University of Southampton

Faculty of Engineering and Physical Sciences

Institute of Sound and Vibration Research

Vehicle-seat-passenger System Dynamics on High-speed Train

by

Jun Wu

Thesis for the degree of Doctor of Philosophy

Nov 2019

University of Southampton

Abstract

Faculty of Engineering and Physical Sciences
Institute of Sound and Vibration Research
Thesis for the degree of Doctor of Philosophy

Vehicle-seat-passenger System Dynamics on High-speed Train

by Jun Wu

As the increase of train speed and the adoption of lightweight technology, the vibration induced by wheel-rail interaction transmitted to the passengers via suspensions, bogies, carbody and seat becomes intensified, which worsens ride comfort. The human-seat system is always ignored in the study of ride comfort. And the existing studies of the biodynamics of human body and the dynamic characteristics of human-seat system are mainly focused on single-axis vibrations, which shows their limitations when applied to typical multi-axis vibration environment of rail vehicles. Further comprehensive research needs to be carried out to advance the understanding under typical multi-axis vibrations and apply to the study of ride comfort of rail vehicles.

Firstly, a vertical train model incorporated with calibrated human-seat systems was developed for studying ride comfort. The relationship between the ride comfort and geometry filter effect of vehicle was analyzed, and the influencing factors of ride comfort were revealed and discussed. In addition, the contribution of different modes of carbody to ride comfort was defined and analyzed.

A field measurement was carried out on a high-speed train for the vibration transmission of the seat, and the data were analyzed with a proposed new multi-input and single-output (MISO) system. The new method has the advantage of evaluating the contribution of inputs and their coherent part to the output independently of the sequences of inputs compared with the original method. It was found three inputs (vertical, lateral and roll accelerations) from the carbody floor could well account for the vertical, lateral or roll vibrations at the seat pan or backrest.

An experimental study of the biodynamics of seated human body exposed to vertical, lateral and roll vibration was carried out. The principal resonance frequencies of the apparent masses generally had a negative correlation with the weighted root-sum-square (r.s.s.) value of the lateral, vertical and roll excitation magnitudes, which was more significant under low r.s.s value or significant only under low r.s.s value. A seated human model exposed to combined vertical, lateral and roll vibration was developed and calibrated by the experimental data. Three modes of the seated human body were observed by modal analysis to be correlated with the resonances in the measured apparent masses. The first mode (1.01 Hz) was found to be associated with the lateral and roll motions of the upper body, the second (2.53 Hz) with lateral motion of the lower body in addition to these motions, and the third mode (5.54 Hz) was dominated by the vertical motion of the whole body.

The experimental study of the dynamics of the train seat with subjects exposed to vertical, lateral and roll vibration was carried out. There was a decrease in the principal resonance frequencies of the seat transmissibilities as the increase of the weighted r.s.s. value of lateral, vertical and roll magntides, which was more significant at low r.s.s. value or significant only at low r.s.s. value. Models of the double-unit train seat, the seat with one and two subjects were developed and calibrated. It was found the primary peak around 5 Hz in the vertical transmissibility on the seat pan arose from a whole-body vertical mode of human body with slightly higher modal frequency. Two modes around 15 and 27 Hz of the seat contributed to the peaks with approximate frequencies in the seat transmissibilities. What is more, human body had a tendency of increasing the modal damping of the seat modes.

Finally, a 3D rigid-flexible coupled track-train-seat-human model was developed with the developed human-seat model. The influence of train speed, carbody damping, suspension parameters and seat position on ride comfort as well as the proportion of different vibration positions and directions in the overall ride comfort index were studied with this model. In addition, the contribution of the rigid and flexible modes of carbody to the ride comfort was also defined and studied. This study gives a useful guide for the design of rail vehicles and the matching of the human-seat system with the vehicle.

Table of Contents

List of Figures

List of Tables

Research Thesis: Declaration of Authorship

Print name:	Jun Wu

Title of thesis:	Vehicle-seat-passenger System Dynamics on High-speed Train

I declare that this thesis and the work presented in it are my own and has been generated by me as the result of my own original research.

I confirm that:

1. This work was done wholly or mainly while in candidature for a research degree at this University;
2. Where any part of this thesis has previously been submitted for a degree or any other qualification at this University or any other institution, this has been clearly stated;
3. Where I have consulted the published work of others, this is always clearly attributed;
4. Where I have quoted from the work of others, the source is always given. With the exception of such quotations, this thesis is entirely my own work;
5. I have acknowledged all main sources of help;
6. Where the thesis is based on work done by myself jointly with others, I have made clear exactly what was done by others and what I have contributed myself;
7. Parts of this work have been published as:

Wu J and Qiu Y. (2017) Ride comfort analysis of high-speed train based on geometry filter effect of carbody bending, Presented on *52nd Human Response to Vibration Conference*, UK.

Wu J and Qiu Y. (2018) Modelling of seated human body exposed to vertical, lateral and roll excitations, Presented on *53rd Human Response to Vibration Conference*, UK.

Wu J and Qiu Y. (2019) Modelling of a train seat with subject exposed to lateral, vertical and roll vibration, Journal of Physics: Conference Series, 1264, 012018. (Presented on *13th International Conference on Recent Advances in Structural Dynamics*, France)

Wu J and Qiu Y. (2019) Analysis of ride comfort of a high-speed train based on a coupled track-train-seat-human model with lateral, vertical and roll vibrations, Presented on *26th IAVSD Symposium on Dynamics of Vehicles on Roads and Tracks*, Sweden.

Wu J and Qiu Y. (2020) The study of seat vibration transmission of a high-speed train based on improved MISO method, *Mechanical System and Signal Processing*, 143. DOI: 10.1016/j.ymssp.2020.106844.

Wu J, Wang M. and Qiu Y. (2020) Approaches to predicting the vertical transmissibility of a suspension seat with a seated subject, *Journal of Vibration and Acoustics*, 142. DOI: 10.1115/1.4046748.

Wu J and Qiu Y. (2019) Modelling of seated human body exposed to vertical, lateral and roll vibrations, submitted to *Journal of Sound and Vibration* (accepted).

Wu J, Qiu Y. (2019) Ride comfort analysis of high-speed train based on a train-seat-human model in the vertical direction, submitted to *Vehicle System Dynamics*.

Signature:		Date:	05/06/2020

Acknowledgements

I would like to express my gratitude to my supervisors Dr. Yi Qiu and Prof. Roberto Lot for their supervision and guidance during my PhD research. It was a pleasant experience to work and do research with them.

Many thanks to Dr. Mingliang Yang and Dr. Haibo Huang from Southwest Jiaotong University for the assistance with the field measurement in Chengdu, and to Mr Peter Russell and Mr Gary Parker for their technical support in the laboratory experiment.

I'm grateful to Prof. Luis Baeza for taking part in my first and second reviews, to Dr. Maryam Ghandchi Tehrani for taking part in the second review, to Dr. Neil Ferguson for being the examiner of the viva voce and giving valuable suggestions for improving my thesis.

I would like to thank University of Southampton for providing a good learning environment for me to focus on my research. Thank all the other members of Human Science Group for spending the most precious years in my life with me.

I would like to thank Prof. Lijun Zhang from Tongji University for recommending me to pursue my PhD in ISVR, which is proved to be a valuable experience.

Finally, I would like to thank my family members for their love, understanding and encouragement. Especially, I want to thank my mother who unfortunately passed away in the third year of my PhD for everything she did for me.

Nomenclature

Variables

A	Cross-sectional area of the carbody
c_{px}, c_{py}, c_{pz}	Damping of primary suspension along x, y and z direction, respectively
c_{pv}, c_{ph}	Damping of fastener in vertical and lateral direction, respectively
c_{sx}, c_{sy}, c_{sz}	Damping of second suspension along x, y and z direction, respectively
$\mathbf{D}_i^{B_j}$	The coordinate of $\mathbf{D}_i$ in the relative coordinate system of B_j
D_k	Flexural rigidity of the plates
E_b	Young's modulus of the carbody
E_r	Elastic modulus of rail
E_s	Elastic modulus of sleeper
f_i^t	i[th] natural bending frequency of the carbody
$\mathcal{F}(*)$	The Fourier transform of *
$\mathbf{f}_{ij}^{\mathbf{C}}$	The force transmitted between B_i and B_j at the point $\mathbf{C}$ (point $\mathbf{C}$ can be left out if there is only one contact or connection point)
g	Acceleration of gravity
GK_r	Torsional stiffness of rail
H	The height of the subject
h_C	Vertical distance between center of gravity of carbody and lateral second suspension
h_k	Thickness of the plates of the multi-plate carbody model

h_T	Vertical distance between center of gravity of bogie and lateral second suspension
h_W	Vertical distance between center of gravity of bogie and lateral primary suspension
I , I_b	Second moment and rotational inertia of the cross-section of carbody, respectively
I_i	The rotational inertia of the human body segment B_i around its x axis $\mathbf{n}_{ix}$
I_{cx} , I_{cy} , I_{cz}	Rotational inertia of carbody about x, y and z axis, respectively
I_{bx} , I_{by} , I_{bz}	Rotational inertia of bogie about x, y and z axis, respectively
I_r	Torsional inertia of rail
I_{ry} , I_{rz}	Second moment of area of the rail about y, z axis, respectively
I_s	Second moment of area of the sleeper about x axis
I_{wx}	Rotational inertia of wheelset about x axis
J_{bg}	Rotational inertia of bogie
k_{bh} , c_{bh}	Stiffness and damping of ballast in the lateral direction, respectively
k_{bv} , c_{bv}	Stiffness and damping of ballast in the vertical direction, respectively
k_{fv} , c_{fv}	Stiffness and damping of subgrade, respectively
k_p , c_p	Stiffness and damping of the primary suspension, respectively
k_s , c_s	Stiffness and damping of the second suspension, respectively
k_{px} , k_{py} , k_{pz}	Stiffness of primary suspension along x, y and z direction, respectively

k_{pv}, k_{ph}	Stiffness of fastener in the vertical and lateral direction, respectively
k_{sx}, k_{sy}, k_{sz}	Stiffness of second suspension along x, y and z direction, respectively
k_w, c_w	Shear stiffness and damping of ballast, respectively
L	Length of the carbody
l_b, l_w	Half the distance between two bogies and between two wheels under one bogie, respectively
l_{hs}	The spacing between two adjacent human-seat systems
l_i	The length of human body segment B_i
$\mathbf{l}_{ij}^{\mathrm{C}}$	The relative displacement between B_j and B_i at the point $\mathbf{C}$ (point $\mathbf{C}$ can be left out if there is only one contact or connection point)
l_r	Calculated length of the rail
L_s	Sleeper spacing
l_s	Sleeper length
m	The total mass of the subject
m_b, m_{bg}, m_w	The mass of the carbody, bogie and wheelset, respectively
m_{ba}	Mass of ballast
m_i	The mass of human body segment B_i
m_r	Mass per unit length of rail
m_s	Mass per unit length of sleeper
$\mathbf{O}_i^O$	The coordinate of $\mathbf{O}_i$ in the absolute coordinate system
ρ_k	Density of the plate of the multi-plate carbody model

ρ_r	Density of rail
$\mathrm{Re}(*)$, $\mathrm{Im}(*)$	The real part and imaginary part of *, respectively
r_0	Nominal wheel radius
s_i	Position of the i[th] seat on the carbody
V	Train speed
μ_k	Poisson ratio of the plates of the multi-plate carbody model
$w(x,t)$	Transverse displacement at the position of x on carbody due to bending at the time of t
w_b , φ_b	Bounce displacement and pitch angle of the carbody, respectively
w_{bgf} , w_{bgr}	Bounce displacement of the front and rear bogies, respectively
w_{wf1} , w_{wf2}	Bounce displacement of the first and second front wheels, respectively
w_{wr1} , w_{wr2}	Bounce displacement of the first and second rear wheels, respectively
$x_{\mathbf{C}_i}^{B_j}$, $y_{\mathbf{C}_i}^{B_j}$, $z_{\mathbf{C}_i}^{B_j}$	The x, y and z coordinate of $\mathbf{C}_i$ in the relative coordinate system of B_j
α	The inclination angle of the backrest relative to the vertical plane
ρ	Density of the carbody
ξ_i	Damping ratio of i[th] bending mode of the carbody
φ_{bgf} , φ_{bgr}	Pitch angle of the front and rear bogies, respectively
ω_i^t	i[th] natural bending circular frequency of the carbody
λ	Wavelength
$\delta(\cdot)$	Dirac delta function

Left superscript

l , r	Symbols defined in the left and right unit of the seat, respectively
Right superscript	
(I)	Ith derivative with respect to the coordinate
Subscript	
b	Carbody
bg	Bogie
f	Front
$i \cdot j$	The part of ith signal not due to jth signal
$i : j$	The part of ith signal due to jth signal
$i \cdot (m!/i)$	$i \cdot m, (m-1), \cdots, (i+1), (i-1)!$
p	Primary suspension
r	Rear
s	Second suspension
w	Wheel
Abbreviation	
DOF	Degree of freedom
FE	Finite element
FRF	Frequency response function
ISVR	Institute of Sound and Vibration Research
MISO	Multi-input and single-output
PSD	Power spectral density
r.m.s.	Root-mean-square
r.s.s.	Root-sum-square

SD	Standard deviation
SISO	Single-input and single-output
VDV	Vibration dose value

Chapter 1 Introduction

1.1 Motivation

Following the emergence of the 'bullet train' in Japan in 1964, the high-speed train industry has been developed for over fifty years. It is during the last few decades that the high-speed train industry has gained rapid development and expansion. Many countries such as Germany, France, Japan and China have built high-speed rails to connect major cities.

Main leading high-speed train companies globally have developed a great many technologies for trains to achieve the required essential functions. Nevertheless, the ride comfort of the train has become the next level of competition. This is especially the case in Europe as comfort and customer experience are viewed as important factors in the transportation industry.

Currently, the operating speed of the high-speed train has been increasing significantly. Lightweight technology is also gradually adopted for carbody in order to save energy. With the increase of train speed and implementation of the lightweight structure, the vibration induced by wheel-rail interaction and other sources is amplified and transmitted to passengers through the suspensions, bogies, carbody, and seats. Undesirable vibration can worsen passenger experiences such as reducing the ride comfort, causing fatigue and other health problems, especially during a long-time train journey. Aside from the dynamics of the train, the biodynamics of the seated human body and the seating dynamics are closely related to the ride comfort, which are always ignored in the relevant studies. In terms of the biodynamic response of seated subject and the dynamic characteristics of the seat with subject, the existing research is mainly focused on single-axis vibrations, showing their limitations when applied to typical multi-axis vibration environment of rail vehicles including high-speed train. To advance understanding in this field and promote ride comfort of rail vehicles, further comprehensive research needs to be carried out with the consideration of the typical multi-axis vibration. Due to lack of relative studies, how to design and develop high-speed trains with human-seat sub-system with a low level of vibration and a high level of ride comfort remains to be a challenging task.

In order to understand the dynamics of the human-seat system and optimize the ride comfort of high-speed trains, the objective biodynamic response of seated human body should be studied in detail from the experimental perspective, based on which suitable mathematical model of seated human body needs to be developed for the prediction of human response to typical vibrations on trains. Also, the seating dynamics characterizing the vibration transmission of the train seat and the

dynamic coupling of the seat with human body needs to be experimentally studied, based on which modelling of the human-seat systems needs to be carried out for the prediction of the vibration transmitted to the human body. Further development of the track-train system model incorporated with the developed model of human-seat system can provide guidance and assist in the design and optimization of the dynamics and ride comfort of the coupled track-train-seat-human system.

1.2 Research objectives

The main objectives of this Ph.D. project are to research into the biodynamics of seated human body and seating dynamics and develop corresponding models under typical multi-axis vibrations on trains and then apply the models to the study of ride comfort. Details are as follows:

- Research into and advance understanding of the biodynamics of seated human body exposed to combined vertical, lateral and roll vibration; research into and advance understanding of the dynamic characteristics of a train seat with subjects exposed to the combined multi-axis vibration.
- Develop and validate mathematical models of seated human body under the combined vibration and find out the association between the resonances in the apparent mass of the human body and modal properties of the human body; develop and validate mathematical models of the train seat and the train seat with subject under the combined vibration to predict the vibration transmitted to passengers seated on the seat, find out the association between the resonances in the seat transmissibility and modal properties of the human body or the seat, and reveal the variation of the modal properties resulting from the coupling between the seat and human body.
- Analytically study the relationship between the geometry filter effect of the vehicle (a phenomenon revealing the dependence of resonant or anti-resonant vibration of carbody modes on the geometrical parameter of the train and the train speed) and ride comfort based on a vertical train-seat-human model;
- Develop a mathematical model of a track-train system incorporated with the developed human-seat model to analyze the ride comfort from the perspective of lateral, vertical and roll vibration; Study the influence of train speed, carbody damping, suspension parameters and seat position, etc on ride comfort based on the model; Investigate the contribution of different modes of carbody to the ride comfort; Compare among different vibration positions and directions at the feet, on the seat-buttock and human-backrest interface; Finally, suggest recommendations aiming at improving the ride dynamics and comfort of high-speed trains.

1.3 Research questions

Based on the literature review, the research questions can be defined as follows:

(1) Based on a train-seat-human model in the vertical direction, how will the geometry filter effect of the vehicle influence the ride comfort? How can the contribution of the rigid modes and flexible modes of carbody to the ride comfort be defined and what is their contribution? What are the most important influencing factors of ride comfort and how do these factors influence the ride comfort? (answered in Chapter 4)

(2) For multi-input and single-output system, how can a new MISO model with partial coherences that are independent of the sequence of inputs be put forward to uniquely evaluate the contribution of one specific conditioned input to the output so as to overcome the limitation of the existing MISO model? When computing the vibration transmission of a human-seat system of a high-speed train in a working environment, how many and which inputs at the seat base should be taken into account in order to sufficiently predict the lateral, vertical and roll accelerations at the seat pan and backrest? What is the difference between field measurement and laboratory measurement? (answered in Section 3.2 and Chapter 5)

(3) What is the effect of magnitudes of single-axis, bi-axis and tri-axis vibration in lateral, vertical and roll directions on the biodynamic response of the seated human body; what is the effect of adding excitations in one or two axes on the apparent mass in another axis? (answered in Chapter 6)

(4) How can a multi-body dynamic model of a seated human body exposed to combined lateral, vertical and roll vibrations be developed based on the measured biodynamics of subjects to be applicable to subjects of different weights and heights and vibrations of different magnitudes? What is the association between the resonances in the apparent mass of the human body and the modal properties of the human body? (answered in Chapter 7)

(5) What are the dynamic characteristics of the train seat and the effect of magnitude of single-axis, bi-axis and tri-axis vibration in lateral, vertical and roll directions on the seat transmissibility of a train seat with a seated subject? What is the effect of adding excitations in one or two axes on the transmissibility in another axis? What is the difference between the seat transmissibilities of a train seat with double units (simplified as ‘double-unit seat’ next) seated with no subject (bare seat), with one subject and with two subjects? (answered in Chapter 8)

(6) How can the double-unit train seat model under exposure to combined lateral, vertical and roll vibrations be developed and how can the coupled double-unit-seat-one-subject model and double-unit-seat-two-subject model be developed on the basis of the developed seated human model and seat model under exposure to combined lateral, vertical and roll vibrations? What is the association between the resonances in the seat transmissibility and the modal properties of the human body or the seat? How do the modal properties change due to the coupling between the seat and human body? (answered in Chapter 9)

(7) How can a 3D rigid-flexible coupled track-train-seat-human model with a flexible 3D carbody that can accurately reflect its bending, breathing and torsional modes and two columns of human-seat systems under excitations of vertical profile, alignment and cross level of the track be developed? What is the influence of train speed, carbody damping, suspension parameters and seat position on ride comfort? What is the proportion of different vibration positions and directions at the feet, human-backrest interface and seat-buttock interface in the overall ride comfort index? What is the contribution of different carbody modes to ride comfort? (answered in Chapter 10)

1.4 Research scope

Chapter 2 reviews and discusses the up-to-date knowledge of relevant research in the biodynamic response of the seated human body to vibrations, seating dynamics, modelling of the seated human body, modelling of the human-seat system as well as ride dynamics and comfort of trains.

Chapter 3 gives an introduction to the research methods that are to be used in the following chapters, including the calculation of the frequency response function, model calibration method, Wilcoxon signed-rank test and linear regression analysis as well as the modal analysis method. Especially, in the method for the calculation of the frequency response function, a new multi-input and single-output (MISO) method is proposed with the new partial coherence functions defined to be independent of the sequence of inputs. (answering research question 2)

Chapter 4 proposes an analytical model of a train-seat-human system in the vertical direction to study the influence of geometry filter effect of the vehicle on the ride comfort and the contribution of rigid modes and flexible modes of carbody to ride comfort. The key influencing factors of ride comfort and their detailed influences are studied. (answering research question 1)

Chapter 5 introduces a field study of vibration transmission of a train seat with passengers on a high-speed train in operation using the proposed new multi-input and single-output method, and studies how many and which inputs at the carbody floor should be taken into account for the

calculation of the acceleration responses on the seat pan and backrest. The advantages and disadvantages of the field and laboratory measurements are also compared. (answering research question 2)

Chapter 6 introduces the experimental study of the biodynamic response of subjects sitting on a rigid seat with backrest, and analyzes the effect of magnitudes of single-axis, bi-axis and tri-axis vibration in lateral, vertical and roll directions on the biodynamic response of seated human body and the effect of adding excitations in one or two axes on the apparent mass in another axis. (answering research question 3)

Chapter 7 introduces the modelling of the seated human body exposed to combined lateral, vertical and roll excitations, and the model calibration using the experimental data from Chapter 6. Modal analysis is conducted with the calibrated human body model to examine the association of the modal properties of the human body with the resonances in apparent masses. (answering research question 4)

Chapter 8 introduces an experimental study in the laboratory about the transmissibility of a double-unit train seat subjected to lateral, vertical and roll excitations. The influence of adding vibrations in other directions on the transmissibility of the train seat with one subject in one direction and the effect of magnitudes of single-axis, bi-axis and tri-axis vibration in lateral, vertical and roll directions on the transmissibility are examined and discussed in detail. The effects of seated subjects on the seat transmissibility are also studied. (answering research question 5)

Chapter 9 introduces the modelling of a double-unit train seat exposed to combined lateral, vertical and roll excitations, and the model calibration with the experimental data from Chapter 8. Double-unit-seat-one-subject and double-unit-seat-two-subject models are developed separately with the use of the human model developed in Chapter 7 and calibrated with the experimental data from Chapter 8. Modal analysis is conducted to find out the association of the modal properties of the seat and human body with the resonances in seat transmissibilities. Furthermore, the variation of the modal properties due to the coupling between the seat and the human body is also examined. (answering research question 6)

Chapter 10 introduces a 3D modelling of the flexible carbody and its validation against the results of a modal test from a published paper. A model of the track-train-seat-human system is developed with the flexible carbody, two bogies, four wheelsets, two flexible tracks supported by several sleepers and ballasts, as well as two columns of double-unit-seat-one-subject models developed in Chapter 9. The ride comfort is evaluated according to ISO 2631-1. The vibration transmission from the alignment, vertical profile and cross level of the track to the lateral, vertical and roll

accelerations at the carbody floor, seat-buttock interface and human-backrest interface is analyzed for different seat positions and train speeds. The influence of the track rigidity on the acceleration PSDs of the carbody floor in the lateral, vertical and roll direction and on the ride comfort is identified. The influence of train speed, carbody damping, suspension parameters and seat position on ride comfort is studied. The contribution of rigid modes, flexible modes of carbody and their coherent part to ride comfort is defined and analyzed. The ride comfort evaluated with the flexible carbody model is compared with that evaluated with a rigid carbody model. In addition, the proportion of different vibration positions and directions in the overall ride comfort index is studied. (answering research question 7)

Chapter 11 provides a summary of the thesis, draws some relevant conclusions, has a discussion and gives recommendations for future work.

1.5 Research flowchart

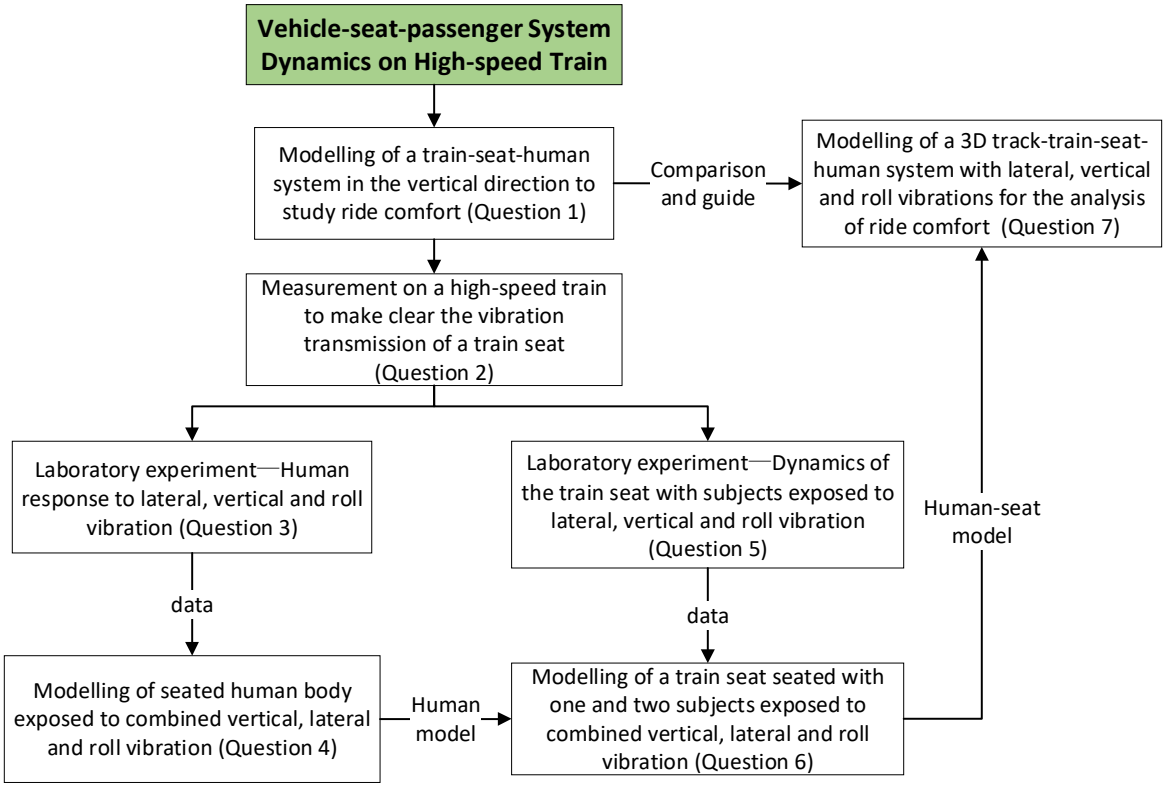

Chapter 2 Literature review

According to the objectives of the research, the literature review was conducted mainly in terms of the biodynamics of the human body, the seating dynamics, the modelling of human body and human-seat system, as well as the dynamics and ride comfort of high-speed train.

2.1 The biodynamic response of seated human body to vibration

The biodynamic response of seated human body exposed to different vibrations has been studied extensively. Objectively, the biodynamic response of the human body is evaluated by apparent mass and driving point impedance, etc. Apparent mass (driving point impedance) of the seated human body is the frequency response function from the acceleration (velocity) to the force measured at the same point, frequently on the human-seat interface. If the acceleration (velocity) and force are in the same direction, the apparent mass (impedance) is called in-line apparent mass (impedance); on the contrary, if they are in two different directions, the apparent mass (impedance) is named cross-axis apparent mass (impedance). However, a comparative study by Wu *et al.* (1999) indicated that the apparent mass was more likely to reveal the inherent damped resonant frequency of the human body than impedance. Using apparent mass to evaluate the biodynamic response of the seated human body is more widely-recognized in related research. So far, the biodynamic response of the seated human body to single-axis excitation (vertical, lateral or fore-and-aft excitation) has been studied extensively. There are also more and more studies working on the biodynamic response of the seated human body to bi-axis and tri-axis translational vibrations.

2.1.1 Apparent mass of the seated human body in the vertical direction

It was generally reported that the vertical apparent mass on the seat pan had a primary peak in the range from 4 to 8 Hz; what is more, some people also exhibited a second peak between 9 and 15 Hz (Fairley and Griffin, 1989; Kitazaki and Griffin, 1997; Qiu and Griffin, 2010). Kitazaki and Griffin (1997) found that the principal resonance about 5 Hz resulted from a whole-body vertical mode—the axial and shear deformation of tissue beneath pelvis vibrating in phase with a vertical visceral mode while the head, spinal column and the pelvis are moving almost rigidly by modal analysis of a finite element model. The second principal resonance corresponded to a rotational mode of the pelvis with contribution from a second visceral mode. There are many factors influencing the apparent mass in the vertical direction, such as vibration magnitude, backrest inclination, posture, inter-subject variability, muscle tension, etc.

The influence of vibration magnitude on apparent mass in the vertical direction was extensively investigated. Commonly, the vibration magnitude was considered to decrease the principal resonance frequency because of the 'softening effect' of the human body (Fig. 2-1), however, there was no consistent conclusion about the influence of vibration magnitude on the modulus of apparent mass at resonance (Mansfield and Griffin, 2000; Matsumoto and Griffin, 2002b; Nawayseh and Griffin, 2003; Huang and Griffin, 2008). Mansfield and Griffin (2000) thought that the resonance frequencies reduced with increasing vibration magnitude was probably caused by a complex combination of factors, including the stiffness of the tissue beneath the ischial tuberosities decreasing with increasing excitation magnitude.

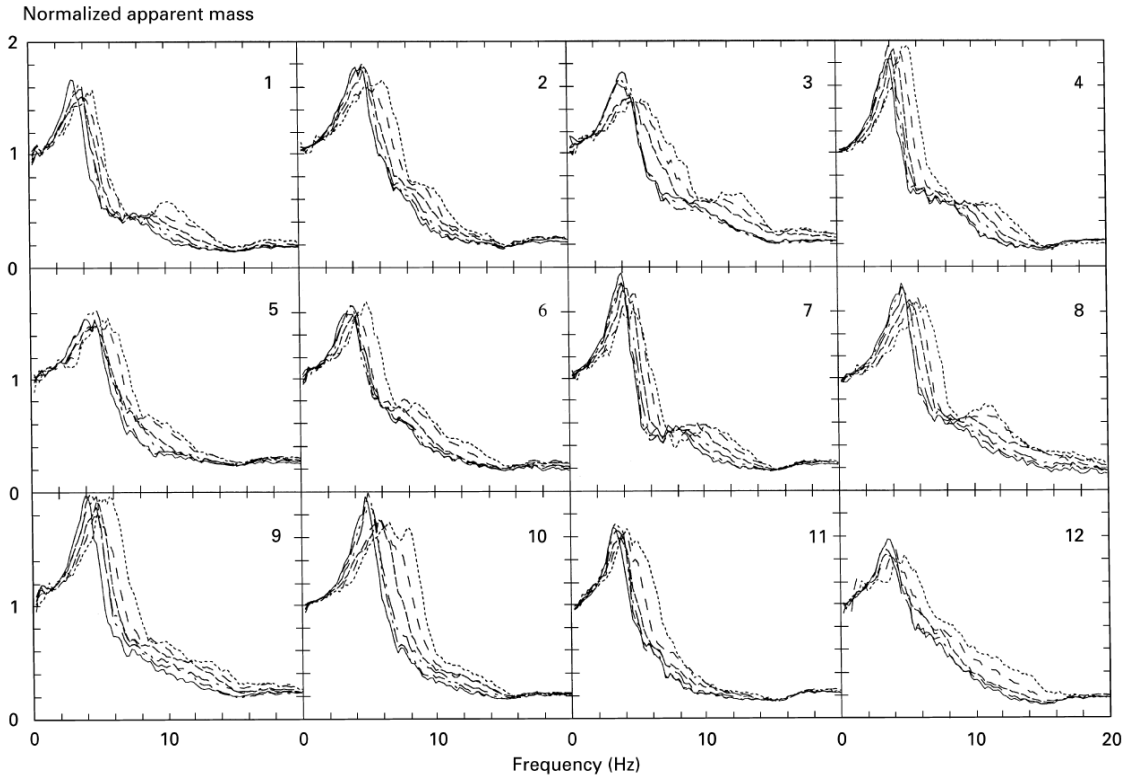

Fig. 2-1 Normalised apparent masses of 12 subjects measured at 0.25 (……), 0.5 (- - -), 1.0(———), 1.5 (- ·- ·-), 2.0 (- -···- -), 2.5 (—) ms^{-2} r.m.s.. Resonance frequencies decrease with increasing vibration magnitude. (Mansfield and Griffin, 2000).

Because apparent mass showed great variability among subjects with different weights, to reduce the variability of apparent mass resulting from subjects' weights, many people studied the normalized apparent mass that could be calculated by the apparent mass divided by the weight supported on the seat. In this way, many studies illustrated much less variability among subjects with different weights for normalized apparent mass than for apparent mass (Fairley and Griffin, 1989; Huang and Griffin, 2006).

The vertical apparent mass on the vertical backrest was seldom measured and very small, with a principal resonance frequency about 5-7 Hz and modulus at resonance varying from 5 to 15 kg across subjects (Fig. 2-2) (Nawayseh and Griffin, 2004). If a vertical backrest is used, the forces at the back arise from the relative motion between the vertical motions of the backrest and upper human body. If an inclined backrest is used, the vertical force is produced by the mass of the human upper body supported on the backrest and the relative motion (Nawayseh and Griffin, 2004).

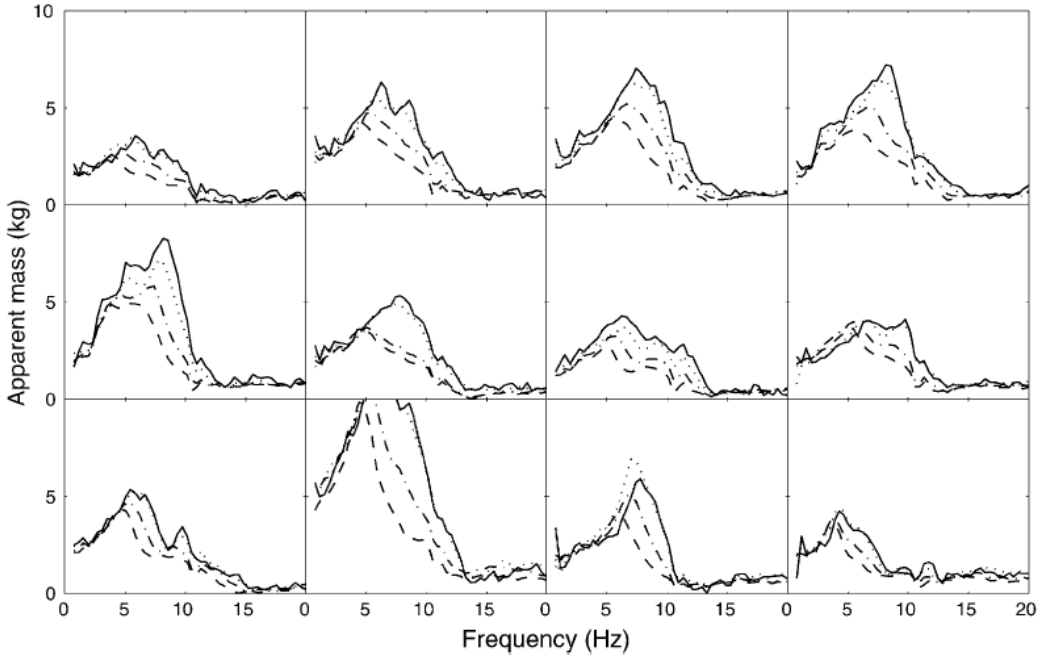

Fig. 2-2 Vertical median apparent masses of 12 subjects measured at the back in the minimum thigh contact posture at four vibration magnitudes. —, 0.125 ms^{-2} r.m.s.; ……, 0.25 ms^{-2} r.m.s.; – .– . –, 0.625 ms^{-2} r.m.s.; – – – –, 1.25 ms^{-2} r.m.s. (Nawayseh and Griffin, 2004).

2.1.2 Apparent mass of the seated human body in the horizontal directions

There is a certain inconsistency in the resonances of the apparent mass on the seat pan in the horizontal direction. Fairley and Griffin (1990) reported the first peak of fore-and-aft apparent mass at 0.7 Hz, and the second one around 2.5 Hz when sitting on a rigid seat without backrest. With backrest contact, only one resonance around 3.5 Hz was clearly visible (Fig. 2-3(a)). However, Nawayseh and Griffin (2005a) showed there were three vibration modes exhibited in the fore-and-aft apparent mass on the seat pan below 10 Hz in all postures (around 1 Hz, 1-3 Hz, and 3-5 Hz, respectively). The three modes varied between subjects and depended on the vibration magnitude. The median modulus and phase of the apparent masses showed nonlinearity in all postures (feet hanging, maximum thigh contact, average thigh contact and minimum thigh contact) (Fig. 2-4). What is more, Hinz *et al.* (2006) reported the first peak around 1 Hz and the second (the maximum

peak) around 3 Hz in the fore-and-aft apparent mass. However, these peaks were not always observed, either at different vibration magnitudes or in all subjects. Several peaks could only be found for some subjects, mainly with the lowest vibration magnitude. Qiu and Griffin (2010) found a primary peak between 2 and 6 Hz, and the peak frequency reduced with increasing fore-and-aft excitation.

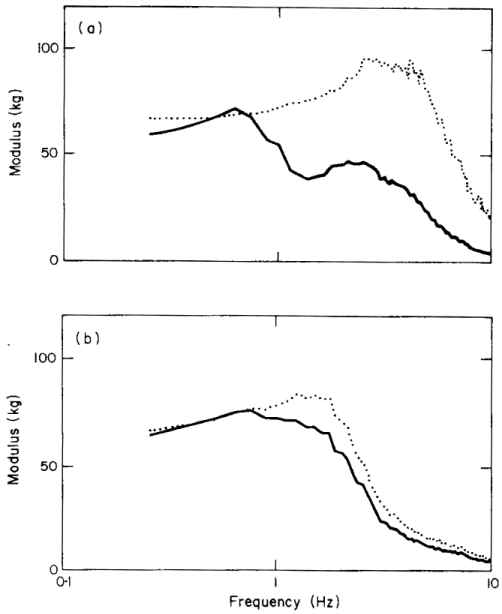

Fig. 2-3 Effect of a backrest on the mean apparent mass of eight people: (a) fore-and-aft; (b) lateral. (⋯, with backrest; —, without backrest) (Fairley and Griffin, 1990).

The fore-and-aft apparent mass on the backrest showed the first peak at less than 2 Hz for most of the subjects, and the second peak clearly present between 3 and 5 Hz, as well as the third peak between 4 and 7 Hz for a few subjects (Fig. 2-5) (Nawayseh and Griffin, 2005b).

In the lateral direction, two or three peaks were found in the lateral apparent mass on the seat pan and the nonlinearity arising from increasing excitation magnitude was clearly exhibited. Fairley and Griffin (1990) registered the first resonance of the apparent mass on the seat pan at about 0.7 Hz with no backrest contact, but the second one was less pronounced, at around 2 Hz for the posture 'without backrest contact'. There appeared to be only one resonance frequency about 1.5 Hz 'with backrest contact' (Fig. 2-3(b)). A reduction of the second resonance frequency in 1.5-3 Hz with increasing vibration magnitude for the lateral apparent mass on the seat pan without backrest contact was observed. Mandapuram *et al.* (2005) found peaks in the 0.7-1.0 Hz and 1.9-2.1 Hz and around 6.4 Hz in the lateral apparent mass at the seat pan with no backrest support. He thought the peak near 0.7 Hz was associated with rocking and swaying of the upper body. With vertical backrest support, low-level excitation yielded two peaks in 0.9-2.1 Hz, which converged to one single peak in 1-1.25 Hz as the increase of excitation level. In addition, a smaller peak in the vicinity

of 6.6 Hz was also observed. Hinz *et al.* (2006) reported a second smaller peak occurred below 1 Hz whose magnitude increased, whereas the modulus of the main peak (around 2 Hz) decreased with increasing vibration magnitude. But the normalized mean peak moduli remained nearly unchanged. The frequency at the normalized main peak values decreased from 2.04 to 1.37 Hz with rising vibration magnitude.

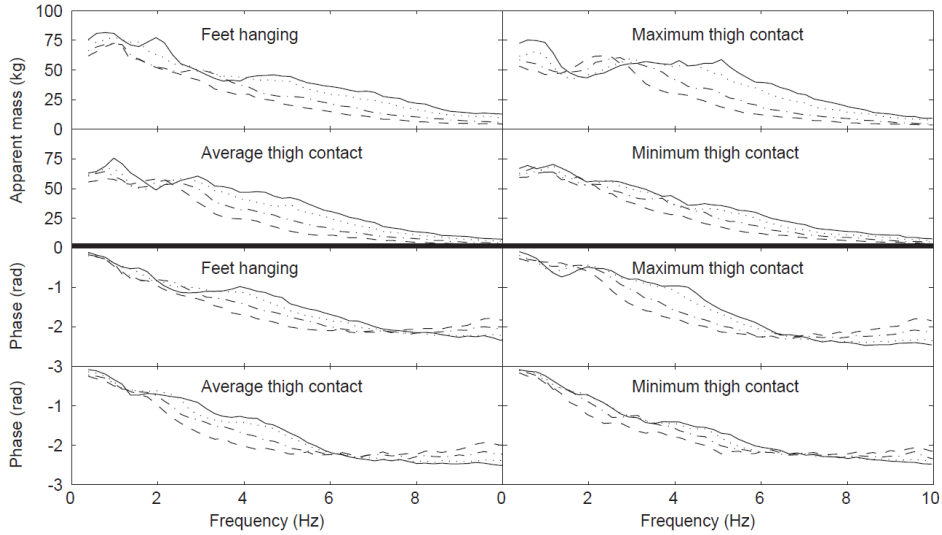

Fig. 2-4 Median fore-and-aft apparent mass and phase angle of 12 subjects at the seat pan: effect of vibration magnitude. —, 0.125ms^{-2} r.m.s.; ·····, 0.25ms^{-2} r.m.s.; – · – · – · –, 0.625ms^{-2} r.m.s.; – – – –, 1.25ms^{-2} r.m.s. (Nawayseh and Griffin, 2005a).

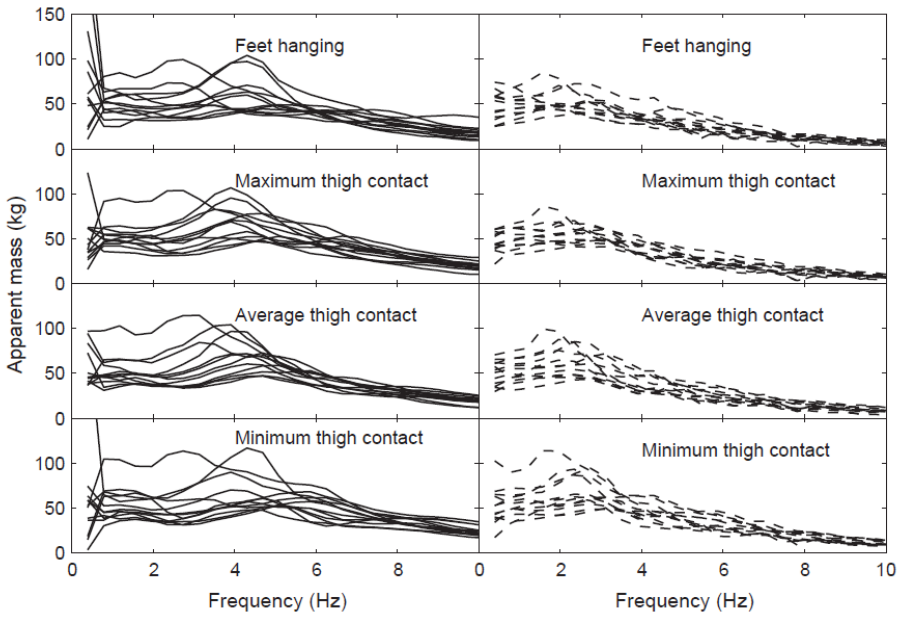

Fig. 2-5 Inter-subject variability in the fore-and-aft apparent mass at the back for each posture at two vibration magnitudes. (—) 0.125 ms^{-2} r.m.s.; and (---) 1.25 ms^{-2} r.m.s. (Nawayseh and Griffin, 2005b).

For the lateral apparent masses on the backrest, they were much smaller than those on the seat pan. The primary peak tended to occur around 1 Hz with backrest support under low-level excitation, which shifted towards a lower frequency that may be below 0.5 Hz as the increase of excitation level. Increasing excitation magnitude reduced the magnitude of apparent mass on the backrest in the entire frequency range (Mandapuram *et al.*, 2005).

2.1.3 Cross-axis apparent mass of the seated human body

Usually, vibration in one direction of the human body can result in the forces and vibrations not only in the same direction but also in other directions, so the cross-axis apparent mass of seated human body cannot be ignored. For the fore-and-aft cross-axis apparent mass during vertical vibration, Nawayseh and Griffin (2003) found the force on the seat pan in the fore-and-aft direction resulting from vertical vibration was high and varied with posture. It showed a principal peak around 5 Hz (Fig. 2-6), which was close to the primary resonance in the vertical inline apparent mass on the seat pan. However, the lateral cross-axis apparent masses on the seat pan were very small for all vibration magnitudes, less than 6 kg (Fig. 2-7) (Nawayseh and Griffin, 2003). With a backrest, Nawayseh and Griffin (2004) found during the vertical vibration, there were not only high vertical inline apparent masses on the seat pan but also high fore-and-aft cross-axis apparent masses on both the seat pan and backrest, however, the cross-axis apparent masses in the lateral direction on the backrest were small. Later on, Nawayseh and Griffin (2005b) also found that considerable vertical cross-axis apparent masses at the seat pan and backrest can be generated by fore-and-aft vibration, however, the lateral cross-axis apparent masses during fore-and-aft vibration were very small (Fig. 2-8).

Telling from these results, the cross-talk of the seated human body between vertical and fore-and-aft directions is great whether on the seat pan or backrest, however, between vertical and lateral directions as well as between fore-and-aft and lateral directions is relatively small because the seated human body is symmetrical about the mid-sagittal plane.

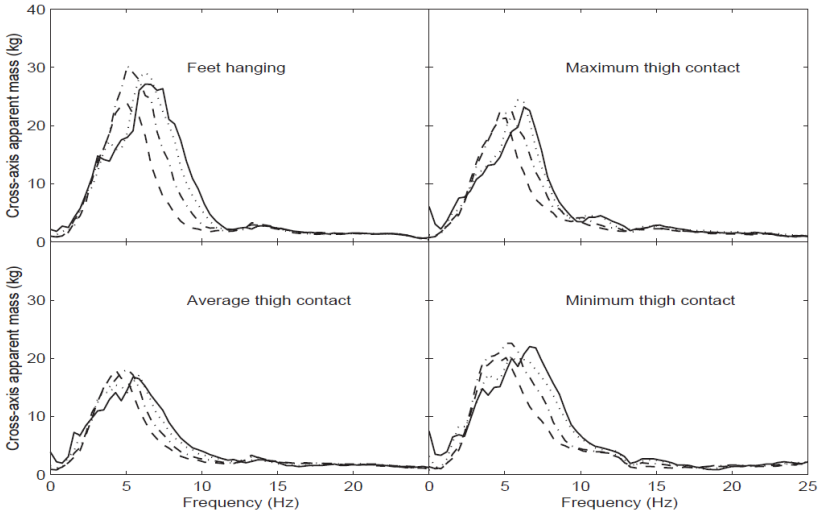

Fig. 2-6 Median cross-axis apparent masses of 12 subjects in the fore-and-aft direction on the seat pan during vertical excitations: effect of vibration magnitudes. —, 0.125 ms^{-2} r.m.s.; ····, 0.25 ms^{-2} r.m.s.; –·–·–, 0.625 ms^{-2} r.m.s.; -----, 1.25 ms^{-2} r.m.s. (Nawayseh and Griffin, 2003)

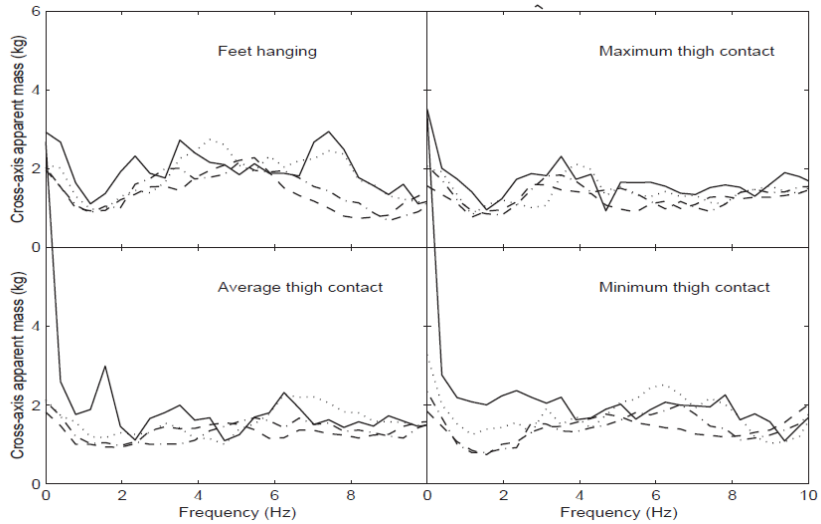

Fig. 2-7 Median cross-axis apparent mass of 12 subjects in the lateral direction on the seat pan during vertical excitations: effect of vibration magnitudes. —, 0.125 ms^{-2} r.m.s.; ····, 0.25 ms^{-2} r.m.s.; –·–·–, 0.625 ms^{-2} r.m.s.; -----, 1.25 ms^{-2} r.m.s. (Nawayseh and Griffin, 2003)

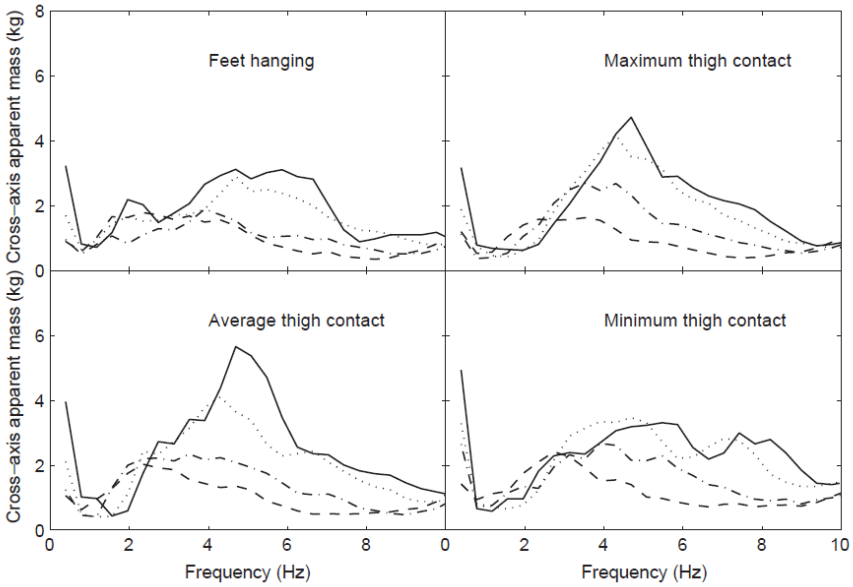

Fig. 2-8 Median lateral cross-axis apparent mass of 12 subjects measured on the seat pan during fore-and-aft excitations: effect of vibration magnitudes. —, 0.125 ms^{-2} r.m.s.; ····, 0.25 ms^{-2} r.m.s.; –·–·–, 0.625 ms^{-2} r.m.s.; -----, 1.25 ms^{-2} r.m.s. (Nawayseh and Griffin, 2005b)

2.1.4 The biodynamic response of the seated human body to multi-axis vibration

Compared with single-axis vibration, there is much less research about the biodynamic response to multi-axis excitations. Because the human body is nonlinear, the biodynamics under multi-axis vibration does not conform to the principle of linear superposition of those under single-axis vibrations. Current research is mainly focused on the biodynamic response of seated subjects to multi-axis translational excitations. The apparent mass curves during vibration exposures with more than one axis showed general similar dependency on the frequency to those apparent masses during single-axis excitation (Hinz *et al.*, 2006; Mansfield and Maeda, 2006). It was extensively reported that the resonance frequency would reduce as the increase of vibration axes and vibration magnitude in every direction (Hinz *et al.*, 2006; Mansfield and Maeda, 2006, 2007; Zheng *et al.*, 2012, 2019).

Hinz *et al.* (2006) investigated the apparent masses of subjects exposed to single-axis and multi-axis random vibration at three magnitudes and reported that the resonance frequencies in the apparent masses reduced with an increase in the number of vibration axes as well as the vibration magnitudes in the fore-and-aft, lateral and vertical directions. Similarly, Mansfield and Maeda (2006) reported that the in-line apparent masses and cross-axis apparent masses of seated subjects exposed to single-axis vibration (fore-and-aft, lateral or vertical) and dual-axis vibration (fore-and-aft and lateral, fore-and-aft and vertical, lateral and vertical) at one magnitude of vibration (0.4 ms^{-}

^{2} r.m.s.) in every direction were close. However, in most cases, the peak frequencies in the in-line apparent masses and the cross-axis apparent masses were slightly lower for the dual-axis vibration than for the single-axis vibration because of a nonlinear effect. And a similar study (Mansfield and Maeda, 2007) also showed that increasing the magnitude of vibration in directions orthogonal to that being measured affected the apparent mass, causing a reduction in the resonance frequency as the total magnitude of vibration evaluated by root-sum-square value increased. Qiu and Griffin (2010) showed that with dual-axis excitation (combined fore-and-aft and vertical vibration), the vibration in one axis affected the apparent mass of the human body measured in the other axis. The resonance frequency in the vertical apparent mass reduced as the magnitude of fore-and-aft excitation increased, and similarly the resonance frequency in the fore-and-aft apparent mass reduced as the magnitude of vertical vibration increased (Fig. 2-9). A similar study by Qiu and Griffin (2012) drew the same conclusion when the effect of backrest was taken into consideration.

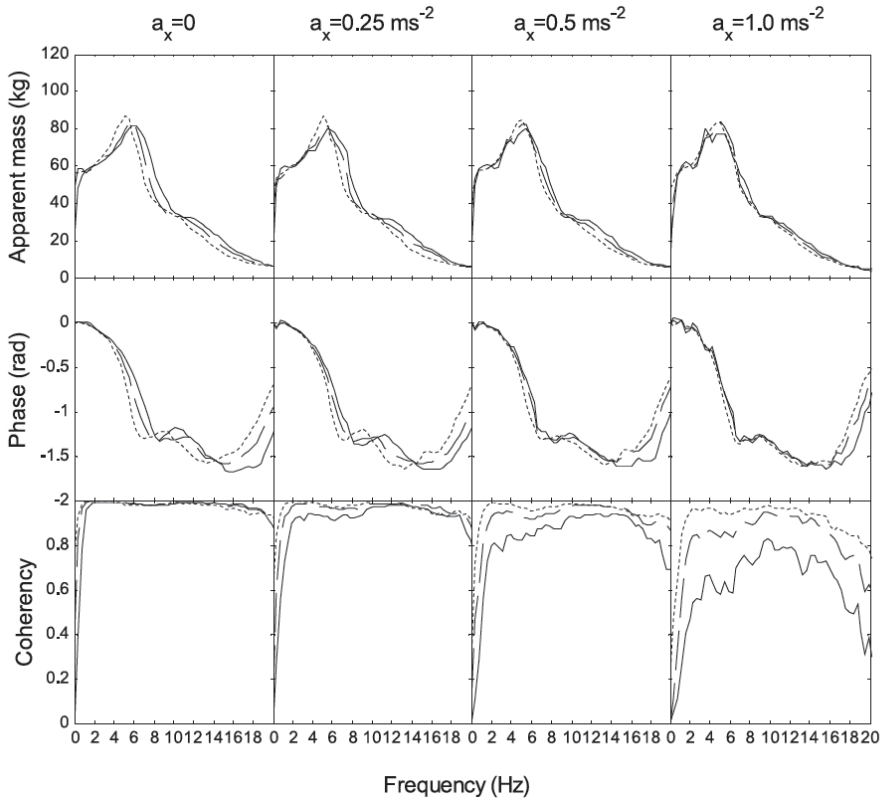

Fig. 2-9 Median in-line apparent mass of 12 subjects in the vertical direction with single-axis and dual-axis excitation. —, a_z=0.25 ms^{-2} r.m.s.; — — —, a_z=0.5 ms^{-2} r.m.s.; - - - -, a_z=1.0 ms^{-2} r.m.s. (Qiu and Griffin, 2010)

Seeing from the available studies, so far there has rarely been research on the biodynamic response of the seated human body to rotational excitations, little about tri-axis excitations, not to mention combined rotational and translational excitations. In addition, the modal shapes of the human body

associated with the resonances in the lateral apparent mass on the seat pan or backrest possibly involving the motions in the mid-coronal plane have rarely been reported.

2.2 Seating dynamics

The seat having the optimum dynamic properties is one which is designed to minimize the unwanted vibration responses of the occupant in the relevant environment. The dynamic efficiency of a seat is mainly determined by three factors: the vibration environment, the dynamics of the seat and the biodynamics of the seated human body. Ideally, the seating dynamics and the carbody dynamics are considered together so that amplification of vibration by the seat is usually designed to occur at a frequency where there is a trough in the spectrum of the carbody vibration.

2.2.1 Measurement of seat transmissibility with seated subject

The seating dynamics is commonly quantified by the seat transmissibility with seated subjects, which is the frequency response function for vibration transmitted from the seat base to the human-seat interfaces. The signals can be obtained by accelerometers at the seat base and the interface between the seat surface and the human body. The SAE pad (also named SIT pad) is suitable for the measurement of the acceleration at the human-seat interface because it does not compress the seat and thereby does not alter its dynamic properties or the posture of the seated occupant.

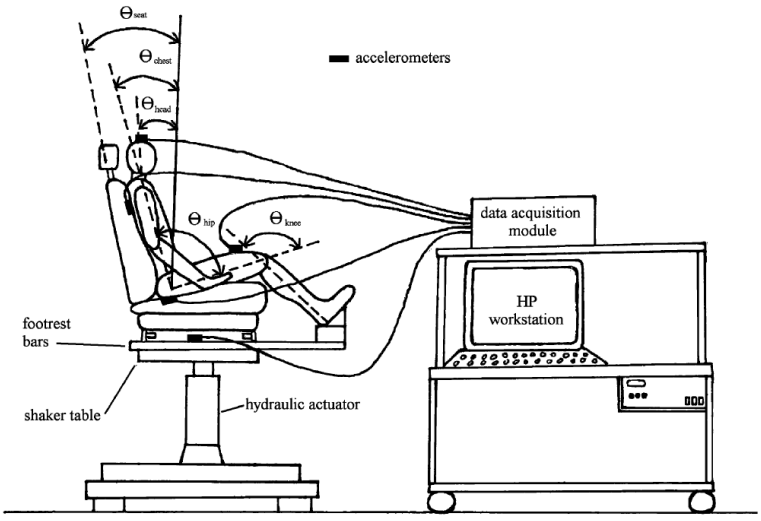

Fig. 2-10 Experimental set-up of the car–seat and mannequin system (Kim *et al.*, 2003a).

A kind of experimental set-up for measuring seat transmissibility is shown in Fig. 2-10, which includes a hydraulic actuator, seat, accelerometers, and data acquisition module (Kim *et al.*, 2003a).

Low-frequency Kistler (Type 8303) and Neuwghent SAA-1000 accelerometers were used to measure the accelerations on the seat base and human-seat interface.

One traditional method to calculate the transmissibility is to divide the cross-spectral density between the i[th] input acceleration $x_i(t)$ at the seat base and the output acceleration $y(t)$ on the human-seat interface, $G_{iy}(f)$, by the auto-spectral density of the i[th] input acceleration $x_i(t)$, $G_{ii}(f)$, as follows:

$$H(f) = \frac{G_{iy}(f)}{G_{ii}(f)} \tag{2-1}$$

where f is the frequency in Hz.

To assist with the interpretation of transfer functions, the coherence function may be determined by

$$\gamma_{iy}^2(f) = \frac{\left|G_{iy}(f)\right|^2}{G_{ii}(f)G_{yy}(f)} \tag{2-2}$$

where $G_{yy}(f)$ is the auto-spectral density of the output $y(t)$.

With the ideal linear system and no noise, the coherence will have its maximum value of unity at all frequencies. Low coherence means the transfer function may only be meaningful at a few isolated frequencies, which may result from noise in the signals, more than one input and nonlinearity of the system, etc.

Another method is to calculate the square root of the ratio of the auto-spectral density of the output to that of the input as

$$H_{iy}(f) = \sqrt{\frac{G_{yy}(f)}{G_{ii}(f)}} \tag{2-3}$$

However, the phase information is missing.

Griffin (1990) compared the two methods finding the differences may arise from several reasons, but they most often occurred at frequencies where there was little vertical vibration in the vehicle (Fig. 2-11). The difference may have little effect on the overall magnitude of vibration occurring on the seat and have little influence on the measurement of seat isolation efficiency.

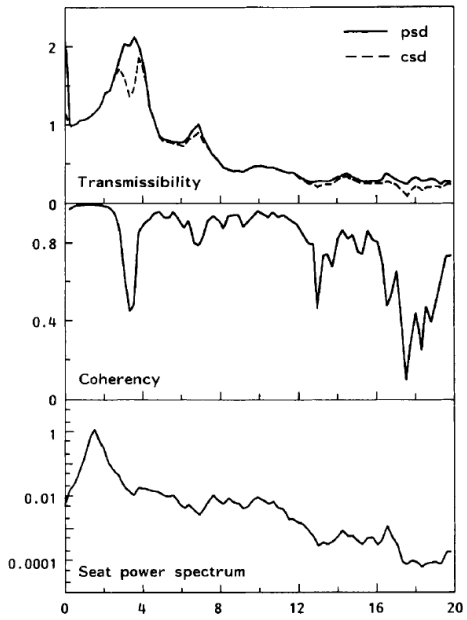

Fig. 2-11 Vertical seat transmissibility determined with cross-spectral density and power spectral density methods: 60 s recording from a 12-seat bus, 0.25 Hz resolution, 58 degrees of freedom (Griffin, 1990).

However, responses in one direction can result from not only vibration in this direction but also vibrations in other directions. In this way, the simple single-input and single-output (SISO) model mentioned above is not always effective when studying vibration transmission in a complex vibration environment because it may always result in a biased estimation of the frequency response function, at least at some frequencies. In order to understand the transmission of seat vibration better, many people measured the vibration at several positions instead of one and tried to develop multi-input and single-output (MISO) models for the vibration transmission of seats (Fig. 2-12). Qiu and Griffin (2004) studied the vertical and horizontal seat transmission on a car using multi-input and single-output models and got a much better coherence function than the single-input and single-output model. Later on, Qiu and Griffin (2005) combined the roll, pitch and yaw motions from the floor with the translational motions to study the seat transmission on a car applying the multi-input and single-output model and obtained even better multiple coherence functions. It can be seen that multi-input and single-output models are more accurate when studying vibration transmission in a complex environment and identifying the number of vibration sources for one specific response.

The partial coherence in the MISO system that is defined as the percentage of the spectrum of the output due to one conditioned input is usually used for evaluating the contribution of one specific input to the output. However, the existing theory introduced in Bendat and Piersol (2010) defined the partial coherence that is dependent on the sequence of the inputs, which will not give unique

results when evaluating the contribution of the inputs. Therefore, a new definition of the partial coherences that are independent of the sequence of inputs is waiting to be put forward.

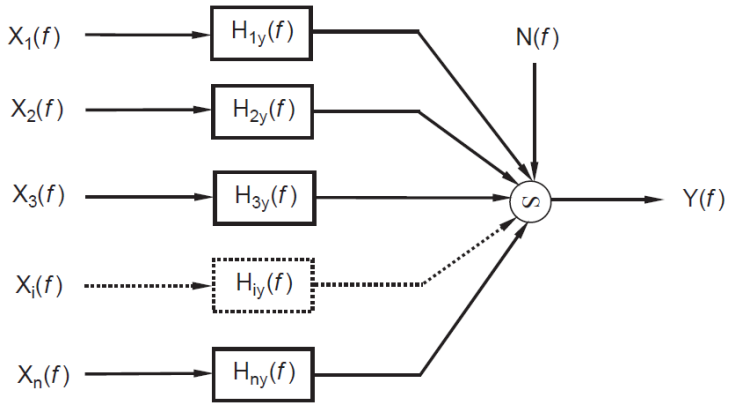

Fig. 2-12 Multi-input and single-output model for original inputs (Qiu and Griffin, 2005)

2.2.2 Seat evaluation methods

Many alternative methods of quantifying dynamic seat comfort have been proposed. A satisfactory general method must take into account the vehicle spectrum, the seat response and the occupant response at all frequencies where there is significant vibration (Griffin, 1990).

One approach is to calculate the seat effective amplitude transmissibility (SEAT). If a seat with low crest factor motions is assessed by measuring the vibration on the seat surface and at the base of the seat, respectively, either in the laboratory or in the field, the SEAT value is given by

$$\mathrm{SEAT}\% = \left[\frac{\int G_{ss}(f)W_i^2(f)\mathrm{d}f}{\int G_{ff}(f)W_i^2(f)\mathrm{d}f}\right]^{\frac{1}{2}} \times 100 \tag{2-4}$$

where $G_{ss}(f)$ and $G_{ff}(f)$ are auto-spectral densities of the accelerations on the seat and floor, respectively, and $W_i(f)$ is the frequency weighting function for the human response to vibration on the seat (Griffin, 1990).

If the motions on either the floor or the seat have a high crest factor, the SEAT value should be obtained using vibration dose values (VDV):

$$\mathrm{SEAT}\% = \frac{\mathrm{VDV\ on\ the\ seat}}{\mathrm{VDV\ on\ the\ floor}} \times 100 \tag{2-5}$$

The physical meaning of the SEAT value is the ratio of the frequency-weighted comfort experienced on the seat to that if the seat is rigid. Thus, a SEAT value of 100% indicates there is no overall

improvement or degradation in vibration discomfort produced by the seat. A SEAT value greater than 100% indicates the discomfort has been increased by the seat, and vice versa.

2.2.3 Seat transmissibility in the vertical direction

Because the human body is a complex dynamic system, the transmissibility of a seat with a seated person shows a great discrepancy with the counterpart with a rigid mass of the same weight (Griffin, 1990). The seat transmissibility is usually measured with a seated subject, and the seat and human body form a coupled dynamic system, so the seat transmissibility depends on the biodynamics of the human body. For conventional seats, the seat transmissibility on the seat pan usually exhibited a primary peak in 4-6 Hz (Toward and Griffin, 2011); sometimes, there would be a second resonance around 10 Hz (Corbridge *et al.*, 1989; Tufano and Griffin, 2013). Seat transmissibility is affected by the excitation magnitude. Generally, the principal resonance frequency would decrease with the increase of vibration magnitude (Fairley and Griffin, 1986; Corbridge *et al.*, 1989; Toward and Griffin, 2011; Tufano and Griffin, 2013). Some people also reported a decreased peak magnitude as the vibration magnitude at the seat base increased (Corbridge *et al.*, 1989; Toward and Griffin, 2011; Tufano and Griffin, 2013).

Fairley and Griffin (1986) showed that the resonance frequency decreased consistently with increasing vibration magnitude (Fig. 2-13). Corbridge *et al.* (1989) found both the resonance frequency of the seat transmissibility and peak magnitude reduced when the random excitation magnitude increased from 0.3 to 0.6 m/s^2 r.m.s.. Similarly, Toward and Griffin (2011) also concluded that there was a decrease of resonance frequency in the seat transmissibility with the increase of vibration magnitude. What is more, Tufano and Griffin (2013) showed with increasing magnitudes of vibration, the resonance frequency of the transmissibility of all three foams reduced significantly ($p<0.05$, Wilcoxon). Similarly, the modulus of the transmissibility at resonance decreased with the increase of vibration magnitude ($p<0.05$, Wilcoxon) (Fig. 2-14).

Seat transmissibility can also be influenced by seat material (Corbridge *et al.*, 1989; Ebe, 1998), subject age, weight and body mass index (Corbridge *et al.*, 1989; Toward and Griffin, 2011) (Fig. 2-15), backrest inclination (Fairley, 1986; Corbridge *et al.*, 1989), leg position (Fairley, 1986), etc. Corbridge *et al.* (1989) showed that the seat/backrest angle from 115° to 105° had little effect on the measured transmissibility. There was an increase in the seat resonance frequency and in the seat transmissibility at resonance when subjects made contact with a reclined backrest, this was because changes in backrest contact and backrest inclination not only changed the posture of the seated occupant and the dynamic response of the person but also altered the mechanical

properties of the seat by changing the contact area and the compression of the seat material (Toward and Griffin, 2011).

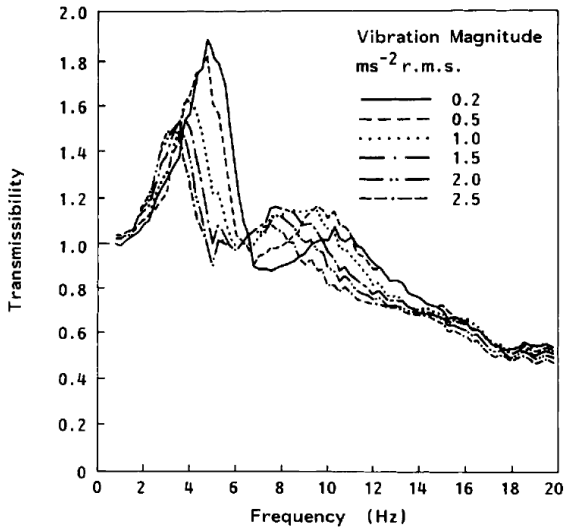

Fig. 2-13 Mean vertical transmissibility of a seat measured with eight subjects at six different magnitudes of random vibration: 0.2, 0.5, 1.0, 1.5, 2.0 and 2.5 ms^{-2} r.m.s.. (Fairley and Griffin, 1986)

The decreasing resonance frequency as the increase of excitation magnitude mainly results from the nonlinearity of both the seat and human body, so there can be significant nonlinearity in the coupled human-seat system (Fairley and Griffin, 1986; Tufano and Griffin, 2013). It was reported that the major contribution to the nonlinearity in the vertical seat transmissibility was the nonlinearity in the human body, with only a minor contribution from the nonlinearity of the seat foam (Griffin, 1990; Tufano and Griffin, 2013).

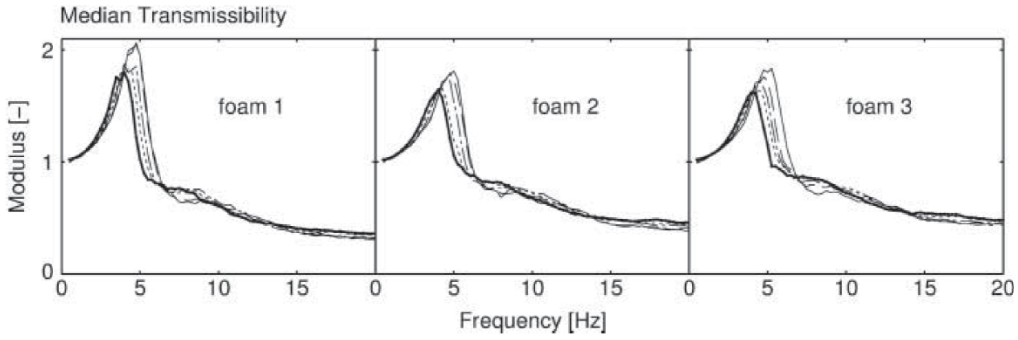

Fig. 2-14 Effect of acceleration magnitude on foam transmissibility (medians of 15 subjects): —0.25, – – 0.4, –·– 0.63, - - - - - 1,—1.6ms^{-2} r.m.s.. (Tufano and Griffin, 2013)

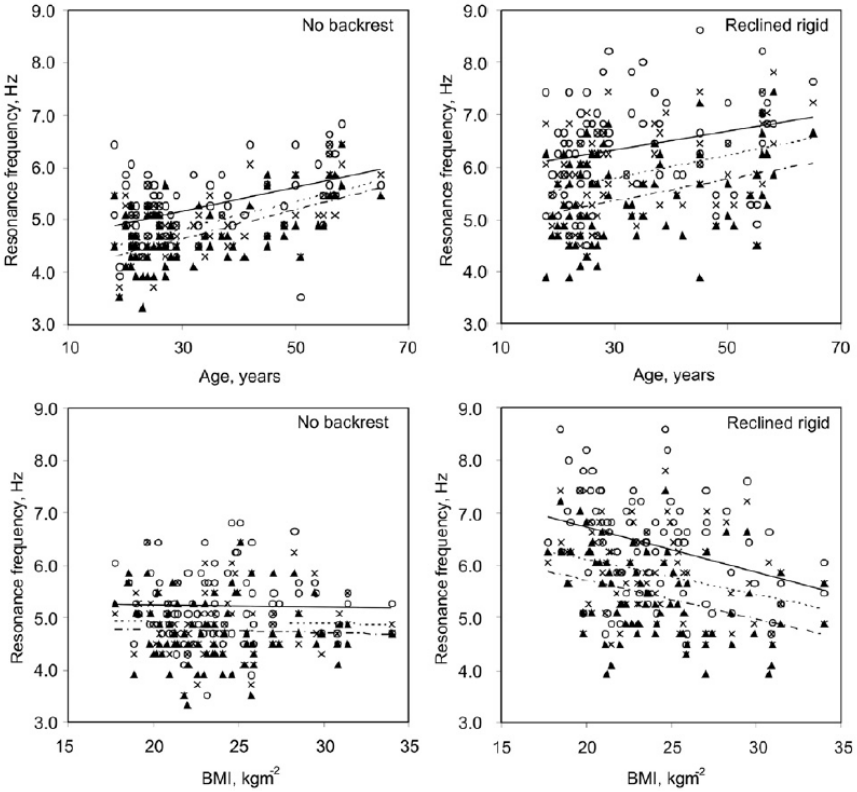

Fig. 2-15 Effect of age and body mass index (BMI) on the resonance frequency of 80 adults at three magnitudes of vertical vibration excitation (no backrest and reclined rigid backrest): 0.5 ms^{-2} rms (○), 1.0 (×) and 1.5 ms^{-2} rms (▲). Bivariate regression trend lines are also shown: 0.5 (—), 1 (·····), and 1.5 ms^{-2} rms (·—·—·—). (Toward and Griffin, 2011)

There have been few studies of the vertical transmissibility on the backrest. Zhang *et al.* (2015b) reported a primary resonance frequency similar to that on the seat pan (at about 4 Hz), but with a modulus at resonance much less than that on the seat pan. The resonance frequency decreased as the increasing thickness of foam at the seat pan, but was not influenced by the thickness of foam at the backrest. Gong and Griffin (2018) showed a primary peak around 25 Hz in the vertical transmissibility on the backrest with no obvious peak around 4 Hz, which was possibly because the peak around 4 Hz with small modulus was covered up by the primary peak around 25 Hz.

2.2.4 Seat transmissibility in the horizontal directions

According to BSI (1987), the fore-and-aft motion at the backrest is one of the three most dominant inputs. There are fewer studies of seat transmissibility in the fore-and-aft direction than in the vertical direction. Qiu and Griffin (2003) showed that in the car the fore-and-aft vibration at the seat pan and the backrest depended on not only the fore-and-aft vibration of the floor but also the vertical vibration of the floor. What's more, the fore-and-aft transmissibilities of the seat from the

base to both the backrest and the seat pan exhibited three resonance frequencies in the ranges 4–5, 25–30 and 45–50 Hz (Fig. 2-16). For the transmissibility to the backrest, the primary peak decreased with little change of frequency with increasing vibration magnitude. And both the peak and resonance frequency reduced with increasing vibration magnitude for the second resonance. The difference is that for the transmissibility to the seat pan, the first and second resonance frequencies decreased with increasing vibration magnitude, and the first peak magnitude reduced, however, the second one rose as the increasing vibration magnitude.

Jalil and Griffin (2007a) studied the effect of backrest inclination, seat pan inclination, and measurement location on the fore-and-aft transmissibility of backrests; for all these cases, a primary resonance was reported in 4-5 Hz. In the same year, Jalil and Griffin (2007b) studied the fore-and-aft vibration transmitted from the floor to a backrest varying with height above the seat surface, and demonstrated that the backrest transmissibilities were nonlinear at all measurement locations on the backrest, that is, both the resonance frequencies and transmissibilities at resonance decreased with the increase of vibration magnitude. Zhang *et al.* (2016) studied the fore-and-aft transmissibility of a car seat from the seat base to surfaces on the seat pan cushion, the backrest cushion and the headrest, as well as to the seat frame at these three locations. The transmissibilities with 12 human subjects to all the six locations showed a principal resonance around 4 Hz, and the resonance frequency decreased as the increasing vibration magnitude. It was concluded the nonlinearity of the seat transmissibility with human subjects may be explained by both the nonlinear biodynamics of the human body and the nonlinear dynamics of the seat itself.

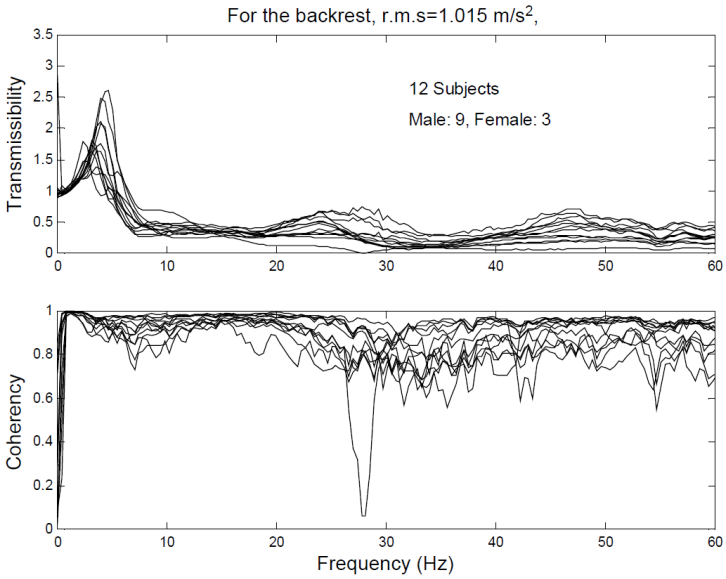

Fig. 2-16 Transmissibility and coherency of the backrest in the fore-and-aft direction (0.39 Hz resolution, 96 degrees of freedom), random vibration input with acceleration r.m.s. value=1.015 ms^{-2}, laboratory simulation. (Qiu and Griffin, 2003)

To date, there have been rarely studies of the seat transmissibility in the lateral direction. Ittianuwat *et al.* (2014) measured the lateral seat transmissibility from the seat base to 19 locations on the seat pan surface, backrest surface and seat frame, and all of them showed obvious peaks around 17 Hz, which was related to a lateral seat mode with a modal frequency of about 17 Hz. Gong and Griffin (2018) found a resonance around 25 Hz in the lateral transmissibility of a train seat with one seated subject on both the seat pan and backrest. The resonances in the lateral transmissibility on the seat pan and backrest possibly arise from a lateral seat mode, since the human body will not add new resonances in the lateral transmissibility above 10 Hz (Lo *et al.*, 2013).

Before being applied to a vehicle, the seat is required to undergo standardized laboratory test and the transmissibility of the seat needs to be measured with different seated subjects to be proved suitable for sale, which is usually costly, time-consuming and inefficient for the understanding and improvement of the dynamic performance of the seat, sometimes even constrained by the maximum vibration magnitude the human body can tolerate. The test also requires the use of vibrators and transducers, which are not always available. However, these problems can be avoided if the transmissibility of the seat with a seated person can be predicted without exposing subjects to vibration.

Many people put forward methods to predict the transmissibility of the seat with the seated subject. One approach is to replace the subjects with dummies of similar dynamic characteristics, however, manufacturing such a dummy is a challenging task. Another method was based on developing human-seat combined model and calibrating the parameters of the human body by apparent mass and the seat by transmissibility or impedance (Wei and Griffin, 1998b; Qiu, 2012). The advantage of mathematical models is that it can not only reflect the dynamic characteristics of the human body and seat very well, but also enhance the understanding of the dynamic performance of the human-seat coupled system. The modelling of human body and human-seat systems will be introduced in detail in the following section. On the other hand, some people made predictions without the modelling of the seat or human body. Fairley and Griffin (1983) predicted the transmissibility of a seat with a seated subject using the apparent mass of the subject and mechanical impedance of the seat without directly modelling the human body and the seat, but the prediction was not very ideal. After taking the apparent mass of the legs into consideration, the predicted magnitude of the transmissibility became much better in the frequency range from 0 to 10 Hz (Fairley, 1990).

2.2.5 Seat transmissibility under multi-axis vibration

To date, there have rarely been studies of the seat transmissibility under multi-axis vibration. To the best of author's knowledge, the only study under multi-axis vibration was reported by Gong and Griffin (2018), where the transmissibilities of a train seat with one seated subject under single-axis vibrations in three translational directions were compared with those under tri-axis vibrations in these directions. It was concluded that there were small differences in seat transmissibilities in three translational directions obtained using single-axis and tri-axis vibrations.

There is almost no existing research on what the effect of vibration magnitude on the seat transmissibility with seated subjects under multi-axis translational excitations or combined translational and rotational excitations is and how the excitation in one axis influences the transmissibility of the seat with subjects in other directions. Compared with the dynamic characteristics of the car seat, there are much fewer studies of the train seat, which has quite a different structure from the car seat.

2.3 Modelling of seated human body and human-seat system

2.3.1 Modelling of seated human body

Different human models to study the biodynamic responses to whole-body vibration have been proposed for different purposes. Generally, the models can be categorized into three types: lumped parameter models, multi-body dynamic models, and finite element models.

2.3.1.1 Lumped parameter models

When simulating the dynamic response of the human body to vibration, the lumped parameter models are widely used because it's easy to develop and calculate. In these models, the human body is usually simplified as several point masses for translational vibration which are interconnected by springs and dampers. Some models also include rotational masses to investigate the rotational motion. Typical models are reported by Wei and Griffin (1998a), Matsumoto and Griffin (2001), Stein *et al.* (2007), Stein *et al.* (2009) and Nawayseh and Griffin (2009), etc.

Wei and Griffin (1998a) put forward two single-degree-of-freedom models and two two-degree-of-freedom models, and single-degree-of-freedom and two-degree-of-freedom models with rigid support structures are proved to be better because of a better fit to the phase (Fig. 2-17). It was also found the two-degree-of-freedom model with rigid support fit better to the phase of the apparent mass at frequencies greater than about 8 Hz and the modulus of the apparent mass at

principal resonance around 5 Hz. But no matter how well the model provided fit to the experimental apparent masses, this did not represent the movement of the human body was the same as the optimized two-degree-of-freedom model.

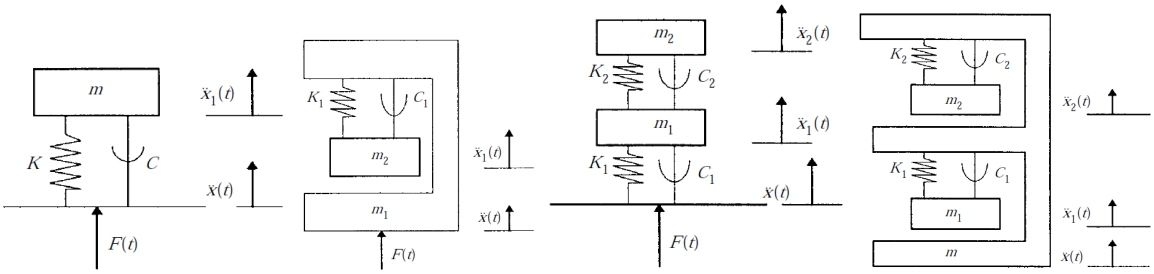

(a) (b) (c) (d)

Fig. 2-17 Different human models exposed to vertical excitation (a) Single degree-of-freedom model; (b) Single degree-of-freedom model with rigid support; (c) Two-degree-of-freedom model; (d) Two-degree-of-freedom model with rigid support (Wei and Griffin, 1998a).

Matsumoto and Griffin (2001) developed simple lumped parameter models with rotational degrees-of-freedom and calibrated the model using previously obtained experimental data (Fig. 2-18). It was found by modal analysis that the resonance of the apparent mass at about 5 Hz may result from a vibration mode— vertical motion of the pelvis and legs and pitch motion of the pelvis, along with the vertical motion of the upper body above the pelvis, bending motion of the spine and vertical motion of the viscera. The models appeared to provide reasonable dynamic responses of the seated human body exposed to vertical excitation.

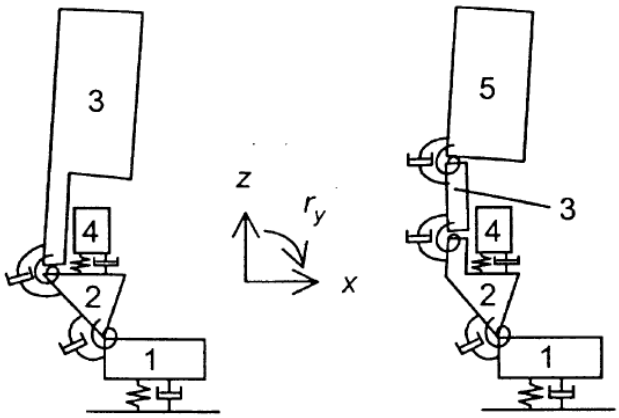

(a) Model 1 (b) Model 2

Fig. 2-18 Two alternative lumped parameter models of seated human body exposed to vertical seat vibration. (Matsumoto and Griffin, 2001)

Nawayseh and Griffin (2009) defined a model that could predict the vertical apparent mass as well as the fore-and-aft cross-axis apparent mass of the seated human body during vertical excitation.

Twelve model parameters with vertical, fore-and-aft and rotational degrees of freedom were optimized using the measured vertical apparent mass and the measured fore-and-aft cross-axis apparent mass of the body (Fig. 2-19). The model showed the seated human body exhibited fore-and-aft motion on a seat pan when only exposed to vertical excitation and the vertical motion of the body resulted in the primary resonance frequency of the apparent mass.

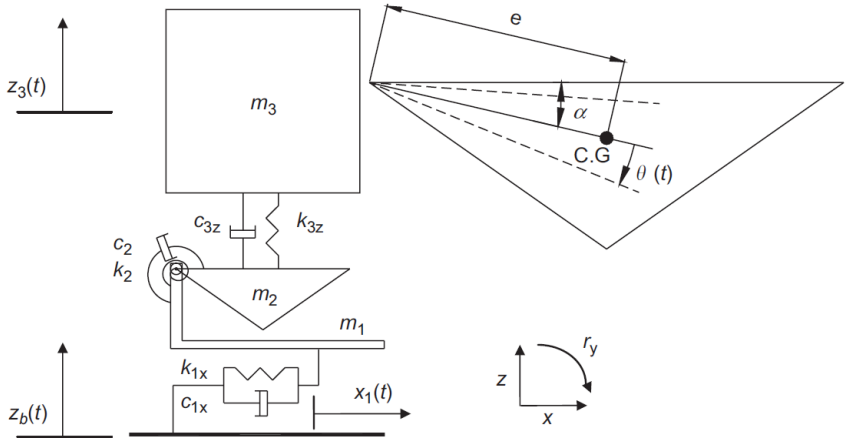

Fig. 2-19 Lumped parameter model for the seated human body exposed to vertical vibration. (Nawayseh and Griffin, 2009)

It is obvious that the lumped parameter model is probably one of the most popular analytical methods for the study of the biodynamic responses of a seated body. This kind of model is simple and easy to implement, but it usually cannot have proper representativeness of the anatomy of the human body.

2.3.1.2 Multi-body dynamic models

Multi-body dynamic models are usually made up of several rigid bodies interconnected by translational and rotational springs and dampers, and each of the rigid bodies has several degrees of freedom, having a good representation of the body dimensions and relative positions. The multi-body dynamic model of the human body can be more anatomically representative than lumped parameter model and less computationally expensive than FE model. Typical multi-body human body models are reported by Liang and Chiang (2008), Kim *et al*. (2011), Zheng *et al.* (2011) and Desai *et al*. (2018), etc.

Liang and Chiang (2008) developed a multi-body model of a seated human body exposed to vertical vibrations (Fig. 2-20). The model was calibrated and analyzed in terms of seat-to-head transmissibility and apparent mass by experimental data from published literature. On the basis of the analytical study and the experimental validation, the proposed fourteen-degrees-of-freedom model was found to be fitted to the test results in different automotive sitting environments well,

therefore, was recommended for studying the biodynamic responses of a seated human body exposed to vertical vibrations in various automotive postures.

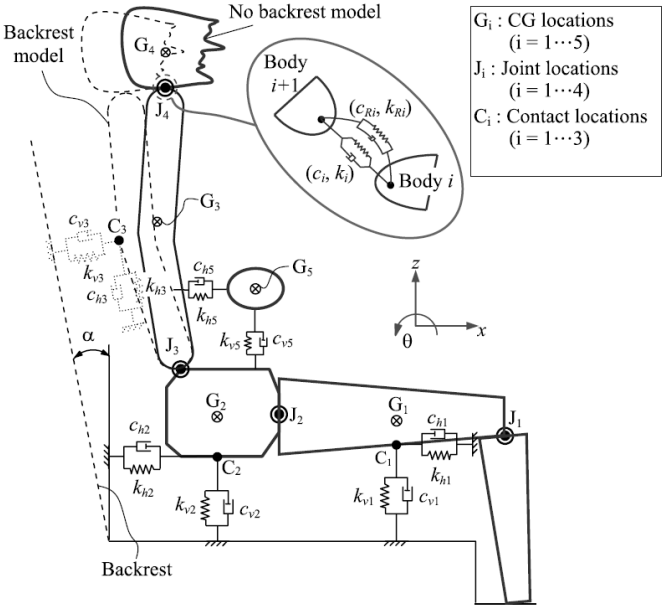

Fig. 2-20 The multi-body model of a seated human body exposed to vertical vibrations (Liang and Chiang, 2008).

The multi-body model is a compromise between the lumped parameter model and finite element model, owning part of their advantages. Generally, the existing multi-body models usually are two-dimensional models, having some rigid parts that can only move or rotate in the mid-sagittal plane with in-plane excitations (vertical, fore-and-aft or pitch excitations). Because the human body is symmetrical about this plane, the development of such models is relatively straightforward. However, these models cannot be applicable to out-of-plane excitations or reflect the motion out of this plane, namely, lateral, roll or yaw motions. A more complex vibration environment may involve not only in-plane vibrations but also out-of-plane ones, where these models are not applicable. Thus, models that are suitable for studying the biodynamics of seated human body exposed to both in-plane and out-of-plane vibrations are still not available and need to be developed.

2.3.1.3 Finite element models

FE model is usually accurately anatomically depicted with detailed skeleton structure and muscle in regions of interest such as the spine, back, pelvis and thigh. This type of model can be developed to predict not only body motion but also internal forces contributing to injury. Typical finite element models can be found in Kitazaki and Griffin (1997), Pankoke *et al.* (1998) and Liu *et al.* (2015), etc.

Kitazaki and Griffin (1997) developed a two-dimensional model using beam, spring, and mass elements to model the spine, viscera, head, pelvis and buttocks tissue in the mid-sagittal plane. The FE model was validated by comparing the calculated mode shapes with those measured in the laboratory (Fig. 2-21). Seven modes below 10 Hz were found for a normal body posture, the mode shapes of which matched well with those obtained from the experiment (Kitazaki and Griffin, 1998). The model could be used to identify the body deformation in the mid-sagittal plane and the effect of posture change on the principal resonance, etc.

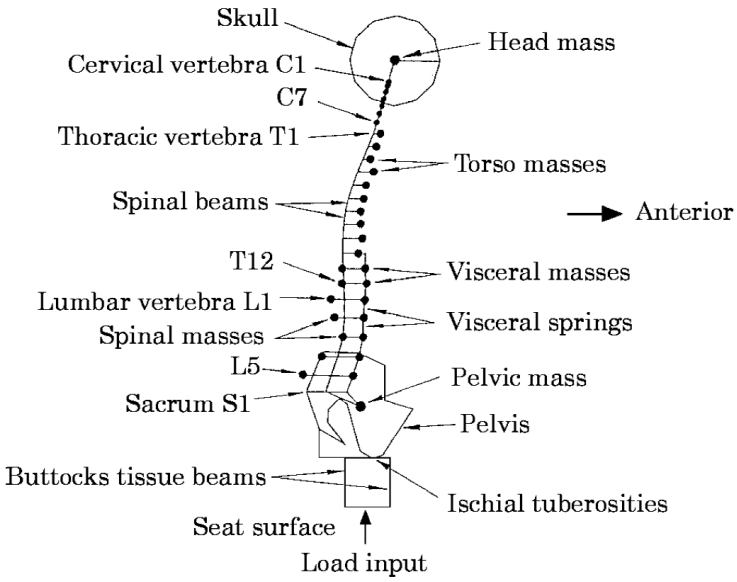

Fig. 2-21 The two-dimensional biomechanical model in the normal posture (Kitazaki and Griffin, 1997).

Pankoke *et al.* (1998) presented a two-dimensional dynamic FE model of sitting man, which could be used for calculating the internal forces that were difficult to be measured in experiments. The whole model incorporated the upper torso with neck, head and arms as well as the lower lumbar spine (L3-L5) with pelvis and legs (Fig. 2-22). All the parts in this model were represented as rigid bodies that were connected by linear stiffness, with their geometry and inertial properties determined by human anatomy. The model could be used as a tool for predicting compressive forces and shear forces in the lumbar vertebral disks for three different postures under arbitrary vertical excitation. Another advantage of this model is it allows adjustment of body height and mass to the values of the subject whose internal forces are to be studied.

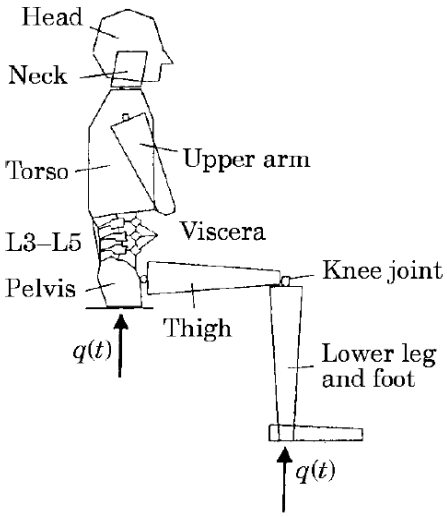

Fig. 2-22 The complete FE model exposed to vertical excitation (Pankoke *et al.*, 1998).

Liu *et al.* (2015) developed a linear FE model with mainly five body segments (torso, pelvis, femurs, buttock, and thighs, etc) interconnected by stiffness and damping. This model can reflect the vertical in-line apparent mass and fore-and-aft cross-axis apparent mass during exposure to vertical excitation well (Fig. 2-23). Furthermore, it could also be developed to analyze the dynamic pressure distribution between the human body and seat pan.

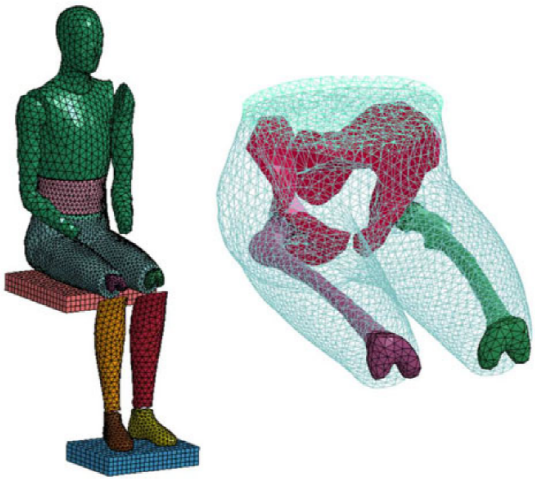

Fig. 2-23 FE model of the seated human body: (left) the complete model; (right) the pelvis-thigh segment (Liu *et al.*, 2015).

However, the FE model, being complex to be applied in dynamic simulations and inefficient to compute, also requires knowledge of the mechanical properties of a seated human body and measurements of dynamic response data to do the calibration. The calibration of an FE model is more difficult and time-consuming than a lumped parameter model or a multi-body dynamic model. The existing human model usually only applies to one specific subject or subjects with the same

body mass and height. A parameterization model that can easily accommodate to subjects with different weights and heights is usually difficult to develop.

2.3.2 Modelling of the human-seat system

Some seat or human-seat system models have been developed for the study of seating dynamics and human-seat interaction. Similar to seated human models, the models can also be divided into three types: lumped parameter models, multi-body dynamic models, and finite element models.

2.3.2.1 Lumped parameter models

Lumped parameter human-seat models are very common, typical models are reported by Qiu and Griffin (2011), Qiu (2012), Wei and Griffin (1998b), etc.

Qiu and Griffin (2011) put forward a combined human body–seat system model for fore-and-aft vibration by calibrating the human body parameters by driving point apparent mass, and then calibrating the seat parameters by median backrest transmissibility separately (Fig. 2-24). The model was capable of predicting the backrest transmissibility with different subjects with fixed parameters of the seat model and predicting the backrest transmissibility for different seats after fixing the human body parameters.

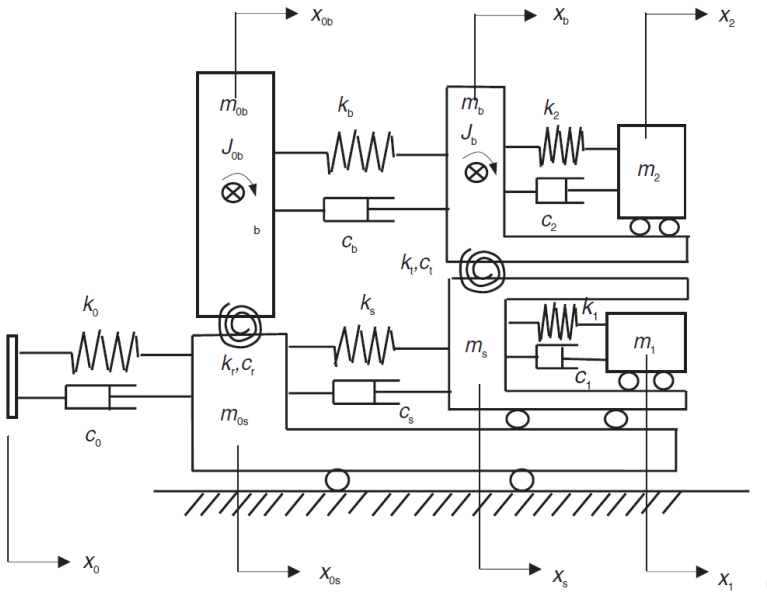

Fig. 2-24 Combined human body-seat model for fore-and-aft vibration (Qiu and Griffin, 2011).

2.3.2.2 Multi-body dynamic models

Many people developed multi-body human-seat dynamic models, including Cho and Yoon (2001), Ippili *et al.* (2008) and Kim *et al.* (2003a), etc.

Cho and Yoon (2001) developed a biomechanical model of a human-seat system with backrest for evaluating the ride quality (Fig. 2-25). This 9 DOF model included the z-axis motion of the hip and the x-axis motion of back that can be used for the evaluation of ride quality. What's more, the 9 DOF model showed a good match for transmissibility at both the first 4.2 Hz mode and second 7.7 Hz mode, which was proved to work better than some simple lumped parameter models. This model showed its advantage over lumped parameter models when it came to the description of human and seat motions.

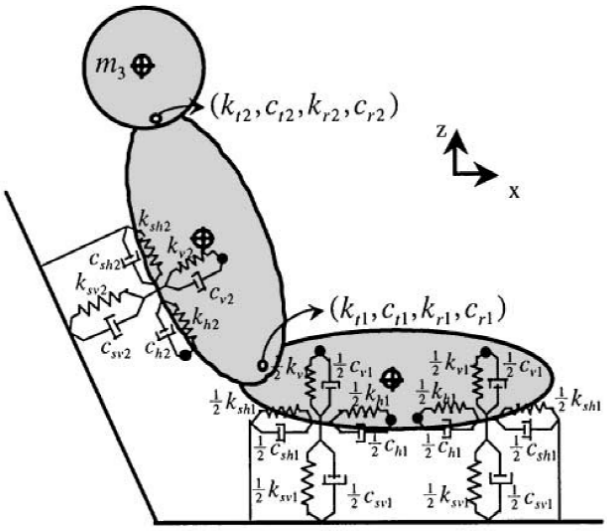

Fig. 2-25 Nine DOF biomechanical model (Cho and Yoon, 2001).

Kim *et al.* (2003a) demonstrated a simplified two-dimensional modelling approach for occupied car seats with geometric nonlinearity and nonlinear torsional dampers at joints (Fig. 2-26). The model was capable of simulating the system response for a given vertical excitation. The mannequin-seat system was broken down into subsystems to determine baseline model parameters by experiment. After that, the model was linearized under the assumption of small deflection, which allowed a detailed parameter study of the effects of changing model parameters on the natural frequencies and the mode shapes. Good agreement between experiment and simulation was obtained in terms of resonance frequencies and deflection shapes at resonance after adjusting the baseline model parameters according to the parameter study.

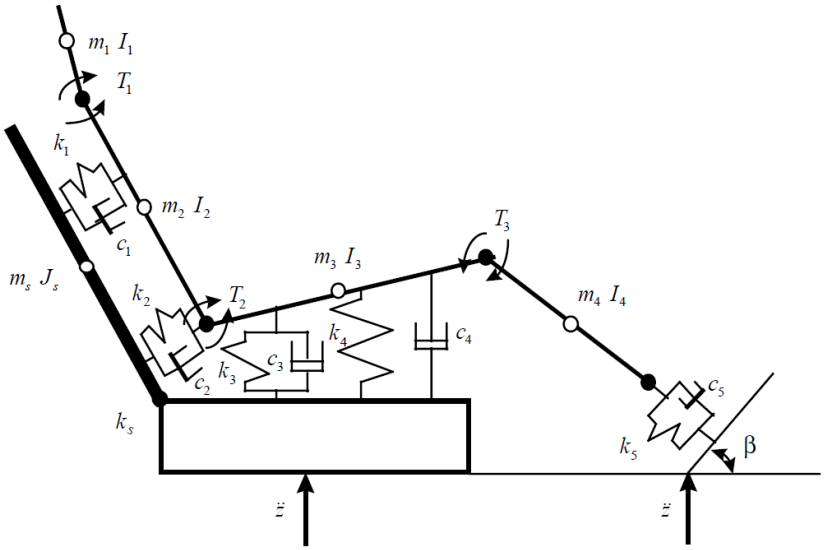

Fig. 2-26 Seven-degree-of-freedom model of the car seat and mannequin system (Kim *et al.*, 2003a).

2.3.2.3 Finite element models

The human-seat models developed by means of finite element software for different purposes are also commonly reported, including Siefert *et al.* (2008), Grujicic *et al.* (2009), Zhang *et al.* (2015a), etc.

Grujicic *et al.* (2009) developed detailed finite element models of a prototypical car seat with a seated subject, which could be used for the study of human-seat interactions and the seating comfort. A skeletal model containing 16 bone assemblies and 15 joints was combined with 'skin' model of the human to obtain a realistic human model (Fig. 2-27). The difficulty of developing this model was to model the materials of different parts of the seat and the human body. The models were validated by comparing the computational results related to the pressure distribution on the human-seat interface with the experimental studies obtained in the relevant literature. The advantage of this detailed finite element model is that it can be used for the investigation of human-seat interactions, which seems almost impossible for lumped parameter models and multi-body models.

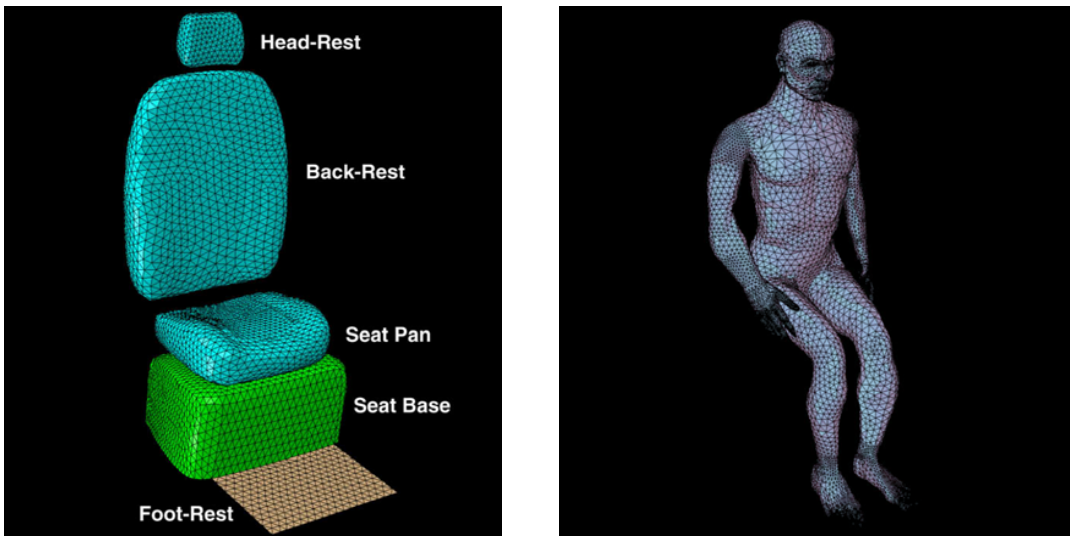

(a) (b)

Fig. 2-27 (a) Finite element model for the car seat (b) Finite element model for the muscular portion of the seated human (Grujicic *et al.*, 2009).

Detailed FE models can reflect not only the motion of the human body and seat, but also the dynamic contact force and pressure at any contact area, so the advantages of them are obvious. However, when it comes to solely reflecting the motion of the human body and seat, a multi-body model is more suitable due to its simplicity and easy calculation, etc.

Generally speaking, all three kinds of human-seat models have similar benefits and drawbacks to the seated human models. After taking into account the aim of our research, we can choose the most suitable models for our study. However, almost all the models are developed in the mid-sagittal plane of the human body or the symmetrical plane of the seat, which is only suitable for in-plane excitation. There are no existing models that are applicable to combined in-plane and out-of-plane excitations, so the dynamic motion of the human body and the seat exposed to combined in-plane and out-of-plane excitations cannot be reflected by these models. What is more, the modelling of the seat is generally limited to car seats, almost no models for multi-unit train seats that have quite different structures from the car seats can be found in the available literature.

2.4 Dynamics and ride comfort of high-speed train

2.4.1 The structure of high-speed train

Nearly all rail vehicles used in passenger transportation have a similar design principle, which is shown in Fig. 2-28. Generally, the carbody rests on two bogies each containing two wheelsets. The wheelset is comprised of two wheels connected by an axle rigidly. The spring and damper elements

connecting the wheelset bearings and the bogie frame as well as the bogie frame and the carbody are called the primary suspension and the second suspension, respectively. One function of the suspension system is to reduce the vibration induced by the track irregularities transmitted to the carbody so as to improve ride comfort. The yaw motion of the carbody is usually prevented by the yaw dampers. Seats are connected with the carbody to provide seating support for passengers, whose dynamics also plays an essential role in ride comfort. Aside from the dynamics of the train, the proper design of seats is also of great importance to passengers' ride comfort as discussed above.

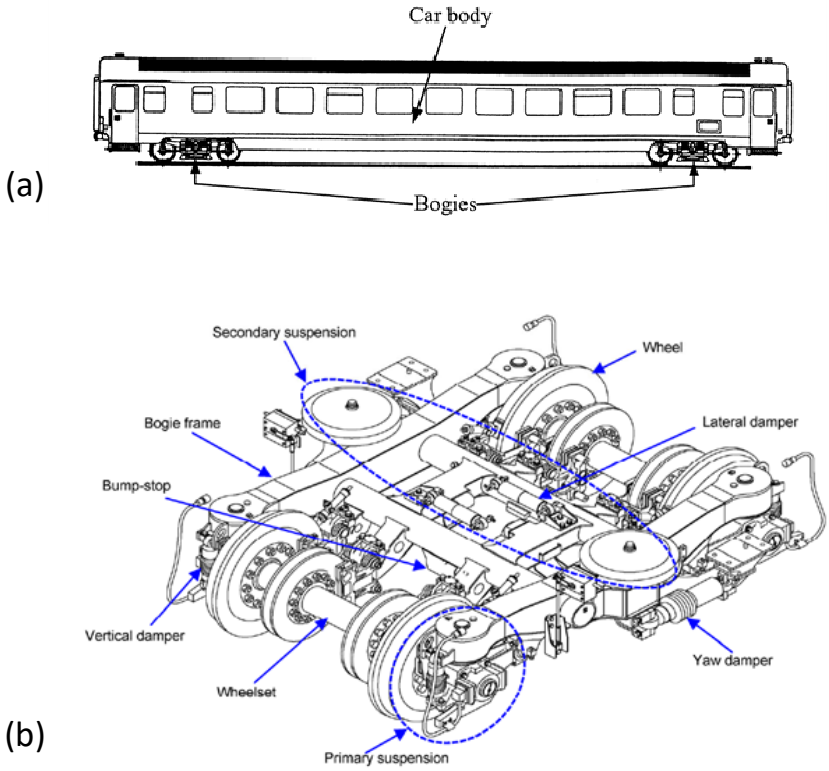

Fig. 2-28 Components of high-speed trains (a) side view of a high-speed train (Popp *et al.*, 1999) (b) bogie of a Chinese high-speed train (Ling *et al.*, 2014).

2.4.2 Track geometry

Track geometry is essentially the variation of lateral and vertical track position in relation to the longitudinal position. Track geometry is defined in terms of four irregularities consisting of gage, cross level, alignment and vertical profile (Garg and Dukkipati, 1984). Gage is defined as the horizontal distance between two rails. Cross level is the difference between the elevation of two rails. Alignment is the average of the lateral positions of two rails (often referred to as the centre line). Vertical profile is the average elevation of the two rails (Fig. 2-29).

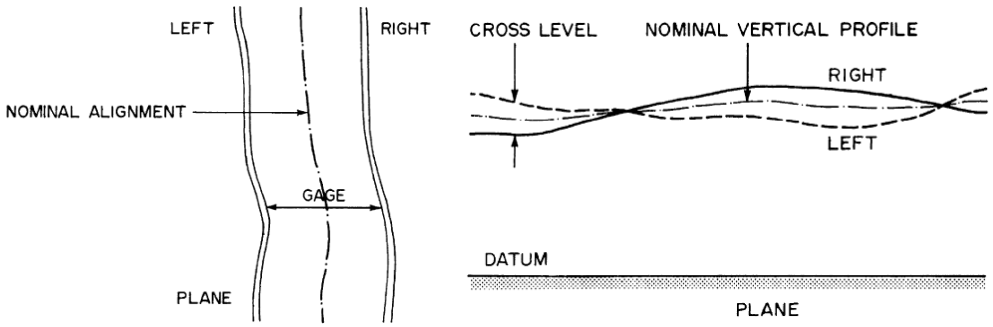

(a) (b)

Fig. 2-29 Definitions of track irregularities (a) gage and alignment; (b) cross level and vertical profile (Garg and Dukkipati, 1984).

Alignment and cross level are often the major causes of lateral and roll vibrations in rail vehicles, whereas vertical profile may have little influence on lateral vehicle dynamics, however, is usually considered as a reason for vertical vibration.

A description of the track geometry usually can be given by the power spectral density (PSD) of the measured track irregularity in the spatial domain. Different countries have different track spectrums. For example, America has 6 levels of track spectrums, Germany has two levels of track spectrums. The expressions of the track spectrums are listed in Table 2-1.

Table 2-1 Track spectrums for America and Germany (Lei, 2015)

Countries	America	Germany
Vertical profile	$S_v(\Omega)=\dfrac{kA_v\Omega_c^{\,2}}{\Omega^2(\Omega^2+\Omega_c^{\,2})}$ $(\mathrm{cm}^2/\mathrm{rad}/\mathrm{m})$	$S_v(\Omega)=\dfrac{A_v\Omega_c^{\,2}}{(\Omega^2+\Omega_r^{\,2})(\Omega^2+\Omega_c^{\,2})}$ $(\mathrm{m}^2/\mathrm{rad}/\mathrm{m})$
Alignment	$S_a(\Omega)=\dfrac{kA_a\Omega_c^{\,2}}{\Omega^2(\Omega^2+\Omega_c^{\,2})}$ $(\mathrm{cm}^2/\mathrm{rad}/\mathrm{m})$	$S_a(\Omega)=\dfrac{A_a\Omega_c^{\,2}}{(\Omega^2+\Omega_r^{\,2})(\Omega^2+\Omega_c^{\,2})}$ $(\mathrm{m}^2/\mathrm{rad}/\mathrm{m})$
Cross level	$S_c(\Omega)=\dfrac{4kA_v\Omega_c^{\,2}}{(\Omega^2+\Omega_c^{\,2})(\Omega^2+\Omega_s^{\,2})}$ $(\mathrm{cm}^2/\mathrm{rad}/\mathrm{m})$	$S_c(\Omega)=\dfrac{A_v\Omega_c^{\,2}\Omega^2/b^2}{(\Omega^2+\Omega_r^{\,2})(\Omega^2+\Omega_c^{\,2})(\Omega^2+\Omega_s^{\,2})}$ $(\mathrm{m}^2/\mathrm{rad}/\mathrm{m})$

Note that Ω is the spatial frequency, Ω_c, Ω_r and Ω_s are the cut-off frequencies, A_v, A_a, k and b are constants.

The direct measurement of the track geometry is usually difficult and time-consuming. Usually, for dynamic simulations in the frequency domain, the PSDs of track geometry can be used directly. On the other hand, for nonlinear models the simulation in the time domain is necessary, random track geometry can be generated from spatial PSD expressions. For PSD expression $\Phi(\Omega)$, the following method can be applied:

(a) To assume a constant speed V and derive the temporal power spectrum by the relationship $\psi(\omega) = \Phi(\Omega)\frac{1}{V}$, where V is the speed, $\psi(\omega)$ is the temporal power spectrum and ω (rad/s) is the angular frequency, $\Phi(\Omega)$ is the spatial PSD and Ω (rad/m) is the angular spatial frequency. The relationship between ω and Ω is $\omega = V\Omega$.

(b) For a signal with a duration of T, divide the frequency range of the desired signal using a frequency resolution of $\Delta f = \frac{1}{T}$, convert the PSD into amplitude $\sqrt{2\Delta f \cdot \psi(f)}$ at every frequency and give each amplitude a random phase $\phi(f)$ that is uniformly distributed between 0 and 2π, then the signal in the frequency domain can be constructed as $\sqrt{2\Delta f \cdot \psi(f)}e^{j\phi(f)}$, where $j = \sqrt{-1}$.

(c) Finally, apply the inverse Fourier transform to obtain the track geometry in the time domain.

This method is very powerful, convenient and suitable for very complex, even piecewise PSD definitions as long as the expression of the PSD is known.

However, using PSD to express track geometry is a limited tool. Firstly, the PSD is defined losing its phase information, so using the PSDs to generate the time-domain signal is not unique, every time the results in the time domain can be totally different because of the random phase at every frequency. Secondly, the PSD is an averaging power spectral density defined at every frequency instead of an exact value, and the variance of the magnitudes at every frequency is missing.

2.4.3 Ride comfort evaluation index

The human's feeling of vibration is dependent on frequency, in order to take this into account, different frequency weighting curves need to be applied. The weighting curves are dependent on position, direction and evaluation index applied.

Three widely-used evaluation indexes are rms-method defined in ISO 2631-1 (ISO, 1997), comfort index according to UIC 513 (Railways, 1994), and Sperling index (Garg and Dukkipati, 1984). ISO 2631-1 suggests individually calculating the root-mean-square (r.m.s.) values for the accelerations at different positions and directions from 0.5 to 80 Hz after weighting, and calculating their root-sum-square value after multiplying by the corresponding multiplying factors. In a simplified method of UIC 513, only fore-and-aft, lateral and vertical accelerations on the floor are used for the evaluation. However, in a full method, vertical acceleration on the floor, lateral and vertical accelerations on the human-seat pan interface as well as fore-and-aft acceleration on the human-backrest interface are used. Sperling index recommends evaluating the ride index Wz value

separately in vertical and lateral directions. It should be noted that one index cannot be transformed into another easily without a complete analysis, and a relevant study regarding the correlation among these indexes has been carried out by Kim *et al.* (2003b).

2.4.4 Vehicle system dynamics

Ride comfort of rail vehicles, which is affected by many factors such as vibration, noise, smell, temperature, visual stimuli, interface pressure between occupants and seat (Park *et al.*, 2014), humidity and seat design, is becoming as important as safety and speed in evaluating the characteristics of rail vehicles. Among these influencing factors, vibration is generally considered to be an important factor that influences ride comfort, especially in railway engineering (Suzuki, 1998). The vibration of the rail vehicles is affected not only by the vehicle structure, such as carbody, suspension and bogies, but also by the track geometry, such as cross level and vertical profile, etc. The ride comfort problem involves not only the study of the dynamics of the train but also the biodynamics of passengers and the seating dynamics. The passenger sensation is dependent on the frequency of vibration, therefore, the objective vibration needs to be weighted by different frequency weighting curves to transform into the one perceived by subjects.

2.4.4.1 Experimental study

An experimental study was conducted by Kim *et al.* (2009) on HSR350x, measuring accelerations at the carbody, the bogie and the wheelset in the vertical and lateral directions. The results showed due to the attenuation effect of the two suspensions, the r.m.s. acceleration at the wheelset was the greatest, and then at the bogie, the r.m.s. acceleration at the carbody was the smallest almost at every train speed (Fig. 2-30). Furthermore, the accelerations at the carbody, the bogie and the wheelset generally increased with the increase of the speed (Fig. 2-30), which was consistent with Zhai *et al.* (2013).

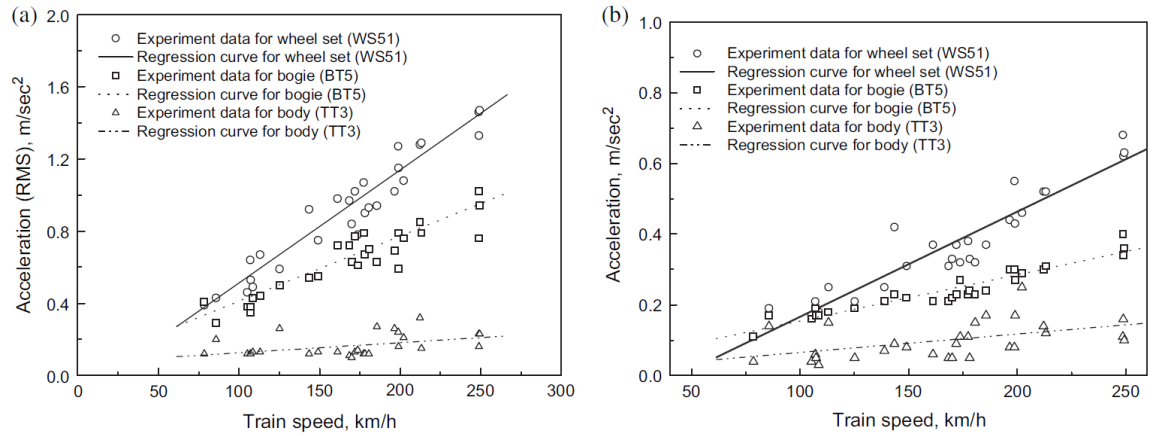

Fig. 2-30 Acceleration (r.m.s.) for the wheelset, the bogie and the carbody versus train speed (a) vertical direction and (b) lateral direction (Kim *et al.*, 2009).

An experimental study by Zhai *et al.* (2015a) also reported a decrease in vibration from the wheel-rail interface, axle box, bogie frame to the carbody in both the vertical and lateral directions. The vibration attenuated to 1/3-1/5 from axle box to bogie frame, while attenuated to 1/10 level from the bogie frame to the carbody. The dominant frequencies of the vibration of the carbody arose from the natural frequency of the suspension system, the natural frequency of the carbody elastic vibration and the forced vibration induced by wheel perimeter in both the vertical and lateral directions.

Konowrocki and Bajer (2008) investigated the vibration on the curve of the track and the straight segments and found the magnitudes of vibration were higher on the curved track than straight one in both the transverse and vertical directions, which may result from the lateral slip in rail/wheel contact zone. Diana *et al.* (2002) measured a train running at 220 km/h on a straight track, finding a probable local vibration mode around 7 Hz contributed to the vibration at the centre of the carbody. In the specific case the vibration at the carbody centre was as significant as that at the extremities for comfort evaluation, which proved the significance of taking local modes and global flexibility into consideration in the study of ride comfort.

2.4.4.2 Flexible modes of the carbody

Because of reduced weight and rigidity of the carbody, elastic vibration of carbody is of great importance, some frequencies of which lie in the human sensitive frequency range in the vertical direction, suppressing these elastic vibrations of the carbody is important to improve ride comfort (Carlbom, 2000, 2001; Carlbom and Berg, 2002; Tomioka *et al.*, 2003). Therefore, the modal analysis of the carbody has been studied and various models have been proposed for the ride comfort simulation.

Carlbom (2000, 2001) modelled the carbody by means of finite element software, finding eight lowest eigenmodes ranging from 9.1 to 16.2 Hz, mainly including bending, torsional and breathing modes, three of which are illustrated in Fig. 2-31. Then a multi-body model of the vehicle which included carbody, suspension and bogie, etc was developed with track data measured on a real track as input. Simulation results fit well with on-track measurements carried out on the real vehicle. Carlbom (2000) also compared the eigenfrequencies of experimental modal analysis (EMA) and finite element modelling (FEM) with operational-deflection shapes (ODS)/PSD peaks and most of the results showed good agreement.

Diana *et al.* (2002) showed the real vehicle behaviour could only be reproduced by the introduction of carbody flexibility, which was the limitation of the rigid-body model. He proposed two parameters playing an important role in ride comfort were the flexibility of carbody and vehicle speed. Among all the bending modes of carbody, the first bending mode was the most significant.

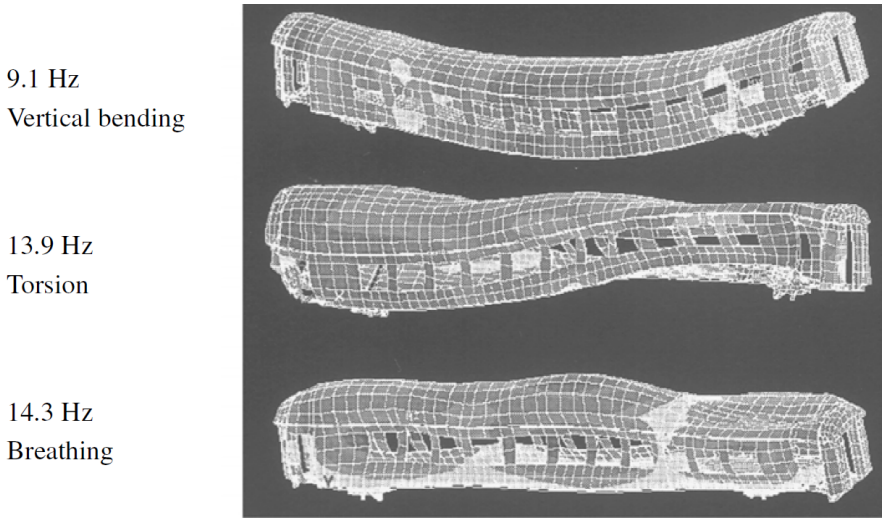

Fig. 2-31 Three calculated eigenmodes (Carlbom, 2001).

Most of the analytical train models just simplified the carbody as a beam for vertical vibration and took the bending modes into account. Zhou *et al.* (2009) developed a vertical railway vehicle model to study the effect of carbody flexibility on ride comfort. The flexural resonant vibration of the carbody mainly resulted from bogie spacing filter phenomena, that is, when bending frequency of carbody coincided with the maximum input gains for bounce mode, there would be violent resonant flexural vibration. What is more, the way to avoid resonant vibration could be increasing stiffness and damping of the primary suspension, however, increasing the damping of the primary suspension too much may worsen the wheel-rail contact, deteriorating the maximum dynamic wheel-rail forces. Besides bogie spacing filter effect, Gong *et al.* (2012) also reported the effect of wheelbase filter effect on frequency response functions (FRFs) of the carbody rigid-body modes,

which occurred when there was neither carbody bounce nor pitch response at certain track wavelengths.

Sun *et al.* (2014) compared the effect of rigid and flexible carbody, finding that the flexibility of the carbody had a different influence at different positions of the carbody, but had no influence on the bogie response. What's more, a smaller stiffness, larger damping of the primary suspension and smaller stiffness of the second suspension could all improve the ride quality. Cao *et al.* (2015) studied the resonant effect and filtering effect existing in elastic vibrations based on a rigid-flexible coupled model and analyzed the factors influencing ride comfort.

The above-mentioned studies were mainly focused on the vertical vibration of the vehicle, where a flexible beam model may seem sufficient to model the overall dynamic response of the carbody. However, for vibrations in other directions (e.g., lateral and roll), the beam model is no longer suitable. In addition, from the experimental modal test (Carlbom, 2000, 2001; Tomioka *et al.*, 2003), the lightweight train could show some more complicated vibration modes than what a simple beam model could reflect, and the frequencies of these modes lied in the human sensitivity frequency range, and such modes would worsen ride comfort. This required to treat the carbody as a three-dimensional (3D) structure.

Some people developed finite element models for the analysis of 3D dynamic vibration of the carbody, e.g. Ling *et al.* (2018). However, the FE model is computationally expensive and still not easy to express the exact vibration of an actual carbody even if the detailed information is available. What is more, modifying an FE carbody model for another carbody is not an easy task. Therefore, 3D analytical modelling of the carbody is another option considering the disadvantage of FE model. Tomioka *et al.* (2003) measured accelerations of more than 40 points on the carbody, from which the modal shapes were identified, showing that in some modes, the roof and floor vibrated in phase, while in some complicated modes, both sides or the roof and floor vibrated out of phase. The complex elastic mode shapes of the commuter vehicle in human sensitive frequency range may be the reason for poor ride comfort. What is more, an analytical approach for 3D elastic vibration of carbody was presented. The carbody was modelled as a box-type structure by means of plates and beams, the modal frequencies, modal shapes and the PSDs of which agreed well with the experiment in the range 0.5-20 Hz. Tomioka *et al.* (2006) also used the same 3D elastic model consisting of plates and beams to model a lightweight commuter vehicle (Fig. 2-32), however, the results for the modes containing shear deformation of the cross-section of carbody were poor.

Seeing from these research, analytical modelling is a good way to study the ride comfort in depth from a mathematical point of view. However, no matter for the beam model or the 3D box model,

almost all the existing models were only focused on the vertical vibration of the carbody. When it comes to vibrations in other directions (e.g., lateral and roll), these models are not applicable any more. Thus, to take into account the multi-axis vibrations (e.g., vertical, lateral and roll) of the carbody simultaneously, a 3D analytical model of the carbody that can reflect the vertical bending, lateral bending, torsional and breathing modes needs to be developed for characterizing the dynamic response of the vehicle accurately. On the other hand, although the geometry filter effect (including bogie spacing filter effect and wheelbase filter effect) can cause resonant or anti-resonant vibration of a specific carbody mode, its relationship with ride comfort has never been studied.

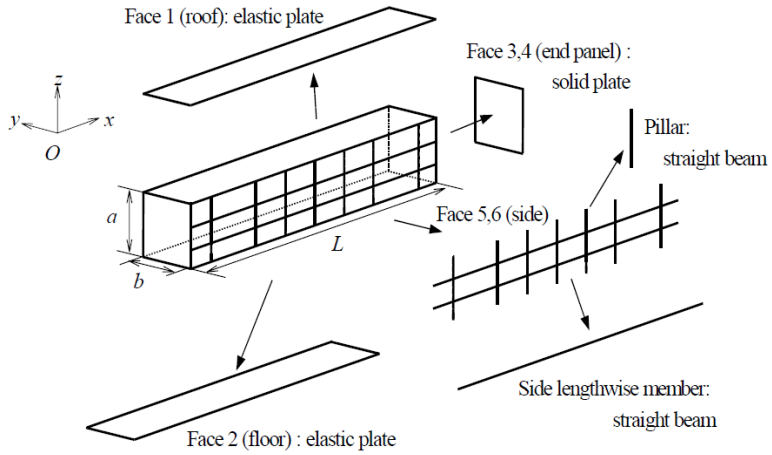

Fig. 2-32 The analytical model of the carbody of a railway vehicle (Tomioka *et al.*, 2006).

2.4.4.3 Flexibility of the track

In traditional railway vehicle dynamics simulations and track modelling using commercial software, such as SIMPACK and NUCARS, etc, the railway track is often assumed to be a rigid or nearly rigid structure. However, the flexibility of track is an important factor that will influence the dynamic response of the whole system. Neglecting track dynamic behaviour may lead to significant overestimation of dynamic performance including hunting and stability, etc (Di Gialleonardo *et al.*, 2012), so how to choose a proper track model for the study of ride comfort is important.

Kargarnovin *et al.* (2005) studied the ride comfort of high-speed trains travelling over railway bridges and a discretely supported Timoshenko beam was used to model the rail, which was on two foundation layers representing the rail pad and ballast. The effects of some design parameters such as damping, stiffness of the suspension and ballast stiffness, etc on ride comfort were investigated.

In the vertical direction, Lu *et al.* (2008) analyzed the coupled vehicle-track system using pseudo-excitation method and compared with the traditional rigid track model, finding the difference was

small in the low-frequency range (0.5-10 Hz) in the vertical direction. Sun *et al.* (2014) compared three track models—a rigid track model, a track stiffness model and a Timoshenko beam model, and found that track flexibility could have a great effect at high frequencies in the vertical direction. Track flexibility could influence the vibration transmitted to the bogies and carbody, but as was evaluated by Sperling Index, this high-frequency vibration didn't influence ride quality. It was recommended that the Timoshenko beam model, which was more suitable and accurate for vibration beyond 40 Hz, was preferred for wheel/rail vibration and contact forces. Furthermore, increasing track stiffness could lead to stronger vibration of carbody at higher frequencies. Cheli and Corradi (2011) compared the results obtained from a flexible ballasted track with those from an infinitely rigid track, concluding the track flexibility played a minor role in the carbody dynamic response in 0-25 Hz in the vertical direction.

In the lateral direction, Zhai *et al.* (2009) compared an elastic track model with a rigid track model, finding the lateral wheel-rail forces showed little difference below 20 Hz. On the other hand, Di Gialleonardo *et al.* (2012) compared three kinds of track modelling, that is, a perfectly rigid track model, a sectional track model, and a three-dimensional finite element track model, and it was found the consideration of track flexibility didn't affect the wheel-rail contact force significantly up to 20 Hz in the lateral direction whether for a tangent or curved track.

As the increase of train speed, the dynamic interaction between the vehicle and track becomes intensified, and systematically investigating the dynamics of a vehicle from the perspective of an entire vehicle–track system is always preferred. However, for the study of ride comfort, the frequency range under consideration is usually very low, sometimes a flexible track model may seem to increase the difficulty in modelling without improving accuracy greatly in the low-frequency range, so for simplification, a rigid track is usually also acceptable when studying ride comfort.

2.4.4.4 Introduction to human-seat system

Till now, few studies on the ride comfort of railway system took the human-seat system into consideration. The interest in the human-seat system in railway vehicles has been low so far, but the development of biodynamics of passengers and seating dynamics is rapid in recent years as engineers are putting much more emphasis directly on the comfort of passengers.

Carlbom and Berg (2002) studied the passenger-carbody interaction to estimate the main influence of the passengers on the carbody dynamics, passenger load parameters were used to describe how the passengers affected each individual carbody mode, and how carbody modes are coupled with each other. A vertical seat model was proposed to describe how seat stiffness and damping could

affect the passenger-carbody interaction. It was also reported that the passengers, seen as increased damping of the carbody structural modes, would have an appreciable influence on the dynamics of the carbody and ride comfort. For a more complete analysis of dynamics, the passenger-seat-carbody model was recommended. Kumar *et al.* (2017) incorporated a human-seat biodynamic model in a low-median speed rail vehicle, studying the comfort of the human body as exposed to vibrations from a rail vehicle.

Most people evaluated the ride comfort using the acceleration measured on the seat base directly. However, a train seat has the potential to modify the vibration transmitted to the seated subjects. For example, a train seat with a seated subject with a resonance between 4 and 8 Hz in the vertical transmissibility will amplify the vibration in this frequency range and attenuate the vibration higher than about 10 Hz, which leads to the accelerations on the floor and human-seat interface being quite different. In addition, the coupling with several human-seat systems may have a significant influence on the dynamics of the carbody. Furthermore, the biodynamics of the human body and seating dynamics have been developing rapidly in recent decades. Therefore, taking into account the human-seat system when studying ride comfort seems to be necessary.

2.4.4.5 Methods of improving ride comfort

The control methods of ride comfort can be classified as passive control and active control. Passive control is usually cheap and easy to implement, often applied to improve ride comfort. The suppression of the first bending mode and rigid modes of the carbody by passive control can achieve satisfactory results. Tomioka and Takigami (2010) utilized the longitudinal vibration in bogies as a dynamic absorber to reduce the vertical bending vibration of a railway vehicle without any additional weight. And the effectiveness of the method was confirmed by a running test with a Shinkansen train on a commercial line. Furthermore, Gong *et al.* (2012) and Shi *et al.* (2014) designed dynamic vibration absorber (DVA) to suspend under the carbody underframe to suppress the flexural resonant vibration of the carbody that was simplified as a beam model.

Aside from these methods, many people studied the key influencing factors of ride comfort and tried to make changes to them in order to achieve better ride comfort.

To summarize, in terms of the vehicle dynamics, most of the research just studied the ride comfort from the perspective of vertical vibration. For a rail vehicle including high-speed train, the vibration environment is usually complex, involving multi-axis vibrations, so the passengers are exposed to not only vertical vibration, but also lateral and roll vibrations, etc, the analysis of ride comfort based on a train model coupled with human-seat sub-systems from the perspective of these vibrations

has rarely been seen. In terms of the evaluation of ride comfort, usually only the vibration in one position and one direction was used for the evaluation, but for multi-axis vibrations, more positions and directions should be taken into account. Based on a train model with multi-axis vibrations, the influence of train speed, carbody damping, suspension parameters and seat position, etc on ride comfort, and the proportion of different vibration positions and directions in the overall ride comfort index are still waiting to be studied. In addition, the contribution of different modes (rigid modes, torsional, bending and breathing modes) to ride comfort can be defined. The answer to these questions can provide guidance on how to modify the design of the seat and train as well as how to match the train system with the human-seat sub-system so as to achieve better ride comfort performance.

2.5 Conclusions

This chapter makes a comprehensive literature review about the up-to-date research on the biodynamic response of the seated human body to vibrations, seating dynamics, modelling of seated human body, modelling of human-seat system and the ride dynamics of high-speed trains, which plays an important role in putting forward the research questions and defining the research scope of this thesis. This review also provides a useful guide for the research methods, the following research and relative conclusions.

The train seat has the potential to modify the vibration transmitted to the seated subjects. And the coupling of several human-seat systems with the carbody may have a significant influence on the dynamics of the carbody. However, the human-seat system is usually ignored when studying the vehicle dynamics and evaluating the ride comfort. On the other hand, although the geometry filter effect can cause resonant or anti-resonant vibration of a specific carbody mode, what its relationship with ride comfort is has never been studied. Therefore, Chapter 4 analytically studied the relationship between the geometry filter effect of the vehicle and ride comfort index based on a vertical train-seat-human model.

When applying the original MISO method introduced in Bendat and Piersol (2010) to evaluate the contribution of the conditioned inputs, the results are not unique and dependent on the sequence of inputs. A new MISO method was proposed in Section 3.2.2 to overcome the limitation of the original method. Based on the new method, Chapter 5 maninly studied how many and which inputs at the seat base should be taken into account in order to sufficiently predict the lateral, vertical and roll accelerations at the seat pan and backrest, so as to make clear the vibration transmission of a human-seat system of a high-speed train in a working environment.

Considering that there are limited studies on the biodynamics of seated human body to multi-axis vibration, especially the typical vibrations on rail vehicles, Chapter 6 studied the biodynamics of the seated human body exposed to lateral, vertical and roll vibrations, and the influence of vibration magnitude on the nonlinearity of biodynamics.

Since the existing seated human models are usually two-dimensional with some rigid parts that can only move or rotate in the mid-sagittal plane under in-plane excitations, they are not applicable to out-of-plane excitation and cannot reflect the out-of-plane motion. In view of this, Chapter 7 developed and validated a multi-body seated human model exposed to combined lateral, vertical and roll vibration.

There have rarely been studies on the seat transmissibility under multi-axis vibration, and the existing research on seating dynamics is more focused on car seat. Chapter 8 studied the seat transmissibility of a train seat with subjects exposed to lateral, vertical and roll vibrations, and the influence of vibration magnitude on the seat transmissibility.

Because almost all the human-seat models are developed in the symmetrical plane of the seat, which is only applicable to in-plane excitation, Chapter 9 proposed and validated multi-body models for the train seat and the seat with one and two subjects under exposed to combined lateral, vertical and roll vibration.

In terms of the vehicle dynamics, most of the research restricted the analysis of ride comfort to vertical vibration. However, the passengers are exposed to not only vertical vibration, but also lateral and roll vibrations, etc. Therefore, Chapter 10 analyzed the ride comfort based on a track-train model coupled with human-seat sub-systems from the perspective of lateral, vertical and roll vibrations, and studied the influence of different factors on ride comfort.

Chapter 3 Research methods used in following chapters

3.1 Introduction

This chapter outlines the research methods that will be used in the following chapters, including the calculation of FRF, the method for model calibration, the Wilcoxon signed-rank test, linear regression analysis and modal analysis method. Especially, to overcome the limitation of the original MISO method, a new MISO method in which the partial coherences are independent of the sequence of the inputs was proposed. For the model calibration, a combined algorithm that is suitable for a large number of optimization variables was introduced. For plotting the animation of complex modes, a modal analysis method based on complex mode theory was introduced.

3.2 The calculation of frequency response function

The frequency response functions are frequently calculated in the study of the biodynamic response of the human body to vibration evaluated by apparent mass and seat vibration transmission assessed by seat transmissibility. Two ways of calculating the FRFs have been adopted in this thesis, which are suitable for single-input and multiple-input systems, respectively.

3.2.1 Single input

Single-input and single-output (SISO) model is commonly used for the calculation of FRF. For the single-input system, the FRF can be calculated as

$$H(f)=\frac{G_{iy}(f)}{G_{ii}(f)} \tag{3-1}$$

where $G_{iy}(f)$ is the cross-spectral density between the input signal $x_i(t)$ and the output $y(t)$; $G_{ii}(f)$ is the auto-spectral density of the input signal $x_i(t)$.

The coherence function between the input and output signals is

$$\gamma_{iy}^2(f)=\frac{\left|G_{iy}(f)\right|^2}{G_{ii}(f)G_{yy}(f)} \tag{3-2}$$

where $G_{yy}(f)$ is the auto-spectral density of the output signal $y(t)$.

3.2.2 Multiple inputs

3.2.2.1 Brief introduction to the existing MISO method

When there are multiple inputs, the SISO model can cause biased estimation of the FRF. Under this situation, the MISO model is designed instead for the more accurate calculation of FRF.

The details of multi-input and single-output systems can refer to Bendat and Piersol (2010). The general multi-input and single-output model for original inputs is illustrated in Fig. 3-1, and the corresponding multi-input and single-output model for conditioned inputs is shown in Fig. 3-2, where $X_i(f)$ ($i=1,2,...,m$), $Y(f)$ and $N(f)$ represent the Fourier transforms of the input signals $x_i(t)$, the output signal $y(t)$, and the noise $n(t)$, respectively; $H_{iy}(f)$ ($i=1,2,...,m$) are the constant-parameter linear frequency response functions for the original system; $X_{i\cdot(i-1)!}$ are the Fourier transforms of the conditioned inputs $x_{i\cdot(i-1)!}(t)$. For any i, the subscript notation $i\cdot j$ stands for removing the coherent part with $x_j(t)$ from $x_i(t)$ by the optimum linear system. For example, $i\cdot(i-1)!$ represents the i[th] record conditioned on the previous $(i-1)$ records, that is, removing the linear effects of $x_1(t)$, $x_2(t)$, up to $x_{i-1}(t)$ that are coherent with $x_i(t)$ from $x_i(t)$ by the optimum linear system. Thus, these conditioned inputs in Fig. 3-2 are mutually incoherent. Similarly, $L_{iy}(f)$ are the constant-parameter linear frequency response functions for the conditioned inputs.

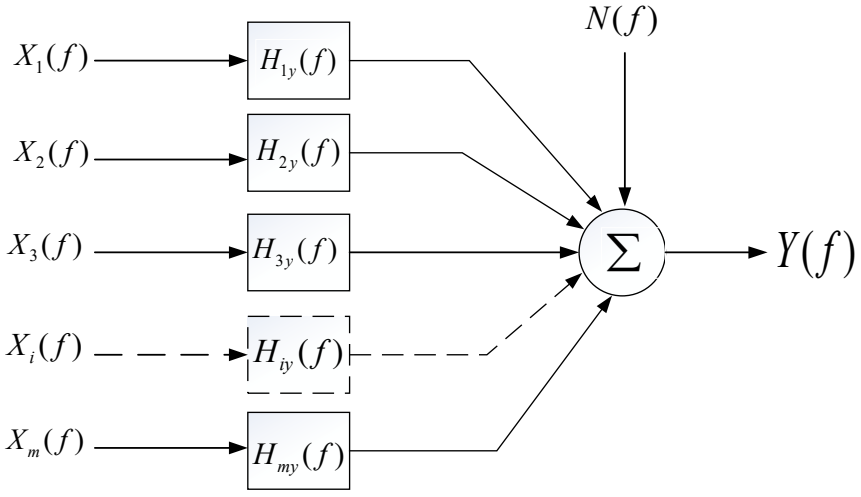

Fig. 3-1 Multi-input and single-output model for original inputs for the original MISO method.

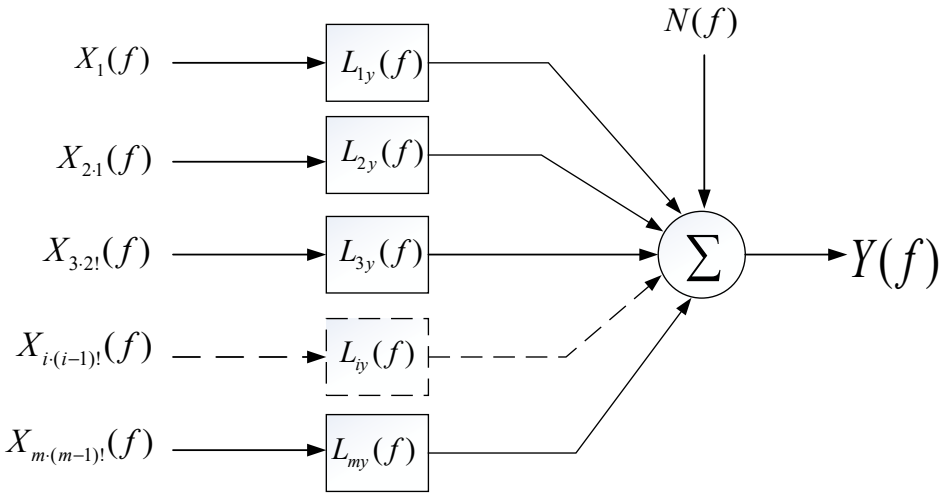

Fig. 3-2 Multi-input and single-output model for ordered conditioned inputs for the original MISO method.

Note that the inputs can be in any order, however, the order is usually determined by the magnitudes of the ordinary coherence functions computed between each input and the output in descending order.

The optimum linear system (also FRF) from one conditioned input $x_{i\cdot(i-1)!}$ to another $x_{j\cdot(i-1)!}$ is defined as the ratio of the cross-spectral density function between the two conditioned inputs and the auto-spectral density function of the former conditioned input as

$$L_{ij} = \frac{G_{ij\cdot(i-1)!}}{G_{ii\cdot(i-1)!}},\ j > i-1 \tag{3-3}$$

where $G_{ij\cdot(i-1)!}$ is the cross-spectral density function between $x_{i\cdot(i-1)!}$ and $x_{j\cdot(i-1)!}$, and $G_{ii\cdot(i-1)!}$ is the auto-spectral density function of the conditioned input $x_{i\cdot(i-1)!}$.

Similarly, the optimum linear system (also FRF) from the conditioned input $x_{i\cdot(i-1)!}$ to the output $y(t)$ is

$$L_{iy} = \frac{G_{iy\cdot(i-1)!}}{G_{ii\cdot(i-1)!}} \tag{3-4}$$

where $G_{iy\cdot(i-1)!}$ is the cross-spectral density function between $x_{i\cdot(i-1)!}$ and $y(t)$.

The conditioned spectral density functions between the conditioned inputs have the following recurrence relationship as

$$G_{jk\cdot(i-1)!} = G_{jk\cdot(i-2)!} - L_{(i-1)k} G_{j(i-1)\cdot(i-2)!},\ j > i-1 \text{ and } k > i-1 \tag{3-5}$$

where $G_{jk\cdot(i-1)!}$, $G_{jk\cdot(i-2)!}$ and $G_{j(i-1)\cdot(i-2)!}$ are the spectral density functions between $x_{j\cdot(i-1)!}$ and $x_{k\cdot(i-1)!}$, between $x_{j\cdot(i-2)!}$ and $x_{k\cdot(i-2)!}$ as well as between $x_{j\cdot(i-2)!}$ and $x_{(i-1)\cdot(i-2)!}$, respectively.

Similarly, the spectral density functions between conditioned input and the output have the following recurrence relationship as

$$G_{jy\cdot(i-1)!} = G_{jy\cdot(i-2)!} - L_{(i-1)y} G_{j(i-1)\cdot(i-2)!},\ j > i-1 \tag{3-6}$$

where $G_{jy\cdot(i-1)!}$ and $G_{jy\cdot(i-2)!}$ are the cross-spectral density functions between the conditioned input $x_{j\cdot(i-1)!}$ and the output $y(t)$, between $x_{j\cdot(i-2)!}$ and $y(t)$, respectively.

The partial coherence function is defined as the coherence function between the conditioned input $x_{j\cdot(i-1)!}$ and the output $y(t)$ as

$$\gamma^2_{jy\cdot(i-1)!} = \frac{\left|G_{jy\cdot(i-1)}\right|^2}{G_{jj\cdot(i-1)!} G_{yy}} = \frac{\left|L_{jy}\right|^2 G_{jj\cdot(i-1)!}}{G_{yy}},\ j > i-1 \tag{3-7}$$

where G_{yy} is the auto-spectral density function of the output $y(t)$. This partial coherence function defines the percentage of the spectrum of output due to the conditioned input $x_{j\cdot(i-1)!}$.

For a general multi-input and single-output model having *m* inputs, the multiple coherence function is

$$\gamma^2_{y:m!} = \sum_{i=1}^{m} \gamma^2_{iy\cdot(i-1)!} \tag{3-8}$$

The relationship between the optimum systems for the original inputs and for the conditioned inputs is

$$\begin{cases} H_{my} = L_{my} \\ H_{iy} = L_{iy} - \sum_{j=i+1}^{m} L_{ij} H_{jy} \quad 1 \le i \le m-1 \end{cases} \tag{3-9}$$

where $H_{iy} = \dfrac{G_{iy\cdot(m!/i)}}{G_{ii\cdot(m!/i)}}$ is the FRF from the conditioned input $x_{i\cdot(m!/i)}$ to the output $y(t)$.

A flowchart of computational algorithm for any number of inputs applying the existing method is described in Fig. 3-3.

3.2.2.2 The new MISO method

However, the existing MISO method provides the partial coherence that is dependent on the sequence of inputs. One specific partial coherence stands for the percentage of the spectrum of the output due to one specific (conditioned) input, used to evaluate the contribution from this specific input to the output. And the multiple coherence stands for the percentage of the spectrum of the output due to all the inputs, used to evaluate the total contribution from all the inputs. However, in the existing MISO method, the evaluation of partial coherences is dependent on the sequence of inputs, which gives no unique results. To date, the researchers have been adopting the method directly (Qiu and Griffin, 2004, 2005) or inversely (Huang and Ferguson, 2018), but the above-mentioned problem remains unsolved. Thus, how to propose a new MISO method and define partial coherences that are independent of the sequence of inputs is still a question. In this chapter, a new MISO method is proposed with new partial coherences defined, and the theory is introduced as follows.

If x_i is taken as the last input, then the incoherent conditioned inputs can be reorganized in the order: x_1, $x_{2\cdot 1}$, $x_{3\cdot 2!}$,..., $x_{(i-1)\cdot(i-2)!}$, $x_{(i+1)\cdot(i-1)!}$, ..., $x_{k\cdot((k-1)!/i)}$, ..., $x_{i\cdot(m!/i)}$. The conditioned input $x_{k\cdot((k-1)!/i)}$ represents the linear effects of $x_1(t)$, $x_2(t)$,..., $x_{i-1}(t)$, $x_{i+1}(t)$,..., $x_{k-1}(t)$ have been removed from $x_k(t)$ by the optimum linear system.

$x_{s\cdot(k!/i)}$ ($s > k \; or \; s = i$) can be obtained by removing the linear effects of x_1, $x_{2\cdot 1}$, $x_{3\cdot 2!}$,..., $x_{(i-1)\cdot(i-2)!}$, $x_{(i+1)\cdot(i-1)!}$, ..., $x_{k\cdot((k-1)!/i)}$ from x_s one by one by the optimum linear system. After removing the linear effects of x_1, $x_{2\cdot 1}$, $x_{3\cdot 2!}$,..., $x_{(i-1)\cdot(i-2)!}$ from x_s, the remaining part of x_s is $x_{s\cdot(i-1)!}$.

Then, the conditioned input $x_{s\cdot((i+1)!/i)}$ ($s > i+1 \text{ or } s = i$) can be calculated by removing the coherent part with $x_{(i+1)\cdot(i-1)!}$ from $x_{s\cdot(i-1)!}$ by the optimum linear system as

$$X_{s\cdot((i+1)!/i)} = X_{s\cdot(i-1)!} - \frac{G_{(i+1)s\cdot(i-1)!}}{G_{(i+1)(i+1)\cdot(i-1)!}} X_{(i+1)\cdot(i-1)!}, \text{ for } s > i+1 \text{ or } s = i \qquad (3\text{-}10)$$

where $X_{s\cdot((i+1)!/i)}$, $X_{s\cdot(i-1)!}$ and $X_{(i+1)\cdot(i-1)!}$ are respectively the Fourier transforms of the conditioned inputs $x_{s\cdot((i+1)!/i)}$, $x_{s\cdot(i-1)!}$ and $x_{(i+1)\cdot(i-1)!}$; $G_{(i+1)s\cdot(i-1)!}$ and $G_{(i+1)(i+1)\cdot(i-1)!}$ are respectively the cross-spectral density between $x_{(i+1)\cdot(i-1)!}(t)$ and $x_{s\cdot(i-1)!}(t)$ and the auto-spectral density function of $x_{(i+1)\cdot(i-1)!}(t)$.

So the cross-spectral density function between $x_{j\cdot((i+1)!/i)}$ and $x_{s\cdot((i+1)!/i)}$ is

$$G_{js\cdot((i+1)!/i)} = G_{js\cdot(i-1)!} - \frac{G_{(i+1)s\cdot(i-1)!}}{G_{(i+1)(i+1)\cdot(i-1)!}} G_{j(i+1)\cdot(i-1)!}, \text{ for } \begin{cases} s > i+1 \text{ or } s = i \\ j > i+1 \text{ or } j = i \end{cases} \tag{3-11}$$

By the same token, the conditioned input $x_{s\cdot((i+2)!/i)}$ ($s > i+2$ or $s = i$) can be calculated by removing the coherent part with $x_{(i+2)\cdot((i+1)!/i)}$ from $x_{s\cdot((i+1)!/i)}$ by the optimum linear system as

$$X_{s\cdot((i+2)!/i)} = X_{s\cdot((i+1)!/i)} - \frac{G_{(i+2)s\cdot((i+1)!/i)}}{G_{(i+2)(i+2)\cdot((i+1)!/i)}} X_{(i+2)\cdot((i+1)!/i)}, \text{ for } s > i+2 \text{ or } s = i \tag{3-12}$$

So the cross-spectral density function between $x_{j\cdot((i+2)!/i)}$ and $x_{s\cdot((i+2)!/i)}$ is

$$G_{js\cdot((i+2)!/i)} = G_{js\cdot((i+1)!/i)} - \frac{G_{(i+2)s\cdot((i+1)!/i)}}{G_{(i+2)(i+2)\cdot((i+1)!/i)}} G_{j(i+2)\cdot((i+1)!/i)}, \text{ for } \begin{cases} s > i+2 \text{ or } s = i \\ j > i+2 \text{ or } j = i \end{cases} \tag{3-13}$$

Following this pattern, the cross-spectral density function between the conditioned inputs $x_{j\cdot(k!/i)}$ and $x_{s\cdot(k!/i)}$ is

$$G_{js\cdot(k!/i)} = G_{js\cdot((k-1)!/i)} - \frac{G_{ks\cdot((k-1)!/i)}}{G_{kk\cdot((k-1)!/i)}} G_{jk\cdot((k-1)!/i)}, \text{ for } \begin{cases} s > k \text{ or } s = i \\ j > k \text{ or } j = i \\ i+1 \le k \le m \end{cases} \tag{3-14}$$

Note that in Eq. (3-14), if $k = i+1$, then

$$G_{js\cdot((i+1)!/i)} = G_{js\cdot(i-1)!} - \frac{G_{(i+1)s\cdot(i-1)!}}{G_{(i+1)(i+1)\cdot(i-1)!}} G_{j(i+1)\cdot(i-1)!}, \text{ for } \begin{cases} s > i+1 \text{ or } s = i \\ j > i+1 \text{ or } j = i \end{cases} \tag{3-15}$$

For the original inputs in Fig. 3-1, the governing equation is

$$Y(f) = \sum_{j=1}^{m} H_{jy}(f) X_j(f) + N(f) \tag{3-16}$$

So the auto-spectral density of the output (G_{yy}) is

$$G_{yy}=\begin{bmatrix}H_{1y}^{*}\\H_{2y}^{*}\\\vdots\\H_{my}^{*}\end{bmatrix}^{\mathrm{T}}\begin{bmatrix}G_{11}&G_{12}&\cdots&G_{1m}\\G_{21}&G_{22}&\cdots&G_{2m}\\\vdots&\vdots&\ddots&\vdots\\G_{m1}&G_{m2}&\cdots&G_{mm}\end{bmatrix}\begin{bmatrix}H_{1y}\\H_{2y}\\\vdots\\H_{my}\end{bmatrix}+G_{nn} \tag{3-17}$$

where G_{ij} ($i\neq j$) is the cross-spectral density between x_i and x_j, G_{ii} is the auto-spectral density of x_i, and G_{nn} is the auto-spectral density of the noise $n(t)$.

In Eq. (3-14), if $j=s=i$, then

$$G_{ii\cdot(k!/i)}=G_{ii\cdot((k-1)!/i)}-\frac{G_{ki\cdot((k-1)!/i)}}{G_{kk\cdot((k-1)!/i)}}G_{ik\cdot((k-1)!/i)}=G_{ii\cdot((k-1)!/i)}(1-\gamma^{2}_{ik\cdot((k-1)!/i)}),\ \text{for}\ k\neq i \tag{3-18}$$

where $\gamma^{2}_{ik\cdot((k-1)!/i)}=\dfrac{G_{ki\cdot((k-1)!/i)}G_{ik\cdot((k-1)!/i)}}{G_{kk\cdot((k-1)!/i)}G_{ii\cdot((k-1)!/i)}}$ is the coherence between the conditioned inputs $x_{i\cdot((k-1)!/i)}$ and $x_{k\cdot((k-1)!/i)}$.

So in this way,

$$\begin{aligned}&G_{ii\cdot(m!/i)}=G_{ii\cdot((m-1)!/i)}(1-\gamma^{2}_{im\cdot((m-1)!/i)})\\&=G_{ii\cdot((m-2)!/i)}(1-\gamma^{2}_{i(m-1)\cdot((m-2)!/i)})(1-\gamma^{2}_{im\cdot((m-1)!/i)}),\ \text{for}\ 1\le i\le m\\&=\cdots=G_{ii}\prod_{\substack{s=1\\s\neq i}}^{m}(1-\gamma^{2}_{is\cdot((s-1)!/i)})\end{aligned} \tag{3-19}$$

where $G_{ii\cdot(m!/i)}$ is the auto-spectral density of the conditioned input $x_{i\cdot(m!/i)}$, which also represents the spectrum of the 'noise' if x_i is taken as the output, all the other (*m-1*) signals x_j ($j\neq i, 1\le j\le m$) as the inputs.

So Eq. (3-17) can be re-expressed as

$$G_{yy}=\begin{bmatrix}H_{1y}^{*}\\H_{2y}^{*}\\\vdots\\H_{my}^{*}\end{bmatrix}^{\mathrm{T}}\begin{bmatrix}G_{11}\gamma^{2}_{11}&G_{12}&\cdots&G_{1m}\\G_{21}&G_{22}\gamma^{2}_{22}&\cdots&G_{2m}\\\vdots&\vdots&\ddots&\vdots\\G_{m1}&G_{m2}&\cdots&G_{mm}\gamma^{2}_{mm}\end{bmatrix}\begin{bmatrix}H_{1y}\\H_{2y}\\\vdots\\H_{my}\end{bmatrix}+\sum_{i=1}^{m}\left|H_{iy}\right|^{2}G_{ii\cdot(m!/i)}+G_{nn} \tag{3-20}$$

where $\gamma_{ii}^2 = 1 - \prod_{\substack{s=1 \\ s \neq i}}^{m} (1 - \gamma_{is\cdot((s-1)!/i)}^2)$ is the multiple coherence function if x_i is taken as the output, all the other (*m-1*) signals x_j ($j \neq i, 1 \leq j \leq m$) as the inputs; $G_{ii}\gamma_{ii}^2$ stands for the spectrum of x_i that is due to all the other (*m-1*) signals x_j ($j \neq i,\ 1 \leq j \leq m$).

Therefore, the partial coherence function between $x_{i\cdot(m!/i)}$ and $y(t)$ is defined as

$$\gamma_{iy\cdot(m!/i)}^2 = \frac{\left|G_{iy\cdot(m!/i)}\right|^2}{G_{ii\cdot(m!/i)}G_{yy}} = \frac{\left|H_{iy}\right|^2 G_{ii\cdot(m!/i)}}{G_{yy}}, \text{ for } 1 \leq i \leq m \tag{3-21}$$

According to Eq. (3-20), the correlation function between the coherent parts and the output $y(t)$ (called 'coherent correlation function' next) can be defined as

$$\begin{aligned}
\gamma_{cy} &= \begin{bmatrix} H_{1y}^* \\ H_{2y}^* \\ \vdots \\ H_{my}^* \end{bmatrix}^{\mathrm{T}} \begin{bmatrix} G_{11}\gamma_{11}^2 & G_{12} & \cdots & G_{1m} \\ G_{21} & G_{22}\gamma_{22}^2 & \cdots & G_{2m} \\ \vdots & \vdots & \ddots & \vdots \\ G_{m1} & G_{m2} & \cdots & G_{mm}\gamma_{mm}^2 \end{bmatrix} \begin{bmatrix} H_{1y} \\ H_{2y} \\ \vdots \\ H_{my} \end{bmatrix} / G_{yy} \\
&= \left(\sum_{i=1}^{m} \left|H_{iy}\right|^2 G_{ii}\gamma_{ii}^2 + \sum_{i=1}^{m}\sum_{j=1, j\neq i}^{m} H_{iy}^* G_{ij} H_{jy}\right) / G_{yy} \\
&= 1 - \frac{G_{nn}}{G_{yy}} - \sum_{i=1}^{m} \gamma_{iy\cdot(m!/i)}^2 = \gamma_{y:m!}^2 - \sum_{i=1}^{m} \gamma_{iy\cdot(m!/i)}^2
\end{aligned} \tag{3-22}$$

where $(H_{iy}^* G_{ij} H_{jy} + H_{jy}^* G_{ji} H_{iy}) / G_{yy}$ ($j \neq i$) is a real value that can be negative, standing for the proportion of the spectrum of output due to the coherent part between x_i and x_j ; while $\left|H_{iy}\right|^2 G_{ii}\gamma_{ii}^2 / G_{yy}$ stands for the proportion of the spectrum of output resulting from the part of x_i that is due to all the other (*m-1*) signals x_j ($j \neq i,\ 1 \leq j \leq m$).

The partial coherence function $\gamma_{iy\cdot(m!/i)}^2$ denotes the percentage of the spectrum of the output $y(t)$ due to the conditioned input $x_{i\cdot(m!/i)}$, and γ_{cy} defines the percentage of the spectrum of output due to the coherent parts (first item in Eq. (3-20)) between the inputs $x_i(t)$ ($i = 1, 2, ..., m$). And $\gamma_{y:m!}^2$ is the multiple coherence function, standing for the percentage of the spectrum of output due to all the inputs, which is the same as the original method.

In the new method, the conditioned inputs are respectively $x_{i\cdot(m!/i)}$ ($1 \le i \le m$), so the coherent parts of x_i with all the other inputs have been removed from x_i, and the new partial coherence function is defined as the coherence between $x_{i\cdot(m!/i)}$ and the output $y(t)$, which is therefore independent of the sequence of inputs. If all the input signals are incoherent with each other, then $\gamma_{cy} = 0$. The closer γ_{cy} is to zero, the less the coherence between the inputs $x_i(t)$ ($i = 1, 2, ..., m$) is. Note that $0 \le \gamma^2_{iy\cdot(m!/i)} \le 1$, but γ_{cy} can be less than 0 and $\sum_{i=1}^{m} \gamma^2_{iy\cdot(m!/i)}$ can be greater than 1. To better illustrate it, an example in Fig. 5-16 of Chapter 5 is made here in advance. The blue line stands for the partial coherence function between the conditioned input $x_{1\cdot2,3}$ and the output $y(t)$, the difference between the red and blue lines stands for the partial coherence between the conditioned input $x_{2\cdot1,3}$ and the output $y(t)$, while the difference between the cyan and red lines stands for the partial coherence between the conditioned input $x_{3\cdot1,2}$ and the output $y(t)$. The black line stands for the multiple coherence function $\gamma^2_{y:3!}$. The multiple coherence $\gamma^2_{y:3!}$ can be greater or less than the summation of three partial coherences ($\gamma^2_{1y\cdot2,3} + \gamma^2_{2y\cdot1,3} + \gamma^2_{3y\cdot1,2}$), which is because the coherent correlation function γ_{cy} can be negative or positive. The summation of the three partial coherence functions can be greater than unity because the three conditioned inputs are not totally incoherent with each other. The partial coherences denote the percentage of the spectrum of output due to the conditioned inputs, while the coherent correlation function defines the percentage of the spectrum of output due to the coherent parts between the three inputs.

Thus, the multiple coherence is equal to the summation of all the new partial coherences and γ_{cy}. And the new partial coherence $\gamma^2_{iy\cdot(m!/i)}$ and γ_{cy} are used to evaluate the contribution of the individual input and the coherent parts between the inputs to the output, respectively in the following analysis. To help the readers understand the difference between the new MISO method and the original method, a special example of three inputs is provided in Appendix A.

The modulus of the FRF is

$$|H(f)| = \sqrt{(\mathrm{Re}(H(f))^2 + \mathrm{Im}(H(f))^2)} \tag{3-23}$$

where $H(f)$ can be any FRF, $\mathrm{Re}()$ and $\mathrm{Im}()$ stand for the real part and imaginary part, respectively.

The phase of the FRF is

$$\theta(f) = \arctan \frac{\mathrm{Im}(H(f))}{\mathrm{Re}(H(f))} \tag{3-24}$$

The flowchart of computational algorithm for any number of inputs for the new method and its relationship with the original method is described in Fig. 3-3, and a Matlab function was developed for any number of inputs according to this algorithm.

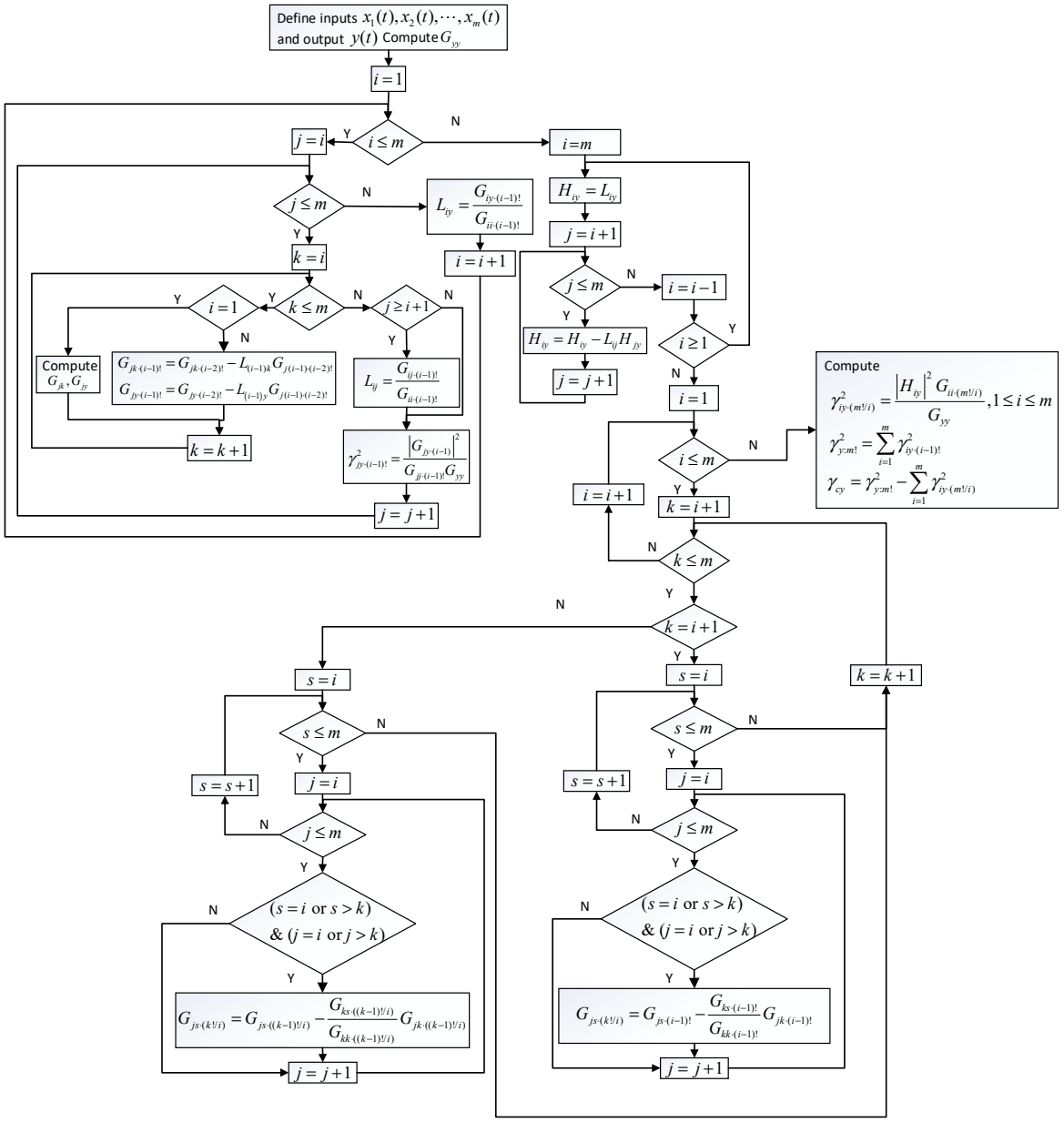

Fig. 3-3 The flowchart of computational algorithm for any number of inputs.

3.3 The method of calibration

Genetic algorithm (GA) is a widely used computational optimization algorithm attempting to mimic the process taking place in biological evolution (Sivanandam and Deepa, 2007). GAs start with a

randomly chosen set of chromosomes, which is the first generation (initial population). Then the evolution starts with encoding and carries out by the use of selection, crossover, mutation and replacement operators to form a new generation, and each chromosome in the population is evaluated by the fitness function (also objective function). Although GAs are global optimization algorithms, GAs have a tendency to converge to local optimum instead of the global optimum. In terms of the speed of convergence, GAs may be less efficient than some other optimization algorithms.

The optimization by GAs is realized by means of 'ga' function in Matlab. The features of this function are that the convergence is very slow and dependent on the randomly chosen first generation. The evolution is usually relatively fast in the first several generations, however, it slows down greatly afterwards during the course of converging to the optimum. This function is more suitable for finding globally an area that may contain an optimum than local in-depth optimization in a small region.

Another optimization algorithm is 'fmincon' function in Matlab that applies to the minimization of nonlinear multivariate function in constraint problems. This function is suitable for linear and nonlinear equality and inequality constraints, and shows great dependence on the initial values. The algorithm implemented in 'fmincon' function seems to perform better than that in 'ga' function at in-depth optimization in a local area.

To take advantage of both functions, a strategy of optimization combining both algorithms was formed. This procedure is summarized as follows:

(1) The objective function and the lower and upper bounds of the optimization parameters were defined with reference to relevant literature available.

(2) Start the phase of global optimization. The genetic algorithm with randomly generated first generation of initial parameter values was adopted for finding next several generations with all the constraints being satisfied, until the number of the optimization (or generation) reached a predefined value or the difference between the two values of the optimization objective function in two consecutive runs reached a predefined value and a set of the optimization parameters was obtained. It is suggested that the more variables there are, the larger population should be used. From this point the procedure entered into the following optimization phase;

(3) Switch into the phase of local optimization. The algorithm in 'fmincon' function in Matlab was then adopted by setting the initial values as the obtained parameters in the previous phase of global optimization with all the constraints being satisfied. The local optimization was terminated when

the number of iteration or the difference between the two values of the optimization objective function in two consecutive runs reached a predefined value.

(4) This process was repeated several times with different sets of initial values of the optimization parameters so as to increase the probability of converging to the global optimum. The best set of the optimization parameters was obtained as the final calibration result.

This combined algorithm combines the benefits of these two functions and is suitable for problems with a large number of optimization variables and linear and nonlinear equality and inequality constraints. This algorithm has a relatively fast optimization speed and is better than any of the two algorithms working alone.

In this thesis, all the model calibrations are done using this combined algorithm.

Note that the ‘fmincon’ function can also be replaced by another function called ‘fminsearchcon’ released by John D'Errico that is a bound constrained optimization algorithm with linear and nonlinear constraints based on ‘fminsearch’ function in Matlab (D’Errico, 2012). A flowchart for the calibration method was illustrated in Fig. 3-4.

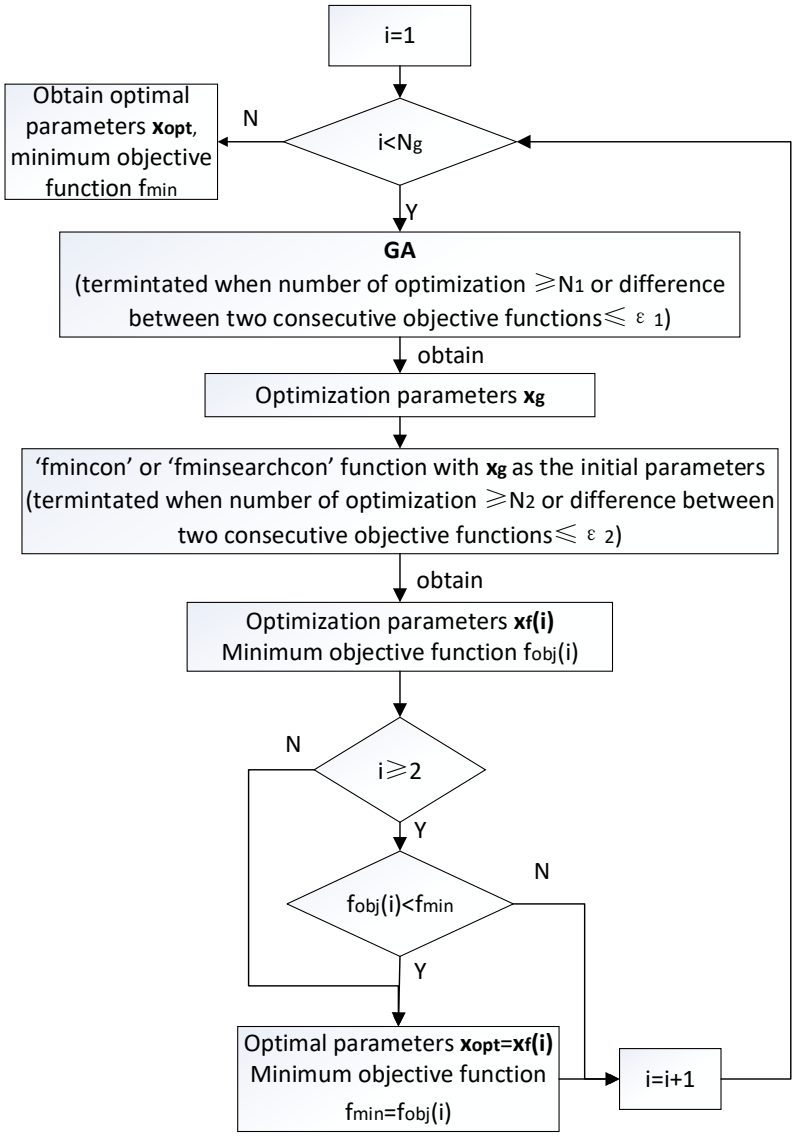

Fig. 3-4 Flowchart for the calibration method (N_1 and N_2 are the predefined optimization numbers, while ε_1 and ε_2 are predefined values for the difference between two consecutive objective functions)

3.4 Wilcoxon signed-rank test

Wilcoxon signed-rank test is a non-parametric statistical test that can be used for determining whether the median difference of two independent samples is zero (Hollander *et al.*, 2013). This test does not make the assumption that samples are normally distributed. The two samples of data should be matched one by one and the differences can be calculated and ranked.

For pairwise comparisons, the null hypothesis is H_0: The medians of the two samples are the same; and the alternative hypothesis is H_1: The medians of the two samples are different.

Then the hypotheses are tested by Wilcoxon signed-rank test with a significance level of α, if the calculated p-value is less than α, then there is a significant difference between the medians of the two samples, and vice versa.

Wilcoxon signed-rank test in the thesis is realized by 'signrank' function in Matlab with a chosen significance level α of 0.05. For example, to study the influence of vertical vibration magnitude on the resonance frequency of the vertical apparent mass on the seat pan, the resonance frequencies for all the subjects under two vibration mangitudes are picked and matched with each other. Then Wilcoxon signed-rank test can be carried out to tell whether the resonance frequencies under these two vibration magnitudes show significant difference or not.

However, it should be noted that for multiple comparisons, if there are N (≥3) samples, for the null hypothesis H_0': The medians of all the samples are the same; and the alternative hypothesis H_1': Two or more medians of the samples are different from each other. Even though there are no differences in the pairwise comparisons tested by Wilcoxon signed-rank test between all the samples, it's wrong to accept H_0' with a significance level of α. Actually, the significance level is different, according to Sidak correction method, the real significance level approximately becomes

$$\alpha_c = 1-(1-\alpha)^{\frac{N(N-1)}{2}} \tag{3-25}$$

where N is the number of samples, so $N(N-1)/2$ is the total number of pairwise comparisons; α is the significance level for Wilcoxon signed-rank test.

Therefore, it's not right to accept H_0' or reject H_1' with a significance level of α.

3.5 Linear regression analysis

Linear regression analysis is used for testing the linear relationship between the dependent variable and the independent ones. The simple linear model involves only one independent variable (X_i) as follows:

$$Y_i = \beta_0 + \beta_1 X_i \tag{3-26}$$

where the subscript $i = 1, 2, ..., n$ represents the ith observation of the dependent and independent variables; β_0 is the intercept and β_1 is the slope.

Then β_0 and β_1 can be estimated by the least square estimation method using data of n observations. The coefficient of determination, R^2 value, ranges from 0 to 1.0, evaluating the proportion of variation in the dependent variable explained by the linear relationship with the independent variable. The closer R^2 value is to 1.0, the better the linearity between the dependent and independent variables is, and vice versa.

The hypothesis H_0: the slope $\beta_1 = 0$, and the alternative hypothesis H_1: the slope $\beta_1 \neq 0$ are tested by F-test. For a given significance level α, if the calculated p-value is less than α, then H_0 is rejected and H_1 is accepted, and vice versa.

The linear regression analysis is conducted by means of 'regress' function in Matlab. Details about linear regression analysis can refer to Rawlings *et al.* (2001). For example, to study the linear relationship between the resonance frequency of the vertical apparent mass on the seat pan and vibration r.s.s. magnitude, all the resonance frequencies (dependent variable) and the corresponding vibration r.s.s. magnitudes (independent variable) for one subject are picked and matched, then linear regression analysis can be carried out to obtain the intercept β_0 and the slope β_1. For other subjects, the linear regression analysis can also be carried out in the same way.

3.6 Modal analysis

Modal analysis is to study the dynamic properties of a system in the frequency domain. When the structural damping is small and the modal frequency is very large, the difference of the modal frequency between the damped and undamped systems usually can be ignored, so can the difference between the actual complex modal shape and the undamped real modal shape. However, in the field of human vibration, the modal frequency is very small, the damping is usually very large, and the damping matrix usually cannot be diagonalized by the eigenvectors of the undamped system. Therefore, the difference between the modal frequencies and modal shapes of the damped and undamped systems is great. The modal shape is actually a complex modal shape instead of a real one. The modal frequencies and modal shapes can be obtained by complex mode theory.

For the motion equations of free vibration as follows:

$$\mathbf{M}\ddot{\mathbf{X}} + \mathbf{C}\dot{\mathbf{X}} + \mathbf{K}\mathbf{X} = \mathbf{0} \tag{3-27}$$

where $\mathbf{M}$, $\mathbf{C}$ and $\mathbf{K}$ are respectively the mass, damping and stiffness matrices.

Eq. (3-27) can be transformed into state space equation as follows:

$$\begin{bmatrix} \mathbf{C} & \mathbf{M} \\ \mathbf{M} & \mathbf{0} \end{bmatrix} \begin{Bmatrix} \dot{\mathbf{X}} \\ \ddot{\mathbf{X}} \end{Bmatrix} + \begin{bmatrix} \mathbf{K} & \mathbf{0} \\ \mathbf{0} & -\mathbf{M} \end{bmatrix} \begin{Bmatrix} \mathbf{X} \\ \dot{\mathbf{X}} \end{Bmatrix} = \mathbf{0} \tag{3-28}$$

If we assume $\begin{Bmatrix} \mathbf{X} \\ \dot{\mathbf{X}} \end{Bmatrix} = \begin{Bmatrix} \mathbf{A} \\ s\mathbf{A} \end{Bmatrix} \mathrm{e}^{st}$, then the modal frequencies are the imaginary parts of conjugate eigenvalues s_i, s_i^* ($i = 1, 2, \cdots, N_1$), which can be solved from

$$\left| s \begin{bmatrix} \mathbf{C} & \mathbf{M} \\ \mathbf{M} & \mathbf{0} \end{bmatrix} + \begin{bmatrix} \mathbf{K} & \mathbf{0} \\ \mathbf{0} & -\mathbf{M} \end{bmatrix} \right| = 0 \tag{3-29}$$

The corresponding eigenvectors of s_i and s_i^* can be solved as $\begin{Bmatrix} \mathbf{A}_i \\ s_i \mathbf{A}_i \end{Bmatrix}$ and $\begin{Bmatrix} \mathbf{A}_i^* \\ s_i^* \mathbf{A}_i^* \end{Bmatrix}$, respectively.

The motion corresponding to the conjugate eigenvalues s_i and s_i^* can be expressed as $\mathbf{A}_i \mathrm{e}^{s_i t}$ and $\mathbf{A}_i^* \mathrm{e}^{s_i^* t}$, respectively; apparently, they are conjugate. So for a pair of conjugate eigenvalues s_i and s_i^*, the displacement vector can be obtained as $|\mathbf{A}_i| \sin(\theta_{\mathbf{A}_i} + \mathrm{Im}(s_i)t)$, where $|\mathbf{A}_i|$ and $\theta_{\mathbf{A}_i}$ are the modulus and phase of the elements in $\mathbf{A}_i$. For one specific mode, the variation of every displacement vector with time is known, so that the complex modal shape can be plotted by animation. Then the damping ratio of i[th] mode can be calculated by $\frac{-\mathrm{Re}(s_i)}{\sqrt{\mathrm{Re}(s_i)^2 + \mathrm{Im}(s_i)^2}}$.

In this way, the modal frequency, modal damping ratio and modal shape can be obtained for every complex mode.

3.7 Conclusion

This chapter introduced the research methods that are to be used in the following chapters. A new MISO method was proposed with partial coherences defined to be independent of the sequence of the inputs. A combined optimization algorithm that has a relatively fast optimization speed and good optimization capability was proposed for model calibration. Wilcoxon signed-rank test was introduced for the pairwise comparison. In addition, linear regression analysis was introduced for finding out the linear relationship between two variables. Finally, modal analysis method based on complex mode theory was proposed for obtaining the modal frequency and complex modal shape of a system with non-negligible damping.

Chapter 4 Analysis of ride comfort of high-speed train based on a train-seat-human model in the vertical direction

4.1 Introduction

Ride comfort has become an important index in evaluating the performance of rail vehicles. The ride comfort of rail vehicles including high-speed trains is affected by many factors, e.g., vibration, noise, smell, temperature, humidity and visual stimuli. Among these influencing factors, vibration is generally considered to be an important factor, especially in railway engineering (Suzuki, 1998). Although the vibration on rail vehicles is multi-axis, the vertical direction is always an important one concerning ride comfort, getting the most attention in relevant research.

As the adoption of lightweight technology and the increase of train speed, the elastic vibration of the carbody becomes more and more drastic (Tomioka *et al.*, 2006; Zhou *et al.*, 2009). For analytical models, many studies simplified the carbody as a beam for characterizing its flexural vibration in the vertical direction, and the first bending mode of the carbody with a modal frequency within the human sensitive frequency range was thought to be the primary mode worsening the ride comfort (Diana *et al.*, 2002; Cheli and Corradi, 2011; Shi and Wu, 2016), as discussed in Section 2.4.4.2. Thus, suppressing the first bending mode of the carbody was thought to be a good approach to improving ride comfort (Tomioka and Takigami, 2010; Gong *et al.*, 2012; Shi *et al.*, 2014).

The geometry filter effect of the vehicle including bogie spacing filter effect and wheelbase filter effect is a phenomenon revealing the dependence of resonant or anti-resonant vibration of carbody modes on the geometrical parameter of the train and the train speed (Tanifuji, 1991; Zhou *et al.*, 2009; Cheli and Corradi, 2011; Gong *et al.*, 2012; Cao *et al.*, 2015; Dumitriu, 2015). Zhou et al. (2009), Gong et al. (2012) and Cao et al. (2015) explained the resonant vibration of the rigid-flexible coupled vehicle model by the geometry filter effect and analyzed the factors influencing ride comfort. Because this effect is directly related to intensified vibration of the vehicle that worsens ride comfort, studying the ride comfort from the perspective of this effect and making clear the relationship between the ride comfort index and the geometry filter effect are necessary in order to promote the ride comfort.

Passengers, as the vibration receptor, are interacted with the dynamics of the vehicle by means of the seat. As the development of ergodynamics, it is found the biodynamics of the human body and seating dynamics are complex (Griffin, 1990), which, however, were frequently ignored in the relevant studies about ride comfort. Investigating the coupling of the human-seat system with the vehicle and evaluating the ride comfort directly from the vibration at the human-seat interface is the trend for future research (Carlbom and Berg, 2002; Kumar *et al.*, 2017) (Section 2.4.4.4).

To make clear which modes of the carbody contribute the most to ride comfort is an important step towards the suppression of them. Carlbom and Berg (2002) simply considered the vibration in the frequency range from 0.3 to 7 Hz was induced by rigid modes, and that from 7 to 20 Hz by flexible modes, which is not accurate. Other studies compared a rigid carbody model with a flexible one to illustrate the contribution of flexible modes, e.g., Ling *et al.* (2018). To the best of author's knowledge, the contribution from different modes of the carbody to ride comfort has never been defined accurately or properly, which poses difficulty in finding out the major modes worsening ride comfort.

In this chapter, a rigid-flexible coupled train-seat-human model in the vertical direction was developed. The resonant and anti-resonant vibration of the carbody caused by geometry filter effect was analyzed based on the model and its relationship with the ride comfort was revealed. The ride comfort at the human-seat interface was evaluated and compared with the evaluation on the floor. The contribution from different modes of the carbody to ride comfort was defined and finally, the effects of different parameters on ride comfort were discussed.

4.2 Train-seat-human model for vertical vibration

Aside from the influence of flexible modes of the carbody on ride comfort, rigid-body modes of the carbody normally lie in a relatively low-frequency range around 1 Hz, which also has considerable influence on the ride comfort. The track has much more influence on the dynamics of the vehicle in the high-frequency range than in the low-frequency one (Lu *et al.*, 2008; Cheli and Corradi, 2011; Sun *et al.*, 2014). In this chapter, the frequency range under consideration is very low (0.5-20 Hz), so for simplification, the track was considered to be rigid. The vertical primary and second suspensions were modelled as linear spring-damper units. A total of 19 human-seat subsystems were evenly distributed on the carbody floor with a spacing of l_{hs}, as shown in Fig. 4-1.

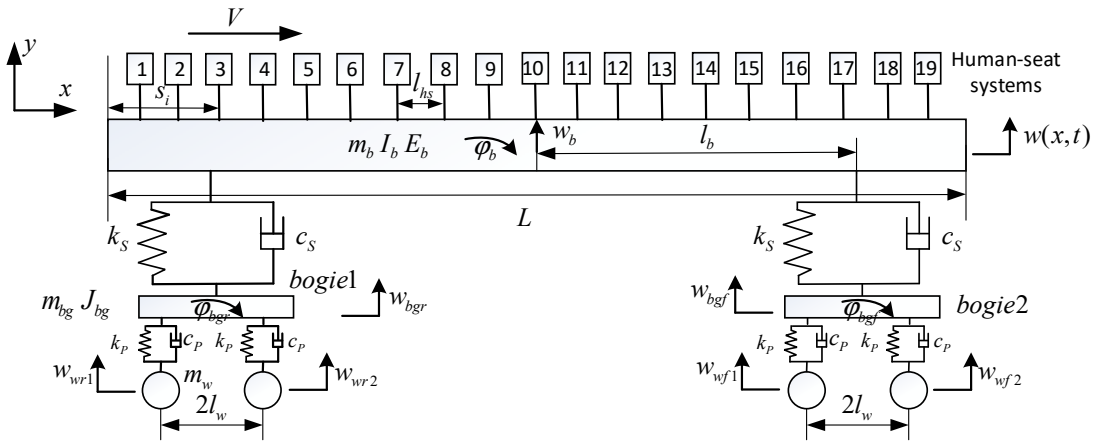

Fig. 4-1 The theoretical model of the train-seat-human system for vertical vibration.

4.2.1 Modelling of the train sub-system

The carbody was modelled as an Euler-Bernoulli beam (Fig. 4-1). Only bounce, pitch and first several bending modes of the carbody were considered. For the analysis purpose set out in this study, this reasonably simple and ideal beam model was adopted to characterize the dynamics of the carbody approximately in the low-frequency range (below 20 Hz). But for more complex carbody or for accurate analysis of the dynamics in the high-frequency range, a carbody model with more realistic structural features is needed. The primary and second suspensions were modelled by springs and dampers. The wheelsets were excited by the vertical profile of a rigid track.

For the carbody, the undamped transverse vibration is characterized by

$$E_b I \frac{\partial^4 w}{\partial x^4} + \rho A \frac{\partial^2 w}{\partial t^2} = -F_{su1}(t)\delta(x-(\frac{L}{2}-l_b)) - F_{su2}(t)\delta(x-(\frac{L}{2}+l_b)) \tag{4-1}$$

where $F_{su1}(t)$ and $F_{su2}(t)$ are the forces from the rear and front second suspensions, respectively.

For the vertical and pitch motions of the carbody, the motion equations are respectively

$$m_b\ddot{w}_b = -m_b g - F_{su1} - F_{su2} \tag{4-2}$$

$$I_b\ddot{\varphi}_b = -F_{su1}l_b + F_{su2}l_b \tag{4-3}$$

For the vertical and pitch motions of the rear and front bogies, the motion equations are respectively

$$m_{bg}\ddot{w}_{bgj} = F_{sui} - F_{bgj1} - F_{bgj2} - m_{bg}g \tag{4-4}$$

$$J_{bg}\ddot{\varphi}_{bgj} = l_w(F_{bgj2} - F_{bgj1}) \tag{4-5}$$

where for the rear bogie, j=r, i=1; for the front bogie, j=f, i=2; F_{bgj1} and F_{bgj2} are the forces transmitted from the first and second wheelsets under the j[th] bogie, respectively.

The wheels were assumed to be closely attached to the rail with no relative motion, just as the treatment in Zhou *et al.* (2009), so the vertical displacements of the wheels equal the vertical profile of the track. All the detailed equations were listed in Appendix B.

The transverse vibration of the carbody due to bending can be expressed by the summation of the product of the modal shapes and modal coordinates as

$$w(x,t) = \sum_{i=1}^{N} \varphi_i(x) p_i(t) \tag{4-6}$$

where $p_i(t)$ is the i[th] generalized modal coordinate and $\varphi_i(x)$ is the corresponding mass normalized bending modal shape of the carbody with free-free boundary condition, which satisfies the ortho-normality conditions:

$$\begin{cases} \rho A \int_0^L \varphi_i(x)\varphi_s(x)\mathrm{d}x = \delta_{is} \\ E_b I \int_0^L \dfrac{\mathrm{d}^4\varphi_i(x)}{\mathrm{d}x^4}\varphi_s(x)\mathrm{d}x = \omega_i^{t2}\delta_{is} \end{cases} \tag{4-7}$$

where $\delta_{is} = \begin{cases} 1, & i = s \\ 0, & i \neq s \end{cases}$.

The natural frequencies of the undamped carbody can be calculated by

$$f_n^t = \frac{v_n^2}{2\pi}\sqrt{\frac{E_b I}{\rho A}},\ n = 1, 2, \cdots \tag{4-8}$$

where v_n ($n = 1, 2, \cdots$) can be solved from the characteristic equation. The parameters of the train from Wu and Yang (2003) were adopted as a simulation example without loss of generality and listed in Table B-1. The modal frequencies of the carbody were then calculated and listed in Table 4-1 (In this chapter, only the first four bending modes were considered). The damping ratio of the n[th] carbody bending mode was assumed as ξ_n ($n = 1, 2, 3, \cdots$).

Table 4-1 Calculated natural frequencies of bending modes of carbody.

Bending mode	1st mode	2nd mode	3rd mode	4th mode
Bending frequency f_n^t (Hz)	9.70	26.76	52.43	86.72

For the train sub-system, the motion equations in matrix form are

$$\mathbf{M}_t\ddot{\mathbf{y}}_t+\mathbf{C}_t\dot{\mathbf{y}}_t+\mathbf{K}_t\mathbf{y}_t=\mathbf{K}_w\mathbf{z}_w+\mathbf{C}_w\dot{\mathbf{z}}_w \tag{4-9}$$

where $\mathbf{y}_t=\left[p_1,p_2,\cdots,p_N,w_b,\varphi_b,w_{bgr},\varphi_{bgr},w_{bgf},\varphi_{bgf}\right]^{\mathrm{T}}$, $\mathbf{z}_w=\left[w_{wf2},w_{wf1},w_{wr2},w_{wr1}\right]^{\mathrm{T}}$, $\mathbf{M}_t$, $\mathbf{C}_t$ and $\mathbf{K}_t$ are respectively the mass, damping and stiffness matrices of the train sub-system; $\mathbf{K}_w$ and $\mathbf{C}_w$ are respectively the stiffness and damping matrices associated with the excitation.

4.2.2 Modelling of the human-seat sub-system

The human model was adopted from Nawayseh and Griffin (2009), which could reflect both the vertical and fore-and-aft motions of the human body under exposure to vertical vibration. The seat was simplified as a rigid body of the mass m_0. The connection between the seat and floor and the contacts between the human body and seat on both the seat pan and backrest interfaces were modelled as springs and dampers (Fig. 4-2).

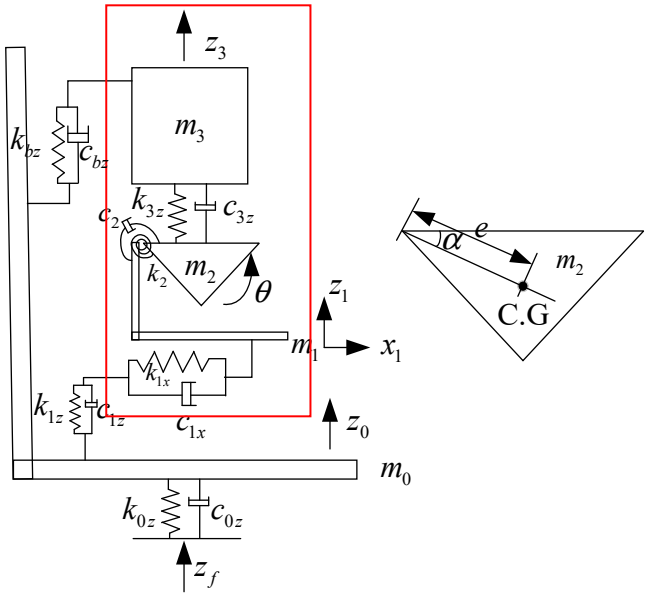

Fig. 4-2 Human-seat model (the adopted human model from Nawayseh and Griffin (2009) is in the red frame).

4.2.2.1 Human model

The motion equations of the human body are expressed in matrix form as follows (refer to Nawayseh and Griffin (2009) for detail)

$$\mathbf{M}_h\ddot{\mathbf{y}}_h + \mathbf{C}_h\dot{\mathbf{y}}_h + \mathbf{K}_h\mathbf{y}_h = \mathbf{M}_{z_1}\ddot{z}_1 + \mathbf{C}_{z_1}\dot{z}_1 + \mathbf{K}_{z_1}z_1 \tag{4-10}$$

where $\mathbf{y}_h = [x_1, z_3, \theta]^{\mathrm{T}}$.

So the transmissibilities can be obtained as

$$\begin{bmatrix} H_{x_1/z_1} & H_{z_3/z_1} & H_{\theta/z_1} \end{bmatrix}^{\mathrm{T}} = (-\omega^2\mathbf{M}_h + \mathrm{j}\omega\mathbf{C}_h + \mathbf{K}_h)^{-1}(-\omega^2\mathbf{M}_{z_1} + \mathrm{j}\omega\mathbf{C}_{z_1} + \mathbf{K}_{z_1}) \tag{4-11}$$

Then the vertical inline and fore-and-aft cross-axis apparent masses on the seat pan are respectively

$$AP_{zz} = m_1 + m_2 + m_3 H_{z_3/z_1} + m_2 e\cos\alpha H_{\theta/z_1} \tag{4-12}$$

$$AP_{zx} = (m_1 + m_2 + m_3)H_{x_1/z_1} + m_2 e\sin\alpha H_{\theta/z_1} \tag{4-13}$$

4.2.2.2 Human-seat model

The kinetic, potential and dissipation energies of the human-seat model are respectively

$$\begin{aligned} T_{hs} &= \frac{1}{2}m_3(\dot{z}_3^2 + \dot{x}_1^2) + \frac{1}{2}I_2\dot{\theta}^2 + \frac{1}{2}m_2[(e\sin\alpha\dot{\theta} + \dot{x}_1)^2 + (e\cos\alpha\dot{\theta} + \dot{z}_1)^2] \\ &+ \frac{1}{2}m_1(\dot{x}_1^2 + \dot{z}_1^2) + \frac{1}{2}m_0\dot{z}_0^2 \end{aligned} \tag{4-14}$$

$$\begin{aligned} U_{hs} &= \frac{1}{2}k_{3z}(z_3 - z_1 - e\theta\cos\alpha)^2 + \frac{1}{2}k_{1x}x_1^2 + \frac{1}{2}k_2\theta^2 + \frac{1}{2}k_{0z}(z_0 - z_f(s_i))^2 \\ &+ \frac{1}{2}k_{bz}(z_3 - z_0)^2 + \frac{1}{2}k_{1z}(z_1 - z_0)^2 \end{aligned} \tag{4-15}$$

$$\begin{aligned} D_{hs} &= \frac{1}{2}c_{3z}(\dot{z}_3 - \dot{z}_1 - e\dot{\theta}\cos\alpha)^2 + \frac{1}{2}c_{1x}\dot{x}_1^2 + \frac{1}{2}c_2\dot{\theta}^2 + \frac{1}{2}c_{0z}(\dot{z}_0 - \dot{z}_f(s_i))^2 \\ &+ \frac{1}{2}c_{bz}(\dot{z}_3 - \dot{z}_0)^2 + \frac{1}{2}c_{1z}(\dot{z}_1 - \dot{z}_0)^2 \end{aligned} \tag{4-16}$$

where

$$z_f(s_i) = w(s_i,t) + w_b(t) - \varphi_b(t)(s_i - \frac{L}{2}) = \mathbf{U}_f(s_i)\mathbf{y}_t,\ i = 1,2,\cdots,N_1 \tag{4-17}$$

is the vertical displacement of the carbody floor under the i[th] seat, where $\mathbf{U}_f(s_i) = [\varphi_1(s_i), \varphi_2(s_i), \cdots, \varphi_N(s_i), \varphi_B(s_i), \varphi_P(s_i), 0, 0, 0, 0]^{\mathrm{T}}$, $\varphi_B(x) = 1$ and $\varphi_P(x) = \frac{L}{2} - x$ are respectively the mode shapes of bounce mode and pitch mode; and N_1 is the number of human-seat sub-systems incorporated with the carbody.

Applying Lagrange's equation,

$$\frac{\mathrm{d}}{\mathrm{d}t}(\frac{\partial T_{hs}}{\partial \dot{\mathbf{y}}_{hs}}) - \frac{\partial T_{hs}}{\partial \mathbf{y}_{hs}} + \frac{\partial U_{hs}}{\partial \mathbf{y}_{hs}} + \frac{\partial D_{hs}}{\partial \dot{\mathbf{y}}_{hs}} = \mathbf{0} \tag{4-18}$$

where $\mathbf{y}_{hs} = [z_0, z_1, x_1, z_3, \theta]^{\mathrm{T}}$.

The motion equations of the human-seat model were obtained and written in matrix form as

$$\mathbf{M}_{hs}\ddot{\mathbf{y}}_{hs} + \mathbf{C}_{hs}\dot{\mathbf{y}}_{hs} + \mathbf{K}_{hs}\mathbf{y}_{hs} = \mathbf{C}_f\dot{z}_f(s_i) + \mathbf{K}_f z_f(s_i) \tag{4-19}$$

where $\mathbf{M}_{hs}$, $\mathbf{C}_{hs}$ and $\mathbf{K}_{hs}$ are respectively the mass, damping and stiffness matrices of the human-seat sub-system, $\mathbf{C}_f$ and $\mathbf{K}_f$ are respectively the damping and stiffness matrices associated with the excitation.

So the transfer matrix from z_f to $\mathbf{y}_{hs}$ is

$$\mathbf{H}_s(\omega) = (-\omega^2\mathbf{M}_{hs} + \mathrm{j}\omega\mathbf{C}_{hs} + \mathbf{K}_{hs})^{-1}(\mathrm{j}\omega\mathbf{C}_f + \mathbf{K}_f) \tag{4-20}$$

The transmissibility from the floor z_f to the human-seat interface z_1 (H_{z_1/z_f}) is the second element in $\mathbf{H}_s(\omega)$.

4.2.2.3 Model calibration

Firstly, calibration of the human model was carried out in which the parameters related to the human model, that is, m_2, m_3, I_2, k_{1x}, c_{1x}, k_2, c_2, k_{3z}, c_{3z}, e, α, m_1, were determined.

The objective function for the calibration is the error between the vertical in-line and fore-and-aft cross-axis apparent masses calculated by the model and those measured in the experiment as follows:

$$\text{error} = \sum_{j=zz,zx} w_j \left\{ \sqrt{\frac{\sum_{i=1}^{N_2} (\text{Re}(AP_j(f_i))_e - \text{Re}(AP_j(f_i))_m)^2}{N_2}} + \sqrt{\frac{\sum_{i=1}^{N_2} (\text{Im}(AP_j(f_i))_e - \text{Im}(AP_j(f_i))_m)^2}{N_2}} \right\} \tag{4-21}$$

where the subscripts e and m represent the data from the experiment and model, respectively, N_2 stands for the total number of the corresponding apparent mass points; w_{zz} and w_{zx} are the weighting factors.

The apparent mass for calibration was derived from the experimental data in Chapter 6. The subject of 83.5 kg in weight and 171 cm in height seated on a rigid seat under 0.25 m/s^2 r.m.s. single-axis vertical random vibration was chosen as the target for calibration. The model was calibrated in 0.5-20 Hz with the optimization algorithm introduced in Section 3.3 and all the data obtained from the calibration were listed in Table B-1. Fig. 4-3 showed good agreement between the model and experiment for both the vertical in-line apparent mass and the fore-and-aft cross-axis apparent mass.

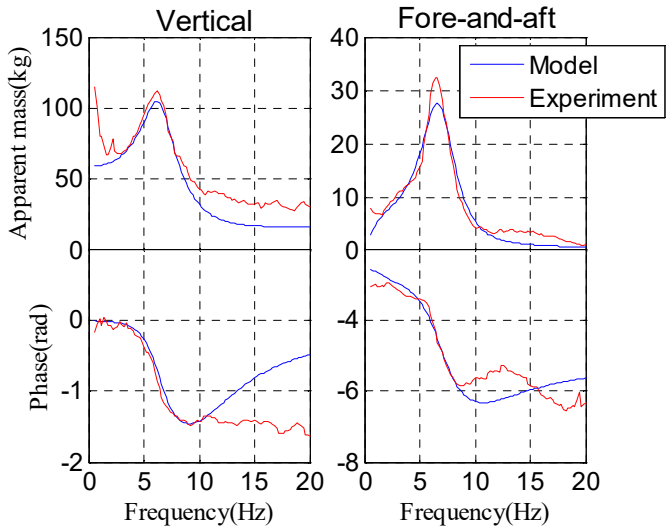

Fig. 4-3 Comparison of the vertical inline apparent mass (left) and fore-and-aft cross-axis apparent mass (right) between the model and experiment.

Then the human-seat model was calibrated by the seat vertical transmissibility with the determined parameters for the human model. The other parameters, that is, k_{bz}, c_{bz}, k_{1z}, c_{1z}, k_{0z} and c_{0z}, were calibrated by minimizing the error between the calculated vertical transmissibility (floor to the human-seat interface) of the model and that obtained experimentally with the same subject sitting on a train seat under the vertical random excitation of 0.25 m/s^2 r.m.s. in the laboratory experiment of Chapter 8 in 0.5-20 Hz. The error between the transmissibility calculated by the model and that measured in the experiment was taken as the calibration objective function as follows:

$$\text{error} = \sqrt{\frac{\sum_{i=1}^{N_3}(\text{Re}(H_{z_1/z_f}(f_i))_e - \text{Re}(H_{z_1/z_f}(f_i))_m)^2}{N_3}} + \sqrt{\frac{\sum_{i=1}^{N_3}(\text{Im}(H_{z_1/z_f}(f_i))_e - \text{Im}(H_{z_1/z_f}(f_i))_m)^2}{N_3}} \quad (4\text{-}22)$$

where the subscripts e and m represent the data from the experiment and model, respectively, N_3 stands for the total number of the transmissibility points.

In the same way, the calibration was carried out by means of the optimization algorithm mentioned in Section 3.3 and the obtained parameters were listed in Table B-1. The calculated transmissibility by the model was compared with the experiment in Fig. 4-4, which showed good agreement. It can be seen that the developed seat-human model is reasonably acceptable for the current study.

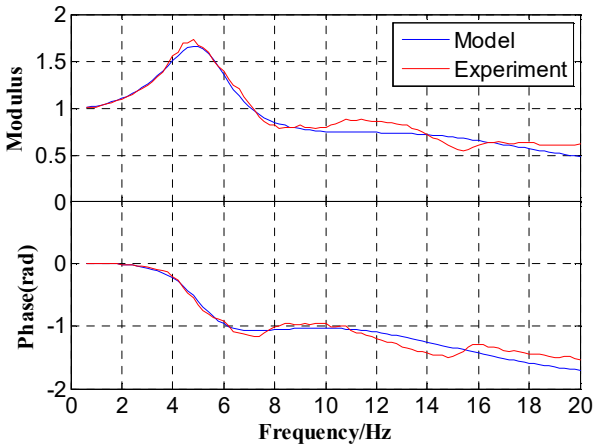

Fig. 4-4 The comparison of the vertical transmissibility from the floor z_f to the seat-human interface z_1 between the model and experiment.

4.2.3 Coupling between the train sub-system and human-seat sub-systems

For simplicity, all the human-seat sub-systems are assumed to be the same. For the coupled train-seat-human system, the motion equations are expressed in matrix form as follows:

$$\mathbf{M}_c\ddot{\mathbf{y}}_c+\mathbf{C}_c\dot{\mathbf{y}}_c+\mathbf{K}_c\mathbf{y}_c=\mathbf{K}_{cw}\mathbf{z}_w+\mathbf{C}_{cw}\dot{\mathbf{z}}_w \tag{4-23}$$

where $\mathbf{M}_c=\begin{bmatrix}\mathbf{M}_t & & & \\ & \mathbf{M}_{hs} & & \\ & & \ddots & \\ & & & \mathbf{M}_{hs}\end{bmatrix}$, $\mathbf{C}_c=\begin{bmatrix}\mathbf{C}_t+c_{0z}\sum_{i=1}^{N_1}\mathbf{U}_f(s_i)^{\mathrm{T}}\mathbf{U}_f(s_i) & -(\mathbf{C}_f\mathbf{U}_f(s_1))^{\mathrm{T}} & \cdots & -(\mathbf{C}_f\mathbf{U}_f(s_{N_1}))^{\mathrm{T}} \\ -\mathbf{C}_f\mathbf{U}_f(s_1) & \mathbf{C}_{hs} & & \\ \vdots & & \ddots & \\ -\mathbf{C}_f\mathbf{U}_f(s_{N_1}) & & & \mathbf{C}_{hs}\end{bmatrix}$

and $\mathbf{K}_c=\begin{bmatrix}\mathbf{K}_t+k_{0z}\sum_{i=1}^{N_1}\mathbf{U}_f(s_i)^{\mathrm{T}}\mathbf{U}_f(s_i) & -(\mathbf{K}_f\mathbf{U}_f(s_1))^{\mathrm{T}} & \cdots & -(\mathbf{K}_f\mathbf{U}_f(s_{N_1}))^{\mathrm{T}} \\ -\mathbf{K}_f\mathbf{U}_f(s_1) & \mathbf{K}_{hs} & & \\ \vdots & & \ddots & \\ -\mathbf{K}_f\mathbf{U}_f(s_{N_1}) & & & \mathbf{K}_{hs}\end{bmatrix}$ are respectively the mass, damping and stiffness matrices of the train-seat-human system; $\mathbf{y}_c=\begin{bmatrix}\mathbf{y}_t \\ \mathbf{y}_{hs1} \\ \vdots \\ \mathbf{y}_{hsN_1}\end{bmatrix}$, where $\mathbf{y}_{hsi}$ is the coordinate vector for i[th] human-seat sub-system; $\mathbf{K}_{cw}=\begin{bmatrix}\mathbf{K}_w \\ \mathbf{O}\end{bmatrix}$ and $\mathbf{C}_w=\begin{bmatrix}\mathbf{C}_w \\ \mathbf{O}\end{bmatrix}$ are respectively the stiffness and damping matrices associated with the wheel inputs.

4.2.4 Vertical input—Vertical profile

Since the real irregularity of the track was not available, the simulation was conducted by considering a track irregularity having the same PSD as German vertical profile (Section 2.4.2). Assume the train runs at a constant speed of V, so the temporal spectrum is

$$S_w(\omega,V)=S(\frac{\omega}{V})\frac{1}{V}=\frac{A_v\Omega_c^2V^3}{(V\Omega_r+\mathrm{j}\omega)(V\Omega_r-\mathrm{j}\omega)(V\Omega_c+\mathrm{j}\omega)(V\Omega_c-\mathrm{j}\omega)} \tag{4-24}$$

where $S(\Omega)$ is the spatial spectrum of track vertical profile, ω is the angular frequency (rad/s), A_v is an amplitude constant, Ω_r and Ω_c are two frequency constants.

The temporal spectrum of the vertical profile increases with the growth of wavelength and the drop of speed, but the wavelength dominates over the speed. The parameters were adopted from the 6th track class in Kargarnovin *et al.* (2005), and listed in Table B-1.

4.3 The effect of human-seat systems on the carbody

4.3.1 Modelling of carbody with different distributions of human-seat system

Different human-seat system distributions may influence the dynamic properties of the carbody, so the effect of human-seat systems on the carbody was studied in the frequency domain. Only four kinds of human-seat system distributions were studied and listed in Table 4-2 and Fig. 4-5. All the human-seat systems incorporated were the same as Section 4.2.2.

Table 4-2 The four kinds of distributions of human-seat systems with reference to Fig. 4-5

Four cases	Human-seat systems
Empty	none
Uniformly distributed	Part A + Part B
Middle	Part B
Ends	Part A

Fig. 4-5 The diagram of different distributions of human-seat systems (Note one square represents one human-seat system and the seat positions are the same as Fig. 4-1).

The motion equation of the undamped carbody with human-seat systems is

$$\rho A\frac{\partial^2 w}{\partial t^2}+E_b I\frac{\partial^4 w}{\partial x^4}=-\sum_{j=1}^{K}F_{pj}(x,t)\delta(x-s_j) \tag{4-25}$$

where $F_{pj}=(k_{0z})_j((z_F)_j-(z_0)_j)+(c_{0z})_j((\dot{z}_F)_j-(\dot{z}_0)_j)$ represents the force transmitted from the jth human-seat system, where $(*)_i$ represents * from ith human-seat system, and K is the total number of human-seat systems; $(z_F)_j$ is the displacement from the floor due to carbody bending under the jth human-seat system as follows

$$(z_F)_j=\sum_{i=1}^{N}\phi_i(s_j)p_i(t) \tag{4-26}$$

The displacement vector from the floor is expressed as

$$\mathbf{z}_F = ((z_F)_1, (z_F)_2, \cdots, (z_F)_K)^{\mathrm{T}} = \mathbf{D}\mathbf{p} \tag{4-27}$$

where $\mathbf{D} = \begin{bmatrix} \phi_1(s_1) & \phi_2(s_1) & \cdots & \phi_N(s_1) \\ \phi_1(s_2) & \phi_2(s_2) & \cdots & \phi_N(s_2) \\ \vdots & \vdots & & \vdots \\ \phi_1(s_K) & \phi_2(s_K) & \cdots & \phi_N(s_K) \end{bmatrix}$, $\mathbf{p} = (p_1, p_2, \cdots, p_N)^{\mathrm{T}}$, N is the number of carbody bending modes considered.

Then Eq. (4-25) can be transformed into the differential equation by the modal summation method, and the damped carbody model with K human-seat systems can be organized in matrix form as follows:

$$\mathbf{M}_W \ddot{\mathbf{X}} + \mathbf{C}_W \dot{\mathbf{X}} + \mathbf{K}_W \mathbf{X} = \mathbf{0} \tag{4-28}$$

where $\mathbf{M}_W$, $\mathbf{C}_W$ and $\mathbf{K}_W$ are respectively the mass, damping and stiffness matrices of the complete system, and $\mathbf{X} = (\mathbf{p}, \mathbf{x}_1, \mathbf{z}_3, \boldsymbol{\theta}, \mathbf{z}_0, \mathbf{z}_1)^{\mathrm{T}}$, $\mathbf{x}_1 = [(x_1)_1, (x_1)_2, \cdots, (x_1)_N]^{\mathrm{T}}$, and the same applies to $\mathbf{z}_3$, $\boldsymbol{\theta}$, $\mathbf{z}_0$ and $\mathbf{z}_1$.

4.3.2 A reduced-order model

If the FRFs from the floor z_f to x_1, z_3, θ, z_0, z_1 are the same for every human-seat system, then they can be denoted as T_{fx_1}, T_{fz_3}, $T_{f\theta}$, T_{fz_0} and T_{fz_1}, respectively. That is the case if all the human-seat systems considered are the same. So the following is satisfied after Fourier transform,

$$\mathcal{F}(\mathbf{Y}) = T_{fY}\mathcal{F}(\mathbf{z}_F) = T_{fY}\mathbf{D}\mathcal{F}(\mathbf{p}) \tag{4-29}$$

where the subscript Y can be x_1, z_3, θ, z_0 and z_1; correspondingly, $\mathbf{Y}$ can be $\mathbf{x}_1$, $\mathbf{z}_3$, $\boldsymbol{\theta}$, $\mathbf{z}_0$ and $\mathbf{z}_1$. Define $\mathcal{F}(\mathbf{p}_Y) = T_{fY}\mathcal{F}(\mathbf{p})$, after inverse Fourier transform, the following relation can be obtained as

$$\mathbf{Y} = \mathbf{D}\mathbf{p}_Y \tag{4-30}$$

With this relation, the dimension of $\mathbf{Y}$ (K, the number of human-seat systems) can be reduced to the dimension of $\mathbf{p}_Y$ (N, the number of carbody bending modes considered). Then the model can be reduced from $N+5K$ to $6N$ only when K is larger than N that is usually satisfied.

Then a reduced-order model of Eq. (4-28) can be put forward as follows:

$$\mathbf{M}_R\ddot{\mathbf{X}}_R+\mathbf{C}_R\dot{\mathbf{X}}_R+\mathbf{K}_R\mathbf{X}_R=\mathbf{0} \tag{4-31}$$

where $\mathbf{X}_R=(\mathbf{p},\mathbf{p}_{x_1},\mathbf{p}_{z_3},\mathbf{p}_\theta,\mathbf{p}_{z_0},\mathbf{p}_{z_1})^{\mathrm{T}}$, $\mathbf{M}_R$, $\mathbf{C}_R$ and $\mathbf{K}_R$ are the corresponding mass, damping and stiffness matrices of the reduced-order system, respectively.

4.3.3 The comparison among different distributions

The modal frequency and damping can be obtained by solving the complex eigenvalues s_i (in conjugate pairs) ($i=1,2,..,6N$) from the following equation according to Eq (4-31),

$$\left|s_i\begin{bmatrix}\mathbf{C}_R & \mathbf{M}_R\\ \mathbf{M}_R & \mathbf{O}\end{bmatrix}+\begin{bmatrix}\mathbf{K}_R & \mathbf{O}\\ \mathbf{O} & -\mathbf{M}_R\end{bmatrix}\right|=0 \tag{4-32}$$

The modal frequency is $\mathrm{Im}(s_i)/2\pi$ Hz, and the modal damping ratio is calculated by $-\mathrm{Re}(s_i)/\sqrt{\mathrm{Re}(s_i)^2+\mathrm{Im}(s_i)^2}$.

Table 4-3 The modal frequencies and modal damping ratios of the first four modes of the carbody with different human-seat distributions.

Different distributions	1st mode*	2nd mode	3rd mode	4th mode
Empty	9.70/0.0050	26.75/0.0050	52.43/0.0050	86.72/0.0050
Uniformly distributed	9.66/0.0113	26.61/0.0064	52.11/0.0056	86.17/0.0054
Middle	9.68/0.0084	26.67/0.0058	52.30/0.0053	86.42/0.0052
Ends	9.68/0.0078	26.69/0.0056	52.25/0.0054	86.47/0.0052

*The values before the slash are modal frequencies with the unit of Hz, those after the slash are modal damping ratios.

The carbody bending frequencies and the corresponding damping ratios were listed in Table 4-3. Compared to 'empty' carbody, 'Middle', 'Ends' and 'Uniformly distributed' distributions have lower frequencies and higher modal damping ratios. The frequencies and damping ratios of the two distributions—'Middle' and 'Ends' are very close. 'Uniformly distributed' always has the lowest modal frequency and highest damping ratio, followed by 'Middle' and 'Ends'. The effect of human-seat systems on the bending modes of the carbody is overall small, however, sometimes their effect cannot be ignored, because the damping ratio can be changed to more than twice the original one,

the conclusion of which is similar to Dossing (1984) and Carlbom (2000). It can be seen that human-seat systems have the tendency to reduce the modal frequencies and increase the modal damping ratios of the carbody modes, and usually, the larger the decrease of the modal frequency is, the larger the increase of the modal damping ratio is.

In the following analysis, the human-seat systems were uniformly distributed on the carbody, as shown in Fig. 4-1.

4.4 The application of bogie spacing filter effect

The frequency response functions (FRF) from the input $\mathbf{z}_w$ to the displacement $\mathbf{y}_c$ ($\mathbf{H}_c(\omega)$) and the acceleration $\ddot{\mathbf{y}}_c$ ($\mathbf{H}_{\mathrm{c}}^a(\omega)$) were respectively obtained as follows:

$$\mathbf{H}_c(\omega)=[-\omega^2\mathbf{M}_c+\mathrm{j}\omega\mathbf{C}_c+\mathbf{K}_c]^{-1}(\mathbf{K}_w+\mathrm{j}\omega\mathbf{C}_w)=[\mathbf{H}_{c1}(\omega),\mathbf{H}_{c2}(\omega),\mathbf{H}_{c3}(\omega),\mathbf{H}_{c4}(\omega)] \tag{4-33}$$

$$\mathbf{H}_{\mathrm{c}}^a(\omega)=-\omega^2\mathbf{H}_c(\omega) \tag{4-34}$$

where $\mathbf{H}_{ci}(\omega)$ ($i=1,...,4$) is the frequency response function from the i[th] wheelset.

Taking into account the time delay between four wheelsets, the system can be considered as a single-input and multiple-output (SIMO) system, the FRF from w_{wf2} to $\mathbf{y}_c$ then becomes

$$\mathbf{H}_c^t(\omega,V)=\mathbf{H}_c(\omega)\mathbf{H}_w(\omega,V) \tag{4-35}$$

where $\mathbf{H}_w(\omega,V)=\begin{bmatrix}1 & e^{-\mathrm{j}\omega\tau_1} & e^{-\mathrm{j}\omega\tau_2} & e^{-\mathrm{j}\omega(\tau_1+\tau_2)}\end{bmatrix}^{\mathrm{T}}$, $\tau_1=\dfrac{2l_w}{V}$ and $\tau_2=\dfrac{2l_b}{V}$ are the time delays.

In the train-seat-human model (Eq.(4-23)), the power spectral densities (PSD) of $\mathbf{y}_c$ and $\ddot{\mathbf{y}}_c$ are respectively

$$\mathbf{S}_{\mathbf{y}_c}(\omega,V)=\mathbf{H}_c^{t\,*}(\omega,V)S_w(\omega,V)\mathbf{H}_c^{t\,\mathrm{T}}(\omega,V) \tag{4-36}$$

$$\mathbf{S}_{\ddot{\mathbf{y}}_c}(\omega,V)=\omega^4\mathbf{S}_{\mathbf{y}_c}(\omega,V) \tag{4-37}$$

where $S_w(\omega,V)$ is the PSD of the wheel input in Eq. (4-24). The auto-spectral densities located in the diagonal of $\mathbf{S}_{\mathbf{y}_c}(\omega,V)$ and $\mathbf{S}_{\ddot{\mathbf{y}}_c}(\omega,V)$.

According to the principle of geometry filter effect analyzed in Appendix B, because every mode shows a global maximum around its natural frequency in FRF (Fig. B-1), so does it in PSD. Taking advantage of the bogie spacing filter effect of the carbody, in order to cause the resonant or anti-resonant vibration of ith carbody mode (f_i^t), the excited frequency must equal the modal frequency of the carbody, that is, to cause the resonant vibration of carbody's anti-symmetrical modes or anti-resonant vibration of symmetrical modes, it should satisfy $f_i^t = \frac{V(2n-1)}{4l_b}$; Similarly, to cause resonant vibration of symmetrical modes or anti-resonant vibration of anti-symmetrical modes, it should satisfy $f_i^t = \frac{Vn}{2l_b}$. Since $\frac{V}{\lambda} = f_i^t$, if λ is fixed, only one speed can cause resonant or anti-resonant vibration of a certain mode; If V is fixed, only one specific wavelength can result in resonant or anti-resonant vibration of a specific mode.

The resonant and anti-resonant speeds of bounce and pitch modes are usually less than 150 km/h that is not under consideration given that the natural frequencies of bounce and picth modes are usually around 1 Hz, so the bogie spacing filter effect of these two modes is not obvious in the considered speed range (150-350 km/h). The acceleration PSDs of the first four bending modal coordinates, that is, $S_{\ddot{p}_1}(\omega)$, $S_{\ddot{p}_2}(\omega)$, $S_{\ddot{p}_3}(\omega)$, $S_{\ddot{p}_4}(\omega)$, were calculated in the speed range from 150 km/h to 350 km/h. At each speed, the peak of the PSD around the modal frequencies of every mode was selected, as shown in Fig. 4-6. The peak and trough values that can be predicted from the bogie spacing filter effect were labelled with red and green circles, respectively. All the peaks and troughs that were predicted by the bogie spacing filter effect were listed in Table 4-4, and those that can be found in Fig. 4-6 were labelled by '+'. It could be seen from Fig. 4-6 that the peaks and troughs generated by the bogie spacing filter effect was clear and almost all the peaks and troughs can be predicted by the bogie spacing filter effect.

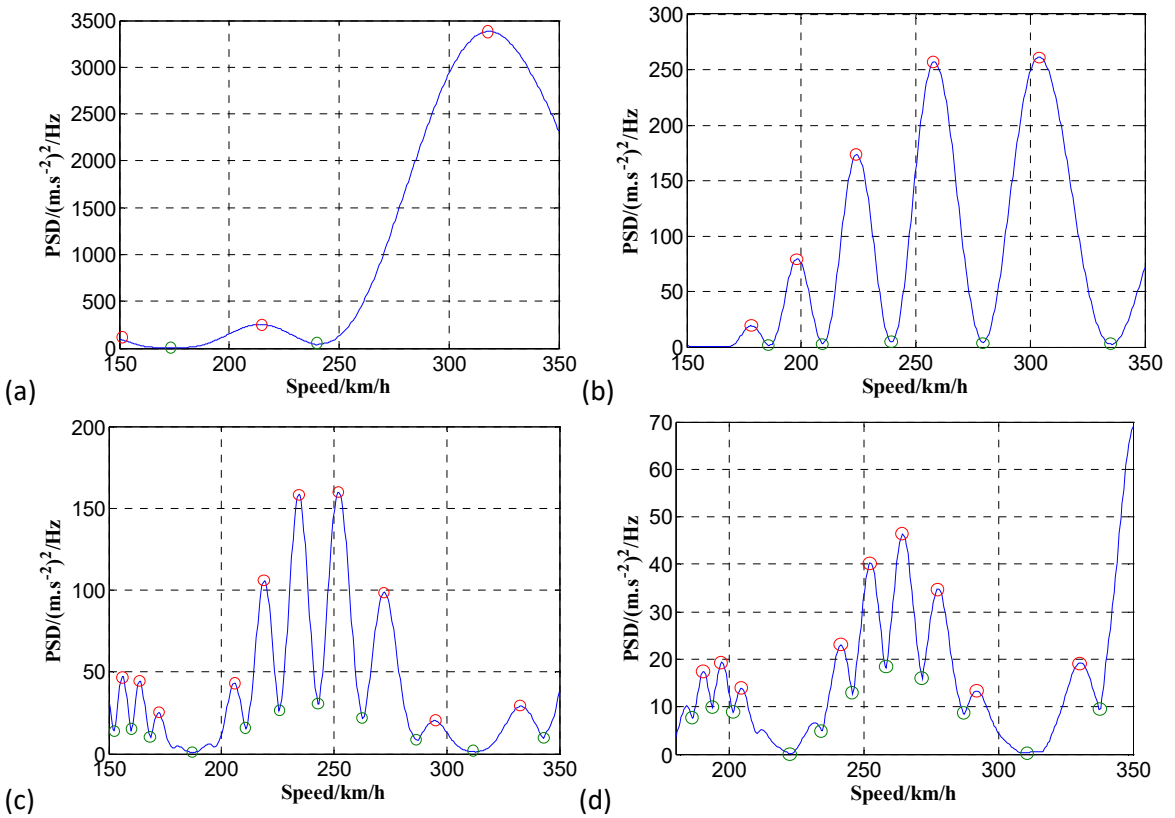

Fig. 4-6 Peak acceleration PSD of the first four bending modal coordinates varying with speed (a) 1st bending mode, $S_{\ddot{p}_1}(\omega)$; (b) 2nd bending mode, $S_{\ddot{p}_2}(\omega)$; (c) 3rd bending mode, $S_{\ddot{p}_3}(\omega)$; (d) 4th bending mode, $S_{\ddot{p}_4}(\omega)$ (red circle and green circle stand for peak and trough respectively that can be predicted by the bogie spacing filter effect).

When the speed is constant, the higher the bending mode frequency is, the lower the wavelength is, the smaller the PSD introduced by the track irregularity is. Therefore, less PSD is introduced into higher mode, resulting in smaller output PSD.

For the same mode, the higher the speed is, the higher the wavelength is, the larger the PSD introduced by the track irregularity usually is. This is because the wavelength dominates over speed in the PSD of the track irregularity.

It is clear that the resonant vibration of the first bending mode is the most drastic compared with the other three (Fig. 4-6), so among all the bending modes of the carbody, the first one is the most significant.

Table 4-4 Comparison of the calculated peak and trough speeds between the complete model and bogie spacing filter analysis.

Bending mode*	1st mode	2nd mode	3rd mode	4th mode
$n=2$	306(+)/NA			
$n=3$	204(+)/244(+)			
$n=4$	153(+)/175(+)			
$n=5$		NA/337(+)		
$n=6$		306(+)/281(+)		
$n=7$		259(+)/241(+)		
$n=8$		225(+)/211(+)		
$n=9$		198(+)/187(+)		
$n=10$		177(+)/169	330(+)/348(+)	
$n=11$		160/153	300(+)/315(+)	
$n=12$			275(+)/287(+)	
$n=13$			254(+)/264(+)	
$n=14$			236(+)/245(+)	
$n=15$			220(+)/228(+)	
$n=16$			206(+)/213(+)	NA/341(+)
$n=17$			194/200	331(+)/321(+)
$n=18$			183/189(+)	312/304
$n=19$			173(+)/179	295(+)/288(+)
$n=20$			165(+)/169(+)	280(+)/273(+)
$n=21$			157(+)/161(+)	267(+)/260(+)
$n=22$			NA/153(+)	254(+)/248(+)
$n=23$				242(+)/238(+)
$n=24$				232/227
$n=25$				223/218(+)
$n=26$				214/210
$n=27$				206(+)/202(+)
$n=28$				199(+)/195(+)
$n=29$				192(+)/188(+)

*Peak value/trough value predicted by bogie spacing filter effect, separated by slash; sign '+' indicates the values that can be found in Fig. 4-6, labelled with red and green circles.

4.5 Analysis of ride comfort

4.5.1 Evaluation of ride comfort

The frequency response function of the acceleration under the i[th] seat on the carbody floor from w_{wf2} can be expressed as

$$H_{cb}^{a}(s_i,\omega)=-\omega^2[\mathbf{U}_f(s_i),\underbrace{0,\cdots,0}_{5N_1}]\mathbf{H}_c^t(\omega,V),\ i=1,2,\cdots,N_1 \tag{4-38}$$

The PSD of the vertical acceleration at the i[th] seat position on the floor is

$$S_{\ddot{z}_f}(s_i,\omega,V)=\left|H_{cb}^{a}(s_i,\omega)\right|^2 S_w(\omega,V) \tag{4-39}$$

At different seat positions, the modes that play major roles in the response will be different. If the symmetrical modes dominate, the geometry filter effect of these modes will dominate in the PSD of the response, and the same applies to anti-symmetrical modes.

To transform the vibration into the one perceived by the human body, ISO (1997) suggests the vertical vibration at the seat surface be frequency weighted by W_k. So the weighted PSD becomes

$$S_{\ddot{z}_1 p}(s_i,\omega,V)=\left|W_k(\mathrm{j}\omega)\right|^2 S_{\ddot{z}_1}(s_i,\omega,V) \tag{4-40}$$

where $S_{\ddot{z}_1}(s_i,\omega,V)$ is auto-spectral density of the vertical acceleration at the human-seat interface $\ddot{z}_1$ for i[th] human-seat system obtained from Eq. (4-37), while $S_{\ddot{z}_1 p}(s_i,\omega,V)$ is the corresponding weighted auto-spectral density. After the human-seat system is determined, the transmissibility T_{z_1/z_f} from the floor (z_f) to the human-seat interface (z_1) is determined accordingly, so it satisfies that

$$S_{\ddot{z}_1}(s_i,\omega,V)=\left|T_{z_1/z_f}\right|^2 S_{\ddot{z}_f}(s_i,\omega,V) \tag{4-41}$$

The PSDs of the accelerations at the floor of carbody and the human-seat interface for seat 10 (center) before weighting and after weighting were compared, as shown in Fig. 4-7. The PSD at the floor was amplified below 7 Hz, however, attenuated above 7 Hz because of the effect of the human-seat system (Fig. 4-4). There was an obvious peak at the first bending frequency (about 9.7 Hz). After the frequency weighting, this peak remained almost the same, but the magnitude of PSD beyond 4-12.5 Hz was attenuated. In addition, because of the significant effect of the first bending mode, the geometry filter effect of the symmetrical modes was dominant over anti-symmetrical modes and retained in the acceleration PSD on the floor, at the human-seat interface as well as in the weighted acceleration PSD at the human-seat interface.

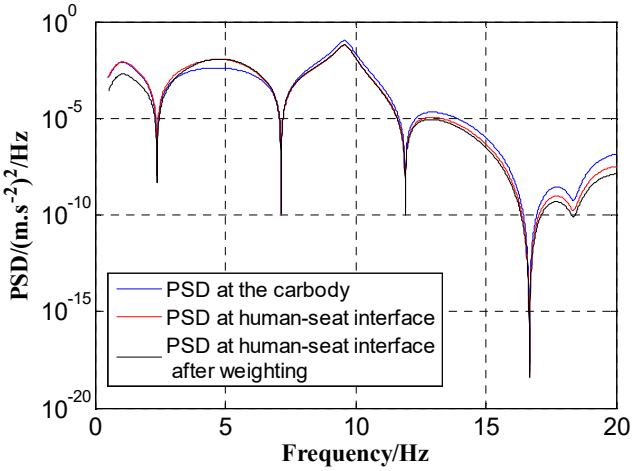

Fig. 4-7 The comparison between the acceleration PSD on the carbody floor and at the human-seat interface before weighting and after weighting at seat 10 (center) when V=300 km/h.

The ride comfort was evaluated using the r.m.s. value of the weighted vertical acceleration at the human-seat interface (called 'equivalent acceleration' next), calculated by

$$a_w(s_i,V)=\left[\int_{0.5}^{20} S_{\ddot{z}_1 p}(s_i,\omega,V)\mathrm{d}f\right]^{\frac{1}{2}} \tag{4-42}$$

A narrower frequency range than ISO (1997) was adopted in this integral, considering that the weighting function drops sharply and the seat will usually attenuate the acceleration greatly above 20 Hz. In addition, other evaluation methods may be used and one can be transformed into another according to Kim *et al.* (2003b).

4.5.2 Prediction of peaks and troughs

Through the above analysis, the first bending mode alone seems sufficient to explain the resonant or anti-resonant vibration of the vehicle because its PSD is much larger than other bending modes (Fig. 4-6), and the geometry filter effect of the rigid-body modes is not obvious at high speed. In addition, when the first bending mode is dominant, the geometry filter effect of symmetrical modes was retained in the weighted acceleration PSD at the human-seat interface. Thus, when the bogies' position and the seat position are both far from the nodes of the first bending mode, and when the resonant (or anti-resonant) vibration of the first bending mode takes place, the equivalent acceleration will correspondingly reach a peak (or trough). Based on this observation, the following prediction according to Section 4.4 may be made:

(a) For the curve of a_w varying with the first bending frequency or bending rigidity, at a specific speed V, the first bending frequency corresponding to the peaks can be predicted by $f_1^t = \frac{V}{2l_b / n}$, and the first bending frequency corresponding to the troughs can be predicted by $f_1^t = \frac{V}{4l_b / (2n-1)}$. The corresponding bending rigidity can be calculated from Eq. (4-8).

(b) For the curve of a_w varying with speed, at a specific first bending frequency, the speeds corresponding to the peaks can be predicted by $V = f_1^t \frac{2l_b}{n}$, and the speeds that correspond to the trough can be predicted by $V = f_1^t \frac{4l_b}{2n-1}$.

This prediction will be validated in the following analysis.

4.5.3 The contribution of different modes

The contribution of different modes of carbody to the equivalent acceleration can be defined from the perspective of power spectral density. The vertical displacement on the floor under the ith seat is the summation of different modes, that is,

$$z_f(s_i,t) = z_{m_1}(s_i,t) + z_{m_2}(s_i,t) + \cdots + z_{m_n}(s_i,t) \tag{4-43}$$

where z_{m_j} is the contribution from the jth set of modes, n is the total number of mode sets.

According to Eqs. (4-40)-(4-42), the equivalent acceleration evaluated on the human-seat interface of ith seat in Eq. (4-42) can be expressed as

$$a_w(s_i,V) = \left[\int_{0.5}^{20} \left|W_k(\mathrm{j}\omega)\right|^2 \omega^4 \left|T_{z_1/z_f}\right|^2 S_{z_f}(s_i,\omega,V)\mathrm{d}f \right]^{\frac{1}{2}} \tag{4-44}$$

$S_{z_f}(s_i,\omega,V)$ is the summation of every element in the matrix $\begin{bmatrix} S_{m_1} & S_{m_1m_2} & \cdots & S_{m_1m_n} \\ S_{m_2m_1} & S_{m_2} & \cdots & S_{m_2m_n} \\ \vdots & \vdots & \ddots & \vdots \\ S_{m_nm_1} & S_{m_nm_2} & \cdots & S_{m_n} \end{bmatrix}$,

where $S_{m_im_j}$ is the cross-spectral density (CSD) between $z_{m_i}(t)$ and $z_{m_j}(t)$ ($i \neq j$), S_{m_i} is the auto-spectral density of $z_{m_i}(t)$. The ideal case is all the off-diagonal elements are zero, that is, the CSDs are zero. In reality, the off-diagonal elements cannot all be zero because of the dynamic interaction between different modes.

The contribution from i[th] mode set (a_{m_i}) can be defined by substituting S_{z_f} in Eq. (4-44) only by S_{m_i}, the contribution from the coherent part (a_{coh}) by substituting S_{z_f} by all the off-diagonal elements. So it satisfies that

$$a_w{}^2 = \sum_{i=1}^{n} a_{m_i}{}^2 + a_{coh}{}^2 \tag{4-45}$$

where $a_{m_i} \geq 0$, but $a_{coh}{}^2$ can be negative, so when the coherent part has a positive effect on a_w, a_{coh} is a real value; on the contrary, a_{coh} is a pure imaginary value.

In the following analysis, four mode sets were taken into account, that is, bounce mode, pitch mode, the first bending mode, and other bending modes. The contribution of these mode sets and their coherent parts was evaluated.

4.5.4 Results of analyses in ride comfort

This section was to analyze the ride comfort of high-speed trains, and to examine the effect of different factors (i.e., bending rigidity of carbody, speed, damping ratio of carbody bending modes, seat position, as well as the stiffness and damping of the suspensions and seat-human contact) on the ride comfort of high-speed trains.

4.5.4.1 The necessity of the human-seat system

Most of the papers evaluated the ride comfort by the acceleration measured on the floor, ignoring the effect of the human-seat system (Xu *et al.*, 2009; Zhang *et al.*, 2013). However, considering the

low-frequency amplification and high-frequency attenuation effects of the human-seat system, the accelerations on the floor and on the human-seat interface can differ a lot.

In Eq. (4-42), if z_1 was replaced by z_f, the acceleration on the floor would be adopted instead of that on the human-seat interface in the evaluation of ride comfort, results were compared to show the necessity of human-seat system.

The performance of the seat could also be evaluated by the SEAT value (Griffin, 1990), defined as

$$\mathrm{SEAT}\% = \left[\frac{\int_{0.5}^{20} \left| W_k(\mathrm{j}\omega) \right|^2 S_{\ddot{z}_1}(s_i, \omega, V) \mathrm{d}f}{\int_{0.5}^{20} \left| W_k(\mathrm{j}\omega) \right|^2 S_{\ddot{z}_f}(s_i, \omega, V) \mathrm{d}f} \right]^{\frac{1}{2}} \times 100 \tag{4-46}$$

It is the ratio of a_w value evaluated at the human-seat interface to that on the floor.

Changing the bending rigidity ($E_b I$) of the carbody, the natural frequencies of the carbody would change accordingly (Eq. (4-8)). Based on this change, the ride comfort was evaluated on the floor and human-seat interface, respectively. As illustrated in Fig. 4-8, two evaluations of ride comfort at seat 10 (center) differed a lot for different speeds with different bending rigidities, especially at low bending rigidity. Because the geometry filter effect was retained in the accelerations on both the floor and the human-seat interface, according to the prediction in Section 4.5.2, the prediction results were quite close to those in Fig. 4-8. For example, when the speed is 350 km/h, the predicted first bending frequencies corresponding to the peaks are 5.55 and 11.11 Hz, corresponding to troughs are 8.33 and 13.89 Hz respectively. The predicted values were quite close to those in Fig. 4-8 on both the floor and the human-seat interface.

The dynamic performance of the seat can be reflected from the SEAT value in Fig. 4-9(a). For a speed of 200 km/h, the seat had always been amplifying the vibration. For speeds such as 250, 300 and 350 km/h, when the first bending frequency was located in 7.5-9, 8.5-11 Hz and 9.5-13 Hz respectively, the seat had the function of attenuating the vibration.

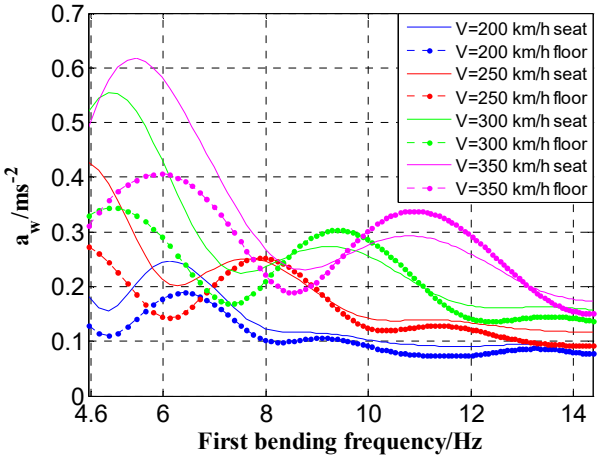

Fig. 4-8 The relationship between a_w and the first bending frequency as the variation of bending rigidity $E_b I$ at different speeds at seat 10 (center) (straight line: evaluated at the human-seat interface; dash-dot line: evaluated at the floor).

If the train speed changed while other parameters were kept constant, the relationship between a_w and the train speed under different damping ratios of carbody bending modes can be obtained. Similarly, according to the prediction in Section 4.5.2, the predictive results were quite accurate as well. For example, in the case of the first bending frequency f_1^t being 9.7 Hz, the predicted speeds corresponding to the peaks are 305.7 and 203.8 km/h, corresponding to troughs are 244.5 and 174.7 km/h respectively. The predicted values were quite close to those in Fig. 4-10. In addition, the evaluation on the floor caused overestimation or underestimation for most of the speed (Fig. 4-10).

The function of the seat was shown in the SEAT value in Fig. 4-9(b). For different damping ratios of carbody bending modes, the seat could attenuate the vibration at high speed, above about 260 km/h. At low speed, the seat tended to amplify the vibration transmitted to the subject. Increasing the damping of the carbody bending modes decreased the attenuation effect of the seat (increasing SEAT value).

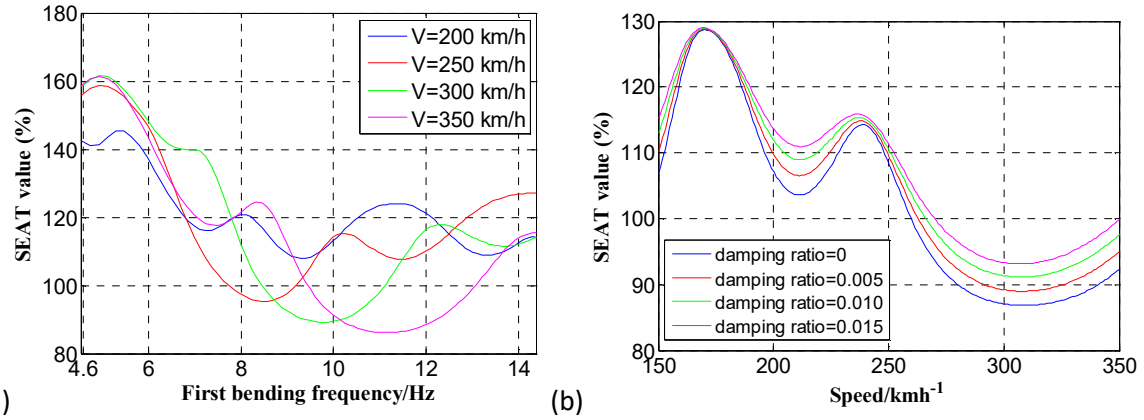

(a) (b)

Fig. 4-9 The SEAT value at seat 10 (center) (a) varying with the first bending frequency (or bending rigidity E_bI) at different speeds (b) varying with speed at different damping ratios of carbody bending modes.

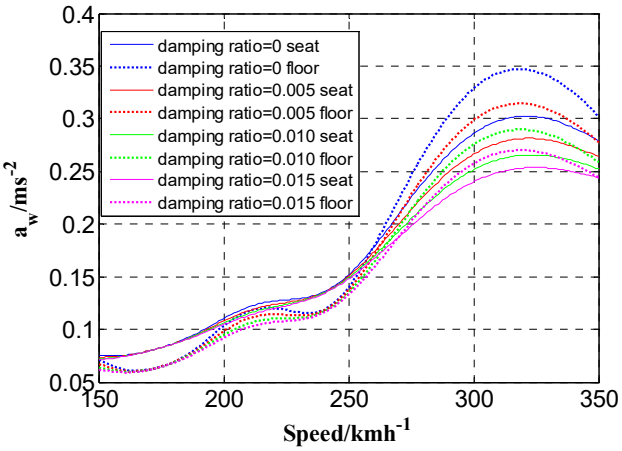

Fig. 4-10 The relationship between a_w and train speed under different damping ratios of carbody bending modes at seat 10 (center) (straight line: evaluated at the human-seat interface; dash-dot line: evaluated at the floor).

The vibration on the human-seat interface is the main vibration perceived by the seated passenger, and ISO (1997) defined frequency weighting method for assessing ride comfort based on this vibration. ISO (1997) suggests applying a multiplying factor of 1.0 for the vertical acceleration on the human-seat interface and a multiplying factor of 0.4 for the vertical acceleration at the feet if these two accelerations are to be combined to evaluate the ride comfort. Obviously, the vertical acceleration on the human-seat interface plays a much more important role in evaluating ride comfort than the vertical acceleration at the feet. Also using the vertical acceleration on the human-seat interface to evaluate the ride comfort is closer to the subjective perception. Based on the above analysis, the evaluation by the acceleration on the floor can result in a biased estimation. Therefore, the incorporation of the human-seat system looks necessary in order to give accurate

evaluation of ride comfort. In the following sections, the ride comfort was evaluated on the human-seat interface.

4.5.4.2 The effect of bending rigidity

Changing the bending rigidity ($E_b I$) of the carbody, the natural frequencies of the carbody would change accordingly. For different speeds, a_w evaluated on the human-seat interface can be calculated with the change of bending rigidity. The relationships between a_w and the first bending frequency at different speeds at seat 10 (center) and seat 17 (near front bogie center) were shown in Fig. 4-8 and Fig. 4-11, respectively. Whether at the center or near the front bogie center, as the increase of bending rigidity (or the first bending frequency), the ride comfort exhibited a global trend of improvement (decreased a_w). This is because when the speed was constant, the higher the bending mode frequency was, the lower the wavelength was, the smaller the PSD introduced by the track irregularity was. The contribution of different modes to ride comfort at seat 10 and seat 17 can be seen from Fig. 4-12. At the seat 10 (center), the contribution from bounce mode was almost constant and from pitch mode was zero because the modal node of the pitch mode was at the center. The contribution from other bending modes was marginal and from the first bending mode was the most significant below about 11 Hz. The contribution of the coherent parts was real, representing its contribution was to increase the equivalent acceleration. At seat 17 (near front bogie center), the contributions from bounce and pitch modes had little variation. The contribution of the first bending mode at seat 17 was much less compared with that at the center because the position was closer to the node of the first bending mode. The contribution of the coherent parts (purely imaginary) was to decrease the equivalent acceleration between 6 and 14 Hz. For both seat positions, the equivalent acceleration a_w showed similar fluctuation to the contribution of the first bending mode because of the significant contribution from the first bending mode, so the prediction in Section 4.5.2 was applicable well at both seats. For example, when the speed is 300 km/h, the predicted first bending frequencies corresponding to the peaks are 4.76 and 9.52 Hz, corresponding to troughs are 7.14 and 11.90 Hz respectively, which are quite close to those in Fig. 4-8 and Fig. 4-11.

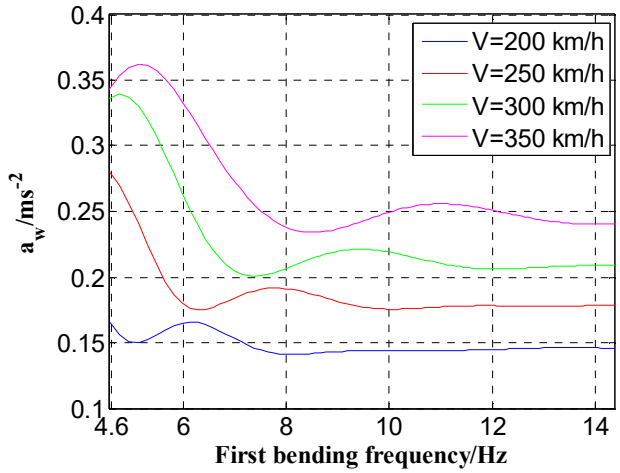

Fig. 4-11 The relationship between a_w evaluated on the human-seat interface and the first bending frequency with the variation of bending rigidity $E_b I$ at different speeds at seat 17 (near the front bogie center).

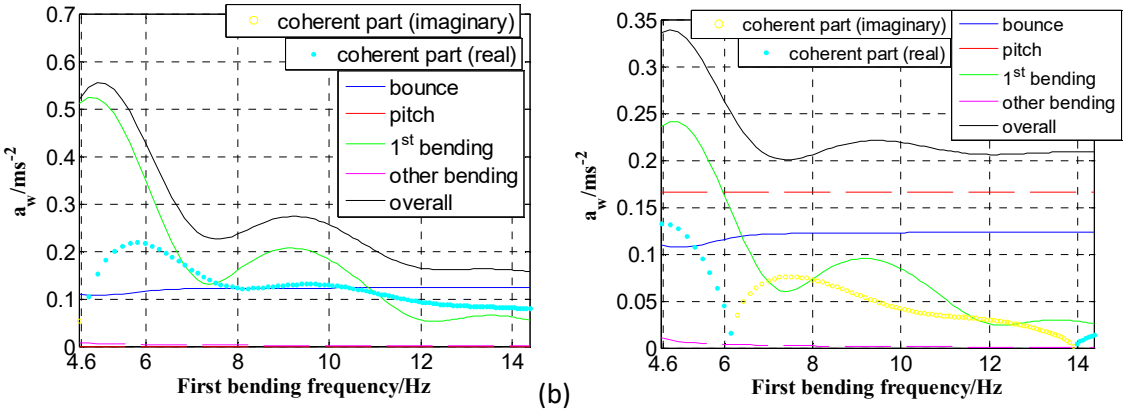

Fig. 4-12 The contribution of different modes to a_w evaluated on the human-seat interface as the change of the first bending frequency (or bending rigidity) (V=300 km/h, damping ratio=0.005) (a) at seat 10 (b) at seat 17.

4.5.4.3 The effect of speed

If the train speed changed while other parameters were kept the same, the relationship between a_w and the train speed under different damping ratios of the carbody bending modes at seat 10 (center) and seat 17 (near front bogie center) was obtained, as shown in Fig. 4-10 and Fig. 4-13, respectively. Increasing the speed had the tendency to worsen the ride comfort regardless of the damping ratio. This is because the higher the speed was, the higher the wavelength was, the larger the PSD introduced by the track irregularity would usually be. The contribution of different modes to ride comfort at different positions can be seen from Fig. 4-14. Wherever the seat position was, the contribution of other bending modes was always negligible. At seat 10 (center), the contribution

of the pitch mode was zero, while the contribution of pitch mode was significant at seat 17 (near the front bogie center), increasing with the speed. The contribution of the bounce mode at both seat positions was also significant and similar, increasing with the speed. The contribution of the coherent part always increased the equivalent acceleration at seat 10 in the considered speed range, while it reduced the equivalent acceleration at seat 17 above about 200 km/h. The contribution of the first bending mode was much greater at seat 10 than that at seat 17. For the same reason, the prediction in Section 4.5.2 was reasonably accurate at seat 10, however, the peaks and troughs were not obvious at seat 17 because the seat position was close to the node of the first bending mode.

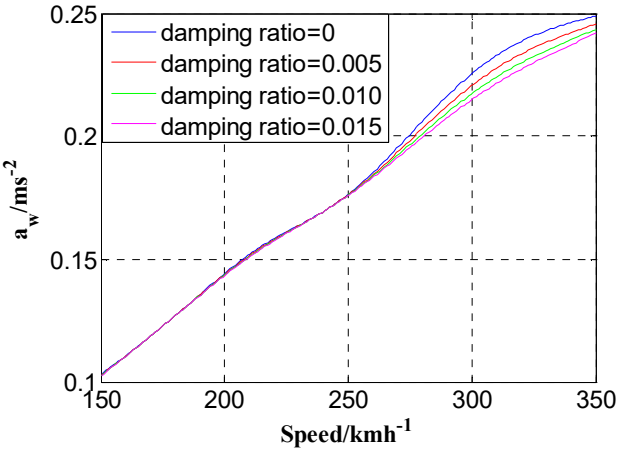

Fig. 4-13 The relationship between a_w evaluated on the human-seat interface and train speed under different damping ratios of carbody bending modes at seat 17 (near front bogie center).

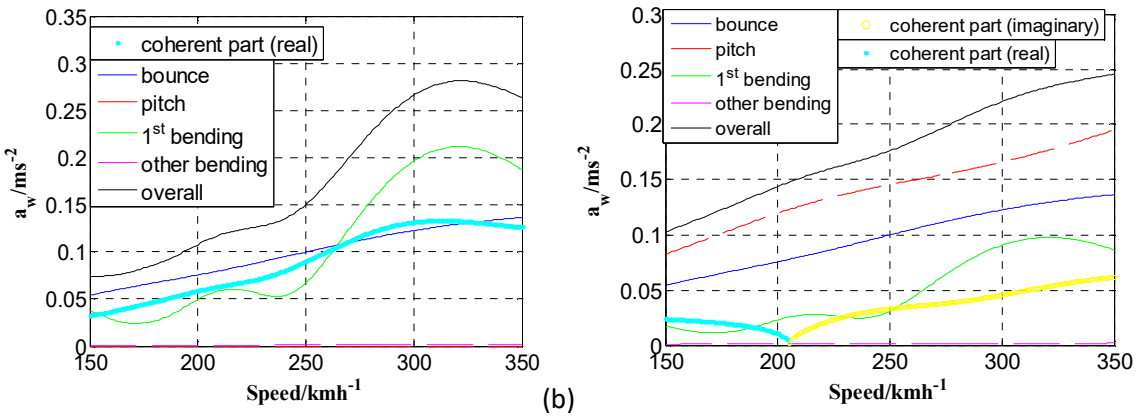

Fig. 4-14 The contribution of different modes to a_w evaluated on the human-seat interface as the change of speed ($f_1^t = 9.7Hz$) (a) at seat 10 (b) at seat 17 (damping ratio=0.005).

4.5.4.4 The effect of carbody damping

It can be seen from Fig. 4-10, Fig. 4-13 and Fig. 4-15 that increasing the damping ratio of carbody bending modes was effective in improving ride comfort (reducing a_w) regardless of speed and bending rigidity. Comparing Fig. 4-16 with Fig. 4-12(a), the damping ratio can reduce the contribution of the first bending mode greatly so as to improve ride comfort, especially at the peaks, while the contribution of other modes made little change. Thus, the smaller the damping ratio was, the more obvious the peaks and troughs were because the geometry filter effect of the first bending mode was more significant.

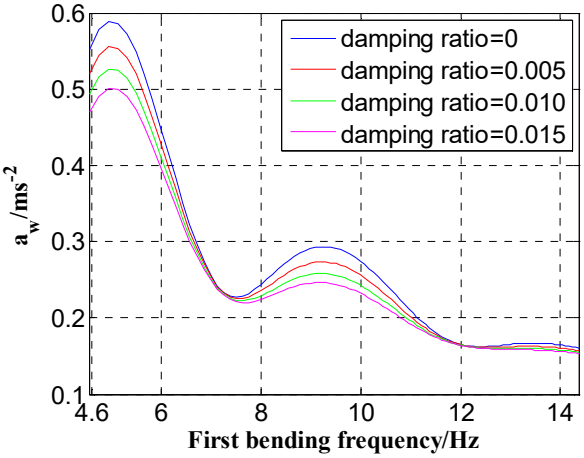

Fig. 4-15 The relationship between a_w evaluated on the human-seat interface and the first bending frequency (bending rigidity E_bI) under different damping ratios of carbody bending modes (V=300 km/h) at seat 10 (center).

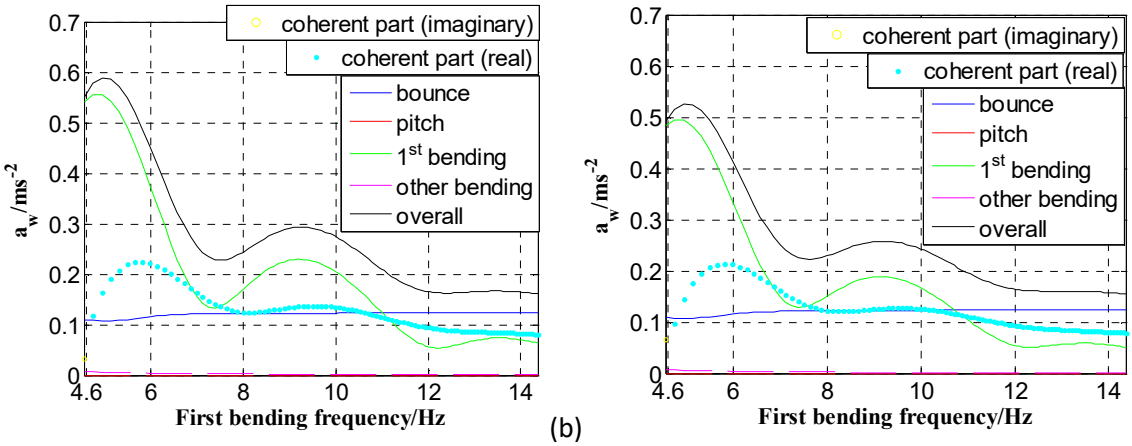

Fig. 4-16 The contribution of different modes to a_w evaluated on the human-seat interface as the change of damping ratio of carbody bending modes (V=300 km/h) at seat 10 (a) damping ratio=0 (b) damping ratio=0.01.

4.5.4.5 The effect of suspension and contact

The effect of the stiffness and damping of the seat-floor connection (k_{0z} and c_{0z}) on ride comfort was negligible (not shown), because the connection between the seat and floor was very rigid. Increasing the stiffness and damping of the primary and second suspensions usually increased the equivalent acceleration (worsening the ride comfort) (Fig. 4-17(a)(b)(c)(d)). What is more, a_w value seemed to increase (worsening ride comfort) as the increase of the stiffness of human-seat contact (k_{1z}), especially at high speed (Fig. 4-17(e)). While as the increase of the damping of human-seat contact (c_{1z}), a_w value decreased (improving ride comfort) (Fig. 4-17(f)).

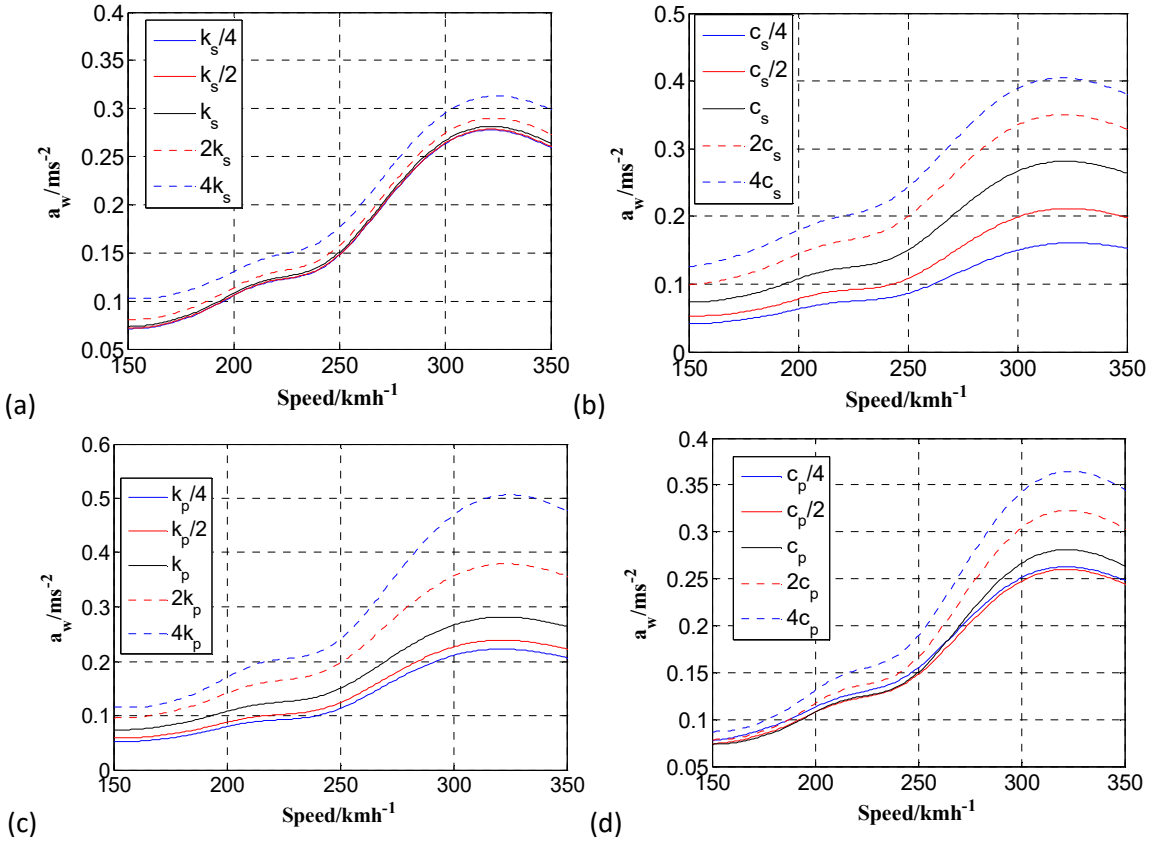

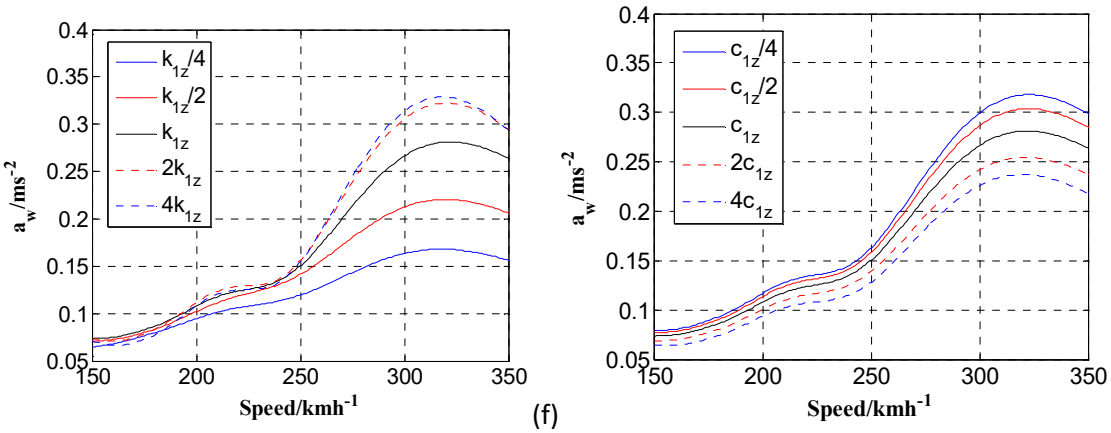

(e) (f)

Fig. 4-17 The influence of the stiffness and damping of suspensions and seat-human contact on ride comfort evaluated on the human-seat interface at seat 10 (center) (a) Change k_s (b) Change c_s (c) Change k_p (d) Change c_p (e) Change k_{1z} (f) Change c_{1z}.

4.5.4.6 The effect of seat position

According to Eq. (4-38), the carbody modes playing major roles in the response will be different at different seat positions. Fig. 4-18 illustrated that different seat positions can result in quite different equivalent accelerations. The equivalent accelerations at symmetrical positions showed analogous tendency as the speed. Ride comfort was worst at two ends whatever the speed was. Ride comfort near the front bogie center (seat 17) and rear bogie center (seat 3) was better than that at the center (seat 10) between 270-350 km/h, however, worse when the speed was lower than 270 km/h. In addition, the ride comfort at seat 6 and seat 14 was always among the best whatever the speed was. Comparing Fig. 4-19 with Fig. 4-14, whatever the position was, the contribution of the bounce mode was almost the same, increasing monotonically with speed. The contribution of the pitch mode was the least at seat 10 (center), followed by seat 14 and seat 6, then seat 17 and seat 3 (near the front and rear bogie centers), finally seat 1 and seat 19 (two ends). This is because the farther the distance from the node was, the more severe the pitch motion was. What is more, regardless of the seat position and speed, the contribution of other bending modes was always negligible. The contribution of the first bending mode was the most at seat 1 and seat 19 (both ends), then seat 10 (center), finally seat 3, 6, 14 and 17 (close to the node of the first bending mode). Because of the first bending mode, the geometry filter effect was obvious at seat 10 (center), seat 1 and seat 19 (two ends), the prediction in Section 4.5.2 applied better at these positions. While for those positions close to the node of the first bending mode (seats 3, 6, 14 and 17), the equivalent acceleration tended to increase monotonically with the speed. Last but not the least, a_w values

were not exactly the same at two symmetrical positions (Fig. 4-18) because the relationship between the symmetrical modes and anti-symmetrical modes can be summation at one side and subtraction at the other side, resulting in the difference of the contribution of coherent parts (comparing Fig. 4-19(b) and (c)).

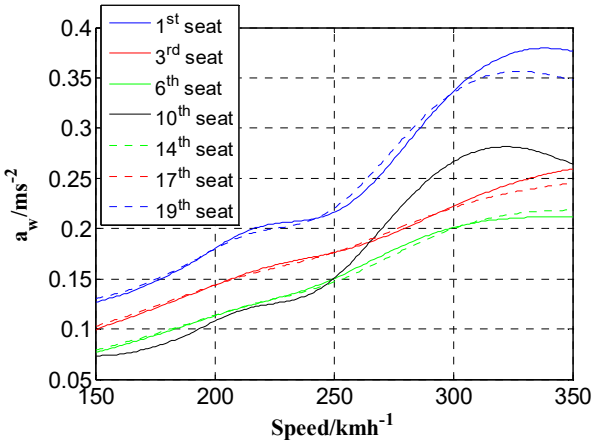

Fig. 4-18 The influence of the seat position on ride comfort evaluated on the human-seat interface (damping ratio=0.005).

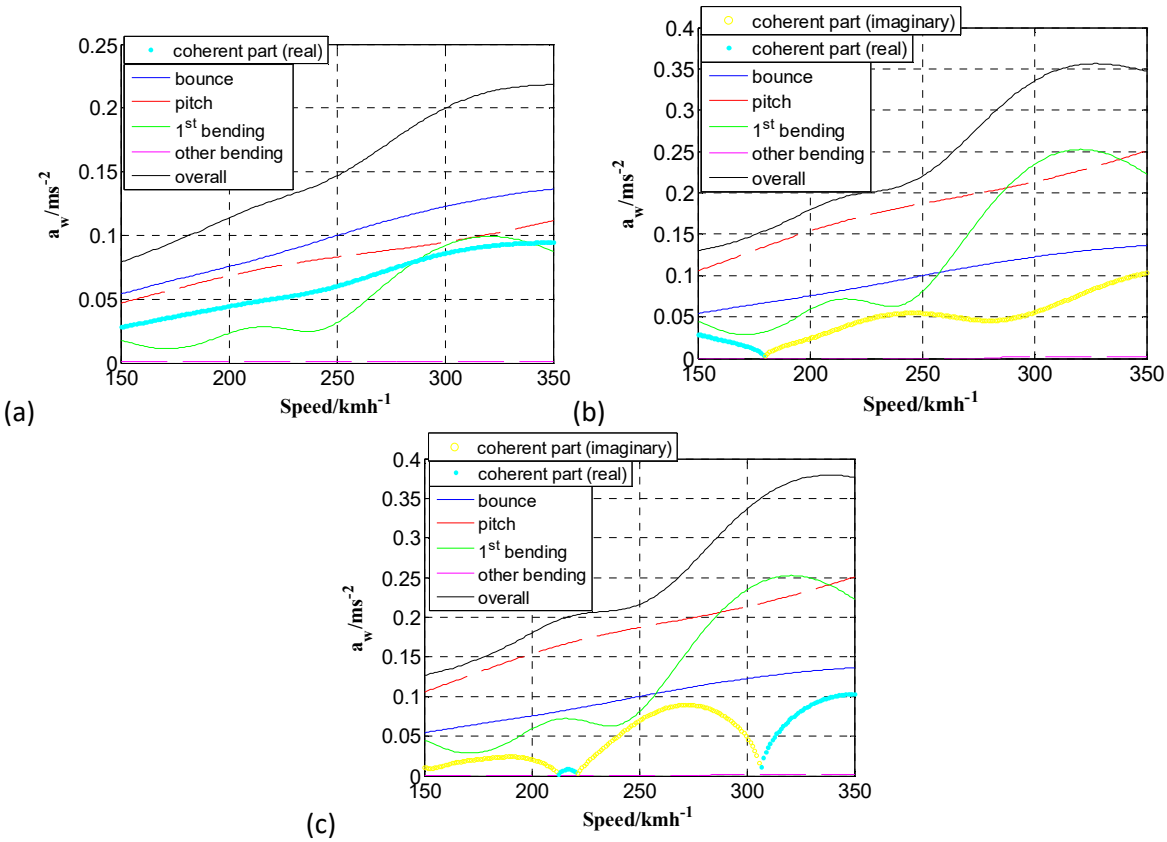

Fig. 4-19 The contribution of different modes to a_w evaluated on the human-seat interface as the change of speed (a) at seat 14 (b) at seat 19 (c) at seat 1.

4.5.4.7 The easiest way to improve ride comfort

Since the first bending mode plays a significant role in ride comfort, one of the possible ways to suppress it is to place the bogies under the nodes of the first bending mode. That is to say, the value of l_b is changed to 0.2758*L*. The effect of this change can be seen from Fig. 4-20. Comparing Fig. 4-20(a) with Fig. 4-12(a) and comparing Fig. 4-20(b) with Fig. 4-14(a), the first bending mode was greatly suppressed so that a_w reduced greatly, because the first bending mode can hardly be excited by the forces transmitted from the bogies. However, this method may not be feasible in reality because it is difficult to change the design of the bogie position.

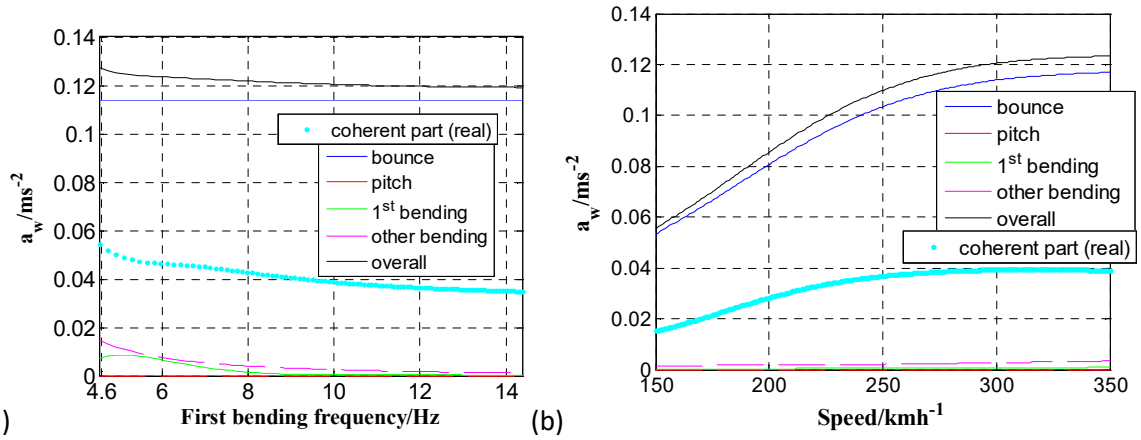

(a) (b)

Fig. 4-20 The contribution of different modes to a_w evaluated on the human-seat interface at seat 10 (center) after the change of bogie positions (a) as the change of the first bending frequency (bending rigidity) (V=300 km/h) (b) as the change of speeds ($f_1^t = 9.7\,Hz$).

4.5.4.8 Speed variation

In the above analysis, the speed was assumed to be constant. However, the speed of a train cannot be constant at all times. Thus, the speed of the train was assumed to obey normal distribution with the probability density function being $P(V)$. The mean speed is $\bar{V}$, and the standard deviation is σ_V.

The equivalent acceleration considering speed variation is defined as

$$\bar{a}_w(s_i) = \int_{\bar{V}-3\sigma_V}^{\bar{V}+3\sigma_V} a_w(s_i, V) P(V) \mathrm{d}V \tag{4-47}$$

For example, when $\bar{V} = 300\ km/h$ and $\sigma_V = 15\ km/h$, the effect of bending rigidity ($E_b I$) on ride comfort can be reevaluated at the seat 10 (center) and seat 17 (near front bogie center), as shown in Fig. 4-21. It can be seen the equivalent accelerations at seat 10 and seat 17 with a varying speed were very close to those running at a constant speed of the mean value, respectively. Therefore, the peaks and troughs can still be approximately predicted by Section 4.5.2 adopting the mean speed.

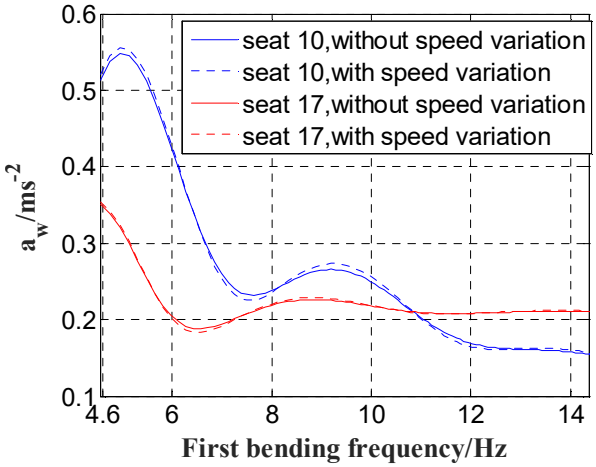

Fig. 4-21 The comparison of equivalent accelerations evaluated on the human-seat interface when a train runs at a varying speed (mean speed: 300 km/h, standard deviation: 15 km/h) and when a train runs at a constant speed of 300 km/h at two seat positions.

4.6 Conclusion

To study the ride comfort of the high-speed train, an analytical model of the train-seat-human system in the vertical direction was developed. Based on the analysis of the geometry filter effect and ride comfort, the following conclusions can be drawn.

By comparing different human-seat system distributions, the effect of human-seat systems on the bending modes of the carbody is usually small, however, these systems can have a tendency to reduce the modal frequencies and increase damping ratios and sometimes the change is so great that it cannot be ignored.

The role of the first bending mode is significant compared with other bending modes when the bogie and seat positions are both far from the nodes of the first bending mode. Under this situation, the geometry filter effect of the first bending mode was retained in the acceleration PSD on the floor and on the human-seat interface as well as in the weighted acceleration PSD on the human-

seat interface. And when the relationship between speed and the first bending frequency satisfies $\frac{V}{2l_b / n} = f_1^t$, the weighted acceleration r.m.s. value evaluated on the human-seat interface in the vertical direction will reach a peak. When the relationship between speed and the first bending frequency satisfies $\frac{V}{4l_b / (2n-1)} = f_1^t$, the r.m.s. value will reach a trough. When the bogie or seat position is close to the nodes of the first bending mode, the predictions are less obvious because of the suppression of the first bending mode. What is more, the same prediction also applies to the r.m.s. value evaluated on the floor. However, the evaluation on the floor will result in a biased estimation, so the incorporation of the human-seat system looks necessary in order to give an accurate evaluation of ride comfort.

Many parameters can have influences on ride comfort. Increasing the bending rigidity, the ride comfort exhibited a global trend of improvement, while increasing the train speed had a global tendency to worsen the ride comfort. Increasing the damping ratio of carbody bending modes can improve ride comfort effectively. Changing the stiffness and damping of seat-floor connection did not show a significant effect on ride comfort. However, increasing the stiffness or decreasing the damping of seat-human vertical contact on the seat pan can worsen ride comfort. Increasing the stiffness and damping of the primary and second suspensions usually increased the equivalent acceleration (worsen the ride comfort). What is more, the equivalent accelerations at symmetrical positions showed an analogous tendency as the speed. Ride comfort was worst at two ends whatever the speed was, followed by the carbody center at high speed, while the ride comfort of a seat close to the node of the first bending mode was relatively good.

After speed variation was taken into account, the equivalent acceleration was defined and found to be close to that evaluated with a constant speed of the mean value.

Chapter 5 The study of seat vibration transmission of a high-speed train based on a new MISO method

5.1 Introduction

Passengers are always exposed to vibrations from six axes at the same time when taking a train. Overall, vertical, lateral and roll vibrations on the seat are three very significant vibrations to passengers of rail vehicles including high-speed trains (ISO, 2001). The riding experience of the passengers may greatly depend on the manner in which the seat modifies the vibration from the floor, which is frequently evaluated by seat transmissibility and SEAT value (Section 2.2). Thus, understanding which vibration at the floor results in these vibrations at the seat-occupant interfaces is an important step towards the reduction of the vibration transmitted to passengers. To this end, vibration transmission from the floor to the seat pan and backrest needs to be studied in detail.

Many studies investigated the vibration transmission of car or train seats in either vertical, lateral or fore-and-aft direction using a single-input and single-output (SISO) model (e.g., Corbridge *et al.* (1989), Qiu and Griffin (2003), Jalil and Griffin (2007a, 2007b), Lo *et al.* (2013), Zhang *et al.* (2016), Gong and Griffin (2018)). For some cases, such as the measurement of seat transmissibility in the laboratory using a vertical vibrator, the vertical acceleration at the seat pan is purely induced by the vertical excitation of the vibrator. In this and similar situations, the traditional SISO model would be sufficient to evaluate the transmissibility of the seat-occupant system. However, for a rail vehicle including high-speed trains, multi-axis vibrations can be generated from the rigid modes, vertical bending, lateral bending, breathing or torsional modes of the carbody (Carlbom and Berg, 2002; Ling *et al.*, 2018). The passenger-seat system is exposed to such a complex vibration environment on a train that the vibration response on the seat in one direction (e.g., the vertical acceleration at the seat pan) may not only arise from the vibration at the floor in that direction but also be induced by the excitations in other directions (e.g., the lateral and roll accelerations at the floor). As a result, the SISO model is not suitable for this case partly because of the coherence between these input signals. In order to understand the vibration transmission of the seat better in a complex vibration environment, researchers started to try to apply or develop suitable multi-input and single-output (MISO) models for the vibration transmission of seats considering multiple vibration inputs on the floor, as discussed in Section 2.2.1, e.g., Qiu and Griffin (2004, 2005). In the subsequent use of this method to study the contribution of individual inputs to the vibration response of the seat-human

system, the author found that there exists an inconvenience in the original MISO method, i.e., the evaluation of the partial coherence is dependent on the sequence of the inputs. A specific partial coherence stands for the percentage of the spectrum of the output due to a specific (conditioned) input, used to evaluate the contribution from this specific input to the output. The multiple coherence stands for the percentage of the spectrum of the output due to all the inputs, used to evaluate the total contribution from all the inputs. However, the dependence on the sequence of inputs when using the original MISO model to evaluate partial coherences would give no unique results. Thus, a new MISO method was proposed and introduced in Section 3.2.2.

To date, most studies on the seat transmissibility have been focused on car seats (Qiu and Griffin, 2004, 2005; Fard, 2011). The structure of a car seat is quite different from a train seat. For example, the first-class seat on a train to be studied is a double-unit seat, but the front seat on a car is usually a single-unit seat. The structure of the seat influences the modal properties and the vibration transmission greatly. And whether the seat transmissibility of the double-unit seat with one seated subject is different from that with two seated subjects is to be studied. If so, these two cases need to be separated for the research of seat transmissibility. This will provide a basis for the subsequent modelling of human-seat system and motivate the study of the effect of seated human body on the dynamics of the train seat. To date, there has been little research about the field measurement of vibration transmission of a seat on a high-speed train, partly because having a train available to make the measurement we desire is not an easy thing, and for the study of ride comfort, people used to evaluate the vibration at the seat base instead of human-seat interface. However, since the biodynamics of human body and seating dynamics have been developing rapidly in recent decades (Griffin, 1990; Mansfield, 2004), it is found the function of the seat in transmitting the vibration perceived by the passengers cannot be ignored. Thus, the field measurement of seat vibration transmission is becoming more and more important.

In this chapter, vibration transmission of the seat-occupant system of a high-speed train from combined vertical, lateral and roll vibrations at the seat base to the responses at the seat pan and backrest were studied via field and laboratory measurements. The objective of this study is to investigate and understand whether the assumed tri-axial inputs at the seat base are sufficient to account for the acceleration responses at the seat pan or backrest, or in other words, how many and which vibration inputs at the seat base should be taken into account in order to sufficiently predict the responses in lateral, vertical and roll directions at the seat pan or backrest. The proposed new MISO model introduced in Section 3.2.2 was adopted to compute the transmissibility of the seat-passenger system exposed to vertical, lateral and roll vibration, and the corresponding coherence analysis was conducted to evaluate the contribution of each of the inputs to the

response (output). In addition, the laboratory measurement was compared with the field measurement in terms of seat transmissibility and coherence. Finally, the difference of the seat transmissibility between the seat with one subject and with two subjects was also examined.

5.2 Measurements on the high-speed train

5.2.1 Vibration measurement method

During the measurement, the train was always running at a constant speed of about 295 km/h. The measurement was carried out in a carriage in which the rear two-thirds is a first-class chamber while the front one-third is a VIP chamber. Vibration measurements were made with two double-unit seats at different positions of the first-class chamber, one near the center of the carriage (the front seat) and the other close to the end (the rear seat) (Fig. 5-1). The seats consisted of a backrest and a seat pan (almost horizontal). The angle of the backrest could be adjusted, however, was kept vertical during the measurement (Fig. 5-2). During the measurement, two seating conditions were considered, one with the seat seated with one subject and the other occupied by two subjects. The measurement for the two seating conditions was made with the same male subject (test subject for whom the vibration was measured) sitting on the left. The weight and height of this subject were 177 cm and 62 kg, respectively. For the rear seat, the other subject with a weight of 62 kg and height of 175 cm sat next to the test subject, while for the front seat, the other subject who sat beside the test subject had a weight of 72 kg and height of 172 cm. During the measurement, all the subjects sat in a comfortable upright posture with the back in contact with the backrest and hands resting on the thighs. (Note that in this chapter, ‘left’ and ‘right’ are defined from the perspective of the subject sitting on the seat.)

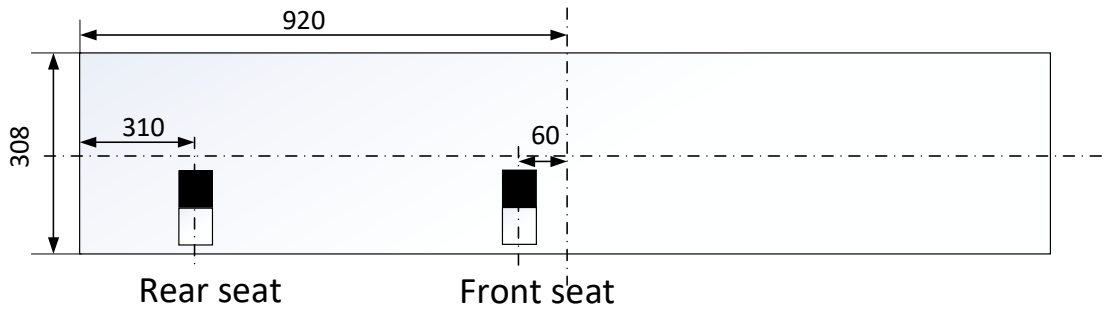

Fig. 5-1 The positions of the seats under test on the high-speed train (the test subject was seated in the black unit).

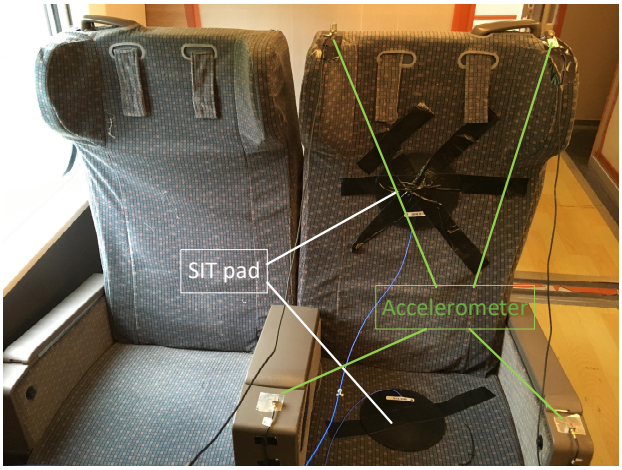

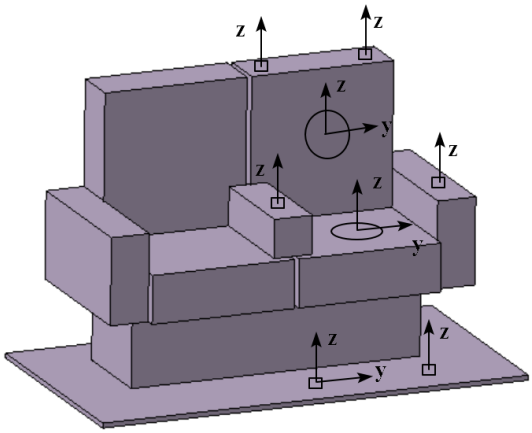

(a) (b)

Fig. 5-2 The layout of the accelerometers on the seat (a) on a high-speed train (b) schematic diagram.

A total of 11 channels of accelerations were recorded, as shown in Fig. 5-2(b). Two SIT-pads conforming to ISO 10326-1 with a sensitivity of 10 mV/ms^{-2} in every axis were positioned at the seat pan and backrest to measure the vertical and lateral accelerations at these positions. The SIT-pad on the seat pan was positioned beneath the ischial tuberosity of the test subject. The SIT-pad on the backrest was centrally located z_d = 450 mm above the seat pan surface. For calculating the roll motion of the seat pan, two single-axis accelerometers from B&W Tech with sensitivities of 10 mV/ms^{-2} were mounted on the left and right armrests to measure their vertical accelerations. (Note that the armrest is much more rigid than the seat pan.) Similarly, two single-axis accelerometers from B&W Tech with sensitivities of 10 mV/ms^{-2} were mounted on the top left and right sides of the backrest for the measurement of their vertical accelerations. The accelerations of the floor beneath the seat were measured by two tri-axial accelerometers from B&W Tech with the sensitivity of 10 mV/ms^{-2} in every axis, with the right one measuring the vertical and lateral accelerations, and the left one only vertical. From the two vertical accelerations at the floor, the roll acceleration on the floor can be calculated. The data were recorded by the LMS SCADAS Mobile data acquisition system with a sampling frequency of 256 Hz and a low-pass filter of 83 Hz.

The roll accelerations on the floor, the seat pan and backrest were calculated by (ISO, 2001)

$$\ddot{\theta}_{\text{roll}} = \frac{\ddot{z}_l - \ddot{z}_r}{d} (\text{rad/s}^2) \tag{5-1}$$

where $\ddot{z}_r$ and $\ddot{z}_l$ were the z-axis acceleration on the right and the corresponding left one, respectively; d was the distance between them.

5.2.2 Vibration inputs from the floor

The front and rear seats with one and two subjects were measured for ten times respectively. Every measurement lasted 60 s and the analysis in the frequency domain was performed using a frequency resolution of 0.2 Hz with a hanning window of 5 s and an overlap of 50%. Because the inputs from the track were random signals conforming to the same spectra, there was no great discrepancy among these ten measurements. Firstly, the median PSD of the ten measurements of acceleration inputs from the floor for the front and rear seats seated with one subject were analyzed, as plotted in Fig. 5-3. (The individual data for the front seat with one subject were illustrated in Fig. C-1 to show the variability.)

In the lateral direction, there are three obvious peaks at about 0.8, 12 and 30.4 Hz. The lowest one may result from the lateral rigid mode of the carbody and the second from a flexible mode (Carlbom, 2000), and the third one may correspond to the excitation from the non-circular wheel. In the vertical direction, there also exist three distinct dominant frequencies. The first one is about 1.0 Hz, probably from the vertical rigid mode of the carbody. The second is about 13.6 Hz, possibly corresponding to one flexible mode (Carlbom, 2000; Tomioka *et al.*, 2003), and the third one is 30.4 Hz, which may arise from the forced vibration induced by the wheel perimeter as well. In the roll direction, there exist three similar resonances, at about 1.0, 12.2 and 30.4 Hz respectively, which may arise from the rigid roll mode, one flexible mode and the excitation from the non-circular wheel. The three dominant frequencies in the vertical and lateral directions are also visible from the field test carried out by Zhai *et al.* (2015a).

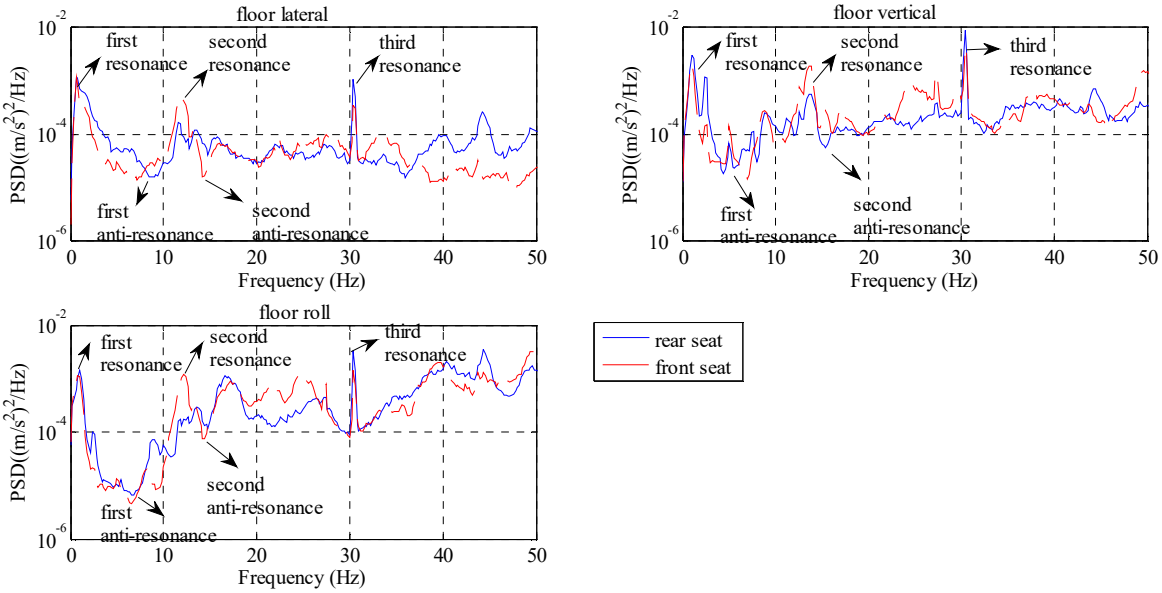

Fig. 5-3 The comparison of the median PSDs of the acceleration inputs from the floor for the rear seat and the front one with one subject.

In all the three directions, there appear two anti-resonances with the first one around 5-8 Hz and the other around 14-16 Hz. Therefore, there may not be enough energy around these two anti-resonances to excite the vibrations on the seat. Because the excitation from the track is random, there is no obvious difference between the spectra of acceleration inputs from the floor seated with one subject and with two subjects.

The ordinary coherence functions were calculated between these three acceleration inputs. Still, the median coherences of the ten measurements of vibration inputs from the floor for both seats seated with one subject was plotted in Fig. 5-4. (The individual data for the front seat with one subject were illustrated in Fig. C-2 to show the variability.) All the three coherences showed high value around 30.4 Hz, further proving the third peaks for all these inputs arose from the same source— the excitation of the non-circular wheel. For the front seat, these three inputs had strong mutual coherences around 12.2 Hz, indicating the second peaks in the PSDs of the three inputs resulted from the same flexible mode of the carbody. However, the three coherences were much smaller for the rear seat because the second peak was less obvious for the rear seat, signifying this flexible mode played a less significant role close to the end of the carbody than the center. What is more, the coherence was also high around 15.6 Hz between the lateral and roll accelerations for the front seat, and around 8.8 Hz between the vertical and roll accelerations for the rear seat, as well as in 20-30 Hz between the vertical and roll accelerations for both seats. These high coherences also implied the two accelerations in different directions at one specific frequency were probably from the same sources.

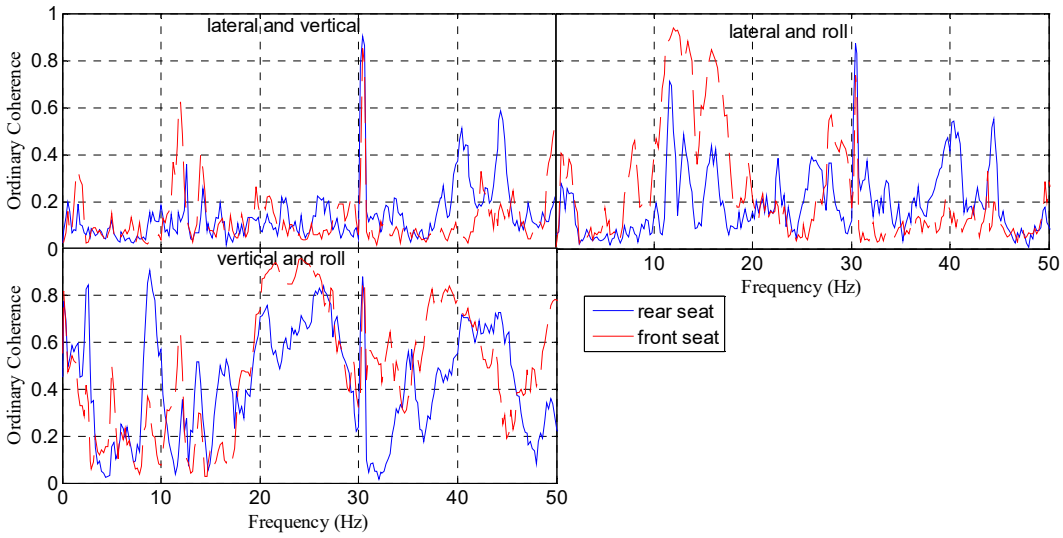

Fig. 5-4 The median ordinary coherence between the three acceleration inputs measured under both the front and rear seats with one subject.

5.2.3 Data processing

The simple single-input and single-output model is not suitable for calculating the frequency response function of the seat exposed to multi-axis excitations on a real high-speed train, which can cause overestimation or underestimation of the FRF because of the coherence between the inputs, so the transmission from the floor to the vertical, lateral and roll responses at the seat pan and backrest was studied by the new multi-input and single-output system (Section 3.2.2.2).

The inputs were the lateral, vertical and roll accelerations from the seat base. The data processing was based on the procedure of multiple inputs introduced in Section 3.2.2. As for the FRF, the FRF for the original inputs H_{jy} ($j = 1, 2, 3$) in Eq. (3-9) was adopted here, so the inputs and outputs for the calculation of FRFs have been got rid of the coherent parts with all the other inputs. The coherences in Eqs. (3-21) and (3-22) were to be calculated for representing the contribution from the different inputs and their coherent part to the output. Therefore, all the calculations of FRF and coherence were independent of the sequence of inputs.

5.3 Seat vibration transmission via multi-input system

The multi-input technique was used to study whether three inputs from the floor (the lateral acceleration on the right, the vertical acceleration on the right, and the roll acceleration) were sufficient to account for the responses at the seat pan and the backrest. The analysis was divided into six cases, that is, transmission to the vertical, lateral and roll accelerations on the seat pan, transmission to vertical, lateral and roll accelerations on the backrest, respectively. Because the transmissibilities and coherences were independent of the sequence of the inputs, the sequence of the inputs was always arranged in the same order: lateral, vertical and roll accelerations on the floor, corresponding to 1, 2 and 3 in the subscript of variables, respectively. In the subscript, *y* refers to the output to be considered, which can be vertical, lateral, or roll accelerations on the seat pan or backrest. Because the locations of the transducers on the floor were not totally identical for the front and rear seats, and the spectrums of the inputs on the floor showed much difference (Fig. 5-3) as well as due to the difference of the neighbouring subjects, the transmissibilities of the front and rear seats would not be compared with each other. For ten measurements, only the median transmissibilities and coherences were plotted in place of ten individual ones in the following results.

5.3.1 Transmission to the vertical acceleration on the seat pan

A three-input and one-output model was adopted for both seats, and the output was the vertical acceleration on the seat pan. The coherence functions and transmissibilities for both seats with one and two subjects were illustrated in Fig. 5-5 and Fig. 5-6. The difference between the multiple coherence and the summation of three partial coherences ($\gamma^2_{1\cdot2,3}+\gamma^2_{2\cdot1,3}+\gamma^2_{3\cdot1,2}$) arose from the coherent parts, indicating non-negligible coherence among the three inputs on the floor contributed greatly to the vertical vibration on the seat pan, especially above 20 Hz. The high contribution of the coherent parts in 20-30 Hz and around 40 Hz may arise from the coherent part between the vertical and roll accelerations (Fig. 5-4). From the coherence functions, it can be seen that among the three inputs, the vertical input made the most contribution to the vertical acceleration on the seat pan, except in about 20-25 Hz and around 40 Hz. On the other hand, these three inputs combining together made a strong multiple coherence function that was greater than 0.8 for most of the frequencies, but the coherence dropped at two anti-resonances (around 6 Hz and 16 Hz) where the energy from inputs was too low to excite the vertical vibration so that noise dominated in the response. The presumed reason would be further verified by the following experiment in the laboratory. Generally, the coherence functions for one seated subject and two were similar even though the neighbouring subject may have the potential to modify the vibration transmission of the seat. As for the transmissibilities, the inline transmissibility H_{2y} showed a primary resonance at about 5 Hz, close to the resonance frequency in other papers (e.g. Corbridge *et al.* (1989), Toward and Griffin (2011) and Gong and Griffin (2018)).

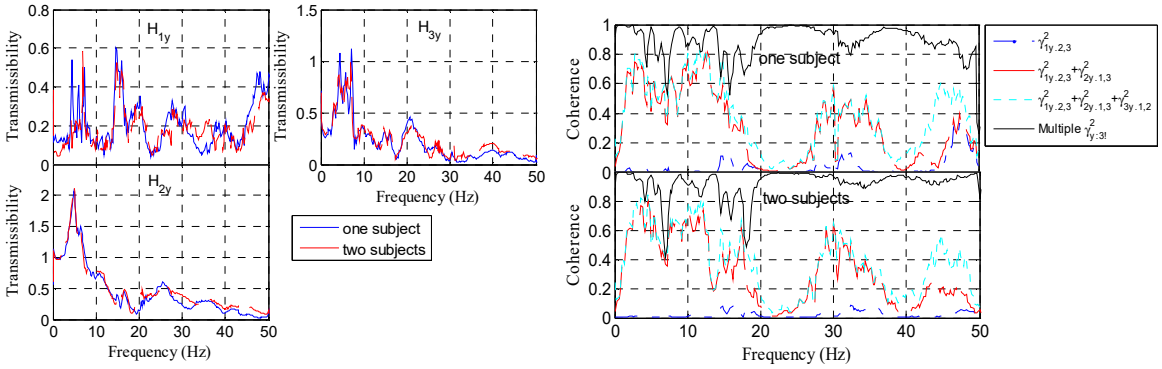

Fig. 5-5 Median transmissibilities (left) and coherences (right) for front seat seated with one subject and two subjects in the transmission to vertical acceleration on the seat pan (output *y*). (The subscripts 1, 2 and 3 correspond to lateral, vertical and roll accelerations on the floor, respectively)

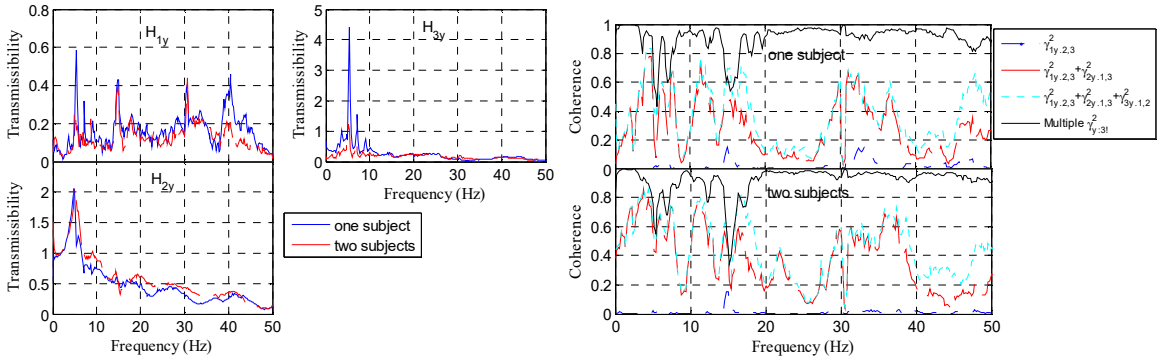

Fig. 5-6 Median transmissibilities (left) and coherences (right) for rear seat seated with one subject and two subjects in the transmission to the vertical acceleration on the seat pan (output *y*). (The subscripts 1, 2 and 3 correspond to lateral, vertical and roll accelerations on the floor, respectively)

5.3.2 Transmission to the lateral acceleration on the seat pan

A three-input and one-output model was designed for both seats for the study of transmission to the lateral acceleration on the seat pan (output) (Fig. 5-7 and Fig. 5-8). Among the three inputs, the lateral acceleration at the floor had a greater effect on the lateral acceleration on the seat pan than the other two inputs, however, cannot generate a strong coherence with the output in the whole frequency range if working alone, e.g. in 10-20 Hz and 40-50 Hz. The vertical and roll accelerations on the floor compensated for the low coherence, so three inputs working together resulted in a strong coherence in the multiple coherence function that was greater than 0.8 for most of the frequencies, especially for the front seat. The discrepancy between the black and cyan lines indicated the contribution from the coherent parts to the lateral vibration on the seat pan was great. The contribution in 10-20 Hz may be mainly from the coherent part between the lateral and roll accelerations, around 40 Hz from the coherent part between the vertical and roll accelerations (Fig. 5-4). For the rear seat, the seat seated with two subjects showed a lower multiple coherence in 0-10 Hz than that with one subject. As for the inline lateral transmissibility H_{1y}, two resonances around 35 and 48 Hz were obvious. The transmissibility was close to 1.0 below 30 Hz, indicating the seat vibrated rigidly in the lateral direction in the low-frequency range.

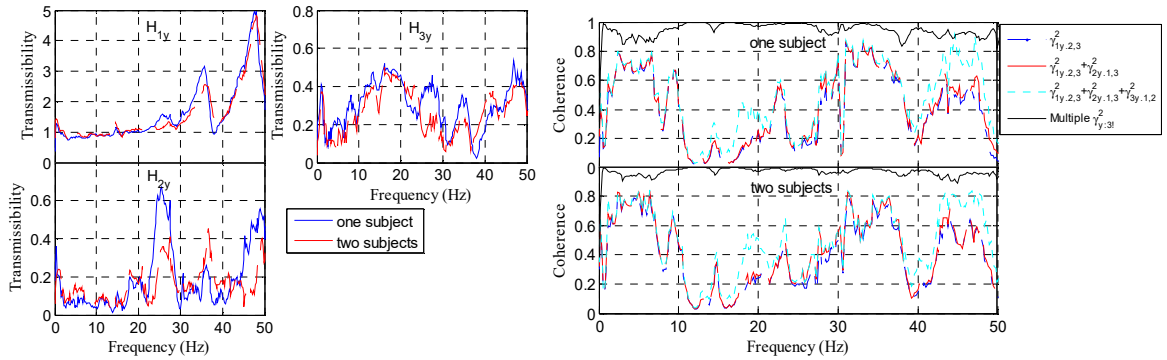

Fig. 5-7 Median transmissibilities (left) and coherences (right) for front seat seated with one subject and two subjects in the transmission to lateral acceleration on the seat pan (output *y*). (The subscripts 1, 2 and 3 correspond to lateral, vertical and roll accelerations on the floor, respectively)

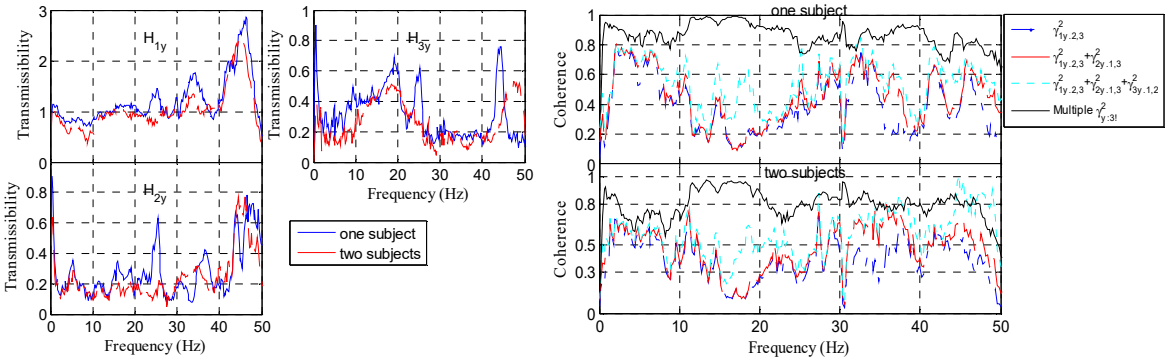

Fig. 5-8 Median transmissibilities (left) and coherences (right) for rear seat seated with one subject and two subjects in the transmission to lateral acceleration on the seat pan (output *y*). (The subscripts 1, 2 and 3 correspond to lateral, vertical and roll accelerations on the floor, respectively)

5.3.3 Transmission to the roll acceleration on the seat pan

A three-input and one-output model was developed for both seats for the vibration transmission to the roll acceleration on the seat pan (output) (Fig. 5-9 and Fig. 5-10). It can be seen that the multiple coherence may not be as good as that in the vertical and lateral directions, but was still satisfactory except for the drop at the anti-resonance (around 6 Hz). The discrepancy between the black and cyan lines was great, indicating the significant contribution of the coherent part. The contribution in 10-20 Hz was probably mainly from the coherent part between the lateral and roll accelerations and that in 20-30 Hz from the coherent part between the vertical and roll accelerations (Fig. 5-4). On the other hand, the inline transmissibilities H_{3y} showed one obvious peak around 20 Hz possibly due to a seat mode with roll vibration of the seat pan.

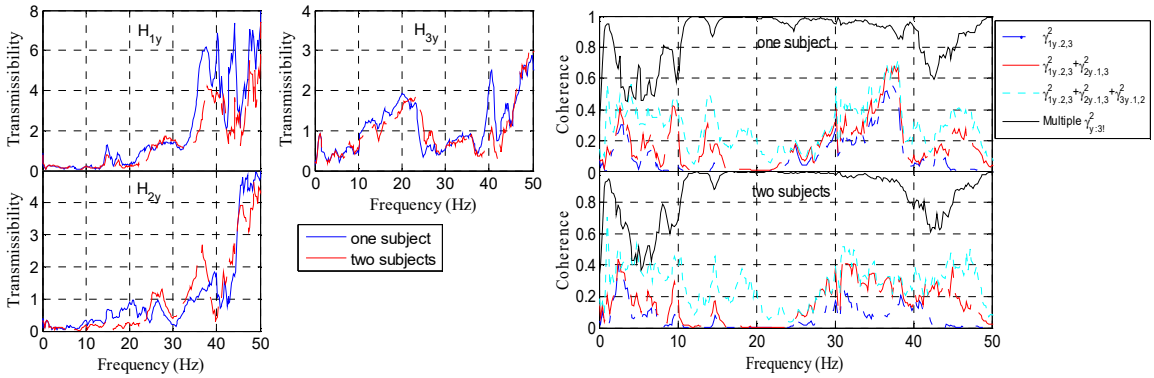

Fig. 5-9 Median transmissibilities (left) and coherences (right) for front seat seated with one subject and two subjects in the transmission to the roll acceleration on the seat pan (output *y*). (The subscripts 1, 2 and 3 correspond to lateral, vertical and roll accelerations on the floor, respectively)

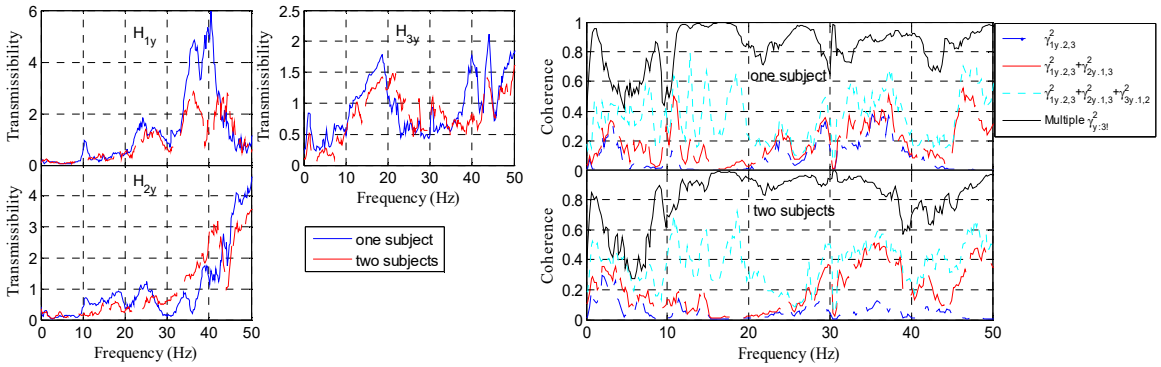

Fig. 5-10 Median transmissibilities (left) and coherences (right) for rear seat seated with one subject and two subjects in the transmission to the roll acceleration on the seat pan (output *y*). (The subscripts 1, 2 and 3 correspond to lateral, vertical and roll accelerations on the floor, respectively)

5.3.4 Transmission to the vertical acceleration on the backrest

A three-input and one-output model was adopted for both seats to study the vibration transmission to the vertical acceleration on the backrest (output) (Fig. 5-11 and Fig. 5-12). Similar to the transmission to the seat pan in the vertical direction, the contribution from the vertical acceleration on the floor to the vertical acceleration on the backrest was much greater than the other two inputs. The coherent part between the vertical and roll accelerations on the floor in 20-30 Hz and 35-50 Hz (Fig. 5-4) probably played an important role in the vertical response of the backrest. Overall, the multiple coherence was quite good, close to unity in 0.5-50 Hz. As for the inline transmissibility H_{2y}, there was an obvious peak around 45 Hz, however, it attenuated with a neighbouring subject possibly due to the damping brought from this subject. What is more, the transmissibility was close to 1.0 at frequencies lower than 20 Hz, signifying the backrest vibrated rigidly in the vertical direction in this frequency range.

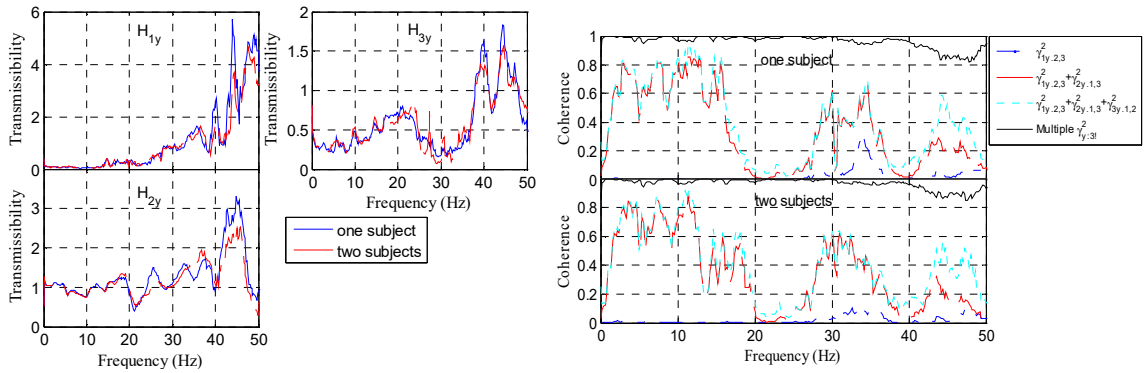

Fig. 5-11 Median transmissibilities (left) and coherences (right) for front seat seated with one subject and two subjects in the transmission to the vertical acceleration on the backrest (output *y*). (The subscripts 1, 2 and 3 correspond to lateral, vertical and roll accelerations on the floor, respectively)

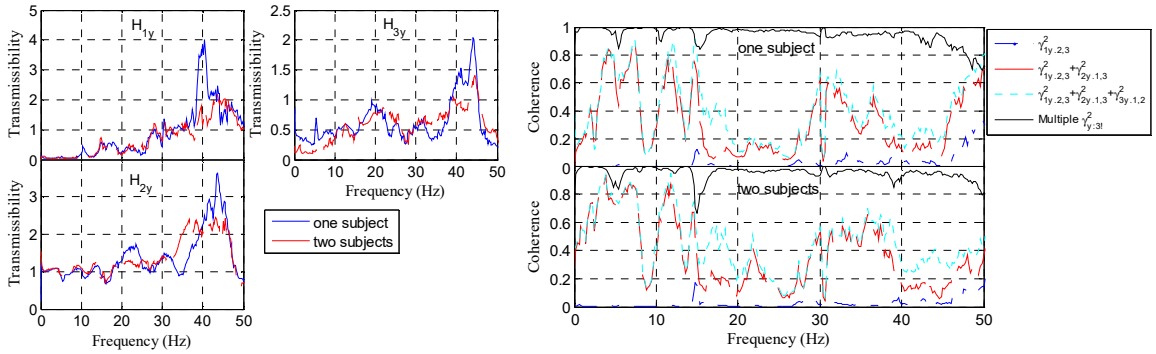

Fig. 5-12 Median transmissibilities (left) and coherences (right) for rear seat seated with one subject and two subjects in the transmission to the vertical acceleration on the backrest (output *y*). (The subscripts 1, 2 and 3 correspond to lateral, vertical and roll accelerations on the floor, respectively)

5.3.5 Transmission to the lateral acceleration on the backrest

A three-input and one-output model was designed for both seats to study the vibration transmission to the lateral acceleration on the backrest (output) (Fig. 5-13 and Fig. 5-14). Any of the three inputs from the floor was not sufficient to account for the lateral vibration at the backrest, but all of them combined together made a very good multiple coherence that was greater than 0.8 in the whole frequency range. The contribution from the lateral acceleration on the floor was the greatest in 0-10 Hz, however, in the range of 25-40 Hz, the vertical acceleration from the floor played the most important role. In addition, the coherent part between the lateral and roll inputs mainly resulted in the lateral acceleration in 10-20 Hz, and that between vertical and roll inputs played an important role in the lateral acceleration in 20-30 Hz and 35-50 Hz (Fig. 5-4). As for the transmissibilities, in the inline transmissibility H_{1y}, there were two resonances for both seats around 15 and 27 Hz that was likely to arise from two modes of the seat both with lateral vibration

of the backrest. The second resonance around 27 Hz was reduced obviously with a neighbouring subject because of the damping brought from that subject.

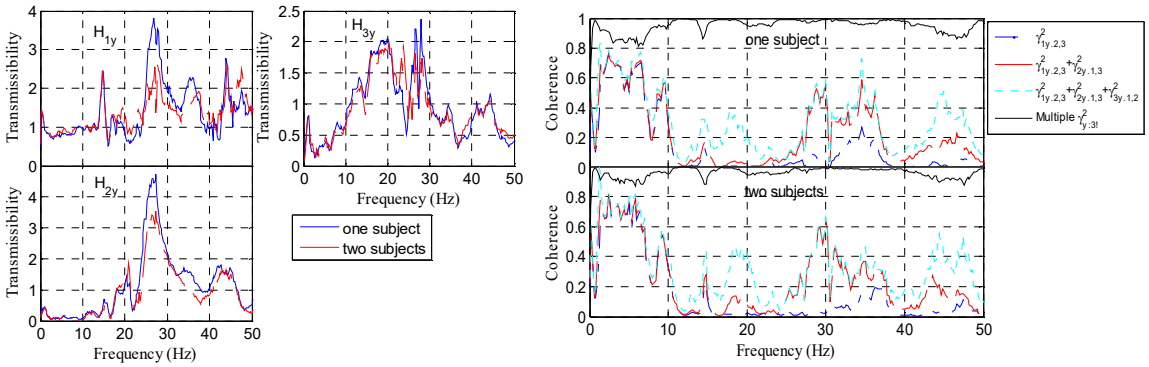

Fig. 5-13 Median transmissibilities (left) and coherences (right) for front seat seated with one subject and two subjects in the transmission to the lateral acceleration on the backrest (output *y*). (The subscripts 1, 2 and 3 correspond to lateral, vertical and roll accelerations on the floor, respectively)

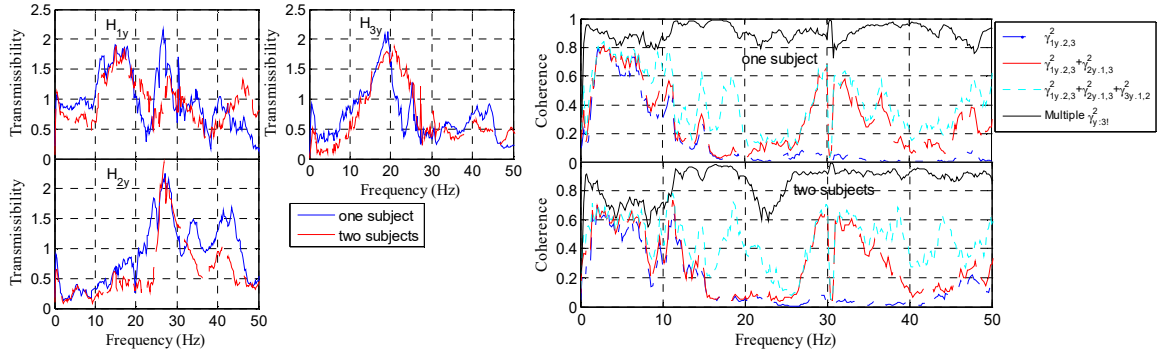

Fig. 5-14 Median transmissibilities (left) and coherences (right) for rear seat seated with one subject and two subjects in the transmission to the lateral acceleration on the backrest (output *y*). (The subscripts 1, 2 and 3 correspond to lateral, vertical and roll accelerations on the floor, respectively)

5.3.6 Transmission to the roll acceleration on the backrest

A three-input and one-output model was adopted for both seats for the study of vibration transmission to the roll acceleration of the backrest (output) (Fig. 5-15 and Fig. 5-16). It can be seen that the multiple coherence was not as good as that in the vertical and lateral directions, but was still satisfactory except at the anti-resonance (around 6 Hz) where the vibration could not be excited by the low energy. The difference between the black and cyan lines indicated the coherent parts in 10-20 Hz, 20-30 Hz and 35-50 Hz still played an important part in the roll acceleration on the backrest, just like the lateral direction. On the other hand, for the inline transmissibility H_{3y}, two resonances around 15 and 27 Hz were registered, identical to the lateral direction. The possible reason was there were two separate seat modes with both lateral and roll vibrations on the

backrest. What is more, the transmissibility with two subjects seemed to be lower than that with only one subject at 27 Hz, which may be explained by the more damping brought from the neighbouring subject.

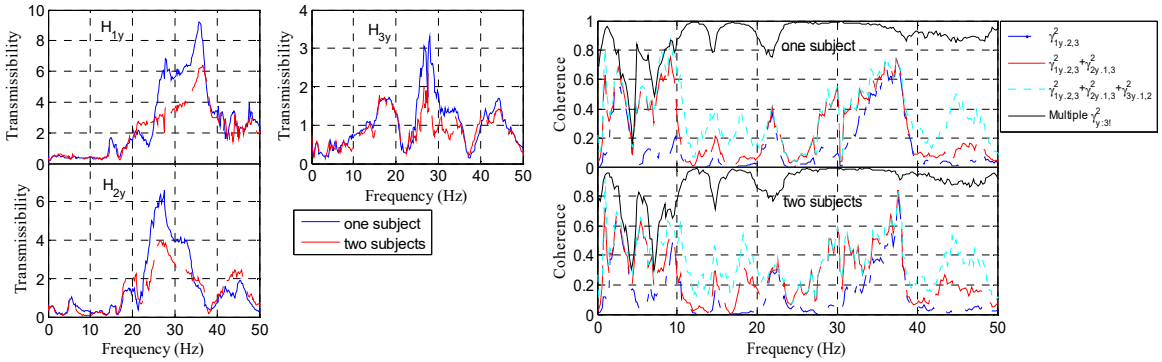

Fig. 5-15 Median transmissibilities (left) and coherences (right) for front seat seated with one subject and two subjects in the transmission to the roll acceleration on the backrest (output *y*). (The subscripts 1, 2 and 3 correspond to lateral, vertical and roll accelerations on the floor, respectively)

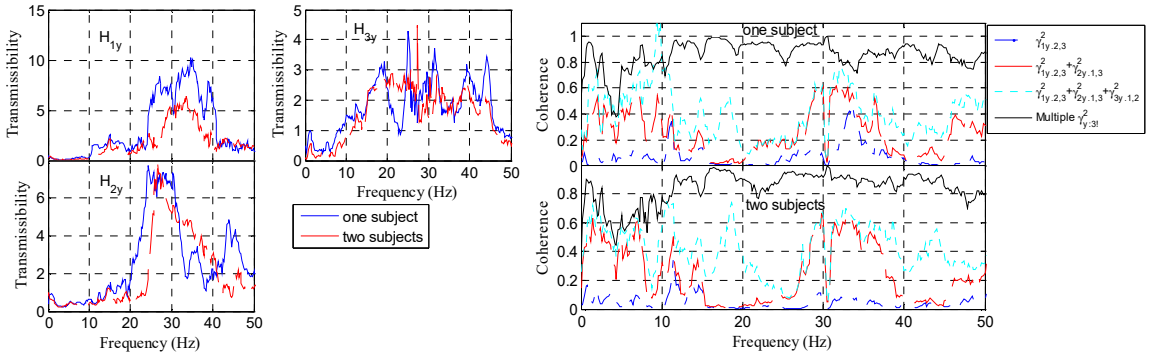

Fig. 5-16 Median transmissibilities (left) and coherences (right) for rear seat seated with one subject and two subjects in the transmission to the roll acceleration on the backrest (output *y*). (The subscripts 1, 2 and 3 correspond to lateral, vertical and roll accelerations on the floor, respectively)

5.4 Comparison with measurements in the laboratory

Compared with on-site measurement, the measurement in the laboratory can have well-defined input spectrums, well-controlled mutual coherence between inputs, low noise disturbance, etc. Under these considerations, similar measurements in the laboratory were carried out using a 6-axis motion simulator in the Institute of Sound and Vibration Research (ISVR) at the University of Southampton. The drop in the multiple coherence at anti-resonances of the input signals can be further proved by the laboratory measurement.

5.4.1 Introduction to the laboratory experiment

A seat of the same type was mounted on the 6-axis motion simulator. Twelve male subjects (different from those participating in the field measurement) having a mean age of 29.7 years (SD 6.8 years), a mean stature of 175.3 cm (SD 6.4 cm) and a mean weight of 80.4 kg (SD 9.98 kg) participated in the experiment, sitting on the left unit of the train seat one by one. There were two kinds of excitations, and the first one was one of the ten measurements of the vertical, lateral and roll accelerations measured at the floor under the front and rear seats on the train, respectively, conforming to the spectrum in Fig. 5-3. The second one was a tri-axial random acceleration signal defined in the range from 0.5 to 50 Hz. The root-mean-square (r.m.s.) values of the random signal were 0.5 m/s^2 in the lateral direction, 0.5 m/s^2 in the vertical direction and 0.75 rad/s^2 in the roll direction, and signals in different directions were almost incoherent with each other. The measurement method was the same as that on the train (Fig. 5-2), and all the data were recorded by *HVlab* data acquisition system at 512 samples per second via anti-aliasing filter set at 100 Hz. The experiment was approved by Human Experimentation Safety and Ethics Committee of the ISVR at the University of Southampton.

5.4.2 Results

For the on-site measurement, the low multiple coherence at some frequencies can be caused by the low energy of the inputs that is not enough to excite the vibration, or the dominating noise in the response. In the laboratory measurement, the latter can be reduced to some degree.

An example of the median coherences of the laboratory measurement with 12 different seated subjects adopting the measured inputs of the front and rear seats, respectively was depicted in Fig. 5-17. (The individual data were illustrated in Fig. C-3 to show the variability.) It can be seen that the multiple coherences still dropped around 6 Hz and 16 Hz, however, were higher than the counterparts in Fig. 5-5 and Fig. 5-6. This was because the noise in the laboratory was less than that on the train. However, the energies in the inputs at these frequencies were still too small to excite the vertical vibration on the seat pan, so even a little noise could have a great effect on the multiple coherence. And the low energy at these frequencies could attribute to the two anti-resonances in Fig. 5-3. On the other hand, the contributions from the three inputs were similar to those in Fig. 5-5 and Fig. 5-6, and the effect of the coherent parts on the response was also great in the laboratory, which could be put down to the high mutual coherence between these three inputs on the train.

An example of the median coherences of laboratory measurement with 12 different seated subjects adopting the random input was illustrated in Fig. 5-18. The discrepancy between multiple

coherence and unity could be put down to the noise, and the nonlinearity of human-seat system, etc. The multiple coherence was very close to unity, indicating the noise in the laboratory measurement was negligible and the human-seat system under random excitation with constant and evenly distributed energy in the whole frequency range could be approximately regarded as a linear system. On the other hand, telling from the partial coherences, the contribution from the vertical input (the difference between the blue and red lines) was much greater than the other two inputs, which indicated the vertical vibration on the seat pan was mainly induced by the vertical input on the floor instead of the lateral and roll inputs. What is more, the small gap between the black and cyan lines signified the low coherence between the inputs, which was the advantage of the laboratory measurement. However, the coherence between the inputs cannot be got rid of completely.

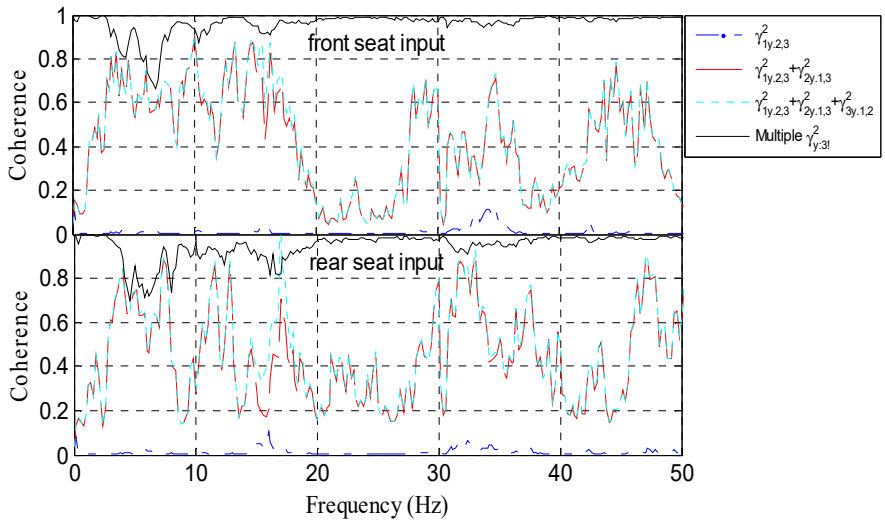

Fig. 5-17 Median coherences of the laboratory measurement with 12 different seated subjects adopting the measured inputs of the front and rear seats in the transmission to the vertical acceleration on the seat pan (output *y*). (The subscripts 1, 2 and 3 correspond to lateral, vertical and roll accelerations on the floor, respectively)

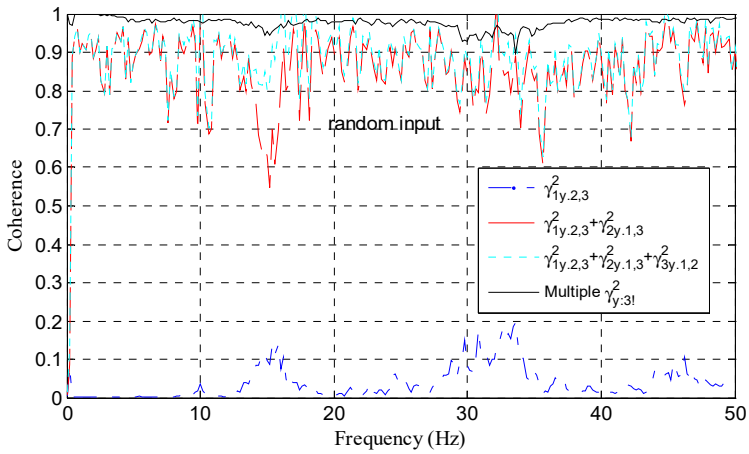

Fig. 5-18 Median coherences of the laboratory measurement with 12 different seated subjects adopting the random input in the transmission to the vertical acceleration on the seat pan (output *y*). (The subscripts 1, 2 and 3 correspond to lateral, vertical and roll accelerations on the floor, respectively)

When the frequency response function (FRF) for the on-site measurement is calculated, it may not be accurate for the following two reasons.

Firstly, in the on-site measurement on a high-speed train, 'noise' is the signal that is not taken as inputs, actually may not be noise at all. The 'noise' can have high coherence with the inputs and some part in the response can arise from the 'noise'. When estimating the FRF, the FRF can either be overestimated or underestimated, depending on the phase difference between the FRF from the input to the response and that from the 'noise' to the response. For example, in Fig. 5-19, only $x_1(t)$ is taken as input, other signals ('noise') that are coherent with $x_1(t)$ can pass through a linear system to make up the output $y(t)$, so $x_1(t)$ can go through two paths to make up $y(t)$, which causes the erroneous estimation of FRF. However, if there is no coherence between $x_1(t)$ and 'noise', there is only one path left for $x_1(t)$, then the estimation is more accurate. Therefore, the FRF estimation for the on-site measurement is usually not convincing, especially when the modulus of FRF from the input to the output is small or when the modulus of FRF from the noise to the output is large. However, the 'noise' in the laboratory is usually incoherent with the inputs, so it will not influence the estimation of FRF, which is another advantage of the laboratory experiment.

Secondly, the strong mutual coherence between the inputs makes where the response arises from unclear. For example, in Fig. 5-20, there are two inputs $x_1(t)$ and $x_2(t)$ with strong coherence, and they can respectively generate the response signals $y_1(t)$ and $y_2(t)$ by means of a linear system, then the output is the summation of these two response signals. Thus, where the output

signal arises from is not clear, because both inputs can reach the output by going through the other' linear system. However, this problem can somehow be solved by adopting an MISO system to some degree as long as the inputs are not totally coherent at one specific frequency. This also requires generating the input signals as incoherent with each other as possible in the laboratory experiment.

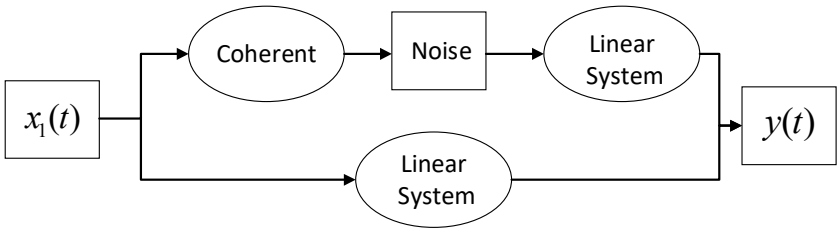

Fig. 5-19 Illustration of erroneous estimation of FRF because of 'noise'.

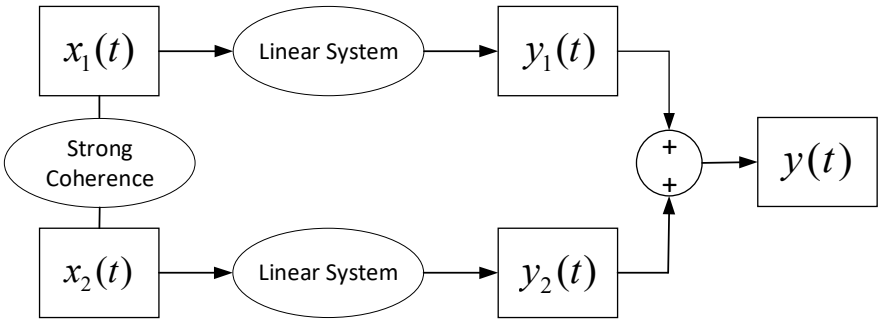

Fig. 5-20 Illustration of erroneous estimation of FRF because of strong coherence between inputs.

The comparison between transmissibilities in on-site measurement, laboratory measurement using inputs in the on-site measurement and laboratory measurement using random inputs was illustrated in Fig. 5-21. The estimations of the transmissibility in two laboratory measurements were overall close, which proved the erroneous estimation resulting from the coherence between the inputs can to some degree be figured out by adopting the MISO system. However, strictly speaking, laboratory measurement using random inputs incoherent between different axes was preferred in order to obtain more accurate FRFs. The estimation of the transmissibility differed a lot between the laboratory measurement and on-site measurement, the main reason for which could be the inputs were coherent with the 'noise', as discussed above, which showed consistency with Qiu and Griffin (2003). In addition, the slight difference between the seats in the on-site measurement and in the laboratory one, the inevitable discrepancy between the layout of the transducers, the different seated subjects between the on-site measurement and the laboratory one as well as the nonlinearity of the human-seat system under excitations of different magnitudes could also in part account for the difference between the estimations of the transmissibility, however, the difference caused by them could not be very large.

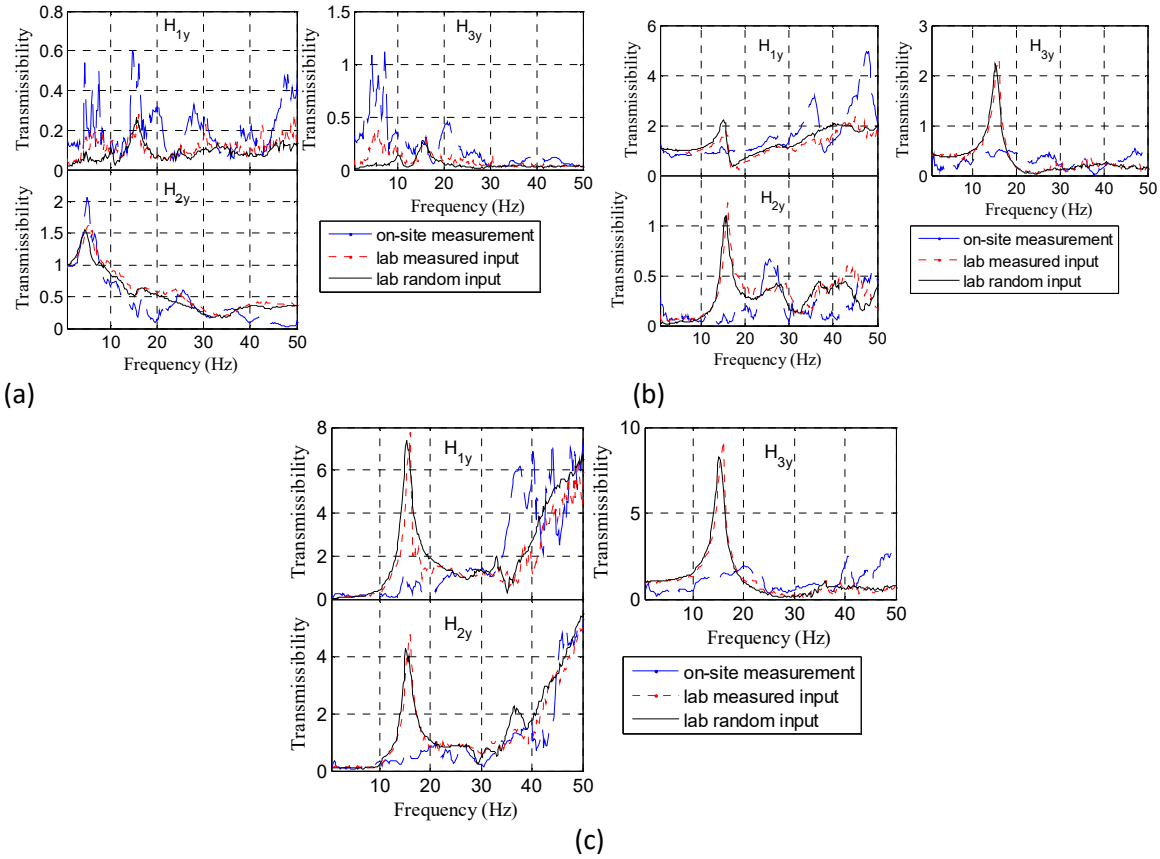

Fig. 5-21 The comparison among the median transmissibility in on-site measurement for the front seat, laboratory measurement using on-site measured inputs of the front seat and laboratory measurement using random inputs (a) the transmissibility to the vertical acceleration on seat pan (output *y*); (b) the transmissibility to the lateral acceleration on the seat pan (output *y*); (c) the transmissibility to the roll acceleration on seat pan (output *y*). (The subscripts 1, 2 and 3 correspond to lateral, vertical and roll accelerations on the floor, respectively)

5.5 Comparison of transmissibility

The seated subjects on the seat would have an influence on the seat transmissibility due to its complex dynamics. For the double-unit train seat, the transmissibility with one seated subject may show difference from the counterpart with two subjects, which has not been studied yet.

The inline seat transmissibilities with one and two seated subjects were compared in Fig. 5-22. It can be seen that the neighbouring subject on the right usually would reduce the transmissibilities at the peaks, except for the vertical transmissibility on the seat pan. This was probably because the modal damping of the train seat modes was amplified by the human body that was a dynamic system with large damping, which was consistent with the following modelling of the human-seat system in Chapter 9 and Lo *et al.* (2013). And the peak around 5 Hz in the vertical transmissibility of the seat pan was probably induced by the whole-body vertical mode of the human body, so the

magnitude was not influenced by the damping of the neighbouring subject, which was also in good agreement with the results in Chapter 9.

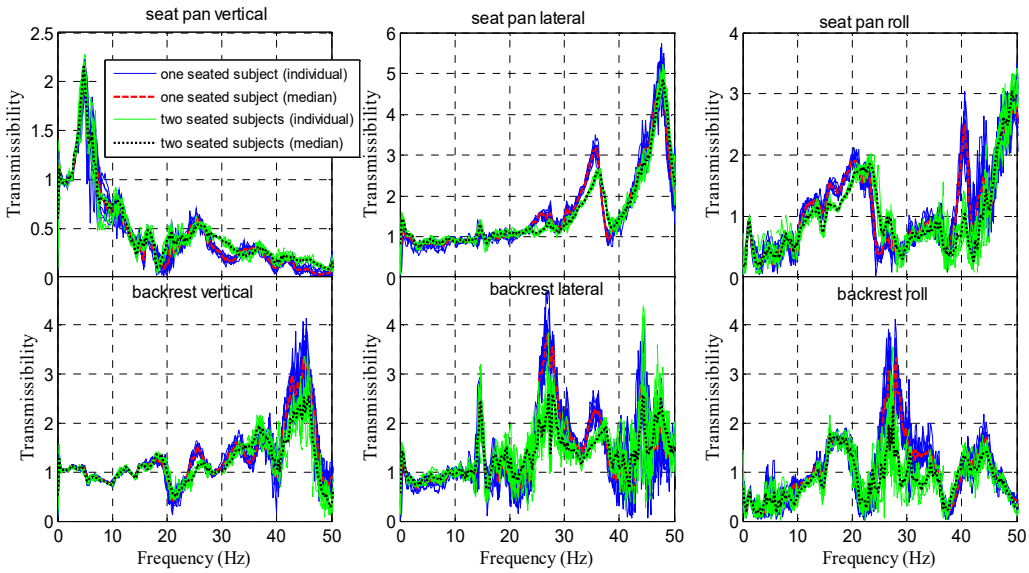

Fig. 5-22 The comparison between the seat inline transmissibilities with one and two subjects (blue line: seat transmissibility with one seated subject for ten individual measurements; red dotted line: median seat transmissibility with one seated subject; green dotted line: seat transmissibility with two seated subjects for ten individual measurements; black dashed line: median seat transmissibility with two seated subjects).

Actually, judging from the structure of a train seat, the frames of two units of the train seat were connected by two rod-like structures (Fig. C-4), that is, there were forces and moments transmitted between them. Since the seat transmissibility with one subject showed a significant difference from that with two subjects, the function of transmitting force and moments cannot be ignored. This is a good guide for the following modelling of the train seat, and in the further laboratory experiment about seat transmissibility, the seat seated with one subject and two should be studied separately.

5.6 Discussion

5.6.1 Comparison between different methods

In the on-site measurement on a high-speed train, the mutual coherence between the inputs could not be avoided. The strong coherence between the three inputs can result from the reason that some inputs arise from the same source, e.g. the same mode of the carbody (for example, the lateral, vertical and roll vibrations can all arise from breathing modes), the excitation from the non-circular wheel, the cross-axis sensitivity of the multi-axis transducers, the misalignment of transducers, etc.

In a complicated vibration environment, if the SISO method is applied to the estimation of FRF, that means only one signal is chosen as input, just as illustrated in Fig. 5-19. At some frequencies, the input is partially coherent with the 'noise' that passes through a linear system to make up the output, so at these frequencies, the output is generated by both the 'noise' and input, which would cause biased estimation of FRF. This is especially the case when the FRF from the input to the output is small or the FRF from the 'noise' to the output is large. This problem can be solved to some extent by taking into account multiple inputs and as many inputs in different directions as possible. So the MISO method is preferable in a complicated vibration environment.

For the newly defined partial coherences $\gamma^2_{iy\cdot(m!/i)}$ ($i=1,2,\cdots,m$) (*m* is the total number of inputs), the advantage is that they are independent of the order of inputs and can reflect the contribution of different inputs to the output separately and uniquely. And γ_{cy} can demonstrate how much the contribution of the coherent parts between the inputs to the output is; the smaller the coherence among the inputs is, the less the contribution from the coherent part to the output is, and the closer γ_{cy} is to zero. On the other hand, for the original partial coherences $\gamma^2_{iy\cdot(i-1)!}$ ($i=1,2,\cdots,m$), they do not have such advantages. Fig. 5-23 illustrated the partial coherences with three different input sequences by adopting the original MISO method. Although the multiple coherences for different input sequences were the same, the partial coherences that were dependent on the sequence of the input could not give unique results when evaluating the contribution of individual input to the output. For the FRF estimation, H_{iy} ($i=1,2,\cdots,m$) is an estimation by getting rid of the coherent parts with all the other inputs from both the ith input and the output, so it is also independent of the sequence of inputs. However, as for the FRF for the conditioned inputs L_{iy} ($i=1,2,\cdots,m$), the ith FRF (except the mth input) will be influenced by the following inputs (x_{i+1}, x_{i+2},..., x_m), so as to cause biased estimation if these following inputs are coherent with x_i and go through individual linear systems to make up the output $y(t)$. Fig. 5-24 showed the estimations of the transmissibilities with the same three input sequences as Fig. 5-23 by adopting the original MISO method. The dependence of the transmissibility on the sequence of inputs posed difficulty for evaluating the transmissibility uniquely. Therefore, H_{iy} is preferable in the data analysis of this chapter.

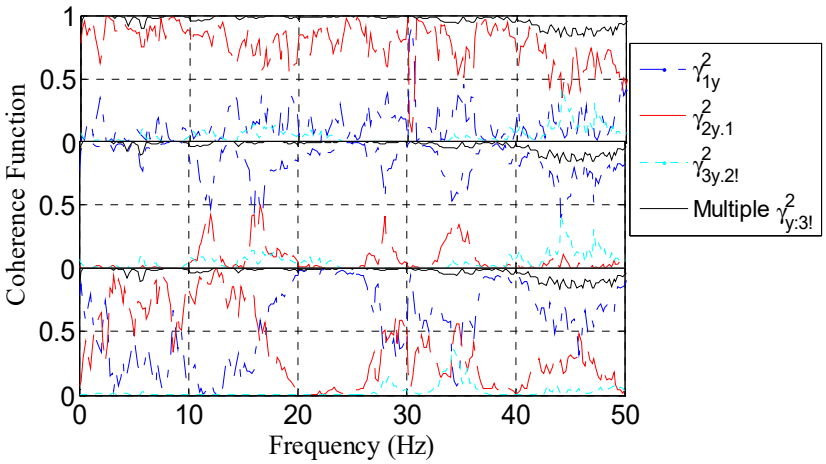

Fig. 5-23 Comparison of partial coherences among different sequences of inputs for the transmissibility to the vertical acceleration on the backrest (output *y*) obtained from the front seat seated with one subject adopting the original MISO method. (sequence 1: lateral acceleration, vertical acceleration, roll acceleration on the floor for the top subfigure; sequence 2: vertical acceleration, lateral acceleration, roll acceleration on the floor for the middle subfigure; sequence 3: roll acceleration, vertical acceleration, lateral acceleration on the floor for the bottom subfigure)

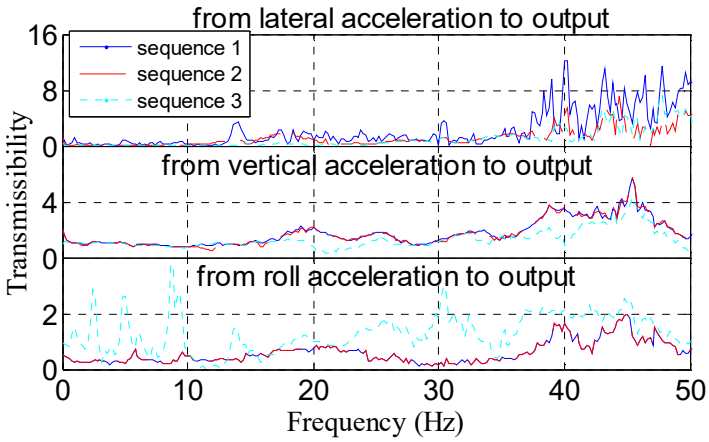

Fig. 5-24 Comparison of transmissibility among different sequences of inputs for the transmissibility to the vertical acceleration on the backrest (output) obtained from the front seat seated with one subject adopting the original MISO method. (sequence 1: lateral acceleration, vertical acceleration, roll acceleration on the floor for the top subfigure; sequence 2: vertical acceleration, lateral acceleration, roll acceleration on the floor for the middle subfigure; sequence 3: roll acceleration, vertical acceleration, lateral acceleration on the floor for the bottom subfigure)

5.6.2 The choice of inputs

Because the roll acceleration on the floor is a linear combination of two vertical accelerations on the right and left (Eq.(5-1)), using any two of the three will get exactly the same multiple coherence

with the previous one, that is to say, if the roll acceleration of the floor ($\ddot{\theta}_f$) is replaced by the vertical one on the left ($\ddot{z}_{fl}$), or the vertical acceleration on the right ($\ddot{z}_{fr}$) is replaced by the counterpart on the left ($\ddot{z}_{fl}$), it will generate exactly the same multiple coherence as the previous one. Also, note that changing the order of the inputs will make no difference to the multiple coherence function. Fig. 5-25 illustrates when the inputs of the front seat are replaced by two groups of other inputs, that is, vertical accelerations on the right and left ($\ddot{z}_{fl}$, $\ddot{z}_{fr}$), lateral acceleration ($\ddot{y}_{fr}$), as well as vertical acceleration on the left ($\ddot{z}_{fl}$), lateral and roll accelerations ($\ddot{y}_{fr}$, $\ddot{\theta}_f$), respectively, the three multiple coherence functions are exactly coincident. Thus, the vibration transmission from the floor to the seat pan and backrest in the three directions can be taken into account by either taking into account any one of the vertical accelerations ($\ddot{z}_{fl}$ or $\ddot{z}_{fr}$), lateral acceleration ($\ddot{y}_{fr}$) and roll acceleration ($\ddot{\theta}_f$) at the floor, or the vertical accelerations at two sides ($\ddot{z}_{fl}$ and $\ddot{z}_{fr}$) combined with lateral acceleration at one side ($\ddot{y}_{fr}$).

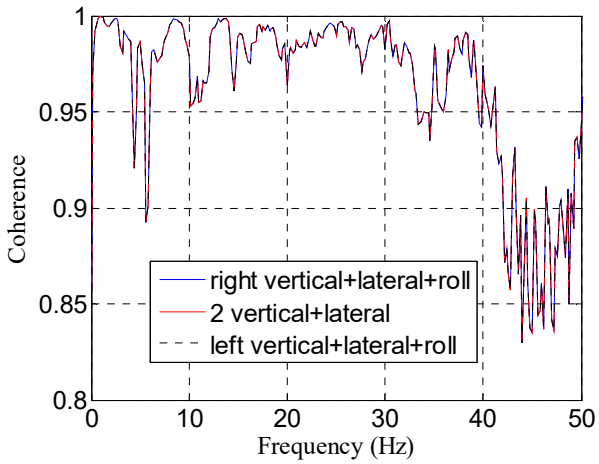

Fig. 5-25 Comparison of multiple coherence functions for the transmissibility to the vertical acceleration on the backrest (output) obtained from the front seat seated with one subject using three different groups of inputs from the floor.

5.6.3 Reason for low multiple coherence

The low multiple coherence at some frequencies can mainly be explained by three reasons: firstly, the inputs on the train were not well-defined, that is, low-level inputs at some frequencies can result in low-level responses, which were prone to be covered up by the noise; Secondly, even when the vibration was fully caused by the vertical, lateral and roll vibrations of the floor, the multiple coherence function would not be unity because of the nonlinearity of human-seat system. Finally, three inputs were not enough to fully explain the responses at the seat pan and backrest because

of complex multiple inputs of the seats on the train and flexibility of the floor. But from all the six cases above, it can be seen that although the high-speed train seat was exposed to various vibrations from different sources, the three inputs (vertical, lateral and roll accelerations) from the floor can almost account for the vertical, lateral and roll responses at the seat pan and backrest. The unsatisfactory multiple coherences at some frequencies were explained by the first reason, so ignoring the effect of the second and third reasons can still obtain satisfactory results, that is to say, the human-seat system can be approximately regarded as a linear system, and other inputs can be ignored.

5.6.4 Field measurement vs laboratory measurement

The field measurement and the laboratory one can be carried out for different purposes. In a real complex vibration environment, the on-site measurements intended to make clear how many and which inputs from the floor could account for the responses on the seat pan and backrest. However, for the laboratory measurements, this could not be achieved because of the self-defined inputs and the randomness of the noise. The laboratory measurement aimed to estimate the FRF accurately, because the input spectrums were well-defined, and the designed multiple inputs could be almost incoherent with each other, as well as the low noise disturbance.

5.7 Conclusions

By the measurement of seat vibration on a high-speed train, the coherences and transmissibilities from the floor to seat pan and backrest were studied using a proposed new multi-input and single-output model, some conclusions could be drawn by this study.

Although the high-speed train seat was exposed to complex vibrations from different sources, when the three inputs (vertical, lateral and roll accelerations) from the floor were used as the inputs for multi-input and single-output models, good multiple coherence functions could be obtained when studying the seat transmissibilities to the vertical, lateral and roll vibrations at the seat pan and backrest except in the frequency range where the anti-resonance of the inputs located. The unsatisfactory multiple coherence could be explained by the anti-resonances of the input signals, which was further verified by the laboratory experiment. When the vertical vibration at the other side took the place of either the roll vibration or the original vertical vibration, they would generate exactly the same multiple coherence.

Then the on-site measurement was compared with the laboratory measurement in terms of the estimation of the coherence and transmissibility, and their advantages and disadvantages were

analyzed. The laboratory experiment can have well-defined spectra of inputs, low disturbance from the noise, well-controlled mutual coherence between inputs, etc, so the contribution from the coherent parts between the inputs is smaller, and the multiple coherence is higher than field measurement. In the field measurement, that the inputs were coherent with the 'noise' was the main reason for the erroneous estimation of FRF, but the erroneous estimation of FRF resulting from the coherence between the inputs can to some degree be figured out by adopting an MISO system.

Finally, the seat transmissibility of one seat seated with one subject was compared with the counterpart with two subjects. It was found the peaks in the seat transmissibilities caused by the seat modes usually got reduced by the neighbouring subject because of the damping brought from that subject. This gave us guidance to separate the cases of different numbers of subjects sitting on the train seat in the following study of seat transmissibility.

Chapter 6 Experimental study of biodynamic response of seated subject to lateral, vertical and roll excitations

6.1 Introduction

The vibration environment in rail vehicles including high-speed trains is usually complex involving multi-axis vibration. Since the human body is a complex nonlinear dynamic system, its biodynamics shows difference under single-axis and multi-axis vibration. Nevertheless, most previous studies were focused on the biodynamic response of seated subjects to single-axis excitations, largely due to the constraint of equipment available and the more complexity of experimental design for multi-axis excitations, etc.

For a linear system, the dynamic characteristics are independent of the vibration magnitude. Since the human body is a nonlinear system, its biodynamics exhibits nonlinearity with the change of vibration magnitudes in all three translational directions. In the vertical direction, the excitation magnitude was considered to decrease the principal resonance frequency of the vertical apparent mass on the seat pan because of the 'softening effect' of the human body. On the other hand, there was no consistent conclusion about the influence of the excitation magnitude on the modulus of apparent mass at resonance (Mansfield and Griffin, 2000; Matsumoto and Griffin, 2002b; Nawayseh and Griffin, 2003; Huang and Griffin, 2008). Mansfield and Griffin (2000) thought the resonance frequency reducing with increasing excitation magnitude was probably caused by a complex combination of factors, including the stiffness of the tissue beneath the ischial tuberosities decreasing with increasing excitation magnitude. In the fore-and-aft direction, Fairley and Griffin (1989) reported a decrease in the second resonance frequency of the fore-and-aft apparent mass as the increase of vibration magnitude. Besides the second one, Mansfield and Lundström (1999) also reported a decrease in the first resonance frequency. Nawayseh and Griffin (2005a) reported that the median magnitude and phase of the fore-and-aft apparent mass showed nonlinearity in all the four postures (feet hanging, maximum thigh contact, average thigh contact, and minimum thigh contact) with the change of the vibration magnitude. Qiu and Griffin (2010) found a primary peak between 2 and 6 Hz, and the peak frequency reduced with increasing fore-and-aft excitation. In the lateral direction, Fairley and Griffin (1990) reported a decrease in the resonance frequency of the second mode in the lateral apparent mass as the increase of vibration magnitude. The reduction of resonance frequency with vibration magnitude was also reported in Mansfield and Lundström (1999) and Mandapuram *et al.* (2005).

Due to the nonlinearity of the human body, whether the biodynamic characteristics of the seated subject under single-axis vibration are applicable to a multi-axis vibration environment is still to be studied. Relative studies have been reported by Hinz *et al.* (2006), Mansfield and Maeda (2006, 2007), Qiu and Griffin (2010, 2012) and Mandapuram *et al.* (2010) as well as Zheng *et al.* (2012, 2019) for different combinations of three translational vibrations. The general conclusion from these studies is that compared with single-axis excitation, the addition of vibration in an orthogonal axis can also result in nonlinearity in the human body similar to increasing vibration magnitude in the single-axis vibration. It is well known the main vibrations on a high-speed train and other rail vehicles concerning passengers' ride comfort are vertical, lateral and roll vibrations, what the biodynamic response of the seated human body to the single-axis, bi-axis and tri-axis vibrations in these three directions with different vibration magnitudes is has rarely been studied.

On the other hand, under multiple inputs, the acceleration can go through more than one path to reach the forces due to the inevitable coherence between the multiple vibrations, so the traditional single-input and single-output (SISO) method may cause erroneous estimation of the apparent mass, which requires to adopt a new method to estimate the apparent mass under multiple inputs.

In this chapter, the biodynamic response of the human body exposed to vertical, lateral and roll vibration was studied by a laboratory experiment. The calculation of inline and cross-axis apparent masses (defined in Section 2.1) was based on the proposed improved multi-input and single-output (MISO) system (Section 3.2) or SISO system according to the number of vibration inputs. The contributions of different vibration inputs to the forces on the seat pan and backrest were analyzed by the analysis of coherence functions. What the effect of vibration magnitude on the biodynamic response of the seated human body to the combined lateral, vertical and roll vibrations is and what the effect of adding on excitations in one or two axes on the apparent mass in another axis is were explored and answered, so as to advance understanding on the biodynamics of the human body.

6.2 Experimental methods

6.2.1 Experimental set-up

The experiment was carried out using a 6-axis motion simulator in ISVR at the University of Southampton. The simulator was capable of producing ±1 m vertical displacement, ±0.5 m fore-and-aft and lateral displacements, ±20 degrees of roll and pitch and ±10 degrees of yaw motion. The simulator had low cross-talk (within 5%) between axes. Twelve male subjects having a mean age of 29.7 years (standard deviation (SD) 6.8 years), a mean stature of 175.3 cm (SD 6.4 cm) and a mean weight of 80.4 kg (SD 9.98 kg) participated in the experiment. The experiment was approved

by Human Experimentation Safety and Ethics Committee of the ISVR at the University of Southampton (approval number: 40309).

The seat used for the experiment was rigid, having a vertical backrest (Fig. 6-1). During the experiment, the participants were asked to sit in an upright posture in contact with the backrest, with the feet resting on the footrest (average thigh contact), a hand holding an emergency button and the other on the lap. Another emergency button was within the reachable distance of the experimenter.

The excitation in every direction was random acceleration signal with approximately flat spectra defined in the range from 0.5 to 30 Hz. Every participant was exposed to 63 excitations which were the combination of the vertical excitation with four magnitudes (0, 0.25, 0.5 and 1.0 m/s^2 r.m.s.), lateral excitation with four magnitudes (0, 0.25, 0.5 and 1.0 m/s^2 r.m.s.), as well as roll excitation with four magnitudes (0, 0.5, 0.75 and 1.0 rad/s^2 r.m.s.). The multi-axis excitations were almost incoherent between different directions. The rotational axis of roll excitation is defined as the intersection line between the seat pan upper surface and the symmetrical (x-z) plane of the seat. Every stimulus lasted 60 s with necessary repetition.

The tri-axial forces F_{sx}, F_{sy} and F_{sz} at the seat pan were measured by a force plate (Kistler 9281 B) with four tri-axial transducers at the four corners of the plate amplified by Kistler 5001 charger amplifiers, and the tri-axial forces F_{bx}, F_{by} and F_{bz} at the backrest were respectively the summation of the forces in x, y and z directions measured by two tri-axial force transducers (Kistler 9602) placed at the two ends in a diagonal amplified by Kistler 5073 charger amplifiers (Fig. 6-1). The tri-axial accelerations at the seat pan (a_{sx}, a_{sy} and a_{sz}) and backrest (a_{bx}, a_{by} and a_{bz}) were measured by two tri-axial SIT-pads. The SIT-pad on the seat pan was positioned beneath the ischial tuberosity of seated subjects. The SIT-pad on the backrest was centrally located $z_d = 470$ mm above the seat pan surface (Fig. 6-1). All the data were recorded by *HVLab* data acquisition system at 512 samples per second via anti-aliasing filter set at 50 Hz, and then data analysis was conducted in Matlab. The participants' safety was ensured over the whole process with the vibration exposure controlled within the safety range in accordance with the standard BS 6841:1987.

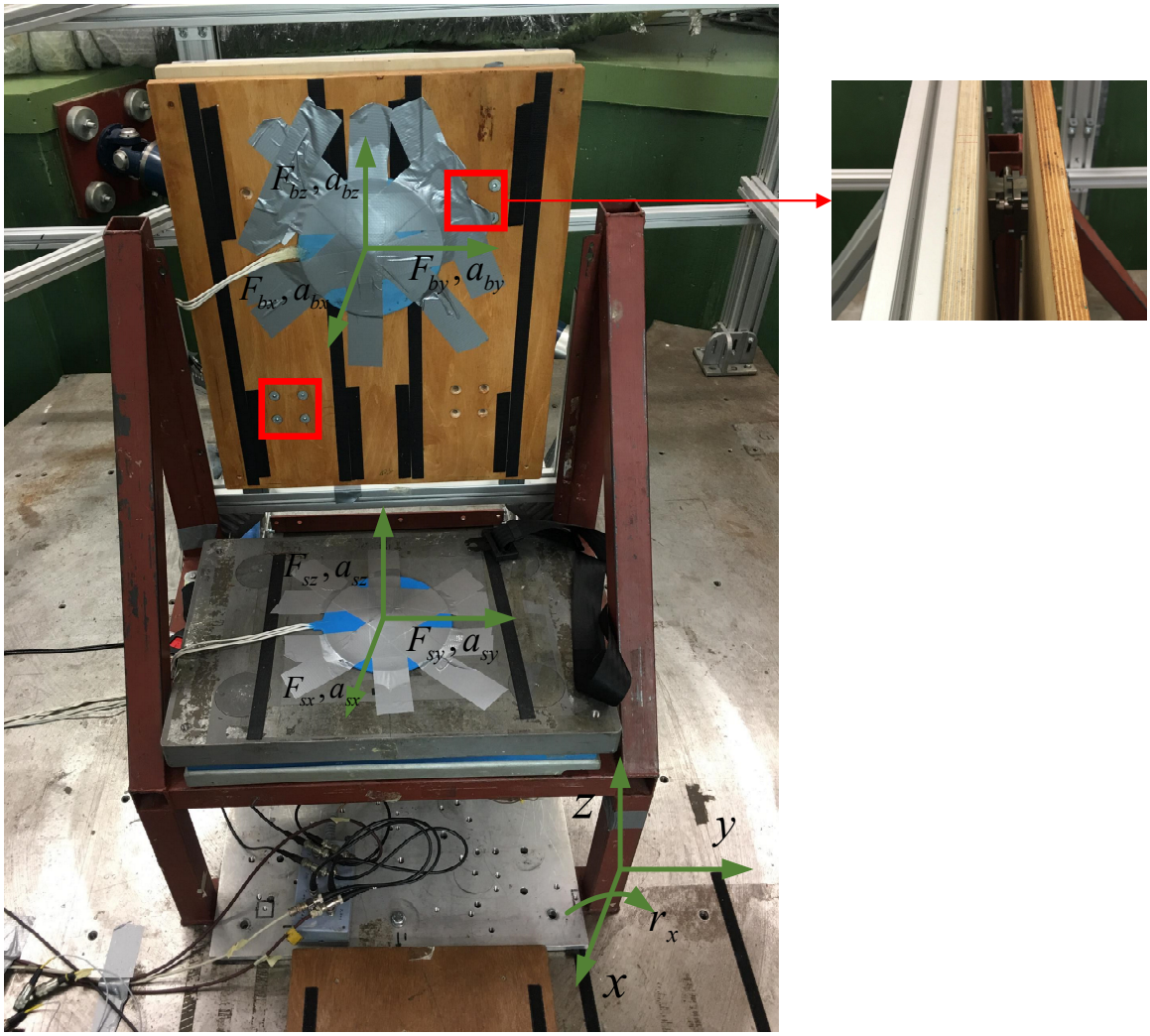

Fig. 6-1 Experimental set-up (the locations of the two force transducers are in the red boxes, the layout is shown in the right subgraph).

6.2.2 Convention of the symbols

The expression of the symbols follows a similar convention to Mansfield and Maeda (2006). For multi-axis inline FRF, the first sequence of characters denotes the directions of the excitations, and the second sequence represents the direction of the calculation of FRF. Acceleration excitation in roll direction is denoted as r_x. For example, 'yzr_x, y' refers to the FRF in y direction while exposed to excitations in y, z and roll directions simultaneously. For cross-axis FRF, the first sequence has the same definition as the inline FRF. Whereas in the second sequence, the character before '-' denotes the direction of acceleration excitation, and that after '-' denotes the direction of the calculation of FRF. For example, 'yzr_x, y-z' means the cross-axis FRF from the vibration in y direction to the vibration or force in z direction, when exposed to excitations in y, z and roll directions simultaneously.

Apparent mass, a kind of FRF, is simplified as 'AM'. For the cross-axis apparent mass, 'AM' is followed by a subscript with three letters. The first one can be either 's' or 'b', standing for the apparent mass on the seat pan or backrest. The following two letters stand for the directions of vibration and the direction of the calculation of apparent mass, same as above. For example, AM_{by-z} means the cross-axis apparent mass from the acceleration in y direction on the backrest to the force in z direction on the backrest. For the inline apparent mass, 'AM' is followed by a subscript with two letters and the first letter has the same meaning as cross-axis apparent mass. The second letter means both the direction of vibration and the direction of the calculation of apparent mass. For example, AM_{sy} means the inline apparent mass in y direction on the seat pan.

For cross-axis apparent mass, the apparent mass from i-axis acceleration to j-axis force is expressed as i-j apparent mass for simplicity. For example, z-x apparent mass means the apparent mass from the acceleration in z axis to the force in x axis.

6.3 Data analysis and results

Prior to the calculation of apparent mass, mass cancellation for the forces at the seat pan and backrest was performed in the time domain by removing the mass attached to the force transducers multiplying by the acceleration in each direction from the measured forces in the same direction. The frequency resolution for the following analysis is 0.2 Hz.

For single-axis excitations, the SISO system usually is applicable. However, for multi-input systems, SISO model can cause overestimation or underestimation of the FRF because of the coherence between the inputs, which is unavoidable in the laboratory experiment and can result from the following reasons: (1) When generating two random signals, they cannot be completely incoherent; (2) When using the 6-axis motion simulator to reproduce the desired signal, the error between the desired signal and the generated one is inevitable; (3) The cross-talk between orthogonal axes of the simulator; (4) The limited rigidity of the seat; (5) The cross-axis sensitivity of the multi-axis transducers; (6) Measuring error of transducers due to misalignment. The mutual coherence can be controlled very small, however, it cannot be eliminated at every frequency. In this situation, the MISO model is designed for the more accurate estimation of FRF.

Because the roll motion of the backrest could also generate lateral acceleration and tri-axis forces on the backrest, for consistency with the cases without roll excitation and ruling out the influence of lateral acceleration and tri-axial forces on the backrest induced by roll excitation on the

calculation of the lateral and y-z, y-x apparent masses on the backrest, MISO system is also designed for this purpose. The roll acceleration on the backrest can be calculated by

$$a_{r_x} = \frac{a_{by} - a_{sy}}{z_d} \tag{6-1}$$

The apparent masses were calculated by designing either SISO or MISO system in accordance with Table 6-1 and Table 6-2. For example, when calculating the lateral apparent mass on the backrest under exposure to lateral, vertical and roll excitations, MISO system should be designed by taking a_{by}, a_{bz} and a_{r_x} as inputs, and F_{by} as output. The tri-axis forces on the seat pan generated by the roll excitation were negligible, so the roll excitation was not taken as the input for the apparent mass on the seat pan.

For the calculation of the apparent mass using the MISO method, the frequency response function for the original system $H_{my}(m=1,2,3)$ in Eq. (3-9) is adopted here, so the input and output for the calculation of apparent mass have been got rid of the coherent parts with all the other inputs. The coherences in Eqs. (3-21)-(3-22) are to be calculated for making clear the contribution of the different inputs to the output. Therefore, all the calculations of apparent mass and coherence do not depend on the sequence of inputs.

Table 6-1 Estimation method (MISO or SISO system) for the apparent mass on the seat pan

Excitation*	$y \neq 0$, $z \neq 0$	$y \neq 0$, $z = 0$	$y = 0$, $z \neq 0$
Method	MISO	SISO	SISO
Input	a_{sy}, a_{sz}	a_{sy}	a_{sz}
Output	F_{sx}, F_{sy}, F_{sz}		

*Being equal or not equal to zero means the excitation in that direction is zero or non-zero.

Table 6-2 Estimation method (MISO or SISO system) for the apparent mass on the backrest

Excitation*	$y \neq 0$, $z \neq 0$, $r_x \neq 0$	$y \neq 0$, $z \neq 0$, $r_x = 0$	$y \neq 0$, $z = 0$, $r_x \neq 0$	$y \neq 0$, $z = 0$, $r_x = 0$	$y = 0$, $z \neq 0$, $r_x \neq 0$	$y = 0$, $z \neq 0$, $r_x = 0$
Method	MISO	MISO	MISO	SISO	MISO	SISO
Input	a_{by}, a_{bz}, a_{r_x}	a_{by}, a_{bz}	a_{by}, a_{r_x}	a_{by}	a_{bz}, a_{r_x}	a_{bz}
Output	F_{bx}, F_{by}, F_{bz}					

*Being equal or not equal to zero means the excitation in that direction is zero or non-zero.

Data analysis was carried out using Matlab (2010b). Wilcoxon signed-rank test introduced in Section 3.4 was used to test the difference between paired samples with a chosen significance level α of 0.05. In the following results, m/M means m pairs show significant change out of M pairs in M pairwise comparisons.

A number of studies on vertical and lateral apparent mass have attributed the discrepancy of apparent mass to the difference of body mass (Fairley and Griffin, 1989; Wang *et al.*, 2004) (Fig. 6-2). In the present study, to reduce the inter-subject variability in apparent masses brought from different subjects' weights, the apparent masses were normalized by the total body mass of the subject. It was noticed that in the experimental data a sudden change occurred at about 10 Hz in the phase of the apparent mass at the backrest in the *z* direction. This was because the apparent mass of the human body above 10 Hz was small in comparison with the gross (measured) apparent mass, and the subtraction of the mass of the backrest from the gross apparent mass when conducting mass cancellation resulted in the phase shift.

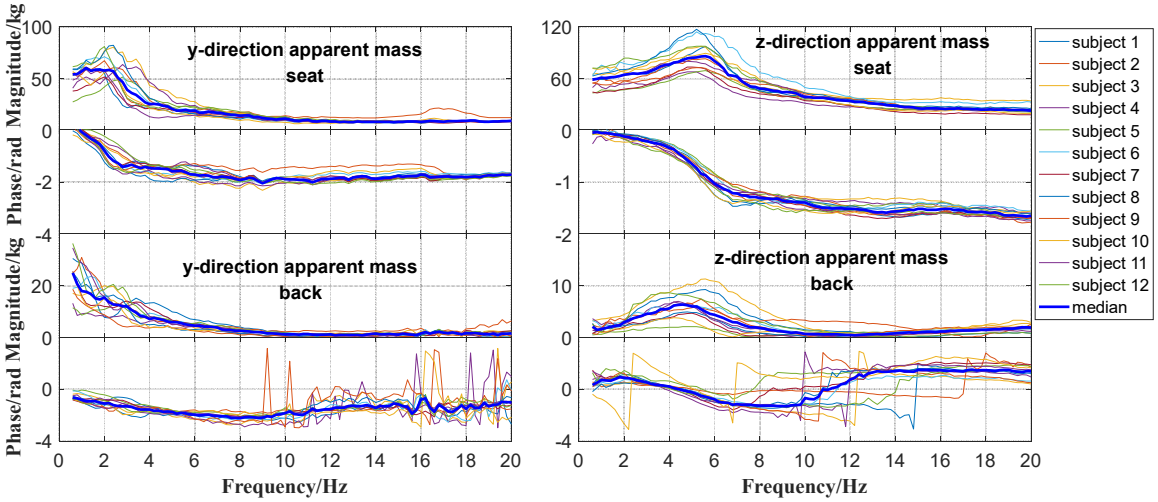

Fig. 6-2 The inline apparent masses in y direction and z direction on the seat pan and backrest for 12 different subjects and the median ones under the excitation of 0.5 ms^{-2} r.m.s. lateral, 1.0 ms^{-2} r.m.s. vertical and 0.75 rad/s^2 r.m.s. roll vibration.

6.3.1 Inline apparent mass

6.3.1.1 Apparent mass in y direction

For the apparent mass in y direction on the seat pan, the primary resonance frequencies for almost all the subjects lied in 0.8-3.5 Hz (Fig. 6-2). No matter how many axes of excitations and what the magnitudes of z-axis and roll excitations were, the resonance frequencies decreased as the increase of excitation magnitude in y direction with a large proportion of significant changes (Fig. 6-3) (33/48 in total, Table 6-3), however, showed much smaller proportion of significant changes as the increasing magnitude in z direction (8/72 in total, Table D-1) and in roll direction (8/72 in total, not shown). The proportion of significant changes of resonance frequency with y-axis excitation magnitude showed a decreasing trend as the increase of roll magnitude (from 9/12 to 6/12, Table 6-3) and no consistent variation as z-axis excitation magnitude (between 7/12 and 10/12, Table 6-3).

On the other hand, no matter what the z-axis and roll magnitudes were, the differences between y=0.25 and y=1.0 and between y=0.5 and y=1.0 were usually more significant than those between y=0.25 and y=0.5 (Table 6-3).

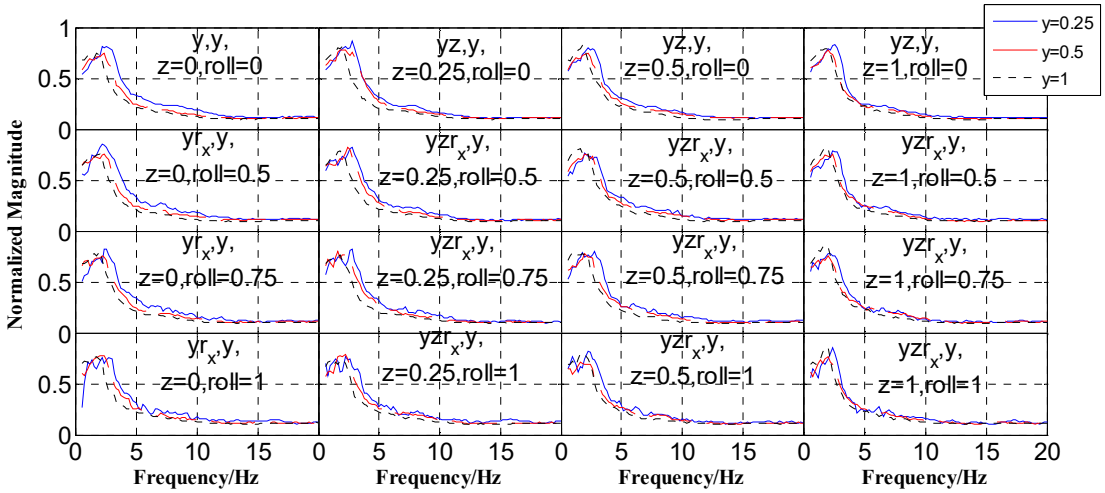

Fig. 6-3 Comparison between median normalized apparent masses in y direction on the seat pan for 12 subjects under different excitation magnitudes in y direction.

Table 6-3 Wilcoxon signed-rank test for the effect of excitation magnitude in y direction on the resonance frequency and modulus at resonance for the apparent mass in y direction on the seat pan

y magnitude	y=0.5	y=1.0	Significant difference proportion (different r_x)
(a)r_x=0			
y=0.25	***/ns/ns/*; ns/*/ns/ns	***/***/ns/***; ns/*/ns/*	9/12; 3/12
y=0.5		***/***/**/***; ns/ns/ns/ns	
(b)r_x=0.5			
y=0.25	ns/*/ns/*; ns/ns/ns/ns	***/***/*/***; ns/*/ns/ns	10/12; 1/12
y=0.5		*/***/***/***; ns/ns/ns/ns	
(c)r_x=0.75			
y=0.25	*/ns/ns/ns; */ns/ns/ns	***/***/***/***; ns/*/ns/ns	8/12; 2/12
y=0.5		ns/***/***/*; ns/ns/ns/ns	
(d)r_x=1.0			
y=0.25	***/ns/ns/ns; ns/ns/***/*	***/ns/***/***; ns/ns/ns/ns	6/12; 3/12
y=0.5		*/ns/*/ns; ns/**/ns/ns	
Significant difference proportion (different z)	z=0: 10/12; 1/12 z=0.25: 7/12; 5/12 z=0.5: 7/12; 1/12 z=1.0: 9/12; 2/12		

ns=not significant, p>0.05; *= p<0.05;**= p<0.01;***= p<0.005, Wilcoxon;
The p-value for different excitation magnitudes in z direction is ranked as z=0/z=0.25/z=0.5/z=1.0, separated by slash;
The effect on resonance frequency and modulus at resonance is shown before and after ';', respectively.

As for the modulus at resonance, the porportion of significant variations was small as the increase of y-axis excitation magnitude (9/48 in total, Table 6-3), z-axis excitation magnitude (6/72 in total, Table D-1) or roll excitation magnitude (3/72 in total, not shown).

For the apparent masses in y direction on the backrest, some subjects exhibited a principal resonance in 0.5-2 Hz, especially under low-magnitude y-axis excitation. The resonance frequency was even frequently lower than 0.5 Hz (not in the band limiting), especially under high-magnitude y-axis excitation, which resulted in the non-parametric study of resonance frequency not being able to be done. Some subjects also showed a second resonance between 2-5 Hz. Sometimes, a third peak was clearly visible between 3-6 Hz for two subjects. Interestingly, from the median apparent masses, there was a clear reduction of the magnitude of apparent mass as the increase of excitation magnitude in y direction (Fig. 6-4). This reduction was clearer in the low-frequency range (<10 Hz) with low excitation magnitude in z and roll directions. The Wilcoxon signed-rank test was conducted at 0.8, 1.0, 2.0, 4.0 Hz, and the results were shown in Table 6-4. The proportion of significant changes seemed to reduce as the increase of frequency (totally 33/48 at 0.8 Hz; 32/48 at 1.0 Hz; 22/48 at 2.0 Hz; 24/48 at 4.0 Hz, Table 6-4). The proportion of significant changes tended to reduce as the increase of magnitude in z axis (from 9/12 to 4/12 at 2.0 Hz, from 8/12 to 5/12 at 4.0 Hz, Table 6-4) and in roll axis (from 9/12 to 6/12 at 1.0 Hz; from 6/12 to 4/12 at 2.0 Hz; from 9/12 to 5/12 at 4.0 Hz, Table 6-4). On the other hand, whatever the z-axis and roll magnitudes were, the difference between y=0.25 and y=1.0 was usually more significant than that between y=0.25 and y=0.5 and between y=0.5 and y=1.0 (Table 6-4), which agrees with common sense.

However, a small proportion of significant changes of the modulus of apparent mass as excitation magnitude in z (totally 6/72 at 0.8 Hz; 9/72 at 1.0 Hz; 10/72 at 2.0 Hz; 9/72 at 4.0 Hz, not shown) and roll (Fig. D-1; totally 5/72 at 0.8 Hz; 8/72 at 1.0 Hz; 7/72 at 2.0 Hz; 11/72 at 4.0 Hz, not shown) directions were detected by Wilcoxon test.

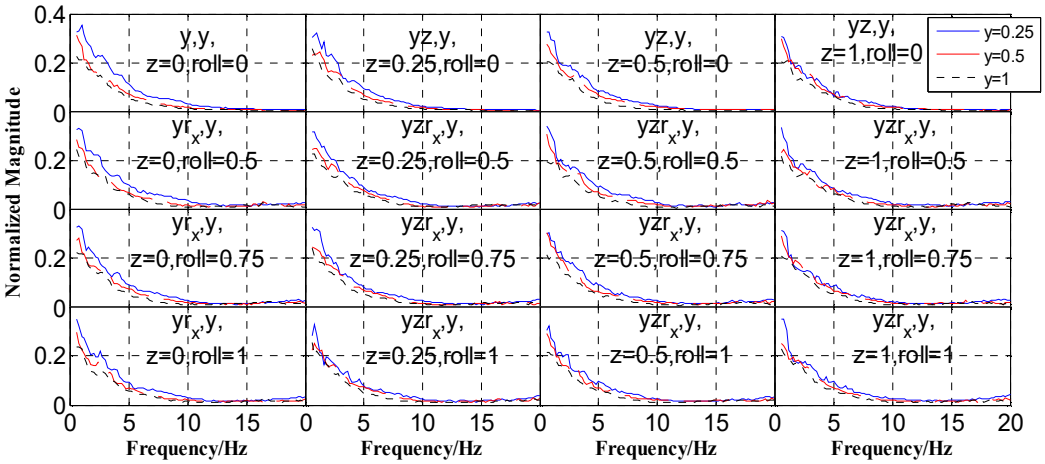

Fig. 6-4 Comparison between median normalized apparent masses in y direction on the backrest for 12 subjects under different excitation magnitudes in y direction.

Table 6-4 Wilcoxon signed-rank test for the effect of excitation magnitude in y direction on the magnitude at specific frequencies for the apparent mass in y direction on the backrest

y magnitude	y=0.5 (Frequencies: 0.8;1.0;2.0;4.0 Hz)	y=1.0 (Frequencies: 0.8;1.0;2.0;4.0 Hz)	Significant difference proportion (different r_x)
(a)r_x=0			
y=0.25	ns/ns/ns/ns;*/ns/ns/ns; **/ns/ns/ns;***/**/ns/ns	*/***/***/***;**/*/***/***; */***/***/**;***/***/***/**	7/12;9/12; 6/12;9/12
y=0.5		***/ns/***/***;***/*/***/***; ns/ns/ns/**;*/ns/**/*	
(b)r_x=0.5			
y=0.25	ns/***/ns/ns;*/ns/ns/ns; ***/*/ns/ns;***/***/ns/ns	*/***/***/***;***/*/***/***; */***/ns/*;***/***/***/ns	9/12;8/12; 6/12;5/12
y=0.5		*/*/*/*;*/ns/***/**; ns/ns/ns/*;ns/ns/ns/ns	
(c)r_x=0.75			
y=0.25	ns/***/ns/**;**/***/ns/**; **/ns/ns/ns;ns/***/ns/ns	**/**/**/***;***/***/**/***; ***/***/***/ns;***/***/*/*	9/12;9/12; 6/12;5/12
y=0.5		**/ns/***/*;ns/*/*/ns; */ns/*/ns;ns/ns/ns/ns	
(d)r_x=1.0			
y=0.25	*/***/ns/**;ns/*/ns/***; ***/ns/ns/ns;*/ns/ns/ns	**/***/**/***;**/**/ns/***; ***/*/***/ns;***/ns/*/*	8/12;6/12; 4/12;5/12
y=0.5		ns/ns/*/ns;ns/ns/ns/*; ns/ns/ns/ns;ns/ns/ns/***	
Significant difference proportion (different z)	z=0: 8/12; 9/12;9/12;8/12 z=0.25: 8/12; 8/12;5/12;6/12 z=0.5: 8/12; 6/12;4/12;5/12 z=1.0: 9/12; 9/12;4/12;5/12		

ns=not significant, p>0.05; *= p<0.05;**= p<0.01;***= p<0.005, Wilcoxon;
The p-value for different excitation magnitudes in z direction is ranked as z=0/z=0.25/z=0.5/z=1.0, separated by slash;
The results at different frequencies are shown in the order: 0.8; 1.0; 2.0; 4.0 Hz, separated by ';'.

6.3.1.2 Apparent mass in z direction

For the apparent mass in z direction on the seat pan, the resonance frequencies for almost all the subjects lied in 4-7.5 Hz (Fig. 6-2). A large proportion of significant decreases of the resonance frequencies were found by Wilcoxon test as the increase of excitation magnitude in z direction (Fig. 6-5; 30/48 in total, Table 6-5), however, a smaller proportion of significant decreases as the increase of magnitude in y direction (Fig. D-2; 27/72 in total, Table 6-6), and a very small proportion of significant decreases as the increasing magnitudes in roll direction (8/72 in total, not shown) were detected. Interestingly, the proportion of significant changes of resonance frequency with z-axis excitation magnitude decreased as the rise of y-axis excitation magnitude (from 11/12 to 3/12, Table 6-5) and roll excitation magnitude (from 9/12 to 5/12, Table 6-5). Similarly, the proportion of significant changes of resonance frequency with y-axis excitation magnitude reduced as the rise of z-axis excitation magnitude (from 15/24 to 3/24, Table 6-6) and roll excitation magnitude (from 9/18 to 5/18, Table 6-6). On the other hand, as for the modulus at resonance, the proportions of significant variations as the increase of y-axis magnitude (9/72 in total, Table 6-6), z-axis magnitude (8/48 in total, Table 6-5) and roll magnitude (3/72 in total, not shown) were all small.

Table 6-5 Wilcoxon signed-rank test for the effect of excitation magnitude in z direction on the resonance frequency and modulus at resonance for the apparent mass in z direction on the seat pan

z magnitude	z=0.5	z=1.0	Significant difference proportion (different r_x)
(a)r_x=0			
z=0.25	***/*/ns/ns; ns/ns/ns/ns	***/***/*/**;ns/ns/ns/ns	9/12;0/12
z=0.5		*/***/*/ns;ns/ns/ns/ns	
(b)r_x=0.5			
z=0.25	**/**/ns/ns;ns/ns/ns/ns	***/***/*/*;ns/*/ns/*	8/12;2/12
z=0.5		ns/***/***/ns;ns/ns/ns/ns	
(c)r_x=0.75			
z=0.25	***/**/ns/*;ns/*/ns/ns	***/***/ns/ns;ns/***/ns/ns	8/12;3/12
z=0.5		***/*/*/ns;ns/ns/ns/***	
(d)r_x=1.0			
z=0.25	**/ns/ns/ns;ns/ns/***/ns	***/***/ns/ns;ns/*/***/ns	5/12;3/12
z=0.5		***/***/ns/ns;ns/ns/ns/ns	
Significant difference proportion (different y)	y=0: 11/12;0/12 y=0.25: 11/12;4/12 y=0.5: 5/12;2/12 y=1.0: 3/12;2/12		

ns=not significant, p>0.05; *= p<0.05;**= p<0.01;***= p<0.005, Wilcoxon;
The p-value for different excitation magnitudes in y direction is ranked as y=0/y=0.25/y=0.5/y=1.0, separated by slash;
The effect on resonance frequency and modulus at resonance is shown before and after ';', respectively.

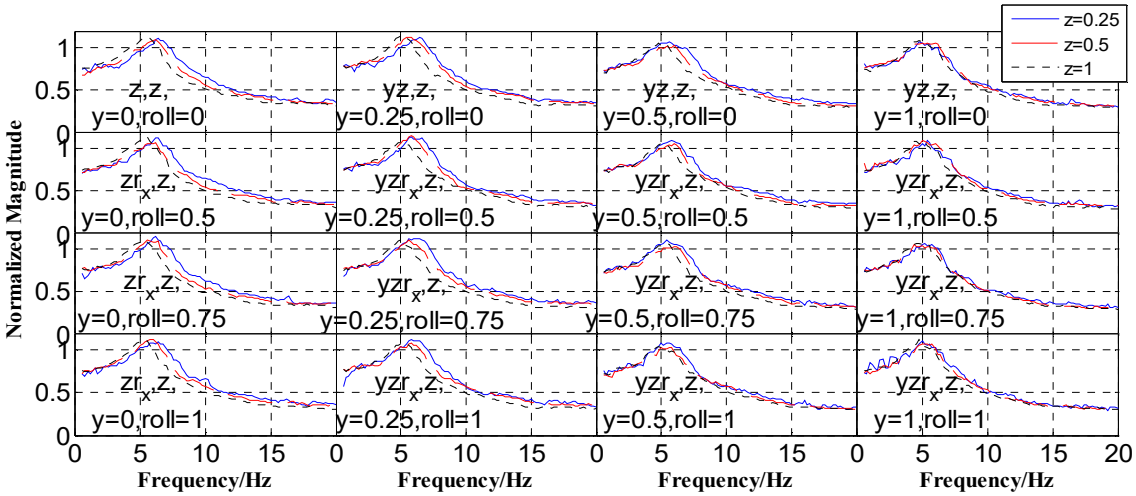

Fig. 6-5 Comparison between median normalized apparent masses in z direction on the seat pan for 12 subjects under different excitation magnitudes in z direction.

Table 6-6 Wilcoxon signed-rank test for the effect of excitation magnitude in y direction on the resonance frequency and modulus at resonance for the apparent mass in z direction on the seat pan

y magnitude	y=0.25	y=0.5	y=1.0	Significant difference proportion (different r_x)
(a)r_x=0				
y=0	ns/ns/***;ns/ns/ns	***/ns/**;ns/*/ns	***/***/**;ns/ns/ns	9/18; 1/18
y=0.25		***/ns/ns;ns/ns/ns	**/*/ns;ns/ns/ns	
y=0.5			ns/ns/ns;ns/ns/ns	
(b)r_x=0.5				
y=0	ns/ns/ns;ns/ns/ns	**/ns/ns;ns/ns/*	***/*/ns;ns/ns/ns	6/18;3/18
y=0.25		*/ns/ns;**/ns/ns	***/ns/ns;**/ns/ns	
y=0.5			ns/*/ns;ns/ns/ns	
(c)r_x=0.75				
y=0	ns/ns/ns;ns/ns/ns	***/ns/ns;ns/ns/ns	***/***/ns;ns/ns/ns	7/18;1/18
y=0.25		***/ns/ns;ns/ns/ns	***/*/ns;*/ns/ns	
y=0.5			ns/***/ns;ns/ns/ns	
(d)r_x=1.0				
y=0	ns/ns/ns;ns/ns/*	*/ns/ns;ns/**/**	***/*/ns;ns/ns/ns	5/18;4/18
y=0.25		ns/ns/ns;ns/ns/ns	**/**/ns;ns/ns/ns	
y=0.5			ns/ns/ns;ns/ns/*	
Significant difference proportion (different z)	z=0.25: 15/24;3/24 z=0.5: 9/24;2/24 z=1.0: 3/24;4/24			

ns=not significant, p>0.05; *= p<0.05;**= p<0.01;***= p<0.005, Wilcoxon;
The p-value for different excitation magnitudes in z direction is ranked as z=0.25/z=0.5/z=1.0, separated by slash;
The effect on resonance frequency and modulus at resonance is shown before and after ';', respectively.

The apparent masses in z direction at the backrest were small compared to those at the seat pan, and most subjects showed a primary resonance between 3 and 7 Hz (Fig. 6-2). This resonance frequency was close to that in the apparent mass in z direction on the seat pan. A large proportion of significant decreases of the resonance frequencies were registered as the increase of excitation magnitude in z direction (18/48 in total, Table 6-7) only with no roll or y-axis excitation (Fig. 6-6; r_x=0, 7/12; y=0, 11/12; Table 6-7). Interestingly, adding or increasing roll and y-axis excitation would reduce the proportion of significant changes of resonance frequency with z-axis magnitude (from 7/12 to 4/12 as r_x-axis magnitude; from 11/12 to 0/12 as y-axis magnitude; Table 6-7).

What is more, the proportion of significant reductions of the resonance frequency was large as the increase of y-axis excitation magnitude (28/72 in total, Table D-2), especially when roll or z-axis magnitude was small (Fig. D-3; r_x=0, 10/18; r_x=0.5, 8/18; z=0.25, 13/24; z=0.5, 13/24; Table D-2). Similarly, adding or increasing roll and z-axis excitation would reduce the proportion of significant changes of resonance frequency with y-axis magnitude (from 10/18 to 5/18 as r_x-axis magnitude; from 13/12 to 2/12 as z-axis magnitude; Table D-2). The change of roll excitation magnitude made little difference to the resonance frequency (2/72 in total, not shown).

As for the modulus at resonance, similar to the apparent mass in z direction on the seat pan, overall, a small proportion of significant changes were found as the increase of y-axis magnitude (8/72 in total, Table D-2), z-axis magnitude (11/48 in total, Table 6-7) and roll magnitude (12/72 in total, not shown), except the relatively large proportion of significant reductions as the increase of z-axis magnitude with no y-axis excitation (7/12, y=0, Table 6-7; the left four subgraphs in Fig. 6-6).

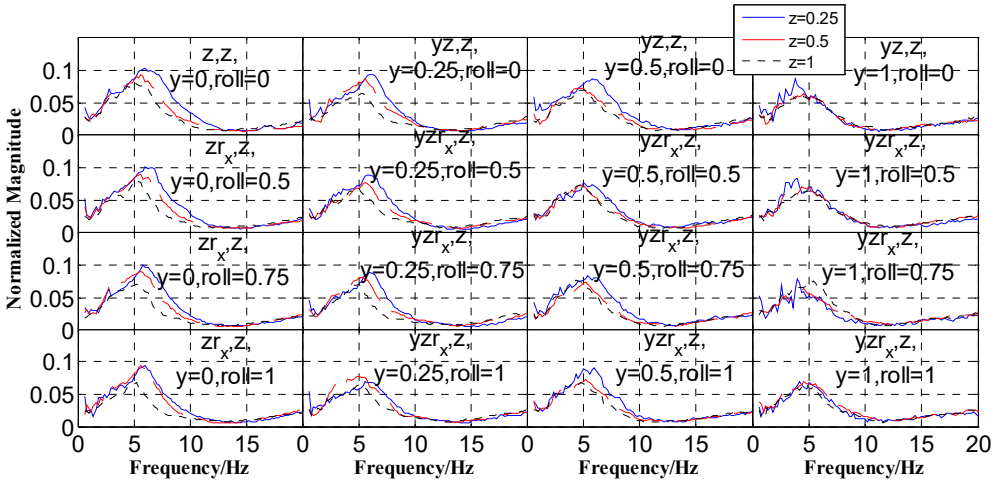

Fig. 6-6 Comparison between median normalized apparent masses in z direction on the backrest for 12 subjects under different excitation magnitudes in z direction.

Table 6-7 Wilcoxon signed-rank test for the effect of excitation magnitude in z direction on the resonance frequency and modulus at resonance for the apparent mass in z direction on the backrest

z magnitude	z=0.5	z=1.0	Significant difference proportion (different r_x)
(a)r_x=0			
z=0.25	*/ns/*/ns;ns/ns/ns/ns	***/ns/***/ns;*/***/ns/ns	7/12;4/12
z=0.5		***/*/***/ns;*/***/ns/ns	
(b)r_x=0.5			
z=0.25	*/ns/ns/ns;ns/ns/ns/ns	***/ns/ns/ns;*/***/ns/ns	4/12;4/12
z=0.5		*/***/ns/ns;**/***/ns/ns	
(c)r_x=0.75			
z=0.25	ns/ns/ns/ns;ns/ns/ns/ns	***/ns/ns/ns;***/ns/ns/ns	3/12;2/12
z=0.5		*/*/ns/ns;***/ns/ns/ns	
(d)r_x=1.0			
z=0.25	*/ns/ns/ns;ns/ns/ns/ns	***/*/ns/ns;ns/ns/ns/ns	4/12;1/12
z=0.5		**/ns/ns/ns;***/ns/ns/ns	
Significant difference proportion (different y)	y=0: 11/12;7/12 y=0.25: 4/12;4/12 y=0.5: 3/12;0/12 y=1.0: 0/12;0/12		

ns=not significant, p>0.05; *= p<0.05;**= p<0.01;***= p<0.005, Wilcoxon;
The p-value for different excitation magnitudes in y direction is ranked as y=0/y=0.25/y=0.5/y=1.0, separated by slash;
The effect on resonance frequency and modulus at resonance is shown before and after ';', respectively.

6.3.2 Cross-axis apparent mass

6.3.2.1 Z-y, y-z and y-x apparent mass

Generally, z-y, y-z and y-x normalized apparent masses on the seat pan and backrest were small at all excitation magnitudes (less than 0.2), which was presumably because of the human body's symmetry about the mid-sagittal plane. The cross-axis apparent masses on the seat pan and backrest measured using single-axis and multi-axis vibrations showed similar trends. One example of these apparent masses under tri-axis vibration was illustrated in Fig. 6-7. The difference between the cross-axis apparent masses for 12 different subjects was clear because of the inter-subject variability.

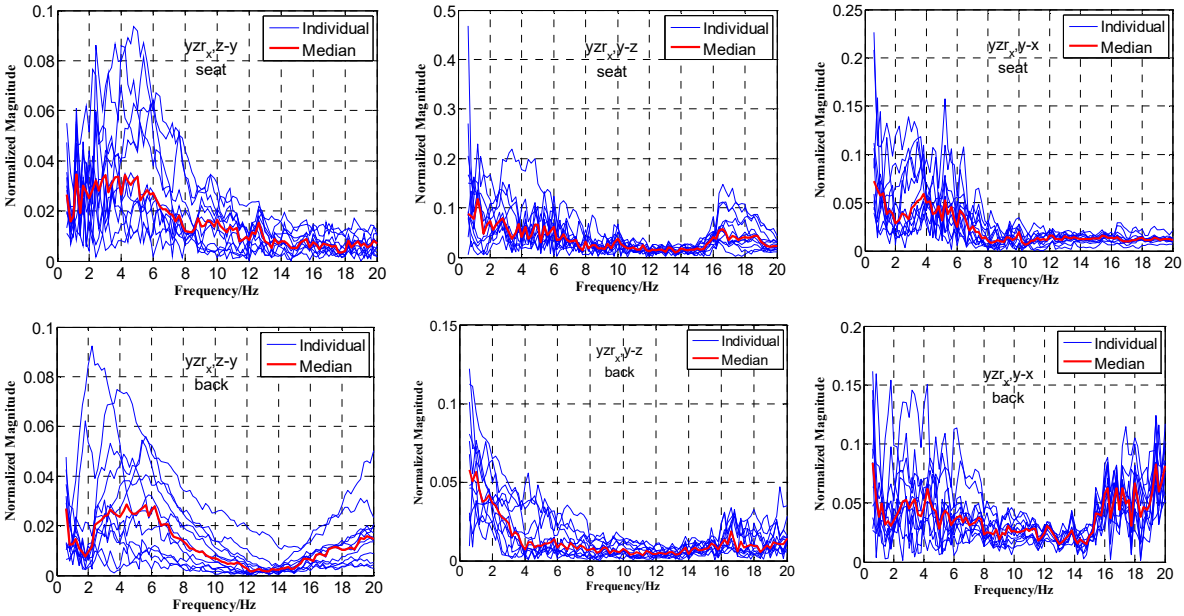

Fig. 6-7 The normalized cross-axis apparent mass on the seat pan and backrest under the excitation of 0.5 ms^{-2} r.m.s. lateral, 1.0 ms^{-2} r.m.s. vertical and 0.75 rad/s^2 r.m.s. roll vibration. Blue lines: individual apparent masses for 12 subjects; Red line: median apparent mass.

6.3.2.2 Z-x apparent mass

Generally speaking, the z-x apparent masses at the seat pan were large compared to other cross-axis apparent masses, showing a clear resonance for most subjects between 3-7.5 Hz (not shown), close to the principal resonance in the vertical apparent mass on the seat pan and backrest and in good agreement with Nawayseh and Griffin (2004).

By means of Wilcoxon signed-rank test, there were a large proportion of significant reductions of the resonance frequencies as the increase of excitation magnitude in z direction (Fig. 6-8; 30/48 in total, Table 6-8), except when y-axis excitation was the largest (y=1.0, 2/12, Table 6-8). The proportion of significant changes of the resonance frequency in z-x apparent mass on the seat pan with z-axis magnitude reduced as the increase of y-axis magnitude (from 12/12 to 2/12, Table 6-8). In a similar way, there were also a large proportion of significant reductions of the resonance frequency as the increase of y-axis excitation magnitude (Fig. D-4; 47/72 in total, Table D-3). However, the proportion of significant changes with y-axis magnitude reduced with the increasing magnitude in z direction from 18/24 to 12/24 (Table D-3). The change of roll excitation magnitude made little difference to the resonance frequency (7/72 in total, not shown).

As for the modulus at resonance, the proportions of significant changes were generally small as the increase of y-axis magnitude (9/72 in total, Table 6-8), z-axis magnitude (0/48 in total, Table D-3) or roll magnitude (4/72 in total, not shown).

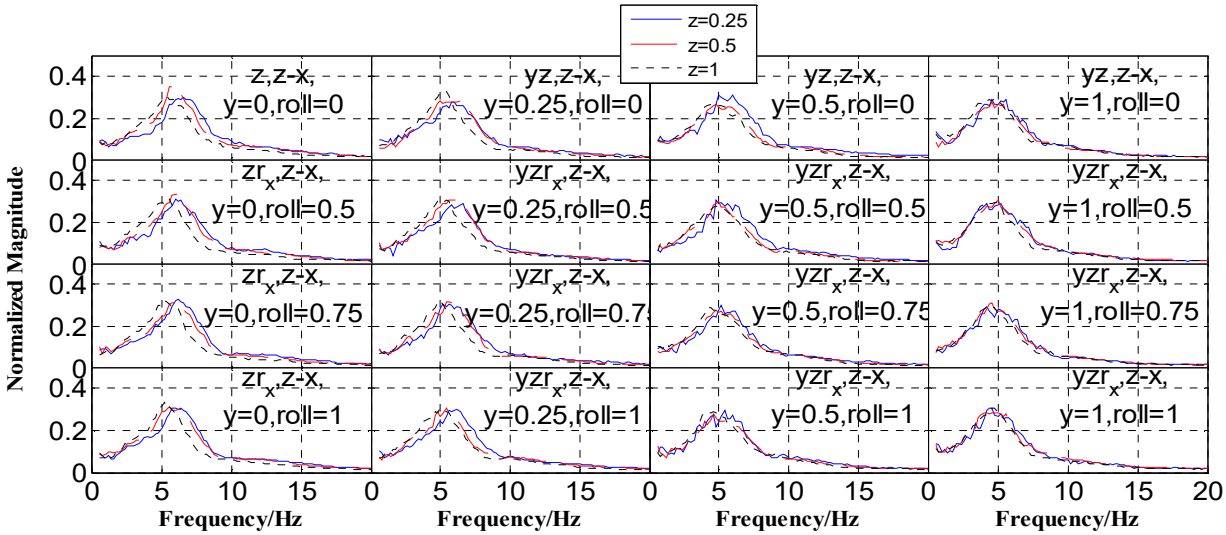

Fig. 6-8 Comparison between median normalized z-x apparent masses on the seat pan for 12 subjects under different excitation magnitudes in z direction.

Table 6-8 Wilcoxon signed-rank test for the effect of excitation magnitude in z direction on the resonance frequency and modulus at resonance for z-x apparent mass on the seat pan

z magnitude	z=0.5	z=1.0	Significant difference proportion (different r_x)
(a)r_x=0			
z=0.25	***/ns/ns/ns; ns/ns/ns/ns	***/***/***/*; ns/ns/ns/ns	8/12;0/12
z=0.5		*/*/**/ns; ns/ns/ns/ns	
(b)r_x=0.5			
z=0.25	**/ns/ns/ns;ns/ns/ns/ns	***/***/***/ns;ns/ns/ns/ns	7/12;0/12
z=0.5		**/***/*/ns;ns/ns/ns/ns	
(c)r_x=0.75			
z=0.25	***/ns/ns/ns;ns/ns/ns/ns	***/***/***/ns;ns/ns/ns/ns	8/12;0/12
z=0.5		**/***/*/*;ns/ns/ns/ns	
(d)r_x=1.0			
z=0.25	**/***/ns/ns;ns/ns/ns/ns	***/***/*/ns;ns/ns/ns/ns	7/12;0/12
z=0.5		***/*/ns/ns;ns/ns/ns/ns	
Significant difference proportion (different y)	y=0: 12/12; 0/12 y=0.25: 9/12; 0/12 y=0.5: 7/12; 0/12 y=1.0: 2/12; 0/12		

ns=not significant, p>0.05; *= p<0.05;**= p<0.01;***= p<0.005, Wilcoxon;
The p-value for different excitation magnitudes in y direction is ranked as y=0/y=0.25/y=0.5/y=1.0, separated by slash;
The effect on resonance frequency and modulus at resonance is shown before and after ';', respectively.

The z-x apparent masses at the back showed high inter-subject variability, overall were large between 2-8 Hz for most subjects, with some subjects showing one resonance frequency and some showing two (not shown). Therefore, Wilcoxon signed-rank test for the magnitude of apparent mass at 2.0, 4.0, 6.0 and 8.0 Hz was carried out to study the influence of vibration magnitude. In general, the proportions of significant changes of the modulus as the z-axis (totally 5/48, at 2.0 Hz;

14/48, 4.0 Hz; 6/48, at 6.0 Hz; 20/48 at 8.0 Hz, not shown; Fig. 6-9), y-axis (totally 1/72 at 2.0 Hz; 12/72 at 4.0 Hz; 3/72 at 6.0 Hz; 23/72 at 8.0 Hz, not shown), or roll (totally 3/72 at 2.0 Hz; 6/72 at 4.0 Hz; 8/72 at 6.0 Hz; 15/72 at 8.0 Hz, not shown; Fig. D-5) magnitude were small. However, at some vibration magnitudes and frequencies, the proportions of significant changes as y-axis (z=0.25, 14/24 at 8.0 Hz) and z-axis (r_x=0.5, 8/12 at 4.0 Hz; r_x=0.5, 7/12 at 8.0 Hz; r_x=0.75, 6/12 at 8.0 Hz; y=0, 6/12 at 4.0 Hz; y=0, 8/12 at 8.0 Hz; y=0.25, 6/12 at 8.0 Hz) were relatively large.

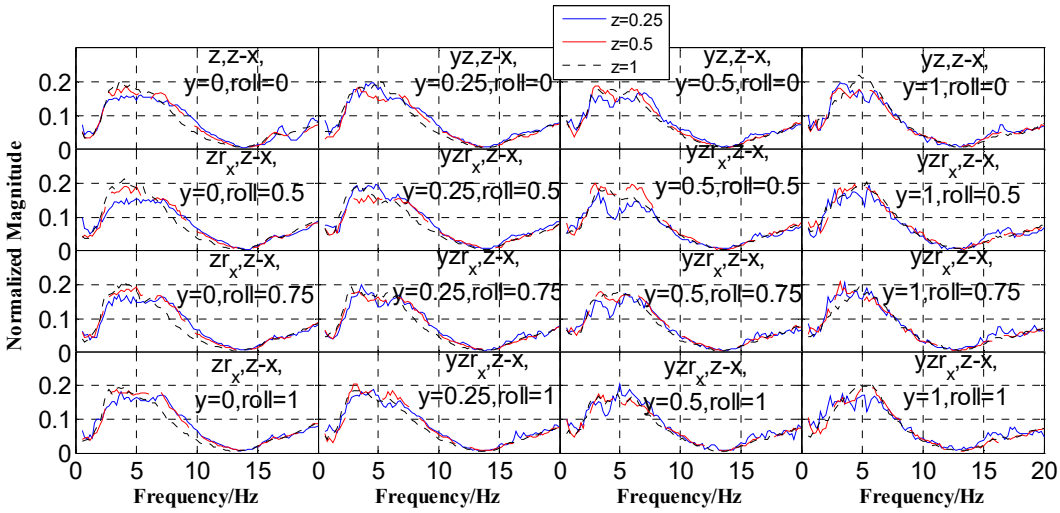

Fig. 6-9 Comparison between median normalized z-x apparent masses on the backrest for 12 subjects under different excitation magnitudes in z direction.

6.3.3 Coherence analysis of multiple inputs

As introduced in Section 3.2.2, the partial coherence function $\gamma^2_{iy\cdot(m!/i)}$ denotes the percentage of the spectrum of output $y(t)$ due to the conditioned input $x_{i\cdot(m!/i)}$, and γ_{cy} stands for the percentage of the spectrum of output due to the coherent parts between the inputs. The role of the accelerations played in the output forces on the seat pan and backrest could be studied in this way.

6.3.3.1 The force in y direction on the seat pan

For multi-axis excitations with non-zero y-axis and z-axis magnitudes, the sequence of the inputs was chosen as a_{sy} and a_{sz}, and the output was the lateral force on the seat pan F_{sy} (Table 6-1). The multiple coherences were very high regardless of the three vibration magnitudes, meaning these two inputs played the most important part in the lateral force on the seat pan F_{sy} (Fig. 6-10). Telling from the partial coherence functions, the contribution from a_{sy} always dominated in the

spectrum of the output, but the contribution from a_{sz} increased as the increasing magnitude of z-axis excitation. The small gap between the red and black lines represented the coherence between a_{sy} and a_{sz} was small, and the contribution from their coherent part was not significant.

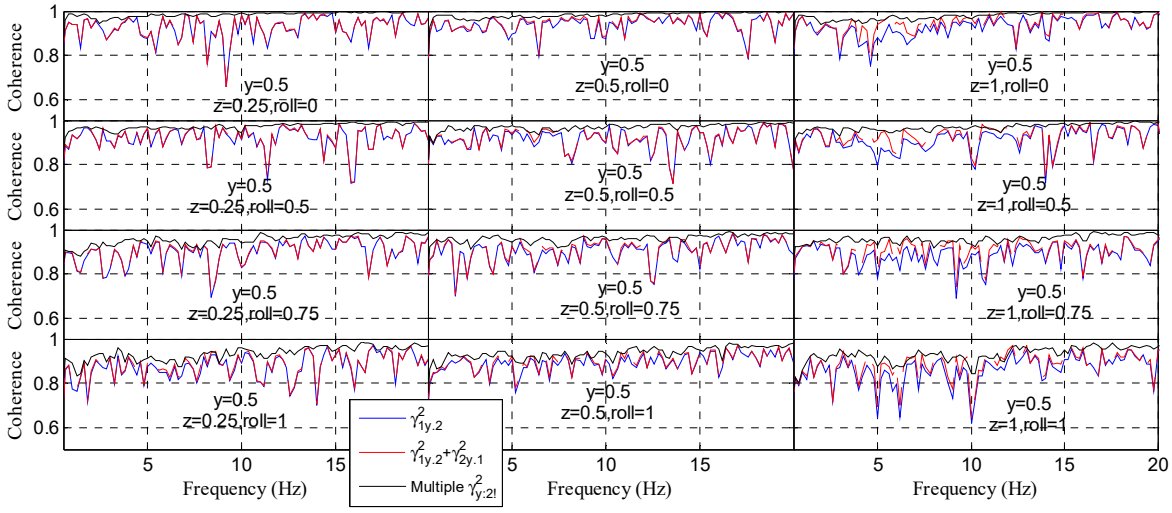

Fig. 6-10 Median coherence in the transmission to the lateral force on the seat pan F_{sy} (output *y*) with y-axis magnitude of 0.5 m/s^2 r.m.s. and varying z-axis and roll excitation magnitudes (The subscripts 1 and 2 correspond to a_{sy} and a_{sz}, respectively).

6.3.3.2 The force in z direction on the seat pan

For multi-axis excitations with non-zero y-axis and z-axis magnitudes, the sequence of the inputs was chosen as a_{sy} and a_{sz}, and the output was the vertical force on the seat pan F_{sz} (Table 6-1). The high multiple coherences for all vibration magnitudes meant these two inputs combined together made a significant contribution to the vertical force on the seat pan F_{sz} (Fig. 6-11). Compared with a_{sy}, a_{sz} played a much more important role in F_{sz}, and as the increase of z-axis magnitude, the contribution from a_{sy} reduced. As the increase of y-axis magnitude, the contribution from a_{sy} rose (not shown). The small discrepancy between the red and black lines meant the coherence between a_{sy} and a_{sz} was well controlled in the experiment, and the contribution of their coherent part was not significant at all.

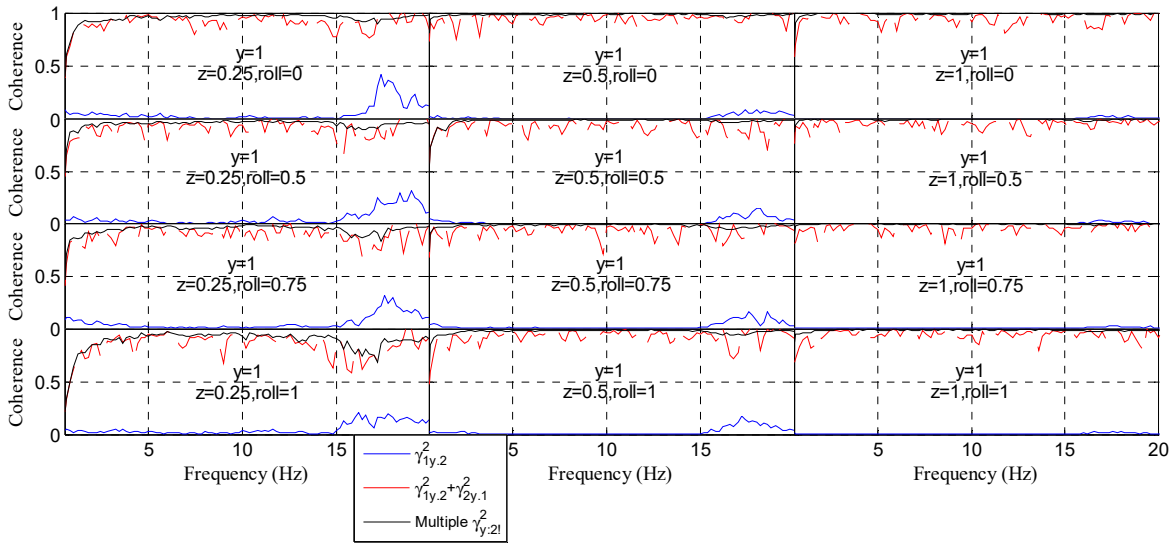

Fig. 6-11 Median coherence in the transmission to the vertical force on the seat pan F_{sz} (output *y*) with y-axis magnitude of 1.0 m/s^2 r.m.s. and varying z-axis and roll excitation magnitudes (The subscripts 1 and 2 correspond to a_{sy} and a_{sz}, respectively).

6.3.3.3 The force in x direction on the seat pan

For multi-axis excitations with non-zero y-axis and z-axis magnitudes, the sequence of the inputs was chosen as a_{sy} and a_{sz}, and the output was the fore-and-aft force on the seat pan F_{sx} (Table 6-1). The high multiple coherences meant except for a_{sy} and a_{sz}, other signals made little contribution to the fore-and-aft force on the seat pan F_{sx}. For equal y-axis and z-axis magnitudes, a_{sz} played a more important role in F_{sx} than a_{sy} (e.g., y=1, z=1, Fig. 6-12), this is because the x-axis force is prone to be induced by z-axis acceleration due to the symmetry of human body in the mid-sagittal (z-x) plane. The contribution from a_{sy} and a_{sz} increased as the rise of y-axis (not shown) and z-axis magnitudes (Fig. 6-12) respectively. The coherence between a_{sy} and a_{sz} was small, and the contribution of their coherent part to F_{sx} was negligible, which was reflected from the difference between red and black lines (Fig. 6-12).

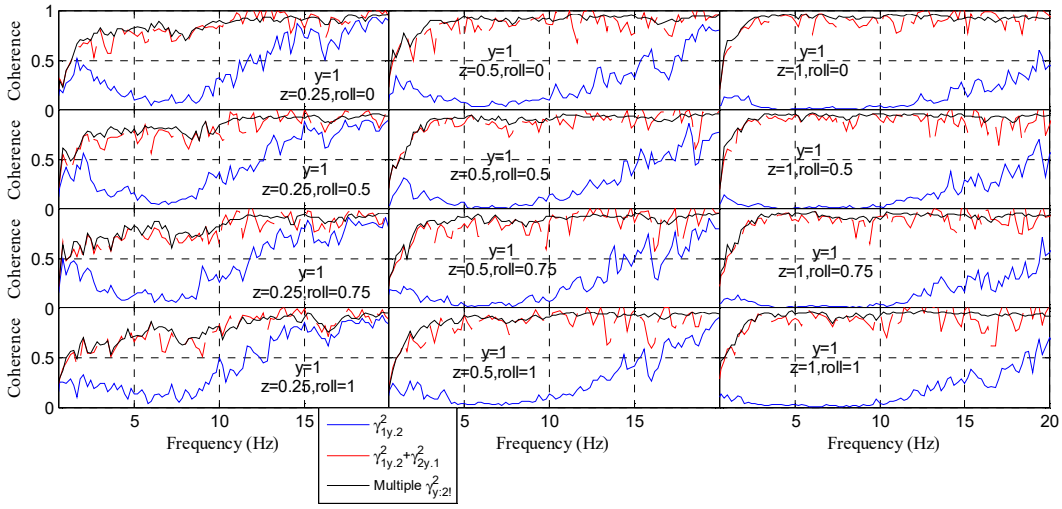

Fig. 6-12 Median coherence in the transmission to the fore-and-aft force on the seat pan F_{sx} (output *y*) with y-axis magnitude of 1.0 m/s^2 r.m.s. and varying z-axis and roll excitation magnitudes (The subscripts 1 and 2 correspond to a_{sy} and a_{sz}, respectively).

6.3.3.4 The force in y direction on the backrest

For multi-axis excitations with non-zero y-axis, z-axis and roll magnitudes, the sequence of the inputs was chosen as a_{by}, a_{bz} and a_{r_x}, and the output was the lateral force on the backrest F_{by} (Table 6-1). The small difference between the cyan and red lines and the great difference between the cyan and black lines indicated the coherence among these three signals was great, and the contribution from a_{r_x} after removing a_{by} was negligible, which was understandable because of a_{r_x} being a linear part of a_{by} (Fig. 6-13). Considering the coherent part among these three inputs was mainly a_{r_x}, the difference between the cyan and black lines could approximately represent the contribution from the roll excitation, so it increased as the rise of roll magnitude. Then the blue line could approximately stand for the contribution from the translational y-axis excitation. The high multiple coherence meant y-axis translational and roll excitations together with a_{bz} almost resulted in F_{by}. However, the contributions from y-axis translational and roll excitations were much more important (Fig. 6-13). In addition, the contribution of one acceleration usually increased as the increase of the corresponding excitation magnitude.

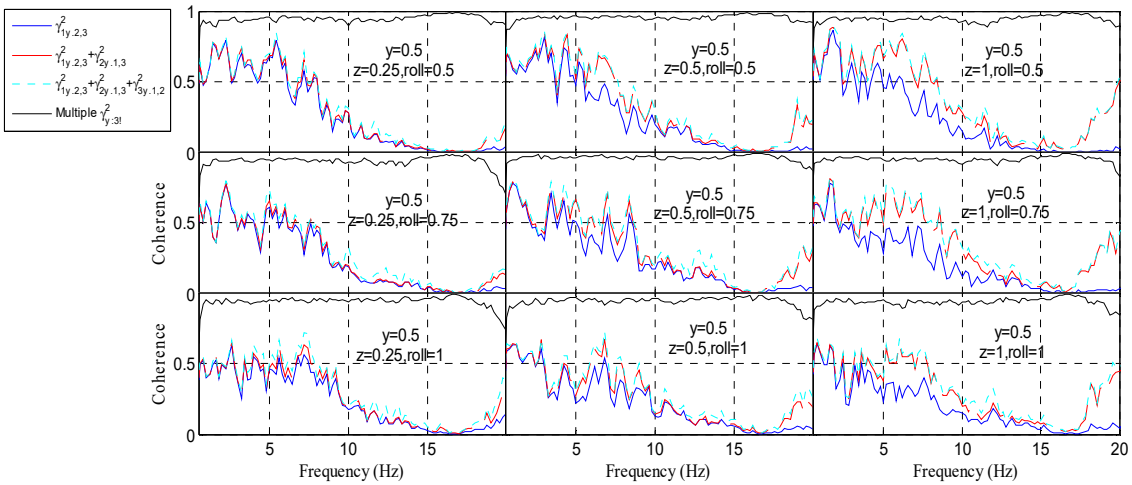

Fig. 6-13 Median coherence in the transmission to the lateral force on the backrest F_{by} (output *y*) with y-axis magnitude of 0.5 m/s^2 r.m.s. and varying z-axis and roll excitation magnitudes (The subscripts 1, 2 and 3 correspond to a_{by}, a_{bz} and a_{r_x}, respectively).

6.3.3.5 The force in z direction on the backrest

For multi-axis excitations with non-zero y-axis, z-axis and roll magnitudes, the sequence of the inputs was chosen as a_{by}, a_{bz} and a_{r_x}, and the output was the vertical force on the backrest F_{bz} (Table 6-1). Because a_{r_x} is a linear part of a_{by}, the contribution from a_{r_x} after removing a_{by} (the difference between the red and cyan lines) was close to zero. Since a_{bz} is almost incoherent with the other two signals, the difference between the cyan and black lines was approximately equal to the contribution from the roll excitation, and the blue line was in close proximity to the contribution from the y-axis translational excitation, and the difference between the red and blue lines represented the contribution from the vertical acceleration a_{bz}. The contribution from the y-axis translational excitation was mainly in 0.5-5 Hz, from the roll excitation in 10-20 Hz, and from a_{bz} in 5-12 Hz (Fig. 6-14). The contribution from the roll excitation and the vertical acceleration a_{bz} tended to increase as the rise of roll magnitude (not shown) and z-axis magnitude (Fig. 6-14), respectively.

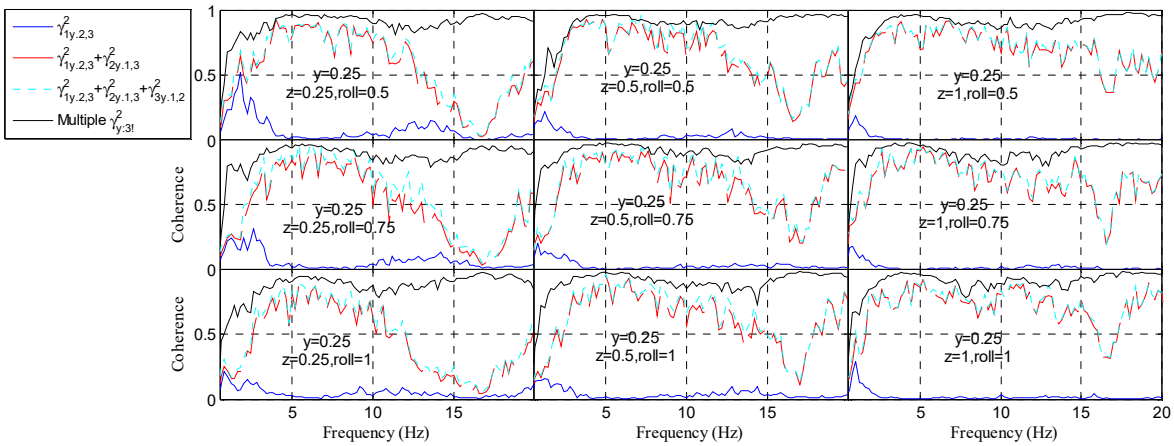

Fig. 6-14 Median coherence in the transmission to the vertical force on the backrest F_{bz} (output *y*) with y-axis magnitude of 0.25 m/s^2 r.m.s. and varying z-axis and roll excitation magnitudes (The subscripts 1, 2 and 3 correspond to a_{by}, a_{bz} and a_{r_x}, respectively).

6.3.3.6 The force in x direction on the backrest

For multi-axis excitations with non-zero y-axis, z-axis and roll magnitudes, the sequence of the inputs was chosen as a_{by}, a_{bz} and a_{r_x}, and the output was the fore-and-aft force on the backrest F_{bx} (Table 6-1). For the same reason, the contribution from the y-axis translational excitation (the blue line) was small, from the vertical acceleration a_{bz} (the difference between the red and blue lines) was significant in 0.5-13 Hz, from the roll excitation was significant in 13-20 Hz (Fig. 6-15). The contribution from the y-axis translational excitation and the vertical acceleration a_{bz} would increase as the rise of y-axis magnitude (not shown) and z-axis magnitude (Fig. 6-15), respectively.

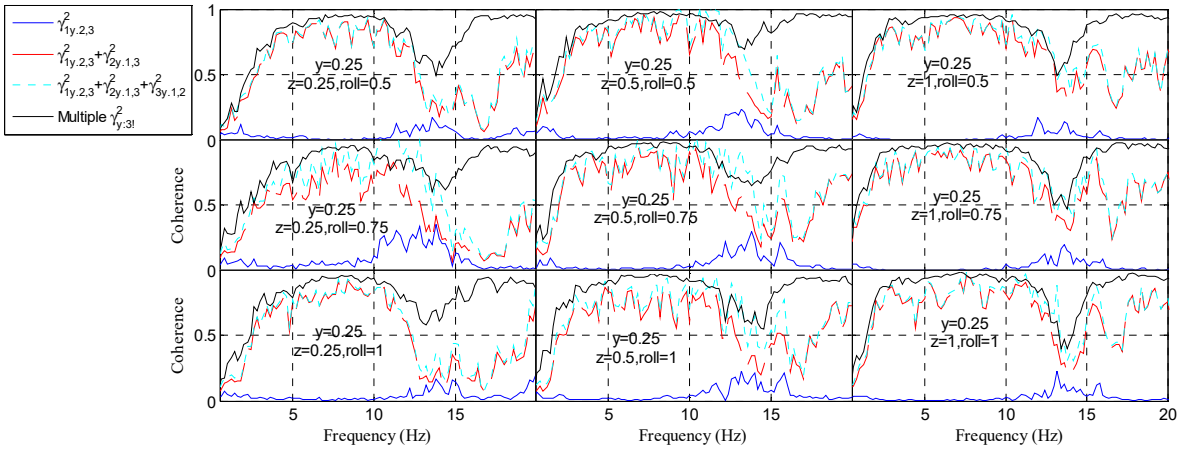

Fig. 6-15 Median coherence in the transmission to the fore-and-aft force on the backrest F_{bx} (output *y*) with y-axis magnitude of 0.25 m/s^2 r.m.s. and varying z-axis and roll excitation magnitudes (The subscripts 1, 2 and 3 correspond to a_{by}, a_{bz} and a_{r_x}, respectively).

6.4 Discussion

6.4.1 Rotational excitation

There have rarely been studies on the biodynamic response of human body to combined translational and rotational vibrations. Without the existence of roll vibration, the lateral inline and the cross-axis (y-z, y-x) apparent masses reported in the existing studies have been solely induced by the translational lateral vibration. With roll vibration, the lateral acceleration and tri-axial forces on the backrest can also be produced by the roll vibration, so some of the apparent masses can be solely induced by roll vibration, or by combined translational lateral and roll vibrations. On the other hand, whether the apparent mass arising from the translational lateral excitation is different from that from the roll excitation has rarely been reported. Under this situation, it is better to keep the calculated apparent masses the same as the commonly-reported ones from the perspective of the vibration direction. The treatment in this study provided the possibility of being consistent with the existing studies in terms of the vibration direction of apparent mass, while the nonlinear biodynamics of the human body arising from the roll excitation that was reflected by the difference of apparent mass caused by the addition of excitation axis or increasing excitation magnitude was retained.

6.4.2 Comparison with existing research

The apparent masses on the seat pan and backrest under single-axis excitations have been widely reported, the results of this study were to be validated by comparing with the existing research.

Under single y-axis vibration and 'back-on' condition, for the lateral apparent mass on the seat pan a peak was reported at around 1.5 Hz at the vibration magnitude of 1.0 ms^{-2} r.m.s. (Fairley and Griffin, 1990), between 0.9-2.1 Hz at the magnitude of 0.25-1.0 ms^{-2} r.m.s. (Mandapuram *et al.*, 2005), around 2.0 and 1.5 Hz at magnitudes of 0.4 and 0.8 ms^{-2} r.m.s., respectively (Mansfield and Maeda, 2007). Mandapuram *et al.* (2010) revealed a principal peak near 1 Hz and a second peak near 2 Hz at a lower lateral magnitude of 0.25 ms^{-2} r.m.s. and a single broad peak near 1.38 Hz at a higher lateral magnitude of 0.4 ms^{-2} r.m.s.. The reduction of resonance frequency with increasing vibration magnitude was also reported by Mandapuram *et al.* (2005) and Mandapuram *et al.* (2010). The results in this study showed agreement with the above-mentioned previous findings (the first subgraph in Fig. 6-3 and Table 6-3).

The relatively low-level interaction between the upper body and the backrest resulted in much smaller apparent masses in y direction on the backrest than those on the seat pan. Under single y-axis vibration and 'back-on' condition, for the lateral apparent mass on the backrest, Mandapuram *et al.* (2005) reported a primary peak around 1 Hz under low-level (0.25 m/s^2 r.m.s.) y-axis excitation, and shifted towards a lower frequency that could be below 0.5 Hz when the excitation magnitude was increased to 0.5 and 1.0 m/s^2 r.m.s.. Mandapuram *et al.* (2010) reported a primary peak around 1 Hz and a second one around 2 Hz under lateral vibration of 0.25 and 0.4 ms^{-2} r.m.s., and the first resonance frequency reduced as the increase of vibration magnitude. The findings of this study agreed with all of the previous results (the first subgraph in Fig. 6-4 and Table 6-4).

Under single z-axis vibration and 'back-on' condition, for the vertical apparent mass on the seat pan a primary peak in the range from 4 to 6 Hz was reported by Fairley and Griffin (1989) under the magnitude of 0.25-2.0 ms^{-2} r.m.s., in 4-7 Hz under the magnitude of 0.125-1.25 ms^{-2} r.m.s. reported by Nawayseh and Griffin (2004), in 4-8 Hz under the magnitude of 0.25-1.0 ms^{-2} r.m.s. reported by Qiu and Griffin (2012). The reduction of resonance frequency as the increase of vibration magnitude was also illustrated in Fairley and Griffin (1989), Nawayseh and Griffin (2004) and Qiu and Griffin (2012). The findings in this study were consistent with the previous results (the first subgraph in Fig. 6-5 and Table 6-5).

The apparent masses in z direction on the backrest were very small, which was due to the relatively stable posture resulting in less relative motion between the upper body and backrest in z direction

than that in y direction. Nawayseh and Griffin (2004) reported under single-axis vertical excitation with magnitudes from 0.125 to 1.25 ms^{-2} r.m.s, resonances of the vertical apparent mass on the backrest were found around 5-7 Hz, the moduli of which were less than 10 kg for most subjects with weights of 62-106 kg, accounting for about 10% of the total body mass. Furthermore, the resonance frequencies showed significant reductions with the increase in vibration magnitudes. The first subgraph in Fig. 6-6 and Table 6-7 were consistent with the previous results.

For z-x apparent mass on the seat pan under single-axis vertical excitation and 'back-on' condition, Mansfield and Maeda (2006) reported a principal peak at 5-6 Hz. Furthermore, Nawayseh and Griffin (2004) reported a principal resonance frequency around 5 Hz, decreasing with increasing vibration magnitude, and showing no significant difference of z-x apparent masses at resonance with vibration magnitude, which was consistent with the finding in this research (the first subgraph in Fig. 6-8 and Table 6-8). What is more, the z-x apparent mass on the backrest under single-axis vertical excitation and 'back-on' condition in the first subgraph in Fig. 6-9 also agreed with Nawayseh and Griffin (2004). For z-y apparent mass on the seat pan and backrest under single-axis vertical excitation and 'back-on' condition, the apparent masses were very small with the median value peaking at about 3 and 2 kg, respectively (Nawayseh and Griffin, 2004), which agreed with Section 6.3.2.1 where the peak median normalized apparent masses on the seat pan and backrest were both about 3% under sole z-axis excitation for the mean weight of about 80.5 kg.

For y-x and y-z apparent masses on the seat pan under single y-axis excitation and 'back-on' condition, on the whole, the magnitudes were less than 10 kg (Mansfield and Maeda, 2006), consistent with the results of this study (Section 6.3.2.1) under single-axis vibration (mean weight was 80.5 kg).

Overall, the data obtained under single-axis excitation were in good agreement with the existing research. For multi-axis excitations, inline and cross-axis apparent masses would be generally analogous to those obtained using single-axis excitations (Mansfield and Maeda, 2006, 2007; Qiu and Griffin, 2010, 2012). This thereby validated the results obtained under multi-axis excitations in this study.

6.4.3 MISO and SISO system

MISO technique was adopted to calculate the apparent mass for the cases of multiple inputs. While the apparent mass was traditionally estimated by the SISO technique, the advantage of applying MISO system over SISO system should be discussed here. As can be seen from Section 6.3.3, the coherence between the input excitations in different directions was inevitable. The biased

estimation of apparent mass should be attributed to the coherences between input signals in Table 6-1 and Table 6-2.

For example, when estimating AM_{sy-z} with excitations in both y direction and z direction (Table 6-1), if a_{sy} and a_{sz} are not totally incoherent, a_{sy} can have two paths (apparent masses) to arrive at F_{sz}; one is by the path of AM_{sy-z}, and the other one is by means of AM_{sz} (Fig. 6-16). If the apparent mass (AM_{sy-z}') from a_{sy} to F_{sz} is estimated by SISO system directly, that is,

$$AM_{sy-z}' = AM_{sy-z} + T_{a_{sz}/a_{sy}} AM_{sz} \tag{6-2}$$

where $T_{a_{sz}/a_{sy}}$ is the frequency response function from a_{sy} to a_{sz}.

From Eq. (6-2), it can be seen the estimation will be influenced greatly by AM_{sz}. On the contrary, when estimating AM_{sz} by SISO method, the estimation will be affected by AM_{sy-z} (Fig. 6-17). However, taking into account that the modulus of the inline apparent mass AM_{sz} is usually much greater than the cross-axis apparent mass AM_{sy-z}, so the estimation error of AM_{sy-z} will be much larger, while the error of AM_{sz} may be negligible. For example, Fig. 6-18 shows the difference between SISO and MISO estimations. For the cross-axis apparent mass AM_{sy-z}, the error of SISO method is very large; but for the inline apparent mass AM_{sz}, the error of SISO method is negligible.

In a word, MISO system is preferable for the more accurate estimation under multiple inputs considering the mutual coherence between the inputs. If using SISO system, the estimation of the inline apparent mass will be influenced by the cross-axis one, and vice versa. Therefore, if applying SISO system to the estimation of apparent mass, the modulus of these apparent masses should be taken into account. If one of them is very large, its influence on the estimation of the others may not be ignored.

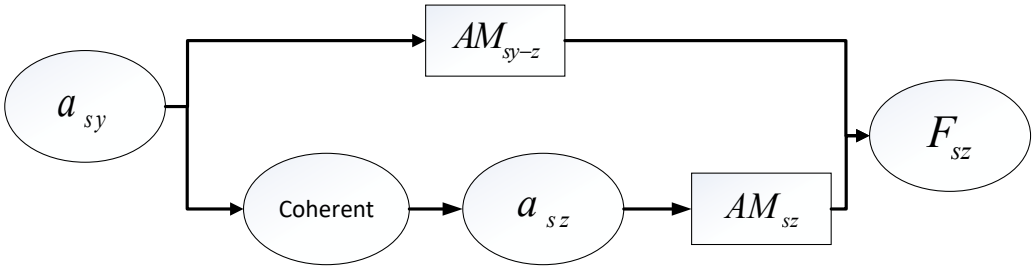

Fig. 6-16 Biased estimation of AM_{sy-z} with both lateral and vertical vibrations using SISO system.

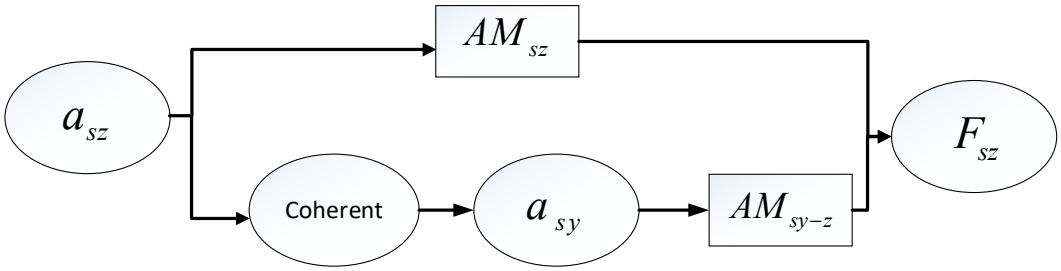

Fig. 6-17 Biased estimation of AM_{sz} with both lateral and vertical vibrations using SISO system.

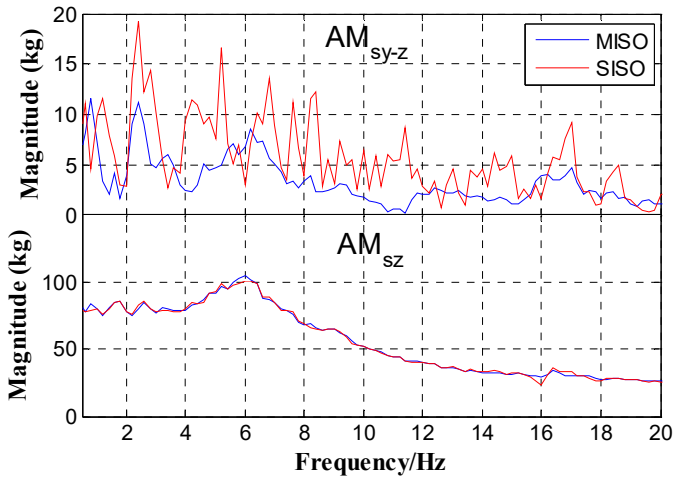

Fig. 6-18 The comparison between SISO and MISO systems when estimating the apparent masses for a subject of 179 cm in height and 93 kg in weight under 0.5 m/s^2 r.m.s. y-axis, 0.25 m/s^2 r.m.s. z-axis and 0.5 rad/s^2 r.m.s. roll excitation.

6.4.4 Multi-axis excitation

For multi-axis excitations, the resonance frequencies of apparent masses were considered to decrease as the increase of the overall excitation magnitudes evaluated by root-sum-square method (Mansfield and Maeda, 2006, 2007). Considering the difference in the sensitivity of the biodynamics of the human body to vibrations in different directions, the relationship between the resonance frequencies and the weighted root-sum-square (r.s.s) value of the excitation magnitudes

was studied. The weighted root-sum-square (r.s.s) value of the excitation magnitudes can be expressed as

$$\text{r.s.s} = [(w_y a_y)^2 + (w_z a_z)^2 + (w_{r_x} a_{r_x})^2]^{0.5} \quad (6\text{-}3)$$

where a_y, a_z and a_{r_x} are the r.m.s. values of the acceleration excitation magnitudes in y, z and roll directions, respectively, and w_y, w_z and w_{r_x} are the corresponding weighting factors.

If the resonance frequency (dependent variable) is assumed to have a linear correlation with the weighted r.s.s. value (independent variable), by conducting linear regression analysis introduced in Section 3.5 by means of 'regress' function in Matlab for every subject (significance level is 0.05), and selecting the mean R^2 value of the 12 subjects as the cost function, the weighting factors maximizing the cost function can be determined by an optimization algorithm introduced in Section 3.3.

For the apparent mass in y direction on the seat pan, the resonance frequency only showed a large proportion of significant reductions as the increase of y-axis magnitude. But the proportion of significant changes reduced as the increase of z-axis magnitude. For the apparent mass in y direction on the backrest, a large proportion of significant reductions of the magnitudes at several frequencies had been illustrated only as the increase of y-axis magnitude (Fig. 6-4 and Table 6-4), which was possibly due to the reduction of a resonance frequency that was less than 0.5 Hz since for low r.s.s. excitation, resonances at 0.5-2 Hz were exhibited. But the proportion of significant changes reduced as the increasing magnitude in z or roll axis. This means for the apparent masses in y direction on the seat pan and backrest, w_y is much larger than w_z and w_{r_x}. However, this nonlinearity is more significant at low r.s.s. magnitudes or significant only at low r.s.s. magnitudes. For the apparent mass in y direction on the seat pan, by maximizing the mean R^2 value of the 12 subjects, the weighting factors can be determined as $w_y = 1$, $w_z \approx 0.358$, $w_{r_x} \approx 0.371$ with the maximum mean R^2 value for 12 subjects being about 0.494 and the mean p-value being only 3×10^{-5}. What is more, the mean correlation coefficient for 12 subjects between the resonance frequency and the weighted r.s.s. value is -1.0578 with a mean constant of 2.8035.

For the apparent mass in z direction on the seat pan, the resonance frequency showed a large proportion of significant reductions as the increase of y-axis magnitude at fixed z-axis and roll magnitudes and as the increase of z-axis magnitude at fixed y-axis and roll magnitudes, respectively, however, the proportion of significant changes reduced as the increase of z-axis or roll magnitude and y-axis or roll magnitude, respectively. For the apparent mass in z direction on the backrest, the

resonance frequency showed a large proportion of significant reductions as the increase of z-axis magnitude only when y-axis or roll magnitude was small (including zero), and similarly, showed a large proportion of significant decreases as the increasing y-axis magnitude only when z-axis or roll magnitude was small (including zero). This means for the apparent masses in z direction on the seat pan and backrest, w_y and w_z are much larger than w_{r_x}. However, this nonlinearity is more significant at low r.s.s. magnitudes or significant only at low r.s.s. magnitudes. For the apparent mass in z direction on the seat pan and backrest, in the same way, the weighting factors, the mean R^2 value for 12 subjects and the mean p-value as well as the mean correlation coefficient were obtained and listed in Table 6-9.

For z-x apparent mass on the seat pan, the resonance frequency showed a large proportion of significant reductions as the increase of y-axis magnitude at fixed z-axis and roll magnitudes and as the increase of z-axis magnitude at fixed y-axis and roll magnitudes, respectively. However, the proportion of significant changes reduced as the increase of z-axis magnitude and y-axis magnitude, respectively. This means for z-x apparent mass at the seat pan, w_y and w_z are much larger than w_{r_x}. And the nonlinearity is more significant at low r.s.s. magnitudes or significant only at low r.s.s. magnitudes. For the z-x apparent mass on the seat pan, in the same way, the weighting factors, the mean R^2 value for 12 subjects and the mean p-value as well as the mean correlation coefficient were obtained and listed in Table 6-9.

These relationships between the resonance frequencies of the apparent masses and the r.s.s. values of excitation magnitudes were summarized in Table 6-9, which could be used for the prediction of the resonance frequency. Therefore, the biodynamic response arising from one direction with increasing vibration magnitudes in orthogonal directions is equivalent to that with a weighted increasing vibration magnitude in the arising direction. Although the p-value is much less than 0.05 (significance level), the R^2 value is not close to unity. This means the negative correlation between the resonance frequencies of the apparent masses and the r.s.s. values of excitation magnitudes is doubtless, but the correlation between them is likely to be nonlinear instead of being linear.

The resonances in the vertical apparent mass on the seat pan and backrest and z-x apparent mass on the seat pan can be associated with the same mode of the human body. Kitazaki and Griffin (1997), Matsumoto and Griffin (2001) and Zheng *et al.* (2011) found by modal analysis of different models a vertical whole-body mode around 5 Hz, usually involving vertical and fore-and-aft (or pitch) motions of the pelvis and upper body. On the other hand, the weighting factors and the mean correlation coefficient were close for these apparent masses (Table 6-9). Therefore, it seems

possible that the resonances of the apparent mass in z direction on the seat pan and backrest and z-x apparent mass on the seat pan found in this experiment are associated with the modes found by Kitazaki and Griffin (1997), Matsumoto and Griffin (2001) and Zheng *et al.* (2011), which is to be further investigated by the modelling of human body in the following chapter. This is also consistent with Nawayseh and Griffin (2003) that the resonances in the vertical apparent mass and z-x apparent mass on the seat pan showed high correlation in all four postures for two higher vibration magnitudes.

The reducing resonance frequency as the increasing weighted r.s.s. value of the vibration magnitude can be put down to the nonlinearity of the human body. However, the nonlinearity is more significant at low r.s.s. value or significant only at low r.s.s. value. This is probably because the subjects tend to adopt more muscle tension to keep the balance under larger vibration level, so as to reduce the involuntary change in muscle tension, thereby reducing the nonlinearity of the human body (Matsumoto and Griffin, 2002a). This finding was similar to the results in Qiu and Griffin (2010, 2012) that during dual-axis excitation in z and x axes, the reducing resonance frequencies as the increase of z-axis or x-axis vibration magnitude became less significant as the increasing excitation magnitude in the other axis. Generally, the magnitudes at resonance for these apparent masses under single-axis vibrations were comparable to those obtained under multi-axis vibrations, which is consistent with other studies (Hinz *et al.*, 2006; Mansfield and Maeda, 2006, 2007; Mandapuram *et al.*, 2010; Qiu and Griffin, 2010, 2012).

Table 6-9 A summary of the relationship between the resonances of the apparent masses (dependent variable) and the r.s.s. excitation magnitudes (independent variable)

Apparent mass	Weighting factors			Mean correlation coefficient	Mean constant	Mean R^2 value	Mean p-value
	w_y	w_z	w_{r_x}				
AM_{sy}	1	0.358	0.371	-1.0578	2.8035	0.494	3×10^{-5}
AM_{sz}	0.842	1	0.242	-1.1258	6.4284	0.441	4×10^{-4}
AM_{bz}	1.391	1	0.297	-0.9886	6.0300	0.418	0.0063
AM_{sz-x}	1.270	1	0.446	-1.2500	6.5455	0.556	4.7×10^{-7}

The smaller cross-axis z-y, y-z and y-x apparent masses on both the seat pan and backrest than z-x apparent masses means the biodynamic cross-axis effect of the seated human body is much greater between z and x axes than between z and y axes, y and x axes, this is because the human body is symmetrical about the mid-sagittal plane (z-x plane).

6.5 Conclusion

The biodynamic response of the seated human body subjected to lateral, vertical and roll excitations has been studied and the data have been analyzed by means of SISO or MISO method and validated by existing research. The following conclusions can be drawn:

The apparent masses under single-axis excitations and multi-axis ones were similar. To summarize, the resonance frequencies of the apparent masses usually have a negative correlation with the weighted r.s.s. value of excitation magnitudes, which is more significant under low r.s.s value or significant only under low r.s.s value. To be specific, for the inline apparent mass, the resonance frequencies of the apparent masses in y direction on the seat pan showed a large proportion of significant reductions as the increase of y-axis magnitude, however, the proportion of significant changes reduced as the increase of z-axis magnitude. For the apparent masses in z direction on the seat pan and backrest, the resonance frequencies tended to reduce as the increasing magnitudes in y axis or z axis, however, the proportion of significant changes reduced as the increasing magnitudes in z or roll direction and y or roll direction, respectively. In addition, for the cross-axis apparent masses, the resonance frequencies of z-x apparent masses on the seat pan had a decreasing tendency as the increasing magnitude in y axis or z axis, however, the proportion of significant decreases reduced as the increasing magnitude in z axis and y axis, respectively. The z-y, y-z, y-x apparent masses were small, however, z-x apparent masses were much larger, indicating the cross-axis effect between z and y axes, y and x axes of seated human body was small, however, between z and x axes was great. On the other hand, the magnitudes at resonance usually did not show significant change as the variation of y-axis, z-axis or roll excitation magnitudes.

From the coherence analysis, for the forces in z direction (y direction) on the seat pan, the contribution from z-axis (y-axis) acceleration on the seat pan was dominant. For the forces in x direction on the seat pan, z-axis and y-axis accelerations on the seat pan could both play important roles in specific frequency ranges. For the force in x direction or z direction on the backrest, the contributions from both z-axis and roll accelerations on the backrest were dominant in specific frequency ranges. What is more, for the y-axis force on the backrest, the role of roll and y-axis translational vibrations were the most important. Overall, the contribution from an acceleration in a specific direction would be greater as the increase of excitation magnitude in that direction.

It was also found MISO system was more suitable for accurate estimation of the apparent masses under multiple inputs than SISO system because of the inevitable mutual coherence between the inputs.

Chapter 7 Modelling of seated human body exposed to combined vertical, lateral and roll excitations

7.1 Introduction

When travelling with rail vehicles such as a high-speed train, passengers experience primarily vertical, lateral and roll motions (ISO, 2001). These vibrations can cause passenger discomfort and fatigue during the journey. It is essential to understand how the human body behaves and responds to the multi-axis vibration before effective measures of reducing the vibration transmitted to the passenger can be proposed and developed so as to promote ride comfort and reduce the health risks caused by vehicular vibration and shocks.

The human body is a complex dynamic system. Its biodynamic response to vibration can be influenced by many factors, e.g., body weight and height, posture, excitation magnitude, etc. Much research has investigated the dynamic response of seated human body in terms of apparent mass and body transmissibility under single-axis or multi-axis translational excitations (e.g., Fairley and Griffin (1989); Toward and Griffin (2009); Qiu and Griffin (2010, 2012); Zheng *et al.* (2019)). They studied the effect of influencing factors including posture, excitation magnitude, body mass on the apparent mass of seated human body using experimental methods. Experiments with the human body are, however, time-consuming and expensive to be conducted. An experiment of such is also possibly constrained by the maximum vibration level the human body can tolerate. Modelling of the human body is complementary or even alternative to the experimental methods for studying the dynamic characteristics of the human body under various excitations, especially when the experiment is impossible.

Different models for studying biodynamic responses of seated human body to whole-body vibration have been proposed. The existing models may be categorized into lumped parameter models, multi-body dynamic models and finite element (FE) models. In the lumped parameter model, the human body is simplified as lumped masses which are connected by springs and dampers. Typical models are reported by Wei and Griffin (1998a), Matsumoto and Griffin (2001), Nawayseh and Griffin (2009), Stein et al. (2009), Qiu and Griffin (2011), etc. The lumped parameter technique is probably one of the most popular analytical methods for the study of biodynamic responses of a seated body partly because of its simplicity. However, most of the models usually do not have a good representation of anatomy of human body. The FE method can model detailed skeleton structure and muscles of the human body in regions of interest such as the spine, back, pelvis and

thigh. This type of model can be developed to predict not only body motion but also surface contact forces and internal forces causing injury. Typical finite element models of the human body include those by Kitazaki and Griffin (1997), Pankoke *et al.* (1998) and Liu *et al.* (2015). However, the FE model is complex and computationally costly to be used in simulations of biodynamics. Calibration of an FE model of the human body is much more difficult and time-consuming than the other types of models. Multi-body dynamic models are to some extent a compromise between lumped parameter models and FE models. This type of models is typically made up of rigid bodies interconnected by joints and force elements (e.g., springs and dampers), in which each of the rigid bodies has several degrees of freedom and some representation of the body dimensions and relative positions. The multibody dynamic model of human body can be more anatomically representative than the lumped parameter model, and less computationally expensive than the FE model. Some multi-body models of the human body are reported by Liang and Chiang (2008), Kim *et al.* (2011), Zheng *et al.* (2011), Desai *et al.* (2018), etc.

Most existing multi-body models are two-dimensional, having the rigid parts moving or rotating in the mid-sagittal plane with in-plane excitations (vertical, fore-and-aft or pitch excitations). Since the human body is treated symmetrical about this plane, the development of such models is relatively straightforward. However, vibration characteristics of a train showed not only in-plane (e.g., vertical) vibration but also out-of-plane (e.g., lateral and roll) vibrations. A model that is suitable for studying biodynamics of seated human body exposed to combined lateral, vertical and roll excitation (i.e. in the mid-coronal plane) is not available and needs to be developed.

The body motions associated with the resonances of the apparent masses have been reported by some researchers. It was reported that the principal resonance around 5 Hz in the apparent mass of human body on the seat pan in the vertical direction was caused by a vertical mode of the entire body based on biodynamic modelling with reference to some experimental observations (Kitazaki and Griffin, 1997; Kitazaki and Griffin, 1998; Matsumoto and Griffin, 2001; Zheng *et al.*, 2011; Liu *et al.*, 2015). However, there are only few studies on the body motion in relation to the resonances of the apparent mass in the lateral direction of the human body measured at the seat pan or backrest. Understanding the association of body motion with the resonances in human biodynamics is particularly important for studying human response to vibration perceived by passengers of rail vehicles.

The objective of this chapter was to propose and develop a model of seated human body exposed to combined lateral, vertical and roll vibration. A multi-body dynamic model of the human body consisting of abdomen, pelvis, thighs, upper torso, head and neck was constructed. An effective approach of model calibration was designed and implemented to determine the model parameters

while the error between the model-predicted and experimentally measured apparent masses of the human body was minimized. A modal analysis was further conducted to reveal the relationship of the modal frequency and mode shape of the seated human body with the resonance of the apparent masses. This study facilitated discussions on the modelling approach, model parameters and modal properties of the human body associated with biodynamics so as to advance understanding in biodynamic response of seated human body to multi-axis vibration. A conclusion beneficial to improving passenger ride comfort of rail vehicles was provided.

7.2 Development of the seated human model

7.2.1 Construction of the model

A multibody dynamic model of seated human body was proposed (Fig. 7-1). The proposed human body model consists of six segments: abdomen (B_1), pelvis (B_2), right thigh (B_3), left thigh (B_4), upper torso (B_7) including the shoulders, thorax and arms, as well as head and neck (B_8). For convenience, a rigid seat used in measuring apparent masses is also included with backrest (B_5) and seat pan (B_6), which are also the locations where vibration inputs are applied. In the model, an absolute coordinate system $\mathbf{S}=(\mathbf{n}_x,\mathbf{n}_y,\mathbf{n}_z)^{\mathrm{T}}$ was defined such that its origin is at the centre of the intersection line of the seat backrest front surface and seat pan upper surface. The others are relative (local) coordinate systems $\mathbf{S}_i=(\mathbf{n}_{ix},\mathbf{n}_{iy},\mathbf{n}_{iz})^{\mathrm{T}}$ ($i=1,2,\cdots,8$) fixed on B_i ($i=1,2,\cdots,8$) with their origins $\mathbf{O}_i$ ($i=1,2,\cdots,8$) defined at the centre of gravity of each segment of the human body and the seat. The backrest can have an inclination with an angle of α relative to the vertical plane. The model has a total of 16 degrees of freedom: each segment of the human body has translational motions in the lateral and vertical directions, y_i and z_i ($i=1,2,3,4,7,8$), and B_1, B_2, B_7 and B_8 are considered to have roll motions, θ_i ($i=1,2,7,8$), around the x-axis in their own relative coordinate systems. Therefore, aside from the translational movements relative to the absolute coordinate system for the coordinate systems $\mathbf{S}_i=(\mathbf{n}_{ix},\mathbf{n}_{iy},\mathbf{n}_{iz})^{\mathrm{T}}$ ($i=3,4$), for $i=2,6$, they have relative rotations θ_i around $\mathbf{n}_{ix}$ to the absolute coordinate system as well; while for $i=1,5,7,8$, they have relative rotations around $\mathbf{n}_y$ with an angle of α as well in addition to the above. The excitation is expressed as lateral vibration (y_0) along $\mathbf{n}_y$, vertical vibration (z_0) along $\mathbf{n}_z$, and roll vibration (θ_0) around $\mathbf{n}_x$ at the seat pan. The foot support is ignored assuming that

the vibration input through the foot support is small. It should be mentioned that although legs were not explicitly modelled in the model, the effective masses of the two legs were included in the thighs, respectively. A pair of contact points between a human body segment and the seat pan or backrest are expressed as $\mathbf{C}_i$ on the human body side and $\mathbf{C}_{is}$ on the seat side ($i = 1,2,3,4,5$). At the equilibrium position, these pairs of points are coincident. Body segments B_2, B_3 and B_4 are in contact with the seat pan at points $\mathbf{C}_2$ ($\mathbf{C}_{2s}$), $\mathbf{C}_3$ ($\mathbf{C}_{3s}$) and $\mathbf{C}_4$ ($\mathbf{C}_{4s}$), respectively. Body segments B_1 and B_7 are in contact with the backrest at points $\mathbf{C}_1$ ($\mathbf{C}_{1s}$) and $\mathbf{C}_5$ ($\mathbf{C}_{5s}$), respectively. The contacts are modelled with translational springs and dampers in y and z directions, as well as rotational springs and dampers around x axis but without rotational springs and dampers at the contact points between thighs and seat pan $-\mathbf{C}_3$ ($\mathbf{C}_{3s}$) and $\mathbf{C}_4$ ($\mathbf{C}_{4s}$).

For the connection between human body segments, B_1, B_3 and B_4 are connected with B_2 at points $\mathbf{D}_1$, $\mathbf{D}_2$ and $\mathbf{D}_3$, respectively. B_1 and B_8 are connected with B_7 at the points $\mathbf{D}_7$ and $\mathbf{D}_8$, respectively. The connections are modelled with translational springs and dampers in y and z directions, and rotational springs and dampers around x direction as well.

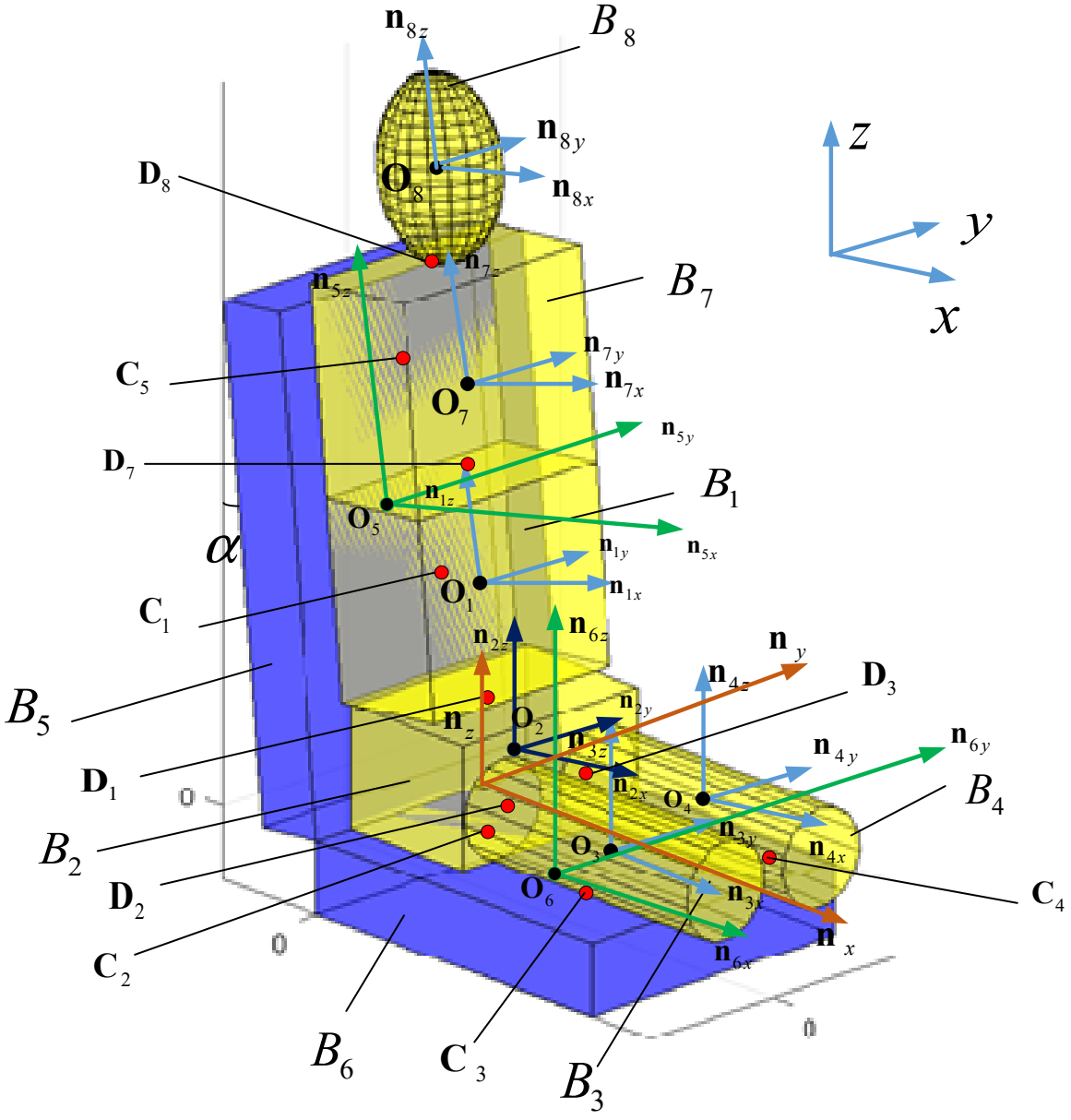

Fig. 7-1 The proposed seated human body model.

7.2.2 Coordinate transformation

Before the development of the model, the transformations between the relative and absolute coordinate systems were calculated, which are explained as follows.

$$\mathbf{S}_i = \begin{cases} \mathbf{T}_{12}(\theta_i)\hat{\mathbf{S}}_i = \mathbf{T}_{12}(\theta_i)\mathbf{T}_{11}(\alpha)\mathbf{S} & i = 1,5,7,8 \\ \mathbf{T}_{12}(\theta_i)\mathbf{S} & i = 2,6 \\ \mathbf{S} & i = 3,4 \end{cases} \tag{7-1}$$

where $\mathbf{T}_{12}(\theta_i)=\begin{bmatrix}1 & 0 & 0\\ 0 & \cos\theta_i & \sin\theta_i\\ 0 & -\sin\theta_i & \cos\theta_i\end{bmatrix}$, $\mathbf{T}_{11}(\alpha)=\begin{bmatrix}\cos\alpha & 0 & \sin\alpha\\ 0 & 1 & 0\\ -\sin\alpha & 0 & \cos\alpha\end{bmatrix}$, $\hat{\mathbf{S}}_i=\begin{bmatrix}\hat{\mathbf{n}}_{ix}\\ \hat{\mathbf{n}}_{iy}\\ \hat{\mathbf{n}}_{iz}\end{bmatrix}$ is the intermediate coordinate system of B_i after rotating α around $\mathbf{n}_y$.

The translational displacements of the center of gravity (CoG) of each human body segment $\mathbf{O}_i^{\ O}$ ($i=1,2,3,4,7,8$) in the absolute coordinate system are expressed as

$$\mathbf{O}_i^{\ O}=\mathbf{O}_{is}^{O}+\mathbf{O}_{id}^{O}=(x_{i0},y_{i0},z_{i0})+(0,y_i,z_i) \tag{7-2}$$

where $\mathbf{O}_{is}^{O}=(x_{i0},y_{i0},z_{i0})$ is the coordinate at the equilibrium position, and $\mathbf{O}_{id}^{O}=(0,y_i,z_i)$ is the dynamic displacement around the equilibrium position during vibration.

7.2.3 Calculation of relative motions

After determining the coordinate transformation, the relative displacements between different segments of the human body can be calculated as follows.

The relative displacement between B_1 and B_2 is

$$\mathbf{l}_{12}^{\mathbf{D}_1}=\mathbf{O}_2^{O}+\mathbf{D}_1^{B_2}\mathbf{T}_{12}(\theta_2)-\mathbf{O}_1^{O}-\mathbf{D}_1^{B_1}\mathbf{T}_{12}(\theta_1)\mathbf{T}_{11}(\alpha) \tag{7-3}$$

The relative displacement between B_2 and B_3 is

$$\mathbf{l}_{23}^{\mathbf{D}_2}=\mathbf{O}_3^{O}+\mathbf{D}_2^{B_3}-\mathbf{O}_2^{O}-\mathbf{D}_2^{B_2}\mathbf{T}_{12}(\theta_2) \tag{7-4}$$

The relative displacement between B_2 and B_4 is

$$\mathbf{l}_{24}^{\mathbf{D}_3}=\mathbf{O}_4^{O}+\mathbf{D}_3^{B_4}-\mathbf{O}_2^{O}-\mathbf{D}_3^{B_2}\mathbf{T}_{12}(\theta_2) \tag{7-5}$$

The relative displacement between B_1 and B_7 is

$$\mathbf{l}_{17}^{\mathbf{D}_7}=\mathbf{O}_7^{O}+\mathbf{D}_7^{B_7}\mathbf{T}_{12}(\theta_7)\mathbf{T}_{11}(\alpha)-\mathbf{O}_1^{O}-\mathbf{D}_7^{B_1}\mathbf{T}_{12}(\theta_1)\mathbf{T}_{11}(\alpha) \tag{7-6}$$

The relative displacement between B_7 and B_8 is

$$\mathbf{l}_{78}^{\mathbf{D}_8}=\mathbf{O}_8^{O}+\mathbf{D}_8^{B_8}\mathbf{T}_{12}(\theta_8)\mathbf{T}_{11}(\alpha)-\mathbf{O}_7^{O}-\mathbf{D}_8^{B_7}\mathbf{T}_{12}(\theta_7)\mathbf{T}_{11}(\alpha) \tag{7-7}$$

The corresponding relative velocities can be derived by the derivative of the relative displacement with respect to time. For example, the relative velocity between B_1 and B_2 is

$$\dot{\mathbf{l}}_{12}^{\mathrm{D}_1} = \frac{\mathrm{d}\mathbf{O}_2^O}{\mathrm{d}t} + \mathbf{D}_1^{B_2}\frac{\mathrm{d}\mathbf{T}_{12}(\theta_2)}{\mathrm{d}t} - \frac{\mathrm{d}\mathbf{O}_1^O}{\mathrm{d}t} - \mathbf{D}_1^{B_1}\frac{\mathrm{d}\mathbf{T}_{12}(\theta_1)}{\mathrm{d}t}\mathbf{T}_{11}(\alpha) \tag{7-8}$$

The pairs of contact points between the human body and the seat are expressed as $\mathbf{C}_i$ on the human body and $\mathbf{C}_{is}$ on the seat accordingly ($i = 1,2,3,4,5$). Similarly, the relative displacements at these contact points can be respectively calculated as

$$\mathbf{l}_{15}^{\mathrm{C}_1} = \mathbf{O}_5^O + \mathbf{C}_{1s}^{B_5}\mathbf{T}_{12}(\theta_5)\mathbf{T}_{11}(\alpha) - \mathbf{O}_1^O - \mathbf{C}_1^{B_1}\mathbf{T}_{12}(\theta_1)\mathbf{T}_{11}(\alpha) \tag{7-9}$$

Because the seat is rigid, the roll angle of the backrest satisfies $\theta_5 = \theta_0\cos\alpha$, and the roll angle of the seat pan satisfies $\theta_6 = \theta_0$.

$$\mathbf{l}_{26}^{\mathrm{C}_2} = \mathbf{O}_6^O + \mathbf{C}_{2s}^{B_6}\mathbf{T}_{12}(\theta_6) - \mathbf{O}_2^O - \mathbf{C}_2^{B_2}\mathbf{T}_{12}(\theta_2) \tag{7-10}$$

$$\mathbf{l}_{36}^{\mathrm{C}_3} = \mathbf{O}_6^O + \mathbf{C}_{3s}^{B_6}\mathbf{T}_{12}(\theta_6) - \mathbf{O}_3^O - \mathbf{C}_3^{B_3} \tag{7-11}$$

$$\mathbf{l}_{46}^{\mathrm{C}_4} = \mathbf{O}_6^O + \mathbf{C}_{4s}^{B_6}\mathbf{T}_{12}(\theta_6) - \mathbf{O}_4^O - \mathbf{C}_4^{B_4} \tag{7-12}$$

$$\mathbf{l}_{57}^{\mathrm{C}_5} = \mathbf{O}_7^O + \mathbf{C}_5^{B_7}\mathbf{T}_{12}(\theta_7)\mathbf{T}_{11}(\alpha) - \mathbf{O}_5^O - \mathbf{C}_{5s}^{B_5}\mathbf{T}_{12}(\theta_5)\mathbf{T}_{11}(\alpha) \tag{7-13}$$

The corresponding relative velocities can be derived by calculating the derivative of the relative displacement with respect to time. For example, the relative velocity between B_1 and B_5 at the point $\mathbf{C}_1$ is

$$\dot{\mathbf{l}}_{15}^{\mathrm{C}_1} = \frac{\mathrm{d}\mathbf{O}_5^O}{\mathrm{d}t} + \mathbf{C}_{1s}^{B_5}\frac{\mathrm{d}\mathbf{T}_{12}(\theta_5)}{\mathrm{d}t}\mathbf{T}_{11}(\alpha) - \frac{\mathrm{d}\mathbf{O}_1^O}{\mathrm{d}t} - \mathbf{C}_1^{B_1}\frac{\mathrm{d}\mathbf{T}_{12}(\theta_1)}{\mathrm{d}t}\mathbf{T}_{11}(\alpha) \tag{7-14}$$

7.2.4 Calculation of forces

For calculating the forces, the translational and rotational springs and dampers between human body segments were defined in Table E-1 in Appendix E. The forces can be calculated as the summation of the spring force (multiplying the relative displacement by the stiffness) and damper force (multiplying the relative velocity by the damping).

Therefore, the force transmitted between the bodies B_1 and B_2 is

$$\mathbf{f}_{12} = \mathbf{l}_{12}^{\mathbf{D}_1}\mathrm{diag}(0, k_{l1}, k_{v1}) + \dot{\mathbf{l}}_{12}^{\mathbf{D}_1}\mathrm{diag}(0, c_{l1}, c_{v1}) = \begin{bmatrix} 0 & f_{12(y)} & f_{12(z)} \end{bmatrix}\mathbf{S} \tag{7-15}$$

Other forces $\mathbf{f}_{23}$, $\mathbf{f}_{24}$, $\mathbf{f}_{17}$ and $\mathbf{f}_{78}$ calculated in this way were listed in Appendix E.

The contact springs and dampers between the human body and the seat were defined in Table E-2 in Appendix E. Then the forces at the contact points can be calculated, for example, at the contact point $\mathbf{C}_1$,

$$\mathbf{f}_{15}^{\mathbf{C}_1} = \mathbf{l}_{15}^{\mathbf{C}_1}\mathbf{T}_{11}^{\mathrm{T}}(\alpha)\mathrm{diag}(0, k_{tl1}, k_{tv1}) + \dot{\mathbf{l}}_{15}^{\mathbf{C}_1}\mathbf{T}_{11}^{\mathrm{T}}(\alpha)\mathrm{diag}(0, c_{tl1}, c_{tv1}) = \begin{bmatrix} 0 & f_{15(y)}^{\mathbf{C}_1} & f_{15(z)}^{\mathbf{C}_1} \end{bmatrix}\hat{\mathbf{S}}_5 \tag{7-16}$$

Other contact forces $\mathbf{f}_{26}^{\mathbf{C}_2}$, $\mathbf{f}_{36}^{\mathbf{C}_3}$, $\mathbf{f}_{46}^{\mathbf{C}_4}$ and $\mathbf{f}_{57}^{\mathbf{C}_5}$ calculated were listed in Appendix E.

7.2.5 Equations of motion of the model

The equations of motion for the human body segment B_1 were derived as

$$m_1\ddot{y}_1 = \mathbf{f}_{15}^{\mathbf{C}_1}\mathbf{T}_{11}(\alpha)\begin{bmatrix} 0 & 1 & 0 \end{bmatrix}^{\mathrm{T}} + f_{12(y)} + \mathbf{f}_{17}\mathbf{T}_{11}(\alpha)\begin{bmatrix} 0 & 1 & 0 \end{bmatrix}^{\mathrm{T}} \tag{7-17}$$

$$m_1\ddot{z}_1 = \mathbf{f}_{15}^{\mathbf{C}_1}\mathbf{T}_{11}(\alpha)\begin{bmatrix} 0 & 0 & 1 \end{bmatrix}^{\mathrm{T}} + f_{12(z)} + \mathbf{f}_{17}\mathbf{T}_{11}(\alpha)\begin{bmatrix} 0 & 0 & 1 \end{bmatrix}^{\mathrm{T}} \tag{7-18}$$

$$\begin{aligned} &I_1\ddot{\theta}_1 = -k_{r3}(\theta_1 - \theta_5) - c_{r3}(\dot{\theta}_1 - \dot{\theta}_5) - k_{r1}(\theta_1 - \theta_2\cos\alpha) - c_{r1}(\dot{\theta}_1 - \dot{\theta}_2\cos\alpha) \\ &+\mathbf{C}_1^{B_1}\times\mathbf{f}_{15}^{\mathbf{C}_1}\begin{bmatrix} 1 & 0 & 0 \end{bmatrix}^{\mathrm{T}} + \mathbf{D}_1^{B_1}\times(\mathbf{f}_{12}\mathbf{T}_{11}^{\mathrm{T}}(\alpha))\begin{bmatrix} 1 & 0 & 0 \end{bmatrix}^{\mathrm{T}} + \mathbf{D}_7^{B_1}\times\mathbf{f}_{17}\begin{bmatrix} 1 & 0 & 0 \end{bmatrix}^{\mathrm{T}} \\ &-k_{r5}(\theta_1 - \theta_7) - c_{r5}(\dot{\theta}_1 - \dot{\theta}_7) \end{aligned} \tag{7-19}$$

Similarly, the equations of motion for the human body segments B_2, B_3, B_4, B_7 and B_8 were obtained, respectively as

$$m_2\ddot{y}_2 = -f_{12(y)} + f_{26(y)}^{\mathbf{C}_2} + f_{23(y)} + f_{24(y)} \tag{7-20}$$

$$m_2\ddot{z}_2 = -f_{12(z)} + f_{26(z)}^{\mathbf{C}_2} + f_{23(z)} + f_{24(z)} \tag{7-21}$$

$$\begin{aligned} &I_2\ddot{\theta}_2 = -k_{r4}(\theta_2 - \theta_6) - c_{r4}(\dot{\theta}_2 - \dot{\theta}_6) - k_{r1}(\theta_2 - \theta_1\cos\alpha) - c_{r1}(\dot{\theta}_2 - \dot{\theta}_1\cos\alpha) \\ &-2k_{r2}\theta_2 - 2c_{r2}\dot{\theta}_2 + \mathbf{D}_1^{B_2}\times(-\mathbf{f}_{12})\begin{bmatrix} 1 & 0 & 0 \end{bmatrix}^{\mathrm{T}} + \mathbf{D}_2^{B_2}\times\mathbf{f}_{23}\begin{bmatrix} 1 & 0 & 0 \end{bmatrix}^{\mathrm{T}} \\ &+\mathbf{D}_3^{B_2}\times\mathbf{f}_{24}\begin{bmatrix} 1 & 0 & 0 \end{bmatrix}^{\mathrm{T}} + \mathbf{C}_2^{B_2}\times\mathbf{f}_{26}^{\mathbf{C}_2}\begin{bmatrix} 1 & 0 & 0 \end{bmatrix}^{\mathrm{T}} \end{aligned} \tag{7-22}$$

$$m_3\ddot{y}_3 = -f_{23(y)} + f_{36(y)}^{\mathbf{C}_3} \tag{7-23}$$

$$m_3\ddot{z}_3 = -f_{23(z)} + f_{36(z)}^{\mathbf{C}_3} \tag{7-24}$$

$$m_3\ddot{y}_4 = -f_{24(y)} + f_{46(y)}^{\mathbf{C}_4} \tag{7-25}$$

$$m_3\ddot{z}_4 = -f_{24(z)} + f_{46(z)}^{\mathbf{C}_4} \tag{7-26}$$

$$m_7\ddot{y}_7 = -\mathbf{f}_{17}\mathbf{T}_{11}(\alpha)\begin{bmatrix}0 & 1 & 0\end{bmatrix}^{\mathrm{T}} + \mathbf{f}_{78}\mathbf{T}_{11}(\alpha)\begin{bmatrix}0 & 1 & 0\end{bmatrix}^{\mathrm{T}} - \mathbf{f}_{57}^{\mathbf{C}_5}\mathbf{T}_{11}(\alpha)\begin{bmatrix}0 & 1 & 0\end{bmatrix}^{\mathrm{T}} \tag{7-27}$$

$$m_7\ddot{z}_7 = -\mathbf{f}_{17}\mathbf{T}_{11}(\alpha)\begin{bmatrix}0 & 0 & 1\end{bmatrix}^{\mathrm{T}} + \mathbf{f}_{78}\mathbf{T}_{11}(\alpha)\begin{bmatrix}0 & 0 & 1\end{bmatrix}^{\mathrm{T}} - \mathbf{f}_{57}^{\mathbf{C}_5}\mathbf{T}_{11}(\alpha)\begin{bmatrix}0 & 0 & 1\end{bmatrix}^{\mathrm{T}} \tag{7-28}$$

$$\begin{aligned} I_7\ddot{\theta}_7 &= k_{r5}(\theta_1-\theta_7) + c_{r5}(\dot{\theta}_1-\dot{\theta}_7) + \mathbf{D}_7^{B_7}\times(-\mathbf{f}_{17})\begin{bmatrix}1 & 0 & 0\end{bmatrix}^{\mathrm{T}} + k_{r6}(\theta_8-\theta_7) \\ &+ c_{r6}(\dot{\theta}_8-\dot{\theta}_7) + \mathbf{D}_8^{B_7}\times\mathbf{f}_{78}\begin{bmatrix}1 & 0 & 0\end{bmatrix}^{\mathrm{T}} + k_{r7}(\theta_5-\theta_7) + c_{r7}(\dot{\theta}_5-\dot{\theta}_7) \\ &+ \mathbf{C}_5^{B_7}\times(-\mathbf{f}_{57}^{\mathbf{C}_5})\begin{bmatrix}1 & 0 & 0\end{bmatrix}^{\mathrm{T}} \end{aligned} \tag{7-29}$$

$$m_8\ddot{y}_8 = -\mathbf{f}_{78}\mathbf{T}_{11}(\alpha)\begin{bmatrix}0 & 1 & 0\end{bmatrix}^{\mathrm{T}} \tag{7-30}$$

$$m_8\ddot{z}_8 = -\mathbf{f}_{78}\mathbf{T}_{11}(\alpha)\begin{bmatrix}0 & 0 & 1\end{bmatrix}^{\mathrm{T}} \tag{7-31}$$

$$I_8\ddot{\theta}_8 = -k_{r6}(\theta_8-\theta_7) - c_{r6}(\dot{\theta}_8-\dot{\theta}_7) + \mathbf{D}_8^{B_8}\times(-\mathbf{f}_{78})\begin{bmatrix}1 & 0 & 0\end{bmatrix}^{\mathrm{T}} \tag{7-32}$$

According to the vibration inputs on the seat pan, the coordinates of the origins $\mathbf{O}_5$ and $\mathbf{O}_6$ in the absolute coordinate system were derived, respectively as

$$\mathbf{O}_5^O = (x_{50}, y_{50}, z_{50}) + (0, y_0 - \theta_0 z_{50}, z_0) \tag{7-33}$$

$$\mathbf{O}_6^O = (x_{60}, y_{60}, z_{60}) + (0, y_0, z_0) \tag{7-34}$$

Assume the roll angles θ_i ($i = 1,2,5,6,7,8$) are small, then the transformation matrix $\mathbf{T}_{12}(\theta_i)$ and its derivative $\dfrac{\mathrm{d}\mathbf{T}_{12}(\theta_i)}{\mathrm{d}t}$ can be linearized by approximating $\sin\theta_i = \theta_i$ and $\cos\theta_i = 1$.

After linearization, the motion equations in Eqs.(7-17)-(7-32) can be expressed in matrix form as

$$\mathbf{M}_p\ddot{\mathbf{X}}_p + \mathbf{C}_p\dot{\mathbf{X}}_p + \mathbf{K}_p\mathbf{X}_p = \mathbf{K}_{pr}\mathbf{X}_{pr} + \mathbf{C}_{pr}\dot{\mathbf{X}}_{pr} \tag{7-35}$$

where $\mathbf{X}_p = [y_1 \quad z_1 \quad \theta_1 \quad y_2 \quad z_2 \quad \theta_2 \quad y_3 \quad z_3 \quad y_4 \quad z_4 \quad y_7 \quad z_7 \quad \theta_7 \quad y_8 \quad z_8 \quad \theta_8]^{\mathrm{T}}$ is the displacement vector, and $\mathbf{X}_{pr} = [y_0 \quad z_0 \quad \theta_0]^{\mathrm{T}}$ is the input displacement vector; $\mathbf{M}_p$, $\mathbf{C}_p$ and $\mathbf{K}_p$ are respectively the mass, damping and stiffness matrices of the modelled human body, and $\mathbf{K}_{pr}$ and $\mathbf{C}_{pr}$ are the stiffness and damping matrices associated with the inputs.

According to Eq.(7-35), the transfer function from $\mathbf{X}_{pr}$ to $\mathbf{X}_p$ can be calculated as

$$\mathbf{T}_p = (-\mathbf{M}_p\omega^2 + \mathrm{j}\omega\mathbf{C}_p + \mathbf{K}_p)^{-1}(\mathbf{K}_{pr} + \mathbf{C}_{pr}\mathrm{j}\omega) \tag{7-36}$$

For the calculation of the transfer function from the accelerations at the backrest to $\ddot{\mathbf{X}}_p$, the displacement vector on the SIT pad of the backrest is $[y_0 - \theta_0 z_d \quad z_0 \quad \theta_0]^{\mathrm{T}}$ (z_d is the vertical distance between the point where the centre of the SIT pad was placed on the backrest during the experimental measurement and the seat pan upper surface). If the roll excitation $\theta_0 \neq 0$, then the first and third displacements in the vector are coherent. For the convenience of calculating the lateral apparent mass on the backrest, the displacement vector on the backrest is expressed as $\mathbf{X}'_{pr} = [y_0 - z_d\theta_0 \quad z_0 \quad y_0 + z_d\theta_0 P_0]^{\mathrm{T}}$. Because the displacements (y_0, z_0 and θ_0) were incoherent white noises during the experiment, when the parameter P_0 satisfies $P_0 = (\frac{(y_0)_{\mathrm{rms}}}{(\theta_0)_{\mathrm{rms}} z_d})^2$ in which $(*)_{\mathrm{rms}}$ represents the r.m.s. value of *, the three displacements in $\mathbf{X}'_{pr}$ are incoherent, then the corresponding transfer function from $\mathbf{X}'_{pr}$ to $\mathbf{X}_p$ can be obtained as

$$\mathbf{T}_p{}' = \mathbf{T}_p \begin{bmatrix} 1 & 0 & -z_d \\ 0 & 1 & 0 \\ 1 & 0 & z_d P_0 \end{bmatrix}^{-1} \tag{7-37}$$

7.3 Parameter estimation and model calibration

7.3.1 General consideration

The model parameters were divided into two groups. One category of the parameters is related to masses and dimensions of the human body segments. They were obtained mainly through measurement or referring to the published anthropometric data. The other category of parameters

is associated with the physical properties (stiffness and damping) at the connection and contact points and locations of connection and contact points. They were mainly determined through a procedure of model calibration.

7.3.2 Parameter estimation

For the estimation of the coordinates of the key construction points, some coordinates can be determined by measurement or referring to literature, e.g., the centre of gravity (CoG) of B_i in the absolute coordinate, $\mathbf{O}_{is}^{O}$ ($i=1,2,\cdots,8$). For some points such as contact points $\mathbf{C}_i$ ($i=1,2,\cdots,5$) or connection points $\mathbf{D}_i$ ($i=1,2,3,7,8$), their coordinates only need to be determined in one of the relative coordinate systems. Then their coordinates in other relative coordinate systems can be determined accordingly given that the relative positions of origins of the relative coordinate systems are known. The determination of the coordinates of these points is shown in Table 7-1.

Table 7-1 The determination of the coordinates of points

Points	Definition of coordinates	Coordinate in other relative coordinate systems
$\mathbf{C}_1$	$\mathbf{C}_1^{B_1}=\left(x_{\mathbf{C}_1}^{B_1} \quad y_{\mathbf{C}_1}^{B_1} \quad z_{\mathbf{C}_1}^{B_1}\right)$	$\mathbf{C}_{1s}^{B_5}=\mathbf{C}_1^{B_1}+(\mathbf{O}_{1s}^{O}-\mathbf{O}_{5s}^{O})\mathbf{T}_{11}{}^{\mathrm{T}}(\alpha)$ *
$\mathbf{C}_2$	$\mathbf{C}_2{}^{B_2}=\left(x_{\mathbf{C}_2}^{B_2} \quad y_{\mathbf{C}_2}^{B_2} \quad z_{\mathbf{C}_2}^{B_2}\right)$	$\mathbf{C}_{2s}^{B_6}=\mathbf{C}_2^{B_2}+\mathbf{O}_{2s}^{O}-\mathbf{O}_{6s}^{O}$
$\mathbf{C}_3$	$\mathbf{C}_3^{B_3}=\left(x_{\mathbf{C}_3}^{B_3} \quad y_{\mathbf{C}_3}^{B_3} \quad z_{\mathbf{C}_3}^{B_3}\right)$	$\mathbf{C}_{3s}^{B_6}=\mathbf{C}_3^{B_3}+\mathbf{O}_{3s}^{O}-\mathbf{O}_{6s}^{O}$
$\mathbf{C}_4$	$\mathbf{C}_4^{B_4}=\left(x_{\mathbf{C}_4}^{B_4} \quad y_{\mathbf{C}_4}^{B_4} \quad z_{\mathbf{C}_3}^{B_3}\right)$	$\mathbf{C}_{4s}^{B_6}=\mathbf{C}_4^{B_4}+\mathbf{O}_{4s}^{O}-\mathbf{O}_{6s}^{O}$
$\mathbf{C}_5$	$\mathbf{C}_5^{B_7}=\left(x_{\mathbf{C}_5}^{B_7} \quad y_{\mathbf{C}_5}^{B_7} \quad z_{\mathbf{C}_5}^{B_7}\right)$	$\mathbf{C}_{5s}^{B_5}=\mathbf{C}_5^{B_7}+(\mathbf{O}_{7s}^{O}-\mathbf{O}_{5s}^{O})\mathbf{T}_{11}{}^{\mathrm{T}}(\alpha)$
$\mathbf{D}_1$	$\mathbf{D}_1^{B_1}=\left(x_{\mathbf{D}_1}^{B_1} \quad 0 \quad z_{\mathbf{D}_1}^{B_1}\right)$	$\mathbf{D}_1^{B_2}=\mathbf{D}_1^{B_1}\mathbf{T}_{11}(\alpha)+\mathbf{O}_{1s}^{O}-\mathbf{O}_{2s}^{O}$
$\mathbf{D}_2$	$\mathbf{D}_2^{B_3}=\left(x_{\mathbf{D}_2}^{B_3} \quad 0 \quad z_{\mathbf{D}_2}^{B_3}\right)$	$\mathbf{D}_2^{B_2}=\mathbf{D}_2^{B_3}+\mathbf{O}_{3s}^{O}-\mathbf{O}_{2s}^{O}$
$\mathbf{D}_3$	$\mathbf{D}_3^{B_4}=\mathbf{D}_2^{B_3}$	$\mathbf{D}_3^{B_2}=\mathbf{D}_3^{B_4}+\mathbf{O}_{4s}^{O}-\mathbf{O}_{2s}^{O}$
$\mathbf{D}_7$	$\mathbf{D}_7{}^{B_1}=\left(x_{\mathbf{D}_7}^{B_1} \quad y_{\mathbf{D}_7}^{B_1} \quad z_{\mathbf{D}_7}^{B_1}\right)$	$\mathbf{D}_7^{B_7}=\mathbf{D}_7^{B_1}+(\mathbf{O}_{1s}^{O}-\mathbf{O}_{7s}^{O})\mathbf{T}_{11}{}^{\mathrm{T}}(\alpha)$
$\mathbf{D}_8$	$\mathbf{D}_8{}^{B_7}=\left(x_{\mathbf{D}_8}^{B_7} \quad y_{\mathbf{D}_8}^{B_7} \quad z_{\mathbf{D}_8}^{B_7}\right)$	$\mathbf{D}_8^{B_8}=\mathbf{D}_8^{B_7}+(\mathbf{O}_{7s}^{O}-\mathbf{O}_{8s}^{O})\mathbf{T}_{11}{}^{\mathrm{T}}(\alpha)$

*Note that $\mathbf{C}_{is}$ and $\mathbf{C}_i$ are coincident at the equilibrium position, however, at different positions during vibration.

Considering subjects of different weights and heights, the masses and dimensions of the human body segments were expressed by the basic parameters — the weight (*m*) and height (*H*) with reference to the published anthropometric data (Dempster and Gaughran, 2010). In this way, the initial masses, moments of inertia, dimensions and coordinates of human body segments can be defined based on the two basic parameters (*m* and *H*) available. In this model, these parameters were obtained as shown in Table 7-2 and Fig. 7-2. Having defined the dimensions, some coordinates of the contact or connection points can be calculated, as listed in Table 7-3.

Table 7-2 The initial masses, dimensions, coordinates and moments of inertia of the segments

Segment	Initial mass	Dimension	Coordinates and moments of inertia
B_1	$m_1 = 0.15m$	$l_1 = 0.14H$	$x_{10} = -(0.07H\cos\alpha + 0.5l_1)\sin\alpha + 0.05H\cos\alpha$ $y_{10} = 0$ $z_{10} = (0.07H\cos\alpha + 0.5l_1)\cos\alpha + 0.05H\sin\alpha$ $I_1 = \frac{1}{12}m_1(l_1^2 + (0.18H)^2)$
B_2	$m_2 = 0.12m$	N/A*	$x_{20} = 0.06H,\ y_{20} = 0,\ z_{20} = 0.035H,$ $I_2 = \frac{1}{12}m_2((0.07H)^2 + (0.18H)^2)$
B_3	$m_3 = 0.1m$	$l_3 = 0.24H$	$x_{30} = 0.12H + 0.43l_3,\ y_{30} = -0.049H$ $z_{30} = 0.035H$
B_4	$m_4 = m_3$	N/A	$x_{40} = x_{30},\ y_{40} = -y_{30},\ z_{40} = z_{30}$
B_5	N/A	N/A	$x_{50} = -0.05\cos\alpha - 0.35\sin\alpha,\ y_{50} = 0,$ $z_{50} = -0.05\sin\alpha + 0.35\cos\alpha$
B_6	N/A	N/A	$x_{60} = 0.25,\ y_{60} = 0,\ z_{60} = -0.05$
B_7	$m_7 = 0.31m$	$l_7 = 0.157H$	$x_{70} = -(0.07H\cos\alpha + 0.5l_7 + l_1)\sin\alpha + 0.05H\cos\alpha$ $y_{70} = 0$ $z_{70} = (0.07H\cos\alpha + 0.5l_7 + l_1)\cos\alpha + 0.05H\sin\alpha$ $I_7 = \frac{1}{12}m_7(l_7^2 + (0.18H)^2)$
B_8	$m_8 = 0.08m$	$l_8 = 0.15H$	$x_{80} = -(0.07H\cos\alpha + l_1 + l_7 + 0.5l_8)\sin\alpha + 0.05H\cos\alpha$ $y_{80} = 0$ $z_{80} = (0.07H\cos\alpha + l_1 + l_7 + 0.5l_8)\cos\alpha + 0.05H\sin\alpha$ $I_8 = \frac{1}{20}m_8(l_8^2 + (0.09H)^2)$

*N/A means 'not applicable'.

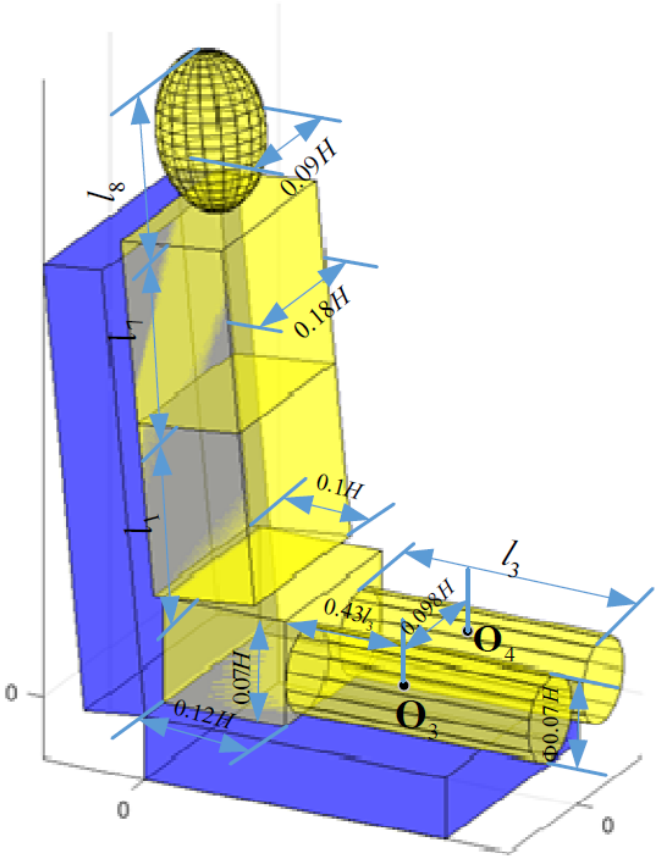

Fig. 7-2 The dimensions of the human body.

Table 7-3 Known coordinates of the contact and connection points

Contact points	Coordinates	Connection points	Coordinates
$\mathbf{C}_1$	$x_{\mathbf{C}_1}^{B_1} = -0.05H$	$\mathbf{D}_1$	$x_{\mathbf{D}_1}^{B_1} = 0$, $z_{\mathbf{D}_1}^{B_1} = -0.5l_1$
$\mathbf{C}_2$	$z_{\mathbf{C}_2}^{B_2} = -0.035H$	$\mathbf{D}_2$	$x_{\mathbf{D}_2}^{B_3} = -0.43l_3$, $z_{\mathbf{D}_2}^{B_3} = 0$
$\mathbf{C}_3$	$z_{\mathbf{C}_3}^{B_3} = -0.035H$	$\mathbf{D}_7$	$z_{\mathbf{D}_7}^{B_1} = 0.5l_1$
$\mathbf{C}_5$	$x_{\mathbf{C}_5}^{B_7} = -0.05H$	$\mathbf{D}_8$	$x_{\mathbf{D}_8}^{B_7} = 0$, $y_{\mathbf{D}_8}^{B_7} = 0$, $z_{\mathbf{D}_8}^{B_7} = 0.5l_7$

7.3.3 Model calibration

7.3.3.1 Model parameters to be determined

To determine the rest of the parameters (stiffness and damping as listed in Table E-1 and Table E-2 in Appendix E) of the model, a procedure of model calibration was carried out in which the error was minimized between the lateral and vertical apparent masses at the seat pan and backrest measured in the experiment of Chapter 6 and those predicted by the model. In addition, position parameters of some contact and connection points ($y_{\mathbf{C}_1}^{B_1}$, $z_{\mathbf{C}_1}^{B_1}$, $x_{\mathbf{C}_2}^{B_2}$, $y_{\mathbf{C}_2}^{B_2}$, $x_{\mathbf{C}_3}^{B_3}$, $y_{\mathbf{C}_3}^{B_3}$, $x_{\mathbf{C}_4}^{B_4}$, $y_{\mathbf{C}_4}^{B_4}$, $y_{\mathbf{C}_5}^{B_7}$, $z_{\mathbf{C}_5}^{B_7}$, $x_{\mathbf{D}_7}^{B_1}$, $y_{\mathbf{D}_7}^{B_1}$), and all the body masses (m_1, m_2, m_3, m_7, m_8) were also determined

through the model calibration. Considering the mass supported on the seat, a constraint for the masses is defined as $0.67m \le m_1 + m_2 + 2m_3 + m_7 + m_8 \le 0.88m$.

The apparent masses in y direction and z direction on the seat pan for the model calibration were calculated in the same way as Table 6-1, however, the apparent masses in y direction and z direction on the backrest were calculated in accordance with Table 7-4, so the lateral acceleration and lateral and vertical forces on the backrest can be generated by both the translational y-axis and roll excitations, which agrees with the calculation of the apparent mass in the model.

Table 7-4 The summary of MISO and SISO systems for the calculation of apparent masses on the backrest for model calibration

Excitation*	$y \neq 0$, $z \neq 0$, $r_x \neq 0$	$y \neq 0$, $z \neq 0$, $r_x = 0$	$y \neq 0$, $z = 0$, $r_x \neq 0$	$y \neq 0$, $z = 0$, $r_x = 0$	$y = 0$, $z \neq 0$, $r_x \neq 0$	$y = 0$, $z \neq 0$, $r_x = 0$	$y = 0$, $z = 0$, $r_x \neq 0$
System	MISO	MISO	SISO	SISO	MISO	SISO	SISO
Input	a_{by}, a_{bz}	a_{by}, a_{bz}	a_{by}	a_{by}	a_{by}, a_{bz}	a_{bz}	a_{by}
Output	F_{by}, F_{bz}						

*Note that being equal or not equal to zero means the excitation in that direction is zero or non-zero.

7.3.3.2 Objective of optimization

The lateral and vertical in-line apparent masses at the seat pan calculated with the model are

$$M_{sy}(\omega) = \frac{\mathcal{F}(f_{26(y)}^{\mathbf{C}_2} + f_{36(y)}^{\mathbf{C}_3} + f_{46(y)}^{\mathbf{C}_4})}{-\omega^2 \mathcal{F}(y_0)} \tag{7-38}$$

$$M_{sz}(\omega) = \frac{\mathcal{F}(f_{26(z)}^{\mathbf{C}_2} + f_{36(z)}^{\mathbf{C}_3} + f_{46(z)}^{\mathbf{C}_4})}{-\omega^2 \mathcal{F}(z_0)} \tag{7-39}$$

The lateral and vertical in-line apparent masses at the backrest are calculated as

$$M_{by}(\omega) = \frac{\mathcal{F}(f_{15(y)}^{\mathbf{C}_1} - f_{57(y)}^{\mathbf{C}_5})}{-\omega^2 \mathcal{F}(y_0 - \theta_0 z_d)} \tag{7-40}$$

$$M_{bz}(\omega) = \frac{\mathcal{F}(f_{15(z)}^{\mathbf{C}_1} - f_{57(z)}^{\mathbf{C}_5})}{-\omega^2 \mathcal{F}(z_0)\cos\alpha} \tag{7-41}$$

All the four apparent masses $M_{sy}(\omega)$, $M_{sz}(\omega)$, $M_{by}(\omega)$ and $M_{bz}(\omega)$ can be expressed by extracting elements from the transfer function matrices $\mathbf{T}_p$ and $\mathbf{T}_p'$ defined in Eq. (7-36)-(7-37).

The error function that is the summation of the average difference of the real and imaginary parts of the apparent masses in y direction and z direction at both the seat pan and backrest between the experimental data and the model is defined as follows. Note that the cross-axis apparent mass was not used in the error function because its value is rather small over the frequency range under consideration.

$$\text{error} = \sum_{j=sy,sz,by,bz} w_j \left\{ \sqrt{\frac{\sum_{i=1}^{N} [\text{Re}(M_j(f_i))_e - \text{Re}(M_j(f_i))_m]^2}{N}} + \sqrt{\frac{\sum_{i=1}^{N} [\text{Im}(M_j(f_i))_e - \text{Im}(M_j(f_i))_m]^2}{N}} \right\} \tag{7-42}$$

where subscripts e and m indicate the apparent masses are from experiment and model, respectively, N stands for the total number of frequency points, and w_j ($j = sy, sz, by, bz$) stand for the weighting factors, which may be different for different subjects or under different excitations. Reasonable constraints for the lower and upper bounds of all the parameters to be determined are defined before the model calibration.

Model calibration has been done with the algorithm introduced in Section 3.3. The frequency range considered for the calibration is 0.5-20 Hz. After that, all parameters can be determined.

7.3.4 Results of calibration

A good agreement in the apparent masses between the experiment and model for subjects of different weights and heights under different magnitudes of multi-axis excitations was achieved. Fig. 7-3- Fig. 7-5 showed three examples, which demonstrated the effectiveness of the model. The model is also good at predicting the resonances of apparent masses at both the seat pan and backrest.

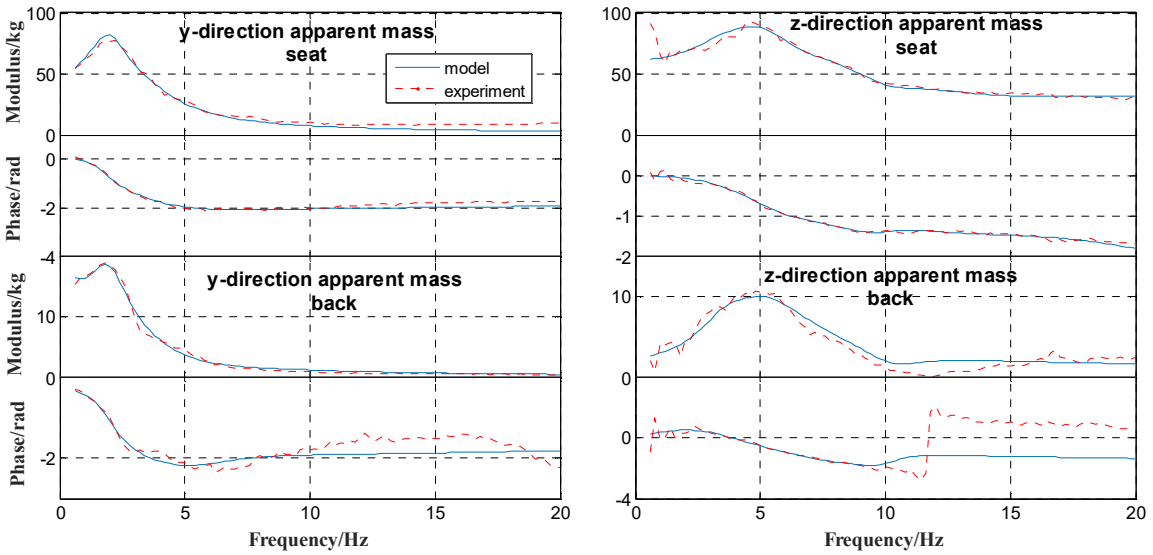

Fig. 7-3 The comparison between model and experiment for y-direction and z-direction apparent masses at the seat pan and backrest for a subject of 170 cm in height and 81 kg in weight under the excitation of 1.0 ms^{-2} r.m.s. lateral, 0.50 ms^{-2} r.m.s. vertical and 0.50 rad/s^2 r.m.s. roll vibration.

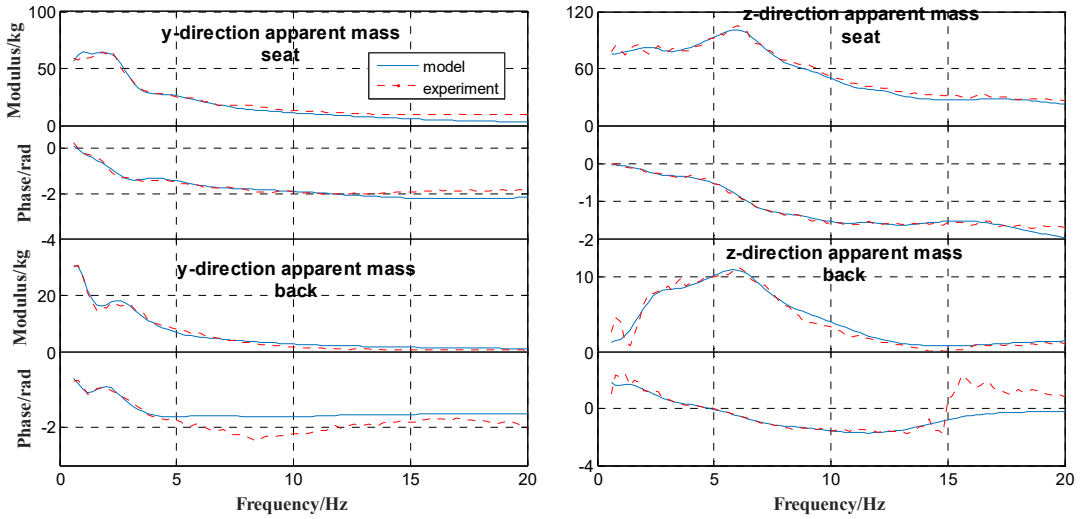

Fig. 7-4The comparison between model and experiment for y-direction and z-direction apparent masses at the seat pan and backrest for a subject of 179 cm in height and 93 kg in weight under the excitation of 0.50 ms^{-2} r.m.s. lateral, 0.25 ms^{-2} r.m.s. vertical and 0.50 rad/s^2 r.m.s. roll vibration.

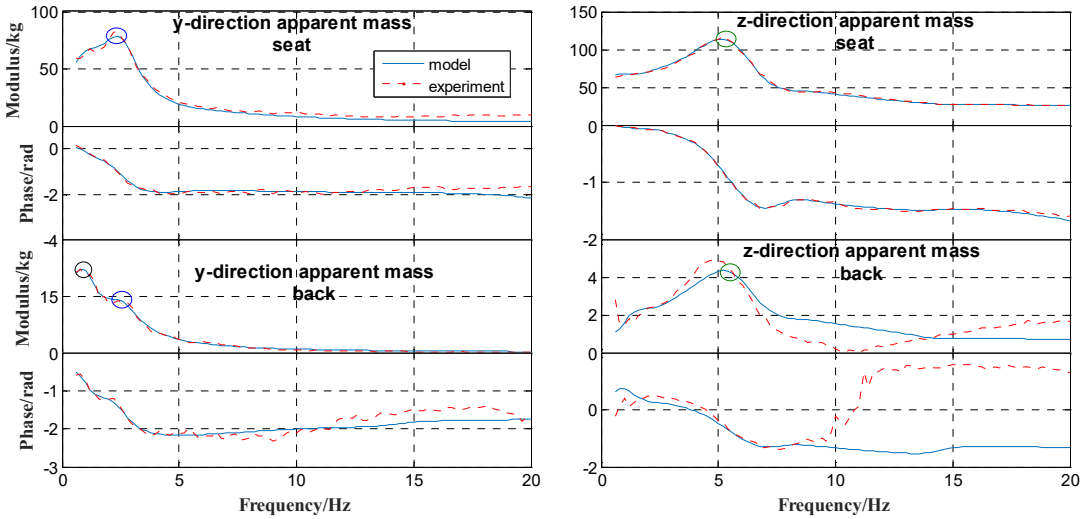

Fig. 7-5 The comparison between model and experiment for apparent masses in y direction and z direction at the seat pan and backrest for a subject of 171 cm in height and 83.5 kg in weight under the excitation of 0.5 ms^{-2} r.m.s. lateral, 1.0 ms^{-2} r.m.s. vertical and 0.75 rad/s^2 r.m.s. roll vibration.

It was noticed that in the experimental data a sudden change occurred at about 10 Hz in the phase of the apparent mass at the backrest in the *z* direction. This was because the apparent mass of the human body above 10 Hz was small in comparison with the gross (measured) apparent mass, and the subtraction of the mass of the backrest from the gross apparent mass when doing mass cancellation resulted in the phase shift.

7.4 Modal analysis

After the model was calibrated, a modal analysis with the model was further conducted allowing to find out the relationship between the modal properties and the resonances in the apparent masses. The damping of the human body is generally high, which cannot be ignored (Griffin, 1990). And the damping matrix cannot be diagonalized by the eigenvectors of the undamped system either. Therefore, the modal shapes of the human body are actually complex ones. The modal shape at each modal frequency can be better to be visualized by animation according to Section 3.6.

For the case of a subject of 171 cm in height and 83.5 kg in weight exposed to combined lateral (0.5 ms^{-2} r.m.s.), vertical (1.0 ms^{-2} r.m.s.) and roll (0.75 rad/s^2 r.m.s.) vibration (Fig. 7-5, the parameters were listed in Table E-3), three modes with modal frequencies of 1.01, 2.53, and 5.54 Hz were detected (corresponding to the peaks with black, blue and green circles in Fig. 7-5), and the corresponding mode shapes are illustrated in Fig. 7-6. For the first mode of 1.01 Hz (Fig. 7-6(a)), the modal vibration is dominated by the roll and lateral motions of the upper torso (B_7), accompanied

by the motion of the head (B_8) in the reverse direction because of its inertia since the head is not in contact with the backrest. For the second mode of 2.53 Hz (Fig. 7-6(b)), the modal shape is the roll and lateral motions of the upper torso (B_7) in the same direction as the lateral motions of the abdomen, pelvis and thighs. For the third mode of 5.54 Hz (Fig. 7-6(c)), the motion is mainly the vertical motions of the whole upper body (head (B_8), upper torso (B_7), abdomen (B_1)), together with the vertical and roll motions of the pelvis (B_2) accompanied by vertical motion of the thighs (B_3 , B_4). For all the 12 subjects, the calculated modal shapes are similar, although not exactly the same due to inter-subject variability.

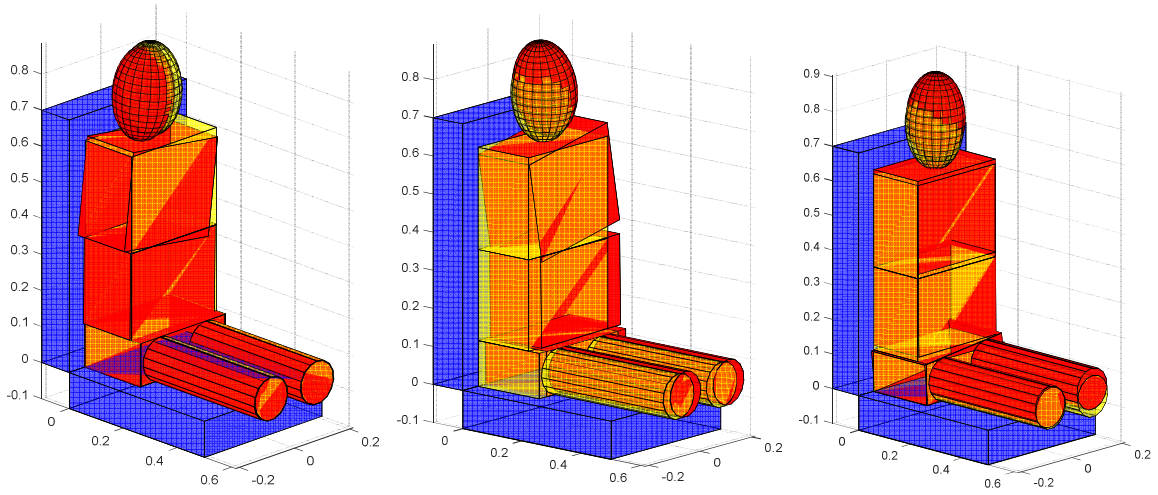

(a) (b) (c)

Fig. 7-6 Modal shapes of a subject of 171 cm in height and 83.5 kg in weight under a combined excitation of lateral (0.5 ms^{-2} r.m.s.), vertical (1.0 ms^{-2} r.m.s.) and roll (0.75 rad/s^2 r.m.s.) vibration: (a) first mode shape (1.01 Hz), (b) second mode shape (2.53 Hz), and (c) third mode shape (5.54 Hz) (red: deformed mode shape; yellow: undeformed mode shape).

7.5 Discussion

7.5.1 Model parameters

As introduced before, one group of model parameters are the stiffness and damping at the contact and connection points or their locations. The surface connection or contact was simplified as point connection or contact with an assumption that the surface force can be taken as a concentrated force acting at the connection or contact point. This group of parameters can hardly be determined from the literature or direct measurement, partly because these parameters from living human

body are difficult to measure. They can be obtained via a properly defined procedure of optimization or calibration with measurement data of human biodynamics.

The other group of the model parameters are those in relation to the size and weight of human body. Two basic parameters (*m* and *H*) were adopted to characterize the geometric size and mass properties of the body segments of different individuals (inter-subject variability) with reference to the literature available (e.g., Dempster and Gaughran (2010)). The masses of the human body segments were included in the parameters to be determined during the model calibration. The ranges of these parameters were constrained to a small band after carefully referring to the relevant literature. This treatment was based on the consideration that although anthropometric data (i.e., m_i) of human body segments may be obtained from literature, the masses of body segments actually show large inter-subject variability, even for those subjects who have similar weights. As mentioned earlier, the two legs were not explicitly modelled in the current model, but part of their masses (except for that portion of the leg weight exerted on the floor through the feet-footrest contact) were included in the thighs. Including the parameter m_i into the to-be-determined variable list also enabled the effective masses of the legs to be more effectively identified and reflected in the mass properties of the thigh. Another consideration for this treatment is that the model can be acclimated to different thigh contacts (minimum thigh contact, maximum thigh contact, average thigh contact, etc) simply by adjusting the initial mass and mass range of the thighs and the range of the mass supported on the seat.

For a model with a large number of calibration parameters, it is important to properly define optimization objective and select suitable and effective optimization algorithms, so that the model parameters are determined while making sure the global dynamics (or apparent masses) of the human body exposed to vibration agrees with the measurement data. This study used both the real and imaginary parts of the lateral and vertical apparent masses at both the seat pan and backrest as the optimization objective function (Eq.(7-42)). This treatment in defining the objective function is more complete compared with the methods reported previously by other researchers. With so many experimental data (four apparent masses and each with both the real and imaginary parts) included in the objective function, it is very important to design an effective optimization strategy and algorithm.

The good agreement between the model-predicted and experimentally measured apparent masses achieved in this study also ascribes to the proper design of the optimization strategy and the selection of optimization algorithm (a genetic algorithm combined with an algorithm for constrained nonlinear multivariable problem). This combined approach was proved to be a more effective and powerful optimization strategy than just adopting one of the above-mentioned

optimization algorithms or the 'Complex' algorithm as used in Qiu and Griffin (2011), increasing the possibility of converging to a better result in a given time.

7.5.2 Modelling

Various seated human models have been developed for different purposes. However, the existing models have been mostly limited to single-axis translational excitation, in fore-and-aft direction (Qiu and Griffin, 2011), lateral direction (Stein *et al.*, 2009) or vertical direction (Matsumoto and Griffin, 2001; Liang and Chiang, 2008; Nawayseh and Griffin, 2009; Liu *et al.*, 2015). Only a few biodynamic models have considered multi-axis excitation, for example, Kim *et al.* (2011) developed a 5 DOF model of seated human body exposed to combined fore-and-aft, vertical and pitch excitation. Desai *et al.* (2018) developed a 20 DOF multi-body dynamic seated human model exposed to fore-and-aft and vertical excitation. Almost all models of such so far, however, were one- or two-dimensional and developed in the mid-sagittal plane. A biodynamic model that considers combined in-plane and out-of-plane excitation suitable for studying ride comfort of rail vehicles has not been available. The model proposed in this chapter is a three-dimensional model of seated human body exposed to combined lateral, vertical and roll vibration. It can be used to predict the motion not only in the vertical direction in the mid-sagittal plane but also in the lateral and roll directions in the mid-coronal plane experienced by passengers on rail vehicles.

How to take into consideration the inter-subject variability in biodynamic modelling is not an easy task (Pankoke *et al.*, 1998; Liu *et al.*, 2015). The proposed model is capable of not only accommodating to simultaneously the in-plane (vertical) and out-of-plane (lateral and roll) vibration inputs, but also representing inter-subject variability. This capability was realized by expressing the body dimensions and masses by the weight (m) and height (H) of subjects and further conducting an effective model calibration procedure to determine the mass property for individuals, as discussed in the preceding section. In addition, the inclination of the upper body was also taken into consideration in the proposed model by introducing an extra variable – inclination angle of the upper body and backrest into the model so as to cope with the situation where passengers are seated with inclined backrest.

7.5.3 Modal properties

There have rarely been any published data about the modal testing of the human body. The existing modal data of the human body were achieved mainly via modal analysis conducted by means of suitable biodynamic models.

The modal shape of the human body in relation to lateral and roll motion has rarely been reported. It was found from this study that the modal frequencies and modal shapes (Fig. 7-6) were related to the resonances in the measured apparent masses. The first modal frequency (1.01 Hz) corresponds to the principal resonance in the lateral apparent mass at the backrest (Fig. 7-5). The modal shape corresponding to this frequency exhibited great lateral motion of the upper torso (Fig. 7-6(a)). It was also found that the second modal frequency (2.53 Hz) was related to the primary peak in the lateral apparent mass on the seat pan and the second peak in the lateral apparent mass at the backrest (Fig. 7-5). From the second mode shape (Fig. 7-6(b)), great lateral motion of the upper torso and the lower body (abdomen, pelvis and thighs) were observed. As can be seen, the modal frequency and modal shape obtained from the modal analysis with the proposed model showed agreement with the resonances in the measured apparent masses. Mandapuram *et al.* (2005) found the first peak frequency in the 0.7-1.0 Hz in the lateral apparent mass at the seat pan and thought it was associated with rocking and swaying of the upper body, which agreed with the first mode in this study.

For the mode shapes under vertical excitation, Kitazaki and Griffin (1997) conducted a modal analysis using a finite element model and reported that the principal resonance about 5 Hz was mainly caused by a whole-body vertical mode: the axial and shear deformation of tissue beneath pelvis vibrating in phase with a vertical visceral mode. Matsumoto and Griffin (2001) carried out a modal analysis with a 2D multi-body dynamic model without damping and suggested that the resonance of the apparent mass at about 5 Hz may result from a vibration mode related to the vertical motion of the pelvis and legs and pitch motion of the pelvis, accompanied by vertical motion of the upper-body and viscera and bending motion of the spine. Zheng *et al.* (2011) found in a modal analysis a mode at 5.29 Hz with body motion in both vertical and fore-and-aft directions along with pitch motion of the pelvis and upper body. Later, Liu *et al.* (2015) reported a similar mode around 6.2 Hz. The modal analysis with the currently proposed model (Fig. 7-6(c)) showed similar modal frequency and modal shape of whole-body vibration in the vertical direction to those reported by the other researchers. However, some difference was observed in the modal shapes of the current analysis compared with the previous results. This was caused by the difference in the model structure and degrees-of-freedom of the human body segments. For example, the models developed by Matsumoto and Griffin (2001) and Zheng *et al.* (2011) were for the seated human body exposed to vertical vibration only, while the proposed model in this study was developed for the seated human body subjected to combined vertical, lateral and roll excitations. The models in the former contain degrees of freedom of fore-and-aft, vertical and pitch motions, whereas the current model accommodates to the degrees of freedom of the body in lateral, vertical and roll directions.

It is worth pointing out that almost all the modal analyses with biodynamic models so far have been conducted without damping for simplicity (e.g., Matsumoto and Griffin (2001); Zheng *et al.* (2011)). In this study, the modal analysis was conducted with damping based on the complex mode theory. In this way, the resulting mode shapes are more accurate and closer to reality than those analyzed without damping.

7.6 Conclusion

A seated human body model consisting of abdomen, pelvis, thighs, upper torso (including the shoulders, thorax, arms), head and neck exposed to lateral, vertical and roll excitations was proposed. The model was calibrated with lateral and vertical apparent masses at both the seat pan and backrest measured from the last chapter. This model has been proved to be applicable for subjects of different weights and heights and different magnitudes of combined lateral, vertical and roll excitations. This model is also potentially suitable for different backrest inclinations that have been taken into consideration in the modelling.

Modal analysis was conducted for the analysis of resonances in the apparent masses. Three vibration modes that are related to the resonances in the measured apparent masses were revealed. It was found the first vibration mode is dominated by the roll and lateral motions of the upper torso, accompanied by the motion of the head in the reverse direction. In the second mode, the modal shape is the roll and lateral motions of the upper torso in the same direction as the lateral motions of the abdomen, pelvis and thighs. In the third mode, the motion is mainly the vertical motion of the whole upper body, together with the vertical and roll motion of the pelvis accompanied by vertical motion of the thighs. The calculated modal frequencies and modal shapes were consistent with the previously reported results and were found to associate with the resonances in the measured apparent masses. This model can be further developed into a human-seat model for predicting vibration transmission to passengers of rail vehicles and assisting in optimization of seat design to promote the ride comfort.

Chapter 8 Experimental study of dynamic characteristics of a train seat with subjects exposed to lateral, vertical and roll excitation

8.1 Introduction

Seats are widely used in high-speed trains and other rail vehicles to isolate the vibration transmitted to passengers, whose dynamics is closely related to the ride comfort. Because the dynamic characteristics of the seat with a seated subject show a great discrepancy from the counterpart with a rigid mass of the same weight (Griffin, 1990), the dynamic characteristics of the seat are usually examined through the seat transmissibility with seated subjects. Thus, the efficiency of a seat depends on not only the dynamic characteristics of the seat itself but also the biodynamics of the subject seated on it. Both the seat and the seated subject exhibit obvious nonlinearity (Qiu and Griffin, 2012; Zheng *et al.*, 2019), showing varying dynamic characteristics with the change of vibration magnitude, so is the seat with seated subjects.

Vibration transmissibility of the seat with subject under exposure to single-axis vibration has been frequently studied, especially in three translational directions. As introduced in Section 2.2.3, in the vertical direction, the transmissibility of conventional seats exhibited a primary peak in 4-6 Hz; sometimes, there would be a second resonance around 10 Hz. The nonlinearity was reflected by that the primary resonance frequency in the seat transmissibility decreased with the increase of vibration magnitude (Corbridge *et al.*, 1989; Toward and Griffin, 2011; Tufano and Griffin, 2013). The nonlinear dynamic characteristics in the vertical direction were found more dependent on the nonlinearity of the human body than the nonlinearity of the seat (cushion) (Tufano and Griffin, 2013). In addition, the seat transmissibility of a car seat in the fore-and-aft direction also exhibited a decreasing tendency in both the resonance frequency and modulus at resonance with increasing vibration magnitude (Jalil and Griffin, 2007b; Zhang *et al.*, 2016). In the lateral direction, Ittianuwat *et al.* (2014) and Gong and Griffin (2018) reported resonances around 17 Hz for a car seat and 25 Hz for a train seat respectively in the lateral seat transmissibilities on both the seat pan and backrest, which were possibly related to a lateral seat mode since the human body would not add new resonances in the lateral transmissibility above 10 Hz (Lo *et al.*, 2013).

The vibration environment on a high-speed train and other rail vehicles is usually complex, involving multi-axis vibration. However, so far, there have rarely been publications about the seat

transmissibility under exposure to multi-axis vibrations because of the limitation of devices and the more complexity of experimental design for multi-axis vibrations. And for a nonlinear system, multi-axis vibration cannot be decomposed into several single-axis ones. Therefore, whether the dynamics of the seat under single-axis vibration can be applied to a multi-axis vibration environment still needs to be studied. It is well known the main vibrations of a high-speed train are vertical, lateral and roll vibrations (ISO, 2001). As found by the above research, the lateral, vertical and roll vibrations on the seat base are three main vibrations for the lateral, vertical and roll vibrations on the seat pan and backrest that would be the main cause of the discomfort of the passengers. The dynamics of the bare train seat and seat with subjects exposed to these combined vibrations has not been studied. Understanding the transmission of these vibrations through the seat may be beneficial to the reduction of the discomfort and risk caused by these vibrations. Furthermore, what the nonlinearity of the train seat with subjects arising from the varying magnitudes of the combined vibrations is remains to be explored.

In terms of the calculation of seat transmissibility, under multiple inputs, the traditional single-input and single-output (SISO) method may cause biased estimation of seat transmissibility because one input acceleration can go through not only its own path but also other inputs' paths to reach the response because of the inevitable mutual coherence among the inputs, so a new estimation method is waiting to be adopted to overcome this problem.

In this chapter, the dynamic characteristics of a double-unit train seat with one and two subjects were studied via a laboratory experiment. The inline and cross-axis seat transmissibilities were evaluated based on MISO or SISO system according to the number of vibration inputs. The objective of this chapter is to advance understanding of the dynamic characteristics of the train seat with subjects. Whether the seat transmissibility under multi-axis vibration is analogous to that under single-axis vibration, how the biodynamics of the subject influences the seat transmissibility and what the effect of adding on excitations in one or two axes on the seat transmissibility in another direction and the effect of combined excitations in vertical, lateral and roll directions of different magnitudes on the seat transmissibility were studied and answered.

8.2 Experimental methods

The experiment was carried out using 6-axis motion simulator in the ISVR at the University of Southampton. The same 12 subjects as Chapter 6 participated in the experiment. During the experiment, the participants were asked to sit in an upright posture in contact with the backrest,

with the feet resting on a footrest (average thigh contact), a hand holding an emergency button and the other on the lap.

8.2.1 Seat description

As shown in Fig. 8-1, the train seat used in this study had two units with a total weight of 64 kg. The left (or right) seat pan frame was connected to the left (or right) backrest via a connecting shaft that forms the pivot of rotation for the backrest (Fig. C-4). The two seat pan frames were integrated together via two rod-like structures and the left (or right) seat pan cushion was stuck to the left (or right) seat pan frame via thread gluing. In addition, the angles of the seat pans and backrests were set at nearly 0° to the horizontal and the vertical, respectively using an SAE H-point manikin.

8.2.2 Vibration design

The vibration in vertical, lateral or roll direction was random acceleration signal with approximately flat spectrum defined in the frequency range from 0.5 to 50 Hz and almost incoherent between directions. Every participant was exposed to 63 vibrations, which was the combination of the vertical vibration with four magnitudes (0, 0.25, 0.5 and 1.0 m/s^2 r.m.s.), lateral vibration with four magnitudes (0, 0.25, 0.5 and 1.0 m/s^2 r.m.s.), as well as roll vibration with four magnitudes (0, 0.5, 0.75 and 1.0 rad/s^2 r.m.s.). The rotational axis of roll vibration was the intersection line between the symmetrical plane of the left unit and the platform ('left' or 'right' is defined from the perspective of the seated subject).

8.2.3 Measurement

As shown in Fig. 8-1, the fore-and-aft acceleration (a_{fx}), lateral acceleration (a_{fy}), and vertical accelerations on the left (a_{fzl}) and right (a_{fzr}) on the platform were measured by four single-axis accelerometers. The tri-axial accelerations at the seat pan (a_{sx}, a_{sy}, a_{sz}) and backrest (a_{bx}, a_{by}, a_{bz}) were measured by two tri-axial SIT-pads. Two vertical accelerations of the left seat pan (a_{sl}, a_{sr}) and left backrest (a_{bl}, a_{br}) were respectively measured by two single-axis accelerometers, from which the roll accelerations of the seat pan and backrest were calculated. The SIT-pad on the left seat pan was positioned beneath the ischial tuberosity of the seated subject. The SIT-pad on the left backrest was centrally located $z_d = 470$ mm above the seat pan upper surface. The roll accelerations of the platform (a_{rf}), left seat pan (a_{rs}) and left backrest (a_{rb}) can be calculated

respectively by dividing the difference between the left vertical acceleration and the right one (a_{fzl} and a_{fzr} for the platform; a_{sl} and a_{sr} for the left seat pan; a_{bl} and a_{br} for the left backrest) by the distance between them.

The measurement was made first with the bare seat, then with 12 subjects seated on the left unit individually, and finally with two pairs of subjects seated on both units individually.

All the data were recorded by *HVlab* data acquisition system at 512 samples per second via anti-aliasing filter set at 100 Hz. The participants' safety was ensured over the whole process with vibration exposure controlled within the safety range in accordance with the standard BS 6841:1987. The experiment was approved by Human Experimentation Safety and Ethics Committee of the ISVR at the University of Southampton (approval number: 40309).

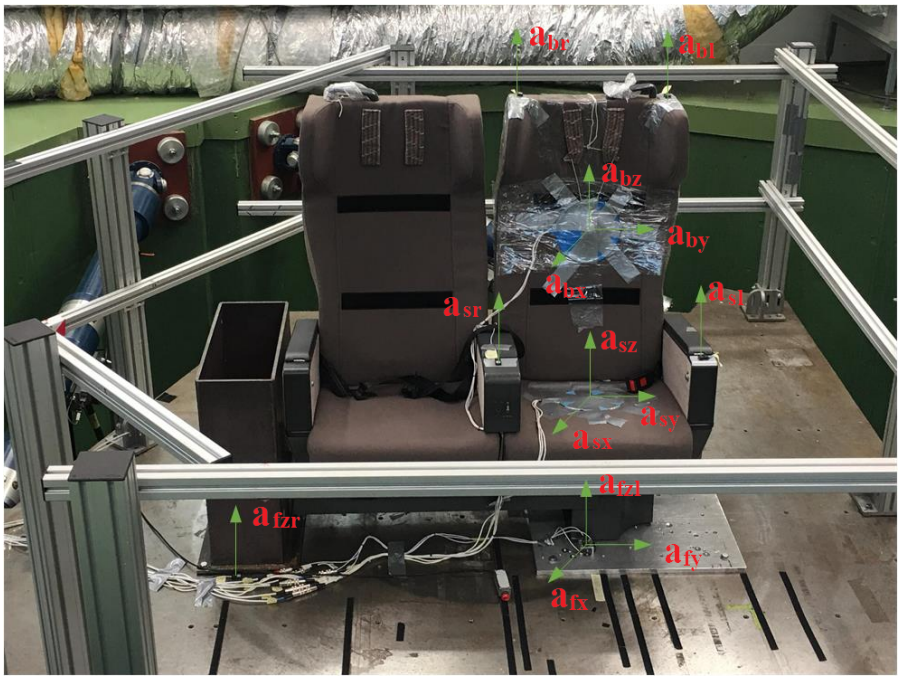

Fig. 8-1 Experimental set-up.

8.2.4 Symbol convention

The convention of the symbols is the same as Section 6.2.2. Transmissibility is simplified as '*T*', and the following subscripts are the same as apparent mass. For example, T_{by-z} means the cross-axis transmissibility from the acceleration in y direction on the platform to the acceleration in z direction on the backrest; T_{sy} means the inline transmissibility in y direction on the seat pan.

For cross-axis transmissibility, the transmissibility from i-axis acceleration on the seat base to j-axis acceleration on the seat pan or backrest is expressed as i-j transmissibility for simplicity. For

example, z-x transmissibility means the transmissibility from the acceleration in z axis on the seat base to the acceleration in x axis.

8.2.5 Data analysis method

For the same reason as Chapter 6, the seat transmissibility under multiple inputs was calculated with MISO method. The transmissibilities were calculated by designing either MISO or SISO system according to the number of inputs, in accordance with Table 8-1. The frequency resolution for the following analysis is 0.2 Hz.

For the calculation of the transmissibility using MISO method, the frequency response function for the original system H_{my} ($m=1,2,3$) in Eq. (3-9) was adopted, so the input and output for the calculation of transmissibilities were got rid of the coherent parts with all the other inputs. The coherences in Eqs. (3-21)-(3-22) were to be calculated for making clear the contribution of the different inputs to the output. Therefore, all the calculations of transmissibilities and coherence were not dependent on the sequence of inputs.

Table 8-1 The summary of MISO and SISO systems for the calculation of seat transmissibility

Excitation*	$y\neq 0$, $z\neq 0$, $r_x\neq 0$	$y\neq 0$, $z\neq 0$, $r_x=0$	$y\neq 0$, $z=0$, $r_x\neq 0$	$y\neq 0$, $z=0$, $r_x=0$	$y=0$, $z\neq 0$, $r_x\neq 0$	$y=0$, $z\neq 0$, $r_x=0$	$y=0$, $z=0$, $r_x\neq 0$
System	MISO	MISO	MISO	SISO	MISO	SISO	SISO
Input	a_{fy}, a_{fz}, a_{rf}	a_{fy}, a_{fz}	a_{fy}, a_{rf}	a_{fy}	a_{fz}, a_{rf}	a_{fz}	a_{rf}
Output	$a_{sx}, a_{sy}, a_{sz}, a_{rs}, a_{bx}, a_{by}, a_{bz}, a_{rb}$						

*Note that being equal or not equal to zero means the excitation in that direction is zero or non-zero.

Data analysis was carried out using Matlab (2010b). Wilcoxon signed-rank test introduced in Section 3.4 was used to test the difference between paired samples with a chosen significance level α of 0.05. In the results, m/M means m pairs show significant changes out of M pairs in M pairwise comparisons.

8.3 Results

8.3.1 The influence of seated subject on seat transmissibility

At first, the seat transmissibility was measured with the bare seat, which was compared with the counterpart with 12 different subjects individually seated on the left unit (Fig. 8-2). For the transmissibilities in y direction and r_x direction on the seat pan and all the transmissibilities on the backrest, the seated subject did not add new resonances and made little difference to the existing

resonance frequencies below 50 Hz, which was consistent with the finding in Lo *et al.* (2013). However, the moduli of the transmissibilities at resonance reduced because of the extra damping introduced from the human body, and those above the resonance decreased due to the increased mass supported on the seat pan and backrest from the seated subject. In addition, the coupling between the human body and the seat made a great change to the transmissibility in z direction on the seat pan, shifting the resonance frequency to around 5 Hz that was close to the principal resonance in the vertical apparent mass of the seated human body on the seat pan (Section 6.3.1.2) (Mansfield and Griffin, 2000; Zheng *et al.*, 2012). In comparison, this coupling had little effect on the transmissibility on the backrest in the vertical direction but reduced the modulus slightly because of the mass of the human body supported on the backrest. However, the mass of the human body interacting with the backrest in the vertical direction was much smaller than that interacting with the seat pan.

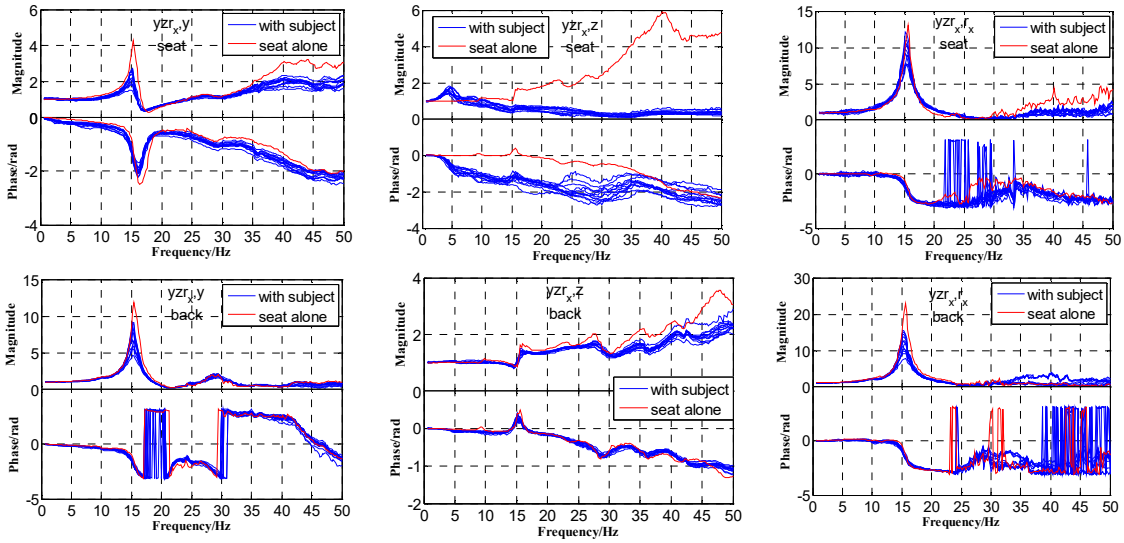

Fig. 8-2 The comparison of seat transmissibility between the bare seat and seat with one seated subject under exposure to 0.5 m/s^2 r.m.s lateral, 0.5 m/s^2 r.m.s vertical and 0.5 rad/s^2 r.m.s roll excitation (blue lines: seat transmissibilities for 12 seated subjects).

Under all excitations, the inter-subject variability resulted in the difference among the seat transmissibilities seated with different subjects, especially for the modulus at resonance, as shown in Fig. 8-2. For the bare seat, all the transmissibilities exhibited a peak or increased around 15 Hz, which was probably due to a seat mode.

8.3.2 Inline transmissibility

The main purpose of this section was to report the results about the inline transmissibility of the train seat with one subject under single-axis, bi-axis and tri-axis vibration of different magnitudes in lateral, vertical and roll directions.

8.3.2.1 Transmissibility in y direction

For the transmissibility in y direction on the seat pan, the principal resonance located around 15 Hz regardless of the number of excitation axes (Fig. 8-2). Wilcoxon signed-rank test was conducted to find out the influence of excitation magnitude on the resonance frequency and modulus at resonance. The resonance frequency tended to decrease with a large proportion of significant reductions as the increase of excitation magnitude in y direction (24/48 in total; Fig. 8-3 and Table 8-2) when the magnitude in z axis was small (z=0, 8/12; z=0.25, 6/12; z=0.5, 7/12; Table 8-2) or the magnitude in roll axis was small (r_x=0, 9/12; r_x=0.5, 8/12; Table 8-2). In addition, there were also a relatively large proportion of significant decreases of the resonance frequency as the increasing magnitude in r_x direction (27/72 in total, Table F-1) at small magnitude of z-axis excitation (z=0, 9/18; z=0.25, 8/18; z=0.5, 9/18; Table F-1) or at y-axis magnitude of 0.5 m/s^2 r.m.s. (y=0.5, 12/24; Table F-1). The resonance frequency only showed a large proportion of significant reductions as the increase of z-axis magnitude (17/72 in total, not shown) with no roll excitation (r_x=0, 11/18, not shown; Fig. F-1), and the proportion of significant changes reduced greatly with the existence of roll excitation (r_x=0.5, 2/18; r_x=0.75, 0/18; r_x=1.0, 4/18; not shown).

As for the modulus at resonance, there were only a relatively large proportion of significant reductions as the increase of roll magnitude with no z-axis excitation (z=0, 10/18; Table F-1) or small y-axis excitation (y=0.25, 12/24; Table F-1) and as the increase of y-axis magnitude when r_x magnitude or z-axis magnitude was the largest (r_x=1.0, 6/12; z=1.0, 6/12; Table 8-2).

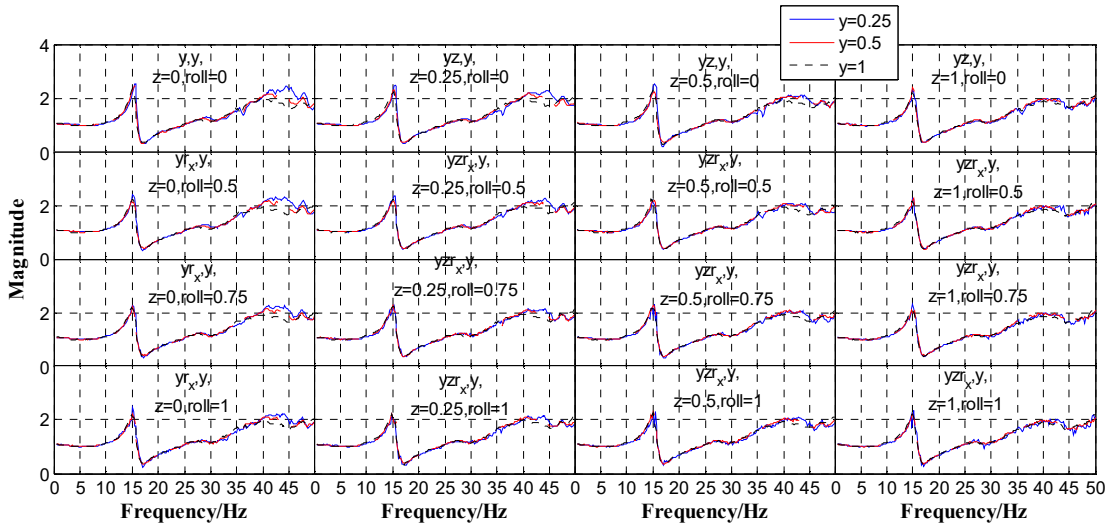

Fig. 8-3 Comparison between median transmissibilities in y direction on the seat pan for 12 subjects under different excitation magnitudes in y direction.

Table 8-2 Wilcoxon signed-rank test for the effect of excitation magnitude in y direction on the principal resonance frequency and modulus at resonance for the transmissibility in y direction on the seat pan

y magnitude	y=0.5	y=1.0	Significant difference proportion (different r_x)
(a)r_x=0			
y=0.25	***/**/***/ns; ns/ns/***/ns	***/***/***/ns; ns/ns/***/*	9/12; 4/12
y=0.5		***/**/ns/*; */ns/ns/ns	
(b)r_x=0.5			
y=0.25	*/**/ns/ns; */*/ns/ns	ns/***/***/*; ns/ns/ns/*	8/12; 3/12
y=0.5		ns/*/***/***; ns/ns/ns/ns	
(c)r_x=0.75			
y=0.25	ns/ns/ns/ns; ns/ns/ns/*	*/ns/*/ns; ns/ns/ns/***	3/12; 2/12
y=0.5		***/ns/ns/ns; ns/ns/ns/ns	
(d)r_x=1.0			
y=0.25	ns/ns/***/ns; ***/ns/*/*	*/ns/***/ns; */ns/*/*	4/12; 6/12
y=0.5		*/ns/ns/ns; ns/ns/ns/ns	
Significant difference proportion (different z)	z=0: 8/12; 4/12 z=0.25: 6/12; 1/12 z=0.5: 7/12; 4/12 z=1.0: 3/12; 6/12		

ns=not significant, p>0.05; *= p<0.05;**= p<0.01;***= p<0.005, Wilcoxon;
The p-value for different excitation magnitudes in z direction is ranked as z=0/z=0.25/z=0.5/z=1.0, separated by slash;
The effect on resonance frequency and modulus at resonance is shown before and after ';', respectively.

For the transmissibility in y direction on the backrest, the principal resonance was around 15 Hz regardless of the number of excitation axes (Fig. 8-2), close to that in the transmissibility in y direction on the seat pan. There were a large proportion of significant decreases of the resonance frequency as the increasing magnitude in y direction (Fig. 8-4; 29/48 in total, Table 8-3), however, the proportion of significant changes reduced with increasing r_x magnitude from 11/12 to 5/12 (Table 8-3). In addition, the proportion of the significant decreases was small when the excitation magnitude in z direction was maximum (z=1.0, 3/12; Table 8-3). On the other hand, the proportion of significant decreases of the resonance frequency as the increase of z-axis magnitude was generally small (26/72 in total, Table F-2), but at some specific y-axis or roll magnitude, the proportion of significant decreases was relatively large (r_x=0.75, 9/18; y=0.25, 13/24; Table F-2). In addition, the proportion of significant reductions of the resonance frequency as roll magnitude (29/72 in total, not shown) was large only at zero or small y-axis or z-axis magnitudes (z=0, 9/18; y=0.25, 12/24; y=0.5, 15/24; not shown).

Table 8-3 Wilcoxon signed-rank test for the effect of excitation magnitude in y direction on the principal resonance frequency and modulus at resonance for the transmissibility in y direction on the backrest

y magnitude	y=0.5	y=1.0	Significant difference proportion (different r_x)
(a)r_x=0			
y=0.25	***/***/***/ns; ns/*/***/ns	***/***/***/***; **/*/***/*	11/12; 7/12
y=0.5		***/***/***/***; **/ns/ns/ns	
(b)r_x=0.5			
y=0.25	ns/***/**/ns; ns/*/ns/ns	***/***/***/ns; ns/ns/*/*	7/12; 4/12
y=0.5		***/ns/*/ns; ns/ns/*/ns	
(c)r_x=0.75			
y=0.25	***/***/**/ns; */*/ns/ns	**/ns/**/ns; ns/ns/***/*	6/12; 5/12
y=0.5		ns/***/ns/ns; ns/ns/*/ns	
(d)r_x=1.0			
y=0.25	ns/**/ns/ns; ns/ns/*/***	ns/ns/***/*; */ns/***/***	5/12; 6/12
y=0.5		ns/*/**/ns; ns/ns/*/ns	
Significant difference proportion (different z)	z=0: 7/12; 4/12 z=0.25: 9/12; 4/12 z=0.5: 10/12; 9/12 z=1.0: 3/12; 5/12		

ns=not significant, p>0.05; *= p<0.05;**= p<0.01;***= p<0.005, Wilcoxon;
The p-value for different excitation magnitudes in z direction is ranked as z=0/z=0.25/z=0.5/z=1.0, separated by slash;
The effect on resonance frequency and modulus at resonance is shown before and after ';', respectively.

For the modulus at resonance, the proportion of significant reductions with y-axis magnitude was large only at some roll or z-axis magnitudes (r_x=0, 7/12; r_x=1.0, 6/12; z=0.5, 9/12; Table 8-3). The proportion of significant changes of the modulus at resonance as z-axis magnitude was small whatever the roll (≤8/18) or y-axis (≤9/24) magnitudes were (Table F-2). In addition, on the whole, the proportion of significant reductions as the increase of roll magnitude was larger than 50% (40/72 in total) except for the small proportion when y=0.5 (9/24) (not shown).

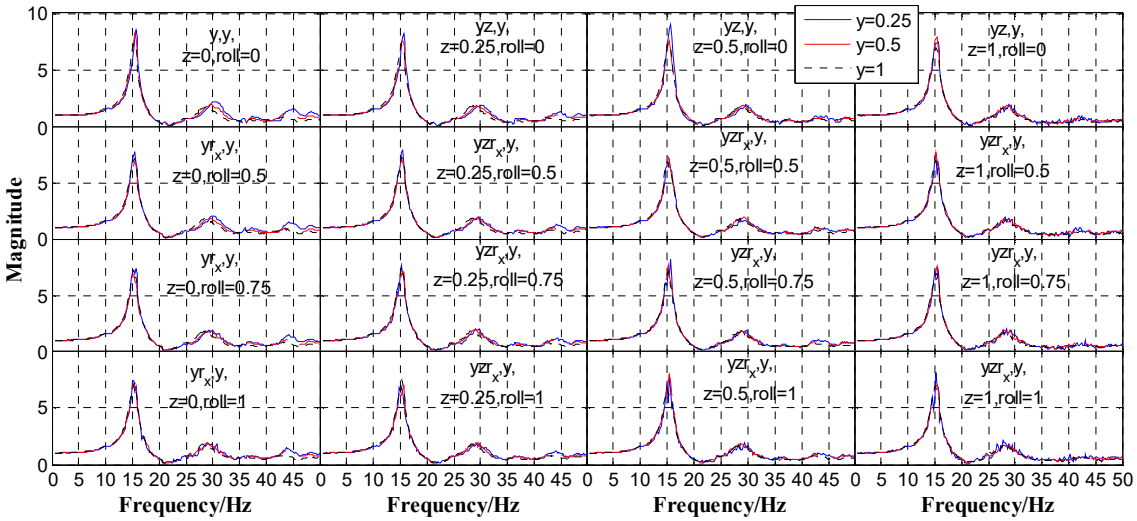

Fig. 8-4 Comparison between median transmissibilities in y direction on the backrest for 12 subjects under different excitation magnitudes in y direction.

8.3.2.2 Transmissibility in z direction

For the vertical seat transmissibility on the seat pan, there was a clear principal resonance around 5 Hz regardless of the number of vibration axes (Fig. 8-2), close to the principal resonance frequency in the vertical apparent mass of seated subject on the seat pan, so this peak was largely related to the human body considering no existence of such resonance in the transmissibility of the bare seat. Some people also exhibited a second resonance around 10 Hz, which was smeared out in the median data (Fig. 8-5). The principal resonance frequency showed a large proportion of significant reductions with the increasing z-axis magnitude (Fig. 8-5; 32/48 in total, Table 8-4), however, the proportion of significant changes reduced as the increasing roll excitation (from 10/12 to 7/12) and y-axis excitation (from 10/12 to 5/12) (Table 8-4). The resonance frequency also exhibited a relatively large proportion of significant reductions as the increase of y-axis excitation (28/72 in total) with no roll excitation (r_x=0, 9/18) or at z-axis magnitude of 0.5 m/s^2 r.m.s. (z=0.5, 12/24) (Table F-3). In addition, there were generally a small proportion of significant changes with the increase of roll excitation (20/72 in total, not shown), but there were still a relatively large proportion of significant changes with no y-axis excitation (y=0, 9/18; not shown).

As for the modulus at resonance, in general, the proportion of significant changes with y-axis (31/72 in total, Table F-3), z-axis (19/48 in total, Table 8-4) or roll (13/72 in total, not shown) magnitude was small. However, it showed a large proportion of significant reductions as the increase of z-axis excitation with small y-axis magnitude (including zero) (y=0, 8/12; y=0.25, 9/12; Table 8-4). What is more, it also exhibited a large proportion of significant reductions with increasing y-axis magnitude with no or small roll or z-axis magnitude (r_x=0, 10/18; z=0.25, 12/24; z=0.5, 14/24; Table F-3).

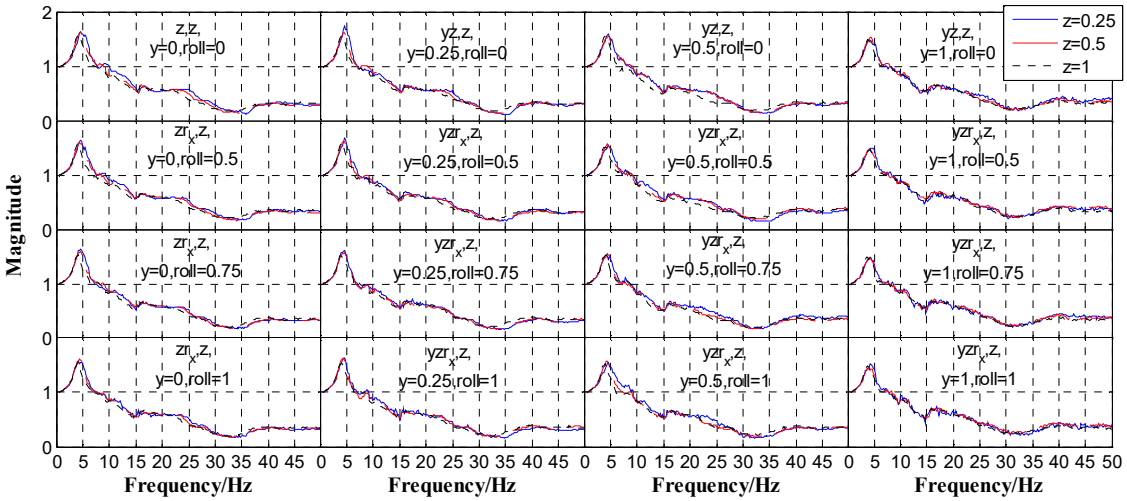

Fig. 8-5 Comparison between median transmissibilities in z direction on the seat pan for 12 subjects under different excitation magnitudes in z direction.

Table 8-4 Wilcoxon signed-rank test for the effect of excitation magnitude in z direction on the principal resonance frequency and modulus at resonance for the transmissibility in z direction on the seat pan

z magnitude	z=0.5	z=1.0	Significant difference proportion (different r_x)
(a)r_x=0			
z=0.25	*/**/ns/ns; ns/***/ns/ns	***/***/***/***;**/***/ns/ns	10/12;5/12
z=0.5		*/**/***/***;**/*/ns/ns	
(b)r_x=0.5			
z=0.25	*/ns/ns/ns;ns/ns/ns/ns	***/***/***/*;*/*/ns/ns	8/12;4/12
z=0.5		***/***/*/ns;*/*/ns/ns	
(c)r_x=0.75			
z=0.25	ns/ns/ns/ns;ns/ns/ns/*	***/***/ns/*;**/*/ns/ns	7/12;5/12
z=0.5		***/***/*/***;*/*/ns/ns	
(d)r_x=1.0			
z=0.25	ns/ns/*/ns;ns/ns/ns/ns	**/***/***/ns;*/***/ns/ns	7/12;5/12
z=0.5		***/***/***/ns;*/***/**/ns	
Significant difference proportion (different y)	y=0: 10/12;8/12 y=0.25: 9/12;9/12 y=0.5: 8/12;1/12 y=1.0: 5/12;1/12		

ns=not significant, p>0.05; *= p<0.05;**= p<0.01;***= p<0.005, Wilcoxon;
The p-value for different excitation magnitudes in y direction is ranked as y=0/y=0.25/y=0.5/y=1.0, separated by slash;
The effect on resonance frequency and modulus at resonance is shown before and after ';', respectively.

For the vertical transmissibility on the backrest, the modulus was nearly constant in 0.5-15 Hz, close to 1.0 (Fig. 8-2), suggesting the backrest worked rigidly in the vertical direction in this frequency range. Most subjects also exhibited a small peak around 5 Hz, possibly resulting from the same human mode as that one generating the principal peak on the seat pan, but it was not clear in the

median transmissibility (Fig. 8-6). The peak was not obvious because only a small portion of the body mass interacted with the backrest. Then the modulus started to increase by the influence of a seat mode around 15 Hz. In addition, judging from the median transmissibility, the modulus tended to shift to the left as the increase of y-axis (not shown), z-axis (Fig. 8-6) and roll excitation (not shown) magnitudes, signifying a nonlinear effect as the increasing vibration magnitude.

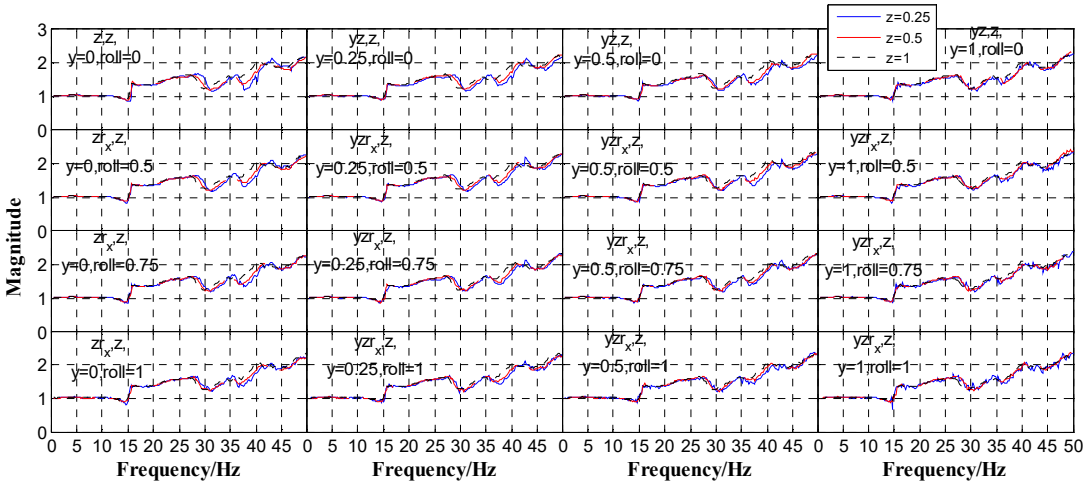

Fig. 8-6 Comparison between median transmissibilities in z direction on the backrest for 12 subjects under different excitation magnitudes in z direction.

8.3.2.3 Transmissibility in r_x direction

For the transmissibility in r_x direction on the seat pan, there was a principal resonance around 15 Hz regardless of the number of vibration axes (Fig. 8-2), in the vicinity of that in the lateral transmissibility on the seat pan and backrest. Overall, the proportion of significant changes of resonance frequency with y-axis (30/72 in total, not shown), z-axis (31/72 in total, Table F-4) and roll excitation (Fig. 8-7; 18/48 in total, Table 8-5) was not very large. The resonance frequency only decreased as the increasing roll magnitude with a considerable proportion of significant changes with no z-axis vibration (z=0, 8/12) or at y-axis magnitude of 0.5 m/s^2 r.m.s. (y=0.5, 6/12) (Table 8-5). The proportion of significant decreases of resonance frequency with increasing z-axis magnitude was only relatively large at y-axis magnitude of 0.25 m/s^2 r.m.s. (y=0.25, 9/18; Table F-4). Similarly, the proportion of significant decreases of resonance frequency with rising y-axis excitation became large only at z-axis magnitude of 0.25 m/s^2 r.m.s. (z=0.25, 9/18) or roll magnitude of 0.75 rad/s^2 r.m.s (r_x=0.75, 12/24) (not shown).

As for the modulus at resonance, it did not show a large proportion of significant changes with the variation of y-axis (19/72 in total, not shown) or z-axis (12/72 in total, Table F-4) magnitude.

However, sometimes it did as the roll magnitude (25/48 in total, Table 8-5) with no clear pattern at some y-axis or z-axis magnitudes (z=0.25, 10/12; z=1.0, 6/12; y=0, 9/12; y=1.0, 7/12; Table 8-5).

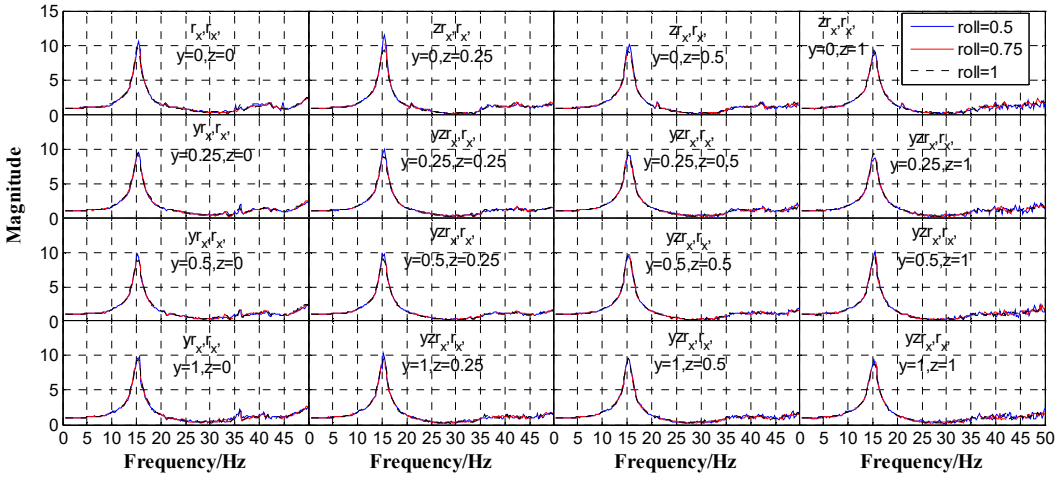

Fig. 8-7 Comparison between median transmissibilities in r_x direction on the seat pan for 12 subjects under different excitation magnitudes in r_x direction.

Table 8-5 Wilcoxon signed-rank test for the effect of roll excitation magnitude on the resonance frequency and modulus at resonance for the transmissibility in r_x direction on the seat pan

r_x magnitude	r_x=0.75	r_x=1.0	Significant difference proportion (different z)
(a)z=0			
r_x=0.5	ns/***/*/***; ***/*/ns/ns	***/***/***/***;***/ns/ns/*	8/12;5/12
r_x=0.75		**/ns/ns/ns;ns/*/ns/ns	
(b)z=0.25			
r_x=0.25	ns/ns/*/ns;***/***/*/***	ns/ns/ns/***;***/***/***/***	3/12;10/12
r_x=0.5		ns/ns/ns/***;***/ns/***/ns	
(c)z=0.5			
r_x=0.25	ns/ns/*/ns;***/ns/ns/*	**/**/ns/ns;***/ns/ns/ns	4/12;4/12
r_x=0.5		ns/***/ns/ns;ns/ns/ns/*	
(d)z=1.0			
r_x=0.25	ns/ns/ns/ns;ns/*/ns/ns	*/ns/***/ns;**/ns/*/***	3/12;6/12
r_x=0.5		ns/ns/***/ns;**/ns/ns/***	
Significant difference proportion (different y)	y=0: 4/12;9/12 y=0.25: 4/12;5/12 y=0.5: 6/12;4/12 y=1.0: 4/12;7/12		

ns=not significant, p>0.05; *= p<0.05;**= p<0.01;***= p<0.005, Wilcoxon;
The p-value for different excitation magnitudes in y direction is ranked as y=0/y=0.25/y=0.5/y=1.0, separated by slash;
The effect on resonance frequency and modulus at resonance is shown before and after ';', respectively.

For the transmissibility in r_x direction on the backrest, there was a principal resonance around 15 Hz regardless of the number of vibration axes (Fig. 8-2), in the vicinity of that in the transmissibility in r_x direction on the seat pan. Overall, by Wilcoxon signed-rank test, the proportion of the

significant variations of resonance frequency with y-axis (31/72 in total, Table F-5), z-axis (30/72 in total, not shown) and roll magnitudes (Fig. 8-8; 22/48 in total, Table 8-6) was not very large. There were a relatively large proportion of significant decreases of the resonance frequency as the increasing roll magnitude with no z-axis vibration (z=0, 8/12) or median y-axis magnitudes (y=0.25, 6/12; y=0.5, 7/12) (Table 8-6). There exhibited a large proportion of significant decreases of resonance frequency as the increasing z-axis magnitude at y-axis magnitude of 0.5 m/s^2 r.m.s. (y=0.5, 9/18; not shown). In addition, there were a large proportion of significant decreases of resonance frequency with rising y-axis excitation at some z-axis or roll magnitudes, following no obvious rule (z=0.25, 10/18; z=1.0, 9/18; r_x=0.75, 13/24; Table F-5).

As for the modulus at resonance, it did not show a large proportion of significant variations with y-axis (10/72 in total, Table F-5) or z-axis (15/72 in total, not shown) magnitude. However, sometimes it did as the roll magnitude with no obvious pattern (19/48 in total, Table 8-6). As exhibited in Table 8-6, the modulus at resonance had a relatively large proportion of significant reductions as increasing roll magnitude at some z-axis or y-axis magnitudes (z=0.25, 9/12; y=0, 8/12; y=1.0, 6/12).

Table 8-6 Wilcoxon signed-rank test for the effect of excitation magnitude in r_x direction on the resonance frequency and modulus at resonance for the transmissibility in r_x direction on the backrest

r_x magnitude	r_x=0.75	r_x=1.0	Significant difference proportion (different z)
(a)z=0			
r_x=0.5	ns/ns/**/***; **/ns/ns/ns	***/***/***/*;*/ns/ns/***	8/12;3/12
r_x=0.75		*/**/ns/ns;ns/ns/ns/ns	
(b)z=0.25			
r_x=0.25	ns/ns/***/ns;*/*/ns/ns	ns/ns/*/***;***/***/***/*	5/12;9/12
r_x=0.5		ns/ns/*/***;***/ns/***/*	
(c)z=0.5			
r_x=0.25	ns/ns/ns/ns;***/ns/ns/ns	*/**/ns/*;*/ns/ns/ns	4/12;3/12
r_x=0.5		ns/***/ns/ns;ns/ns/ns/***	
(d)z=1.0			
r_x=0.25	ns/ns/ns/ns;ns/***/ns/ns	*/***/***/ns;ns/ns/ns/***	5/12;4/12
r_x=0.5		ns/*/***/ns;**/ns/ns/***	
Significant difference proportion (different y)	y=0: 4/12;8/12 y=0.25: 6/12;3/12 y=0.5: 7/12;2/12 y=1.0: 5/12;6/12		

ns=not significant, p>0.05; *= p<0.05;**= p<0.01;***= p<0.005, Wilcoxon;
The p-value for different excitation magnitudes in y direction is ranked as y=0/y=0.25/y=0.5/y=1.0, separated by slash;
The effect on resonance frequency and modulus at resonance is shown before and after ';', respectively.

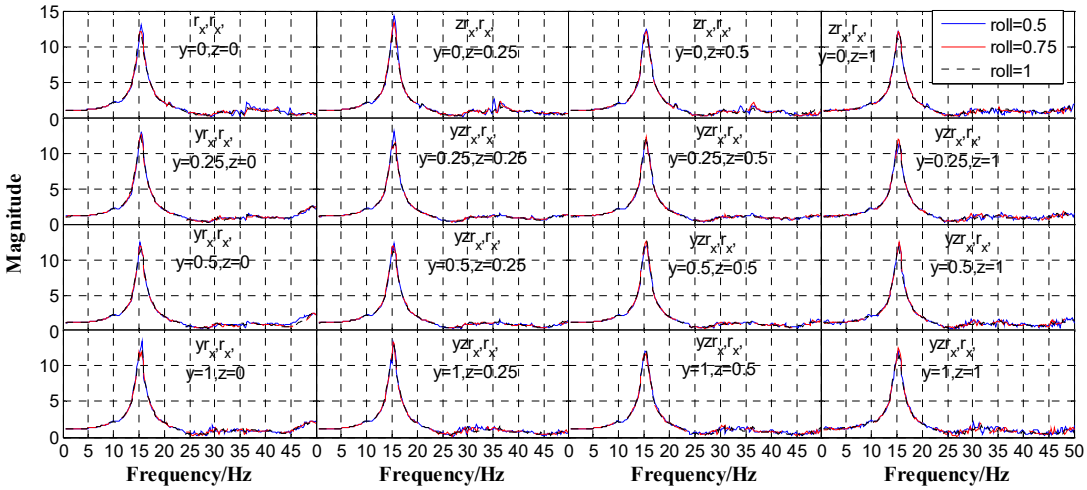

Fig. 8-8 Comparison between median transmissibilities in r_x direction on the backrest for 12 subjects under different excitation magnitudes in r_x direction.

8.3.3 Cross-axis transmissibility

The purpose of this section was to briefly report the results about the cross-axis transmissibility of the train seat with one subject exposed to lateral, vertical and roll vibrations.

8.3.3.1 On the seat pan

The cross-axis transmissibilities on the seat pan measured using single-axis and multi-axis vibrations showed similar trends. One example of these transmissibilities under tri-axis vibration was illustrated in Fig. 8-9. All the cross-axis transmissibilities on the seat pan showed a peak around 15 Hz, close to the principal peaks in the inline transmissibilities in y and r_x directions on the seat pan and backrest (Fig. 8-2). For the transmissibilities to the acceleration in x direction on the seat pan (y-x, z-x and r_x-x), another peak around 25 Hz was visible for almost all the 12 subjects. For the y-z, z-x, z-r_x transmissibilities, there exhibited a peak around 5 Hz for most subjects, which was probably associated with the same human mode as the one generating the peaks around 5 Hz in the vertical seat transmissibilities on the seat pan and backrest. The difference between the seat transmissibilities caused by inter-subject variability was relatively greater for y-z, r_x-z ones than the others.

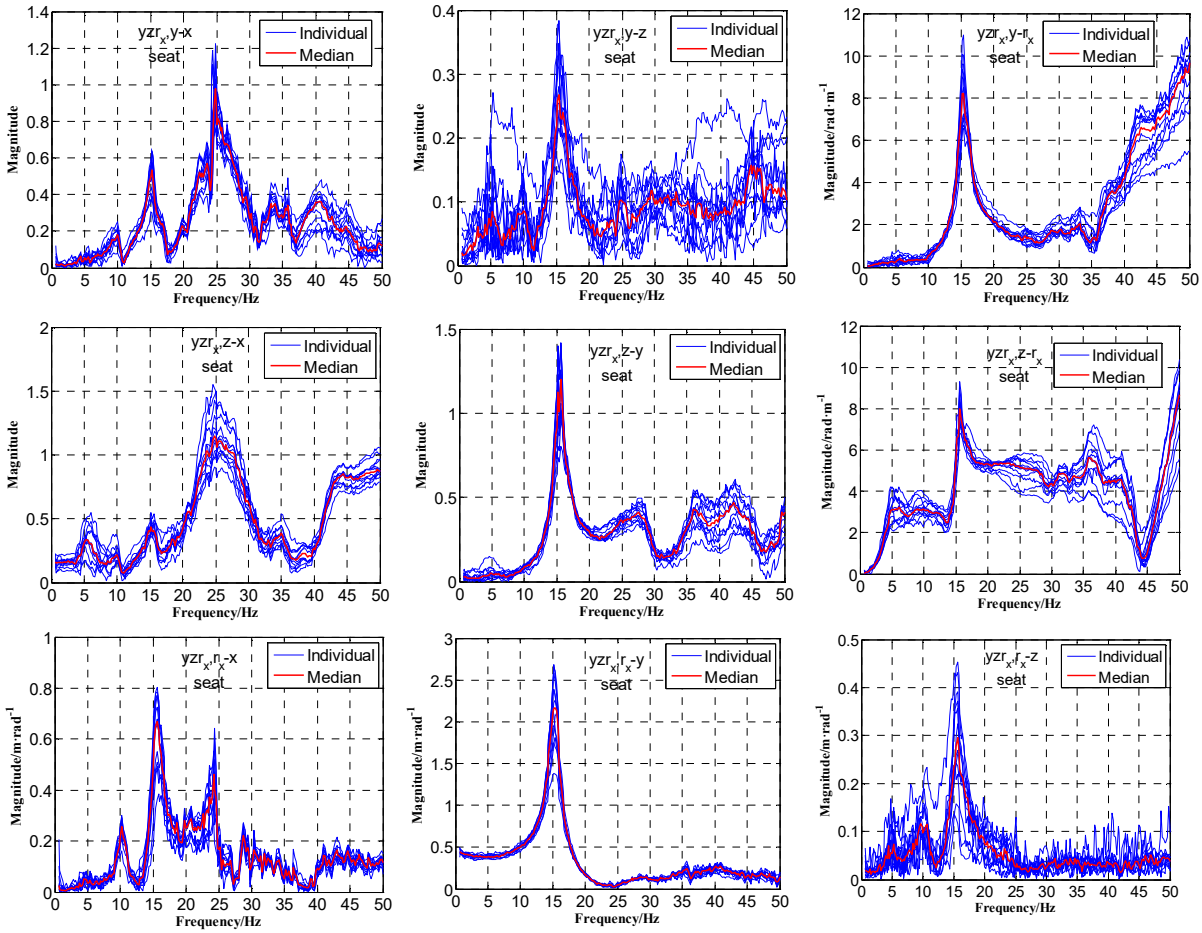

Fig. 8-9 The cross-axis transmissibilities on the seat pan under the excitation of 0.5 ms^{-2} r.m.s. lateral, 0.5 ms^{-2} r.m.s. vertical and 0.5 rad/s^2 r.m.s. roll vibration. Blue line: individual transmissibilities for 12 subjects; Red line: median transmissibility.

8.3.3.2 On the backrest

The cross-axis transmissibilities on the backrest measured using single-axis and multi-axis vibrations also showed similar trends. One example of these transmissibilities under tri-axis vibration was illustrated in Fig. 8-10. Almost all the cross-axis transmissibilities for 12 subjects on the backrest showed a peak around 15 Hz. There also exhibited a resonance around 10 Hz in the transmissibilities to the acceleration in x direction on the backrest (y-x, z-x and r_x-x). For the z-x transmissibility, most subjects exhibited a peak around 5 Hz, which was also possibly associated with the same human mode as the one generating the peaks around 5 Hz in the vertical seat transmissibilities on the seat pan and backrest. Y-x, z-x, r_x-x and z-r_x transmissibilities for 12 subjects showed relatively greater inter-subject variability than the others.

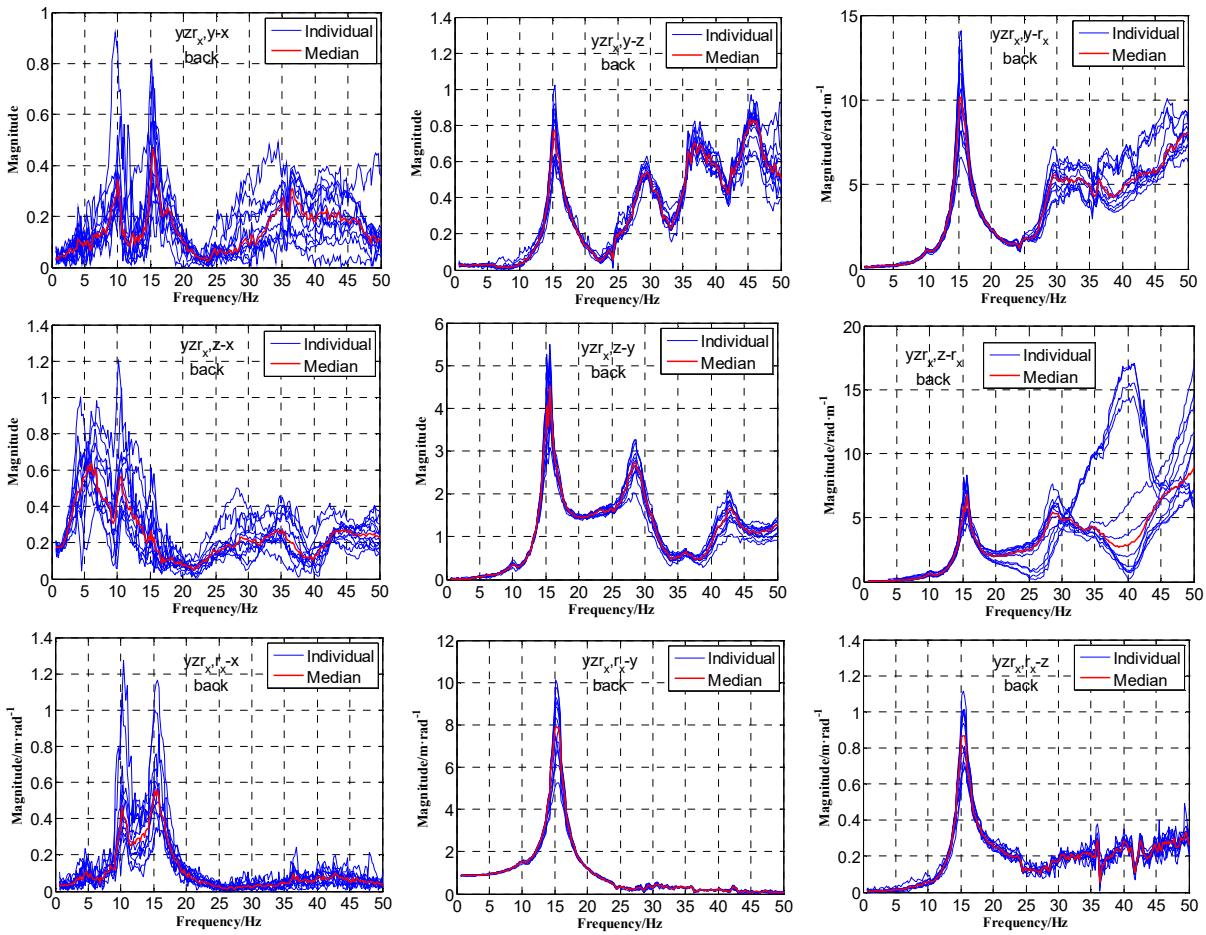

Fig. 8-10 The cross-axis transmissibilities on the backrest under the excitation of 0.5 ms^{-2} r.m.s. lateral, 0.5 ms^{-2} r.m.s. vertical and 0.5 rad/s^2 r.m.s. roll vibration. Blue line: individual transmissibilities for 12 subjects; Red line: median transmissibility.

8.3.4 Coherence analysis of multiple inputs

As introduced in Section 3.2.2, the partial coherence function $\gamma^2_{iy\cdot(m!/i)}$ denotes the percentage of the spectrum of output $y(t)$ due to the conditioned input $x_{i\cdot(m!/i)}$, and γ_{cy} defines the percentage of the spectrum of output due to the coherent parts between inputs. The role of the input accelerations on the seat base playing in the output accelerations on the seat pan and backrest can be studied by coherence analysis.

The inputs were always organized in the order of lateral acceleration on the seat base, vertical acceleration on the seat base and roll acceleration on the seat base, and the output was one of the accelerations on the seat pan or backrest. Generally, the contribution from one input would increase as the increase of the vibration magnitude; the coherence between the three inputs was inevitable but small, and its contribution to the output was small.

8.3.4.1 Acceleration in y direction on the seat pan and backrest

When the output was respectively the lateral acceleration on the seat pan and backrest, the multiple coherences were always close to unity (Fig. 8-11 and Fig. 8-12). For the lateral acceleration on the seat pan, the contribution from the lateral input was the most important, and from the roll input was mainly in 0.5-20 Hz, from the vertical input was the least. However, the contribution of vertical acceleration could not be ignored when the vertical input got maximum (z=1). On the other hand, for the lateral acceleration on the backrest, the contributions from the lateral and roll inputs dominated in the low-frequency range (0.5-15 Hz). Above 15 Hz, the vertical input started to play an important part while the contribution of lateral and roll inputs began to reduce.

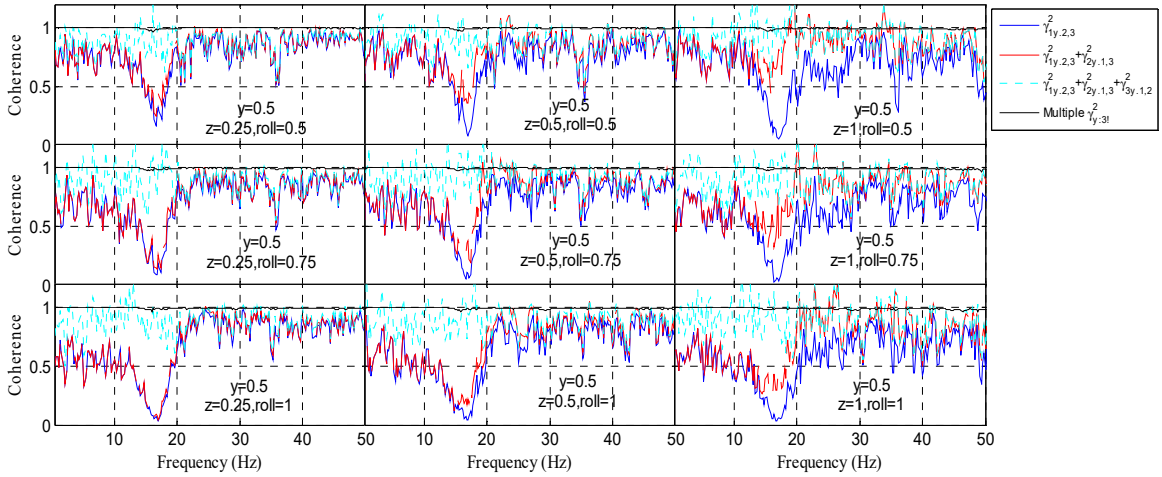

Fig. 8-11 Median coherence in the transmission to the lateral acceleration on the seat pan a_{sy} (output *y*) with y-axis magnitude of 0.5 m/s^2 r.m.s. and varying z-axis and roll excitation magnitudes (The subscripts 1, 2 and 3 correspond to a_{fy}, a_{fz} and a_{rf}, respectively).

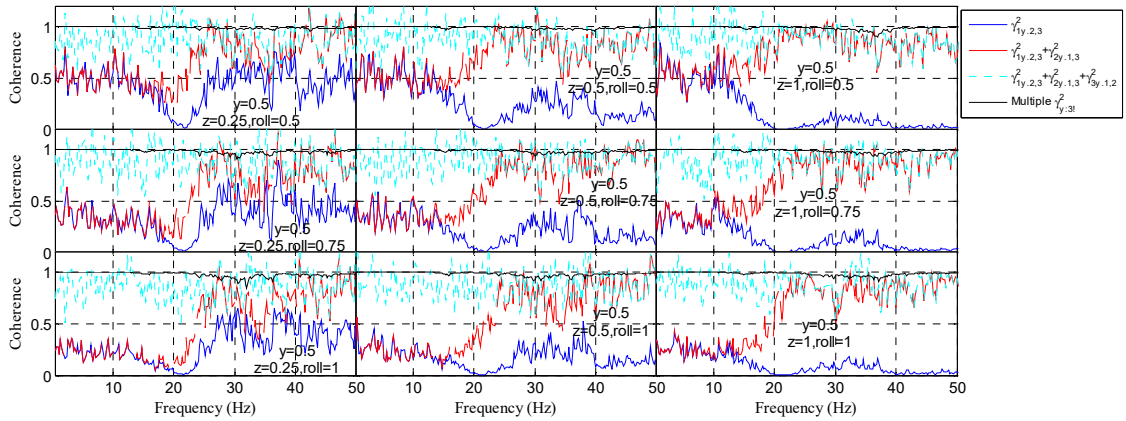

Fig. 8-12 Median coherence in the transmission to the lateral acceleration on the backrest a_{by} (output *y*) with y-axis magnitude of 0.5 m/s^2 r.m.s. and varying z-axis and roll excitation magnitudes (The subscripts 1, 2 and 3 correspond to a_{fy}, a_{fz} and a_{rf}, respectively).

8.3.4.2 Acceleration in z direction on the seat pan and backrest

When the output was respectively the vertical acceleration on the seat pan and backrest, the multiple coherences still trended towards unity (Fig. 8-13 and Fig. 8-14). Whether on the seat pan or the backrest, the vertical input played a dominant role, while the function of roll input was the most obvious around 15 Hz, in agreement with where the peaks of r_x-z transmissibilities located. In addition, the contribution from the lateral input was the most around 15 and 35 Hz for the seat pan, around 15, 30, 38 and 45 Hz for the backrest. These frequencies were consistent with where the peaks of y-z transmissibilities located.

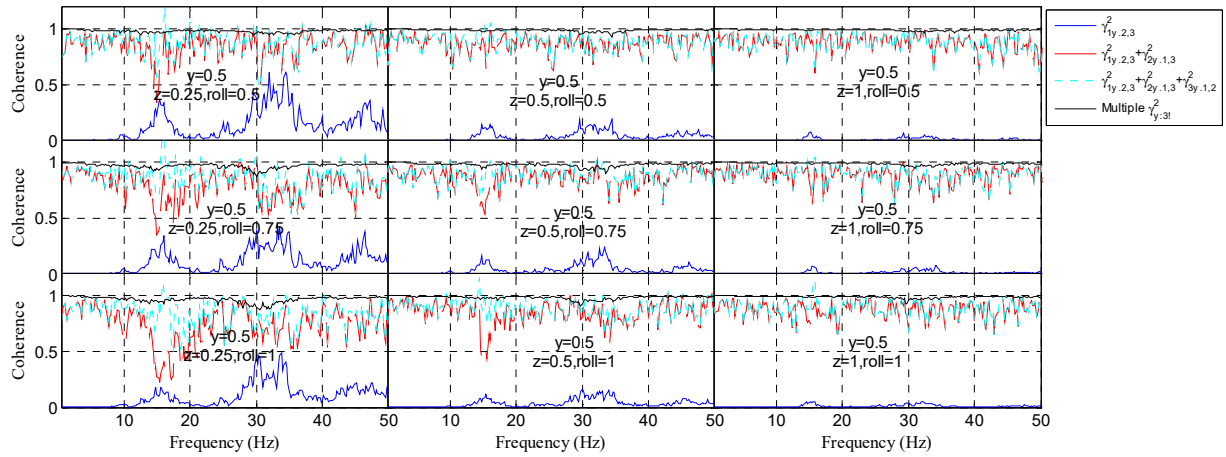

Fig. 8-13 Median coherence in the transmission to the vertical acceleration on the seat pan a_{sz} (output *y*) with y-axis magnitude of 0.5 m/s^2 r.m.s. and varying z-axis and roll excitation magnitudes (The subscripts 1, 2 and 3 correspond to a_{fy}, a_{fz} and a_{rf}, respectively).

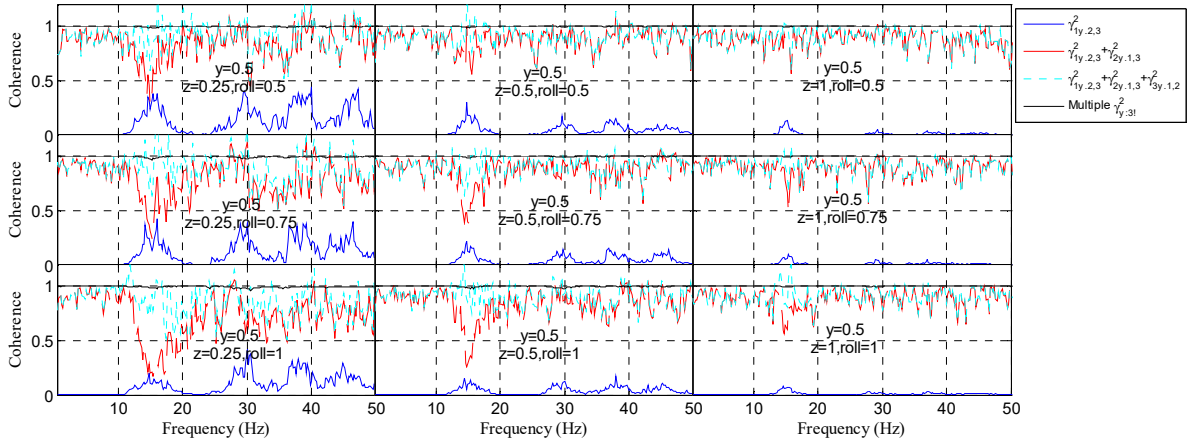

Fig. 8-14 Median coherence in the transmission to the vertical acceleration on the backrest a_{bz} (output *y*) with y-axis magnitude of 0.5 m/s^2 r.m.s. and varying z-axis and roll excitation magnitudes (The subscripts 1, 2 and 3 correspond to a_{fy}, a_{fz} and a_{rf}, respectively).

8.3.4.3 Acceleration in r_x direction on the seat pan and backrest

When the output was respectively the roll acceleration on the seat pan and backrest, the multiple coherences still verged on unity (Fig. 8-15 and Fig. 8-16). Whether on the seat pan or backrest, the contribution from roll input was mainly in the low-frequency range (0.5-20 Hz). The role of lateral input was negligible in 0.5-10 Hz and started to become significant as the increase of frequency. The contribution of vertical input to roll vibration on the seat pan was high in the whole frequency range except around 15 and 45 Hz (Fig. 8-15), while that on the backrest was significant above 15 Hz, especially when the vertical input was greater than (or equal to) 0.5 m/s^2 r.m.s (Fig. 8-16).

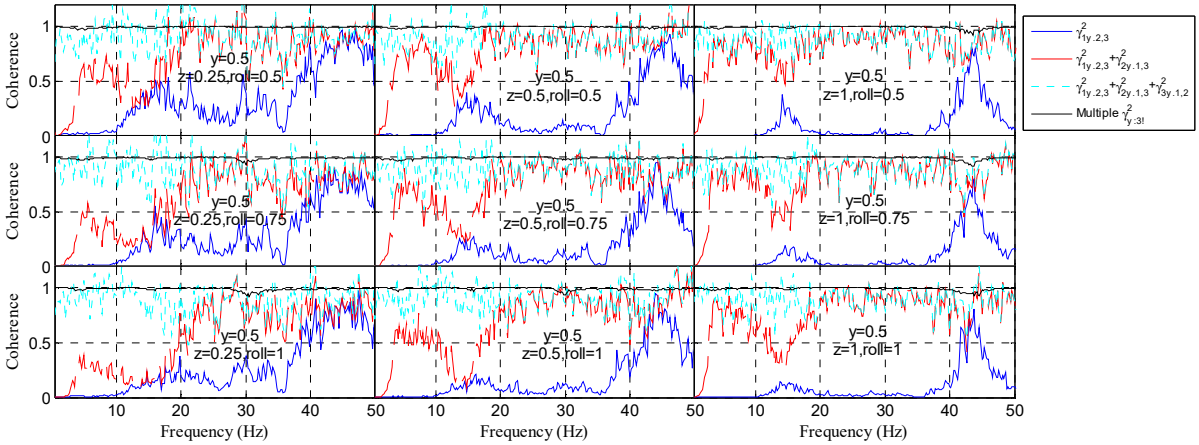

Fig. 8-15 Median coherence in the transmission to the roll acceleration on the seat pan a_{rs} (output *y*) with y-axis magnitude of 0.5 m/s^2 r.m.s. and varying z-axis and roll excitation magnitudes (The subscripts 1, 2 and 3 correspond to a_{fy}, a_{fz} and a_{rf}, respectively).

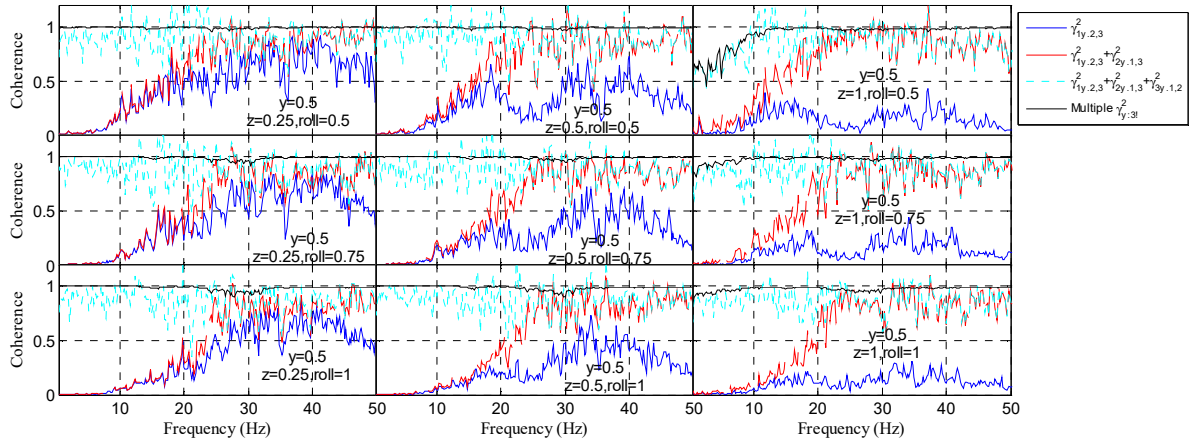

Fig. 8-16 Median coherence in the transmission to the roll acceleration on the backrest a_{rb} (output *y*) with y-axis magnitude of 0.5 m/s^2 r.m.s. and varying z-axis and roll excitation magnitudes (The subscripts 1, 2 and 3 correspond to a_{fy}, a_{fz} and a_{rf}, respectively).

It can be seen the vibration transmission of a train seat with a seated subject was complex. The vibration on the seat pan or backrest can arise from not only the vibration in the same direction on the seat base but also those in other directions, and the cross-axis inputs can frequently dominate over the inline input in the responses on the seat pan or backrest.

8.3.5 Comparison of seat transmissibility with one and two subjects

The seat transmissibilities with one and two subjects were compared to validate the difference found in the on-site measurement in Chapter 5. Two pairs of subjects participated in the experiment, the first pair was a test subject of 178 cm in height and 87 kg in weight on the left with a neighbouring one of 170 cm in height and 81 kg in weight, while the second pair was a test subject of 171 cm in height and 83.5 kg in weight on the left with a neighbouring one of 183 cm in height and 85 kg in weight. Generally speaking, the influence of the neighbouring subject on the seat transmissibility cannot be ignored (Fig. 8-17). The transmissibilities in y direction and r_x direction on both the seat pan and backrest with two subjects were attenuated greatly by the neighbouring subject at the peaks, this was probably because the enhanced damping introduced from the neighbouring subject suppressed the seat mode around 15 Hz. Furthermore, the resonance frequencies around 15 Hz with two subjects showed a little increase compared to those with one subject, probably because the increased modal stiffness by the neighbouring subject dominated slightly over the increased modal mass (Lo *et al.*, 2013). On the other hand, the difference between the primary resonances in the vertical transmissibilities on the seat pan was not so significant, because the resonance around 5 Hz arose from a human mode of the subject on the left, the effect of the neighbouring subject on this mode was negligible. However, the moduli of the vertical

transmissibilities on the seat pan and backrest were more or less changed by the neighbouring subject. The discrepancy between the seat transmissibilities with one and two subjects suggested giving a clear indication of the number of seated subjects when studying the seat transmissibility.

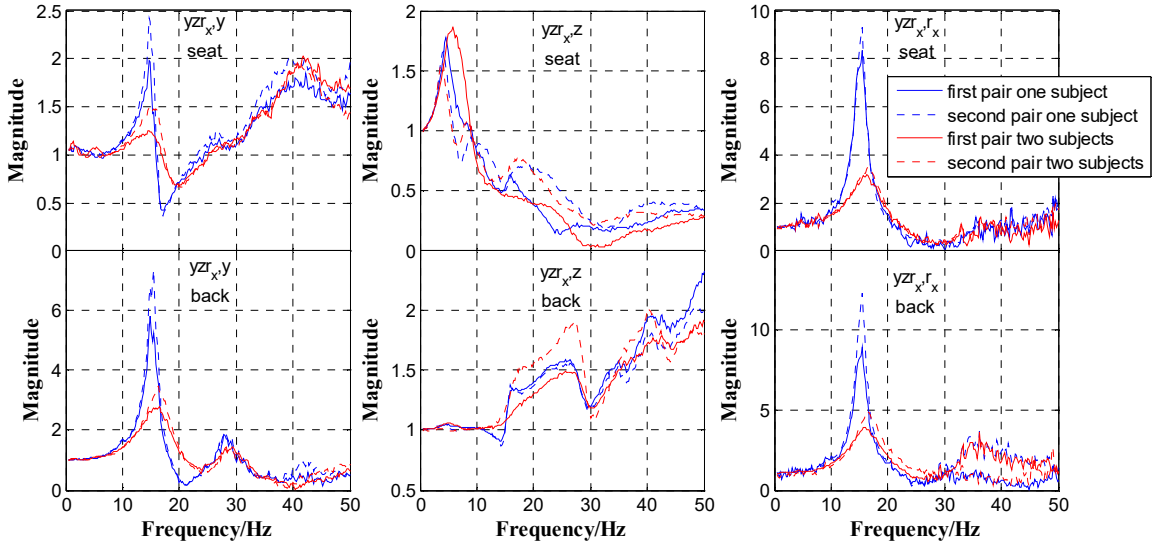

Fig. 8-17 The comparison between seat transmissibilities with one and two subjects for two pairs of subjects under the excitation of 0.5 m/s^2 r.m.s. lateral, 1.0 m/s^2 r.m.s. vertical, 0.75 rad/s^2 r.m.s. roll excitation.

8.4 Discussion

8.4.1 Comparison with existing research

The lateral and vertical transmissibilities on the seat pan and backrest under single-axis excitation have been widely reported, the results of this study were to be validated against the existing research.

For the vertical transmissibility on the seat pan, Corbridge *et al.* (1989) compared the vertical transmissibility on the seat pan of a train seat under vertical excitation of two magnitudes (0.3 and 0.6 m/s^2 r.m.s.), and found the resonance frequency reduced from 3.85 to 3.34 Hz and the modulus at resonance also decreased from 3.08 to 2.86 with the increase of excitation magnitude. Toward and Griffin (2011) reported a reduced frequency of 0.6 Hz (from 4.7 to 4.1 Hz) and decreasing modulus at resonance for the vertical transmissibility of a car seat with a reclined backrest (15°) and reclined seat cushion (12°) as the vibration magnitude increased from 0.5 to 1.5 m/s^2 r.m.s.. Tufano and Griffin (2013) found the same phenomenon by measuring the vertical transmissibility of a rigid seat with foam cushion as the increase of vibration magnitude. The finding in this research

showed consistency with the previous studies (the first subfigure in Fig. 8-5 and Table 8-4 when y=0 and r_x=0).

For the vertical transmissibility on the backrest under single-axis vertical excitation, Zhang *et al.* (2015b) reported a primary resonance frequency similar to that on the seat pan (at about 4 Hz), but with a modulus at resonance much less than that on the seat pan. That most subjects showed a resonance in the vertical transmissibility on the backrest at about 5 Hz with a much smaller modulus than that on the seat pan in this study was consistent with the previous study.

For the lateral transmissibility on both the seat pan and backrest under single-axis lateral excitation, there exhibited a principal resonance at about 17 Hz for a car seat and 25 Hz for a train seat respectively in Ittianuwat *et al.* (2014) and Gong and Griffin (2018), and these resonances were very likely to be related to a lateral seat mode. Therefore, the resonances in the lateral transmissibility around 15 Hz in this study may also arise from a lateral seat mode. The difference between the resonance frequencies can be explained by the different structures of the seat resulting in different modal frequencies.

However, there have been few studies about the inline seat transmissibility in roll direction. The only study about seat transmissibility under multi-axis vibration was reported by Gong and Griffin (2018), where the transmissibilities of a train seat under single-axis vibrations in three translational directions were compared with those under tri-axis vibrations in these directions. It was concluded that there were small differences in seat transmissibilities in three translational directions obtained using single-axis and tri-axis vibrations. The seat transmissibilities under single-axis vibrations and multi-axis ones were very close in this study, which thereby validated the results obtained under multi-axis excitations in this study.

8.4.2 MISO and SISO system

MISO technique was adopted to calculate the seat transmissibility under multiple inputs as shown in Table 8-1. Since the seat transmissibility was traditionally estimated by the SISO technique, the advantage of applying MISO system over SISO system should be discussed. When estimating the seat transmissibility under multiple inputs, biased estimation of the transmissibility can result from the inevitable coherence among the multiple inputs as discussed above. For example, when estimating T_{sy-z} under combined lateral, vertical and roll excitations, if a_{fy}, a_{fz} and a_{rf} are not totally incoherent, a_{fy} can go through three paths (or transmissibilities) to reach a_{sz}, the three

paths are T_{sy-z}, T_{sz} and T_{sr_x-z}, respectively (Fig. 8-18). If estimating T_{sy-z} directly by SISO system, the estimated transmissibility (T_{sy-z}') is

$$T_{sy-z}' = T_{sy-z} + T_{a_{fz}/a_{fy}} T_{sz} + T_{a_{rf}/a_{fy}} T_{sr_x-z} \tag{8-1}$$

where $T_{a_{fz}/a_{fy}}$ and $T_{a_{rf}/a_{fy}}$ are respectively the frequency response functions from a_{fy} to a_{fz} and from a_{fy} to a_{rf}.

From Eq. (8-1), it's obvious the estimation of T_{sy-z} will be influenced by T_{sz} and T_{sr_x-z}, especially when their moduli are large. For the same reason, the estimation of T_{sz} by SISO system will be affected by T_{sy-z} and T_{sr_x-z} (Fig. 8-19).

Therefore, when estimating the transmissibility under multiple inputs by SISO system, the mutual coherence between the inputs must be taken into consideration. If one of the inline or cross-axis transmissibilities has large modulus, its effect on the estimation of others could not be ignored. The comparison between SISO and MISO systems when estimating T_{sy-z} and T_{sz} was shown in Fig. 8-20. T_{sz} estimated by SISO and MISO systems was very close because of the relatively small moduli of T_{sy-z} and T_{sr_x-z}. However, the estimations of T_{sy-z} using SISO and MISO systems differed a lot because of the large modulus of T_{sz}. Therefore, for more accurate estimation of transmissibility with multiple inputs, MISO system is preferred since the mutual coherence among different inputs is practically inevitable.

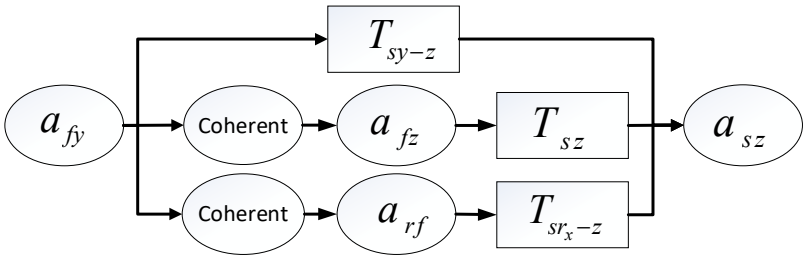

Fig. 8-18 Biased estimation of T_{sy-z} under combined lateral, vertical and roll vibrations using SISO system.

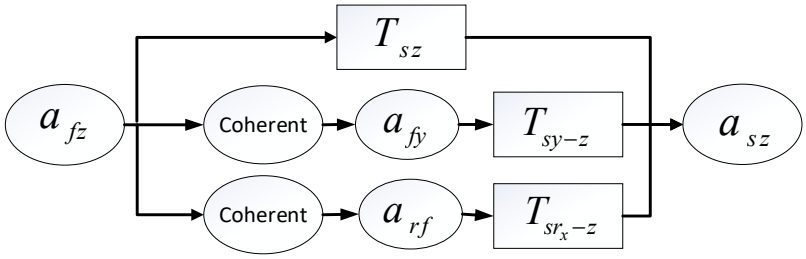

Fig. 8-19 Biased estimation of T_{sz} under combined lateral, vertical and roll vibrations using SISO system.

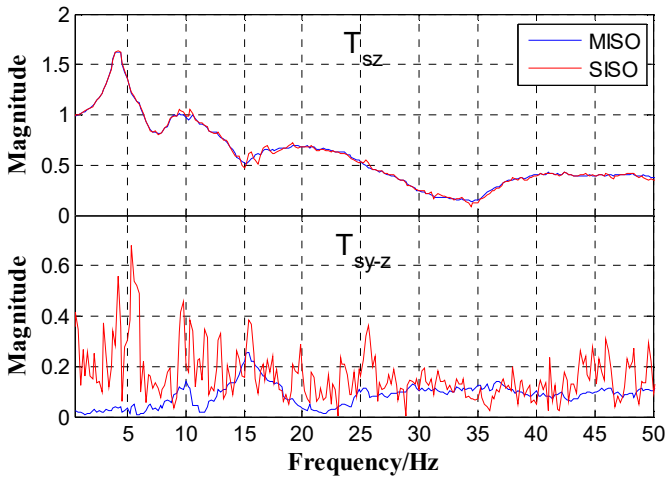

Fig. 8-20 The comparison of SISO and MISO systems when estimating the seat transmissibility with a subject of 171 cm in height and 83.5 kg in weight under 0.5 m/s^2 r.m.s. y-axis, 0.5 m/s^2 r.m.s. z-axis and 0.5 rad/s^2 r.m.s. roll excitation.

8.4.3 Multi-axis excitation

Research on the seat transmissibility under exposure to roll vibration or under multi-axis vibrations has been rarely seen. A study of this topic was conducted in this chapter and results showed that the seat transmissibility under multi-axis excitation was generally analogous to that under single-axis one. During this study, the nonlinearity of the train seat with one subject was observed: the principal resonance frequencies of the transmissibilities tended to reduce as the increase of the overall excitation magnitude, especially under low overall excitation magnitude. In addition, the modulus at resonance sometimes showed a decreasing tendency as the increase of excitation magnitude.

It is assumed that the resonance frequency of the seat transmissibility (dependent variable) has a linear correlation with the weighted root-sum-square (r.s.s.) value of excitation magnitudes (independent variable). The weighted r.s.s. value of the excitation magnitudes can also be expressed by Eq. (6-3). By conducting linear regression analysis between the resonance frequencies

and weighted r.s.s. values as introduced in Section 3.5 by means of 'regress' function in Matlab for every subject (significance level is 0.05), and selecting the mean R^2 value (coefficient of determination) of the 12 subjects as the cost function, the weighting factors that maximize the cost function can be determined by the optimization algorithm introduced in Section 3.3.

For the seat transmissibility in y direction on the seat pan and backrest, the decrease of resonance frequency with y-axis magnitude was the most significant, followed by roll magnitude, finally z-axis magnitude, so w_y and w_{r_x} are expected to be greater than w_z. By maximizing the mean R^2 value, for the transmissibility in y direction on the seat pan and backrest, the weighting factors, the mean R^2 value for 12 subjects, the mean p-value, the mean correlation coefficient for 12 subjects between the resonance frequency and weighted r.s.s. value were obtained and listed in Table 8-7.

For the transmissibility in z direction on the seat pan, the decrease of resonance frequency with the vibration magnitude in z axis was more significant than that in y and roll axes, so w_z is expected to be greater than w_y and w_{r_x}. In the same way, the results were obtained and listed in Table 8-7.

For the transmissibility in roll direction on the seat pan and backrest, the resonance frequency varying with increasing weighted r.s.s. value of excitation magnitude was not very significant as a whole. Therefore, absolute values of the mean correlation coefficients were smaller than the others, and the p-value became close to the significance level (0.05). The obtained results were also listed in Table 8-7.

The nonlinearity of the train seat with one subject can arise from both the nonlinearity of the human body and that of the seat. At some resonances, the nonlinearity of the human body may dominate over that of the seat, and vice versa. It is presumed that the primary resonance in the vertical transmissibility on the seat pan arises from the human body, which is supported by that the nonlinearity in the vertical seat transmissibility on the seat pan was more dependent on the nonlinearity of the human body than that of the seat cushion (Tufano and Griffin, 2013) and by the analysis in Section 8.3.1. On the other hand, the principal resonances of the seat transmissibilities around 15 Hz in the lateral and roll directions may arise from a seat mode since the human body seems not to add any new resonance above 10 Hz to them (Section 8.3.1). Besides, the nonlinearity of the conventional seats (except suspension seats) may be less than that of the human body (Griffin, 1990), so the absolute value of the mean correlation coefficient (0.994) for the vertical transmissibility on the seat pan was much larger than the others, signifying a greater nonlinearity as the increase of vibration magnitude because of the dominant nonlinearity of the human body. On the other hand, the nonlinearity of the principal resonances in the lateral and roll directions

mainly comes from that of the seat (cushion), so the corresponding absolute values of the mean correlation coefficient were much smaller. Although the principal resonances of the seat transmissibilities around 15 Hz in the lateral and roll directions may arise from the same seat mode, the great discrepancy of the weighting factors and the mean correlation coefficients between the seat transmissibilities on the seat pan and backrest in lateral and roll directions may indicate the influence of the human body on the seat mode in different directions is not the same.

These relationships between the resonance frequencies of the seat transmissibility and the r.s.s. values of excitation magnitudes were summarized in Table 8-7, which could be used for the prediction of the resonance frequency. The dynamic response arising from one direction with increasing vibration magnitudes in orthogonal directions was equivalent to that with a weighted increasing vibration magnitude in the arising direction. Although the p-value is much less than 0.05 (significance level), the R^2 value is not close to unity. This means the negative correlation between the resonance frequencies and the r.s.s. values of excitation magnitudes is doubtless, but the correlation between them is likely to be nonlinear instead of being linear.

The reducing resonance frequency as the increasing weighted r.s.s. value of the vibration magnitude can be put down to the nonlinearity of both the human body and the seat. However, the nonlinearity appears more significant at low r.s.s. value or significant only at low r.s.s. value. One reason may be that the nonlinearity of biodynamics of the human body is more significant at low r.s.s. value or significant only at low r.s.s. value, as illustrated in Chapter 6. Another possible reason is the equivalent stiffness of the seat cushion material (polyurethane foam) has relatively large rate of change at small vibration magnitude, and becomes more constant as the increasing vibration magnitude of the cushion material, which is supported by the experimental results of Zhang and Dupuis (2010) under large static compression level.

Table 8-7 A summary of the relationship between the principal resonances of the seat transmissibility (dependent variable) and the r.s.s. excitation magnitudes (independent variable)

Seat transmissibility (resonance)	Weighting factors			Mean correlation coefficient	Mean constant	Mean R^2 value	Mean p-value
	w_y	w_z	w_{r_x}				
T_{sy} (around 15 Hz)	1	0.62	1	-0.39	15.37	0.340	5.7×10^{-4}
T_{by} (around 15 Hz)	1	0.58	0.85	-0.36	15.61	0.310	6.9×10^{-4}
T_{sz} (around 5 Hz)	0.91	1	0.65	-0.994	5.36	0.495	2.3×10^{-4}
T_{sr_x} (around 15 Hz)	0.94	1	1	-0.1836	15.49	0.140	0.0273
T_{br_x} (around 15 Hz)	0.97	1.01	1	-0.1879	15.53	0.144	0.0298

8.4.4 Analysis of modal shape

It was observed the principal resonances around 15 Hz in the lateral and roll seat transmissibilities may arise from a seat mode. From the seat transmissibilities with no occupant (Fig. 8-2), it can be seen the seat had a mode around 15 Hz with large lateral and roll motions but small vertical motion on both the seat and backrest, which was similar to the lateral modal shape of the seat in Ittianuwat *et al.* (2014).

The comparison of seat transmissibility between the bare seat and seat with one subject showed that the coupling with the subject did not have much effect on the modal frequency but the modal damping of the seat mode (Fig. 8-2), which is consistent with Lo *et al.* (2013). This suggested predicting the seat transmissibility with one subject from the transmissibility of the bare seat in the lateral and roll directions on the seat pan and backrest, which can alleviate the trouble of exposing the occupants to vibrations and the need for complex modelling and analysis of the human body.

With one subject, the seat mode around 15 Hz was attenuated by the damping brought from the subject, however, the peak was still obvious in the inline and almost all the cross-axis seat transmissibilities. Thus, the modal shape of the seat with a subject should be similar to that without subject. The lateral motion of the backrest was almost three times that of the seat pan, which can be judged by the relative moduli of the y-direction (or z-y, r_x-y) seat transmissibility on the seat pan and backrest at this peak. In addition, the roll motion of the backrest was approximate to that of the seat pan, which can be deducted from the relative moduli of the r_x-direction (or z-r_x, y-r_x) seat transmissibility on the seat pan and backrest at this peak. With two subjects, the damping of this seat mode was further increased (Fig. 8-17), but the modal shape of the seat was expected to keep almost the same.

There was a principal resonance around 5 Hz in the vertical transmissibility on the seat pan with a seated subject, and some people also exhibited a resonance around 5 Hz in the vertical transmissibility on the backrest with a smaller modulus close to 1.0. This is because much more force was transmitted between the human body and the seat pan than between the human body and the backrest. This mode largely arose from the vertical whole-body mode of the human body, similar to those with a modal frequency about 5 Hz reported by Kitazaki and Griffin (1997), Matsumoto and Griffin (2001), Zheng *et al.* (2011) and Liu *et al.* (2015). This also explained the reason why conventional seats with totally different structures usually have a peak around 5 Hz in the vertical transmissibility on the seat pan (Corbridge *et al.*, 1989; Toward and Griffin, 2011; Gong and Griffin, 2018). Therefore, for the modal shape of the seat with a subject, the motion was expected to be the whole-body motion of the human body resembling the vertical whole-body

human mode together with great vertical motion of the seat pan. With two subjects, because the neighbouring subject had little effect on this mode (Fig. 8-17), the modal shape was expected to keep almost the same along with a little vibration of the neighbouring subject.

These deductions of the modal shapes will be further verified by the human-seat system modelling in the next chapter.

8.5 Conclusions

An experimental study of the vibration transmission of a train seat with no subject, with one and two subjects was carried out in the laboratory under single-axis, bi-axis and tri-axis vibrations in lateral, vertical and roll directions, and some conclusions can be drawn as follows.

For the seat transmissibility on the seat pan and backrest in the y, z and roll directions, the transmissibilities measured with multi-axis vibration were generally analogous to those obtained with single-axis vibration. There was some evidence of a decrease in the principal resonance frequency as the increase of vibration magnitude evaluated by the r.s.s. value, which appeared more significant at low r.s.s. magnitude or significant only at low r.s.s. magnitude. What is more, this decrease was most significant for the vertical transmissibilities on the seat pan, followed by the lateral ones on the seat pan and backrest, and finally the ones in r_x direction on the seat pan and backrest. For some cases, the modulus at resonance also reduced significantly with the increasing r.s.s. vibration magnitude.

Compared with the transmissibility of the bare seat, the addition of human body would add a new resonance around 5 Hz to the vertical transmissibility on the seat pan, and greatly attenuate the resonance around 15 Hz arising from the seat mode due to the introduced damping of the human body. In addition, the addition of the neighbouring subject would further increase the damping of the seat mode and result in slightly higher resonance frequency.

The vibration transmission of a train seat was complex. The vibration on the seat pan or backrest can arise from not only the vibration on the seat base in the same direction but also those in other directions, and the cross-axis inputs can frequently dominate over the inline input in the responses on the seat pan or backrest.

In terms of the calculation of seat transmissibility, MISO system is more suitable for the estimation of transmissibility under multiple inputs than the traditional SISO system.

This experimental study laid the basis for the modelling of human-seat system and gave a useful guide in seat design so as to promote the ride comfort.

Chapter 9 Modelling of a train seat with subject exposed to combined lateral, vertical and roll vibration

9.1 Introduction

Lateral, vertical and roll vibrations are usually three main vibrations on the rail vehicles concerning ride comfort (ISO, 2001). The seat on trains provides the passenger with a place to sit, whose dynamic characteristics are directly associated with the ride comfort of passengers. The human body is also a dynamic system whose biodynamics will influence the dynamics of the seat, so studying the dynamic characteristics of the seat and its interaction with the human body is of great importance to ride comfort. The transmissibility from the seat base to the human-seat interfaces is one of the most important characteristics of the seat, which is frequently adopted for characterizing the seating dynamics. Since the human body is a complex dynamic system, the transmissibility of a seat with a seated person shows a great discrepancy from the counterpart with a rigid mass of the same weight (Griffin, 1990). The experiment is the main approach to studying the seat transmissibility, however, experiment with subjects is time-consuming and expensive, sometimes also limited by the vibration magnitude the subjects can endure. Sometimes, dummies can be used to take the place of subjects, but manufacturing such a dummy having the same biodynamic characteristics as the human body is not an easy task. The experiment also requires the use of single-axis or multi-axis vibrator that is not always available. As an alternative, modelling approach has been widely used to assist with the experiment to understand the vibration transmission of the seat to occupants.

Various kinds of human-seat models have been developed to study the vibration transmission of human-seat systems under exposure to different vibrations (Section 2.3.2). The models can be generally categorized into lumped parameter models, multi-body dynamic models and finite element models. Lumped parameter models are relatively easy to develop and calculate, however, these models usually cannot have good representation of the structure. Typical models were reported by Qiu and Griffin (2011), Qiu (2012), Wei and Griffin (1998b), etc. FE models can model the detailed structures of the human body and the seat, and can predict not only the vibration, but also the dynamic contact pressure on the human-seat interface, etc. Nevertheless, FE models are usually complex, computationally expensive, and take a long time to get calibrated. It is not easy to accommodate to the inter-subject variability such as body dimensions by one model, either. Typical models were developed by Siefert *et al.* (2008), Grujicic *et al.* (2009), etc. The multi-body dynamic

model is a compromise between the lumped parameter model and finite element model, sharing part of their advantages and avoiding part of their drawbacks. For example, the multi-body model is usually anatomically representative, even if it is not as representative as the finite element model, it has the advantage of being less computationally expensive than the finite element model. Typical models can be found in Cho and Yoon (2001), Kim *et al.* (2003a), Ippili *et al.* (2008) and Zheng *et al.* (2011), etc.

However, so far most of the models have been restricted to single-axis translational (fore-and-aft or vertical) vibration. They are usually developed in the symmetrical plane of the seat, so the out-of-plane vibration cannot be predicted by these models. What is more, most of the existing seat models were usually developed for single-unit car seats (e.g., Verver *et al.* (2005)), which have quite a different structure from a double-unit train seat. Therefore, taking into account the characteristics of ride vibration of a train, a kind of human-seat multi-body dynamic models that has the ability of truly reflecting the structure of the double-unit train seat and vibration characteristics under exposure to combined in-plane (vertical) and out-of-plane (lateral and roll) vibrations is still waiting to be developed.

The objective of this chapter was to propose and develop a multi-body dynamic model of a double-unit train seat exposed to lateral, vertical and roll vibrations. With the use of the seated human model developed in Chapter 7, two coupled models of the double-unit seat with one and two subjects were developed. All the models were calibrated using experimental data. The modal analysis was conducted to find out the relationship between the resonances in the seat transmissibilities and the modal properties of the seat or human body and facilitate discussions in relation to the association among the modal properties of the human model, seat model and human-seat models, and the variation of the modal properties due to the coupling between the human body and the seat.

9.2 Development of the seat model

9.2.1 Model description

The train seat has two units: the left one and the right one. The train seat consists of seven parts, that is, the left and right backrests ($^{l}B_5$, $^{r}B_5$), the left and right seat pan frames ($^{l}B_9$, $^{r}B_9$), the left and right cushions ($^{l}B_6$, $^{r}B_6$) as well as the seat base (B_B) (Fig. 9-1). There are eight different coordinate systems defined in the model, one is the absolute coordinate system $\mathbf{S}=(\mathbf{n}_x,\mathbf{n}_y,\mathbf{n}_z)^{\mathrm{T}}$,

whose origin is at the centre of the intersection line of the upper surface of the left cushion and the front surface of the left backrest. $\mathbf{n}_x$ and $\mathbf{n}_y$ that are in the upper surface of the left seat pan are directed along the fore-and-aft and lateral directions, respectively, while $\mathbf{n}_z$ is normal to the surface. The other seven are relative coordinate systems ${}^j\mathbf{S}_i = ({}^j\mathbf{n}_{ix}, {}^j\mathbf{n}_{iy}, {}^j\mathbf{n}_{iz})^{\mathrm{T}}$ ($\begin{cases} i=5,6,9; j=l,r \\ i=B; no\ j \end{cases}$) (there is no superscript j for $i=B$) with their origins defined at the centre of gravity of each segment of the seat ${}^j\mathbf{O}_i$ ($\begin{cases} i=5,6,9; j=l,r \\ i=B; no\ j \end{cases}$). The left and right backrests can respectively have inclinations with angles of ${}^l\alpha$ and ${}^r\alpha$ relative to the vertical plane. The model has a total of 21 degrees-of-freedom: each segment has translational motions in $\mathbf{n}_y$ and $\mathbf{n}_z$ directions, ${}^jy_i$ and ${}^jz_i$ ($\begin{cases} i=5,6,9; j=l,r \\ i=B; no\ j \end{cases}$), and roll motions, ${}^j\theta_i$ ($\begin{cases} i=5,6,9; j=l,r \\ i=B; no\ j \end{cases}$), around the x-axis in their own relative coordinate systems (${}^j\mathbf{n}_{ix}$). Thus, aside from the relative translational movements and relative rotation of ${}^j\theta_i$ around ${}^j\mathbf{n}_{iy}$ to the absolute coordinate system for the coordinate systems ${}^j\mathbf{S}_i$ ($\begin{cases} i=6,9; j=l,r \\ i=B; no\ j \end{cases}$), for $i=5; j=l,r$, they have relative rotations around $\mathbf{n}_y$ to the absolute coordinate system with the same angles as the corresponding backrests as well. The excitation is expressed as lateral excitation (y_0) along $\mathbf{n}_y$, vertical excitation (z_0) along $\mathbf{n}_z$ and roll excitation (θ_0) around the intersection line between the symmetrical (z-x) plane of the left unit of the seat and the platform surface. The excitation point is denoted as $\mathbf{E}_s$ on the platform, corresponding to $\mathbf{E}$ at the seat base (B_B) at the equilibrium position.

Pairs of contact points between the seat pan cushion (${}^jB_6$) and the seat pan frame (${}^jB_9$) are expressed as ${}^j\mathbf{C}_6$ on the frame side and ${}^j\mathbf{C}_{6s}$ on the cushion side ($j=l,r$). The contact points between the left (right) side of the seat base (B_B) and the platform are expressed as ${}^l\mathbf{C}_7$ (${}^r\mathbf{C}_7$) on the seat base and ${}^l\mathbf{C}_{7s}$ (${}^r\mathbf{C}_{7s}$) on the platform. Each pair of points is coincident at the equilibrium position, but at different positions during vibration.

For the connection of the seat segments, the backrest (${}^jB_5$) and seat base (B_B) are connected with the seat pan frame (${}^jB_9$) at points ${}^j\mathbf{D}_4$ and $\mathbf{D}_5$, respectively ($j=l,r$). The left seat pan

frame (${}^{l}B_9$) and the right (${}^{r}B_9$) are connected at the point $\mathbf{D}_6$. The connections and contacts are realized by translational springs and dampers in y and z directions, and rotational springs and dampers around x direction as well.

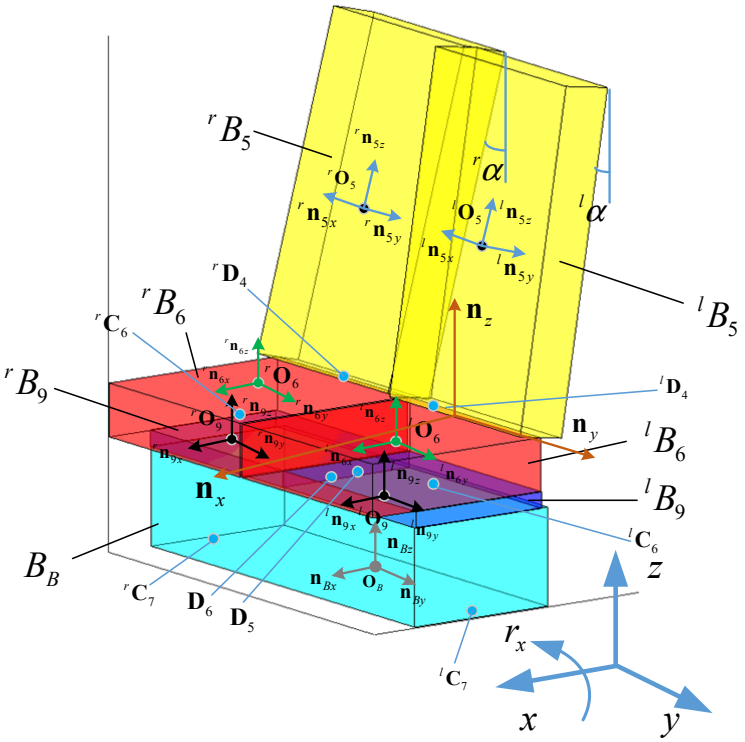

Fig. 9-1 Double-unit train seat model.

9.2.2 Coordinate transformation

Before developing the double-unit seat model, the coordinate transformations between the relative coordinate systems and the absolute one are calculated as follows.

$$ {}^{j}\mathbf{S}_i = \begin{cases} \mathbf{T}_{12}({}^{j}\theta_i)\,{}^{j}\hat{\mathbf{S}}_i = \mathbf{T}_{12}({}^{j}\theta_i)\mathbf{T}_{11}({}^{j}\alpha)\mathbf{S} & i=5;\ j=l,r \\ \mathbf{T}_{12}({}^{j}\theta_i)\mathbf{S} & i=6,9;\ j=l,r \text{ or } i=B;no\ j \end{cases} \tag{9-1} $$

where ${}^{j}\hat{\mathbf{S}}_i = \begin{bmatrix} {}^{j}\hat{\mathbf{n}}_{ix} & {}^{j}\hat{\mathbf{n}}_{iy} & {}^{j}\hat{\mathbf{n}}_{iz} \end{bmatrix}^{\mathrm{T}}$ is the intermediate coordinate system after rotating ${}^{j}\alpha$ around $\mathbf{n}_y$.

The translational displacements of the center of gravity of each segment (${}^{j}\mathbf{O}_i^{\,O}$, $\begin{cases} i=5,6,9;\ j=l,r \\ i=B;no\ j \end{cases}$) in the absolute coordinate system are expressed as

$$ {}^{j}\mathbf{O}_i^{\,O} = {}^{j}\mathbf{O}_{is}^{O} + {}^{j}\mathbf{O}_{id}^{O} = ({}^{j}x_{i0},\ {}^{j}y_{i0},\ {}^{j}z_{i0}) + (0,\ {}^{j}y_i,\ {}^{j}z_i) \tag{9-2} $$

where ${}^{j}\mathbf{O}_{is}^{O}=({}^{j}x_{i0},{}^{j}y_{i0},{}^{j}z_{i0})$ is the coordinate at the equilibrium position, and ${}^{j}\mathbf{O}_{id}^{O}=(0,{}^{j}y_{i},{}^{j}z_{i})$ is the displacement around the equilibrium position during vibration.

9.2.3 Calculation of relative motion

After determining the coordinate transformation, the relative displacements between different segments of the seat can be calculated as follows.

The relative displacement between the backrest (${}^{j}B_5$) and the corresponding seat pan frame (${}^{j}B_9$) at the point ${}^{j}\mathbf{D}_4$ ($j=l,r$) is

$$ {}^{j}\mathbf{l}_{59}^{\mathbf{D}_4}={}^{j}\mathbf{O}_{9}^{O}+{}^{j}\mathbf{D}_{4}^{B_9}\mathbf{T}_{12}({}^{j}\theta_9)-{}^{j}\mathbf{O}_{5}^{O}-{}^{j}\mathbf{D}_{4}^{B_5}\mathbf{T}_{12}({}^{j}\theta_5)\mathbf{T}_{11}({}^{j}\alpha) \tag{9-3}$$

The relative displacement between the seat pan cushion (${}^{j}B_6$) and the corresponding seat pan frame (${}^{j}B_9$) at the point ${}^{j}\mathbf{C}_6$ ($j=l,r$) is

$$ {}^{j}\mathbf{l}_{69}^{\mathbf{C}_6}={}^{j}\mathbf{O}_{9}^{O}+{}^{j}\mathbf{C}_{6}^{B_9}\mathbf{T}_{12}({}^{j}\theta_9)-{}^{j}\mathbf{O}_{6}^{O}-{}^{j}\mathbf{C}_{6s}^{B_6}\mathbf{T}_{12}({}^{j}\theta_6) \tag{9-4}$$

The relative displacement between the seat pan frame (${}^{j}B_9$) and the seat base (B_B) at the point $\mathbf{D}_5$ ($j=l,r$) is

$$ {}^{j}\mathbf{l}_{9B}^{\mathbf{D}_5}=\mathbf{O}_{B}^{O}+\mathbf{D}_{5}^{B_B}\mathbf{T}_{12}(\theta_B)-{}^{j}\mathbf{O}_{9}^{O}-{}^{j}\mathbf{D}_{5}^{B_9}\mathbf{T}_{12}({}^{j}\theta_9) \tag{9-5}$$

The relative displacement between the left seat pan frame (${}^{l}B_9$) and the right one (${}^{r}B_9$) at the point $\mathbf{D}_6$ is

$$ \mathbf{l}_{99}^{\mathbf{D}_6}={}^{r}\mathbf{O}_{9}^{O}+{}^{r}\mathbf{D}_{6}^{B_9}\mathbf{T}_{12}({}^{r}\theta_9)-{}^{l}\mathbf{O}_{9}^{O}-{}^{l}\mathbf{D}_{6}^{B_9}\mathbf{T}_{12}({}^{l}\theta_9) \tag{9-6}$$

The relative displacement between the seat base (B_B) and the platform at the point ${}^{j}\mathbf{C}_7$ ($j=l,r$) is

$$ {}^{j}\mathbf{l}_{B_B}^{\mathbf{C}_7}=\mathbf{O}_{B}^{O}+{}^{j}\mathbf{C}_{7}^{B_B}\mathbf{T}_{12}(\theta_B)-\mathbf{O}_{Bs}^{O}-\mathbf{E}^{B_B}-[0,y_0,z_0]-\overline{\mathbf{E}_s\,{}^{j}\mathbf{C}_{7s}}\mathbf{T}_{12}(\theta_0) \tag{9-7}$$

where $\overline{\mathbf{E}_s\,{}^{j}\mathbf{C}_{7s}}$ is a vector from $\mathbf{E}_s$ to ${}^{j}\mathbf{C}_{7s}$.

The corresponding relative velocities can be derived by the derivative of the relative displacements with respect to time. For example,

$$ {}^{j}\dot{\mathbf{l}}_{59}^{\mathbf{D}_4} = \frac{\mathrm{d}\,{}^{j}\mathbf{O}_9^{O}}{\mathrm{d}t} + {}^{j}\mathbf{D}_4^{B_9}\frac{\mathrm{d}\mathbf{T}_{12}({}^{j}\theta_9)}{\mathrm{d}t} - \frac{\mathrm{d}\,{}^{j}\mathbf{O}_5^{O}}{\mathrm{d}t} - {}^{j}\mathbf{D}_4^{B_5}\frac{\mathrm{d}\mathbf{T}_{12}({}^{j}\theta_5)}{\mathrm{d}t}\mathbf{T}_{11}({}^{j}\alpha) \tag{9-8} $$

9.2.4 Force calculation

For calculating the forces, the translational and rotational springs and dampers between different segments are defined in Table G-1 of Appendix G. The forces can be calculated as the summation of the spring force (multiplying the relative displacement by the stiffness) and damper force (multiplying the relative velocity by the damping).

Therefore, the force transmitted between the backrest (${}^{j}B_5$) and the corresponding seat pan frame (${}^{j}B_9$) at the point ${}^{j}\mathbf{D}_4$ ($j = l, r$) is

$$ {}^{j}\mathbf{f}_{59}^{\mathbf{D}_4} = {}^{j}\mathbf{l}_{59}^{\mathbf{D}_4}\mathrm{diag}(0, k_{sl1}, k_{sv1}) + {}^{j}\dot{\mathbf{l}}_{59}^{\mathbf{D}_4}\mathrm{diag}(0, c_{sl1}, c_{sv1}) = \begin{bmatrix} 0 & {}^{j}f_{59(y)}^{\mathbf{D}_4} & {}^{j}f_{59(z)}^{\mathbf{D}_4} \end{bmatrix}\mathbf{S} \tag{9-9} $$

Other forces ${}^{j}\mathbf{f}_{69}^{\mathbf{C}_6}$, ${}^{j}\mathbf{f}_{9B}^{\mathbf{D}_5}$, $\mathbf{f}_{99}^{\mathbf{D}_6}$ and ${}^{j}\mathbf{f}_{B_B}^{\mathbf{C}_7}$ calculated in this way are listed in Appendix G.

9.2.5 Equations of motion of the model

The equations of motion for the backrest (${}^{j}B_5$, $j = l, r$) are derived respectively as

$$ m_5\,{}^{j}\ddot{y}_5 = {}^{j}f_{59(y)}^{\mathbf{D}_4} \tag{9-10} $$

$$ m_5\,{}^{j}\ddot{z}_5 = {}^{j}f_{59(z)}^{\mathbf{D}_4} \tag{9-11} $$

$$ \begin{aligned} I_5\,{}^{j}\ddot{\theta}_5 = {}^{j}\mathbf{D}_4^{B_5} \times ({}^{j}\mathbf{f}_{59}^{\mathbf{D}_4}\mathbf{T}_{11}^{\mathrm{T}}({}^{j}\alpha))\begin{bmatrix} 1 & 0 & 0 \end{bmatrix}^{\mathrm{T}} + k_{sr1}({}^{j}\theta_9\cos{}^{j}\alpha - {}^{j}\theta_5) \\ + c_{sr1}({}^{j}\dot{\theta}_9\cos{}^{j}\alpha - {}^{j}\dot{\theta}_5) \end{aligned} \tag{9-12} $$

Similarly, the equations of motion for the seat pan frames (${}^{j}B_9$, $j = l, r$), the seat pan cushions (${}^{j}B_6$, $j = l, r$), and the seat base (B_B) are derived respectively as

$$ m_9\,{}^{j}\ddot{y}_9 = -{}^{j}f_{59(y)}^{\mathbf{D}_4} - {}^{j}f_{69(y)}^{\mathbf{C}_6} + c_e f_{99(y)}^{\mathbf{D}_6} + {}^{j}f_{9B(y)}^{\mathbf{D}_5} \tag{9-13} $$

$$ m_9\,{}^{j}\ddot{z}_9 = -{}^{j}f_{59(z)}^{\mathbf{D}_4} - {}^{j}f_{69(z)}^{\mathbf{C}_6} + c_e f_{99(z)}^{\mathbf{D}_6} + {}^{j}f_{9B(z)}^{\mathbf{D}_5} \tag{9-14} $$

$$I_9\,{}^j\ddot{\theta}_9 = {}^j\mathbf{D}_4^{B_9}\times(-{}^j\mathbf{f}_{59}^{\mathbf{D}_4})[1\quad 0\quad 0]^{\mathrm{T}} + {}^j\mathbf{C}_6^{B_9}\times(-{}^j\mathbf{f}_{69}^{\mathbf{C}_6})[1\quad 0\quad 0]^{\mathrm{T}} + {}^j\mathbf{D}_6^{B_9}\times(c_e\mathbf{f}_{99}^{\mathbf{D}_6})[1\quad 0\quad 0]^{\mathrm{T}}$$
$$+{}^j\mathbf{D}_5^{B_9}\times{}^j\mathbf{f}_{9B}^{\mathbf{D}_5}[1\quad 0\quad 0]^{\mathrm{T}} + k_{sr1}({}^j\theta_5\cos{}^j\alpha - {}^j\theta_9) + c_{sr1}({}^j\dot{\theta}_5\cos{}^j\alpha - {}^j\dot{\theta}_9) + k_{sr2}({}^j\theta_6 - {}^j\theta_9)$$
$$+c_{sr2}({}^j\dot{\theta}_6 - {}^j\dot{\theta}_9) + k_{sr3}(\theta_B - {}^j\theta_9) + c_{sr3}(\dot{\theta}_B - {}^j\dot{\theta}_9) + k_{sr4}c_e({}^r\theta_9 - {}^l\theta_9) + c_{sr4}c_e({}^r\dot{\theta}_9 - {}^l\dot{\theta}_9) \tag{9-15}$$

where $c_e = \begin{cases} 1, j = l \\ -1, j = r \end{cases}$.

$$m_6\,{}^j\ddot{y}_6 = {}^jf_{69(y)}^{\mathbf{C}_6} \tag{9-16}$$

$$m_6\,{}^j\ddot{z}_6 = {}^jf_{69(z)}^{\mathbf{C}_6} \tag{9-17}$$

$$I_6\,{}^j\ddot{\theta}_6 = {}^j\mathbf{C}_{6s}^{B_6}\times{}^j\mathbf{f}_{69}^{\mathbf{C}_6}[1\quad 0\quad 0]^{\mathrm{T}} + k_{sr2}({}^j\theta_9 - {}^j\theta_6) + c_{sr2}({}^j\dot{\theta}_9 - {}^j\dot{\theta}_6) \tag{9-18}$$

$$m_B\ddot{y}_B = -{}^lf_{9B(y)}^{\mathbf{D}_5} - {}^rf_{9B(y)}^{\mathbf{D}_5} - {}^lf_{B_B(y)}^{\mathbf{C}_7} - {}^rf_{B_B(y)}^{\mathbf{C}_7} \tag{9-19}$$

$$m_B\ddot{z}_B = -{}^lf_{9B(z)}^{\mathbf{D}_5} - {}^rf_{9B(z)}^{\mathbf{D}_5} - {}^lf_{B_B(z)}^{\mathbf{C}_7} - {}^rf_{B_B(z)}^{\mathbf{C}_7} \tag{9-20}$$

$$I_B\ddot{\theta}_B = \mathbf{D}_5^{B_B}\times(-{}^l\mathbf{f}_{9B}^{\mathbf{D}_5} - {}^r\mathbf{f}_{9B}^{\mathbf{D}_5})[1\quad 0\quad 0]^{\mathrm{T}} + k_{sr3}({}^l\theta_9 - \theta_B) + c_{sr3}({}^l\dot{\theta}_9 - \dot{\theta}_B)$$
$$+k_{sr3}({}^r\theta_9 - \theta_B) + c_{sr3}({}^r\dot{\theta}_9 - \dot{\theta}_B) + {}^l\mathbf{C}_7^{B_B}\times(-{}^l\mathbf{f}_{B_B}^{\mathbf{C}_7})[1\quad 0\quad 0]^{\mathrm{T}}$$
$$+{}^r\mathbf{C}_7^{B_B}\times(-{}^r\mathbf{f}_{B_B}^{\mathbf{C}_7})[1\quad 0\quad 0]^{\mathrm{T}} + ({}^lk_{sr5} + {}^rk_{sr5})(\theta_0 - \theta_B) + ({}^lc_{sr5} + {}^rc_{sr5})(\dot{\theta}_0 - \dot{\theta}_B) \tag{9-21}$$

After linearization of the matrices $\mathbf{T}_{12}({}^j\theta_i)$ and $\frac{\mathrm{d}\mathbf{T}_{12}({}^j\theta_i)}{\mathrm{d}t}$ because of the small roll angles ${}^j\theta_i$ by approximating $\sin{}^j\theta_i = {}^j\theta_i$ and $\cos{}^j\theta_i = 1$, the motion equations in Eqs. (9-10)-(9-21) can be organized in matrix form as

$$\mathbf{M}_{sa}\ddot{\mathbf{X}}_{sa} + \mathbf{C}_{sa}\dot{\mathbf{X}}_{sa} + \mathbf{K}_{sa}\mathbf{X}_{sa} = \mathbf{K}_{sr}\mathbf{X}_{pr} + \mathbf{C}_{sr}\dot{\mathbf{X}}_{pr} \tag{9-22}$$

where $\mathbf{X}_{sa} = [{}^ly_5\quad {}^lz_5\quad {}^l\theta_5\quad {}^ly_9\quad {}^lz_9\quad {}^l\theta_9\quad {}^ry_5\quad {}^rz_5\quad {}^r\theta_5\quad {}^ry_9\quad {}^rz_9\quad {}^r\theta_9\quad {}^ly_6\quad {}^lz_6\quad {}^l\theta_6\quad {}^ry_6\quad {}^rz_6\quad {}^r\theta_6\quad y_B\quad z_B\quad \theta_B]^{\mathrm{T}}$ is the displacement vector, and $\mathbf{X}_{pr} = [y_0\quad z_0\quad \theta_0]^{\mathrm{T}}$ is the input displacement vector, $\mathbf{M}_{sa}$, $\mathbf{C}_{sa}$ and $\mathbf{K}_{sa}$ are respectively the mass, damping, stiffness matrices of the seat model, $\mathbf{K}_{sr}$ and $\mathbf{C}_{sr}$ are the stiffness and damping matrices associated with the inputs.

According to Eq.(9-22), the frequency response function from $\mathbf{X}_{pr}$ to $\mathbf{X}_{sa}$ can be obtained as

$$\mathbf{T}_{sa} = (-\mathbf{M}_{sa}\omega^2 + \mathrm{j}\omega\mathbf{C}_{sa} + \mathbf{K}_{sa})^{-1}(\mathbf{K}_{sr} + \mathbf{C}_{sr}\mathrm{j}\omega) \quad (9\text{-}23)$$

9.2.6 Parameter estimation and model calibration

9.2.6.1 General consideration

The model parameters were divided into two groups. One category of the parameters is related to masses and dimensions of the seat segments. They were obtained mainly through measurement. The other category of parameters is associated with the physical properties (stiffness and damping) at the connection and contact points and locations of connection and contact points. They were mainly determined through a procedure of model calibration.

9.2.6.2 Parameter estimation

For the estimation of the coordinates of the key construction points, some coordinates can be determined by measurement, such as CoG of ${}^{j}B_i$ in the absolute coordinate ${}^{j}\mathbf{O}_{is}^{O}$ ($\begin{cases} i = 5,6,9; j = l,r \\ i = B; no\ j \end{cases}$). For some points such as contact points ${}^{j}\mathbf{C}_i$ ($i = 6,7; j = l,r$) or connection points ${}^{j}\mathbf{D}_4$ ($j = l,r$), $\mathbf{D}_5$ and $\mathbf{D}_6$, their coordinates only need to be determined in one of the relative coordinate systems. Then their coordinates in other relative coordinate systems can be determined accordingly given that the relative positions of origins of the relative coordinate systems are known. The determination of the coordinates of these points is shown in Table 9-1.

By measurement and calculation, the masses, the dimensions, coordinates and moments of inertia of the seat segments can be obtained, as illustrated in Table 9-2. Having known the dimensions, some coordinates of the contact or connection points can be calculated, as listed in Table 9-3.

Table 9-1 The determination of the coordinates of key points

Points	Definition of coordinates	Coordinate in other relative coordinate systems
${}^{l}\mathbf{C}_6$	${}^{l}\mathbf{C}_6^{B_9}=\left({}^{l}x_{\mathbf{C}_6}^{B_9}\quad {}^{l}y_{\mathbf{C}_6}^{B_9}\quad {}^{l}z_{\mathbf{C}_6}^{B_9}\right)^{*}$	${}^{j}\mathbf{C}_{6s}^{B_6}={}^{j}\mathbf{C}_6^{B_9}+{}^{j}\mathbf{O}_{9s}^{O}-{}^{j}\mathbf{O}_{6s}^{O}, j=l,r$
${}^{r}\mathbf{C}_6$	${}^{r}\mathbf{C}_6^{B_9}={}^{l}\mathbf{C}_6^{B_9}$	
${}^{l}\mathbf{C}_7$	${}^{l}\mathbf{C}_7^{B_B}=\left({}^{l}x_{\mathbf{C}_7}^{B_B}\quad {}^{l}y_{\mathbf{C}_7}^{B_B}\quad {}^{l}z_{\mathbf{C}_7}^{B_B}\right)$	${}^{j}\mathbf{C}_7^{O}={}^{j}\mathbf{C}_7^{B_B}+\mathbf{O}_{Bs}^{O}, j=l,r$
${}^{r}\mathbf{C}_7$	${}^{r}\mathbf{C}_7^{B_B}=\left({}^{r}x_{\mathbf{C}_7}^{B_B}\quad {}^{r}y_{\mathbf{C}_7}^{B_B}\quad {}^{r}z_{\mathbf{C}_7}^{B_B}\right)$	
${}^{l}\mathbf{D}_4$	${}^{l}\mathbf{D}_4^{B_5}=\left({}^{l}x_{\mathbf{D}_4}^{B_5}\quad {}^{l}y_{\mathbf{D}_4}^{B_5}\quad {}^{l}z_{\mathbf{D}_4}^{B_5}\right)$	${}^{j}\mathbf{D}_4^{B_9}={}^{j}\mathbf{D}_4^{B_5}\mathbf{T}_{11}({}^{j}\alpha)+{}^{j}\mathbf{O}_{5s}^{O}-{}^{j}\mathbf{O}_{9s}^{O}, j=l,r$
${}^{r}\mathbf{D}_4$	${}^{r}\mathbf{D}_4^{B_5}={}^{l}\mathbf{D}_4^{B_5}$	
$\mathbf{D}_5$	${}^{l}\mathbf{D}_5^{B_9}=\left({}^{l}x_{\mathbf{D}_5}^{B_9}\quad {}^{l}y_{\mathbf{D}_5}^{B_9}\quad {}^{l}z_{\mathbf{D}_5}^{B_9}\right)$	${}^{r}\mathbf{D}_5^{B_9}={}^{l}\mathbf{D}_5^{B_9}+{}^{l}\mathbf{O}_{9s}^{O}-{}^{r}\mathbf{O}_{9s}^{O}$, $\mathbf{D}_5^{B_B}={}^{l}\mathbf{D}_5^{B_9}+{}^{l}\mathbf{O}_{9s}^{O}-\mathbf{O}_{Bs}^{O}$
$\mathbf{D}_6$	${}^{l}\mathbf{D}_6^{B_9}=\left({}^{l}x_{\mathbf{D}_6}^{B_9}\quad {}^{l}y_{\mathbf{D}_6}^{B_9}\quad {}^{l}z_{\mathbf{D}_6}^{B_9}\right)$	${}^{r}\mathbf{D}_6^{B_9}={}^{l}\mathbf{D}_6^{B_9}+{}^{l}\mathbf{O}_{9s}^{O}-{}^{r}\mathbf{O}_{9s}^{O}$
$\mathbf{E}$	$\mathbf{E}^{O}=\left(x_{\mathbf{E}}^{O}\quad y_{\mathbf{E}}^{O}\quad z_{\mathbf{E}}^{O}\right)$	$\mathbf{E}^{B_B}=\mathbf{E}^{O}-\mathbf{O}_{Bs}^{O}$, $\overline{\mathbf{E}_s\,{}^{j}\mathbf{C}_{7s}}={}^{j}\mathbf{C}_7^{O}-\mathbf{E}^{O}, j=l,r$

*Note that ${}^{j}\mathbf{C}_{is}$ and ${}^{j}\mathbf{C}_{i}$ are coincident at the equilibrium position, but at different positions during vibration.

Table 9-2 The masses, dimensions, coordinates and moments of inertia of the seat segments

Part	Mass (kg)	Moment of inertia (kgm^2)	Coordinates (m)
${}^{j}B_5{}^{*}$	$m_5=9.1$	$I_5=\frac{1}{12}(0.52^2+0.84^2)m_5$	${}^{j}x_{50}=-(0.06\sin{}^{j}\alpha+0.48)\sin{}^{j}\alpha-0.06\cos{}^{j}\alpha$ ${}^{l}y_{50}=0$, ${}^{r}y_{50}={}^{l}y_{50}-0.53$, ${}^{j}z_{50}=(0.06\sin{}^{j}\alpha+0.48)\cos{}^{j}\alpha-0.06\sin{}^{j}\alpha$
${}^{j}B_6$	$m_6=2.2$	$I_6=\frac{1}{12}(0.13^2+0.52^2)m_6$	${}^{l}x_{60}={}^{r}x_{60}=0.19$, ${}^{l}y_{60}=0$, ${}^{r}y_{60}={}^{l}y_{60}-0.53$, ${}^{r}z_{60}={}^{l}z_{60}=-0.065$
${}^{j}B_9$	$2m_9+m_B=41.4$	$I_9=\frac{1}{12}\times0.525^2 m_9$	${}^{l}x_{90}={}^{r}x_{90}=0.12$, ${}^{l}y_{90}=0$, ${}^{r}y_{90}={}^{l}y_{90}-0.53$, ${}^{l}z_{90}={}^{r}z_{90}=-0.15$
B_B		$I_B=\frac{1}{12}(1.05^2+0.1^2)m_B$	$x_{B0}=0.11$, $y_{B0}=-0.2$, $z_{B0}=-0.22$

* $j=l$, for the left unit; $j=r$, for the right unit.

Table 9-3 Known coordinates of the contact and connection points

Points	Coordinates (m)	Points	Coordinates (m)
${}^{l}\mathbf{D}_4$	${}^{l}x_{\mathbf{D}_4}^{B_5}=0$, ${}^{l}z_{\mathbf{D}_4}^{B_5}=-0.48$	${}^{l}\mathbf{C}_7$	${}^{l}y_{\mathbf{C}_7}^{B_B}=0.25$, ${}^{l}z_{\mathbf{C}_7}^{B_B}=-0.19$
$\mathbf{D}_5$	${}^{l}x_{\mathbf{D}_5}^{B_9}=0$, ${}^{l}y_{\mathbf{D}_5}^{B_9}=-0.265$, ${}^{l}z_{\mathbf{D}_5}^{B_9}=0$	${}^{r}\mathbf{C}_7$	${}^{r}y_{\mathbf{C}_7}^{B_B}=-0.6$, ${}^{r}z_{\mathbf{C}_7}^{B_B}=0$
$\mathbf{D}_6$	${}^{l}y_{\mathbf{D}_6}^{B_9}=-0.265$, ${}^{l}z_{\mathbf{D}_6}^{B_9}=0$	$\mathbf{E}$	$x_{\mathbf{E}}^{O}=0.185$, $y_{\mathbf{E}}^{O}=0$, $z_{\mathbf{E}}^{O}=-0.41$
${}^{l}\mathbf{C}_6$	${}^{l}z_{\mathbf{C}_6}^{B_9}=0.02$		

9.2.6.3 Model calibration

9.2.6.3.1. Model parameters to be determined

To determine the rest of the parameters, a procedure of model calibration was carried out. The detailed parameters to be determined during the calibration are all the stiffness and damping listed in Table G-1 of Appendix G, other unknown parameters about contact and connection positions (${}^{l}y_{\mathbf{D}_4}^{B_5}$, ${}^{l}x_{\mathbf{C}_6}^{B_9}$, ${}^{l}y_{\mathbf{C}_6}^{B_9}$, ${}^{l}x_{\mathbf{D}_6}^{B_9}$, ${}^{l}x_{\mathbf{C}_7}^{B_B}$, ${}^{r}x_{\mathbf{C}_7}^{B_B}$), and the masses (m_9 , m_B) given that the total mass is about 64 kg.

9.2.6.3.2. Objective of optimization

The lateral, vertical and roll in-line transmissibilities at the left seat pan calculated by the model are respectively

$$T_{sy} = \mathbf{T}_{sa}(13,1) \tag{9-24}$$

$$T_{sz} = \mathbf{T}_{sa}(14,2) \tag{9-25}$$

$$T_{sr} = \mathbf{T}_{sa}(15,3) \tag{9-26}$$

where $\mathbf{T}_{sa}(i,j)$ represents the ith row jth column element in the matrix $\mathbf{T}_{sa}$.

The lateral, vertical and roll in-line transmissibilities at the left backrest calculated by the model are respectively

$$T_{by} = \mathbf{T}_{sa}(1,1) \tag{9-27}$$

$$T_{bz} = \mathbf{T}_{sa}(2,2) \tag{9-28}$$

$$T_{br} = \mathbf{T}_{sa}(3,3) \tag{9-29}$$

As introduced in Chapter 8, in the experiment, the inline seat transmissibilities with no subject from the platform to the left seat pan and left backrest in the lateral, vertical and roll directions were measured and calculated under 27 combinations of the vertical excitation with three magnitudes (0.25, 0.5 and 1.0 m/s^2 r.m.s.), lateral excitation with three magnitudes (0.25, 0.5 and 1.0 m/s^2 r.m.s.), as well as roll excitation with three magnitudes (0.5, 0.75 and 1.0 rad/s^2 r.m.s.). Therefore, the model can be calibrated by minimizing the error between the lateral, vertical and r_x-axis inline transmissibilities at the backrest and seat pan of the left unit measured in the experiment and those calculated by the model.

The cost function that is the sum of the average difference of the real and imaginary parts of the transmissibilities in the y, z and r_x directions on both the seat pan and backrest between the experimental data and the model is defined as follows:

$$\text{error} = \sum_{\substack{j=sy,sz,sr,\\ by,bz,br}} w_j \left\{ \sqrt{\frac{\sum_{i=1}^{N} [\text{Re}(T_j(f_i))_e - \text{Re}(T_j(f_i))_m]^2}{N}} + \sqrt{\frac{\sum_{i=1}^{N} [\text{Im}(T_j(f_i))_e - \text{Im}(T_j(f_i))_m]^2}{N}} \right\} \tag{9-30}$$

where subscripts e and m represent the transmissibilities from experiment and model, respectively, N stands for the total number of frequencies, w_j ($j = sy, sz, sr, by, bz, br$) stands for the weighting factors, which can be different for different vibration magnitudes.

Reasonable constraints for the lower and upper bounds of all the parameters to be calibrated were given before model calibration. Model calibration was completed with a combined genetic algorithm and minimization function of constrained nonlinear multivariable problem that has been introduced in Section 3.3. The frequency range considered for the calibration was 0.5-50 Hz. After that, all parameters of the seat model were determined.

9.2.7 Results of calibration

A good agreement between the experiment and model under different excitations was observed. Fig. 9-2 showed one example of the comparison between the experimental data and the model, proving the effectiveness of the seat model (the parameters of the seat are illustrated in Table G-3). The model is also good at predicting the resonances of the transmissibilities at both the left seat pan and left backrest. The seat model may also be applicable to different backrest inclinations that have also been taken into account in the modelling.

The modal analysis with the seat model was further conducted to find out the relationship between the modal properties and the resonances in the transmissibilities according to the method introduced in Section 3.6.

Because of the phase difference between different degrees of freedom, the modal shape for every modal frequency is better visualized by animation. Taking the excitation in Fig. 9-2 as an example, two main modes were detected, 15.49 and 26.99 Hz, respectively, corresponding to the peaks in black circles and in blue circles. For the first modal shape of 15.49 Hz in Fig. 9-3(a), it is dominated

by the roll and lateral motions of the seat pan and backrest, moving in phase for the left and right units. For the second modal shape of 26.99 Hz in Fig. 9-3(b), the modal vibration is mainly the lateral and roll motions of the two backrests, however, their relative vibrations transform from in-phase vibration to out-of-phase one.

It should be noted that the actual nonlinear seat was simplified as a linear model under one specific excitation, so there were different sets of seat parameters corresponding to different magnitudes of excitations. These two modal shapes of the seat under excitations of different magnitudes were almost the same, this was probably because the nonlinearity of the seat was not significant.

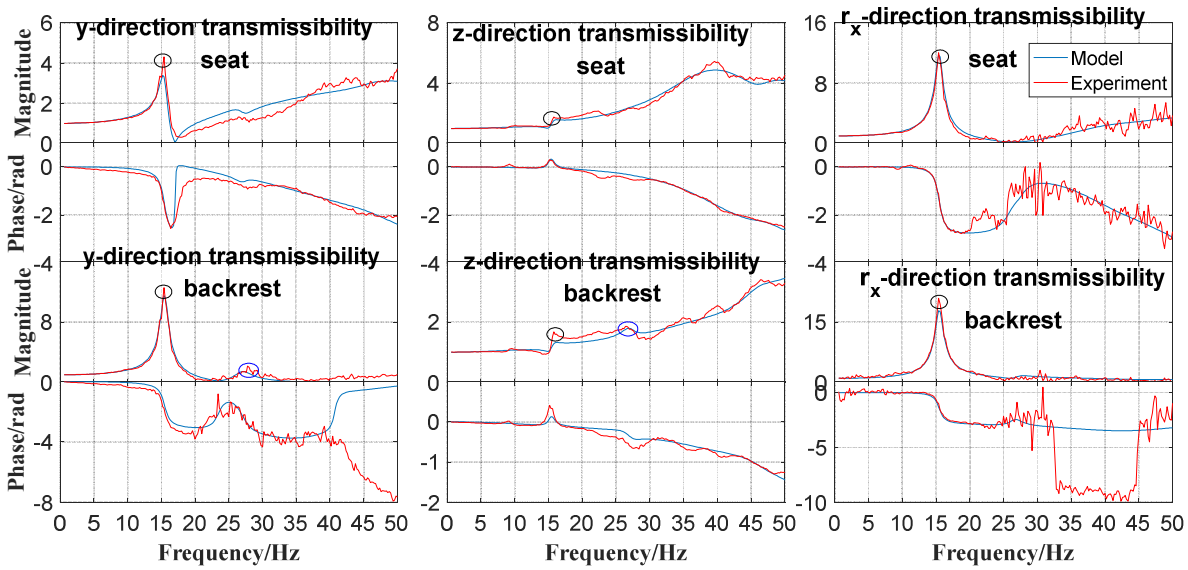

Fig. 9-2 The comparison between the model and experiment for the seat transmissibility in y direction, z direction and r_x direction at the left seat pan and left backrest under the excitation of 0.5 ms^{-2} r.m.s. lateral, 1.0 ms^{-2} r.m.s. vertical and 0.75 rad/s^2 r.m.s. roll vibration.

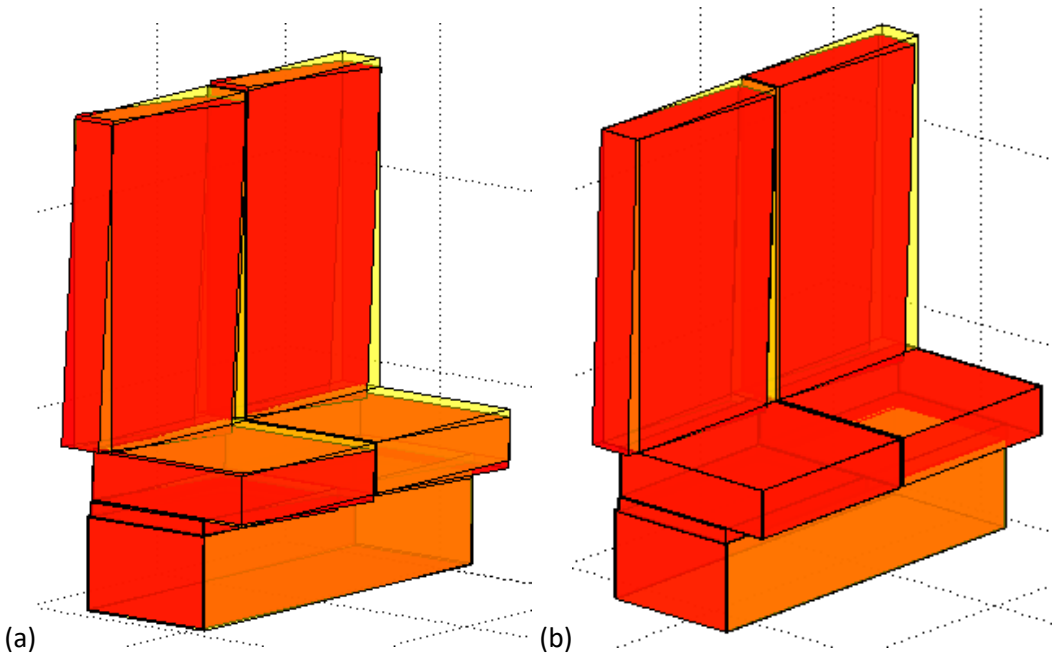

Fig. 9-3 The modal shapes of the seat under the excitation of 0.5 ms^{-2} r.m.s. lateral, 1.0 ms^{-2} r.m.s. vertical and 0.75 rad/s^2 r.m.s. roll vibration (a) first modal shape (15.49 Hz); (b) second modal shape (26.99 Hz) (red: deformed modal shape; yellow: undeformed modal shape).

9.3 Development of coupled human-seat models

Since the seated human model and double-unit train model have been developed separately, their coupled dynamics is going to be studied by means of modelling the coupled human-seat system. From the experiment in Chapter 5 and Chapter 8, the dynamics of the train seat with one seated subject showed a great discrepancy from that with two subjects, so double-unit-seat-one-subject model and double-unit-seat-two-subject model were developed separately.

9.3.1 Development of double-unit-seat-one-subject model

9.3.1.1 Model introduction

For the double-unit-seat-one-subject model shown in Fig. 9-4(a), the mass distribution of the subject seated on the train seat was assumed the same as that seated on the rigid seat. For both the seated human model on the rigid seat and double-unit-seat-one-subject model, the head was not in contact with the backrest. Therefore, the modelling of the human body seated on the train seat was the same as the seated human model. The symbols for the double-unit-seat-one-subject model were also kept the same as the human model and train seat model. However, for distinguishing between the subject seated on the left and the one on the right, 'l' and 'r' were added in left superscript of every symbol for the human model on the left and on the right, respectively.

The development of the double-unit-seat-one-subject model was conducted by integrating the seat model developed in Section 9.2 with the human body model described in Chapter 7.

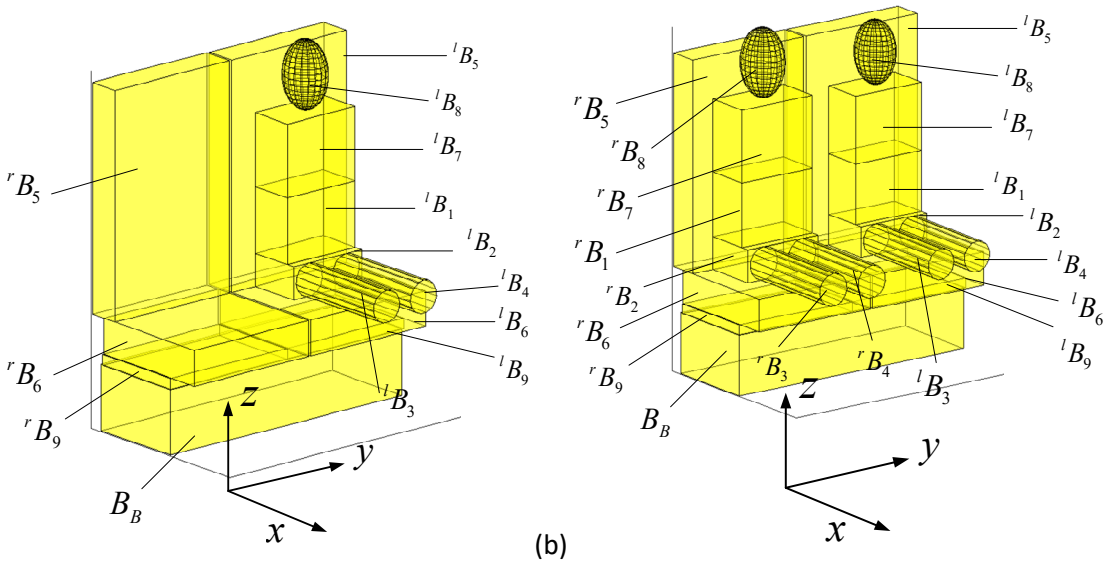

Fig. 9-4 Coupled human-seat models (a) seat with one subject on the left (b) seat with two subjects.

However, for the seated human model on a train seat, the stiffness and damping at the contact points between the human body and the train seat (seat pan and backrest) were different from the seated human model on a rigid seat. The former resulted from the interaction between the human tissue and the seat cushion, but the latter arose merely from human tissue. Therefore, these parameters in relation to the stiffness and damping at the contact points between the human body and the train seat were redefined or readjusted in Table G-2 of Appendix G.

For the double-unit-seat-one-subject model, the motion equations for ${}^{r}B_5$, ${}^{r}B_6$, ${}^{r}B_9$, B_B and ${}^{l}B_9$ were the same as Eqs. (9-10)-(9-21). However, the motion equations of ${}^{l}B_5$ and ${}^{l}B_6$ were modified due to the coupling with the human body.

The motion equations for the left backrest (${}^{l}B_5$) are respectively

$$m_5\,{}^{l}\ddot{y}_5 = {}^{l}f_{59(y)}^{\mathbf{D}_4} - {}^{l}\mathbf{f}_{15}^{\mathbf{C}_1}\mathbf{T}_{11}({}^{l}\alpha)\begin{bmatrix}0 & 1 & 0\end{bmatrix}^{\mathrm{T}} + {}^{l}\mathbf{f}_{57}^{\mathbf{C}_5}\mathbf{T}_{11}({}^{l}\alpha)\begin{bmatrix}0 & 1 & 0\end{bmatrix}^{\mathrm{T}} \tag{9-31}$$

$$m_5\,{}^{l}\ddot{z}_5 = {}^{l}f_{59(z)}^{\mathbf{D}_4} - {}^{l}\mathbf{f}_{15}^{\mathbf{C}_1}\mathbf{T}_{11}({}^{l}\alpha)\begin{bmatrix}0 & 0 & 1\end{bmatrix}^{\mathrm{T}} + {}^{l}\mathbf{f}_{57}^{\mathbf{C}_5}\mathbf{T}_{11}({}^{l}\alpha)\begin{bmatrix}0 & 0 & 1\end{bmatrix}^{\mathrm{T}} \tag{9-32}$$

$$I_5\,{}^l\ddot{\theta}_5 = {}^l\mathbf{D}_4^{B_5}\times({}^l\mathbf{f}_{59}^{\mathbf{D}_4}\mathbf{T}_{11}^{\mathrm{T}}({}^l\alpha)))\begin{bmatrix}1 & 0 & 0\end{bmatrix}^{\mathrm{T}} + k_{sr1}({}^l\theta_9\cos{}^l\alpha - {}^l\theta_5) + c_{sr1}({}^l\dot{\theta}_9\cos{}^l\alpha - {}^l\dot{\theta}_5)$$
$$+{}^l\mathbf{C}_{1s}^{B_5}\times(-{}^l\mathbf{f}_{15}^{\mathbf{C}_1})\begin{bmatrix}1 & 0 & 0\end{bmatrix}^{\mathrm{T}} + {}^lk_{cr3}({}^l\theta_1 - {}^l\theta_5) + {}^lc_{cr3}({}^l\dot{\theta}_1 - {}^l\dot{\theta}_5) + {}^l\mathbf{C}_{5s}^{B_5}\times{}^l\mathbf{f}_{57}^{\mathbf{C}_5}\begin{bmatrix}1 & 0 & 0\end{bmatrix}^{\mathrm{T}}$$
$$+{}^lk_{cr7}({}^l\theta_7 - {}^l\theta_5) + {}^lc_{cr7}({}^l\dot{\theta}_7 - {}^l\dot{\theta}_5)$$

(9-33)

The motion equations for the left seat pan cushion ($^lB_6$) are respectively

$$m_6\,{}^l\ddot{y}_6 = {}^lf_{69(y)}^{\mathbf{C}_6} - {}^lf_{26(y)}^{\mathbf{C}_2} - {}^lf_{36(y)}^{\mathbf{C}_3} - {}^lf_{46(y)}^{\mathbf{C}_4} \tag{9-34}$$

$$m_6\,{}^l\ddot{z}_6 = {}^lf_{69(z)}^{\mathbf{C}_6} - {}^lf_{26(z)}^{\mathbf{C}_2} - {}^lf_{36(z)}^{\mathbf{C}_3} - {}^lf_{46(z)}^{\mathbf{C}_4} \tag{9-35}$$

$$I_6\,{}^l\ddot{\theta}_6 = {}^l\mathbf{C}_{6s}^{B_6}\times{}^l\mathbf{f}_{69}^{\mathbf{C}_6}\begin{bmatrix}1 & 0 & 0\end{bmatrix}^{\mathrm{T}} + k_{sr2}({}^l\theta_9 - {}^l\theta_6) + c_{sr2}({}^l\dot{\theta}_9 - {}^l\dot{\theta}_6) + {}^l\mathbf{C}_{2s}^{B_6}\times(-{}^l\mathbf{f}_{26}^{\mathbf{C}_2})\begin{bmatrix}1 & 0 & 0\end{bmatrix}^{\mathrm{T}}$$
$$+{}^l\mathbf{C}_{3s}^{B_6}\times(-{}^l\mathbf{f}_{36}^{\mathbf{C}_3})\begin{bmatrix}1 & 0 & 0\end{bmatrix}^{\mathrm{T}} + {}^l\mathbf{C}_{4s}^{B_6}\times(-{}^l\mathbf{f}_{46}^{\mathbf{C}_4})\begin{bmatrix}1 & 0 & 0\end{bmatrix}^{\mathrm{T}} + {}^lk_{cr4}({}^l\theta_2 - {}^l\theta_6) + {}^lc_{sr4}({}^l\dot{\theta}_2 - {}^l\dot{\theta}_6)$$

(9-36)

After linearization, the motion equations of the double-unit-seat-one-subject model can be expressed in matrix form as

$$\mathbf{M}_{sh}\ddot{\mathbf{X}}_{sh} + \mathbf{C}_{sh}\dot{\mathbf{X}}_{sh} + \mathbf{K}_{sh}\mathbf{X}_{sh} = \mathbf{K}_{shr}\mathbf{X}_{pr} + \mathbf{C}_{shr}\dot{\mathbf{X}}_{pr} \tag{9-37}$$

where $\mathbf{X}_{sh} = [{}^l\mathbf{X}_p; \mathbf{X}_{sa}]$ is the displacement vector, ${}^l\mathbf{X}_p$ is the displacement vector for the human body on the left (Eq. (7-35)), while $\mathbf{X}_{sa}$ is the displacement vector for the double-unit seat (Eq. (9-22)); and $\mathbf{X}_{pr} = \begin{bmatrix}y_0 & z_0 & \theta_0\end{bmatrix}^{\mathrm{T}}$ is the input displacement vector, $\mathbf{M}_{sh}$, $\mathbf{C}_{sh}$ and $\mathbf{K}_{sh}$ are respectively the mass, damping and stiffness matrices of the double-unit-seat-one-subject model, $\mathbf{K}_{shr}$ and $\mathbf{C}_{shr}$ are the stiffness and damping matrices associated with the inputs.

According to Eq. (9-37), the frequency response function from $\mathbf{X}_{pr}$ to $\mathbf{X}_{sh}$ can be obtained as

$$\mathbf{T}_{sh} = (-\mathbf{M}_{sh}\omega^2 + \mathrm{j}\omega\mathbf{C}_{sh} + \mathbf{K}_{sh})^{-1}(\mathbf{K}_{shr} + \mathbf{C}_{shr}\mathrm{j}\omega) \tag{9-38}$$

The in-line transmissibilities of the double-unit-seat-one-subject model in y direction, z direction and r_x direction at the left seat pan and left backrest were obtained from $\mathbf{T}_{sh}$.

9.3.1.2 Model calibration and results

In the same way, the model was calibrated by minimizing the error between the model and experimental data for these transmissibilities by means of the same algorithm (Section 3.3) in 0.5-

50 Hz. The parameters to be calibrated were all the contact stiffness and damping in Table G-2 of Appendix G, and the parameters concerning the contact positions (${}^{l}y_{\mathbf{C}_1}^{B_1}$, ${}^{l}z_{\mathbf{C}_1}^{B_1}$, ${}^{l}x_{\mathbf{C}_2}^{B_2}$, ${}^{l}y_{\mathbf{C}_2}^{B_2}$, ${}^{l}x_{\mathbf{C}_3}^{B_3}$, ${}^{l}y_{\mathbf{C}_3}^{B_3}$, ${}^{l}x_{\mathbf{C}_4}^{B_4}$, ${}^{l}y_{\mathbf{C}_4}^{B_4}$, ${}^{l}y_{\mathbf{C}_5}^{B_7}$, ${}^{l}z_{\mathbf{C}_5}^{B_7}$). Similar to the train seat and human models, this kind of model simplified the actual nonlinear object as linear model under a specific excitation, so under different excitations, the model had different sets of parameters. Under a specific excitation, the other parameters were kept the same as the double-unit seat model and seated human model that were determined under the same excitation.

An example was taken by coupling the train seat model in Fig. 9-2 with the human model in Fig. 7-5 (the parameters of contact were listed in Table G-4), good agreement between the model and experimental results was shown in Fig. 9-5. Another example was illustrated in Fig. 9-6. All the results proved the effectiveness of the double-unit-seat-one-subject model. By means of modal analysis (Section 3.6) of the example in Fig. 9-5, three main modal frequencies were found, that is, 4.67, 15.27, and 27.73 Hz, respectively, corresponding to the black circle, blue circles and green circle in Fig. 9-5. The first modal shape (4.67 Hz) in Fig. 9-7(a) is dominated by the motion of human body that is similar to the third human mode in Fig. 7-6(c), accompanied by vertical motion of the left seat pan. For the second modal shape (15.27 Hz) in Fig. 9-7(b), the motion is mainly the seat vibration that is analogous to the first seat mode in Fig. 9-3(a), together with a little lateral and roll motions of the human body. The dominating motion in the third modal shape (27.73 Hz) depicted in Fig. 9-7(c) is the seat vibration that resembles the second seat mode in Fig. 9-3(b), along with a little lateral and roll motions of the human body.

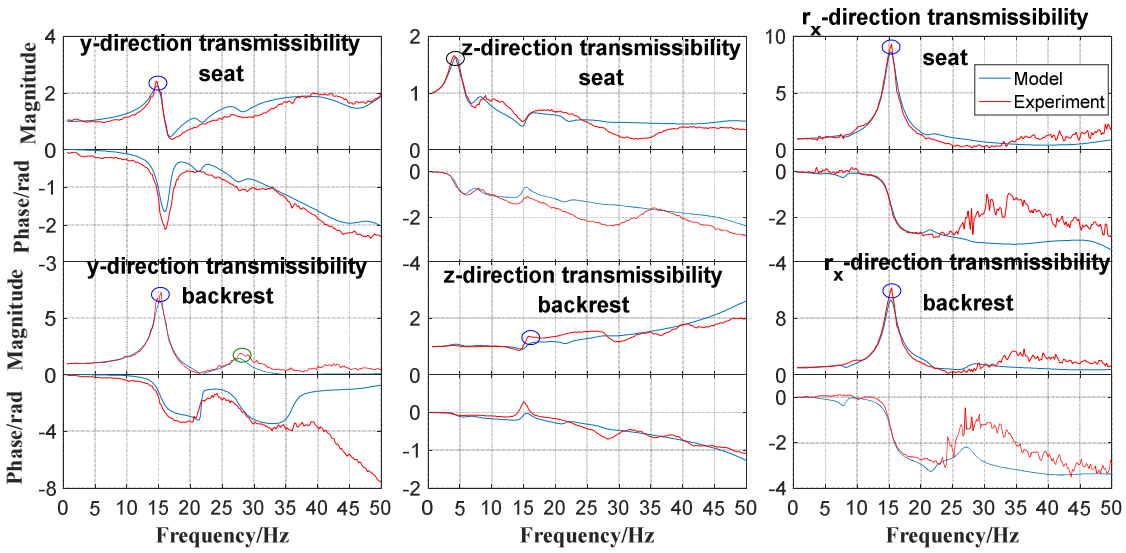

Fig. 9-5 The comparison between model and experiment for the seat transmissibilities in y direction, z direction and r_x direction at the left seat pan and left backrest for a subject of 171 cm in height and 83.5 kg in weight seated on the left of the double-unit train seat under the excitation of 0.5 ms^{-2} r.m.s. lateral, 1.0 ms^{-2} r.m.s. vertical and 0.75 rad/s^2 r.m.s. roll vibration.

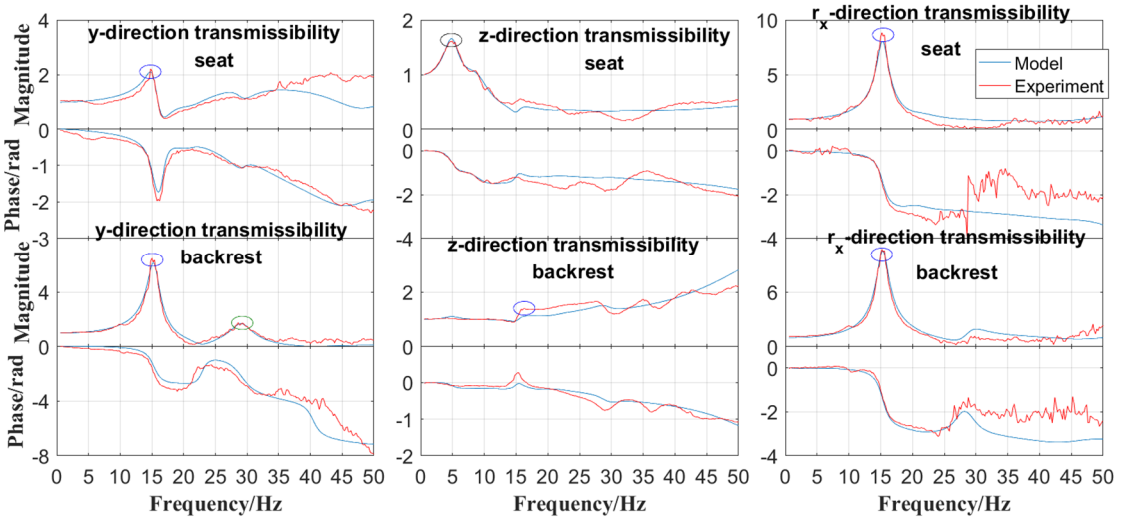

Fig. 9-6 The comparison between model and experiment for the seat transmissibilities in y direction, z direction and r_x direction at the left seat pan and left backrest for a subject of 178 cm in height and 82.8 kg in weight seated on the left of the double-unit train seat under the excitation of 0.25 ms^{-2} r.m.s. lateral, 0.5 ms^{-2} r.m.s. vertical and 0.5 rad/s^2 r.m.s. roll vibration.

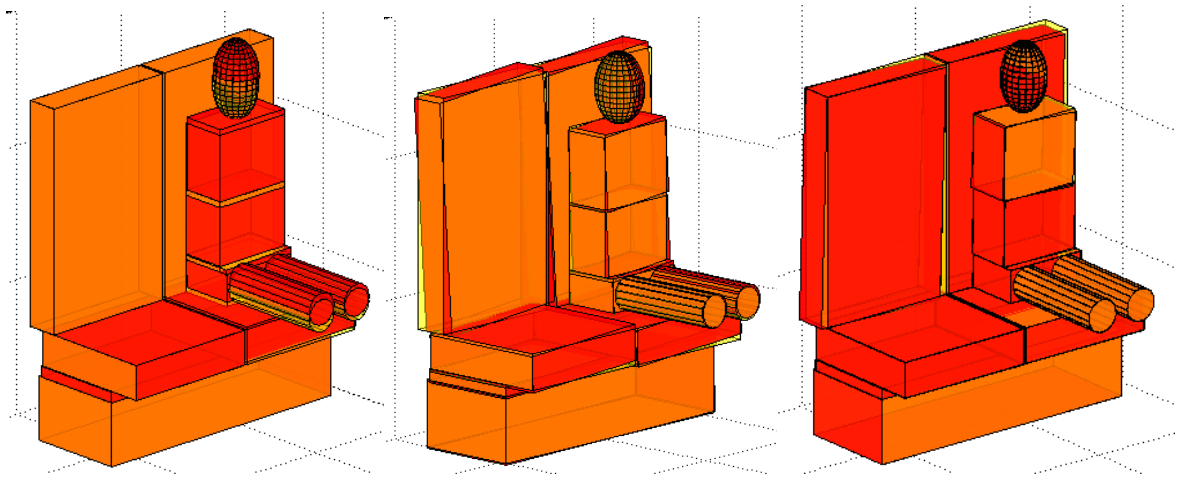

(a) (b) (c)

Fig. 9-7 The modal shapes of the double-unit-seat-one-subject model with a subject of 171 cm in height and 83.5 kg in weight seated on the left under the excitation of 0.5 ms^{-2} r.m.s. lateral, 1.0 ms^{-2} r.m.s. vertical and 0.75 rad/s^2 r.m.s. roll vibration (a) first modal shape (4.67 Hz); (b) second modal shape (15.27 Hz); (c) third modal shape (27.73 Hz) (red: deformed modal shape; yellow: undeformed modal shape).

9.3.2 Development of double-unit-seat-two-subject model

9.3.2.1 Model introduction

Similarly, for the double-unit-seat-two-subject model depicted in Fig. 9-4(b), the modelling of the human body on the right was the same as the seated human model in Chapter 7, with the same symbols and 'r' added in the left superscript of every symbol for the human model on the right.

Compared with the double-unit-seat-one-subject model, because of the coupling with the seated subject on the right, the motion equations of the right backrest (${}^{r}B_5$) and the right seat pan cushion (${}^{r}B_6$) were changed to be the same as ${}^{l}B_5$ and ${}^{l}B_6$, but the left superscript 'l' was substituted with 'r' in Eq. (9-31)-(9-36). For the same reason, the contact parameters between the subject on the right and the seat (seat pan and backrest) were also redefined or readjusted in Table G-2 of Appendix G. Other motion equations were the same as the above double-unit-seat-one-subject model.

9.3.2.2 Model calibration and results

In the same way, after linearization, the lateral, vertical and roll in-line transmissibilities at the left seat pan and left backrest were calculated by the model. Then the model was calibrated by minimizing the error between the model and experimental data for these transmissibilities by

means of the same algorithm (Section 3.3) in 0.5-50 Hz. The parameters to be calibrated were all the contact stiffness and damping in Table G-2 of Appendix G for the subject on the right, and the parameters concerning the contact positions (${}^{r}y_{\mathbf{C}_1}^{B_1}$, ${}^{r}z_{\mathbf{C}_1}^{B_1}$, ${}^{r}x_{\mathbf{C}_2}^{B_2}$, ${}^{r}y_{\mathbf{C}_2}^{B_2}$, ${}^{r}x_{\mathbf{C}_3}^{B_3}$, ${}^{r}y_{\mathbf{C}_3}^{B_3}$, ${}^{r}x_{\mathbf{C}_4}^{B_4}$, ${}^{r}y_{\mathbf{C}_4}^{B_4}$, ${}^{r}y_{\mathbf{C}_5}^{B_7}$, ${}^{r}z_{\mathbf{C}_5}^{B_7}$). Under a specific excitation, the other parameters were kept the same as the double-unit-seat-one-subject model and the human model for the right subject that were determined under the same excitation.

One example was taken by coupling the double-unit-seat-one-subject model in Fig. 9-5 with another seated human model for the right subject of 183 cm in height and 85 kg in weight, Fig. 9-8 illustrated good conformity between the model and the experiment.

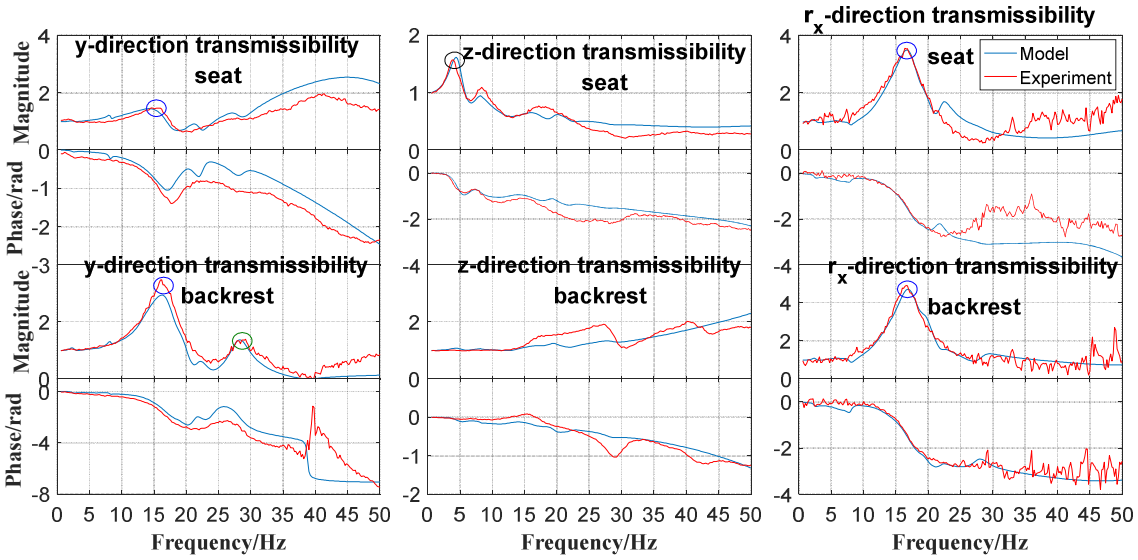

Fig. 9-8 The comparison between model and experiment for the seat transmissibilities in y direction, z direction and r_x direction at the left seat pan and left backrest for a subject of 171 cm in height and 83.5 kg in weight seated on the left of the double-unit train seat and a subject of 183 cm in height and 85 kg in weight on the right under the excitation of 0.5 ms^{-2} r.m.s. lateral, 1.0 ms^{-2} r.m.s. vertical and 0.75 rad/s^2 r.m.s. roll vibration.

Three main modes were still observed by modal analysis (Section 3.6), with modal frequencies of 4.67, 17.08 and 28.20 Hz, corresponding to peaks in the black, blue and green circles in Fig. 9-8, respectively. The modal shapes for the three modes were illustrated in Fig. 9-9(a), (b) and (c), respectively, which were analogous to those in Fig. 9-7(a), (b) and (c) with a little motion of the subject on the right.

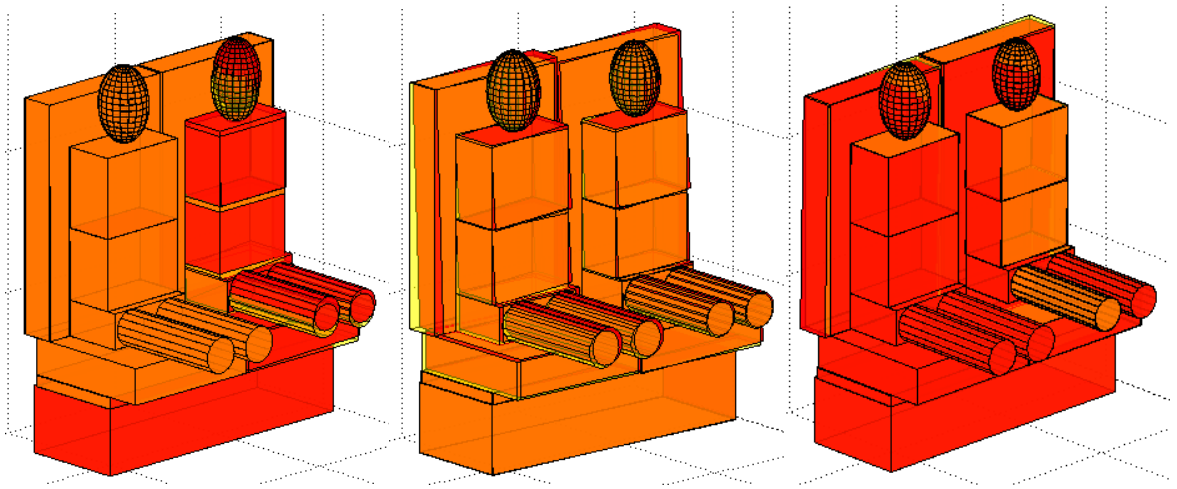

(a) (b) (c)

Fig. 9-9 The modal shapes of the double-unit-seat-two-subject model with a subject of 171 cm in height and 83.5 kg in weight seated on the left and a subject of 183 cm in height and 85 kg in weight on the right under the excitation of 0.5 ms^{-2} r.m.s. lateral, 1.0 ms^{-2} r.m.s. vertical and 0.75 rad/s^2 r.m.s. roll vibration (a) first modal shape (4.67 Hz); (b) second modal shape (17.08 Hz); (c) third modal shape (28.20 Hz) (red: deformed modal shape; yellow: undeformed modal shape).

9.4 Discussion

9.4.1 Model parameters

As introduced before, for the seat model, one group of model parameters are the stiffness and damping at the contact and connection points and their locations. On the other hand, for the double-unit-seat-one-subject model (double-unit-seat-two-subject model), the group of parameters to be determined are the stiffness and damping at the contact points between the subject on the left (right) and the corresponding seat pan and backrest as well as the locations of the contact points. In the models, the surface connection or contact was simplified as point connection or contact with an assumption that the surface force can be taken as a concentrated force acting at the connection or contact point. These groups of parameters can hardly be determined by measurement. So they were obtained via a properly defined procedure of optimization or calibration with measurement data of seat transmissibility, so that the model parameters were determined while making sure the global dynamics of the seat agreed with the measurement data. This study used both the real and imaginary parts of the transmissibilities in y direction, z direction and r_x direction at both the seat pan and backrest as the optimization objective function (Eq.(9-30)). This treatment in defining the objective function is more complete than those reported previously by other researchers. With so many experimental data (six transmissibilities

and each with both the real and imaginary parts) included in the objective function, it is very important to design an effective optimization strategy and algorithm.

The good agreement between the model–calculated and experimentally measured transmissibilities achieved in this study also ascribed to the proper design of the optimization strategy and the selection of optimization algorithm (a genetic algorithm combined with an algorithm for constrained nonlinear multivariable problem). This combined approach was proved to be a more effective and powerful optimization strategy than just adopting one of the above-mentioned optimization algorithms or the 'Complex' algorithm as used in Qiu and Griffin (2011), increasing the possibility of converging to a better result in a given time.

For calibrating the double-unit-seat-one-subject model and double-unit-seat-two-subject model, most of the parameters (except for the stiffness and damping at the contact points and their locations) were directly derived from the corresponding human model and seat model, which reduced the number of parameters to be calibrated and ensured the correctness of the seating dynamics of the human-seat systems together with the biodynamics of the human body and dynamics of the train seat.

9.4.2 Modelling

The existing seat or human-seat models have been mostly limited to single-axis translational excitation, in the fore-and-aft direction (Qiu and Griffin, 2011) or in the vertical direction (Kim *et al.*, 2003a; Grujicic *et al.*, 2009). Almost no model is applicable to lateral or roll vibration or multi-axis vibration. The model proposed in this chapter is a three-dimensional model exposed to combined lateral, vertical and roll vibration that can be used to predict not only the motion in the symmetrical (z-x) plane but also the motion out of the plane. In addition, the existing models are usually single-unit seat models possibly with one seated subject, e.g., Siefert *et al.* (2008) and Grujicic *et al.* (2009), but a double-unit seat model with a more complex structure occupied by one and two subjects in this study have rarely been seen. The inclinations of the two backrests were also taken into consideration in the proposed seat model, and the inclination of the upper body was also considered in the seated human model (Chapter 7), so the situation where passengers are seated with inclined backrest can be coped with by this model.

9.4.3 Modal properties

Although there were some modal tests of seats of different structures reported in others' studies (e.g., Lo *et al.* (2013)), the results cannot be compared with this train seat because of the great

discrepancy in structure. The two modes around 15 Hz and 27 Hz were important modes for the seat and exhibited peaks in the inline and cross-axis seat transmissibilities (Fig. 8-2). From the transmissibilities for the case of the bare seat, it was found that the modal frequencies and modal shapes were related to the resonances in the measured transmissibilities. All the inline transmissibilities in y direction and r_x direction showed a peak and both transmissibilities in z direction showed increased magnitude around the first modal frequency (around 15 Hz) (Fig. 8-2), so the modal shape corresponding to this modal frequency exhibited great lateral and roll motions of the seat pan and backrest along with a little vertical motion (Fig. 9-3(a)). The inline transmissibility in y direction on the backrest and y-r_x cross-axis transmissibility on the backrest (Fig. 8-10) showed a peak around the second modal frequency (about 27 Hz), so the modal shape exhibited great lateral and roll motions on the backrest (Fig. 9-3(b)). As can be seen, the modal frequencies and modal shapes obtained from the modal analysis with the seat model showed good agreement with the resonances in the measured seat transmissibilities.

With a seated subject on the left, the first modal frequency (4.67 Hz) corresponded to the primary resonance in the vertical seat transmissibility on the left seat pan (Fig. 9-5). And this peak possibly arose from the third human mode with modal frequency of 5.54 Hz (Fig. 7-6(c)) because of no existence of such peak in the transmissibility of the bare seat (Fig. 8-2), so the modal shape exhibited motions of human body resembling the third human mode along with vertical motion of the left seat pan (Fig. 9-7(a)). The second (15.27 Hz) and third (27.73 Hz) modal frequencies still corresponded to the resonances in the transmissibilities generated by the first and second seat modes, respectively, so the two modal shapes were mainly the seat motion resembling the first and second seat mode shapes respectively with a little motion of the subject (Fig. 9-7(b)(c)). However, the damping of the second mode (15.27 Hz) was probably increased telling from the reduced and flatter resonances in the transmissibilities.

With two seated subjects, there was no appearance or disappearance of resonance in the transmissibilities compared with those with one seated subject and three modes with close frequencies to the case with one subject were detected, so their modal shapes were similar to these three for the seat with one subject, along with a little motion of the subject on the right (Fig. 9-9). However, the damping of the second mode (17.08 Hz) was probably further increased telling from the reduced and flatter resonances in the transmissibilities.

The above analysis also proved the deduction of the modal shapes in Section 8.4.4.

It is worth mentioning that in this study, the modal analysis was conducted with damping based on the complex mode theory. In this way, the resulting modal shapes are more accurate and closer to reality than those analyzed without damping.

9.4.4 Model correlation

There was some association between the modes for these four models. For the four models—human model, double-unit train seat model, double-unit-seat-one-subject model, and double-unit-seat-two-subject model, those modes with close modal frequencies and similar modal shapes for their shared parts were considered to belong to the same mode set. When one mode of the human-seat system belongs to the same mode set as one human mode (or seat mode), then this mode of the human-seat system possibly arises from this human mode (or seat mode). Take the example of a subject of 171 cm in height and 83.5 kg in weight seated on the left and another subject of 183 cm in height and 85 kg in weight on the right under the excitation of 0.5 ms^{-2} r.m.s. lateral, 1.0 ms^{-2} r.m.s. vertical and 0.75 rad/s^2 r.m.s. roll vibration, the modal frequencies, damping ratios and modal shapes of the four models were compared and summarized in Table 9-4. Furthermore, MAC values between two models for their shared part were calculated. The MAC value is defined as

$$\mathrm{MAC}=\frac{\left|\mathbf{X}_1^{*\mathrm{T}}\mathbf{X}_2\right|^2}{(\mathbf{X}_1^{*\mathrm{T}}\mathbf{X}_1)(\mathbf{X}_2^{*\mathrm{T}}\mathbf{X}_2)} \tag{9-39}$$

where $\mathbf{X}_1$ and $\mathbf{X}_2$ are two modal vectors for the shared part in two models. For example, the shared part for the seated human model ($\mathbf{X}_p$ in Eq. (7-35)) and the double-unit-seat-one-subject model ($\mathbf{X}_{sh}=[{}^{l}\mathbf{X}_p;\mathbf{X}_{sa}]$ in Eq. (9-37)) is the subject on the left, so $\mathbf{X}_1=\mathbf{X}_p$ solved from the seated human model, and $\mathbf{X}_2={}^{l}\mathbf{X}_p$ solved from the double-unit-seat-one-subject model.

For mode set 1, it can be seen the first mode in the two human-seat systems was induced by the third mode of human body. As analyzed in Chapter 7, the third mode of human body is a vertical whole-body mode of the human body, similar to those with a modal frequency about 5 Hz reported by Kitazaki and Griffin (1997), Matsumoto and Griffin (2001), Zheng *et al.* (2011) and Liu *et al.* (2015). Thus, the primary resonance in the vertical transmissibility on the left seat pan for the two human-seat models arose from the third mode of human body (vertical whole-body mode). However, the coupling of the human body with the seat reduced the modal frequency and the damping ratio more or less. For this human mode (mode set 1), the axial stiffness and damping of the tissue beneath pelvis seemed to play an important role in the modal frequency and damping ratio (Kitazaki

and Griffin, 1997; Matsumoto and Griffin, 2001; Liu and Qiu, 2020). When the axial stiffness and damping of the tissue beneath pelvis coupled with the vertical stiffness and damping of the seat in series, the overall stiffness and damping would both decrease, which may be the reason for the reduced modal frequency and damping ratio. What is more, telling from the resonance in the vertical seat transmissibility on the seat pan with the bare seat, the vertical stiffness of the train seat is very large, so the coupled modal frequency was very close to that of the human body since the overall stiffness was only decreased a little compared with the axial stiffness of human tissue. However, the MAC values between the human-seat systems and the seated human model were relatively small, but that between two human-seat systems was close to unity, this is because the coupling with the train seat generated dramatic vertical vibration in the human body since the seat pan had dramatic vertical motion instead of staying static for the rigid seat. The high MAC value between two human-seat systems explained the resemblance in their modal shapes.

On the other hand, for mode set 2 and 3, the second and third modes in the two human-seat systems were induced by the first and second seat modes, respectively, so the resonances around 15 Hz and 27 Hz in the seat transmissibilities of two human-seat models were induced by the first and second seat modes, respectively. The MAC values between any one of the human-seat systems and the seat model or between two human-seat systems were rather high, which explained the similarity in their modal shapes. The coupling with the human bodies increased the modal damping obviously, so the peaks in the seat transmissibilities reduced and changed from ‘sharp’ to ‘flat’ as the increase of subject number, which was more significant for the peaks around 15 Hz (Fig. 8-2 and Fig. 8-17). The modal frequencies usually rose more or less as the increase of subject number except for the modal frequency of the double-unit-seat-one-subject model in mode set 2. This is because the human body will increase modal mass and the modal stiffness of the seat modes at the same time (Lo *et al.*, 2013). When the increased modal stiffness dominates over the increased modal mass, the modal frequency will increase; and vice versa. All the results deduced from the models showed good agreement with the experimental results in Chapter 8.

The above finding also explained the reason why conventional seats (except for suspension seats) of different structures usually have a peak around 5 Hz in the vertical transmissibility on the seat pan (Corbridge *et al.*, 1989; Toward and Griffin, 2011; Gong and Griffin, 2018), however, the other resonance frequencies in the transmissibilities may differ greatly, depending on the modal frequencies of the seats.

Table 9-4 Intercomparison among the modal properties of the four models for a subject of 171 cm in height and 83.5 kg in weight seated on the left and another subject of 183 cm in height and 85 kg in weight on the right under the excitation of 0.5 ms^{-2} r.m.s. lateral, 1.0 ms^{-2} r.m.s. vertical and 0.75 rad/s^2 r.m.s. roll vibration.

	Models	Human model for left subject	Seat model	Double-unit-seat-one-subject model	Double-unit-seat-two-subject model	MAC between two human-seat models
Mode set 1	Frequency(Hz)	5.54	N/A[a]	4.67	4.67	1.0
	Damping ratio	0.28	N/A	0.24	0.24	
	Modal shape	Fig. 7-6(c)	N/A	Fig. 9-7(a)	Fig. 9-9(a)	
	MAC (with left subject)	N/A	N/A	0.18	0.18	
Mode set 2	Frequency(Hz)	N/A	15.47	15.27	17.08	0.80
	Damping ratio	N/A	0.038	0.061	0.113	
	Modal shape	N/A	Fig. 9-3(a)	Fig. 9-7(b)	Fig. 9-9(b)	
	MAC (with seat)	N/A	N/A	0.99	0.78	
Mode set 3	Frequency(Hz)	N/A	26.99	27.73	28.20	0.96
	Damping ratio	N/A	0.044	0.055	0.057	
	Modal shape	N/A	Fig. 9-3(b)	Fig. 9-7(c)	Fig. 9-9(c)	
	MAC (with seat)	N/A	N/A	0.98	0.96	

[a] N/A means 'not applicable'.

9.5 Conclusion

In this chapter, a kind of double-unit train seat model, double-unit-seat-one-subject model and double-unit-seat-two-subject model were developed and calibrated, and the transmissibilities calculated with those models showed good consistency with the transmissibilities measured in the laboratory experiment. These models were applicable to dynamic analysis of the train seat with occupants under combined lateral, vertical and roll vibrations of different magnitudes. The models may potentially be suitable for different backrest inclinations that were also taken into account in the modelling of the human body and the seat. Modal analysis revealed that two modes around 15 Hz and 27 Hz of the seat contributed to the peaks with approximate frequencies in the seat transmissibilities. The modal shape of the former was dominated by the lateral and roll motions of two seat pans and backrests moving in phase, while the modal shape of the latter was mainly the lateral and roll motions of the two backrests moving in phase one minute and out of phase the next. The seated subjects exhibited a tendency of increasing the damping of these two modes, so the peaks of the transmissibilities corresponding to these two modes got reduced and flatter with the increase of subject number. In addition, the primary peak around 5 Hz in the vertical transmissibility on the seat pan arose from a whole-body vertical mode of the human body with a little higher modal frequency because the coupling of the human body with the seat reduced the modal

frequency and modal damping of this human mode slightly. The human-seat models are going to be adopted for the prediction of the vibration transmitted to the passengers on rail vehicles in the following chapter.

Chapter 10 Analysis of ride comfort of a high-speed train based on a coupled track-train-seat-human model with lateral, vertical and roll vibrations

10.1 Introduction

Ride comfort is one of the most important performance indexes of trains, affecting the well-being of the passengers during travel by train (Iwnicki, 2006). It is well-known that human sensation shows different sensitivities to vibrations in different directions and at different frequencies (Griffin, 1990), according to which the vibration directions and frequency range to be taken into account can be determined. Most studies have been focused on the vibration in the vertical direction alone (Kargarnovin *et al.*, 2005; Zhou *et al.*, 2009; Sun *et al.*, 2014), because the vertical direction is the most important direction concerning ride comfort. In recent years, researchers started investigating the ride comfort under multi-axis vibrations, e.g. lateral, vertical and roll vibration (Zhang *et al.*, 2013), because of the non-negligible contribution from other vibrations (lateral and roll) in a complex vibration environment. The main frequency range under consideration concerning ride comfort is usually 0.5-20 Hz (Popp *et al.*, 1999), because human body is not sensitive to vibrations over 20 Hz (ISO, 1997), especially in lateral and roll directions.

The traditional railway vehicle dynamics is usually focused on the dynamics of the vehicle by considering the track structure as rigid (Garg and Dukkipati, 1984; Wickens, 2003). In fact, the track is an elastic structure whose vibration can be transmitted to the vehicle via the wheel-rail contact and suspensions in both lateral and vertical directions (Zhai *et al.*, 2009). The track flexibility has much more influence on the dynamics of the carbody in the high-frequency range than in the low-frequency one. In the vertical direction, Lu *et al*. (2008) reported that track flexibility played a minor role in the dynamic response of the carbody in 0.5-10 Hz by comparing a flexible track with a traditional rigid track, and a wider frequency range of 0.5-25 Hz was reported by Cheli and Corradi (2011). In the lateral direction, Zhai *et al.* (2009) and Di Gialleonardo *et al.* (2012) found the lateral wheel-rail forces did not show much difference below 20 Hz by comparing an elastic track model with a rigid track model. What the effect of track flexibility on the dynamics of the carbody in the lateral and roll directions is has rarely been studied. As the increase of train speed, the dynamic interaction between the vehicle and track becomes intensified, and it seems necessary to

systematically investigate the dynamics of a vehicle from the perspective of an entire vehicle–track system.

Because of the lightweight technology and the increasing speed, many flexible modes of the carbody lie in the sensitive frequency range of the human body and become more easily excited by the wheel-rail interaction, which worsens the ride comfort. For the theoretical studies of the elastic vibration of carbody in the vertical direction, the carbody was frequently approximated as a beam (Zhou *et al.*, 2009; Cheli and Corradi, 2011; Sun *et al.*, 2014; Cao *et al.*, 2015). And the first bending mode was widely recognized as the primary mode affecting ride comfort (Diana *et al.*, 2002; Zhou *et al.*, 2009). Nevertheless, some research showed some more complicated modal shapes of carbody (torsional, breathing modes) than what a simple beam model can reflect (Carlbom, 2000, 2001; Carlbom and Berg, 2002), and such modes were thought to worsen ride comfort, which requires to treat the carbody as a three-dimensional (3D) structure. The finite element (FE) models were commonly used for the analysis of 3D dynamic vibration of the carbody (Ling *et al.*, 2018), however, the FE model with a great number of DOFs requires huge computational capacity and long calculational time. In addition, it is not easy for the FE model to precisely predict the vibration of an actual carbody even if the detailed information of the train is available. What is more, modifying an FE carbody model for another carbody is not an easy task (Tomioka *et al.*, 2006). Therefore, 3D analytical carbody model can be seen as an alternative considering the disadvantages of the FE model. Tomioka *et al.* (2003) and Tomioka *et al.* (2006) adopted an analytical approach for 3D elastic vertical vibration of carbody. The carbody was modeled as a box-type structure with interconnected plates and beams, the modal frequencies, modal shapes and the power spectra of which agreed well with the experiment in the range of 0.5-20 Hz. However, the existing models are only applicable to vertical vibration. For studying the dynamics of the carbody with multi-axis vibrations including vertical vibration, 3D analytical carbody models that can reflect its elastic vibrations in the lateral, vertical and roll directions have rarely been seen.

Most studies concerning ride comfort of vehicles have so far ignored the human-seat system by evaluating the ride comfort using the acceleration measured on the seat base directly for simplicity (Zhou *et al.*, 2009). However, a train seat has the potential to modify the vibration transmitted to the seated subjects, and the coupling of many seats with occupants with the carbody may have a significant effect on the dynamics of the carbody, so systematically investigating the ride comfort from the perspective of an entire track-train-seat-human system becomes necessary (Carlbom and Berg, 2002; Kumar *et al.*, 2017).

In this chapter, a 3D analytical track-train-seat-human model with a flexible carbody that can reflect its vertical, lateral and roll motions was developed. The main purpose was to study the influence of

train speed, carbody damping, suspension parameters and seat position on ride comfort as well as the proportion of different vibration positions and directions in the overall ride comfort index with the help of this model. In addition, the contribution of the rigid and flexible modes to the ride comfort was also defined and studied.

10.2 The modelling of flexible carbody

For reflecting the elastic vibration of the carbody in the lateral, vertical and roll directions, a 3D analytical modelling approach was adopted. The 3D analytical carbody was modelled as a box structure consisting of six elastic plates, as shown in Fig. 10-1, standing for the roof, floor, the right and left sidewalls, as well as the front and rear sidewalls. All the six plates can have both out-of-plane and in-plane vibrations, as shown in Fig. 10-2. To realize a box structure, the six plates were interconnected by large artificial springs (Yuan, 1992). The carbody model was to be developed by Lagrange's method.

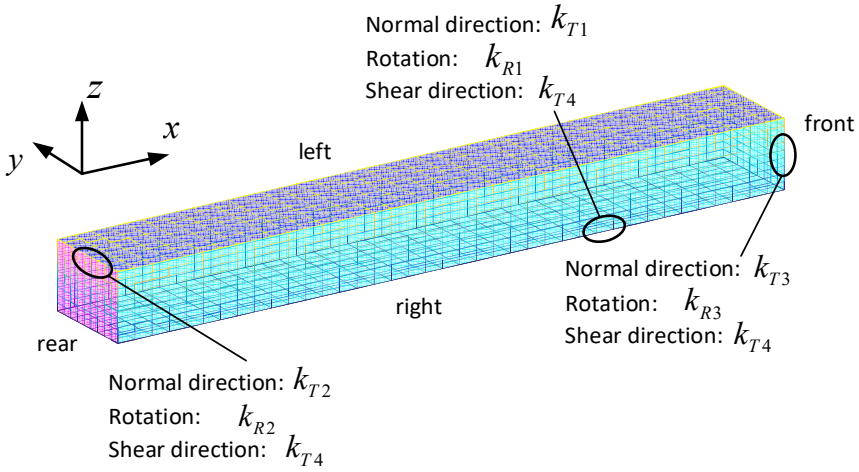

Fig. 10-1 The multi-plate carbody model (k_{Tj} ($j=1,2,3,4$) and k_{Rk} ($k=1,2,3$) are the artificial springs)

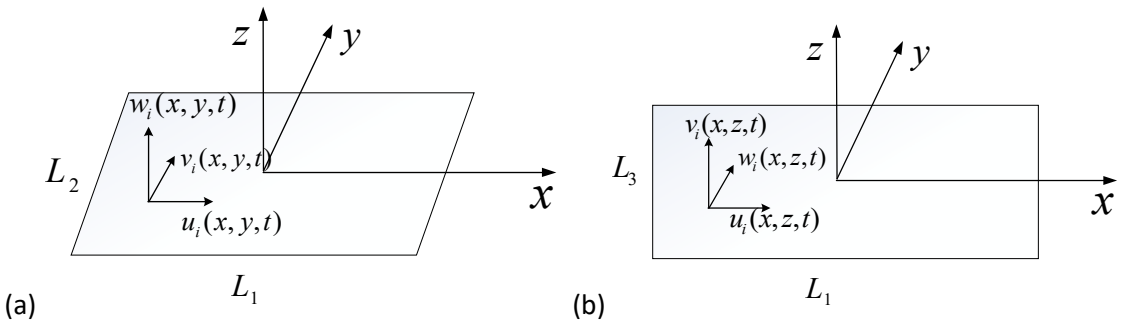

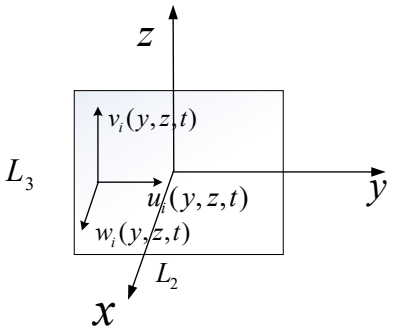

(c)

Fig. 10-2 The detailed displacements of the six plates (a) floor and roof ($i = d$, for floor; $i = u$, for roof); (b) right and left sidewalls ($i = r$, for right plate; $i = l$, for left plate); (c) front and rear sidewalls ($i = f$, for front plate; $i = b$, for rear plate).

10.2.1 The generation of trial functions

The rate of convergence and the accuracy of the analytical model depend on the trial functions used in the series representing the deflection of every plate. There are many choices of trial functions for the plate, such as the products of characteristic beam functions. Here, orthogonal polynomials were adopted for the generation of trial functions, which was first introduced by Bhat (1985). Once the starting polynomial satisfying the geometrical (or natural) boundary condition was selected, the subsequent polynomials were easy to be generated through the Gram-Schmidt orthogonalization process. Finally, all the polynomials were normalized. The trial functions of a plate could be expressed as the product of two normalized polynomials in two directions satisfying their own boundary conditions.

First, given a starting polynomial $\Phi_1(x)$ that at least satisfies the geometrical boundary conditions as

$$\Phi_1(x) = \prod_{n=1}^{2} \varphi_n(x) \tag{10-1}$$

where $\varphi_n(x)$ is the polynomial satisfying the boundary condition of one of the two edges. At edge $x = a$, it is given by: $\varphi_n(x) = x - a$ for simply supported edges; $\varphi_n(x) = (x-a)^2$, for clamped edges; $\varphi_n(x) = 1$, for free edges.

Then a set of orthogonal polynomials in the interval of the length can be generated by using the Gram-Schmidt orthogonalization process as follows:

$$\Phi_2(x) = (x - b_2)\Phi_1(x) \tag{10-2}$$

$$\Phi_k(x) = (x - b_k)\Phi_{k-1}(x) - c_k\Phi_{k-2}(x) \ (k \geq 3) \tag{10-3}$$

where the coefficients are given by $b_k = \dfrac{\int_L x\Phi_{k-1}(x)\Phi_{k-1}(x)\mathrm{d}x}{\int_L \Phi_{k-1}(x)\Phi_{k-1}(x)\mathrm{d}x}$,

$$c_k = \frac{\int_L x\Phi_{k-1}(x)\Phi_{k-2}(x)\mathrm{d}x}{\int_L \Phi_{k-2}(x)\Phi_{k-2}(x)\mathrm{d}x} = \frac{\int_L \Phi_{k-1}(x)\Phi_{k-1}(x)\mathrm{d}x}{\int_L \Phi_{k-2}(x)\Phi_{k-2}(x)\mathrm{d}x}.$$

Then these following polynomials satisfy the (geometrical) boundary conditions naturally.

Finally, all the polynomials are normalized as

$$\hat{\Phi}_n(x) = \frac{\Phi_n(x)}{\sqrt{\int_L \Phi_n^2(x)\mathrm{d}x}}, \ n = 1, 2, \ldots \tag{10-4}$$

All the trial functions of every plate were generated by the product of these normalized polynomials in two directions.

10.2.2 Development of the multi-plate carbody model

The kinetic energy and strain energy stored in the plates and the strain energy of the connection were calculated first, then the motion equations of the carbody model were derived by Lagrange's method.

For the floor and roof (Fig. 10-2(a)), the kinetic energy (T_k) and strain energy (U_k) of the out-of-plane motions ($k = u$, for the roof; $k = d$, for the floor) stored in the plates were

$$T_k = \frac{1}{2}\rho_k h_k \int_{-L_1/2}^{L_1/2}\int_{-L_2/2}^{L_2/2} \dot{w}_k^2 \mathrm{d}y\mathrm{d}x \tag{10-5}$$

$$U_k = \frac{D_k}{2}\int_{-L_1/2}^{L_1/2}\int_{-L_2/2}^{L_2/2}[(\frac{\partial^2 w_k}{\partial x^2})^2 + (\frac{\partial^2 w_k}{\partial y^2})^2 + 2\mu_k \frac{\partial^2 w_k}{\partial x^2}\frac{\partial^2 w_k}{\partial y^2} + 2(1-\mu_k)(\frac{\partial^2 w_k}{\partial x \partial y})^2]\mathrm{d}y\mathrm{d}x \tag{10-6}$$

where w_k is the out-of-plane displacement of the plates, and the dot (.) over the symbol denotes the derivative with respect to time; D_k is the flexural rigidity, μ_k is the Poisson ratio, ρ_k is the density, and h_k is the thickness of the plates.

The out-of-plane displacements were assumed to be the summation of the product of the trial functions and generalized coordinates as

$$w_k(x,y,t) = \sum_{m=1}^{{}^kN_1} \sum_{n=1}^{{}^kN_2} {}^k q_{mn}(t)\, {}^k X_m(x)\, {}^k Y_n(y) \tag{10-7}$$

where ${}^k X_m(x)$ and ${}^k Y_n(y)$ are the normalized orthogonal polynomials generated by the above-mentioned method satisfying the 'free-free' boundary condition, ${}^kN_1$ and ${}^kN_2$ are the numbers of the polynomials used, and ${}^k q_{mn}(t)$ is the generalized coordinate.

Substituting Eq. (10-7) into Eq. (10-5) and Eq. (10-6), and defining ${}^k E_{mi}^{(I,J)} = \int_{-L_1/2}^{L_1/2} {}^k X_m^{(I)}(x)\, {}^k X_i^{(J)}(x)\mathrm{d}x$, ${}^k F_{nj}^{(I,J)} = \int_{-L_2/2}^{L_2/2} {}^k Y_n^{(I)}(y)\, {}^k Y_j^{(J)}(y)\mathrm{d}y$, where the superscript (I) means I[th] derivative with respect to the coordinate, then the energies were simplified as

$$T_k = \frac{1}{2}\rho_k h_k \sum_{m=1}^{{}^kN_1} \sum_{n=1}^{{}^kN_2} {}^k \dot{q}_{mn}^2(t) \tag{10-8}$$

$$U_k = \frac{D_k}{2} \sum_{m=1}^{{}^kN_1} \sum_{n=1}^{{}^kN_2} \sum_{i=1}^{{}^kN_1} \sum_{j=1}^{{}^kN_2} {}^k q_{mn}(t)\, {}^k q_{ij}(t) [{}^k E_{mi}^{(2,2)}\, {}^k F_{nj}^{(0,0)} + {}^k E_{mi}^{(0,0)}\, {}^k F_{nj}^{(2,2)} + \mu_k ({}^k E_{mi}^{(2,0)}\, {}^k F_{nj}^{(0,2)} + {}^k E_{mi}^{(0,2)}\, {}^k F_{nj}^{(2,0)}) + 2(1-\mu_k)\, {}^k E_{mi}^{(1,1)}\, {}^k F_{nj}^{(1,1)}] \tag{10-9}$$

On the other hand, the kinetic energy ${}^{in}T_k$ and strain energy ${}^{in}U_k$ of the in-plane vibrations stored in the plates were

$${}^{in}T_k = \frac{1}{2}\rho_k h_k \int_{-L_1/2}^{L_1/2} \int_{-L_2/2}^{L_2/2} (\dot{u}_k^{\,2} + \dot{v}_k^{\,2}) \mathrm{d}y \mathrm{d}x \tag{10-10}$$

$${}^{in}U_k = \frac{E_k h_k}{2(1-\mu_k^{\,2})} \int_{-L_1/2}^{L_1/2} \int_{-L_2/2}^{L_2/2} [(\frac{\partial u_k}{\partial x})^2 + (\frac{\partial v_k}{\partial y})^2 + 2\mu_k \frac{\partial u_k}{\partial x} \frac{\partial v_k}{\partial y} + \frac{1-\mu_k}{2} (\frac{\partial u_k}{\partial y} + \frac{\partial v_k}{\partial x})^2] \mathrm{d}y \mathrm{d}x \tag{10-11}$$

where u_k and v_k are the in-plane displacements of the plates, as shown in Fig. 10-2(a).

In a similar way, the in-plane displacements were assumed to be the summation of the product of the trial functions and generalized coordinates as

$$\begin{cases} u_k(x,y,t) = \sum_{m=1}^{{}^kN_3}\sum_{n=1}^{{}^kN_4} {}^k p_{mn}(t)\,{}^kU_{1m}(x)\,{}^kU_{2n}(y) \\ v_k(x,y,t) = \sum_{m=1}^{{}^kN_5}\sum_{n=1}^{{}^kN_6} {}^k g_{mn}(t)\,{}^kV_{1m}(x)\,{}^kV_{2n}(y) \end{cases} \tag{10-12}$$

where ${}^kU_{1m}(x)$ and ${}^kU_{2n}(y)$ as well as ${}^kV_{1m}(x)$ and ${}^kV_{2n}(y)$ are two pairs of normalized orthogonal polynomials generated by the above-mentioned method satisfying the 'free-free' boundary condition.

By substituting Eq. (10-12) into Eq. (10-10)-(10-11) and defining

${}^kE_{1mi}^{(I,J)} = \int_{-L_1/2}^{L_1/2} {}^kU_{1m}^{(I)}(x)\,{}^kU_{1i}^{(J)}(x)\mathrm{d}x$, ${}^kF_{1nj}^{(I,J)} = \int_{-L_2/2}^{L_2/2} {}^kU_{2n}^{(I)}(y)\,{}^kU_{2j}^{(J)}(y)\mathrm{d}y$ and

${}^kE_{2mi}^{(I,J)} = \int_{-L_1/2}^{L_1/2} {}^kV_{1m}^{(I)}(x)\,{}^kV_{1i}^{(J)}(x)\mathrm{d}x$, ${}^kF_{2nj}^{(I,J)} = \int_{-L_2/2}^{L_2/2} {}^kV_{2n}^{(I)}(y)\,{}^kV_{2j}^{(J)}(y)\mathrm{d}y$ as well as

${}^kE_{3mi}^{(I,J)} = \int_{-L_1/2}^{L_1/2} {}^kV_{1m}^{(I)}(x)\,{}^kU_{1i}^{(J)}(x)\mathrm{d}x$, ${}^kF_{3nj}^{(I,J)} = \int_{-L_2/2}^{L_2/2} {}^kV_{2n}^{(I)}(y)\,{}^kU_{2j}^{(J)}(y)\mathrm{d}y$, the energies were simplified as

$${}^{in}T_k = \frac{1}{2}\rho_k h_k \left(\sum_{m=1}^{{}^kN_3}\sum_{n=1}^{{}^kN_4} {}^k\dot{p}_{mn}^2 + \sum_{m=1}^{{}^kN_5}\sum_{n=1}^{{}^kN_6} {}^k\dot{g}_{mn}^2\right) \tag{10-13}$$

$$\begin{aligned} {}^{in}U_k = {} & \frac{E_k h_k}{2(1-{\mu_k}^2)}\Bigg[\sum_{m=1}^{{}^kN_3}\sum_{n=1}^{{}^kN_4}\sum_{i=1}^{{}^kN_3}\sum_{j=1}^{{}^kN_4} {}^k p_{mn}(t)\,{}^k p_{ij}(t)\left({}^kE_{1mi}^{(1,1)}\,{}^kF_{1nj}^{(0,0)} + \frac{1-\mu_k}{2}\,{}^kE_{1mi}^{(0,0)}\,{}^kF_{1nj}^{(1,1)}\right) \\ & + \sum_{m=1}^{{}^kN_5}\sum_{n=1}^{{}^kN_6}\sum_{i=1}^{{}^kN_5}\sum_{j=1}^{{}^kN_6} {}^k g_{mn}(t)\,{}^k g_{ij}(t)\left({}^kE_{2mi}^{(0,0)}\,{}^kF_{2nj}^{(1,1)} + \frac{1-\mu_k}{2}\,{}^kE_{2mi}^{(1,1)}\,{}^kF_{2nj}^{(0,0)}\right) \\ & + 2\sum_{m=1}^{{}^kN_5}\sum_{n=1}^{{}^kN_6}\sum_{i=1}^{{}^kN_3}\sum_{j=1}^{{}^kN_4} {}^k g_{mn}(t)\,{}^k p_{ij}(t)\left({}^kE_{3mi}^{(0,1)}\,{}^kF_{3nj}^{(1,0)}\mu_k + \frac{1-\mu_k}{2}\,{}^kE_{3mi}^{(1,0)}\,{}^kF_{3nj}^{(0,1)}\right)\Bigg] \end{aligned} \tag{10-14}$$

The in-plane and out-of-plane kinetic energy and strain energy of the left, right, front and rear plates could be obtained in the same way, but the left superscript or right subscript 'k' should be modified as: $k = r$, for the right plate; $k = l$, for the left plate; $k = f$, for the front plate; $k = b$, for the rear plate. The range of integral should be modified according to Fig. 10-2(b)(c).

The connection between two plates was realized by adopting artificial springs at the joints, as shown in Fig. 10-1. At all the 12 edges, the out-of-plane displacement of one plate was connected

with the in-plane displacement of the other by k_{Tj} ($j=1,2,3$). To keep two connected plates at every connection edge perpendicular, the rotational angles of two plates along the edge were connected by k_{Rj} ($j=1,2,3$). The in-plane shear displacements of two plates at the connection edge were connected by k_{T4} . The connection stiffness at the four edges in the same direction was assumed the same. When the stiffness of artificial springs was large enough, the result would converge.

For example, the strain energy of the connection between the roof and the right plate was

$$U_{c1}=\frac{1}{2}k_{T1}\int_{-L_1/2}^{L_1/2}(w_u(x,-\frac{L_2}{2},t)-v_r(x,\frac{L_3}{2},t))^2\mathrm{d}x+\frac{1}{2}k_{T1}\int_{-L_1/2}^{L_1/2}(w_r(x,\frac{L_3}{2},t)-v_u(x,-\frac{L_2}{2},t))^2\mathrm{d}x$$
$$+\frac{1}{2}k_{R1}\int_{-L_1/2}^{L_1/2}(\frac{\partial w_u(x,-\frac{L_2}{2},t)}{\partial y}+\frac{\partial w_r(x,\frac{L_3}{2},t)}{\partial z})^2\mathrm{d}x+\frac{1}{2}k_{T4}\int_{-L_1/2}^{L_1/2}(u_r(x,\frac{L_3}{2},t)-u_u(x,-\frac{L_2}{2},t))^2\mathrm{d}x \tag{10-15}$$

In the same way, the strain energies at the other 11 edges could be calculated as U_{cj} ($j=2,3,\cdots,12$).

The total kinetic and strain energies of the multi-plate model were respectively

$$T_{mp}=\sum_{k=u,d,r,l,f,b}(T_k+{}^{in}T_k) \tag{10-16}$$

$$U_{mp}=\sum_{k=u,d,r,l,f,b}(U_k+{}^{in}U_k)+\sum_{j=1}^{12}U_{cj} \tag{10-17}$$

Define the coordinate vectors as

$$\mathbf{q}_{mp}=\left\{{}^{u}\mathbf{q}\quad {}^{d}\mathbf{q}\quad {}^{r}\mathbf{q}\quad {}^{r}\mathbf{p}\quad {}^{r}\mathbf{g}\quad {}^{l}\mathbf{q}\quad {}^{l}\mathbf{p}\quad {}^{l}\mathbf{g}\quad {}^{f}\mathbf{q}\quad {}^{f}\mathbf{p}\quad {}^{f}\mathbf{g}\quad {}^{b}\mathbf{q}\quad {}^{b}\mathbf{p}\quad {}^{b}\mathbf{g}\quad {}^{u}\mathbf{p}\quad {}^{u}\mathbf{g}\quad {}^{d}\mathbf{p}\quad {}^{d}\mathbf{g}\right\}^{\mathrm{T}}$$

where ${}^{k}\mathbf{q}=\left[{}^{k}q_{mn}\right]$, $m=1,2,...,{}^{k}N_1$, $n=1,2,...,{}^{k}N_2$; ${}^{k}\mathbf{p}=\left[{}^{k}p_{mn}\right]$, $m=1,2,...,{}^{k}N_3$, $n=1,2,...,{}^{k}N_4$; ${}^{k}\mathbf{g}=\left[{}^{k}g_{mn}\right]$, $m=1,2,...,{}^{k}N_5$, $n=1,2,...,{}^{k}N_6$; $k=u,d,l,r,f,b$; $\left[{}^{k}q_{mn}\right]$, $\left[{}^{k}p_{mn}\right]$ and $\left[{}^{k}g_{mn}\right]$ stand for vectors including all the coordinates of ${}^{k}q_{mn}$, ${}^{k}p_{mn}$ and ${}^{k}g_{mn}$, respectively, first ranking in ascending order of n , then in ascending order of m .

Then substituting Eq. (10-16)-(10-17) into the following Lagrange's equation

$$\frac{\mathrm{d}}{\mathrm{d}t}\left(\frac{\partial T_{mp}}{\partial \dot{\mathbf{q}}_{mp}}\right)-\frac{\partial T_{mp}}{\partial \mathbf{q}_{mp}}+\frac{\partial U_{mp}}{\partial \mathbf{q}_{mp}}=\mathbf{0} \tag{10-18}$$

It was easy to derive the motion equations in matrix form as

$$\mathbf{M}_{mp}\ddot{\mathbf{q}}_{mp}+\mathbf{K}_{mp}\mathbf{q}_{mp}=\mathbf{0} \tag{10-19}$$

where $\mathbf{M}_{mp}$ and $\mathbf{K}_{mp}$ are the mass and stiffness matrices of the multi-plate carbody model, respectively.

The modal analysis of the carbody was conducted by assuming

$$\mathbf{q}_{mp}=\mathbf{Q}_{mp}e^{\mathrm{j}\omega t} \tag{10-20}$$

where $\mathbf{Q}_{mp}$ is the modal vector, ω is the natural circular modal frequency.

The determination of the material properties and the thicknesses was completed by minimizing the error of modal frequencies and modal shapes between the model and the experiment adopted from Tomioka *et al.* (2003) by the optimization algorithm introduced in Section 3.3. The error function was defined as

$$\text{error}=\sum_{i=1}^{6}(f_i-f_{ei})^2-k_M\sum_{i=1}^{6}\text{MAC}_i \tag{10-21}$$

where $k_M>0$ is the weighting factor; f_i is the i$^{\text{th}}$ modal frequency of the carbody model, while f_{ei} is the i$^{\text{th}}$ experimental modal frequency of the carbody, MAC_i is the MAC value between the i$^{\text{th}}$ modal vector of the model and i$^{\text{th}}$ one of the experiment, defined as

$$\text{MAC}_i=\frac{(\mathbf{Q}_{mpi}^{\mathrm{T}}\mathbf{Q}_{ei})^2}{(\mathbf{Q}_{mpi}^{\mathrm{T}}\mathbf{Q}_{mpi})(\mathbf{Q}_{ei}^{\mathrm{T}}\mathbf{Q}_{ei})} \tag{10-22}$$

where $\mathbf{Q}_{mpi}$ and $\mathbf{Q}_{ei}$ are the i$^{\text{th}}$ modal vector for the multi-plate model and the experiment, respectively.

The multi-plate model had the same dimension as the carbody in the experiment. The obtained parameters of the multi-plate model were listed in Appendix H. The analytical model was also cross-checked with an FE model developed in ANSYS 17.1 that was made up of six plates using shell63 elements with the same material properties and thicknesses as the analytical model. The comparison of the modal analysis among the experiment, the analytical model and FE model was

shown in Table 10-1. Six extra modes that were calculated from the analytical model but not available in the experiment were illustrated in Table H-1 of Appendix H. It can be seen that all the modal frequencies and modal shapes of the analytical model were almost identical to the FE model, and both of them showed good agreement with the experiment. The maximum frequency difference between the analytical model and the experiment was about 0.6 Hz, indicating that the analytical model can be accepted for characterizing the elastic vibration of the carbody.

Table 10-1 The comparison among the analytical carbody model, the FE model and the experiment

Mode	Experiment (Tomioka *et al.*, 2003)	Analytical model	FE model
1 First torsional mode	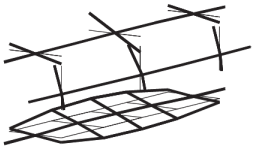 8.87 Hz	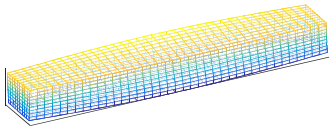 8.82 Hz	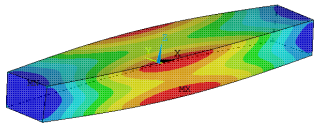 8.82 Hz
2 First vertical bending mode	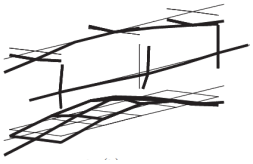 10.15 Hz	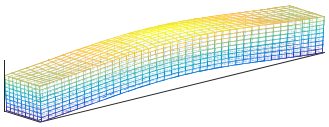 10.14 Hz	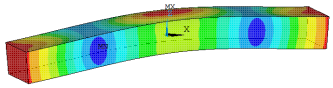 10.14 Hz
3 Second breathing mode	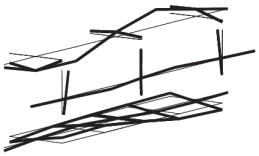 14.15 Hz	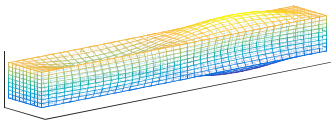 14.76 Hz	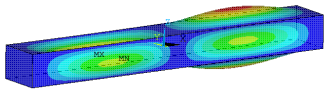 14.75 Hz
4 Second vertical bending mode	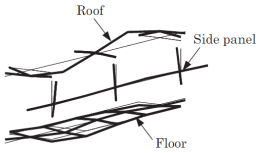 15.44 Hz	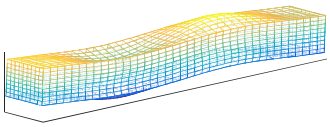 15.66 Hz	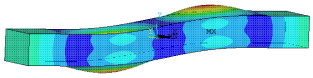 15.65 Hz
5 Third breathing mode	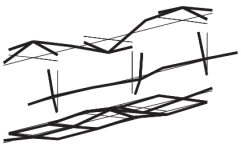 16.59 Hz	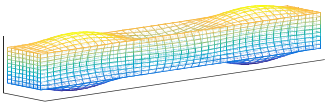 16.05 Hz	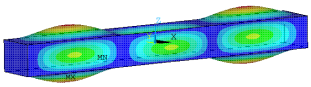 16.04 Hz
6 Third vertical bending mode	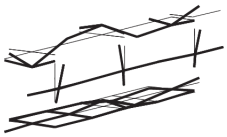 18.81 Hz	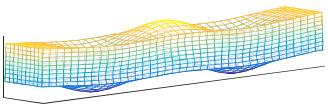 18.63 Hz	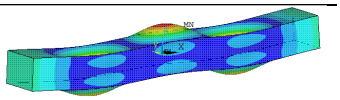 18.62 Hz

10.2.3 Modal summation method

Because the analytical multi-plate carbody model had thousands of degrees-of-freedom, in order to reduce the computational effort, the model was simplified by extracting these 12 useful modes

introduced in Section 10.2.2 by means of the modal summation method. The mode set that was considered in the calculation was assumed as A_s with the total number of N_{A_s}.

The transient displacement vector was expressed as the linear combination of the modal vectors as

$$\mathbf{q}_{mp}(t)=\sum_{i\in A_s}\bar{\mathbf{Q}}_{mpi}p_{si}(t)=\begin{bmatrix}\bar{\mathbf{Q}}_{mp1} & \bar{\mathbf{Q}}_{mp2} & \cdots & \bar{\mathbf{Q}}_{mpN_{A_s}}\end{bmatrix}\mathbf{p}_s \tag{10-23}$$

where $\bar{\mathbf{Q}}_{mpi}$ is the i[th] mass normalized modal vector of $\mathbf{Q}_{mp_i}$, $\mathbf{p}_s=\begin{bmatrix}p_{s1}(t) & p_{s2}(t) & \cdots & p_{sN_{A_s}}(t)\end{bmatrix}^{\mathrm{T}}$ is the modal coordinate vector.

Then the new mass matrix and stiffness matrix became

$$\mathbf{M}_s=\begin{bmatrix}\bar{\mathbf{Q}}_{mp1} & \bar{\mathbf{Q}}_{mp2} & \cdots & \bar{\mathbf{Q}}_{mpN_{A_s}}\end{bmatrix}^{\mathrm{T}}\mathbf{M}_{mp}\begin{bmatrix}\bar{\mathbf{Q}}_{mp1} & \bar{\mathbf{Q}}_{mp2} & \cdots & \bar{\mathbf{Q}}_{mpN_{A_s}}\end{bmatrix}=\mathbf{I} \tag{10-24}$$

$$\mathbf{K}_s=\begin{bmatrix}\bar{\mathbf{Q}}_{mp1} & \bar{\mathbf{Q}}_{mp2} & \cdots & \bar{\mathbf{Q}}_{mpN_{A_s}}\end{bmatrix}^{\mathrm{T}}\mathbf{K}_{mp}\begin{bmatrix}\bar{\mathbf{Q}}_{mp1} & \bar{\mathbf{Q}}_{mp2} & \cdots & \bar{\mathbf{Q}}_{mpN_{A_s}}\end{bmatrix}=\mathrm{diag}(\omega_i^2) \tag{10-25}$$

where $\omega_i=2\pi f_i$ is the i[th] circular modal frequency. The vertical displacement, lateral displacement and roll angle of the floor at any position due to the flexible modes of the carbody were expressed respectively as

$$\bar{d}_v(x,y,t)=\mathbf{C}_{fv}(x,y)\mathbf{p}_s(t) \tag{10-26}$$

$$\bar{d}_l(x,y,t)=\mathbf{C}_{fl}(x,y)\mathbf{p}_s(t) \tag{10-27}$$

$$\bar{d}_\theta(x,y,t)=\mathbf{C}_{f\theta}(x,y)\mathbf{p}_s(t) \tag{10-28}$$

where $\mathbf{C}_{fv}(x,y)=\begin{bmatrix}\underbrace{0 \quad \cdots \quad 0}_{{}^{u}N_1\times{}^{u}N_2} & [{}^{d}X_m(x){}^{d}Y_n(y)] & 0 & \cdots & 0\end{bmatrix}\begin{bmatrix}\bar{\mathbf{Q}}_{mp1} & \bar{\mathbf{Q}}_{mp2} & \cdots & \bar{\mathbf{Q}}_{mpN_{A_s}}\end{bmatrix}$,

$\mathbf{C}_{fl}(x,y)=\begin{bmatrix}0 & \cdots & 0 & [{}^{d}V_{1m}(x){}^{d}V_{2n}(y)]\end{bmatrix}\begin{bmatrix}\bar{\mathbf{Q}}_{mp1} & \bar{\mathbf{Q}}_{mp2} & \cdots & \bar{\mathbf{Q}}_{mpN_{A_s}}\end{bmatrix}$, and

$\mathbf{C}_{f\theta}(x,y)=\begin{bmatrix}\underbrace{0 \quad \cdots \quad 0}_{{}^{u}N_1\times{}^{u}N_2} & [{}^{d}X_m(x)\dfrac{\mathrm{d}\,{}^{d}Y_n(y)}{\mathrm{d}y}] & 0 & \cdots & 0\end{bmatrix}\begin{bmatrix}\bar{\mathbf{Q}}_{mp1} & \bar{\mathbf{Q}}_{mp2} & \cdots & \bar{\mathbf{Q}}_{mpN_{A_s}}\end{bmatrix}$;

$[{}^{d}X_m(x)\,{}^{d}Y_n(y)]$, $[{}^{d}V_{1m}(x)\,{}^{d}V_{2n}(y)]$ and $[{}^{d}X_m(x)\dfrac{\mathrm{d}\,{}^{d}Y_n(y)}{\mathrm{d}y}]$ stand for a vector including all the products of trial functions- ${}^{d}X_m(x)\,{}^{d}Y_n(y)$, ${}^{d}V_{1m}(x)\,{}^{d}V_{2n}(y)$ and ${}^{d}X_m(x)\dfrac{\mathrm{d}\,{}^{d}Y_n(y)}{\mathrm{d}y}$, respectively, first ranking in ascending order of n, then in ascending order of m.

After applying the modal summation method, the DOF of the multi-plate carbody model was greatly reduced.

10.3 Modelling of the track-train-seat-human system

The train was assumed to run at a constant speed of V on a tangent track that was made up of two rails, several sleepers and ballasts. For the convenience of demonstrating the method, there assumed two columns of human-seat systems evenly distributed on the carbody floor. The excitation from the track was alignment, vertical profile and cross level. The structure of the track-train-seat-human system model was illustrated in Fig. 10-3.

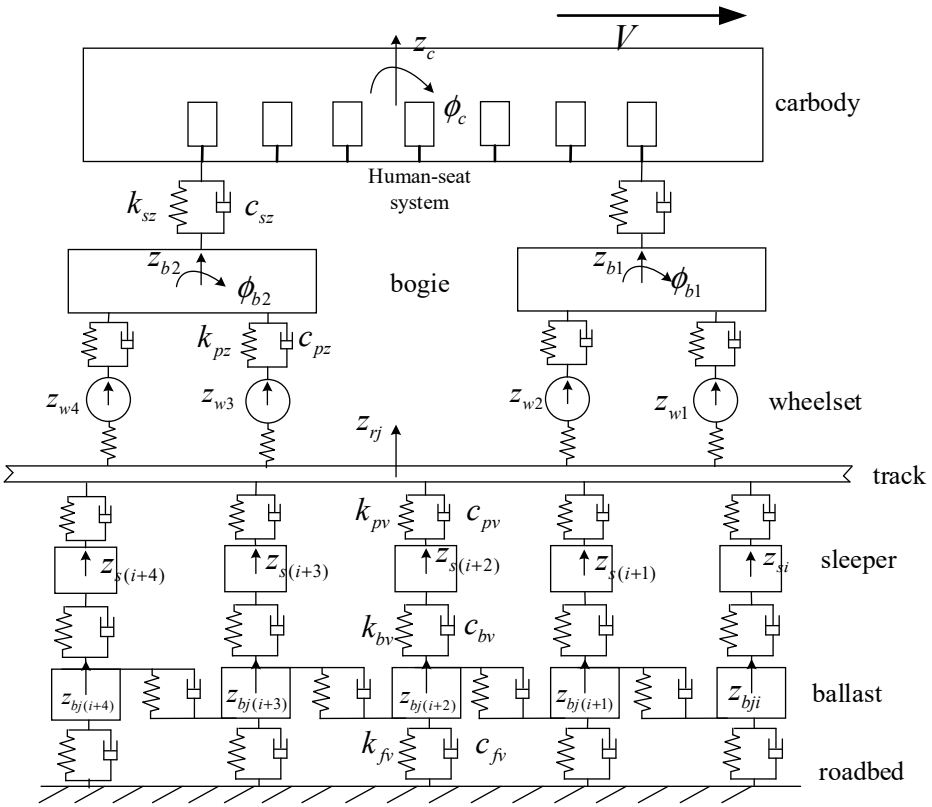

(a)

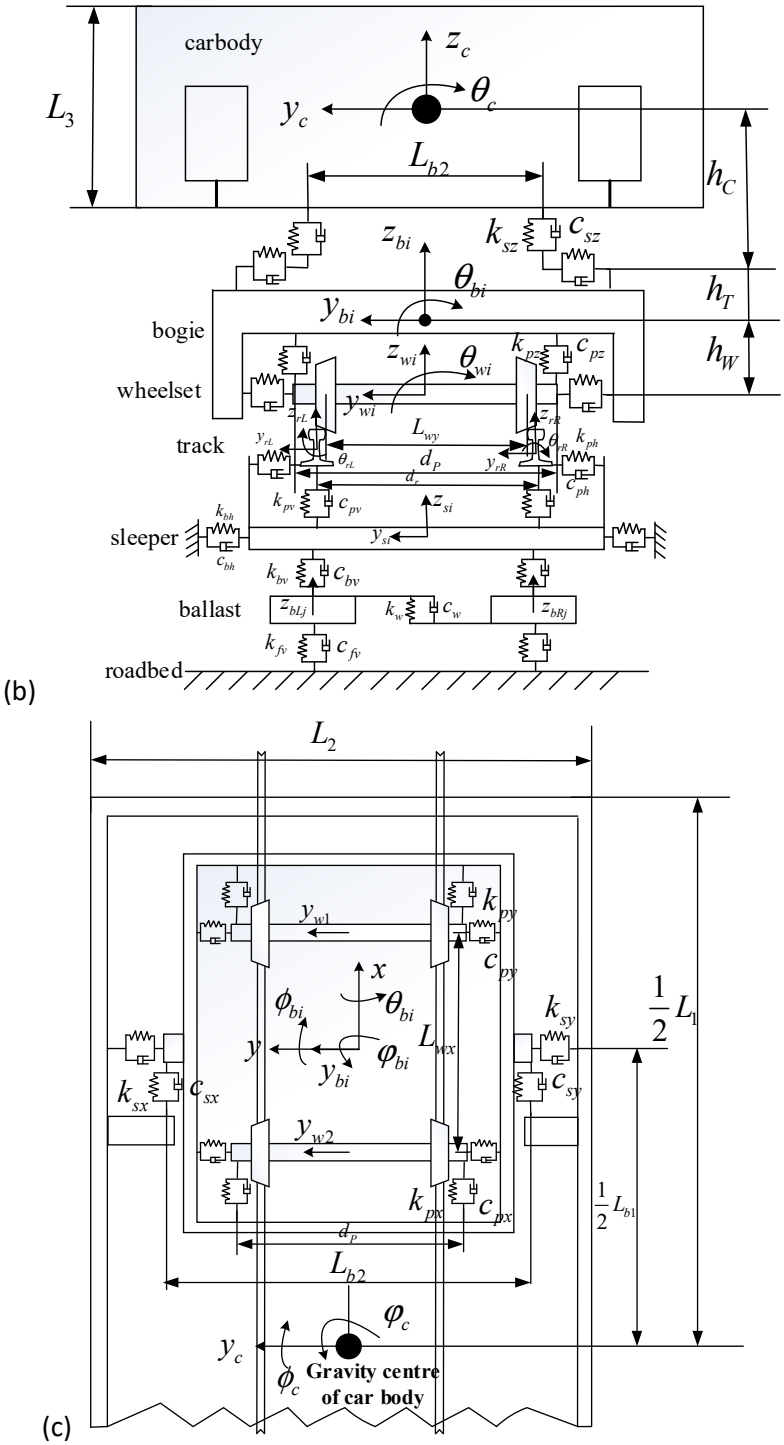

Fig. 10-3 The structure of the track-train-seat-human system (a) Side view; (b) Front view; (c) Top view.

10.3.1 Modelling of train subsystem

The train subsystem consisted of the carbody, two bogies and four wheelsets. For the carbody, in addition to the flexible modes, some rigid DOFs at its center of gravity, i.e. the vertical z_c, lateral y_c, roll θ_c, pitch ϕ_c and yaw φ_c, were also included. For the bogies, the vertical motion z_{bi}, the

lateral motion y_{bi}, the roll θ_{bi}, the pitch ϕ_{bi} and the yaw φ_{bi} (i=1, for the front bogie; i=2, for the rear bogie) at their centers of gravity were considered. The number of four wheelsets was denoted as 1 to 4 starting from the front to the rear. For every wheelset, the lateral motion y_{wi}, vertical motion z_{wi} and roll θ_{wi} ($i=1,...,4$) were taken into account. The fore-and-aft, vertical and lateral primary and second suspension systems were modelled as linear spring-damper units.

The total vertical, lateral and roll displacements of the carbody floor at any position were

$$d_v(x,y,t)=\overline{d}_v(x,y,t)+z_c+\theta_c y-\phi_c x \tag{10-29}$$

$$d_l(x,y,t)=\overline{d}_l(x,y,t)+y_c+\varphi_c x+\frac{1}{2}L_3\theta_c \tag{10-30}$$

$$d_\theta(x,y,t)=\frac{\partial d_v(x,y,t)}{\partial y}=\mathbf{C}_{f\theta}(x,y)\mathbf{p}_s(t)+\theta_c \tag{10-31}$$

The motion equations for the rigid body modes of carbody, front and rear bogies in lateral, vertical, roll, pitch and yaw directions were respectively,

$$m_j\ddot{y}_j=F_{syj} \tag{10-32}$$

$$m_j\ddot{z}_j=-m_j g+F_{szj} \tag{10-33}$$

$$I_{jx}\ddot{\theta}_j=M_{sxj} \tag{10-34}$$

$$I_{jy}\ddot{\phi}_j=M_{syj} \tag{10-35}$$

$$I_{jz}\ddot{\varphi}_j=M_{szj} \tag{10-36}$$

where $j=c$, for carbody; $j=b_1$, for the front bogie; $j=b_2$, for the rear bogie. F_{syj} and F_{szj} denote the suspension forces in the lateral and vertical directions, respectively. M_{sxj}, M_{syj} and M_{szj} denote the suspension moments in the roll, pitch and yaw directions, respectively. The expressions for the forces and moments were listed in Appendix H.

The damping of the flexible modes of carbody was assumed to be Rayleigh damping, so the damping matrix after modal summation was expressed as

$$\mathbf{C}_s=c_M\mathbf{M}_s+c_K\mathbf{K}_s \tag{10-37}$$

where c_M and c_K are constant coefficients.

The motion equation for the flexible body modes of the carbody was

$$\mathbf{M}_s\ddot{\mathbf{p}}_s + \mathbf{C}_s\dot{\mathbf{p}}_s + \mathbf{K}_s\mathbf{p}_s = \sum_{k=z,y}\left(\frac{\partial k_{fl}}{\partial \mathbf{p}_s}F_{kcb1l} + \frac{\partial k_{fr}}{\partial \mathbf{p}_s}F_{kcb1r} + \frac{\partial k_{bl}}{\partial \mathbf{p}_s}F_{kcb2l} + \frac{\partial k_{br}}{\partial \mathbf{p}_s}F_{kcb2r}\right) \quad (10\text{-}38)$$

where y , z and F with subscript represent the lateral and vertical displacements and suspension forces above the second suspensions, which were summarized in Table H-2 of Appendix H.

The motion equations of the j[th] wheelset (j=1,2,3,4) in the lateral, vertical and roll directions were respectively

$$m_w\ddot{y}_{wj} = F_{ywj} \quad (10\text{-}39)$$

$$m_w\ddot{z}_{wj} = F_{zwj} \quad (10\text{-}40)$$

$$I_{wx}\ddot{\theta}_{wj} = M_{xwj} \quad (10\text{-}41)$$

where F_{ywj} and F_{zwj} are the lateral and vertical forces between the bogies and the j[th] wheelsets, M_{xwj} is the moment between the bogies and the j[th] wheelsets in the roll direction, their expressions were listed in Appendix H.

10.3.2 Modelling of track subsystem

The track subsystem consisted of left and right tracks, several evenly distributed sleepers supporting the tracks, and ballasts under the sleepers, as shown in Fig. 10-3.

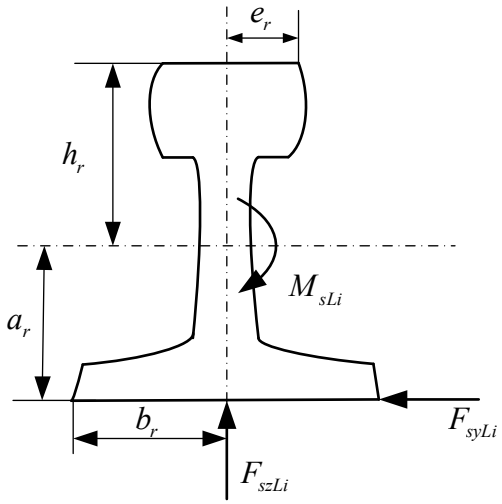

Fig. 10-4 The cross-section of the left track.

The left and right tracks were modelled by Euler-Bernoulli beams with two fixed ends for their vertical, lateral and torsional vibrations, and the cross-section of the left track was shown in Fig. 10-4. The vertical, lateral and torsional motion equations of the left track were respectively

$$E_r I_{ry} \frac{\partial^4 z_{rL}(x,t)}{\partial x^4} + m_r \frac{\partial^2 z_{rL}(x,t)}{\partial t^2} = \sum_{k=1}^{N_s} F_{szLk} \delta(x - x_{sk}) \tag{10-42}$$

$$E_r I_{rz} \frac{\partial^4 y_{rL}(x,t)}{\partial x^4} + m_r \frac{\partial^2 y_{rL}(x,t)}{\partial t^2} = \sum_{k=1}^{N_s} F_{syLk} \delta(x - x_{sk}) \tag{10-43}$$

$$-GK_r \frac{\partial^2 \theta_{rL}(x,t)}{\partial x^2} + \rho_r I_r \frac{\partial^2 \theta_{rL}(x,t)}{\partial t^2} = \sum_{k=1}^{N_s} M_{sLk} \delta(x - x_{sk}) \tag{10-44}$$

where $z_{rL}(x,t)$, $y_{rL}(x,t)$ and $\theta_{rL}(x,t)$ are the vertical, lateral and torsional displacements of the left rail at the coordinate *x* at the time *t*; N_s is the total number of sleepers; F_{szLk} and F_{syLk} are the vertical and lateral forces between the kth sleeper and the left track, respectively; M_{sLk} is the moment acting on the left rail due to the force F_{syLk}, so $M_{sLk} = a_r F_{syLk}$; x_{sk} is the *x* coordinate of the kth sleeper. The expressions were listed in Appendix H.

The above partial differential equations were transformed into ordinary differential equations in terms of generalized coordinates by modal summation method as follows.

$$\ddot{q}_{zrLi} + \frac{E_r I_{ry}}{m_r} \alpha_{ri}{}^4 q_{zrLi} = \sum_{k=1}^{N_s} F_{szLk} Z_{rLi}(x_{sk}) \tag{10-45}$$

$$\ddot{q}_{yrLi}+\frac{E_r I_{rz}}{m_r}\alpha_{ri}{}^4 q_{yrLi}=\sum_{k=1}^{N_s}F_{syLk}Y_{rLi}(x_{sk}) \tag{10-46}$$

$$\ddot{q}_{trLi}+\frac{GK_r}{\rho_r I_r}(\frac{i\pi}{l_r})^2 q_{trLi}=\sum_{k=1}^{N_s}M_{sLk}\Phi_{rLi}(x_{sk}) \tag{10-47}$$

where l_r is the calculated length of the rail, α_{ri} can be determined from $\alpha_{ri}l_r=\begin{cases}4.730, i=1\\(i+0.5)\pi, i\geq 2\end{cases}$, q_{zrLi}, q_{yrLi} and q_{trLi} are the i[th] generalized coordinates of the vertical, lateral and torsional modes, respectively; and the corresponding mass normalized vertical, lateral and torsional modal functions of the rail are respectively as follows:

$$Z_{rLi}(x)=\sqrt{\frac{1}{m_r l_r}}[\cosh\alpha_{ri}x-\cos\alpha_{ri}x-\frac{\sinh\alpha_{ri}l_r+\sin\alpha_{ri}l_r}{\cosh\alpha_{ri}l_r-\cos\alpha_{ri}l_r}(\sinh\alpha_{ri}x-\sin\alpha_{ri}x)] \tag{10-48}$$

$$Y_{rLi}(x)=\sqrt{\frac{1}{m_r l_r}}[\cosh\alpha_{ri}x-\cos\alpha_{ri}x-\frac{\sinh\alpha_{ri}l_r+\sin\alpha_{ri}l_r}{\cosh\alpha_{ri}l_r-\cos\alpha_{ri}l_r}(\sinh\alpha_{ri}x-\sin\alpha_{ri}x)] \tag{10-49}$$

$$\Phi_{rLi}(x)=\sqrt{\frac{2}{\rho_r I_r l_r}}\sin\frac{i\pi x}{l_r} \tag{10-50}$$

The vertical, lateral and torsional displacements of the rail were expressed by modal summation method respectively as

$$z_{rL}(x,t)=\sum_{k=1}^{N_{kv}}Z_{rLk}(x)q_{zrLk}(t) \tag{10-51}$$

$$y_{rL}(x,t)=\sum_{k=1}^{N_{kh}}Y_{rLk}(x)q_{yrLk}(t) \tag{10-52}$$

$$\theta_{rL}(x,t)=\sum_{k=1}^{N_{kt}}\Phi_{rLk}(x)q_{trLk}(t) \tag{10-53}$$

where N_{kv}, N_{kh} and N_{kt} are the total mode numbers selected for the vertical, lateral and torsional vibrations of the left rail, respectively.

The motion equations for the right rail could be obtained by replacing the subscript ‘L’ by ‘R’.

The sleeper was treated as Euler-Bernoulli beam with 'free-free' boundary condition in the vertical direction, but as lumped mass in the lateral direction. The equation for the vertical motion of the ith sleeper was expressed as

$$E_s I_s \frac{\partial^4 z_{si}(y,t)}{\partial y^4} + m_s \frac{\partial^2 z_{si}(y,t)}{\partial t^2} = -F_{szLi}(t)\delta(y - \frac{l_s}{2} - \frac{d_r}{2}) - F_{szRi}(t)\delta(y - \frac{l_s}{2} + \frac{d_r}{2}) - F_{bzLi}(y,t) - F_{bzRi}(y,t) \tag{10-54}$$

where $z_{si}(y,t)$ is the vertical displacement of the ith sleeper at the coordinate *y* at the time *t*; $F_{szLi}(t)$ ($F_{szRi}(t)$) is the vertical force between the ith sleeper and the left (right) rail; $F_{bzLi}(y,t)$ ($F_{bzRi}(y,t)$) denotes the vertical force between the ith sleeper and the left (right) ballast underneath the sleeper, which was considered as a distributed force over the whole length of the sleeper. The expressions for these forces were listed in Appendix H.

The vertical displacement of the ith sleeper was expressed by modal summation method as

$$z_{si}(y,t) = \sum_{j=1}^{N_{ks}} Z_{sj}(y) q_{sij}(t), i = 1,2,\cdots,N_s \tag{10-55}$$

where $q_{sij}(t)$ is the jth generalized coordinate for the ith sleeper, N_{ks} is the total number of modes selected for the calculation for every sleeper, and $Z_{sj}(y)$ is the jth mass normalized modal shape of the sleeper satisfying the 'free-free' boundary condition, which can be expressed as

$$Z_{sj}(y) = \begin{cases} \sqrt{\frac{1}{m_s l_s}}, j = 1 \\ \sqrt{\frac{3}{m_s l_s}}(1 - \frac{2y}{l_s}), j = 2 \\ \sqrt{\frac{1}{m_s l_s}}[(\cosh \alpha_k y + \cos \alpha_k y) - C_k(\sinh \alpha_k y + \sin \alpha_k y)], j \geq 3, k = j - 2 \end{cases} \tag{10-56}$$

where the coefficients α_k and C_k are governed by

$$C_k = \frac{\sinh \alpha_k l_s + \sin \alpha_k l_s}{\cosh \alpha_k l_s - \cos \alpha_k l_s} \tag{10-57}$$

$$\alpha_k l_s = \begin{cases} 4.730, k = 1 \\ (k + 0.5)\pi, k \geq 2 \end{cases} \tag{10-58}$$

Then, the partial differential equation (Eq. (10-54)) was transformed into ordinary differential equation in terms of generalized coordinates as

$$\begin{aligned} \ddot{q}_{sij} + \frac{E_s I_s}{m_s} \alpha_{j-2}^4 q_{sij} = & -F_{szLi} Z_{sj}(\frac{l_s}{2} + \frac{d_r}{2}) - F_{szRi} Z_{sj}(\frac{l_s}{2} - \frac{d_r}{2}) \\ & - \int_{l_s/2}^{l_s} F_{bzLi}(y,t) Z_{sj}(y) \mathrm{d}y - \int_0^{l_s/2} F_{bzRi}(y,t) Z_{sj}(y) \mathrm{d}y \end{aligned} \tag{10-59}$$

where $\alpha_{j-2} = 0$, for j=1,2.

The sleeper was simplified as a lumped mass for the lateral motion as

$$m_s l_s \ddot{y}_{si} = -F_{syLi} - F_{syRi} - F_{ysbi}, i = 1, 2, \cdots, N_s \tag{10-60}$$

where y_{si} is the lateral displacement of the i[th] sleeper; F_{syLi} (F_{syRi}) is the lateral force between the i[th] sleeper and the left (right) rail; F_{ysbi} is the lateral force between the i[th] sleeper and the ballasts. The expressions of these forces were listed in Appendix H.

The modelling of the ballasts can refer to Zhai *et al.* (2004), only the vertical rigid motion was considered. For the left and right ballasts under the i[th] sleeper, the motion equations were respectively

$$m_{ba} \ddot{z}_{bLi} = m_{ba} g + F_{zfLi} + F_{zrLi} + F_{zLRi} + F_{zgLi} + \int_{l_s/2}^{l_s} F_{bzLi}(y) \mathrm{d}y, i = 1, 2, \cdots, N_s \tag{10-61}$$

$$m_{ba} \ddot{z}_{bRi} = m_{ba} g + F_{zfRi} + F_{zrRi} - F_{zLRi} + F_{zgRi} + \int_0^{l_s/2} F_{bzRi}(y) \mathrm{d}y, i = 1, 2, \cdots, N_s \tag{10-62}$$

where z_{bLi} (z_{bRi}) is the vertical displacement of the left (right) ballast under the i[th] sleeper; F_{zfLi} (F_{zfRi}) is the vertical shear force between the left (right) i[th] and (i-1)[th] ballasts; F_{zrLi} (F_{zrRi}) is the vertical shear force between the left (right) i[th] and (i+1)[th] ballast; F_{zLRi} is the vertical shear force between the left i[th] and right i[th] ballasts; F_{zgLi} (F_{zgRi}) is the vertical force between the left (right) i[th] ballast and the roadbed. The expressions of these forces were listed in Appendix H.

10.3.3 Wheel-rail contact

The excitations from the track were the alignment, vertical profile and cross level of the track. The actual wheel-rail contact has strong nonlinearity, for sake of direct analysis in the frequency domain, the wheel-rail normal contact force was calculated by Hertzian contact theory with a linearized contact stiffness K_n (Nguyen *et al.*, 2009), and the tangential wheel-rail creep force was calculated by Kalker's linear creep theory. The spin creepage was ignored and the wheel-rail contact angles were assumed to be zero.

Thus, the strain energy of the contact between the wheelsets and the left rail in the normal direction was

$$U_{cL} = 0.5K_n \sum_{j=1}^{4} [z_{wj} + \frac{1}{2} L_{wy} \theta_{wj} - (z_{rL}(x_{wj},t) - e_r \theta_{rL}(x_{wj},t) + r_v(x_{wj},t) + \frac{1}{2} r_t(x_{wj},t))]^2 \tag{10-63}$$

The dissipation energy of the contact between the wheelsets and the left rail in the tangential direction was

$$D_{cL} = 0.5 \frac{f_{11}}{V} \sum_{j=1}^{4} [\dot{y}_{wj} + r_0 \dot{\theta}_{wj} - (\dot{y}_{rL}(x_{wj},t) - h_r \dot{\theta}_{rL}(x_{wj},t) + \dot{r}_a(x_{wj},t))]^2 \tag{10-64}$$

where $r_a(x_{wj},t)$, $r_v(x_{wj},t)$ and $r_t(x_{wj},t)$ are the alignment, vertical profile and cross level of the track acting on the j[th] wheelset at the position x_{wj} at the time *t*, f_{11} is the lateral creep coefficient. In the same way, the strain energy (U_{cR}) and dissipation energy (D_{cR}) of the contact between the wheelsets and the right rail were obtained and listed in Appendix H.

The moving irregularity model (Knothe and Grassie, 1993) was adopted, in which the wheelsets remained at the fixed positions on the track, while the irregularities were assumed to move backwards at the speed of the train between the wheel and rail.

The motion equations of the track-train system were then organized in matrix form as

$$\mathbf{M}_{tt}\ddot{\mathbf{y}}_{tt} + \mathbf{C}_{tt}\dot{\mathbf{y}}_{tt} + \mathbf{K}_{tt}\mathbf{y}_{tt} = \mathbf{K}_{ttr}\mathbf{r}_r + \mathbf{C}_{ttr}\dot{\mathbf{r}}_r \tag{10-65}$$

where $\mathbf{M}_{tt}$, $\mathbf{C}_{tt}$ and $\mathbf{K}_{tt}$ are the mass, damping and stiffness matrices of the track-train system, $\mathbf{y}_{tt}$ is the coordinate vector of the track-train system, $\mathbf{K}_{ttr}$ and $\mathbf{C}_{ttr}$ are respectively the stiffness

and damping matrices associated with the excitations from track irregularity, and $\mathbf{r}_r$ is the excitation vector of the track irregularity.

10.3.4 Coupling of human-seat systems with carbody

It was assumed there were two columns of double-unit-seat-one-subject systems uniformly distributed on the carbody floor, and the number of human-seat systems in one column was N_{hs}.

According to the motion equation of the double-unit-seat-one-subject system in Eq. (9-37), the equation of ith human-seat system was

$$\mathbf{M}_{shi}\ddot{\mathbf{X}}_{shi}+\mathbf{C}_{shi}\dot{\mathbf{X}}_{shi}+\mathbf{K}_{shi}\mathbf{X}_{shi}=\mathbf{K}_{shri}\mathbf{X}_{pri}+\mathbf{C}_{shri}\dot{\mathbf{X}}_{pri} \tag{10-66}$$

where $\mathbf{M}_{shi}$, $\mathbf{C}_{shi}$ and $\mathbf{K}_{shi}$ are the mass, damping and stiffness matrices of the ith double-unit-seat-one-subject system, and $\mathbf{X}_{shi}$ is the corresponding coordinate vector; $\mathbf{K}_{shri}$ and $\mathbf{C}_{shri}$ are the stiffness and damping matrices associated with the inputs of ith system, $\mathbf{X}_{pri}$ is the corresponding input displacement vector.

When the location of the excitation for ith system from the floor is (x_{fi}, y_{fi}), the excitation vector consisting of the displacement and the roll angle from the carbody floor can be denoted as $\mathbf{X}_{pri}=[d_l(x_{fi},y_{fi},t),d_v(x_{fi},y_{fi},t),d_\theta(x_{fi},y_{fi},t)]^{\mathrm{T}}$.

Then $\mathbf{X}_{pri}$ was expressed by the coordinate vector of the track-train system $\mathbf{y}_{tt}$ as

$$\mathbf{X}_{pri}=\left[\mathbf{C}_{Fl}(x_{fi},y_{fi})^{\mathrm{T}}\quad\mathbf{C}_{Fv}(x_{fi},y_{fi})^{\mathrm{T}}\quad\mathbf{C}_{F\theta}(x_{fi},y_{fi})^{\mathrm{T}}\right]^{\mathrm{T}}\mathbf{y}_{tt} \tag{10-67}$$

where $\mathbf{C}_{Fl}(x_{fi},y_{fi})=[\mathbf{C}_{fl}(x_{fi},y_{fi}),1,0,0.5L_3,0,x_{fi},\mathbf{O}]$, $\mathbf{C}_{Fv}(x_{fi},y_{fi})=[\mathbf{C}_{fv}(x_{fi},y_{fi}),0,1,y_{fi},-x_{fi},0,\mathbf{O}]$, and $\mathbf{C}_{F\theta}(x_{fi},y_{fi})=[\mathbf{C}_{f\theta}(x_{fi},y_{fi}),0,0,1,0,0,\mathbf{O}]$ are the coefficient vectors.

Then the equations for the ith human-seat system (Eq. (10-66)) became

$$\mathbf{M}_{shi}\ddot{\mathbf{X}}_{shi}+\mathbf{C}_{shi}\dot{\mathbf{X}}_{shi}+\mathbf{K}_{shi}\mathbf{X}_{shi}=\mathbf{K}_{sti}\mathbf{y}_{tt}+\mathbf{C}_{sti}\dot{\mathbf{y}}_{tt} \tag{10-68}$$

where $\mathbf{K}_{sti}$ and $\mathbf{C}_{sti}$ are the new stiffness and damping matrices associated with the excitation from the floor.

Because of the forces acting on the carbody floor from the N_{hs} human-seat systems, the motion equations of the track-train system then became

$$\begin{aligned}&\mathbf{M}_{tt}\ddot{\mathbf{y}}_{tt}+(\mathbf{C}_{tt}+\sum_{i=1}^{N_{hs}}\mathbf{C}_{tsi})\dot{\mathbf{y}}_{tt}+(\mathbf{K}_{tt}+\sum_{i=1}^{N_{hs}}\mathbf{K}_{tsi})\mathbf{y}_{tt}\\&=\mathbf{K}_{ttr}\mathbf{r}_r+\mathbf{C}_{ttr}\dot{\mathbf{r}}_r+\sum_{i=1}^{N_{hs}}(\mathbf{K}_{sti}^{\mathrm{T}}\mathbf{X}_{shi}+\mathbf{C}_{sti}^{\mathrm{T}}\dot{\mathbf{X}}_{shi})\end{aligned}\tag{10-69}$$

The motion equations of the coupled track-train-seat-human system were expressed in matrix form as

$$\mathbf{M}_{cc}\ddot{\mathbf{y}}_{cc}+\mathbf{C}_{cc}\dot{\mathbf{y}}_{cc}+\mathbf{K}_{cc}\mathbf{y}_{cc}=\mathbf{K}_{cr}\mathbf{r}_r+\mathbf{C}_{cr}\dot{\mathbf{r}}_r\tag{10-70}$$

where $\mathbf{M}_{cc}=\begin{bmatrix}\mathbf{M}_{tt}&&&\\&\mathbf{M}_{sh1}&&\\&&\ddots&\\&&&\mathbf{M}_{shN_{hs}}\end{bmatrix}$ is the mass matrix,

$\mathbf{C}_{cc}=\begin{bmatrix}\mathbf{C}_{tt}+\sum_{i=1}^{N_{hs}}\mathbf{C}_{tsi}&-\mathbf{C}_{st1}^{\mathrm{T}}&\cdots&-\mathbf{C}_{stN_{hs}}^{\mathrm{T}}\\-\mathbf{C}_{st1}&\mathbf{C}_{sh1}&\mathbf{O}&\mathbf{O}\\\vdots&\mathbf{O}&\ddots&\mathbf{O}\\-\mathbf{C}_{stN_{hs}}&\mathbf{O}&\mathbf{O}&\mathbf{C}_{shN_{hs}}\end{bmatrix}$ is the damping matrix,

$\mathbf{K}_{cc}=\begin{bmatrix}\mathbf{K}_{tt}+\sum_{i=1}^{N_{hs}}\mathbf{K}_{tsi}&-\mathbf{K}_{st1}^{\mathrm{T}}&\cdots&-\mathbf{K}_{stN_{hs}}^{\mathrm{T}}\\-\mathbf{K}_{st1}&\mathbf{K}_{sh1}&\mathbf{O}&\mathbf{O}\\\vdots&\mathbf{O}&\ddots&\mathbf{O}\\-\mathbf{K}_{stN_{hs}}&\mathbf{O}&\mathbf{O}&\mathbf{K}_{shN_{hs}}\end{bmatrix}$ is the stiffness matrix, $\mathbf{y}_{cc}=\begin{bmatrix}\mathbf{y}_{tt}\\\mathbf{X}_{sh1}\\\vdots\\\mathbf{X}_{shN_{hs}}\end{bmatrix}$ is the coordinate vector of the coupled track-train-seat-human system, while $\mathbf{K}_{cr}=\begin{bmatrix}\mathbf{K}_{ttr}\\\mathbf{O}\end{bmatrix}$ and $\mathbf{C}_{cr}=\begin{bmatrix}\mathbf{C}_{ttr}\\\mathbf{O}\end{bmatrix}$ are the stiffness and damping matrices associated with the track excitation, respectively. $\mathbf{K}_{ts_i}$ and $\mathbf{C}_{ts_i}$ are respectively the stiffness and damping matrices generated by the connection between the carbody and i[th] human-seat system.

In the following analysis, the double-unit-seat-one-subject system in Fig. 9-5 was adopted for the human-seat systems and the positions of the two columns of the human-seat systems were shown in Fig. 10-5.

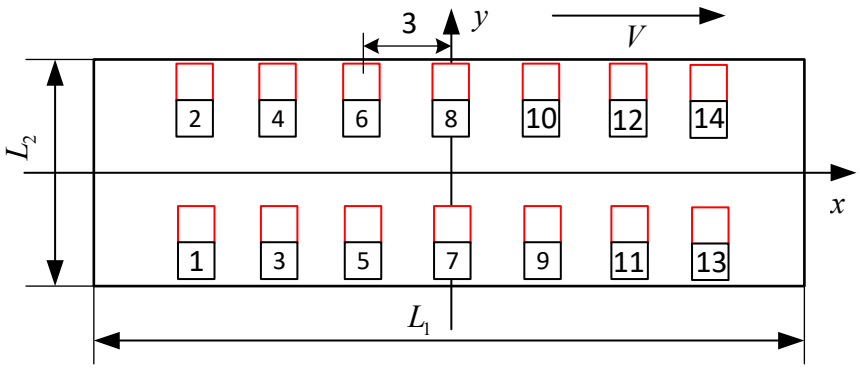

Fig. 10-5 The positions of the seats on the carbody floor (the passengers are seated on the red seats).

10.4 Frequency-domain analysis

The frequency response matrix from the excitation vector of the track irregularity $\mathbf{r}_r$ to the output $\mathbf{y}_{cc}$ was

$$\begin{aligned}\mathbf{H}_{avc}(f) &= (-(2\pi f)^2\mathbf{M}_{cc} + \mathrm{j}2\pi f\mathbf{C}_{cc} + \mathbf{K}_{cc})^{-1}(\mathbf{K}_{cr} + \mathrm{j}2\pi f\mathbf{C}_{cr}) \\ &= [\mathbf{H}_a(f), \mathbf{H}_v(f), \mathbf{H}_c(f)]\end{aligned} \tag{10-71}$$

where $\mathbf{H}_j(f) = [\mathbf{H}_{j1}(f), \mathbf{H}_{j2}(f), \mathbf{H}_{j3}(f), \mathbf{H}_{j4}(f)]$ is the frequency response matrix from alignment ($j = a$), vertical profile ($j = v$) or cross level ($j = c$). The subscript i (i=1,2,3,4) stands for the track irregularity acting on the ith wheelset.

Taking into account the time delay among the four wheelsets, the frequency response matrix from the excitations of the four wheelsets was transformed into the one from the 1st wheelset as follows

$$\mathbf{H}_j^s(f) = \mathbf{H}_j(f)\mathbf{W}_r(f) \tag{10-72}$$

where $j = a, v, c$, $\mathbf{W}_r(f) = [1, e^{-\mathrm{j}\omega\tau_1}, e^{-\mathrm{j}\omega\tau_2}, e^{-\mathrm{j}\omega(\tau_1+\tau_2)}]^{\mathrm{T}}$ is a vector resulting from the phase difference, $\tau_1 = \dfrac{L_{wx}}{V}$ and $\tau_2 = \dfrac{L_{b1}}{V}$ are the time delays.

Thus, the power spectrum density (PSD) of the output $\mathbf{y}_{cc}$ was

$$\mathbf{S}_{\mathbf{y}_{cc}}(f) = \sum_{j=a,v,c} \mathbf{H}_j^{s*}(f) S_{rj}(f) \mathbf{H}_j^{s\mathrm{T}}(f) \tag{10-73}$$

where $S_{rj}(f)$ is the PSD of the track irregularity acting on the 1st wheelset (j=a for alignment, j=v for vertical profile, j=c for cross level). The 5th American track spectra (Lei, 2015) were adopted for

the track irregularity, whose spatial expressions were listed in Table 2-1. The temporal power spectra for alignment, vertical profile and cross level at the speed of *V* were obtained respectively as

$$S_{rv}(\omega)=\frac{kA_v\Omega_c{}^2}{(\omega/V)^2((\omega/V)^2+\Omega_c{}^2)V} \tag{10-74}$$

$$S_{ra}(\omega)=\frac{kA_a\Omega_c{}^2}{(\omega/V)^2((\omega/V)^2+\Omega_c{}^2)V} \tag{10-75}$$

$$S_{rc}(\omega)=\frac{4kA_v\Omega_c{}^2}{((\omega/V)^2+\Omega_c{}^2)((\omega/V)^2+\Omega_s{}^2)} \tag{10-76}$$

All the three spectra decrease as the increase of frequency and three track inputs were assumed to be incoherent with each other.

According to Eq. (10-73), the PSD of the output ($\mathbf{y}_{cc}$) is the summation of the PSDs under individual excitation of alignment, vertical profile and cross level.

The PSD of the acceleration of $\mathbf{y}_{cc}$ was

$$\mathbf{S}_{\ddot{\mathbf{y}}_{cc}}(f)=(2\pi f)^4\mathbf{S}_{\mathbf{y}_{cc}}(f) \tag{10-77}$$

10.4.1 The spectrum on the floor

The frequency response function from the j[th] track irregularity acting on the 1[st] wheelset (j=a for alignment; j=v for vertical profile; j=c for cross level) to the i[th] displacement on the floor (i=l for lateral displacement; i=v for vertical displacement; i=θ for roll angle) was

$$H_{ji}^s(x,y,f)=\mathbf{C}_{Fi}{}'(x,y)\mathbf{H}_j^s(f) \tag{10-78}$$

where $\mathbf{C}_{Fi}{}'(x,y)=[\mathbf{C}_{Fi}(x,y),\mathbf{0}]$ is the corresponding coefficient vector for the i[th] displacement on the floor.

From Eq.(10-77), the PSD of the acceleration on the carbody floor at the position (*x*, *y*) was

$$S_{\ddot{d}_i}(x,y,f)=(2\pi f)^4\sum_{j=a,v,c}H_{ji}^{s\,*}(x,y,f)S_{rj}(f)H_{ji}^s(x,y,f) \tag{10-79}$$

where the subscript i stands for the displacement on the floor, i=l, for lateral displacement; i=v, for vertical displacement; i=θ, for roll angle; the two dots over the symbol stand for the second derivative with respect to time.

It can be seen from Eq. (10-79) that the PSD of the acceleration on the carbody floor is the summation of the PSDs under individual excitation of the track alignment, vertical profile and cross level.

10.4.1.1 Suitable length of track

In actual calculation, the track of infinite length is usually truncated as one of finite length. For the moving irregularity excitation model, the vibration of the track far away from the train is hardly excited, so the boundary condition of the track of finite length is 'fixed-fixed'. According to Zhai *et al.* (2004), satisfactory results can be obtained if the distance between the moving wheelsets and the end of track is more than 15 m for moving irregularity model. The PSDs of the accelerations on the floor for different track lengths were compared and illustrated in Fig. 10-6, while the train was always in the middle of the track. The results for different track lengths were very close, even though there exhibited some difference around 17 Hz. Increasing the track length means more sleepers and ballasts are in need, so the calculation amount is greatly increased. It can be seen 60 m is sufficient for achieving satisfactory results, so 60 m was adopted for the track length in the following analysis.

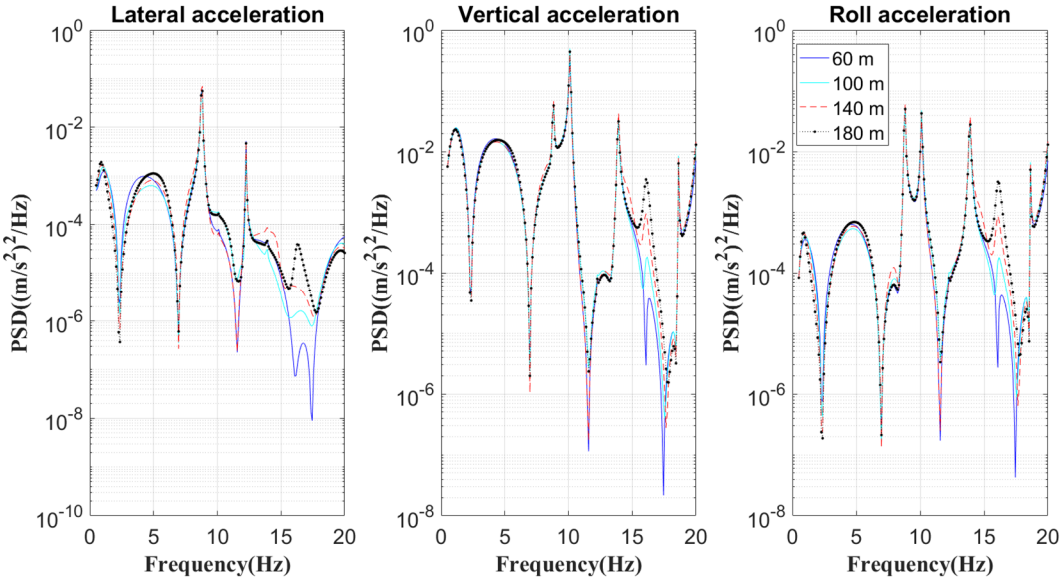

Fig. 10-6 Comparison among different track lengths (60 m, 100 m, 140 m and 180 m) for the PSDs of the accelerations on the floor at the excitation point of seat 7 at the speed of 300 km/h.

10.4.1.2 The contribution of track irregularities

The peaks generated by the carbody modes were clearly visible in the PSDs of the accelerations on the floor (Fig. 10-7 and Fig. 10-8). If there is lateral (vertical or roll) deflection at a particular seat position in the modal shape of a carbody mode, a peak corresponding to that mode may exhibit in the PSD of the lateral (vertical or roll) acceleration on the floor. The carbody modes can play different roles at different seat positions (comparing Fig. 10-7 with Fig. 10-8). For example, a peak around 10.15 Hz exhibited in the PSDs of the lateral, vertical and roll accelerations on the floor under seat 7, which was due to mode 2 of the carbody because this mode had lateral, vertical and roll deflections at the position of seat 7. Furthermore, it can be seen that the flexible modes of the carbody played an important role in the acceleration PSDs on the floor. The peaks and troughs generated by the geometry filter effect were obvious in the PSD of the accelerations on the floor. At different train speeds, the contributions of the track irregularities (alignment, vertical profile and cross level) in a specific frequency range can be revealed, so as to provide the possibility of modifying the track irregularity to reduce the vibration on the carbody floor. For example, the vertical profile played the most important role in the PSDs of the vertical accelerations on the floor at the positions of seat 7 (V=300 km/h) and seat 1 (V=200 km/h) except around 8.8 Hz and 11-13 Hz. More results can be found in Appendix H.

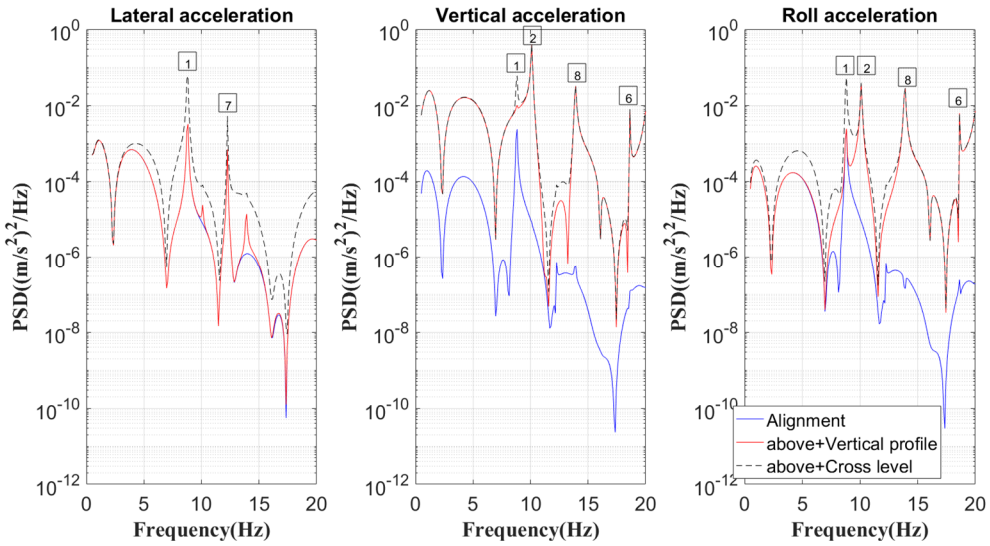

Fig. 10-7 The PSD of the acceleration on the floor at the excitation point of seat 7 at the speed of 300 km/h (blue line: the PSD resulting from alignment alone; red line: PSD resulting from alignment and vertical profile; black line: PSD resulting from alignment, vertical profile and cross level). The number in the box is the number of the carbody modes in Table 10-1 and Table H-1.

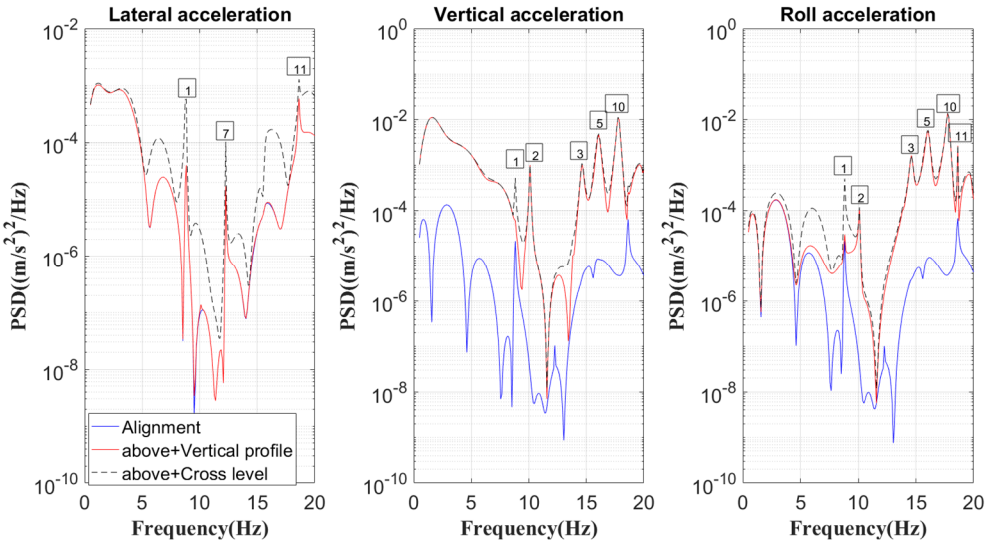

Fig. 10-8 The PSD of the acceleration on the floor at the excitation point of seat 1 at the speed of 200 km/h (blue line: the PSD resulting from alignment alone; red line: PSD resulting from alignment and vertical profile; black line: PSD resulting from alignment, vertical profile and cross level). The number in the box is the number of the carbody modes in Table 10-1 and Table H-1.

10.4.2 The spectrum on human-seat interfaces

According to Eq.(10-73), the PSD of the accelerations on the human-seat interface is the summation of the PSDs under individual excitation of alignment, vertical profile and cross level. The spectra of the accelerations on the carbody floor would be further modified by the seat when the vibration was transmitted to the passengers. The peaks generated by the carbody modes were still clearly visible in the PSDs of the accelerations on the seat-buttock interface (Fig. 10-9) and human-backrest interface (Fig. 10-10). Because of the vibration transmission of the train seat, all the five peaks that were visible in the acceleration PSDs on the floor (Fig. 10-7) exhibited in all the three acceleration PSDs on the seat-buttock interface and human-backrest interface. The role of the track irregularities (alignment, vertical profile and cross level) played in the lateral, vertical and roll acceleration PSDs on the seat-buttock interface and human-backrest interface was clear from Fig. 10-9 and Fig. 10-10. In addition, the peaks and troughs generated by the geometry filter effect were still obvious in the PSD of the accelerations on the seat-buttock interface and human-backrest interface even after the vibration transmission of the train seat. More results can be found in Appendix H.

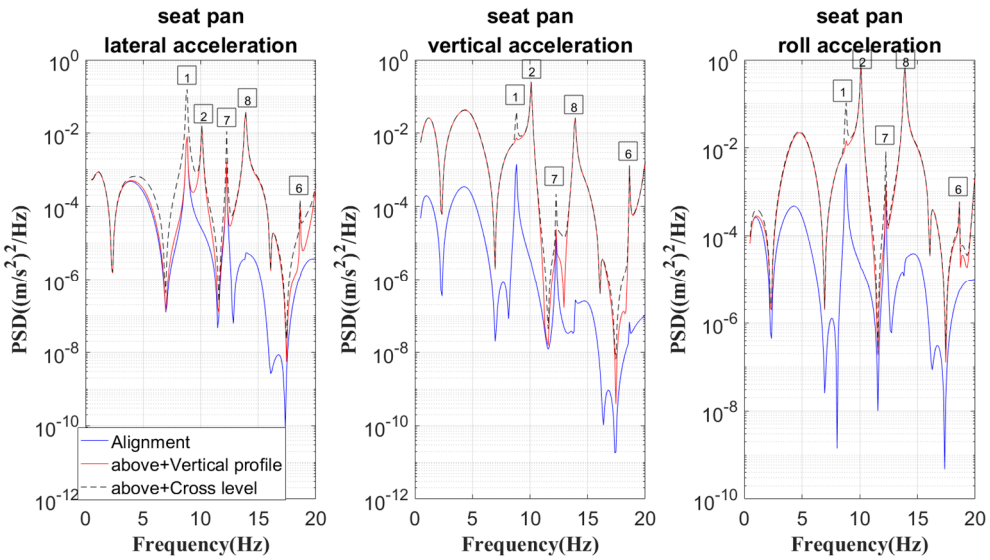

Fig. 10-9 The PSD of the acceleration on the seat-buttock interface of seat 7 at the speed of 300 km/h (blue line: the PSD resulting from alignment alone; red line: PSD resulting from alignment and vertical profile; black line: PSD resulting from alignment, vertical profile and cross level). The number in the box is the number of the carbody modes in Table 10-1 and Table H-1.

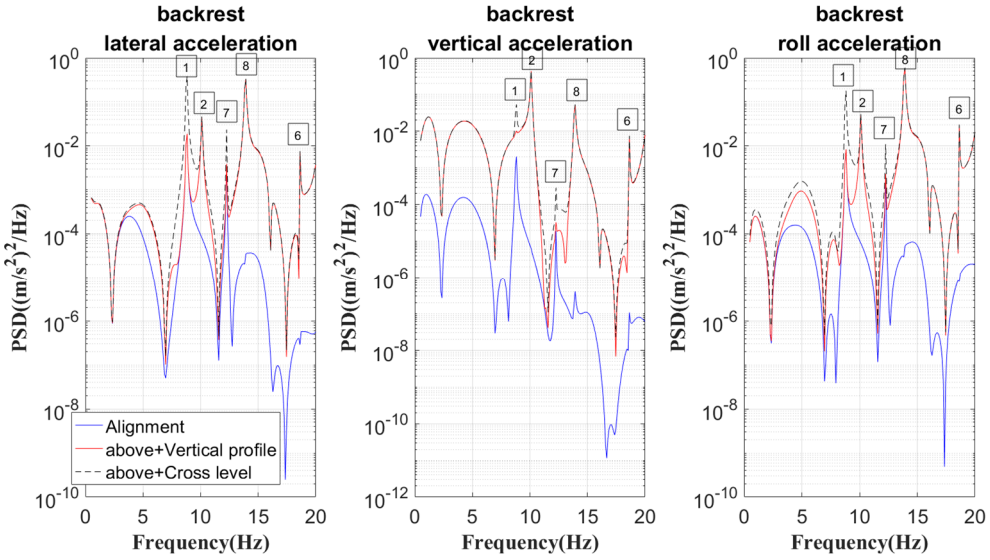

Fig. 10-10 The PSD of the acceleration on the human-backrest interface of seat 7 at the speed of 300 km/h (blue line: the PSD resulting from alignment alone; red line: PSD resulting from alignment and vertical profile; black line: PSD resulting from alignment, vertical profile and cross level). The number in the box is the number of the carbody modes in Table 10-1 and Table H-1.

10.4.3 The influence of track rigidity

It was reported the rigidity of the track would influence the dynamics of the vehicle, especially in the high-frequency range (Cheli and Corradi, 2011). In addition, the rigidity of the track determines whether it can be considered as a rigid track in the modelling, and there is no double that taking the track as a rigid one simplifies the modelling procedure a lot. As depicted in Fig. 10-11, as the

increase of track rigidity, the lateral, vertical and roll acceleration PSDs on the floor showed minor difference below 20 Hz. It is worth mentioning that further increasing the bending and torsional rigidities of the track would make the dynamics of track converge to the case of a traditional rigid track. Thus, in terms of the spectrum on the carbody floor, modelling the track as rigid is usually acceptable below 20 Hz for the sake of reducing computational effort without losing much accuracy.

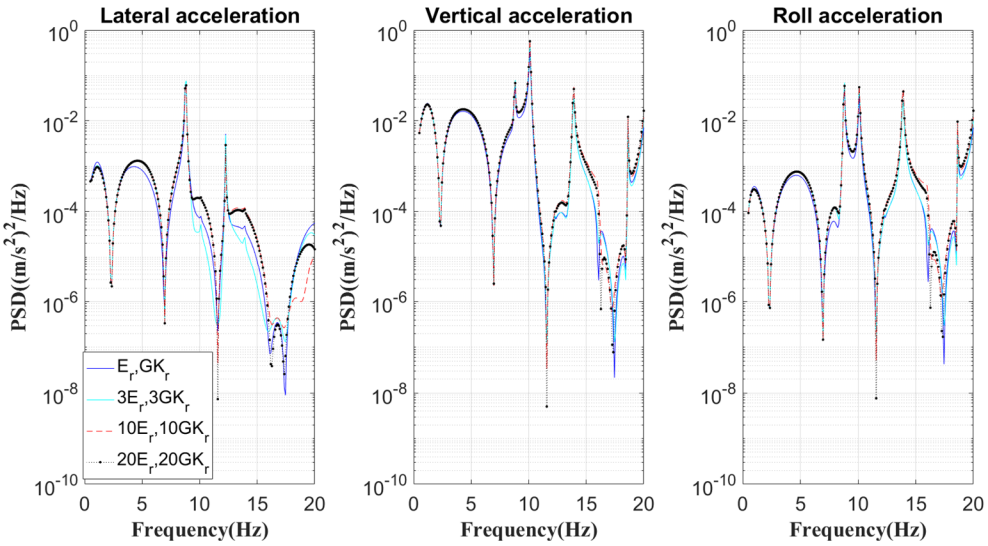

Fig. 10-11 The influence of track rigidity on PSDs of the lateral, vertical and roll accelerations on the floor at the excitation point of seat 7 at the speed of 300 km/h.

10.4.4 Comparison with rigid carbody model

The influence of the flexible carbody was reported in many papers, e.g., Diana *et al.* (2002), Zhou *et al.* (2009), and Ling *et al.* (2018). The comparison was made between a rigid carbody model and a flexible one in terms of the acceleration PSD on the floor (Fig. 10-12). The difference between the rigid carbody model and the flexible one was small below 7.5 Hz, similar to the conclusion in Ling *et al.* (2018). Thus, for the dynamic analysis of the vibration on the carbody below 7.5 Hz, using a rigid carbody model to take the place of the flexible carbody model is acceptable. Because of the flexible modes of the carbody, the flexible carbody model showed intensified vibration on the floor in lateral, vertical and roll directions above 7.5 Hz compared with the rigid carbody model. This also illustrated that the vibration of the carbody in the low-frequency range was dominated by the rigid modes, however, by both the rigid and flexible modes in the high-frequency range because the flexible modes of the carbody were excited by the wheel-rail interaction.

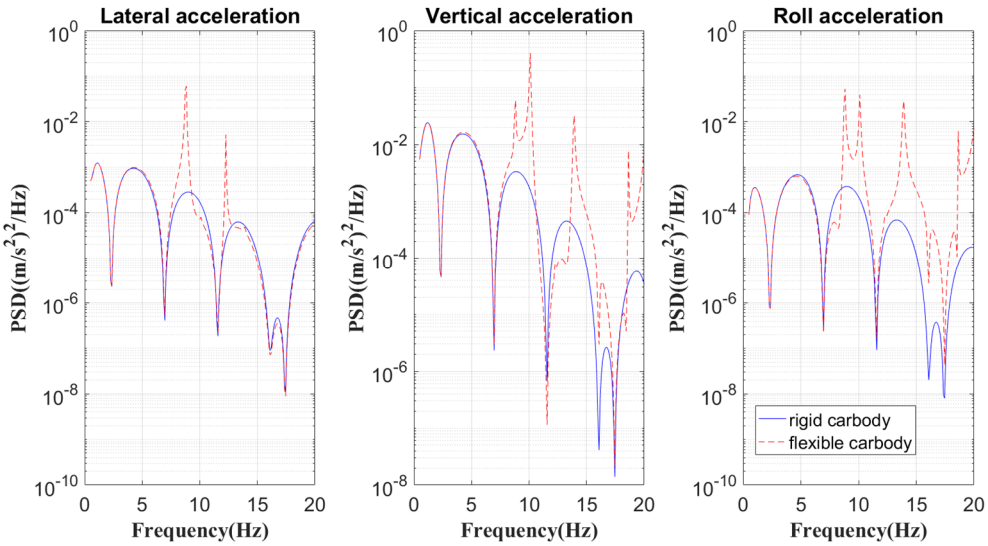

Fig. 10-12 The comparison between rigid and flexible carbody models for the PSD of the accelerations on the floor at the excitation point of seat 7 at the speed of 300 km/h.

10.5 Analysis of ride comfort

10.5.1 Evaluation of ride comfort

According to ISO 2631-1, the ride comfort was evaluated by the weighted root-sum-square (r.s.s.) value of the weighted root-mean-square (r.m.s.) values of the lateral, vertical and roll accelerations on the feet, seat-buttock and human-backrest interfaces as

$$a_t = \sqrt{\sum_{i=sy,sz,sr,by,bz,fy,fz} (b_i a_{wi})^2} \tag{10-80}$$

where a_t is the total equivalent acceleration value; the subscript i stands for the direction and position of the accelerations, the subscripts *sy*, *sz*, *sr* for the lateral, vertical and roll vibrations on the seat-buttock interface, *by* and *bz* for the lateral and vertical vibrations on the human-backrest interface, *fy* and *fz* for the lateral and vertical vibrations at the feet (the feet position was taken as 40 cm in front of the excitation point of the seat on the floor), b_i is the multiplying factor according to ISO 2631-1 (Table H-5), a_{wi} is the weighted acceleration r.m.s. value defined as

$$a_{wi} = \sqrt{\int_{0.5}^{20} S_{a_i}(f) \left| W_i(f) \right|^2 \mathrm{d}f} \tag{10-81}$$

where $S_{a_i}(f)$ is the autospectrum of the acceleration a_i, $W_i(f)$ is the weighting function according to ISO 2631-1 (Table H-5). According to ISO 2631-1, the frequency range 0.5-80 Hz is

recommended. However, the frequency range 0.5-20 Hz was taken into account in this study considering that both the human-seat system and the weighting function have the potential to reduce the vibration above 20 Hz. The larger the total equivalent acceleration a_t is, the worse the ride comfort is, and vice versa.

The equivalent acceleration at every vibration position and direction in the total acceleration a_t can be evaluated by $b_i a_{wi}$.

10.5.2 The contribution of different modes

The contribution of different modes was defined from the perspective of spectrum. Similar to Section 4.5.3, the (lateral, vertical or roll) displacement at any position of the floor is the summation of those from different modes, as shown in Eq. (10-29)-(10-31). If these modes are grouped into several sets, then

$$d_i(x,y,t) = d_{im_1}(x,y,t) + d_{im_2}(x,y,t) + \cdots + d_{im_n}(x,y,t) = \mathbf{C}_{Fi}'(x,y)\mathbf{y}_{cc} \qquad (10\text{-}82)$$

where $d_i(x,y,t)$ is the displacement at the position (*x*,*y*) on the floor ($i = l$ for lateral displacement, $i = v$ for vertical displacement, and $i = \theta$ for roll angle); $d_{im_j}(t)$ is the contribution from the j[th] set of modes to the displacement $d_i(t)$, and the subscript n is the total number of mode sets.

According to Eq. (10-78), the frequency response matrix from the alignment, vertical profile and cross level acting on the 1[st] wheelset to the lateral, vertical and roll displacements on the floor is

$$\mathbf{H}_{tf}(x,y,f) = \begin{bmatrix} H^s_{al}(x,y,f) & H^s_{vl}(x,y,f) & H^s_{cl}(x,y,f) \\ H^s_{av}(x,y,f) & H^s_{vv}(x,y,f) & H^s_{cv}(x,y,f) \\ H^s_{a\theta}(x,y,f) & H^s_{v\theta}(x,y,f) & H^s_{c\theta}(x,y,f) \end{bmatrix} \qquad (10\text{-}83)$$

For the spectrum $S_{a_k}(f)$ at the feet (*k*=*fy*, *fz*) in Eq. (10-81), it can be calculated from Eq. (10-79); While for the spectrum $S_{a_k}(f)$ on the seat (*k*=*sy*, *sz*, *sr*, *by*, *bz*) in Eq. (10-81), it was further expressed as

$$S_{a_k}(f) = [\mathbf{H}_{a_k/d_f}(f)\mathbf{H}_{tf}(x,y,f)]^* \operatorname{diag}(S_{ra}(f), S_{rv}(f), S_{rc}(f))[\mathbf{H}_{a_k/d_f}(f)\mathbf{H}_{tf}(x,y,f)]^{\mathrm{T}} \qquad (10\text{-}84)$$

where $\mathbf{H}_{a_k/d_f}(f)$ is the frequency response vector from the lateral, vertical and roll displacements on the floor to the acceleration on the seat a_k, which could be obtained from Eq. (10-66).

When calculating a_t value in Eq. (10-80), the acceleration resulting from jth (j=1,2,…,n) mode set (a_{m_j}) could be calculated by keeping all the corresponding elements for this mode set in the coefficient vector $\mathbf{C}_{Fi}'(x,y)$ ($i=l,v,\theta$) unchanged, while setting all the other elements zero (Eq. (10-82)) in the calculation of the acceleration spectrum $S_{a_k}(f)$ at the feet and on the seat with the deterimined track-train-seat-human system (Eq. (10-70)). The acceleration resulting from the coherent parts of all the mode sets a_{coh} could be calculated by

$$a_{coh}=(a_t^2-\sum_{i=1}^{n}{a_{m_i}}^2)^{1/2} \tag{10-85}$$

where $a_{m_i}>0$, but ${a_{coh}}^2$ can be negative, so when the coherent part has a positive effect on a_t, a_{coh} is a real value; on the contrary, a_{coh} is a pure imaginary value.

10.5.3 The effect of different influencing factors

10.5.3.1 The effect of train speed and seat position

The ride comfort at different seat positions was compared in Fig. 10-13, similar to Fig. 4-18. On the whole, the equivalent acceleration a_t showed an increasing tendency as the increase of speed because for a specific frequency, the higher the speed was, the higher the wavelength was, the larger the PSD introduced by the track irregularity would usually be. The fluctuations were due to the geometry filter effect of the vehicle. For symmetrical seat positions, the equivalent accelerations showed analogous tendency as the speed. In the whole speed range, the equivalent accelerations at seat 1 and seat 13 (both ends) were the largest, resulting in the worst ride comfort. Above about 280 km/h, what follows is seat 7 (the middle), then seat 5 and seat 9, finally seat 3 and seat 11, while the opposite is true below 280 km/h. The contributions of rigid and flexible modes of carbody to the total equivalent acceleration at different seat positions were analyzed and illustrated in Fig. 10-14. The acceleration resulting from flexible modes showed similar fluctuation with the speed to the total equivalent acceleration because the contribution of rigid modes tended to increase monotonically with the speed given that the geometry filter effect of the rigid modes was not obvious in the considered speed range (150-350 km/h) owing to the low modal frequencies.

This proved the fluctuation of the total equivalent acceleration was mainly due to the flexible modes. At seat 1 and seat 3, the contribution of the rigid modes dominated obviously over that of the flexible modes and the contribution of the coherent part was to decrease the total equivalent acceleration (improving ride comfort), but at seat 5 and seat 7 the contribution of the flexible modes increased and the contribution of the coherent part intended to increase the total equivalent acceleration (worsening ride comfort). It is worth mentioning that the contributions of the rigid and flexible modes are dependent on the carbody model, and different carbody models can result in quite different results.

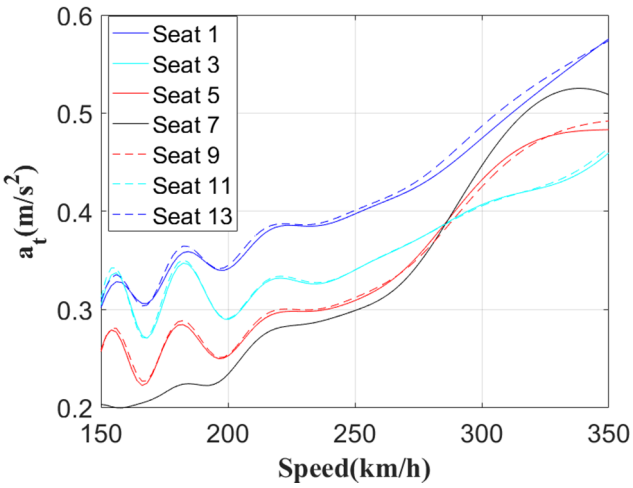

Fig. 10-13 The comparison of ride comfort among different seat positions.

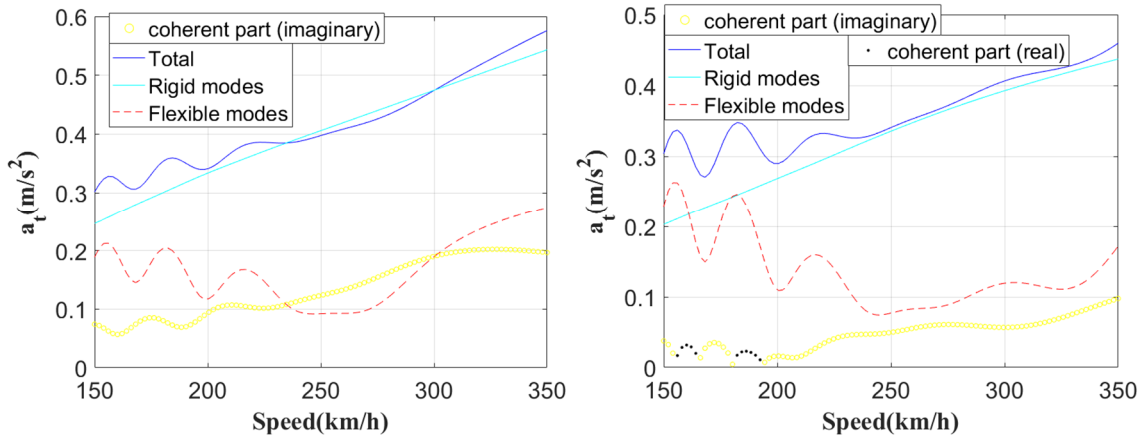

(a) (b)

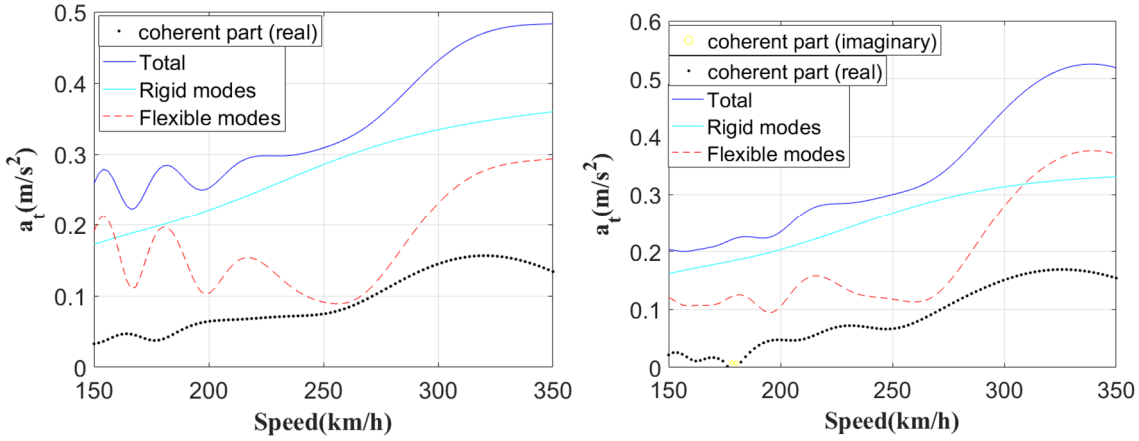

(c) (d)

Fig. 10-14 The contribution of rigid and flexible modes of the carbody to ride comfort for (a) seat 1 (b) seat 3 (c) seat 5 (d) seat 7.

10.5.3.2 Equivalent acceleration at different vibration positions and directions

The equivalent accelerations at different vibration positions and directions were somehow dependent on the human-seat system and human sensitivity to vibration. The accelerations at different vibration positions and directions were plotted for different seat positions, and their contributions to the total equivalent acceleration could be clearly seen from Fig. 10-15. Regardless of the seat position and speed, vertical acceleration on the seat pan was the most severe, usually followed by the vertical acceleration at the feet. Compared with these two accelerations, other accelerations at the feet, on the seat pan or backrest sometimes could be ignored. One reason is that the weighting function W_k for the vertical accelerations at the feet and on the seat pan is the largest between 8.0-12.5 Hz, where the vibration is drastic due to both the elastic and rigid vibrations of the carbody, while other weighting functions W_e and W_d are the largest between 0.5-1.0 Hz and 0.5-2.0 Hz, respectively, where the vibration is less drastic because of the mere rigid-body vibration of the carbody. Another reason is that the vertical direction on the seat pan has the largest multiplying factor of 1.0 (Table H-5). Therefore, controlling the elastic vibration of the carbody may be an effective way to improve ride comfort.

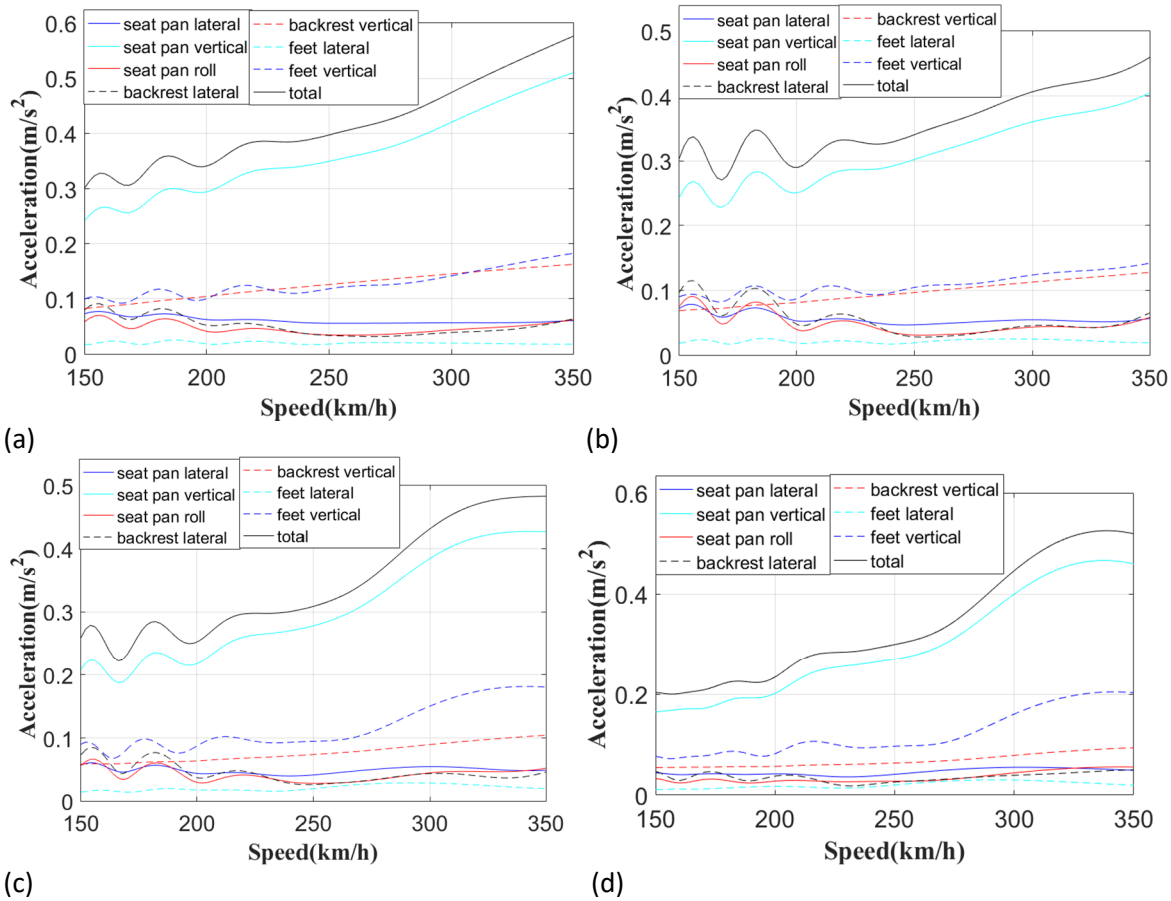

Fig. 10-15 The equivalent accelerations at different vibration positions and directions of (a) seat 1 (b) seat 3 (c) seat 5 (d) seat 7.

10.5.3.3 Comparison with another human-seat system

Because the seating dynamics of the seat with one subject showed great discrepancy from that with two subjects, the effect of the number of seated subjects on ride comfort was studied. If all the double-unit-seat-one-subject systems on the carbody were replaced by double-unit-seat-two-subject systems whose transmissibilities were illustrated in Fig. 9-8, while the subject under evaluation was kept the same. Then the ride comfort was evaluated at different seat positions and illustrated in Fig. 10-16. Telling from Fig. 8-17, the modulus of seat transmissibilities at the resonance around 15 Hz was reduced greatly by the introduced neighbouring subject in the lateral and roll directions. As the reduction of seat transmissibilities around 15 Hz by the neighbouring subject, the contribution from flexible modes reduced accordingly, resulting in reduced total equivalent acceleration (Fig. 10-16). Therefore, for evaluating the ride comfort with a double-unit train seat, the number of subjects seated on the seat should be considered separately.

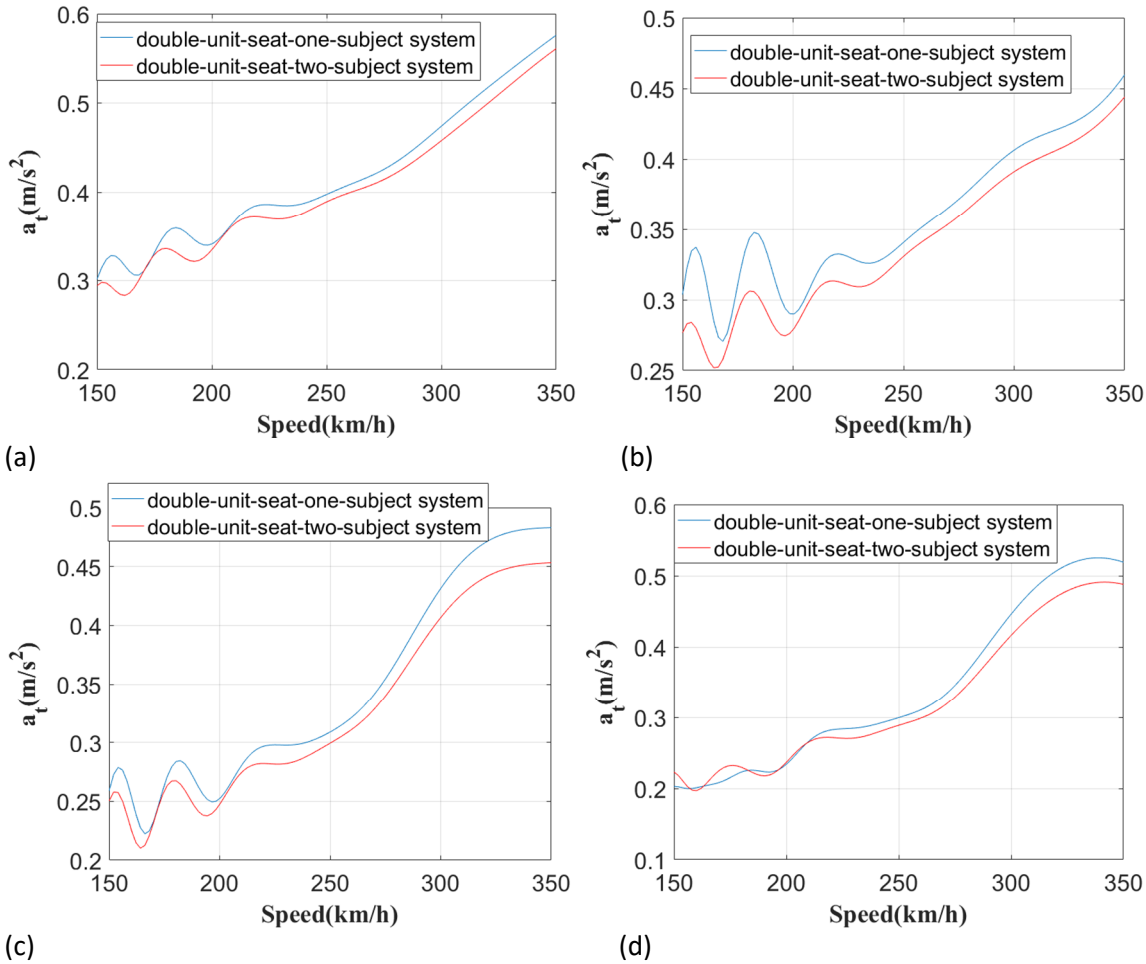

Fig. 10-16 The comparison of ride comfort between two human-seat systems— double-unit-seat-one-subject and double-unit-seat-two-subject systems at the position of (a) seat 1 (b) seat 3 (c) seat 5 (d) seat 7.

10.5.3.4 The effect of carbody damping

When the damping of the carbody increased, the total equivalent acceleration decreased obviously for every speed, especially at the peaks (Fig. 10-17). By analysis of the contribution from the rigid and flexible modes comparing Fig. 10-14(d) with Fig. 10-18, for seat 7, the contribution of the rigid modes and the coherent part kept almost unchanged, while the contribution from the flexible modes was reduced by the increased damping. Therefore, increasing the carbody damping is an effective way to suppress the flexible modes, thereby improving ride comfort.

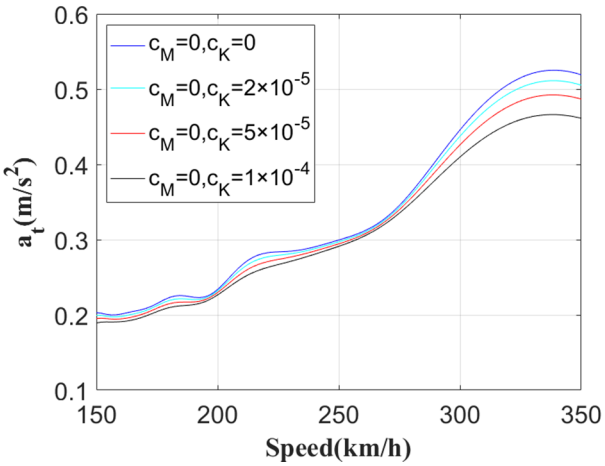

Fig. 10-17 The influence of carbody damping on the total equivalent acceleration a_t at the position of seat 7.

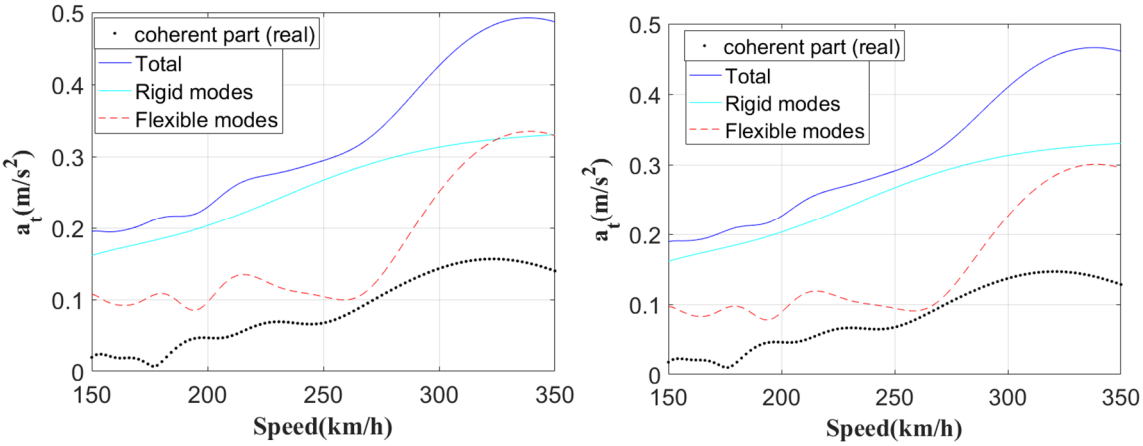

Fig. 10-18 The contribution of rigid and flexible modes to ride comfort for seat 7 when (a) c_M=0 and c_K=5×10^{-5} (b) c_M=0 and c_K=1×10^{-4}.

10.5.3.5 The comparison with rigid carbody model

The ride comfort evaluated with a flexible carbody model was compared with a rigid one, as shown in Fig. 10-19. According to Section 10.4.4, the rigid carbody model underestimated the vibration above 7.5 Hz, given that the weighting function W_k is the largest between 8.0-12.5 Hz, so the vertical equivalent acceleration on the seat-buttock interface and at the feet had great reductions when the flexible carbody model was replaced by a rigid one (comparing Fig. 10-19(b) with Fig. 10-15(d)). Besides, these two accelerations dominated over others in the total equivalent acceleration, so the evaluation of ride comfort with a rigid carbody model exhibited great underestimation of the total equivalent acceleration compared with a flexible one (Fig. 10-19(a)).

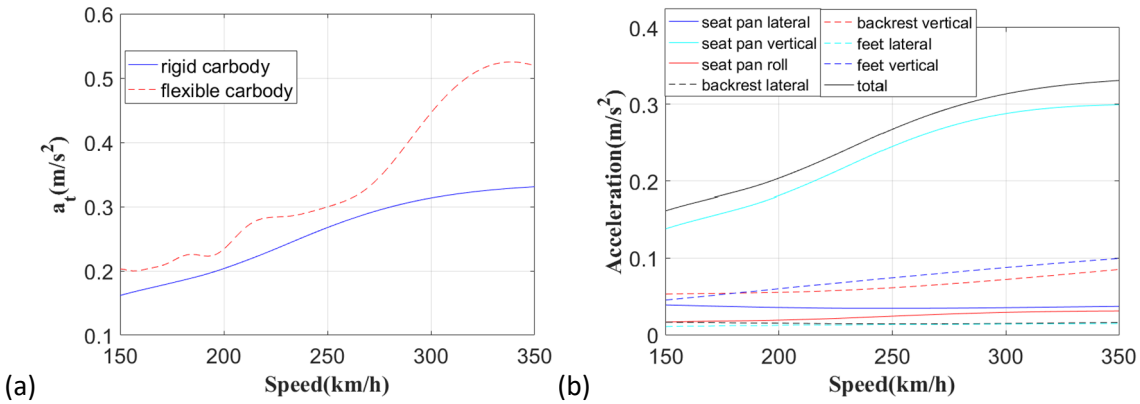

Fig. 10-19 The comparison of the total equivalent acceleration for seat 7 between the rigid and flexible carbody models (a) the total equivalent acceleration (b) the equivalent accelerations at different vibration positions and directions for the rigid carbody model.

10.5.3.6 The influence of track rigidity

Although the track rigidity did not cause much difference to the PSD of the floor accelerations below 20 Hz (Fig. 10-11), the ride comfort evaluated under different track rigidities showed much difference at high speed (Fig. 10-20). The maximum overestimation of the total equivalent acceleration can be over 10 % if a flexible track was taken as a rigid one. This is because as the increase of train speed, the interaction between the wheel and track became intensified, and a rigid track would result in more drastic vibration of the carbody than a flexible track. This means modelling the track as flexible can achieve a more accurate evaluation of total equivalent acceleration and reduce the overestimation than modelling the track as rigid.

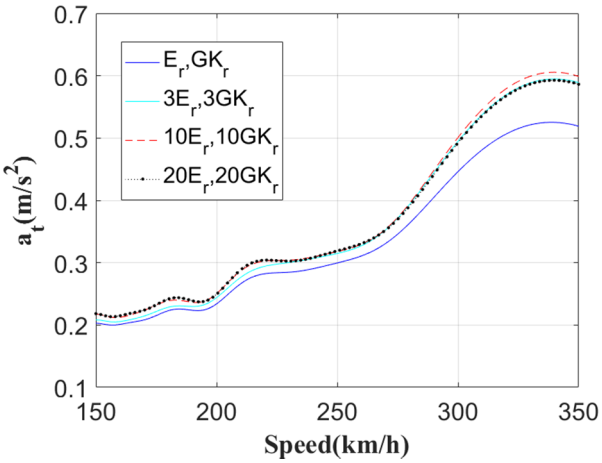

Fig. 10-20 The influence of track rigidity on the ride comfort for seat 7.

10.5.3.7 The effect of suspension parameters

The effect of stiffness and damping of the primary and second suspensions on the ride comfort at the position of seat 7 was studied (Fig. 10-21). Reducing the vertical damping of the second suspension (c_{sz}) improved ride comfort obviously with decreasing a_t for every speed, whose influence on ride comfort was analogous to the vertical stiffness of the primary suspension (k_{pz}) (Fig. 10-21). Increasing the vertical damping of the primary suspension (c_{pz}) above its initial value worsened the ride comfort with increasing a_t for every speed. Reducing it below its initial value improved the ride comfort above 280 km/h. The modal contribution was calculated for seat 7 under different values of the vertical damping of the second suspension c_{sz} (Fig. 10-22). By comparing with Fig. 10-14(d), increasing c_{sz} augmented the contribution of both the rigid and flexible modes. At the position of seat 7, the increase of vertical stiffness of the second suspension (k_{sz}) seemed to cause a slight increase of the total equivalent acceleration (Fig. 10-21(a)). Other suspension parameters (k_{py}, k_{sy}, k_{px}, k_{sx}, c_{sy}) had little influence on the total equivalent acceleration (Fig. H-10 in Appendix H). The vertical stiffness and damping had more influence on ride comfort than the fore-and-aft and lateral ones because the vertical stiffness and damping had significant influence on the vertical accelerations at the feet and on the seat pan that were of great significance to ride comfort, while the effects of lateral and fore-and-aft stiffness and damping of the two suspensions on the vertical vibration were negligible.

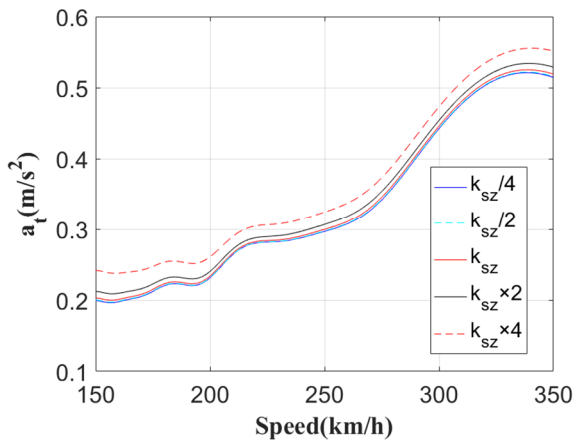

(a)

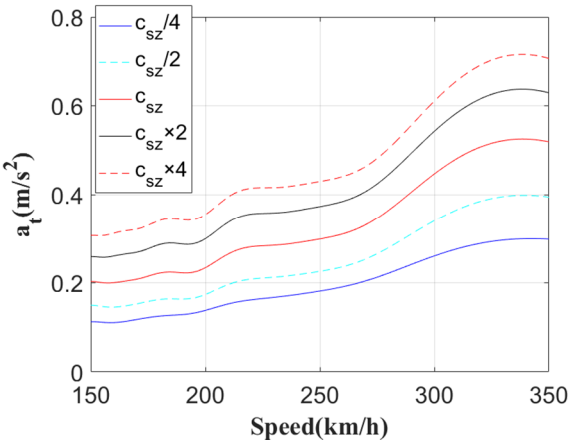

(b)

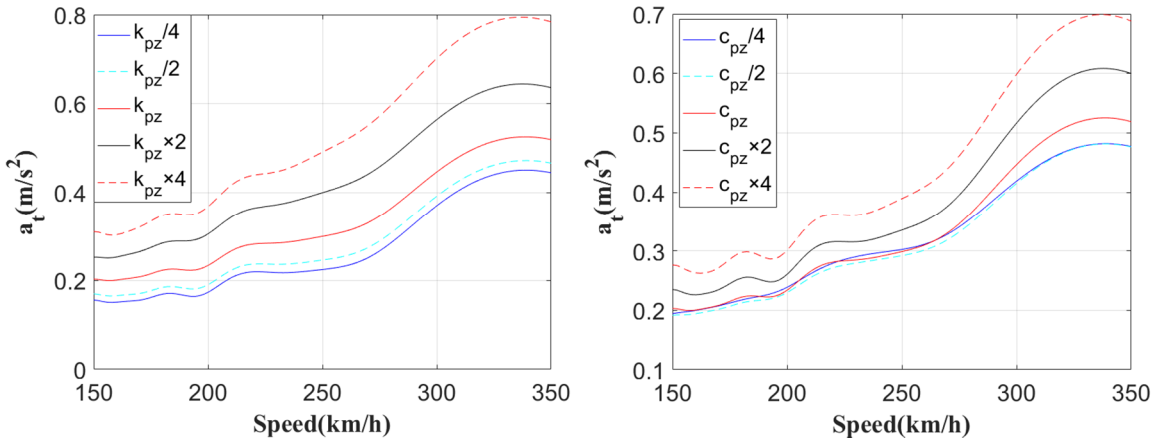

(c) (d)

Fig. 10-21 The effect of suspension stiffness and damping on ride comfort (a) k_{sz} (b) c_{sz} (c) k_{pz} (d) c_{pz} at the position of seat 7.

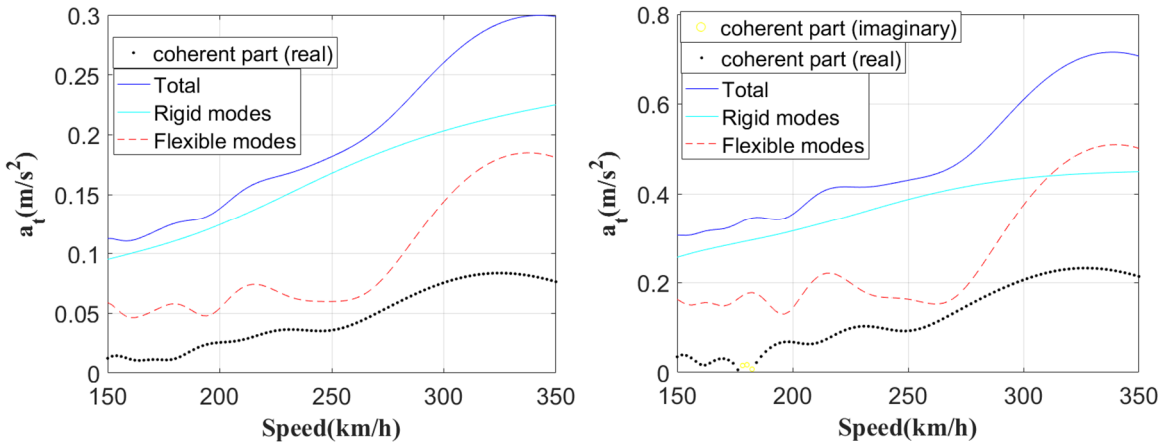

(a) (b)

Fig. 10-22 The contribution of rigid and flexible modes to ride comfort at the position of seat 7 for (a) $c_{sz}/4$ (b) 4 c_{sz}.

10.6 Conclusion

Based on the coupled track-train-seat-human model, the ride comfort was analyzed for a high-speed train running at a constant speed on a tangent track. The following conclusions can be drawn.

The total equivalent acceleration showed an increasing tendency as the increase of speed with some fluctuations because of the geometry filter effect of the vehicle. For symmetrical seat positions, the equivalent accelerations showed analogous tendency as the speed. The ride comfort close to the ends was the worst, followed by the carbody center at high speed. Regardless of the seat position and speed, vertical acceleration on the seat pan was the most severe, usually followed by the vertical acceleration at the feet. Compared with these two accelerations, other accelerations at the feet, on the seat pan or backrest sometimes could be ignored. The total equivalent acceleration was reduced by the introduced neighbouring subject. The damping of the carbody

effectively reduced the contribution from flexible modes, resulting in the reduction of the total equivalent acceleration for every speed, especially at the peaks.

The track rigidity only had a minor influence on the lateral, vertical and roll vibrations of the carbody floor below 20 Hz, but a rigid track can cause an overestimation of the total equivalent acceleration by over 10 % compared with a flexible track at high speed. Because of the flexible modes of the carbody, the flexible carbody model showed intensified vibration on the floor in lateral, vertical and roll directions above 7.5 Hz compared with the rigid carbody model; and the evaluation of ride comfort with a rigid carbody model exhibited great underestimation of the total equivalent acceleration compared with a flexible carbody model.

The total equivalent acceleration increased significantly as the increase of vertical damping of second suspension or vertical stiffness of the primary suspension under every speed, however, only showed a slight increase as the increase of vertical stiffness of the second suspension. The total equivalent acceleration increased significantly as the increase of vertical damping of the primary suspension above its initial value. However, the total equivalent acceleration was insensitive to the stiffness and damping in the fore-and-aft and lateral directions.

This study gives a useful guide for the design of rail vehicles and the matching of the human-seat system with the vehicle. The same methodology can be applied to the analysis of ride comfort of other rail vehicles.

Chapter 11 Conclusions and recommendations

11.1 Conclusions and summary

Chapter 1 introduced the motivation and objectives of this thesis, defined the research questions and research scope.

Chapter 2 reviewed the up-to-date knowledge and research related to this study, covering the topics of the biodynamic response of seated subject to vibration, seating dynamics, modelling of seated human body and human-seat system, dynamics and ride comfort of the high-speed train.

Chapter 3 introduced the research methods used in the thesis, including the method for the calculation of frequency response function, method for model calibration, Wilcoxon signed-rank test and the linear regression analysis as well as modal analysis method. Especially, for the calculation of FRF with MISO system, a new MISO method was proposed and new partial coherences that are independent of the sequence of inputs were defined. For the calibration method, a combined algorithm of genetic algorithm and a minimization algorithm for constrained nonlinear multivariable problem ('fmincon' function in Matlab) that is suitable for a large number of optimization variables was introduced. For plotting the animation of complex modes, modal analysis method based on complex mode theory was introduced.

In Chapter 4, a rigid-flexible coupled train-seat-human model with calibrated human-seat systems in the vertical direction was developed for studying ride comfort of rail vehicles including high-speed trains. The frequency (W_k) weighted acceleration r.m.s. value at the seat pan was used for assessing ride comfort. The contribution of different modes of the carbody to ride comfort was defined from the perspective of power spectral density. It was demonstrated that the role of the first bending mode was more important than other bending modes for ride comfort when bogie and seat positions are both far from the nodes of the first bending mode. Under this situation, the bogie spacing filter effect of the first bending mode can be adopted to predict peaks and troughs of the equivalent acceleration on the carbody floor and on the human-seat interface varying with train speed or first bending frequency (bending rigidity). The incorporation of human-seat system was necessary in order to give accurate evaluation of ride comfort. Many parameters can have influences on ride comfort. Increasing the bending rigidity or reducing the speed, the ride comfort exhibited a global trend of improvement. Increasing the damping ratio of bending modes improved the ride comfort effectively. Increasing the stiffness or decreasing the damping of seat-human vertical contact on the seat pan worsened ride comfort. Increasing the stiffness and damping of the

primary and second suspensions usually increased the equivalent acceleration (worsening the ride comfort). What is more, the equivalent accelerations at symmetrical seat positions showed analogous tendency as the speed. Ride comfort was worst at two ends whatever the speed was, followed by the carbody center at high speed. After speed variation was taken into account, the equivalent acceleration was also defined and found to be close to that evaluated with a constant speed of the mean value.

In Chapter 5, the field measurement was carried out on a high-speed train for the vibration transmission of the seat. The transmissibilities and coherences from the accelerations on the carbody floor to those on the seat pan and backrest were studied by the proposed new multi-input and single-output (MISO) system introduced in Section 3.2. It was found that although the high-speed train seat was exposed to complex vibrations from different sources, when the three inputs (vertical, lateral and roll accelerations) at the seat base were used as the inputs for MISO models, good multiple coherence functions could be obtained when studying the seat transmissibility to the vertical, lateral or roll vibration at the seat pan and backrest except in the frequency range where the anti-resonances of the inputs located. In such an exceptional case, the unsatisfactory multiple coherence could be explained by the anti-resonances of the input signals, which was further verified by the laboratory experiment. Then the on-site measurement was compared with the laboratory measurement in terms of the estimation of the coherence and transmissibility. Due to the advantages of the laboratory experiment, the contribution from the coherent parts was smaller, and the multiple coherence was higher than the field measurement. In the field measurement, that the inputs were coherent with the 'noise' was the main reason for the erroneous estimation of frequency response function (FRF), but the erroneous estimation of FRF resulting from the coherence between the inputs could to some degree be figured out by adopting MISO system. Finally, it was found the peaks in the seat transmissibilities caused by seat modes usually got reduced by the neighboring subject because of the damping brought from the subject.

Chapter 6 presented a study whereby 12 male subjects were exposed to single-axis, bi-axis and tri-axis excitations in lateral, vertical and roll directions when seated on a rigid seat with a vertical backrest using a 6-axis motion simulator. The apparent masses were estimated by either single-input and single-output (SISO) method or multi-input and single-output (MISO) method according to the number of vibration inputs. Generally speaking, the apparent masses under single-axis excitations and multi-axis ones showed comparable results. All the results showed consistency with those of the existing research. The resonance frequencies of the apparent masses usually had a negative correlation with the weighted root-sum-square (r.s.s.) value of excitation magnitudes, which was more significant under lower r.s.s value or significant only under lower r.s.s value.

Therefore, the biodynamic response arising from one direction with increasing vibration magnitudes in orthogonal directions was equivalent to that with a weighted increasing vibration magnitude in the arising direction. On the other hand, the magnitudes of the apparent masses at resonance usually did not show significant change as the variation of y-axis, z-axis or roll excitation magnitudes. It was also found MISO system was suitable for the more accurate estimation of the apparent masses under multiple inputs than SISO system because of the inevitable mutual coherence between the inputs.

In Chapter 7, based on the characteristics of ride dynamics of rail vehicles such as high-speed trains and biodynamic response of seated human body from experiments, a multi-body dynamic model of the seated human body consisting of abdomen, pelvis, thighs, upper torso (including the shoulders, thorax, arms), head and neck exposed to combined lateral, vertical and roll vibrations was developed. While part of the model parameters were derived from literature available, the others were determined by a procedure of model calibration with a combined genetic algorithm and a minimization algorithm for constrained nonlinear multivariable problem using measured lateral and vertical apparent masses at both the seat pan and backrest in 0.5-20 Hz. The model can be used for the analysis of ride vibration and comfort of passengers of rail vehicles with different weights and heights exposed to multiple excitations in lateral, vertical and roll directions. The methodology may also be applicable to similar analyses of other types of vehicles and seats with varied inclination angles of backrest. A modal analysis with the calibrated model was further conducted, which revealed three vibration modes of the seated human body correlated with the resonances observed in the measured apparent masses. The first mode was found to be associated with the lateral and roll motions of the upper body, the second with lateral motion of the lower body in addition to these motions, and the third mode shape was dominated by the vertical motion of the whole body.

Chapter 8 presented a study whereby a train seat was exposed to single-axis, bi-axis and tri-axis vibrations in lateral, vertical and roll directions under the situations of the bare seat, seat with one seated subject (12 subjects in total) and with two seated subjects (2 pairs) using a 6-axis motion simulator. Generally speaking, the transmissibilities measured under multi-axis vibrations were analogous to those obtained under single-axis ones. There was some evidence of a decrease in the principal resonance frequency as the increase of vibration magnitude evaluated by the root-sum-square (r.s.s.) value, which was more significant at low r.s.s. magnitude or significant only at low r.s.s. magnitude. What is more, this decrease was the most significant for the vertical transmissibilities on the seat pan, followed by the lateral ones on the seat pan and backrest, finally the r_x-direction ones on the seat pan and backrest. Compared with the bare seat, when a subject

was seated on the seat, a new resonance around 5 Hz in the vertical transmissibility on the seat pan was generated by a vertical whole-body human mode, and the resonance arising from the seat mode was greatly attenuated by the damping brought from the human body. In addition, a neighbouring subject would increase the resonance frequency slightly and the damping of the seat mode further. Finally, MISO system was found to be more suitable for the estimation of transmissibility under multiple inputs than the SISO system.

In Chapter 9, considering the characteristics of ride vibration of rail vehicles, a multi-body dynamic model of a double-unit train seat exposed to lateral, vertical and roll vibrations was developed and calibrated using measured seat transmissibilities from the accelerations at the seat base to the accelerations at both the seat pan and backrest in lateral, vertical and roll directions. With the use of a seated human model in Chapter 7, two coupled models of the double-unit seat with one and two subjects were then developed and calibrated using the corresponding measured seat transmissibilities. The models showed good agreement with the experimental data. Using these models, modal analysis was conducted to find out the modal properties of the human-seat system and facilitate discussions in relation to the resonances in the seat transmissibilities. It was found the primary peak around 5 Hz in the vertical transmissibility on the seat pan arose from the whole-body vertical mode of human body with slightly higher modal frequency because the coupling of the human body with the seat reduced the modal frequency and modal damping of this human mode slightly. Two vibration modes around 15 and 27 Hz of the seat contributed to the peaks with approximate frequencies in the seat transmissibilities. The modal shape of the former was related to the lateral and roll motions of two seat pans and backrests moving in phase, while that of the latter was mainly associated with the lateral and roll motions of the two backrests. What is more, human bodies had the tendency of increasing the modal damping of the seat modes.

In Chapter 10, to study the ride comfort of a high-speed train running at a constant speed on a tangent track, a 3D rigid-flexible coupled track-train-seat-human model was developed. The flexible carbody model consisted of six plates with both out-of-plane and in-plane vibrations interconnected by artificial springs, and was calibrated using a modal test available in a published paper. The ride comfort was evaluated by the total equivalent acceleration calculated by the weighted root-sum-square value of the weighted root-mean-square values of lateral, vertical and roll accelerations at the feet, seat-buttock and human-backrest interfaces. It was concluded the track rigidity only had a minor influence on the lateral, vertical and roll vibrations of the carbody floor below 20 Hz, but a rigid track can cause an overestimation of the total equivalent acceleration by over 10 % compared with a flexible track at high speed. The flexible carbody model showed intensified vibration at the carbody floor in the lateral, vertical and roll directions above 7.5 Hz

compared with the rigid carbody model, so the rigid carbody model caused great underestimation of total equivalent acceleration. The total equivalent acceleration showed an increasing tendency as the increasing speed. For symmetrical seat positions, the equivalent accelerations showed analogous tendency as the speed. The ride comfort was the worst close to the ends, followed by the carbody center at high speed. Regardless of the seat position and speed, the vertical acceleration on the seat pan was the most severe, usually followed by the vertical acceleration at the feet. The neighbouring subject resulted in reduced total equivalent acceleration. The damping of the carbody effectively reduced the total equivalent acceleration for every speed. The effect of the suspension stiffness and damping on ride comfort was also studied.

11.2 Discussion and recommendations for future work

11.2.1 Excitation and motion

This thesis was mainly focused on three excitations, that is, vertical, lateral and roll excitations, while the motions of the human body or the seat taken into account were mainly vertical, lateral and roll motions. For the modelling of the human body and human-seat systems, fore-and-aft excitation or the fore-and-aft and pitch motions of the human body and the train seat are recommended to be taken into account in the future because the fore-and-aft direction is also an important direction concerning ride comfort although it may not be as significant on the rail vehicles as on cars. Another reason is that relatively great fore-and-aft and pitch vibrations can be induced by vertical excitation. In this way, the coupled vibration in the mid-sagittal plane (fore-and-aft, vertical and pitch) and the mid-coronal (lateral and roll) plane of the seated human body can be studied.

11.2.2 Modelling

Although the biodynamics of human body and seating dynamics exhibited obvious nonlinearity, linear models of human body and seat have been widely proposed and developed. However, the drawback of linear models is that the parameters of the model under one vibration magnitude may not be applicable well to another vibration magnitude because of the nonlinear characteristics of the human body and the seat exhibited under different vibration magnitudes. In addition, the linear models may work well under random vibrations, but may not be suitable for other kinds of vibrations, e.g., shock vibrations. In the future, nonlinear modelling technique can be developed so that these models are able to characterize the nonlinearity of the biodynamics of human body and seating dynamics better.

11.2.3 Nonlinearity in biodynamics and seating dynamics

Following the discussion in Section 6.4.4, the nonlinearity of the biodynamics is more significant at low r.s.s. value or significant only at low r.s.s. value. This is probably because the subjects tend to adopt more muscle tension to keep the balance under larger vibration level, so as to reduce the involuntary change in muscle tension, thereby reducing the nonlinearity of the human body. The evidence can be found in Matsumoto and Griffin (2002a). How the vibration magnitude influences the muscular activity so as to influence the nonlinearity of biodynamics, and whether there are other reasons behind it can be the next step of study.

Following the discussion in Section 8.4.3, the nonlinearity of the seating dynamics appears more significant at low r.s.s. value or significant only at low r.s.s. value, which may be associated with the above-mentioned biodynamics of the human body and the dynamics of the seat material. The material of the seat cushion (polyurethane foam) is showed to have relatively large rate of change at small vibration magnitude, and becomes more constant as the increasing vibration magnitude of the cushion material by the experimental results of Zhang and Dupuis (2010) under large static compression level. Similar testing can be carried out for the cushion of the train seat to validate this assumption, and whether there are other reasons behind it can be the next step of study.

11.2.4 Modal test

The biodynamics of the human body and seating dynamics are highly related to the modal properties of the human body and the seat. The modal analysis of the human body and the train seat as well as the human-seat systems has been carried out by the multi-body dynamic models in this thesis. Although the results of modal analysis have been validated against the measured apparent mass or seat transmissibility measured in the experiment, it is better if a modal test of the seated human body and seat can be conducted to further validate the results. If the experimental equipment is available, procedures of the modal test of the human body and the seat should be set up and relevant tests should be carried out to validate the modal properties found in the models.

11.2.5 Model calibration

For the model calibration, the possibility of a good convergence of the model to the experiment in a given time is dependent on the optimization algorithm and strategy, while how well the model can reflect the biodynamics of human body or the dynamics of the seat with subjects to some extent relies on the model itself and the choice of the calibration objective. In this thesis, a combined algorithm with the use of two existing functions (‘ga’ and ‘fmincon’) available in Matlab was

developed. However, with the advance and development of optimization algorithms, more powerful and suitable algorithms can be adopted for the model calibration to obtain better convergence of the model to the experiment in a given time in the future. To ensure the model has better representation of the biodynamics of the human body or the dynamics of the train seat with subjects so that the modal properties of the model can be closer to the reality, choosing as many and representative frequency response functions as possible as the calibration objectives is suggested.

11.2.6 3D carbody model

For the track-train-seat-human model in Chapter 10, the analysis results are dependent on the modal properties of the carbody. The analytical carbody model is more suitable for a carbody with simple and ideal structures and for theoretical study. However, for a specific train with a carbody with complicated modal shapes, a finite element model with detailed structure and materials of the carbody can be developed to derive the mass and stiffness matrices, taking the place of the corresponding matrices of the analytical carbody model, then the same analyses can be carried out. In this way, more accurate results may be obtained for that train.

11.2.7 Suggestions for improving ride comfort

The ride comfort is possible to be improved from the perspective of track irregularity, the vehicle-track dynamics and seating dynamics. The improvement of track irregularity is a direct solution from the excitation source, and the guidance on which irregularity should be refined in order to reduce the vibration on the carbody floor in a specific frequency range can refer to Section 10.4.3. However, usually improving the track irregularity is a difficult task. The parameters of vehicle-track system can be modified in order to achieve better ride comfort according to similar analyses in Section 10.5.3. However, when one parameter is changed for better ride comfort, its influence of this change on other indexes of train, e.g. derailment and safety, should be taken into account. On the other hand, the modification of seating dynamics usually has relatively minor effect on other indexes of train, which can provide further potential for improving ride comfort. This implies the significance of the work carried out in this thesis.

11.2.8 Comprehensive ride comfort

Aside from vibration, other factors such as noise, lighting, ventilation, smell, temperature, visual stimuli can also influence passengers' ride comfort when taking a high-speed train, future research

on ride comfort can be focused on the influence of the other factors on the ride comfort and how to combine these factors together to quantitatively evaluate the comprehensive ride comfort.

Appendix

Appendix A

To illustrate the advantage of the new MISO method over the original method, an example of three inputs is made as follows. Assume three inputs are $x_1(t)$, $x_2(t)$ and $x_3(t)$, and the output is $y(t)$.

A.1 In the original MISO method

If the inputs are organized in the sequence of $x_1(t)$, $x_2(t)$ and $x_3(t)$, then the corresponding conditioned inputs are $x_1(t)$ as it is, $x_{2\cdot1}(t)$ —part of $x_2(t)$ that is the coherent with the previous input ($x_1(t)$) has been removed from $x_2(t)$, and $x_{3\cdot2!}(t)$ —part of $x_3(t)$ that is coherent with the previous inputs ($x_1(t)$ and $x_2(t)$) has been removed from $x_3(t)$. The partial coherences are defined as the coherences between these conditioned inputs and the output, so they are respectively

$$\gamma_{1y}^2 = \frac{\left|G_{1y}\right|^2}{G_{11}G_{yy}} \tag{A-1}$$

$$\gamma_{2y\cdot1}^2 = \frac{\left|G_{2y\cdot1}\right|^2}{G_{22\cdot1}G_{yy}} \tag{A-2}$$

$$\gamma_{3y\cdot2!}^2 = \frac{\left|G_{3y\cdot2!}\right|^2}{G_{33\cdot2!}G_{yy}} \tag{A-3}$$

where G_{1y}, $G_{2y\cdot1}$ and $G_{3y\cdot2!}$ are respectively the cross-spectral densities between $x_1(t)$ and $y(t)$, between $x_{2\cdot1}(t)$ and $y(t)$, and between $x_{3\cdot2!}(t)$ and $y(t)$, whereas G_{11}, $G_{22\cdot1}$ and $G_{33\cdot2!}$ are respectively the auto-spectral densities of $x_1(t)$, $x_{2\cdot1}(t)$ and $x_{3\cdot2!}(t)$. G_{yy} is the auto-spectral density of the output $y(t)$.

In this method, if the inputs are organized in a different sequence, e.g., $x_3(t)$, $x_2(t)$ and $x_1(t)$, the conditioned inputs become $x_3(t)$, $x_{2\cdot3}(t)$ and $x_{1\cdot3,2}(t)$. The partial coherences then become

$$\gamma_{3y}^2 = \frac{\left|G_{3y}\right|^2}{G_{33}G_{yy}} \tag{A-4}$$

$$\gamma_{2y\cdot 3}^2 = \frac{\left|G_{2y\cdot 3}\right|^2}{G_{22\cdot 3}G_{yy}} \tag{A-5}$$

$$\gamma_{1y\cdot 3,2}^2 = \frac{\left|G_{1y\cdot 3,2}\right|^2}{G_{11\cdot 3,2}G_{yy}} \tag{A-6}$$

where G_{3y} , $G_{2y\cdot 3}$ and $G_{1y\cdot 3,2}$ are respectively the cross-spectral densities between $x_3(t)$ and $y(t)$, between $x_{2\cdot 3}(t)$ and $y(t)$, and between $x_{1\cdot 3,2}(t)$ and $y(t)$, whereas G_{33}, $G_{22\cdot 3}$ and $G_{11\cdot 3,2}$ are respectively the auto-spectral densities of $x_3(t)$, $x_{2\cdot 3}(t)$ and $x_{1\cdot 3,2}(t)$. Again, G_{yy} is the auto-spectral density of the output $y(t)$.

It is clear that the partial coherences are dependent on the sequence of the inputs. If to evaluate the contribution of a specific input to the output using the partial coherence, for example, in inspection of contribution from $x_1(t)$ to $y(t)$, both γ_{1y}^2 and $\gamma_{1y\cdot 3,2}^2$ calculated from the above-mentioned two different input sequences may be used for evaluating the contribution of the input related to $x_1(t)$ to the output $y(t)$, but the results will be different.

The multiple coherence $\gamma_{y:3!}^2$, however, is independent of the sequence of inputs, as it is defined as the summation of all the partial coherence functions as

$$\gamma_{y:3!}^2 = \gamma_{1y}^2 + \gamma_{2y\cdot 1}^2 + \gamma_{3y\cdot 2!}^2 = \gamma_{3y}^2 + \gamma_{2y\cdot 3}^2 + \gamma_{1y\cdot 3,2}^2 \tag{A-7}$$

A.2 In the new MISO method

If the inputs are organized in the sequence of $x_1(t)$, $x_2(t)$ and $x_3(t)$, then the conditioned inputs are $x_{1\cdot 3,2}(t)$ —part of $x_1(t)$ that is coherent with the other two inputs ($x_2(t)$ and $x_3(t)$) has been removed from $x_1(t)$, $x_{2\cdot 3,1}(t)$ —part of $x_2(t)$ that is coherent with the other two inputs ($x_1(t)$ and $x_3(t)$) has been removed from $x_2(t)$, and $x_{3\cdot 2!}(t)$ —part of $x_3(t)$ that is coherent with the other two inputs ($x_1(t)$ and $x_2(t)$) has been removed from $x_3(t)$. The partial coherences are defined as the coherences between these conditioned inputs and the output, so they are respectively

$$\gamma_{1y\cdot 3,2}^2 = \frac{\left|G_{1y\cdot 3,2}\right|^2}{G_{11\cdot 3,2}G_{yy}} \tag{A-8}$$

$$\gamma_{2y\cdot 3,1}^2 = \frac{\left|G_{2y\cdot 3,1}\right|^2}{G_{22\cdot 3,1}G_{yy}} \tag{A-9}$$

$$\gamma_{3y\cdot 2!}^2 = \frac{\left|G_{3y\cdot 2!}\right|^2}{G_{33\cdot 2!}G_{yy}} \tag{A-10}$$

where $G_{1y\cdot 3,2}$, $G_{2y\cdot 3,1}$ and $G_{3y\cdot 2!}$ are respectively the cross-spectral densities between $x_{1\cdot 3,2}(t)$ and $y(t)$, between $x_{2\cdot 3,1}(t)$ and $y(t)$, and between $x_{3\cdot 2!}(t)$ and $y(t)$, whereas $G_{11\cdot 3,2}$, $G_{22\cdot 3,1}$ and $G_{33\cdot 2!}$ are respectively the auto-spectral densities of $x_{1\cdot 3,2}(t)$, $x_{2\cdot 3,1}(t)$ and $x_{3\cdot 2!}(t)$. G_{yy} is the auto-spectral density of the output $y(t)$.

Even if the inputs are organized in a different sequence, e.g., $x_3(t)$, $x_2(t)$ and $x_1(t)$, the corresponding conditioned inputs are the same as the previous ones, that is $x_{3\cdot 2!}(t)$, $x_{2\cdot 3,1}(t)$ and $x_{1\cdot 3,2}(t)$. Therefore, the conditioned inputs are independent of the sequence of inputs, so are the partial coherence functions. Consequently, when one specific partial coherence is used to evaluate the contribution of one specific input to the output, the result is unique. For example, $\gamma_{1y\cdot 3,2}^2$ can be used for evaluating the contribution of the input related to $x_1(t)$ to the output $y(t)$.

However, the summation of all the partial coherence functions is no longer the multiple coherence function. The multiple coherence is

$$\gamma_{y\cdot 3!}^2 = 1 - \frac{G_{nn}}{G_{yy}} = \gamma_{1y\cdot 3,2}^2 + \gamma_{2y\cdot 3,1}^2 + \gamma_{3y\cdot 2!}^2 + \gamma_{cy} \tag{A-11}$$

where $\gamma_{cy} = (\sum_{i=1}^{3}\left|H_{iy}\right|^2 G_{ii}\gamma_{ii}^2 + \sum_{i=1}^{3}\sum_{j=1, j\neq i}^{3} H_{iy}^* G_{ij} H_{jy}) / G_{yy}$ is the percentage of the spectrum of the output due to the coherent parts between the inputs, which can be used to evaluate the contribution of the coherent parts between the three inputs to the output.

Note that the multiple coherences in the original method and the new method are the same.

As can be seen, all the partial coherence functions ($\gamma_{1y\cdot 3,2}^2$, $\gamma_{2y\cdot 3,1}^2$ and $\gamma_{3y\cdot 2!}^2$) and γ_{cy} are independent of the sequence of the inputs in the new method proposed in this thesis.

Appendix B

B.1 The equations and parameters

The forces from the rear and front second suspensions are respectively

$$F_{su1} = k_s[w(\frac{L}{2} - l_b, t) + w_b(t) + \varphi_b(t)l_b - w_{bgr}] + c_s[\frac{\partial w(\frac{L}{2} - l_b, t)}{\partial t} + \dot{w}_b(t) + \dot{\varphi}_b(t)l_b - \dot{w}_{bgr}] \tag{B-1}$$

$$F_{su2} = k_s[w(\frac{L}{2} + l_b, t) + w_b(t) - \varphi_b(t)l_b - w_{bgf}] + c_s[\frac{\partial w(\frac{L}{2} + l_b, t)}{\partial t} + \dot{w}_b(t) - \dot{\varphi}_b(t)l_b - \dot{w}_{bgf}] \tag{B-2}$$

The forces transmitted from the first and second wheelsets of the primary suspensions at the rear bogie are respectively

$$F_{bgr1} = k_P[w_{bgr} + \varphi_{bgr}l_w - w_{wr1}] + c_P[\dot{w}_{bgr} + \dot{\varphi}_{bgr}l_w - \dot{w}_{wr1}] \tag{B-3}$$

$$F_{bgr2} = k_P[w_{bgr} - \varphi_{bgr}l_w - w_{wr2}] + c_P[\dot{w}_{bgr} - \dot{\varphi}_{bgr}l_w - \dot{w}_{wr2}] \tag{B-4}$$

The forces transmitted from the first and second wheelsets of the primary suspensions at the front bogie are respectively

$$F_{bgf1} = k_P[w_{bgf} + \varphi_{bgf}l_w - w_{wf1}] + c_P[\dot{w}_{bgf} + \dot{\varphi}_{bgf}l_w - \dot{w}_{wf1}] \tag{B-5}$$

$$F_{bgf2} = k_P[w_{bgf} - \varphi_{bgf}l_w - w_{wf2}] + c_P[\dot{w}_{bgf} - \dot{\varphi}_{bgf}l_w - \dot{w}_{wf2}] \tag{B-6}$$

The motion equations of the human-seat model are

$$\begin{aligned} &m_0\ddot{z}_0 + k_{0z}(z_0 - z_f(s_i)) + k_{bz}(z_0 - z_3) + k_{1z}(z_0 - z_1) + c_{0z}(\dot{z}_0 - \dot{z}_f(s_i)) \\ &+c_{bz}(\dot{z}_0 - \dot{z}_3) + c_{1z}(\dot{z}_0 - \dot{z}_1) = 0 \end{aligned} \tag{B-7}$$

$$\begin{aligned} &m_2(e\cos\alpha\ddot{\theta} + \ddot{z}_1) + m_1\ddot{z}_1 + k_{1z}(z_1 - z_0) + c_{1z}(\dot{z}_1 - \dot{z}_0) - k_{3z}(z_3 - z_1 - e\theta\cos\alpha) \\ &-c_{3z}(\dot{z}_3 - \dot{z}_1 - e\dot{\theta}\cos\alpha) = 0 \end{aligned} \tag{B-8}$$

$$m_3\ddot{x}_1 + m_1\ddot{x}_1 + m_2(\ddot{x}_1 + e\sin\alpha\ddot{\theta}) + k_{1x}x_1 + c_{1x}\dot{x}_1 = 0 \tag{B-9}$$

$$\begin{aligned} &m_3\ddot{z}_3 + k_{3z}(z_3 - z_1 - e\theta\cos\alpha) + k_{bz}(z_3 - z_0) + c_{3z}(\dot{z}_3 - \dot{z}_1 - e\dot{\theta}\cos\alpha) \\ &+c_{bz}(\dot{z}_3 - \dot{z}_0) = 0 \end{aligned} \tag{B-10}$$

$$\begin{aligned} &J_2\ddot{\theta} + m_2e\sin\alpha\ddot{x}_1 + m_2e\cos\alpha\ddot{z}_1 - e\cos\alpha k_{3z}(z_3 - z_1 - e\theta\cos\alpha) + k_2\theta \\ &-e\cos\alpha c_{3z}(\dot{z}_3 - \dot{z}_1 - e\dot{\theta}\cos\alpha) + c_2\dot{\theta} = 0 \end{aligned} \tag{B-11}$$

where $J_2 = I_2 + m_2 e^2$.

Table B-1 Parameters of the train-seat-human system

Parameters	Values	Parameters	Values
m_b	41750 kg	m_2	18.65 kg
m_{bg}	3040 kg	m_3	41.75 kg
m_w	1780 kg	I_2	0.0055 kgm^2
L	24.5 m	k_{1x}	101418.1 N/m
l_b	8.75 m	c_{1x}	955.92 Ns/m
l_w	1.25 m	k_2	70.66 N/m
J_{bg}	3930 kgm^2	c_2	8.52 Ns/m
k_s	1.06×10^6 N/m	k_{3z}	74331.91 N/m
c_s	1.804×10^5 Ns/m	c_{3z}	833.91 Ns/m
k_p	2.36×10^6 N/m	e	0.2728 m
c_p	7.84×10^4 Ns/m	α	1.4383 rad
I_b	2.08×10^6 kgm^2	m_1	0.138 kg
ξ_i	0.005	k_{bz}	10467.87 N/m
$E_b I$	4.56×10^9 Nm^2	c_{bz}	556.36 Ns/m
m_0	50 kg	k_{1z}	85640.11 N/m
k_{0z}	7065216112 N/m	c_{1z}	517.62 Ns/m
c_{0z}	130.91 Ns/m	A	1.5×10^{-6}
N_1	19	Ω_1	2.06×10^{-2} rad/s
Ω_2	0.825 rad/s	l_{hs}	1.2 m

B.2 The principle of geometry filter effect

The geometry filter effect of the vehicle was analyzed in terms of the train-seat-human model in Eq. (4-23). Similar analyses can be found in Cossalter *et al.* (2006), Zhou *et al.* (2009), Gong *et al.* (2012) and Cao *et al.* (2015). It is easy to find that for the symmetrical modes like 1st, 3rd bending modes and bounce mode,

$$\mathbf{H}_{c1}(\omega)=\mathbf{H}_{c2}(\omega)=\mathbf{H}_{c3}(\omega)=\mathbf{H}_{c4}(\omega) \tag{B-12}$$

However, for the anti-symmetrical modes like 2nd, 4th bending modes and pitch mode,

$$\mathbf{H}_{c1}(\omega)=\mathbf{H}_{c2}(\omega)=-\mathbf{H}_{c3}(\omega)=-\mathbf{H}_{c4}(\omega) \tag{B-13}$$

Thus, for the symmetrical modes,

$$\left|\mathbf{H}_c^t(\omega)\right| = 2\left|\mathbf{H}_{c1}(\omega)\right|\sqrt{1+\cos\omega\tau_1}\sqrt{1+\cos\omega\tau_2} \quad \text{(B-14)}$$

While for the anti-symmetrical modes,

$$\left|\mathbf{H}_c^t(\omega)\right| = 2\left|\mathbf{H}_{c1}(\omega)\right|\sqrt{1+\cos\omega\tau_1}\sqrt{1-\cos\omega\tau_2} \quad \text{(B-15)}$$

It can be seen that when $\omega\tau_1 = (2n-1)\pi$, that is, the frequency satisfies $f_r = \frac{(2n-1)V}{4l_w}, n = 1,2,3\ldots$, $\left|\mathbf{H}_c^t(\omega)\right|$ will be null for all the modes. This frequency (f_r) is related to l_w, so it is called 'wheelbase filter effect'.

On the other hand, for the symmetrical modes, when $\omega\tau_2 = (2n-1)\pi$, that is, the frequency satisfies $f_r^s = \frac{(2n-1)V}{4l_b}, n = 1,2,3\ldots$, $\left|\mathbf{H}_c^t(\omega)\right|$ will be null for these modes. What is more, there will be a local maximum approximately when $\omega\tau_2 = 2n\pi$, that is, $f_r^s = \frac{nV}{2l_b}, n = 1,2,3\ldots$; While for the anti-symmetrical modes, when $\omega\tau_2 = 2n\pi$, that is, the frequency satisfies $f_r^{as} = \frac{nV}{2l_b}, n = 1,2,3\ldots$, $\left|\mathbf{H}_c^t(\omega)\right|$ will be null for these modes. What is more, there will be a local maximum approximately when $\omega\tau_2 = (2n-1)\pi$, that is, $f_r^{as} = \frac{(2n-1)V}{4l_b}, n = 1,2,3\ldots.$

These frequencies (f_r^s and f_r^{as}) are related to l_b, so it is called 'bogie spacing filter effect'.

Both the 'wheelbase filter effect' and 'bogie spacing filter effect' are geometry filter effect of the vehicle.

For a train running at a constant speed of V, if the wavelength of the track irregularity satisfies $\lambda = \frac{4l_b}{2n-1}$, the track irregularity will excite the symmetrical modes least, but the anti-symmetrical modes drastically. On the other hand, if $\lambda = \frac{2l_b}{n}$, the track irregularity will excite the anti-symmetrical modes least, but the symmetrical modes drastically.

Frequency response function $\mathbf{H}_c^t(\omega)$ in Eq. (4-35) when V=300 km/h was calculated for all the modes, as plotted in Fig. B-1. It can be seen that all the FRFs showed troughs at the same frequencies whatever the mode is, which resulted from the wheelbase filter effect. Furthermore,

because of the bogie spacing filter effect, troughs that located at the frequencies $\frac{(2n-1)V}{4l_b}$ appeared in the FRFs of the symmetrical modes; around these frequencies, the FRFs of the anti-symmetrical modes showed peaks. On the contrary, there were troughs at the frequencies $\frac{nV}{2l_b}$ in the FRFs of the anti-symmetrical modes, the FRFs of the symmetrical modes showed peaks around these frequencies. In addition, every mode showed a global maximum around its natural frequency. For example, the FRF of the first bending mode showed a global peak around 9.7 Hz. Finally, FRF of the first bending mode dominated in the frequency range of 0.5—20 Hz that is usually considered for ride comfort.

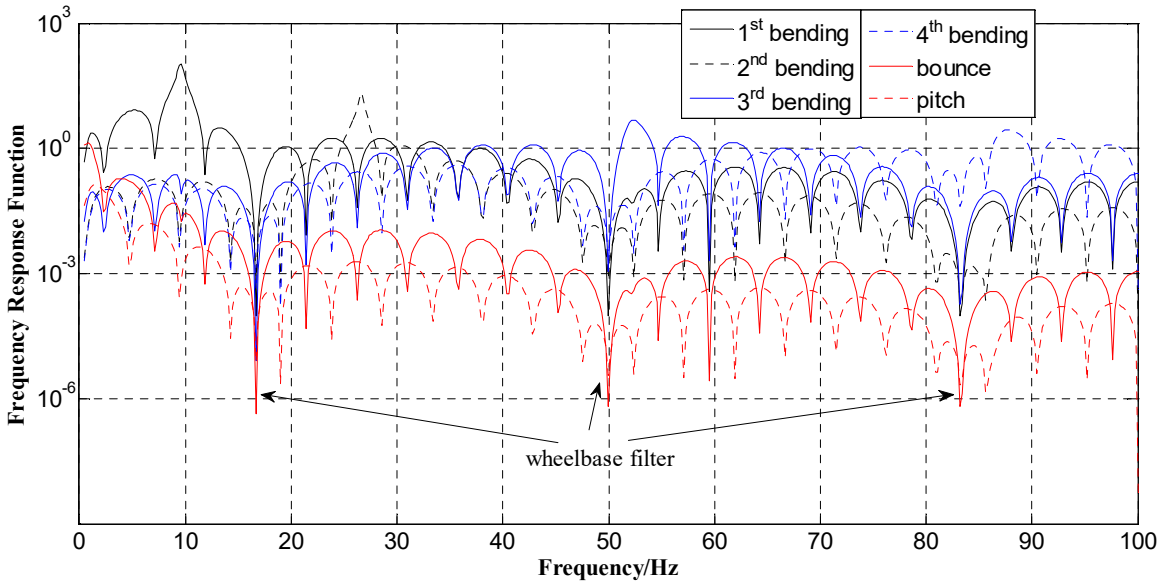

Fig. B-1 Frequency response functions $\mathbf{H}_c^t(\omega)$ when V=300 km/h for all carbody modes.

Appendix C

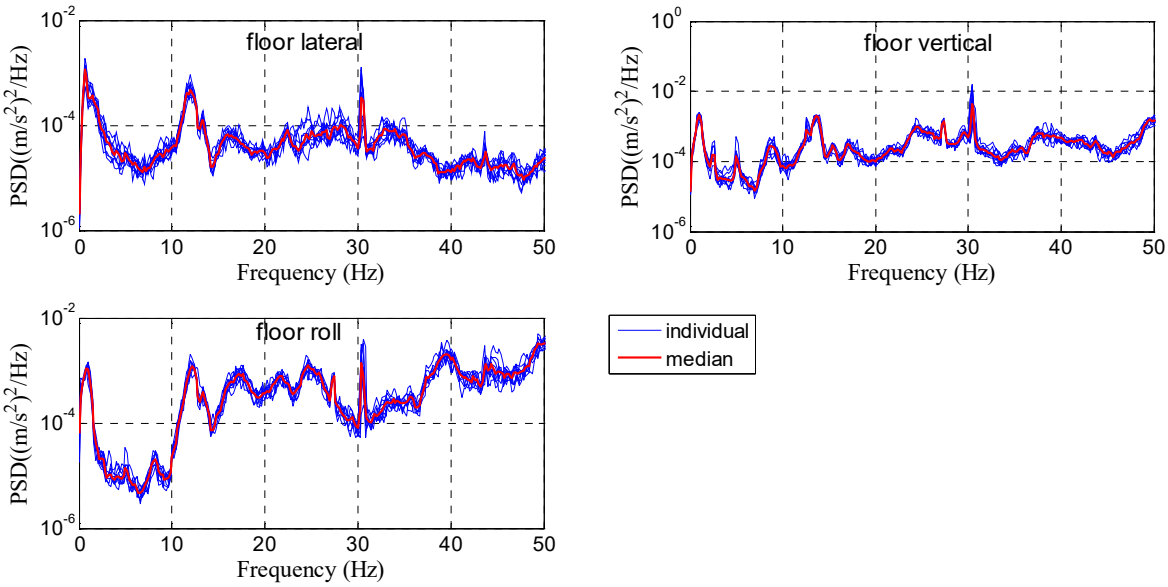

Fig. C-1 The individual and median PSDs of the acceleration inputs from the floor for the front seat with one subject.

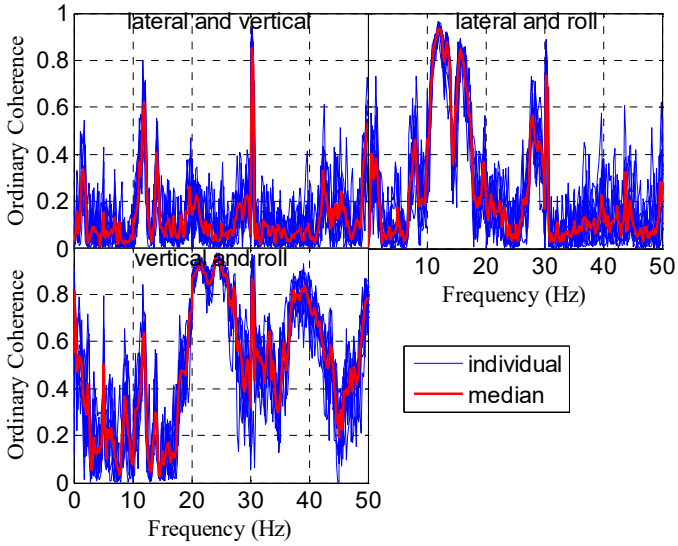

Fig. C-2 The individual and median ordinary coherences between the three acceleration inputs measured under the front seat with one subject.

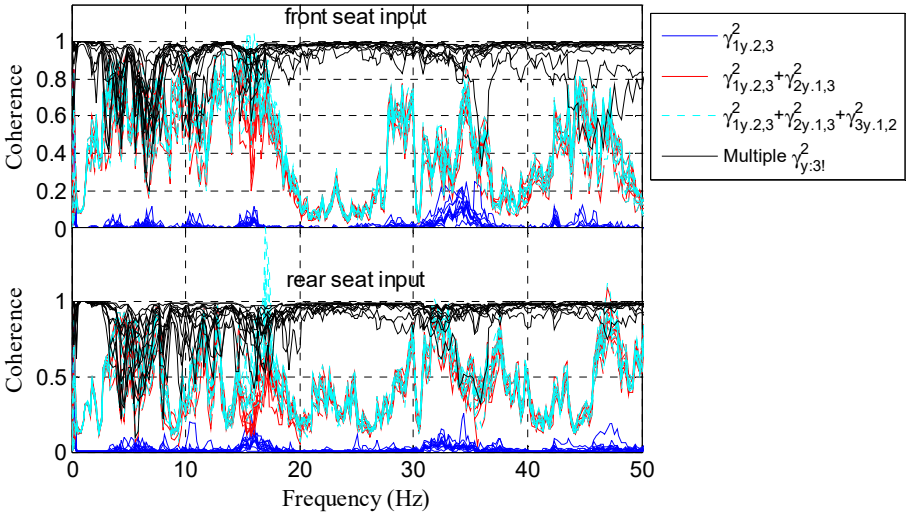

Fig. C-3 Individual coherences of the laboratory measurement with 12 different seated subjects adopting the measured inputs of the front and rear seats in the transmission to the vertical acceleration on the seat pan (output *y*). (The subscripts 1, 2 and 3 correspond to lateral, vertical and roll accelerations on the floor, respectively)

Fig. C-4 The internal structure of the train seat

Appendix D

Table D-1 Wilcoxon signed-rank test for the effect of excitation magnitude in z direction on the resonance frequency and modulus at resonance for the apparent mass in y direction on the seat pan

z magnitude	z=0.25	z=0.5	z=1.0	Significant difference proportion (different r_x)
(a)r_x=0				
z=0	ns/ns/ns; ns/ns/ns	ns/ns/ns; ns/ns/ns	ns/ns/ns; ns/ns/ns	1/18;0/18
z=0.25		ns/ns/ns; ns/ns/ns	ns/*/ns; ns/ns/ns	
z=0.5			ns/ns/ns; ns/ns/ns	
(b)r_x=0.5				
z=0	ns/ns/ns; ns/ns/ns	ns/ns/ns; ns/ns/ns	ns/ns/ns; ns/ns/ns	3/18; 1/18
z=0.25		*/ns/ns; ns/*/ns	***/***/ns; ns/ns/ns	
z=0.5			ns/ns/ns; ns/ns/ns	
(c)r_x=0.75				
z=0	ns/ns/ns; ns/ns/ns	*/ns/ns; ns/ns/ns	ns/ns/ns; ns/ns/ns	1/18; 1/18
z=0.25		ns/ns/ns; ns/ns/ns	ns/ns/ns; ns/ns/*	
z=0.5			ns/ns/ns; ns/ns/ns	
(d)r_x=1.0				
z=0	*/ns/ns; ns/ns/ns	**/ns/ns; ns/ns/ns	**/ns/ns; ns/ns/**	3/18; 4/18
z=0.25		ns/ns/ns; ns/*/ns	ns/ns/ns; ns/ns/*	
z=0.5			ns/ns/ns; ns/ns/*	
Significant difference proportion (different y)	y=0.25: 6/24;0/24 y=0.5: 2/24;2/24 y=1.0: 0/24;4/24			

ns=not significant, p>0.05; *= p<0.05;**= p<0.01;***= p<0.005, Wilcoxon;
The p-value for different excitation magnitudes in y direction is ranked as y=0.25/y=0.5/y=1.0, separated by slash;
The effect on resonance frequency and modulus at resonance is shown before and after ';', respectively.

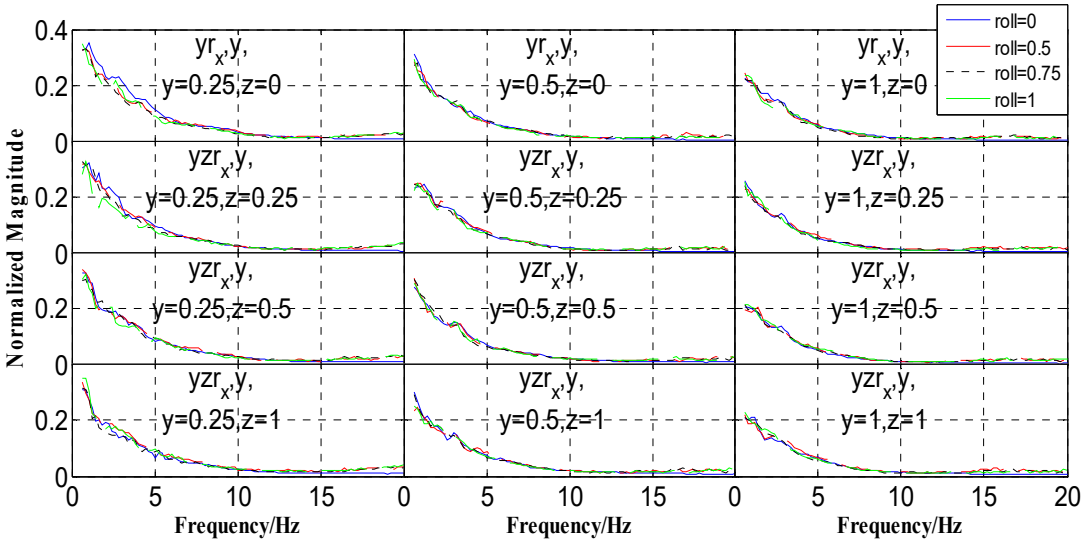

Fig. D-1 Comparison between median normalized apparent masses in y direction on the backrest for 12 subjects under different excitation magnitudes in roll direction.

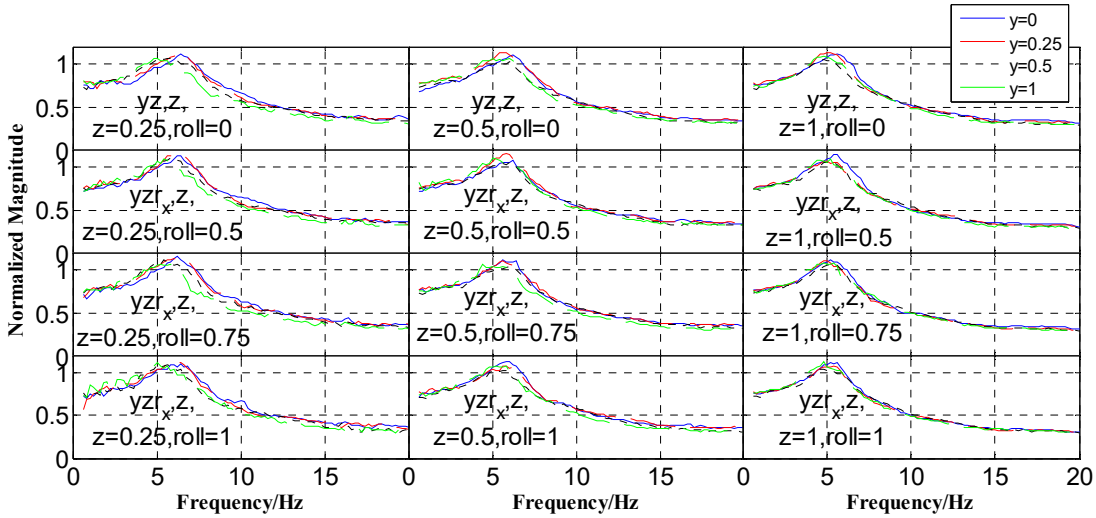

Fig. D-2 Comparison between median normalized apparent masses in z direction on the seat pan for 12 subjects under different excitation magnitudes in y direction.

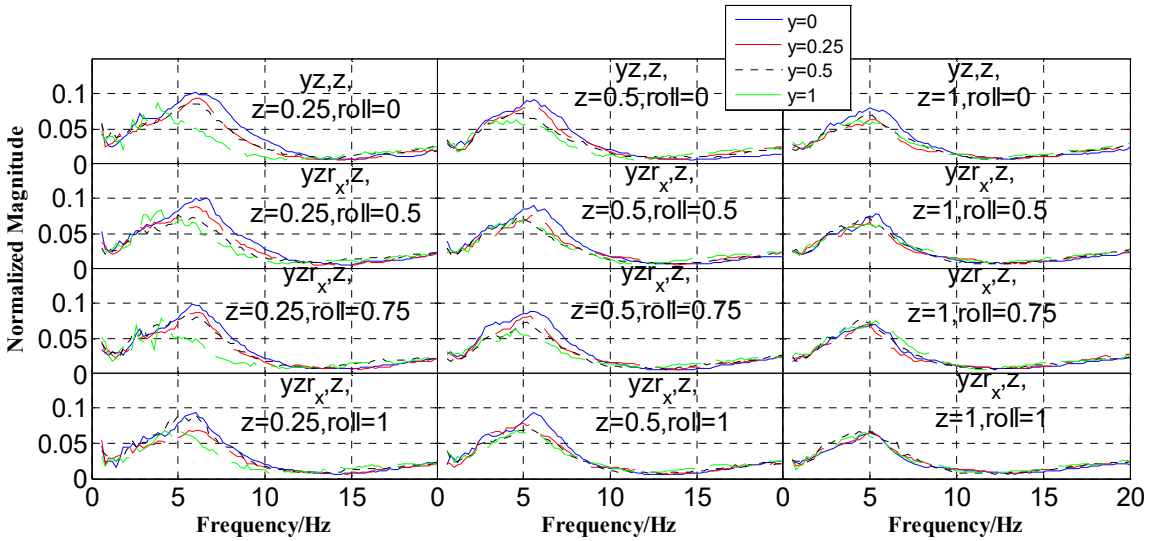

Fig. D-3 Comparison between median normalized apparent masses in z direction on the backrest for 12 subjects under different excitation magnitudes in y direction.

Table D-2 Wilcoxon signed-rank test for the effect of excitation magnitude in y direction on the resonance frequency and modulus at resonance for the apparent mass in z direction on the backrest

y magnitude	y=0.25	y=0.5	y=1.0	Significant difference proportion (different r_x)
(a)r_x=0				
y=0	*/ns/ns;ns/ns/*	ns/**/*;ns/*/ns	***/***/ns;ns/***/ns	10/18; 3/18
y=0.25		ns/ns/ns;ns/ns/ns	***/***/***;ns/ns/ns	
y=0.5			***/**/ns;ns/ns/ns	
(b)r_x=0.5				
y=0	*/ns/ns;ns/ns/*	*/*/ns;ns/*/ns	*/***/ns;**/*/ns	8/18;4/18
y=0.25		ns/***/ns;ns/ns/ns	ns/***/ns;ns/ns/ns	
y=0.5			ns/*/ns;ns/ns/ns	
(c)r_x=0.75				
y=0	ns/ns/ns;ns/ns/ns	***/ns/ns;ns/ns/ns	*/*/ns;***/ns/ns	5/18;1/18
y=0.25		ns/ns/ns;ns/ns/ns	*/***/ns;ns/ns/ns	
y=0.5			ns/ns/ns;ns/ns/ns	
(d)r_x=1.0				
y=0	ns/ns/ns;ns/ns/ns	**/**/ns;ns/ns/ns	**/*/ns;ns/ns/ns	5/18;0/18
y=0.25		ns/ns/ns;ns/ns/ns	***/ns/ns;ns/ns/ns	
y=0.5			ns/ns/ns;ns/ns/ns	
Significant difference proportion (different z)	z=0.25: 13/24;2/24 z=0.5: 13/24;4/24 z=1.0: 2/24;2/24			

ns=not significant, p>0.05; *= p<0.05;**= p<0.01;***= p<0.005, Wilcoxon;
The p-value for different excitation magnitudes in z direction is ranked as z=0.25/z=0.5/z=1.0, separated by slash;
The effect on resonance frequency and modulus at resonance is shown before and after ';', respectively.

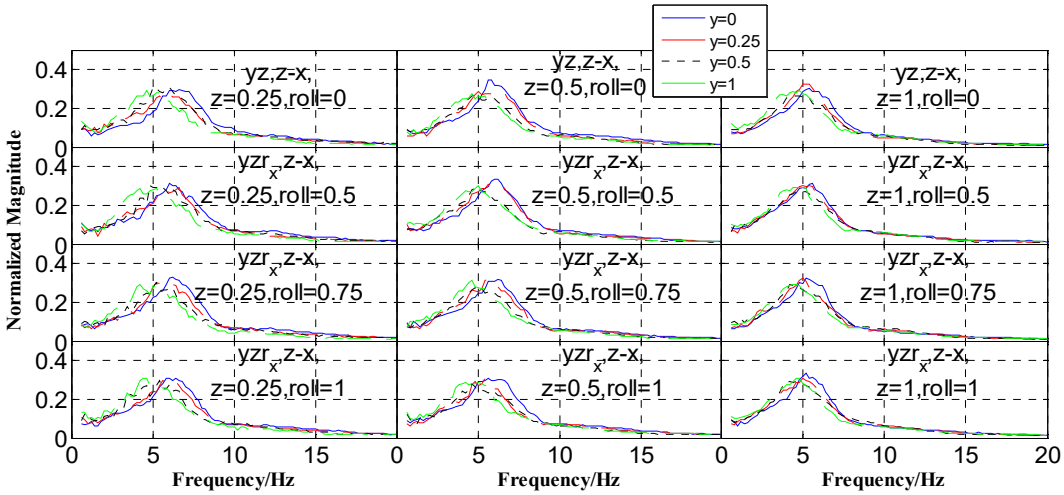

Fig. D-4 Comparison between median normalized z-x apparent masses on the seat pan for 12 subjects under different excitation magnitudes in y direction.

Table D-3 Wilcoxon signed-rank test for the effect of excitation magnitude in y direction on the resonance frequency and modulus at resonance for z-x apparent mass on the seat pan

y magnitude	y=0.25	y=0.5	y=1.0	Significant difference proportion (different r_x)
(a)r_x=0				
y=0	ns/ns/ns;ns/ns/ns	***/***/***;ns/ns/ns	***/***/***;ns/***/ns	11/18;2/18
y=0.25		ns/*/ns;ns/ns/**	***/***/**;ns/ns/ns	
y=0.5			***/ns/ns;ns/ns/ns	
(b)r_x=0.5				
y=0	ns/ns/ns;ns/ns/ns	*/*/***;ns/ns/*	***/***/***;ns/ns/ns	12/18;3/18
y=0.25		*/**/ns;ns/*/*	***/**/*;ns/ns/ns	
y=0.5			***/ns/ns;ns/ns/ns	
(c)r_x=0.75				
y=0	ns/ns/ns;ns/ns/ns	***/**/ns;ns/ns/ns	***/***/*;**/ns/ns	11/18;2/18
y=0.25		ns/ns/ns;ns/*/ns	***/***/*;ns/ns/ns	
y=0.5			*/*/*;ns/ns/ns	
(d)r_x=1.0				
y=0	ns/*/ns;ns/ns/ns	***/***/ns;ns/ns/*	***/***/***;ns/*/ns	13/18;2/18
y=0.25		***/*/ns;ns/ns/ns	***/***/***;ns/ns/ns	
y=0.5			*/ns/*;ns/ns/ns	
Significant difference proportion (different z)	z=0.25: 18/24;1/24 z=0.5: 17/24;4/24 z=1.0: 12/24; 4/24			

ns=not significant, p>0.05; *= p<0.05;**= p<0.01;***= p<0.005, Wilcoxon;
The p-value for different excitation magnitudes in z direction is ranked as z=0.25/z=0.5/z=1.0, separated by slash;
The effect on resonance frequency and modulus at resonance is shown before and after ';', respectively.

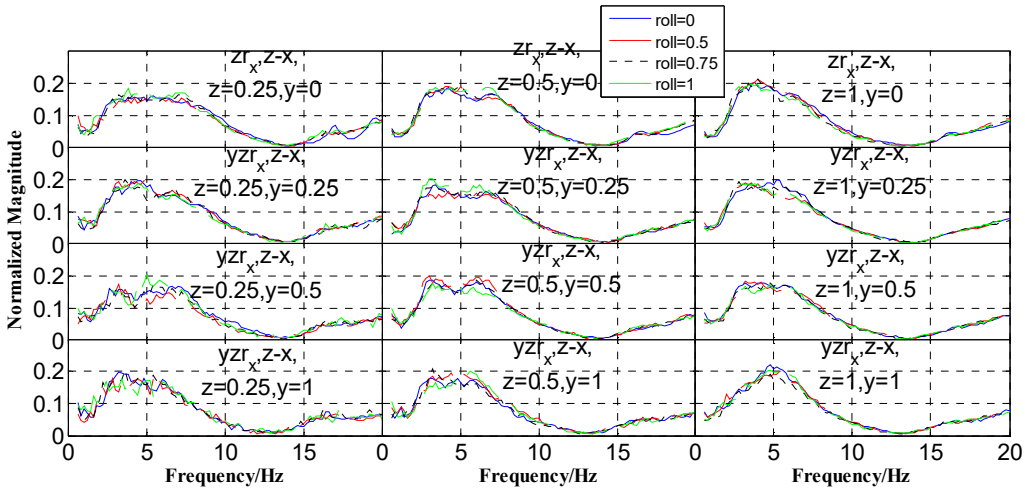

Fig. D-5 Comparison between median normalized z-x apparent masses on the backrest for 12 subjects under different excitation magnitudes in roll direction.

Appendix E

Table E-1 The definition of springs and dampers between human body segments

Springs	Dampers	At which point	Between which bodies	Directions
k_{l1}	c_{l1}	$\mathbf{D}_1$	B_1 and B_2	$\mathbf{n}_y$
k_{v1}	c_{v1}	$\mathbf{D}_1$	B_1 and B_2	$\mathbf{n}_z$
k_{r1}	c_{r1}	N/A*	B_1 and B_2	around $\mathbf{n}_x$
k_{l2}	c_{l2}	$\mathbf{D}_2$	B_2 and B_3	$\mathbf{n}_y$
k_{l2}	c_{l2}	$\mathbf{D}_3$	B_2 and B_4	$\mathbf{n}_y$
k_{v2}	c_{v2}	$\mathbf{D}_2$	B_2 and B_3	$\mathbf{n}_z$
k_{v2}	c_{v2}	$\mathbf{D}_3$	B_2 and B_4	$\mathbf{n}_z$
k_{r2}	c_{r2}	N/A	B_2 and B_3	around $\mathbf{n}_x$
k_{r2}	c_{r2}	N/A	B_2 and B_4	around $\mathbf{n}_x$
k_{l3}	c_{l3}	$\mathbf{D}_7$	B_1 and B_7	$\hat{\mathbf{n}}_{5y}$
k_{v3}	c_{v3}	$\mathbf{D}_7$	B_1 and B_7	$\hat{\mathbf{n}}_{5z}$
k_{r5}	c_{r5}	N/A	B_1 and B_7	around $\hat{\mathbf{n}}_{5x}$
k_{l4}	c_{l4}	$\mathbf{D}_8$	B_7 and B_8	$\hat{\mathbf{n}}_{7y}$
k_{v4}	c_{v4}	$\mathbf{D}_8$	B_7 and B_8	$\hat{\mathbf{n}}_{7z}$
k_{r6}	c_{r6}	N/A	B_7 and B_8	around $\hat{\mathbf{n}}_{7x}$

*N/A means ‘not applicable’.

Table E-2 The definition of springs and dampers between the human body and seat

Springs	Dampers	At which points	Between which bodies	Directions
k_{tl1}	c_{tl1}	$\mathbf{C}_1$ ($\mathbf{C}_{1s}$)	B_1 and B_5	$\hat{\mathbf{n}}_{5y}$
k_{tv1}	c_{tv1}	$\mathbf{C}_1$ ($\mathbf{C}_{1s}$)	B_1 and B_5	$\hat{\mathbf{n}}_{5z}$
k_{r3}	c_{r3}	N/A*	B_1 and B_5	around $\hat{\mathbf{n}}_{5x}$
k_{tl2}	c_{tl2}	$\mathbf{C}_2$ ($\mathbf{C}_{2s}$)	B_2 and B_6	$\mathbf{n}_y$
k_{tv2}	c_{tv2}	$\mathbf{C}_2$ ($\mathbf{C}_{2s}$)	B_2 and B_6	$\mathbf{n}_z$
k_{r4}	c_{r4}	N/A	B_2 and B_6	around $\mathbf{n}_x$
k_{tl3}	c_{tl3}	$\mathbf{C}_3$ ($\mathbf{C}_{3s}$)	B_3 and B_6	$\mathbf{n}_y$
k_{tl3}	c_{tl3}	$\mathbf{C}_4$ ($\mathbf{C}_{4s}$)	B_4 and B_6	$\mathbf{n}_y$
k_{tv3}	c_{tv3}	$\mathbf{C}_3$ ($\mathbf{C}_{3s}$)	B_3 and B_6	$\mathbf{n}_z$
k_{tv3}	c_{tv3}	$\mathbf{C}_4$ ($\mathbf{C}_{4s}$)	B_4 and B_6	$\mathbf{n}_z$
k_{tl4}	c_{tl4}	$\mathbf{C}_5$ ($\mathbf{C}_{5s}$)	B_5 and B_7	$\hat{\mathbf{n}}_{5y}$
k_{tv4}	c_{tv4}	$\mathbf{C}_5$ ($\mathbf{C}_{5s}$)	B_5 and B_7	$\hat{\mathbf{n}}_{5z}$
k_{r7}	c_{r7}	N/A	B_5 and B_7	around $\hat{\mathbf{n}}_{5x}$

*N/A means 'not applicable'.

The forces transmitted between the bodies B_2 and B_3, B_2 and B_4, B_1 and B_7, B_7 and B_8 were respectively computed as

$$\mathbf{f}_{23} = \mathbf{l}_{23}^{\mathbf{D}_2}\mathrm{diag}(0, k_{l2}, k_{v2}) + \dot{\mathbf{l}}_{23}^{\mathbf{D}_2}\mathrm{diag}(0, c_{l2}, c_{v2}) = \begin{bmatrix} 0 & f_{23(y)} & f_{23(z)} \end{bmatrix}\mathbf{S} \tag{E-1}$$

$$\mathbf{f}_{24} = \mathbf{l}_{24}^{\mathbf{D}_3}\mathrm{diag}(0, k_{l2}, k_{v2}) + \dot{\mathbf{l}}_{24}^{\mathbf{D}_3}\mathrm{diag}(0, c_{l2}, c_{v2}) = \begin{bmatrix} 0 & f_{24(y)} & f_{24(z)} \end{bmatrix}\mathbf{S} \tag{E-2}$$

$$\mathbf{f}_{17} = \mathbf{l}_{17}^{\mathbf{D}_7}\mathbf{T}_{11}^{\mathrm{T}}(\alpha)\mathrm{diag}(0, k_{l3}, k_{v3}) + \dot{\mathbf{l}}_{17}^{\mathbf{D}_7}\mathbf{T}_{11}^{\mathrm{T}}(\alpha)\mathrm{diag}(0, c_{l3}, c_{v3}) = \begin{bmatrix} 0 & f_{17(y)} & f_{17(z)} \end{bmatrix}\hat{\mathbf{S}}_5 \tag{E-3}$$

$$\mathbf{f}_{78} = \mathbf{l}_{78}^{\mathbf{D}_8}\mathbf{T}_{11}^{\mathrm{T}}(\alpha)\mathrm{diag}(0, k_{l4}, k_{v4}) + \dot{\mathbf{l}}_{78}^{\mathbf{D}_8}\mathbf{T}_{11}^{\mathrm{T}}(\alpha)\mathrm{diag}(0, c_{l4}, c_{v4}) = \begin{bmatrix} 0 & f_{78(y)} & f_{78(z)} \end{bmatrix}\hat{\mathbf{S}}_7 \tag{E-4}$$

The forces at the contact points ($\mathbf{C}_2$, $\mathbf{C}_3$, $\mathbf{C}_4$ and $\mathbf{C}_5$) were then calculated respectively as

$$\mathbf{f}_{26}^{\mathbf{C}_2} = \mathbf{l}_{26}^{\mathbf{C}_2}\mathrm{diag}(0, k_{tl2}, k_{tv2}) + \dot{\mathbf{l}}_{26}^{\mathbf{C}_2}\mathrm{diag}(0, c_{tl2}, c_{tv2}) = \begin{bmatrix} 0 & f_{26(y)}^{\mathbf{C}_2} & f_{26(z)}^{\mathbf{C}_2} \end{bmatrix}\mathbf{S} \tag{E-5}$$

$$\mathbf{f}_{36}^{\mathbf{C}_3} = \mathbf{l}_{36}^{\mathbf{C}_3}\mathrm{diag}(0, k_{tl3}, k_{tv3}) + \dot{\mathbf{l}}_{36}^{\mathbf{C}_3}\mathrm{diag}(0, c_{tl3}, c_{tv3}) = \begin{bmatrix} 0 & f_{36(y)}^{\mathbf{C}_3} & f_{36(z)}^{\mathbf{C}_3} \end{bmatrix}\mathbf{S} \tag{E-6}$$

$$\mathbf{f}_{46}^{\mathbf{C}_4} = \mathbf{l}_{46}^{\mathbf{C}_4}\mathrm{diag}(0, k_{tl3}, k_{tv3}) + \dot{\mathbf{l}}_{46}^{\mathbf{C}_4}\mathrm{diag}(0, c_{tl3}, c_{tv3}) = \begin{bmatrix} 0 & f_{46(y)}^{\mathbf{C}_4} & f_{46(z)}^{\mathbf{C}_4} \end{bmatrix}\mathbf{S} \tag{E-7}$$

$$\mathbf{f}_{57}^{\mathbf{C}_5} = \mathbf{l}_{57}^{\mathbf{C}_5}\mathbf{T}_{11}^{\mathrm{T}}(\alpha)\mathrm{diag}(0, k_{tl4}, k_{tv4}) + \dot{\mathbf{l}}_{57}^{\mathbf{C}_5}\mathbf{T}_{11}^{\mathrm{T}}(\alpha)\mathrm{diag}(0, c_{tl4}, c_{tv4}) = \begin{bmatrix} 0 & f_{57(y)}^{\mathbf{C}_5} & f_{57(z)}^{\mathbf{C}_5} \end{bmatrix}\hat{\mathbf{S}}_5 \tag{E-8}$$

Table E-3 The calibrated parameter for the subject of 171 cm in height and 83.5 kg in weight under a combined excitation of lateral (0.5 ms^{-2} r.m.s.), vertical (1.0 ms^{-2} r.m.s.) and roll (0.75 rad/s^2 r.m.s.) vibration corresponding to the results in Fig. 7-5 and Fig. 7-6

Parameter	Value	Parameter	Value	Parameter	Value
k_{l1}	10.0 kN/m	c_{v4}	3.6 kN·s/m	k_{tv4}	1.0 kN/m
c_{l1}	6.6 kN·s/m	k_{r6}	144.0 N·m/rad	c_{tv4}	51.2 N·s/m
k_{v1}	81.1 kN/m	c_{r6}	573.4 mN·m·s/rad	k_{r7}	10.0 N·m/rad
c_{v1}	1.1 kN·s/m	k_{tl1}	1.0 kN/m	c_{r7}	10.9 N·m·s/rad
k_{r1}	956.7 N·m/rad	c_{tl1}	7.1 N·s/m	m_1	14.19 kg
c_{r1}	1.9 mN·m·s/rad	k_{tv1}	1.0 kN/m	m_2	10.04 kg
k_{l2}	85.6 kN/m	c_{tv1}	0	m_3	8.31 kg
c_{l2}	101.1 mN·s/m	k_{r3}	289.4 N·m/rad	m_7	20.88 kg
k_{v2}	74.7 kN/m	c_{r3}	26.7 N·m·s/rad	m_8	4.61 kg
c_{v2}	2.0 mN·s/m	k_{tl2}	2.86 kN/m	$z_{\mathbf{C}_1}^{B_1}$	0.0078 m
k_{r2}	14.4 kN·m/rad	c_{tl2}	399.3 N·s/m	$y_{\mathbf{C}_1}^{B_1}$	-0.0196 m
c_{r2}	92.8 kN·m·s/rad	k_{tv2}	48.97 kN/m	$x_{\mathbf{C}_2}^{B_2}$	0
k_{l3}	22.0 kN/m	c_{tv2}	0.170 N·s/m	$y_{\mathbf{C}_2}^{B_2}$	0.1197 m
c_{l3}	29.1 kN·s/m	k_{r4}	2296.7 kN·m/rad	$x_{\mathbf{C}_3}^{B_3}$	0.0287 m
k_{v3}	18.9 kN/m	c_{r4}	2.95 kN·m·s/rad	$y_{\mathbf{C}_3}^{B_3}$	0.0342 m
c_{v3}	84.9 kN·s/m	k_{tl3}	4.80 kN/m	$x_{\mathbf{C}_4}^{B_4}$	0.0286 m
k_{r5}	80.55 N·m/rad	c_{tl3}	0	$y_{\mathbf{C}_4}^{B_4}$	0.0342 m
c_{r5}	0	k_{tv3}	153.9 kN/m	$y_{\mathbf{C}_5}^{B_7}$	0.1197 m
k_{l4}	36.4 kN/m	c_{tv3}	1.8 mN·s/m	$z_{\mathbf{C}_5}^{B_7}$	-0.0605 m
c_{l4}	3.2 N·s/m	k_{tl4}	1.28 kN/m	$x_{\mathbf{D}_7}^{B_1}$	0
k_{v4}	944.8 kN/m	c_{tl4}	60.8 N·s/m	$y_{\mathbf{D}_7}^{B_1}$	0.0912 m

Appendix F

Table F-1 Wilcoxon signed-rank test for the effect of roll excitation magnitude on the principal resonance frequency and modulus at resonance for the transmissibility in y direction on the seat pan

roll magnitude	roll=0.5	roll=0.75	roll=1.0	Significant difference proportion (different z)
(a)z=0				
roll=0	***/***/ns; */***/**	***/***/***; ***/***/ns	***/***/**; ns/***/*	9/18; 10/18
roll=0.5		Ns/*/ns; ***/ns/ns	Ns/ns/ns; ***/ns/ns	
roll=0.75			Ns/ns/ns; ***/ns/ns	
(b)z=0.25				
roll=0	Ns/ns/*; ns/*/*	*/***/ns; ns/ns/ns	***/***/ns; ***/**/ns	8/18; 6/18
roll=0.5		Ns/ns/ns; ns/ns/ns	***/**/ns; */ns/ns	
roll=0.75			Ns/***/ns; ***/ns/ns	
(c)z=0.5				
roll=0	**/ns/*; ***/ns/***	***/ns/*; **/ns/***	Ns/***/*; ***/ns/*	9/18; 8/18
roll=0.5		Ns/*/ns; ns/ns/ns	Ns/***/ns; */ns/ns	
roll=0.75			**/ns/ns; ns/*/ns	
(d)z=1.0				
roll=0	Ns/ns/ns; ns/ns/ns	Ns/ns/ns; ns/*/**	Ns/ns/ns; ns/*/ns	1/18; 5/18
roll=0.5		Ns/ns/ns; ns/ns/*	Ns/*/ns; ns/ns/ns	
roll=0.75			Ns/ns/ns; ns/ns/*	
Significant difference proportion (different y)	y=0.25: 9/24;12/24 y=0.5: 12/24;8/24 y=1.0: 6/24;9/24			

ns=not significant, p>0.05; *= p<0.05;**= p<0.01;***= p<0.005, Wilcoxon;
The p-value for different excitation magnitudes in y direction is ranked as y=0.25/y=0.5/y=1.0, separated by slash;
The effect on resonance frequency and modulus at resonance is shown before and after ';', respectively.

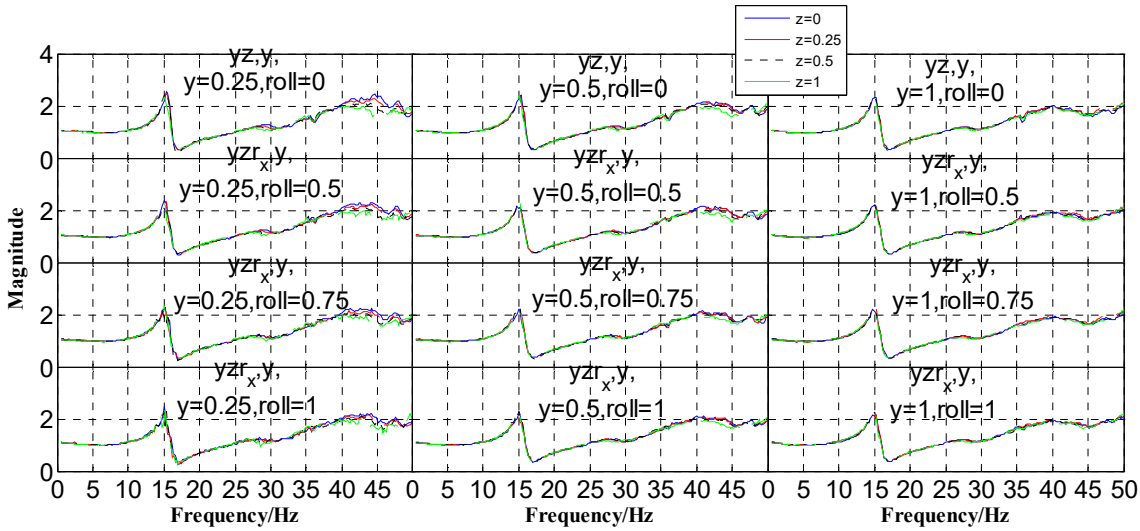

Fig. F-1 Comparison between median transmissibilities in y direction on the seat pan for 12 subjects under different excitation magnitudes in z direction.

Table F-2 Wilcoxon signed-rank test for the effect of excitation magnitude in z direction on the principal resonance frequency and modulus at resonance for the transmissibility in y direction on the backrest

z magnitude	z=0.25	z=0.5	z=1.0	Significant difference proportion (different r_x)
(a)r_x=0				
z=0	ns/ns/ns; ns/***/ns	ns/ns/ns; */***/ns	*/ns/ns; **/*/ns	3/18;8/18
z=0.25		Ns/ns/ns; ***/ns/ns	*/ns/ns; */ns/ns	
z=0.5			*/ns/ns; ***/ns/ns	
(b)r_x=0.5				
z=0	Ns/***/ns; ns/ns/ns	Ns/***/*; ns/ns/*	**/***/ns; ns/ns/ns	7/18; 2/18
z=0.25		ns/ns/ns; ns/ns/*	*/ns/ns; ns/ns/ns	
z=0.5			**/ns/ns; ns/ns/ns	
(c)r_x=0.75				
z=0	***/***/ns; ns/*/*	ns/*/ns; ns/**/ns	*/***/ns; ns/*/ns	9/18; 5/18
z=0.25		**/***/ns; ns/ns/ns	Ns/ns/ns; ns/ns/ns	
z=0.5			*/*/ns; */ns/ns	
(d)r_x=1.0				
z=0	ns/ns/ns; **/**/ns	*/ns/ns; ns/ns/ns	ns/ns/*; ns/ns/ns	7/18; 7/18
z=0.25		***/ns/ns; ***/*/***	Ns/*/*; ***/ns/ns	
z=0.5			***/**/ns; ns/ns/***	
Significant difference proportion (different y)	y=0.25: 13/24;9/24 y=0.5: 10/24;8/24 y=1.0: 3/24;5/24			

ns=not significant, p>0.05; *= p<0.05;**= p<0.01;***= p<0.005, Wilcoxon;
The p-value for different excitation magnitudes in y direction is ranked as y=0.25/y=0.5/y=1.0, separated by slash;
The effect on resonance frequency and modulus at resonance is shown before and after ';', respectively.

Table F-3 Wilcoxon signed-rank test for the effect of excitation magnitude in y direction on the principal resonance frequency and modulus at resonance for the transmissibility in z direction on the seat pan

y magnitude	y=0.25	y=0.5	y=1.0	Significant difference proportion (different r_x)
(a)r_x=0				
y=0	Ns/*/ns;ns/ns/ns	ns/ns/*;ns/*/ns	*/***/***;***/***/*	9/18; 10/18
y=0.25		ns/ns/ns;*/ns/ns	*/*/***;***/***/*	
y=0.5			ns/ns/**;*/**/ns	
(b)r_x=0.5				
y=0	Ns/ns/ns;ns/ns/ns	ns/ns/ns;ns/*/ns	*/***/ns;**/***/*	7/18;8/18
y=0.25		ns/ns/ns;ns/ns/ns	ns/***/*;*/***/*	
y=0.5			*/***/*;ns/*/ns	
(c)r_x=0.75				
y=0	Ns/ns/ns;ns/ns/ns	*/ns/ns;*/ns/ns	*/***/*;**/***/ns	7/18;7/18
y=0.25		ns/ns/ns;*/ns/ns	ns/*/ns;*/***/ns	
y=0.5			Ns/**/***;ns/***/ns	
(d)r_x=1.0				
y=0	Ns/ns/ns;ns/ns/ns	ns/ns/*;ns/ns/ns	ns/***/*;*/***/*	5/18;6/18
y=0.25		Ns/ns/ns;ns/ns/ns	ns/***/ns;**/***/ns	
y=0.5			Ns/*/ns;ns/***/ns	
Significant difference proportion (different z)	z=0.25: 6/24;12/24 z=0.5: 12/24;14/24 z=1.0: 10/24;5/24			

ns=not significant, p>0.05; *= p<0.05;**= p<0.01;***= p<0.005, Wilcoxon;
The p-value for different excitation magnitudes in z direction is ranked as z=0.25/z=0.5/z=1.0, separated by slash;
The effect on resonance frequency and modulus at resonance is shown before and after ';', respectively.

Table F-4 Wilcoxon signed-rank test for the effect of excitation magnitude in z direction on the resonance frequency and modulus at resonance for the transmissibility in r_x direction on the seat pan

z magnitude	z=0.25	z=0.5	z=1.0	Significant difference proportion (different r_x)
(a)r_x=0.5				
z=0	Ns/ns/*/**;*/ns/ns/ns	ns/ns/ns/ns;ns/ns/ns/ns	***/**/***/**;ns/*/ns/ns	11/24;9/24
z=0.25		ns/ns/ns/ns;***/***/*/*	***/*/ns/ns;***/***/ns/*	
z=0.5			***/***/ns/*;ns/ns/ns/ns	
(b)r_x=0.75				
z=0	Ns/ns/*/ns;***/ns/ns/ns	ns/**/ns/ns;ns/ns/*/ns	***/ns/ns/ns;ns/ns/ns/ns	9/24;5/24
z=0.25		ns/ns/***/ns;***/ns/*/ns	***/*/***/ns;**/ns/ns/ns	
z=0.5			*/***/ns/ns;ns/ns/ns/ns	
(c)r_x=1.0				
z=0	***/***/*/*;ns/ns/*/ns	ns/ns/ns/ns;ns/ns/ns/ns	ns/ns/***/ns;ns/ns/ns/***	11/24;5/24
z=0.25		***/**/ns/**;ns/ns/*/ns	ns/***/ns/***;ns/ns/ns/*	
z=0.5			Ns/ns/*/ns;ns/ns/ns/***	
Significant difference proportion (different y)	y=0: 8/18;6/18 y=0.25: 9/18;3/18 y=0.5: 8/18;5/18 y=1.0: 6/18;5/18			

ns=not significant, p>0.05; *= p<0.05;**= p<0.01;***= p<0.005, Wilcoxon;
The p-value for different excitation magnitudes in y direction is ranked as y=0/y=0.25/y=0.5/y=1.0, separated by slash;
The effect on resonance frequency and modulus at resonance is shown before and after ';', respectively.

Table F-5 Wilcoxon signed-rank test for the effect of excitation magnitude in y direction on the resonance frequency and modulus at resonance for the transmissibility in r_x direction on the backrest

y magnitude	y=0.5	y=0.75	y=1.0	Significant difference proportion (different z)
(a)z=0				
y=0	ns/ns/ns;ns/ns/ns	***/ns/ns;*/ns/ns	ns/*/ns;ns/ns/ns	7/18;1/18
y=0.5		***/ns/**;ns/ns/ns	ns/*/ns;ns/ns/ns	
y=0.75			***/*/ns;ns/ns/ns	
(b)z=0.25				
y=0	Ns/ns/ns;**/***/*	Ns/***/**;***/***/***	***/***/ns;ns/ns/ns	10/18;7/18
y=0.5		Ns/***/***;ns/ns/ns	***/**/ns;ns/ns/ns	
y=0.75			*/ns/**;ns/ns/***	
(c)z=0.5				
y=0	Ns/ns/ns;ns/ns/ns	*/ns/ns;ns/ns/ns	Ns/*/ns;ns/ns/ns	5/18;0/18
y=0.5		ns/ns/**;ns/ns/ns	Ns/*/ns;ns/ns/ns	
y=0.75			Ns/*/ns;ns/ns/ns	
(d)z=1.0				
y=0	*/ns/*;*/ns/ns	***/***/*;ns/ns/ns	ns/ns/ns;ns/ns/ns	9/18;2/18
y=0.5		Ns/***/ns;**/ns/ns	*/ns/ns;ns/ns/ns	
y=0.75			***/***/ns;ns/ns/ns	
Significant difference proportion (different r_x)	r_x=0.5: 11/24;5/24 r_x=0.75: 13/24;2/24 r_x=1.0: 7/24;3/24			

ns=not significant, p>0.05; *= p<0.05;**= p<0.01;***= p<0.005, Wilcoxon;

The p-value for different excitation magnitudes in r_x direction is ranked as r_x =0.25/ r_x =0.5/ r_x =1.0, separated by slash;

The effect on resonance frequency and modulus at resonance is shown before and after ';', respectively.

Appendix G

Table G-1 The definition of springs and dampers between seat segments

Springs	Dampers	Points	Between which bodies	Directions
k_{sl1}	c_{sl1}	${}^{j}\mathbf{D}_4$	${}^{j}B_5$ and ${}^{j}B_9$	$\mathbf{n}_y$
k_{sv1}	c_{sv1}	${}^{j}\mathbf{D}_4$	${}^{j}B_5$ and ${}^{j}B_9$	$\mathbf{n}_z$
k_{sr1}	c_{sr1}	N/A*	${}^{j}B_5$ and ${}^{j}B_9$	around $\mathbf{n}_x$
k_{sl2}	c_{sl2}	${}^{j}\mathbf{C}_6$ (${}^{j}\mathbf{C}_{6s}$)	${}^{j}B_6$ and ${}^{j}B_9$	$\mathbf{n}_y$
k_{sv2}	c_{sv2}	${}^{j}\mathbf{C}_6$ (${}^{j}\mathbf{C}_{6s}$)	${}^{j}B_6$ and ${}^{j}B_9$	$\mathbf{n}_z$
k_{sr2}	c_{sr2}	N/A	${}^{j}B_6$ and ${}^{j}B_9$	around $\mathbf{n}_x$
k_{sl3}	c_{sl3}	$\mathbf{D}_5$	${}^{j}B_9$ and B_B	$\mathbf{n}_y$
k_{sv3}	c_{sv3}	$\mathbf{D}_5$	${}^{j}B_9$ and B_B	$\mathbf{n}_z$
k_{sr3}	c_{sr3}	N/A	${}^{j}B_9$ and B_B	around $\mathbf{n}_x$
k_{sl4}	c_{sl4}	$\mathbf{D}_6$	${}^{r}B_9$ and ${}^{l}B_9$	$\mathbf{n}_y$
k_{sv4}	c_{sv4}	$\mathbf{D}_6$	${}^{r}B_9$ and ${}^{l}B_9$	$\mathbf{n}_z$
k_{sr4}	c_{sr4}	N/A	${}^{r}B_9$ and ${}^{l}B_9$	around $\mathbf{n}_x$
${}^{j}k_{sl5}$	${}^{j}c_{sl5}$	${}^{j}\mathbf{C}_7$ (${}^{j}\mathbf{C}_{7s}$)	B_B and platform	$\mathbf{n}_y$
${}^{j}k_{sv5}$	${}^{j}c_{sv5}$	${}^{j}\mathbf{C}_7$ (${}^{j}\mathbf{C}_{7s}$)	B_B and platform	$\mathbf{n}_z$
${}^{j}k_{sr5}$	${}^{j}c_{sr5}$	N/A	B_B and platform	around $\mathbf{n}_x$

*N/A means 'not applicable'. $j = l, r$.

The force transmitted between the seat pan cushion (${}^{j}B_6$) and corresponding seat pan frame (${}^{j}B_9$) at the point ${}^{j}\mathbf{C}_6$ ($j = l, r$) is

$$ {}^{j}\mathbf{f}_{69}^{\mathbf{C}_6} = {}^{j}\mathbf{l}_{69}^{\mathbf{C}_6}\mathrm{diag}(0, k_{sl2}, k_{sv2}) + {}^{j}\dot{\mathbf{l}}_{69}^{\mathbf{C}_6}\mathrm{diag}(0, c_{sl2}, c_{sv2}) = \begin{bmatrix} 0 & {}^{j}f_{69(y)}^{\mathbf{C}_6} & {}^{j}f_{69(z)}^{\mathbf{C}_6} \end{bmatrix}\mathbf{S} \quad \text{(G-1)} $$

The force transmitted between the seat base (B_B) and the seat pan frame (${}^{j}B_9$) at the point $\mathbf{D}_5$ ($j = l, r$) is

$$ {}^{j}\mathbf{f}_{9B}^{\mathbf{D}_5} = {}^{j}\mathbf{l}_{9B}^{\mathbf{D}_5}\mathrm{diag}(0, k_{sl3}, k_{sv3}) + {}^{j}\dot{\mathbf{l}}_{9B}^{\mathbf{D}_5}\mathrm{diag}(0, c_{sl3}, c_{sv3}) = \begin{bmatrix} 0 & {}^{j}f_{9B(y)}^{\mathbf{D}_5} & {}^{j}f_{9B(z)}^{\mathbf{D}_5} \end{bmatrix}\mathbf{S} \quad \text{(G-2)} $$

The force transmitted between the left seat pan frame (${}^{l}B_9$) and the right one (${}^{r}B_9$) at the point $\mathbf{D}_6$ is

$$ \mathbf{f}_{99}^{\mathbf{D}_6} = \mathbf{l}_{99}^{\mathbf{D}_6}\mathrm{diag}(0, k_{sl4}, k_{sv4}) + \dot{\mathbf{l}}_{99}^{\mathbf{D}_6}\mathrm{diag}(0, c_{sl4}, c_{sv4}) = \begin{bmatrix} 0 & f_{99(y)}^{\mathbf{D}_6} & f_{99(z)}^{\mathbf{D}_6} \end{bmatrix}\mathbf{S} \quad \text{(G-3)} $$

The force transmitted between the seat base (${}^{j}B_{B}$) and the platform at the point ${}^{j}\mathbf{C}_{7}$ ($j = l, r$) is

$$ {}^{j}\mathbf{f}_{B_B}^{\mathbf{C}_7} = {}^{j}\mathbf{l}_{B_B}^{\mathbf{C}_7}\mathrm{diag}(0, {}^{j}k_{sl5}, {}^{j}k_{sv5}) + {}^{j}\mathbf{i}_{B_B}^{\mathbf{C}_7}\mathrm{diag}(0, {}^{j}c_{sl5}, {}^{j}c_{sv5}) = \begin{bmatrix} 0 & {}^{j}f_{B_B(y)}^{\mathbf{C}_7} & {}^{j}f_{B_B(z)}^{\mathbf{C}_7} \end{bmatrix}\mathbf{S} \quad \text{(G-4)} $$

Table G-2 The definition of springs and dampers between the human body and the train seat

Springs	Dampers	Points	Between which bodies	Directions
${}^{j}k_{cl1}$	${}^{j}c_{cl1}$	${}^{j}\mathbf{C}_1$ (${}^{j}\mathbf{C}_{1s}$)	${}^{j}B_1$ and ${}^{j}B_5$	${}^{j}\hat{\mathbf{n}}_{5y}$
${}^{j}k_{cv1}$	${}^{j}c_{cv1}$	${}^{j}\mathbf{C}_1$ (${}^{j}\mathbf{C}_{1s}$)	${}^{j}B_1$ and ${}^{j}B_5$	${}^{j}\hat{\mathbf{n}}_{5z}$
${}^{j}k_{cr3}$	${}^{j}c_{cr3}$	N/A	${}^{j}B_1$ and ${}^{j}B_5$	around ${}^{j}\hat{\mathbf{n}}_{5x}$
${}^{j}k_{cl2}$	${}^{j}c_{cl2}$	${}^{j}\mathbf{C}_2$ (${}^{j}\mathbf{C}_{2s}$)	${}^{j}B_2$ and ${}^{j}B_6$	$\mathbf{n}_y$
${}^{j}k_{cv2}$	${}^{j}c_{cv2}$	${}^{j}\mathbf{C}_2$ (${}^{j}\mathbf{C}_{2s}$)	${}^{j}B_2$ and ${}^{j}B_6$	$\mathbf{n}_z$
${}^{j}k_{cr4}$	${}^{j}c_{cr4}$	N/A	${}^{j}B_2$ and ${}^{j}B_6$	around $\mathbf{n}_x$
${}^{j}k_{cl3}$	${}^{j}c_{cl3}$	${}^{j}\mathbf{C}_3$ (${}^{j}\mathbf{C}_{3s}$)	${}^{j}B_3$ and ${}^{j}B_6$	$\mathbf{n}_y$
${}^{j}k_{cl3}$	${}^{j}c_{cl3}$	${}^{j}\mathbf{C}_4$ (${}^{j}\mathbf{C}_{4s}$)	${}^{j}B_4$ and ${}^{j}B_6$	$\mathbf{n}_y$
${}^{j}k_{cv3}$	${}^{j}c_{cv3}$	${}^{j}\mathbf{C}_3$ (${}^{j}\mathbf{C}_{3s}$)	${}^{j}B_3$ and ${}^{j}B_6$	$\mathbf{n}_z$
${}^{j}k_{cv3}$	${}^{j}c_{cv3}$	${}^{j}\mathbf{C}_4$ (${}^{j}\mathbf{C}_{4s}$)	${}^{j}B_4$ and ${}^{j}B_6$	$\mathbf{n}_z$
${}^{j}k_{cl4}$	${}^{j}c_{cl4}$	${}^{j}\mathbf{C}_5$ (${}^{j}\mathbf{C}_{5s}$)	${}^{j}B_5$ and ${}^{j}B_7$	${}^{j}\hat{\mathbf{n}}_{5y}$
${}^{j}k_{cv4}$	${}^{j}c_{cv4}$	${}^{j}\mathbf{C}_5$ (${}^{j}\mathbf{C}_{5s}$)	${}^{j}B_5$ and ${}^{j}B_7$	${}^{j}\hat{\mathbf{n}}_{5z}$
${}^{j}k_{cr7}$	${}^{j}c_{cr7}$	N/A	${}^{j}B_5$ and ${}^{j}B_7$	around ${}^{j}\hat{\mathbf{n}}_{5x}$

*N/A means 'not applicable'. $j = l$, for the subject on the left; $j = r$, for the subject on the right.

Table G-3 The calibrated parameters for the train seat under a combined excitation of lateral (0.5 ms^{-2} r.m.s.), vertical (1.0 ms^{-2} r.m.s.) and roll (0.75 rad/s^2 r.m.s.) vibration corresponding to the results in Fig. 9-2 and Fig. 9-3

Parameter	Value	Parameter	Value	Parameter	Value
k_{sl1}	10.08 MN/m	c_{sl3}	2.87 kN·s/m	${}^{r}k_{sl5}$	582.1 MN/m
k_{sv1}	673.2 kN/m	c_{sv3}	67.68 kN·s/m	${}^{r}k_{sv5}$	1.55 MN/m
k_{sr1}	100.9 kN·m/rad	c_{sr3}	3.0 mN·m·s/rad	${}^{r}k_{sr5}$	4.86 kN·m/rad
c_{sl1}	10.56 MN·s/m	k_{sl4}	772.4 kN/m	${}^{r}c_{sl5}$	979.3 N·s/m
c_{sv1}	8.6 kN·s/m	k_{sv4}	129.0 kN/m	${}^{r}c_{sv5}$	0.063 N·s/m
c_{sr1}	2.1 mN·m·s/rad	k_{sr4}	102.0 N·m/rad	${}^{r}c_{sr5}$	0.98 mN·m·s/rad
k_{sl2}	225.3 kN/m	c_{sl4}	33.5 mN·s/m	m_9	9.97 kg
k_{sv2}	194.4 kN/m	c_{sv4}	46.2 MN·s/m	m_B	21.88 kg
k_{sr2}	17.7 kN·m/rad	c_{sr4}	7.5 kN·m·s/rad	${}^{l}y_{\mathbf{D}_4}^{B_5}$	0.177 m
c_{sl2}	0.147 mN·s/m	${}^{l}k_{sl5}$	21.6 kN/m	${}^{l}x_{\mathbf{C}_6}^{B_9}$	0.046 m
c_{sv2}	597.8 N·s/m	${}^{l}k_{sv5}$	9.17 MN/m	${}^{l}y_{\mathbf{C}_6}^{B_9}$	0.20 m
c_{sr2}	3.1 N·m·s/rad	${}^{l}k_{sr5}$	29.99 kN·m/rad	${}^{l}x_{\mathbf{D}_6}^{B_9}$	0.150 m
k_{sl3}	552.4 kN/m	${}^{l}c_{sl5}$	34.3 N·s/m	${}^{l}x_{\mathbf{C}_7}^{B_B}$	0.0038 m
k_{sv3}	3.47 MN/m	${}^{l}c_{sv5}$	16.0 N·s/m	${}^{r}x_{\mathbf{C}_7}^{B_B}$	-0.142 m
k_{sr3}	111.4 kN·m/rad	${}^{l}c_{sr5}$	0.029 N·m·s/rad		

Table G-4 The calibrated parameters of the contact between the train seat and the subject of 171 cm in height and 83.5 kg in weight seated on the left under a combined excitation of lateral (0.5 ms^{-2} r.m.s.), vertical (1.0 ms^{-2} r.m.s.) and roll (0.75 rad/s^2 r.m.s.) vibration corresponding to the results in Fig. 9-5 and Fig. 9-7

Parameter	Value	Parameter	Value	Parameter	Value
${}^{l}k_{cl1}$	100 N/m	${}^{l}k_{cv3}$	100 N/m	${}^{l}k_{cr7}$	7.0 kN·m/rad
${}^{l}c_{cl1}$	0	${}^{l}c_{cv3}$	736.0 N·s/m	${}^{l}c_{cr7}$	1.68 N·m·s/rad
${}^{l}k_{cv1}$	1.0 kN/m	${}^{l}k_{cl4}$	100 N/m	${}^{l}z_{\mathbf{C}_1}^{B_1}$	0.039 m
${}^{l}c_{cv1}$	357.0 N·s/m	${}^{l}c_{cl4}$	0	${}^{l}x_{\mathbf{C}_2}^{B_2}$	-0.061 m
${}^{l}k_{cl2}$	100 N/m	${}^{l}k_{cv4}$	100.0 N/m	${}^{l}x_{\mathbf{C}_3}^{B_3}$	0.062 m
${}^{l}c_{cl2}$	0	${}^{l}c_{cv4}$	125.7 N·s/m	${}^{l}y_{\mathbf{C}_1}^{B_1}$	0.0386 m
${}^{l}k_{cv2}$	225.6 kN/m	${}^{l}k_{cr3}$	44.3 MN·m/rad	${}^{l}y_{\mathbf{C}_2}^{B_2}$	0.1197 m
${}^{l}c_{cv2}$	2.1 kN·s/m	${}^{l}c_{cr3}$	34.3 kN·m·s/rad	${}^{l}y_{\mathbf{C}_3}^{B_3}$	-0.0342 m
${}^{l}k_{cl3}$	100 N/m	${}^{l}k_{cr4}$	3.6 kN·m/rad	${}^{l}x_{\mathbf{C}_4}^{B_4}$	-0.0897 m
${}^{l}c_{cl3}$	73.9 N·s/m	${}^{l}c_{cr4}$	0	${}^{l}y_{\mathbf{C}_4}^{B_4}$	-0.029 m
${}^{l}y_{\mathbf{C}_5}^{B_7}$	0.1196 m	${}^{l}z_{\mathbf{C}_5}^{B_7}$	0.080 m		

Appendix H

The lateral forces between the carbody and front bogie on the left and right are respectively

$$F_{ycb1l} = k_{sy}(-y_{fl} + y_{b1} - \theta_{b1}h_T) + c_{sy}(-\dot{y}_{fl} + \dot{y}_{b1} - \dot{\theta}_{b1}h_T) \tag{H-1}$$

$$F_{ycb1r} = k_{sy}(-y_{fr} + y_{b1} - \theta_{b1}h_T) + c_{sy}(-\dot{y}_{fr} + \dot{y}_{b1} - \dot{\theta}_{b1}h_T) \tag{H-2}$$

The lateral forces between the carbody and rear bogie on the left and right are respectively

$$F_{ycb2l} = k_{sy}(-y_{bl} + y_{b2} - \theta_{b2}h_T) + c_{sy}(-\dot{y}_{bl} + \dot{y}_{b2} - \dot{\theta}_{b2}h_T) \tag{H-3}$$

$$F_{ycb2r} = k_{sy}(-y_{br} + y_{b2} - \theta_{b2}h_T) + c_{sy}(-\dot{y}_{br} + \dot{y}_{b2} - \dot{\theta}_{b2}h_T) \tag{H-4}$$

The lateral suspension force acting on the carbody is

$$F_{syc} = F_{ycb1l} + F_{ycb1r} + F_{ycb2l} + F_{ycb2r} \tag{H-5}$$

The vertical forces between the carbody and front bogie on the left and right are respectively

$$F_{zcb1l} = k_{sz}(-z_{fl} + z_{b1} + \frac{1}{2}\theta_{b1}L_{b2}) + c_{sz}(-\dot{z}_{fl} + \dot{z}_{b1} + \frac{1}{2}\dot{\theta}_{b1}L_{b2}) \tag{H-6}$$

$$F_{zcb1r} = k_{sz}(-z_{fr} + z_{b1} - \frac{1}{2}\theta_{b1}L_{b2}) + c_{sz}(-\dot{z}_{fr} + \dot{z}_{b1} - \frac{1}{2}\dot{\theta}_{b1}L_{b2}) \tag{H-7}$$

The vertical forces between the carbody and rear bogie on the left and right are respectively

$$F_{zcb2l} = k_{sz}(-z_{bl} + z_{b2} + \frac{1}{2}\theta_{b2}L_{b2}) + c_{sz}(-\dot{z}_{bl} + \dot{z}_{b2} + \frac{1}{2}\dot{\theta}_{b2}L_{b2}) \tag{H-8}$$

$$F_{zcb2r} = k_{sz}(-z_{br} + z_{b2} - \frac{1}{2}\theta_{b2}L_{b2}) + c_{sz}(-\dot{z}_{br} + \dot{z}_{b2} - \frac{1}{2}\dot{\theta}_{b2}L_{b2}) \tag{H-9}$$

The vertical suspension force acting on the carbody is

$$F_{szc} = F_{zcb1l} + F_{zcb1r} + F_{zcb2l} + F_{zcb2r} \tag{H-10}$$

The lateral forces between the front bogie and the first wheelset on the left and right are

$$F_{yb1w1l} = F_{yb1w1r} = k_{py}(y_{w1} - y_{b1} - \frac{1}{2}L_{wx}\varphi_{b1} - h_W\theta_{b1}) \\ +c_{py}(\dot{y}_{w1} - \dot{y}_{b1} - \frac{1}{2}L_{wx}\dot{\varphi}_{b1} - h_W\dot{\theta}_{b1}) \tag{H-11}$$

The lateral forces between the front bogie and the second wheelset on the left and right are

$$F_{yb1w2l} = F_{yb1w2r} = k_{py}(y_{w2} - y_{b1} + \frac{1}{2}L_{wx}\varphi_{b1} - h_W\theta_{b1}) \\ +c_{py}(\dot{y}_{w2} - \dot{y}_{b1} + \frac{1}{2}L_{wx}\dot{\varphi}_{b1} - h_W\dot{\theta}_{b1}) \tag{H-12}$$

The lateral forces between the rear bogie and the third wheelset on the left and right are

$$F_{yb2w3l} = F_{yb2w3r} = k_{py}(y_{w3} - y_{b2} - \frac{1}{2}L_{wx}\varphi_{b2} - h_W\theta_{b2}) \\ +c_{py}(\dot{y}_{w3} - \dot{y}_{b2} - \frac{1}{2}L_{wx}\dot{\varphi}_{b2} - h_W\dot{\theta}_{b2}) \tag{H-13}$$

The lateral forces between the rear bogie and the fourth wheelset on the left and right are

$$F_{yb2w4l} = F_{yb2w4r} = k_{py}(y_{w4} - y_{b2} + \frac{1}{2}L_{wx}\varphi_{b2} - h_W\theta_{b2}) \\ +c_{py}(\dot{y}_{w4} - \dot{y}_{b2} + \frac{1}{2}L_{wx}\dot{\varphi}_{b2} - h_W\dot{\theta}_{b2}) \tag{H-14}$$

The lateral suspension forces acting on the front and rear bogies are respectively

$$F_{syb1} = -F_{ycb1l} - F_{ycb1r} + F_{yb1w1l} + F_{yb1w1r} + F_{yb1w2l} + F_{yb1w2r} \tag{H-15}$$

$$F_{syb2} = -F_{ycb2l} - F_{ycb2r} + F_{yb2w3l} + F_{yb2w3r} + F_{yb2w4l} + F_{yb2w4r} \tag{H-16}$$

The vertical forces between the front bogie and the first wheelset on the left and right are respectively

$$F_{zb1w1l} = k_{pz}(z_{w1} + \frac{1}{2}d_P\theta_{w1} - z_{b1} - \frac{1}{2}d_P\theta_{b1} + \frac{1}{2}L_{wx}\phi_{b1}) \\ +c_{pz}(\dot{z}_{w1} + \frac{1}{2}d_P\dot{\theta}_{w1} - \dot{z}_{b1} - \frac{1}{2}d_P\dot{\theta}_{b1} + \frac{1}{2}L_{wx}\dot{\phi}_{b1}) \tag{H-17}$$

$$F_{zb1w1r} = k_{pz}(z_{w1} - \frac{1}{2}d_P\theta_{w1} - z_{b1} + \frac{1}{2}d_P\theta_{b1} + \frac{1}{2}L_{wx}\phi_{b1}) + c_{pz}(\dot{z}_{w1} - \frac{1}{2}d_P\dot{\theta}_{w1} - \dot{z}_{b1} + \frac{1}{2}d_P\dot{\theta}_{b1} + \frac{1}{2}L_{wx}\dot{\phi}_{b1}) \quad \text{(H-18)}$$

The vertical forces between the front bogie and the second wheelset on the left and right are respectively

$$F_{zb1w2l} = k_{pz}(z_{w2} + \frac{1}{2}d_P\theta_{w2} - z_{b1} - \frac{1}{2}d_P\theta_{b1} - \frac{1}{2}L_{wx}\phi_{b1}) + c_{pz}(\dot{z}_{w2} + \frac{1}{2}d_P\dot{\theta}_{w2} - \dot{z}_{b1} - \frac{1}{2}d_P\dot{\theta}_{b1} - \frac{1}{2}L_{wx}\dot{\phi}_{b1}) \quad \text{(H-19)}$$

$$F_{zb1w2r} = k_{pz}(z_{w2} - \frac{1}{2}d_P\theta_{w2} - z_{b1} + \frac{1}{2}d_P\theta_{b1} - \frac{1}{2}L_{wx}\phi_{b1}) + c_{pz}(\dot{z}_{w2} - \frac{1}{2}d_P\dot{\theta}_{w2} - \dot{z}_{b1} + \frac{1}{2}d_P\dot{\theta}_{b1} - \frac{1}{2}L_{wx}\dot{\phi}_{b1}) \quad \text{(H-20)}$$

The vertical forces between the rear bogie and the third wheelset on the left and right are respectively

$$F_{zb2w3l} = k_{pz}(z_{w3} + \frac{1}{2}d_P\theta_{w3} - z_{b2} - \frac{1}{2}d_P\theta_{b2} + \frac{1}{2}L_{wx}\phi_{b2}) + c_{pz}(\dot{z}_{w3} + \frac{1}{2}d_P\dot{\theta}_{w3} - \dot{z}_{b2} - \frac{1}{2}d_P\dot{\theta}_{b2} + \frac{1}{2}L_{wx}\dot{\phi}_{b2}) \quad \text{(H-21)}$$

$$F_{zb2w3r} = k_{pz}(z_{w3} - \frac{1}{2}d_P\theta_{w3} - z_{b2} + \frac{1}{2}d_P\theta_{b2} + \frac{1}{2}L_{wx}\phi_{b2}) + c_{pz}(\dot{z}_{w3} - \frac{1}{2}d_P\dot{\theta}_{w3} - \dot{z}_{b2} + \frac{1}{2}d_P\dot{\theta}_{b2} + \frac{1}{2}L_{wx}\dot{\phi}_{b2}) \quad \text{(H-22)}$$

The vertical forces between the rear bogie and the fourth wheelset on the left and right are respectively

$$F_{zb2w4l} = k_{pz}(z_{w4} + \frac{1}{2}d_P\theta_{w4} - z_{b2} - \frac{1}{2}d_P\theta_{b2} - \frac{1}{2}L_{wx}\phi_{b2}) + c_{pz}(\dot{z}_{w4} + \frac{1}{2}d_P\dot{\theta}_{w4} - \dot{z}_{b2} - \frac{1}{2}d_P\dot{\theta}_{b2} - \frac{1}{2}L_{wx}\dot{\phi}_{b2}) \quad \text{(H-23)}$$

$$F_{zb2w4r} = k_{pz}(z_{w4} - \frac{1}{2}d_P\theta_{w4} - z_{b2} + \frac{1}{2}d_P\theta_{b2} - \frac{1}{2}L_{wx}\phi_{b2}) + c_{pz}(\dot{z}_{w4} - \frac{1}{2}d_P\dot{\theta}_{w4} - \dot{z}_{b2} + \frac{1}{2}d_P\dot{\theta}_{b2} - \frac{1}{2}L_{wx}\dot{\phi}_{b2}) \quad \text{(H-24)}$$

The vertical suspension forces acting on the front and rear bogies are respectively

$$F_{szb1} = -F_{zcb1l} - F_{zcb1r} + F_{zb1w1l} + F_{zb1w1r} + F_{zb1w2l} + F_{zb1w2r} \tag{H-25}$$

$$F_{szb2} = -F_{zcb2l} - F_{zcb2r} + F_{zb2w3l} + F_{zb2w3r} + F_{zb2w4l} + F_{zb2w4r} \tag{H-26}$$

The fore-and-aft force between the carbody and front bogie on the left is

$$F_{xcb1l} = -k_{sx}(\varphi_c - \varphi_{b1})\frac{1}{2}L_{b2} - c_{sx}(\dot{\varphi}_c - \dot{\varphi}_{b1})\frac{1}{2}L_{b2} \tag{H-27}$$

The fore-and-aft force between the carbody and rear bogie on the left is

$$F_{xcb2l} = -k_{sx}(\varphi_c - \varphi_{b2})\frac{1}{2}L_{b2} - c_{sx}(\dot{\varphi}_c - \dot{\varphi}_{b2})\frac{1}{2}L_{b2} \tag{H-28}$$

The fore-and-aft forces between the front bogie and the first, second wheelsets on the left are respectively

$$F_{xb1w1l} = F_{xb1w2l} = k_{px}(-\varphi_{b1})\frac{1}{2}d_P + c_{px}(-\dot{\varphi}_{b1})\frac{1}{2}d_P \tag{H-29}$$

The fore-and-aft forces between the rear bogie and the third, fourth wheelsets on the left are respectively

$$F_{xb2w3l} = F_{xb2w4l} = k_{px}(-\varphi_{b2})\frac{1}{2}d_P + c_{px}(-\dot{\varphi}_{b2})\frac{1}{2}d_P \tag{H-30}$$

The suspension moments acting on the carbody in roll, pitch and yaw directions are respectively

$$M_{sxc} = F_{zcb1l}\frac{1}{2}L_{b2} - F_{zcb1r}\frac{1}{2}L_{b2} + F_{zcb2l}\frac{1}{2}L_{b2} - F_{zcb2r}\frac{1}{2}L_{b2} + F_{syc}\frac{1}{2}L_3 \tag{H-31}$$

$$M_{syc} = -F_{zcb1l}\frac{1}{2}L_{b1} - F_{zcb1r}\frac{1}{2}L_{b1} + F_{zcb2l}\frac{1}{2}L_{b1} + F_{zcb2r}\frac{1}{2}L_{b1} \tag{H-32}$$

$$M_{szc} = F_{xcb1l}L_{b2} + F_{xcb2l}L_{b2} + (F_{ycb1l} + F_{ycb1r})\frac{1}{2}L_{b1} - (F_{ycb2l} + F_{ycb2r})\frac{1}{2}L_{b1} \tag{H-33}$$

The suspension moments acting on the front bogie in roll, pitch and yaw directions are respectively

$$M_{sxb1} = -F_{zcb1l}\frac{1}{2}L_{b2} + F_{zcb1r}\frac{1}{2}L_{b2} + F_{ycb1l}h_T + F_{ycb1r}h_T + (F_{yb1w1l} + F_{yb1w1r})h_W$$
$$+(F_{yb1w2l} + F_{yb1w2r})h_W + F_{zb1w1l}\frac{1}{2}d_P - F_{zb1w1r}\frac{1}{2}d_P + F_{zb1w2l}\frac{1}{2}d_P - F_{zb1w2r}\frac{1}{2}d_P \quad \text{(H-34)}$$

$$M_{syb1} = -(F_{zb1w1l} + F_{zb1w1r})\frac{1}{2}L_{wx} + (F_{zb1w2l} + F_{zb1w2r})\frac{1}{2}L_{wx} \quad \text{(H-35)}$$

$$M_{szb1} = -F_{xcb1l}L_{b2} + (F_{yb1w1l} + F_{yb1w1r})\frac{1}{2}L_{wx}$$
$$-(F_{yb1w2l} + F_{yb1w2r})\frac{1}{2}L_{wx} + F_{xb1w1l}d_P + F_{xb1w2l}d_P \quad \text{(H-36)}$$

The suspension moments acting on the rear bogie in roll, pitch and yaw directions are respectively

$$M_{sxb2} = -F_{zcb2l}\frac{1}{2}L_{b2} + F_{zcb2r}\frac{1}{2}L_{b2} + F_{ycb2l}h_T + F_{ycb2r}h_T + (F_{yb2w3l} + F_{yb2w3r})h_W$$
$$+(F_{yb2w4l} + F_{yb2w4r})h_W + F_{zb2w3l}\frac{1}{2}d_P - F_{zb2w3r}\frac{1}{2}d_P + F_{zb2w4l}\frac{1}{2}d_P - F_{zb2w4r}\frac{1}{2}d_P \quad \text{(H-37)}$$

$$M_{syb2} = -(F_{zb2w3l} + F_{zb2w3r})\frac{1}{2}L_{wx} + (F_{zb2w4l} + F_{zb2w4r})\frac{1}{2}L_{wx} \quad \text{(H-38)}$$

$$M_{szb2} = -F_{xcb2l}L_{b2} + (F_{yb2w3l} + F_{yb2w3r})\frac{1}{2}L_{wx}$$
$$-(F_{yb2w4l} + F_{yb2w4r})\frac{1}{2}L_{wx} + F_{xb2w3l}d_P + F_{xb2w4l}d_P \quad \text{(H-39)}$$

The forces and moments of the wheelsets can be expressed as

$$F_{ywj} = -F_{ybiwjl} - F_{ybiwjr} \quad \text{(H-40)}$$

$$F_{zwj} = -F_{zbiwjl} - F_{zbiwjr} \quad \text{(H-41)}$$

$$M_{xwj} = -F_{zbiwjl}\frac{d_P}{2} + F_{zbiwjr}\frac{d_P}{2} \quad \text{(H-42)}$$

For the first wheelset, j=1 and i=1; for the second wheelset, j=2 and i=1; for the third wheelset, j=3 and i=2; for the fourth wheelset, j=4 and i=2.

The forces between the i^{th} sleeper and the left, right rail are respectively

$$F_{szLi}(t) = -k_{pv}(z_{rL}(x_{si},t) - z_{si}(\frac{l_s}{2} + \frac{d_r}{2},t)) - c_{pv}(\dot{z}_{rL}(x_{si},t) - \dot{z}_{si}(\frac{l_s}{2} + \frac{d_r}{2},t)) \quad \text{(H-43)}$$

$$F_{szRi}(t) = -k_{pv}(z_{rR}(x_{si},t) - z_{si}(\frac{l_s}{2} - \frac{d_r}{2},t)) - c_{pv}(\dot{z}_{rR}(x_{si},t) - \dot{z}_{si}(\frac{l_s}{2} - \frac{d_r}{2},t)) \quad \text{(H-44)}$$

The forces between the i[th] sleeper and the left, right ballast can be expressed respectively as

$$F_{bzLi}(y,t) = k_{bv}(z_{si}(y,t) - z_{bLi}(t)), \frac{l_s}{2} \le y \le l_s \quad \text{(H-45)}$$

$$F_{bzRi}(y,t) = k_{bv}(z_{si}(y,t) - z_{bRi}(t)), 0 \le y < \frac{l_s}{2} \quad \text{(H-46)}$$

The lateral forces between the i[th] sleeper and the left, right rail respectively are

$$\begin{aligned} F_{syLi} &= k_{ph}(-y_{rL}(x_{si},t) - \theta_{rL}(x_{si},t)a_r + y_{si}(t)) \\ &+ c_{ph}(-\dot{y}_{rL}(x_{si},t) - \dot{\theta}_{rL}(x_{si},t)a_r + \dot{y}_{si}(t)) \end{aligned} \quad \text{(H-47)}$$

$$\begin{aligned} F_{syRi} &= k_{ph}(-y_{rR}(x_{si},t) - \theta_{rR}(x_{si},t)a_r + y_{si}(t)) \\ &+ c_{ph}(-\dot{y}_{rR}(x_{si},t) - \dot{\theta}_{rR}(x_{si},t)a_r + \dot{y}_{si}(t)) \end{aligned} \quad \text{(H-48)}$$

The lateral force between the i[th] sleeper and the ballasts is

$$F_{ysbi} = 2k_{bh}y_{si} + 2c_{bh}\dot{y}_{si} \quad \text{(H-49)}$$

The vertical shear forces between the left, right i[th] ballast and the corresponding (i-1)[th] one, respectively are

$$F_{zfLi} = -k_w(z_{bLi} - z_{bL(i-1)}) - c_w(\dot{z}_{bLi} - \dot{z}_{bL(i-1)}) \quad \text{(H-50)}$$

$$F_{zfRi} = -k_w(z_{bRi} - z_{bR(i-1)}) - c_w(\dot{z}_{bRi} - \dot{z}_{bR(i-1)}) \quad \text{(H-51)}$$

where $z_{bL(i-1)} = z_{bR(i-1)} = 0$ when $i = 1$.

The vertical shear forces between the left, right i[th] ballasts and the corresponding (i+1)[th] one, respectively are

$$F_{zrLi} = k_w(z_{bL(i+1)} - z_{bLi}) + c_w(\dot{z}_{bL(i+1)} - \dot{z}_{bLi}) \quad \text{(H-52)}$$

$$F_{zrRi} = k_w(z_{bR(i+1)} - z_{bRi}) + c_w(\dot{z}_{bR(i+1)} - \dot{z}_{bRi}) \quad \text{(H-53)}$$

where $z_{bL(i+1)} = z_{bR(i+1)} = 0$ when $i = N_s$.

The vertical shear force between the left i[th] and the right i[th] ballasts is

$$F_{zLRi} = -k_w(z_{bLi} - z_{bRi}) - c_w(\dot{z}_{bLi} - \dot{z}_{bRi}) \tag{H-54}$$

The vertical forces between the left, right i[th] ballasts and the roadbed, respectively are

$$F_{zgLi} = -k_{fv} z_{bLi} - c_{fv} \dot{z}_{bLi} \tag{H-55}$$

$$F_{zgRi} = -k_{fv} z_{bRi} - c_{fv} \dot{z}_{bRi} \tag{H-56}$$

The strain energy of the contact between the wheelsets and the right rail in the normal direction is

$$U_{cR} = 0.5K_n \sum_{j=1}^{4} [z_{wj} - \frac{1}{2} L_{wy} \theta_{wj} - (z_{rR}(x_{wj}, t) + e_r \theta_{rR}(x_{wj}, t) + r_v(x_{wj}, t) - \frac{1}{2} r_t(x_{wj}, t))]^2 \tag{H-57}$$

The dissipation energy of the contact between the wheelsets and the right rail in the tangential direction is

$$D_{cR} = 0.5 \frac{f_{11}}{V} \sum_{j=1}^{4} [\dot{y}_{wj} + r_0 \dot{\theta}_{wj} - (\dot{y}_{rR}(x_{wj}, t) - h_r \dot{\theta}_{rR}(x_{wj}, t) + \dot{r}_a(x_{wj}, t))]^2 \tag{H-58}$$

The stiffness and damping matrices generated by the connection between the carbody and i[th] human-seat system ($i = 1, 2, \cdots, N_{hs}$) are respectively

$$\begin{aligned}
&\mathbf{K}_{tsi} = \left[\mathbf{C}_{Fl}(x_{fi}, y_{fi})^{\mathrm{T}} \quad \mathbf{C}_{Fv}(x_{fi}, y_{fi})^{\mathrm{T}} \quad \mathbf{C}_{F\theta}(x_{fi}, y_{fi})^{\mathrm{T}} \right] \\
&({}^{l}k_{sl5} \left[-1 \quad 0 \quad {}^{l}z_{\mathbf{C}_7}^{B_B} - z_{\mathbf{E}}^{O} + z_{B0} \right]^{\mathrm{T}} \left[-1 \quad 0 \quad {}^{l}z_{\mathbf{C}_7}^{B_B} - z_{\mathbf{E}}^{O} + z_{B0} \right] + \\
&{}^{r}k_{sl5} \left[-1 \quad 0 \quad {}^{r}z_{\mathbf{C}_7}^{B_B} - z_{\mathbf{E}}^{O} + z_{B0} \right]^{\mathrm{T}} \left[-1 \quad 0 \quad {}^{r}z_{\mathbf{C}_7}^{B_B} - z_{\mathbf{E}}^{O} + z_{B0} \right] + \\
&{}^{l}k_{sv5} \left[0 \quad -1 \quad -({}^{l}y_{\mathbf{C}_7}^{B_B} - y_{\mathbf{E}}^{O} + y_{B0}) \right]^{\mathrm{T}} \left[0 \quad -1 \quad -({}^{l}y_{\mathbf{C}_7}^{B_B} - y_{\mathbf{E}}^{O} + y_{B0}) \right] + \\
&{}^{r}k_{sv5} \left[0 \quad -1 \quad -({}^{r}y_{\mathbf{C}_7}^{B_B} - y_{\mathbf{E}}^{O} + y_{B0}) \right]^{\mathrm{T}} \left[0 \quad -1 \quad -({}^{r}y_{\mathbf{C}_7}^{B_B} - y_{\mathbf{E}}^{O} + y_{B0}) \right] + \\
&({}^{l}k_{sr5} + {}^{r}k_{sr5}) [0 \quad 0 \quad 1]^{\mathrm{T}} [0 \quad 0 \quad 1]) \left[\mathbf{C}_{Fl}(x_{fi}, y_{fi})^{\mathrm{T}} \quad \mathbf{C}_{Fv}(x_{fi}, y_{fi})^{\mathrm{T}} \quad \mathbf{C}_{F\theta}(x_{fi}, y_{fi})^{\mathrm{T}} \right]^{\mathrm{T}}
\end{aligned} \tag{H-59}$$

$$\mathbf{C}_{tsi}=\left[\mathbf{C}_{Fl}(x_{fi},y_{fi})^{\mathrm{T}}\quad \mathbf{C}_{Fv}(x_{fi},y_{fi})^{\mathrm{T}}\quad \mathbf{C}_{F\theta}(x_{fi},y_{fi})^{\mathrm{T}}\right]$$
$$({}^{l}c_{sl5}\left[-1\quad 0\quad {}^{l}z_{\mathbf{C}_7}^{B_B}-z_{\mathbf{E}}^{O}+z_{B0}\right]^{\mathrm{T}}\left[-1\quad 0\quad {}^{l}z_{\mathbf{C}_7}^{B_B}-z_{\mathbf{E}}^{O}+z_{B0}\right]+$$
$${}^{r}c_{sl5}\left[-1\quad 0\quad {}^{r}z_{\mathbf{C}_7}^{B_B}-z_{\mathbf{E}}^{O}+z_{B0}\right]^{\mathrm{T}}\left[-1\quad 0\quad {}^{r}z_{\mathbf{C}_7}^{B_B}-z_{\mathbf{E}}^{O}+z_{B0}\right]+$$
$${}^{l}c_{sv5}\left[0\quad -1\quad -({}^{l}y_{\mathbf{C}_7}^{B_B}-y_{\mathbf{E}}^{O}+y_{B0})\right]^{\mathrm{T}}\left[0\quad -1\quad -({}^{l}y_{\mathbf{C}_7}^{B_B}-y_{\mathbf{E}}^{O}+y_{B0})\right]+$$
$${}^{r}c_{sv5}\left[0\quad -1\quad -({}^{r}y_{\mathbf{C}_7}^{B_B}-y_{\mathbf{E}}^{O}+y_{B0})\right]^{\mathrm{T}}\left[0\quad -1\quad -({}^{r}y_{\mathbf{C}_7}^{B_B}-y_{\mathbf{E}}^{O}+y_{B0})\right]+$$
$$({}^{l}c_{sr5}+{}^{r}c_{sr5})\left[0\quad 0\quad 1\right]^{\mathrm{T}}\left[0\quad 0\quad 1\right])\left[\mathbf{C}_{Fl}(x_{fi},y_{fi})^{\mathrm{T}}\quad \mathbf{C}_{Fv}(x_{fi},y_{fi})^{\mathrm{T}}\quad \mathbf{C}_{F\theta}(x_{fi},y_{fi})^{\mathrm{T}}\right]^{\mathrm{T}}$$

(H-60)

The numbers of the polynomials used for the multi-plate model are

${}^{u}N_1={}^{d}N_1=15$, ${}^{u}N_2={}^{d}N_2=7$, ${}^{u}N_3={}^{d}N_3=15$, ${}^{u}N_4={}^{d}N_4=7$, ${}^{u}N_5={}^{d}N_5=15$, ${}^{u}N_6={}^{d}N_6=7$, ${}^{r}N_1={}^{l}N_1=15$, ${}^{r}N_2={}^{l}N_2=7$, ${}^{r}N_3={}^{l}N_3=15$, ${}^{r}N_4={}^{l}N_4=7$, ${}^{r}N_5={}^{l}N_5=15$, ${}^{r}N_6={}^{l}N_6=7$, ${}^{f}N_i={}^{b}N_i=6$, for $i=1,2,...,6$; The dimensions of the carbody are $L_1=24.5\,\mathrm{m}$, $L_2=3.4\,\mathrm{m}$, $L_3=2.4\,\mathrm{m}$; The thickness of the plates is $h_u=0.14689\,\mathrm{m}$, $h_d=0.14151\,\mathrm{m}$, $h_r=h_l=0.13618\,\mathrm{m}$, $h_f=h_b=0.14819\,\mathrm{m}$; The density of the plates is $\rho_u=7251\ \mathrm{kg/m^3}$, $\rho_d=6899\ \mathrm{kg/m^3}$, $\rho_r=\rho_l=2925\ \mathrm{kg/m^3}$, $\rho_f=\rho_b=1399\ \mathrm{kg/m^3}$; The passion ratio of the plates is $\mu_u=\mu_d=\mu_r=\mu_l=\mu_f=\mu_b=0.3$; The elastic modulus of the plates is $E_u=33893852125\ \mathrm{Pa}$, $E_d=33872470722\ \mathrm{Pa}$, $E_r=E_l=8586985066\ \mathrm{Pa}$, $E_f=E_b=99647621739\ \mathrm{Pa}$; The flexural rigidity of the plates is $D_i=\dfrac{E_i h_i^3}{12(1-v_i^2)}$, $i=u,d,r,l,f,b$.

The stiffness of the artificial springs is

$k_{T1}=k_{T2}=k_{T3}=k_{T4}=10^{12}\ \mathrm{N/m}$ and $k_{R1}=k_{R2}=k_{R3}=10^{12}\ \mathrm{N/rad}$.

The parameters of the train and track subsystems can refer to Ren *et al.* (2005), Zhai *et al.* (2009) and Zhai *et al.* (2015b), which were listed in Table H-3 and Table H-4.

Table H-1 Extra modes calculated from the analytical model and FE model

Mode	Analytical model	FE model
7 First lateral bending mode	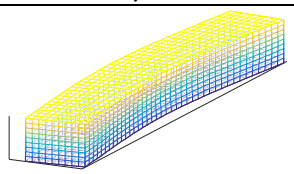 12.27 Hz	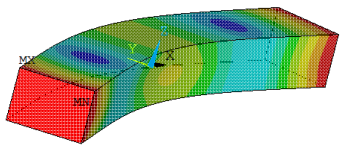 12.27 Hz
8 First breathing mode	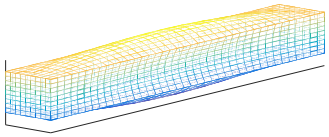 13.98 Hz	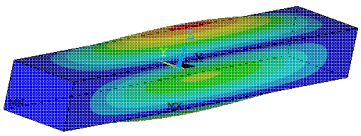 13.98 Hz
9 Torsional and breathing mode	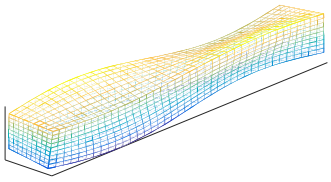 15.66 Hz	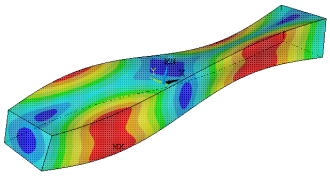 15.66 Hz
10 Fourth breathing mode	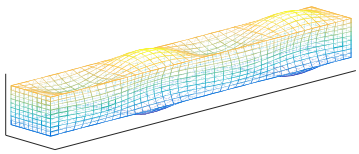 17.85 Hz	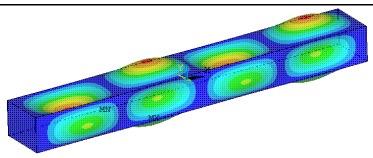 17.83 Hz
11 Second torsional mode	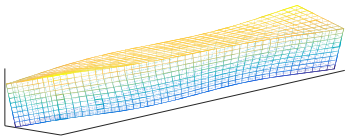 18.60 Hz	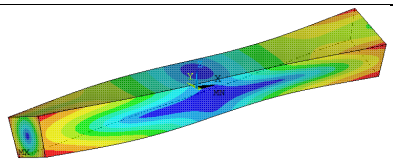 18.60 Hz
12 Fifth breathing mode	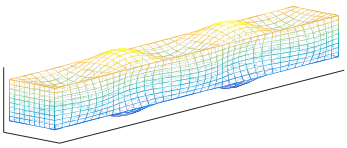 20.15 Hz	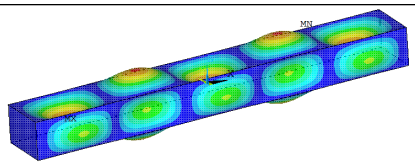 20.13 Hz

Table H-2 The summary of the lateral and vertical displacements and suspension forces above the second suspensions

Positions	Lateral displacement	Vertical displacement	Lateral suspension force	Vertical suspension force
Above front left second suspension	$y_{fl}=d_l(\frac{1}{2}L_{b1},\frac{1}{2}L_{b2},t)$	$z_{fl}=d_v(\frac{1}{2}L_{b1},\frac{1}{2}L_{b2},t)$	F_{ycb1l}	F_{zcb1l}
Above front right second suspension	$y_{fr}=d_l(\frac{1}{2}L_{b1},-\frac{1}{2}L_{b2},t)$	$z_{fr}=d_v(\frac{1}{2}L_{b1},-\frac{1}{2}L_{b2},t)$	F_{ycb1r}	F_{zcb1r}
Above rear left second suspension	$y_{bl}=d_l(-\frac{1}{2}L_{b1},\frac{1}{2}L_{b2},t)$	$z_{bl}=d_v(-\frac{1}{2}L_{b1},\frac{1}{2}L_{b2},t)$	F_{ycb2l}	F_{zcb2l}
Above rear right second suspension	$y_{br}=d_l(-\frac{1}{2}L_{b1},-\frac{1}{2}L_{b2},t)$	$z_{br}=d_v(-\frac{1}{2}L_{b1},-\frac{1}{2}L_{b2},t)$	F_{ycb2r}	F_{zcb2r}

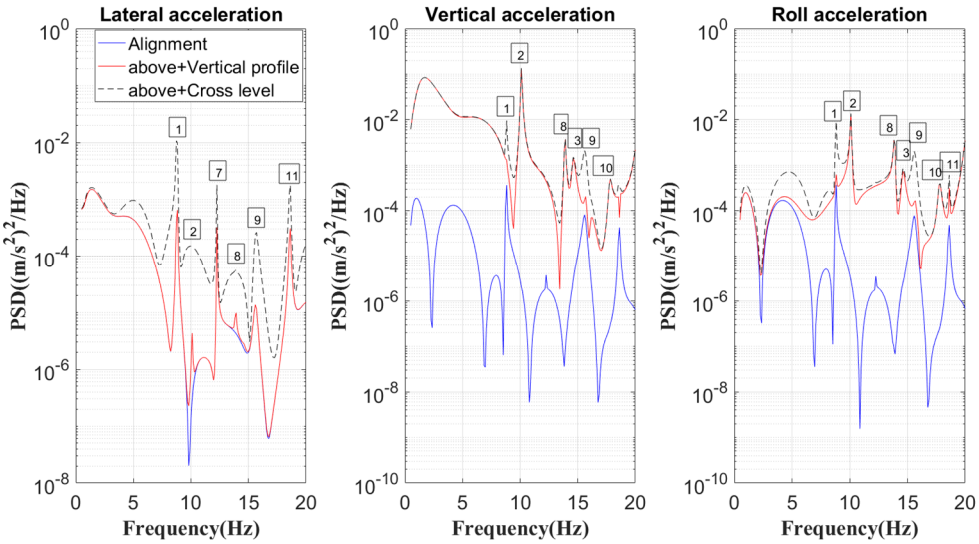

Fig. H-1 The PSD of the acceleration on the floor at the excitation point of seat 1 at the speed of 300 km/h (blue line: the PSD resulting from alignment alone; red line: PSD resulting from alignment and vertical profile; black line: PSD resulting from alignment, vertical profile and cross level). The number in the box is the number of the carbody modes in Table 10-1 and Table H-1.

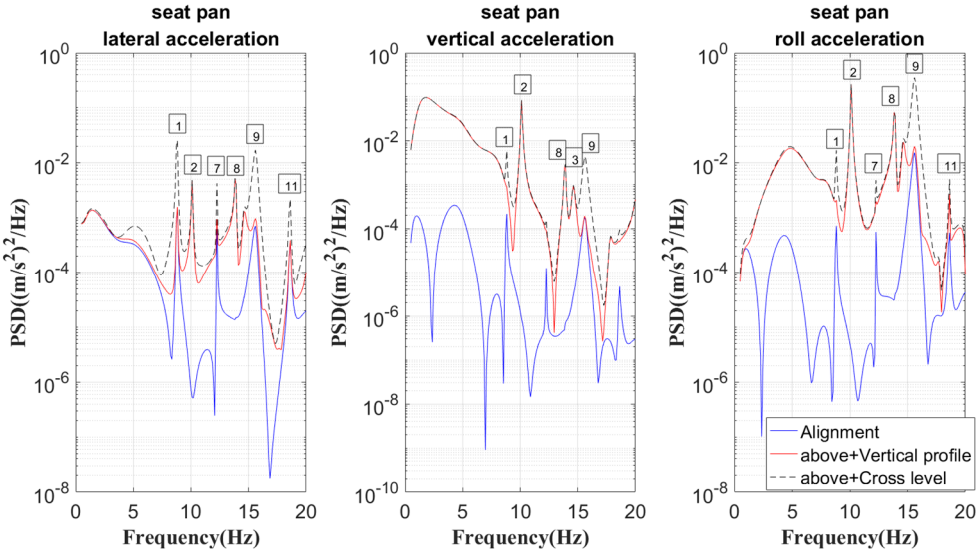

Fig. H-2 The PSD of the acceleration on the seat-buttock interface of seat 1 at the speed of 300 km/h (blue line: the PSD resulting from alignment alone; red line: PSD resulting from alignment and vertical profile; black line: PSD resulting from alignment, vertical profile and cross level). The number in the box is the number of the carbody modes in Table 10-1 and Table H-1.

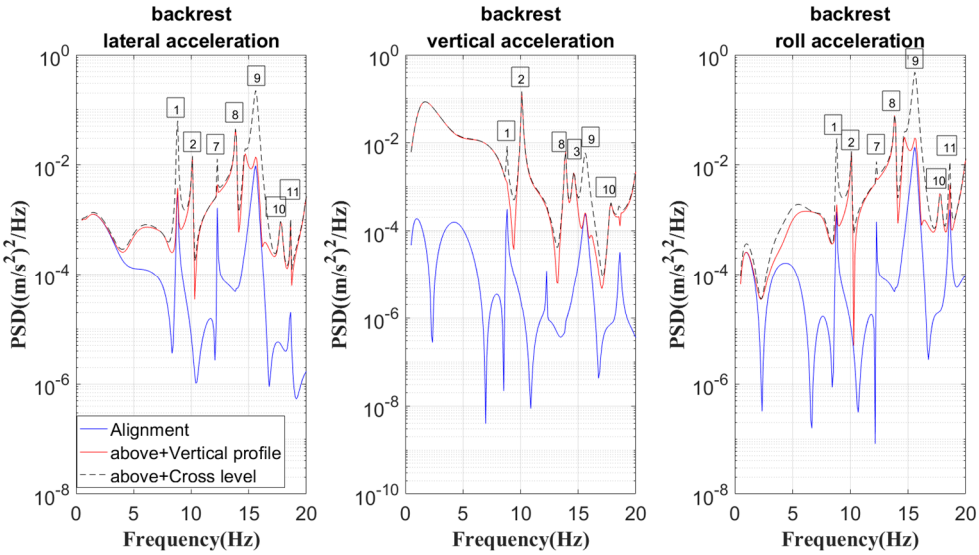

Fig. H-3 The PSD of the acceleration on the human-backrest interface of seat 1 at the speed of 300 km/h (blue line: the PSD resulting from alignment alone; red line: PSD resulting from alignment and vertical profile; black line: PSD resulting from alignment, vertical profile and cross level). The number in the box is the number of the carbody modes in Table 10-1 and Table H-1.

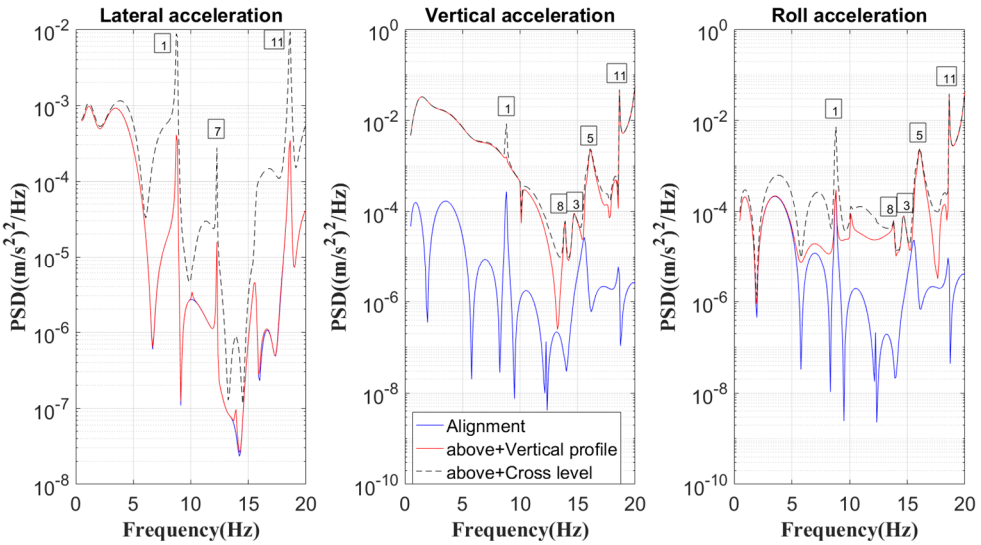

Fig. H-4 The PSD of the acceleration on the floor at the excitation point of seat 3 at the speed of 250 km/h (blue line: the PSD resulting from alignment alone; red line: PSD resulting from alignment and vertical profile; black line: PSD resulting from alignment, vertical profile and cross level). The number in the box is the number of the carbody modes in Table 10-1 and Table H-1.

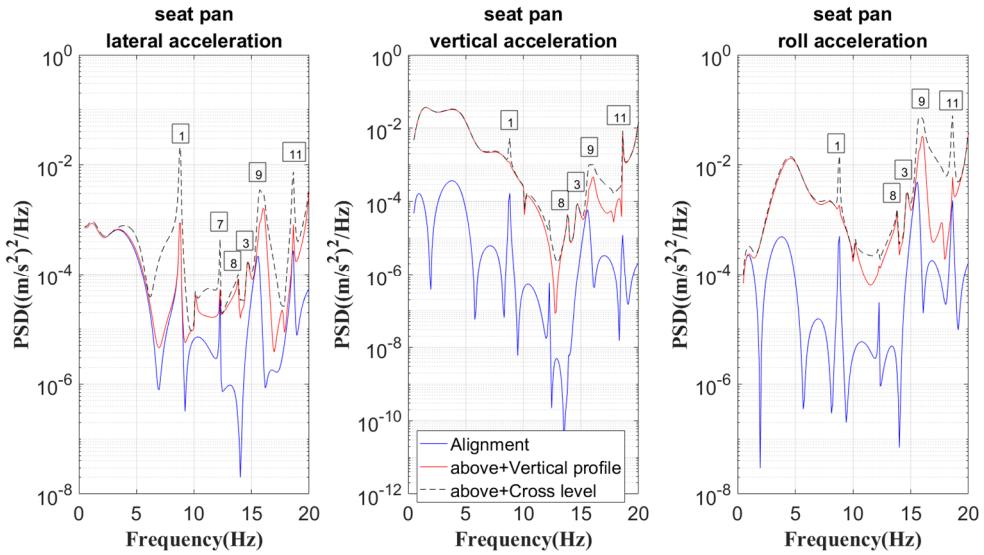

Fig. H-5 The PSD of the acceleration on the seat-buttock interface of seat 3 at the speed of 250 km/h (blue line: the PSD resulting from alignment alone; red line: PSD resulting from alignment and vertical profile; black line: PSD resulting from alignment, vertical profile and cross level). The number in the box is the number of the carbody modes in Table 10-1 and Table H-1.

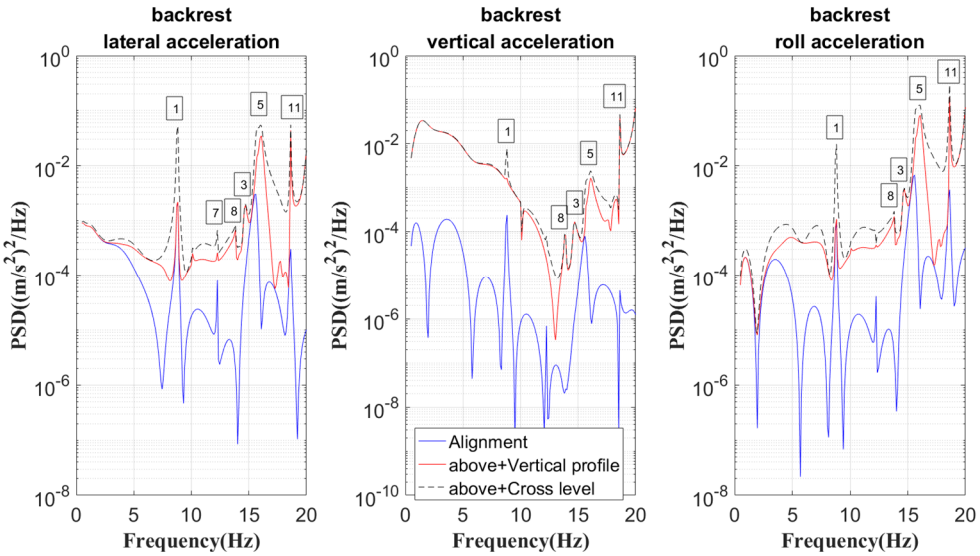

Fig. H-6 The PSD of the acceleration on the human-backrest interface of seat 3 at the speed of 250 km/h (blue line: the PSD resulting from alignment alone; red line: PSD resulting from alignment and vertical profile; black line: PSD resulting from alignment, vertical profile and cross level). The number in the box is the number of the carbody modes in Table 10-1 and Table H-1.

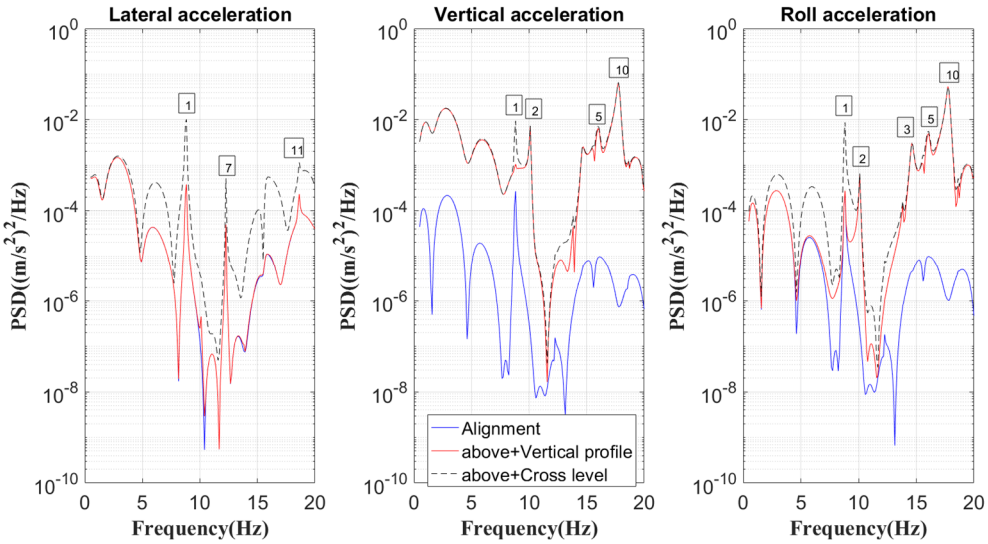

Fig. H-7 The PSD of the acceleration on the floor at the excitation point of seat 5 at the speed of 200 km/h (blue line: the PSD resulting from alignment alone; red line: PSD resulting from alignment and vertical profile; black line: PSD resulting from alignment, vertical profile and cross level). The number in the box is the number of the carbody modes in Table 10-1 and Table H-1.

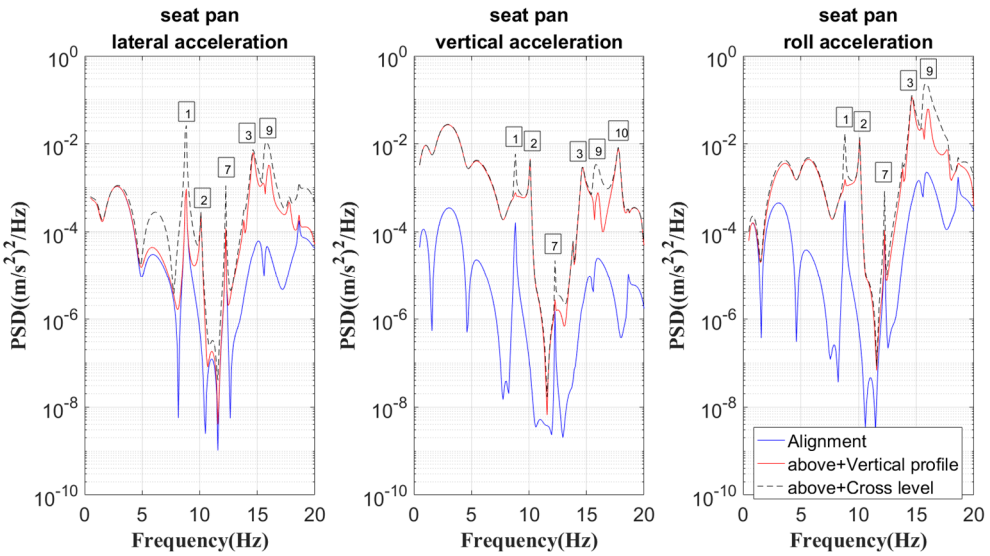

Fig. H-8 The PSD of the acceleration on the seat-buttock interface of seat 5 at the speed of 200 km/h (blue line: the PSD resulting from alignment alone; red line: PSD resulting from alignment and vertical profile; black line: PSD resulting from alignment, vertical profile and cross level). The number in the box is the number of the carbody modes in Table 10-1 and Table H-1.

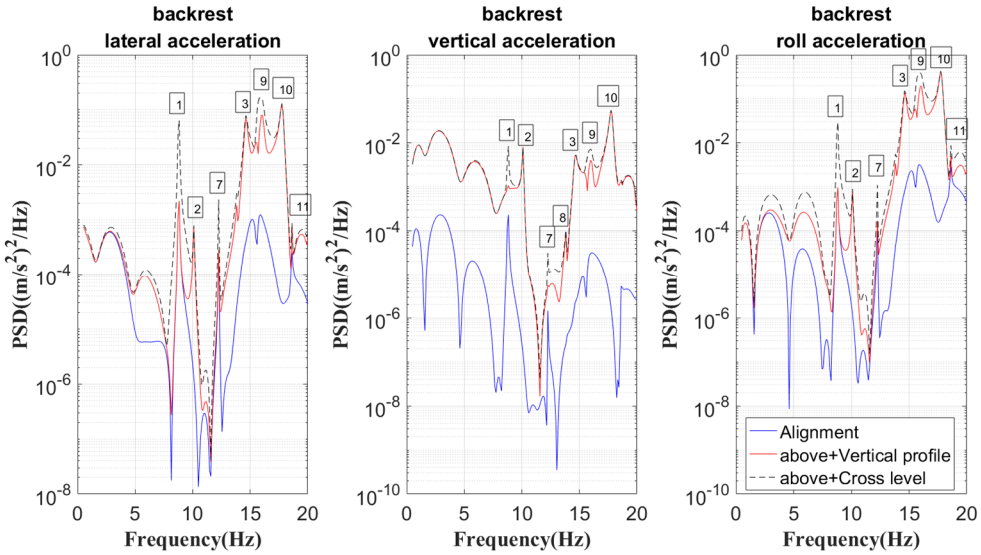

Fig. H-9 The PSD of the acceleration on the human-backrest interface of seat 5 at the speed of 200 km/h (blue line: the PSD resulting from alignment alone; red line: PSD resulting from alignment and vertical profile; black line: PSD resulting from alignment, vertical profile and cross level). The number in the box is the number of the carbody modes in Table 10-1 and Table H-1.

Table H-3 Main parameters of the train subsystem

Notation	Parameter (Unit)	Value
m_c	Carbody mass (kg)	29600
m_b	Bogie mass (kg)	1700
m_w	Wheelset mass (kg)	1900
I_{cx}	Rotational inertia of carbody about x axis (kgm^2)	5.802×10^4
I_{cy}	Rotational inertia of carbody about y axis (kgm^2)	2.139×10^6
I_{cz}	Rotational inertia of carbody about z axis (kgm^2)	2.139×10^6
I_{bx}	Rotational inertia of bogie about x axis (kgm^2)	1600
I_{by}	Rotational inertia of bogie about y axis (kgm^2)	1700
I_{bz}	Rotational inertia of bogie about z axis (kgm^2)	1700
I_{wx}	Rotational inertia of wheelset about x axis (kgm^2)	1067
k_{px}	Stiffness of primary suspension along x direction (MN/m)	24
k_{py}	Stiffness of primary suspension along y direction (MN/m)	5.1
k_{pz}	Stiffness of primary suspension along z direction (MN/m)	0.873
k_{sx}	Stiffness of second suspension along x direction (MN/m)	1.2
k_{sy}	Stiffness of second suspension along y direction (MN/m)	0.3
k_{sz}	Stiffness of second suspension along z direction (MN/m)	0.41
c_{px}	Damping of primary suspension along x direction (kNs/m)	0
c_{py}	Damping of primary suspension along y direction (kNs/m)	0
c_{pz}	Damping of primary suspension along z direction (kNs/m)	30
c_{sx}	Damping of second suspension along x direction (kNs/m)	0
c_{sy}	Damping of second suspension along y direction (kNs/m)	25
c_{sz}	Damping of second suspension along z direction (kNs/m)	108.7
L_{b1}	Distance between two bogies (m)	18
L_{b2}	Distance between two second suspension lateral spring and damper arms (m)	2
L_{wx}	Wheelbase (m)	2.4
d_P	Distance between two primary suspension lateral spring and damper arms (m)	2
L_{wy}	The lateral distance between two contact points of wheel and rail (m)	1.5
h_W	Vertical distance between center of gravity of bogie and lateral primary suspension (m)	0.14
r_0	Nominal wheel radius (m)	0.4575
h_T	Vertical distance between center of gravity of bogie and lateral second suspension (m)	0.081
h_C	Vertical distance between center of gravity of carbody and lateral second suspension (m)	1.415
c_M	Rayleigh damping coefficient of the mass matrix	0
c_K	Rayleigh damping coefficient of the stiffness matrix	0

Table H-4 Main parameters of the track subsystem

Notation	Parameter (Unit)	Value
E_r	Elastic modulus of rail (N/m^2)	2.059×10^{11}
ρ_r	Density of rail (kg/m^3)	7.86×10^3
I_r	Torsional inertia of rail (m^4)	3.741×10^{-5}
I_{ry}	Second moment of area of rail about y axis (m^4)	3.217×10^{-5}
I_{rz}	Second moment of area of rail about z axis (m^4)	5.24×10^{-6}
GK_r	Torsional stiffness of rail (Nm/rad)	5.0×10^5
m_r	Mass per unit length of rail (kg/m)	60.64
l_r	Calculated length of rail (m)	60
m_s	Mass per unit length of sleeper (kg/m)	100.4
E_s	Elastic modulus of sleeper (N/m^2)	4.13×10^{10}
I_s	Second moment of inertia of sleeper about x axis (m^4)	1.65×10^{-4}
k_{pv}	Stiffness of fastener in vertical direction (N/m)	6.5×10^7
k_{ph}	Stiffness of fastener in lateral direction (N/m)	2.0×10^7
c_{pv}	Damping of fastener in vertical direction (Ns/m)	7.5×10^4
c_{ph}	Damping of fastener in lateral direction (Ns/m)	5.0×10^4
L_s	Sleeper spacing (m)	0.545
l_s	Sleeper length (m)	2.5
m_{ba}	Mass of ballast (kg)	531.422
k_{bv}	Stiffness of ballast in vertical direction (N/m)	8.0×10^7
c_{bv}	Damping of ballast in vertical direction (Ns/m)	5.88×10^4
k_{bh}	Stiffness of ballast in lateral direction (N/m)	5.0×10^7
c_{bh}	Damping of ballast in lateral direction (Ns/m)	1.0×10^5
k_w	Shear stiffness of ballast (N/m)	7.84×10^7
c_w	Shear damping of ballast (Ns/m)	8.0×10^4
k_{fv}	Stiffness of subgrade (N/m)	6.5×10^7
c_{fv}	Damping of subgrade (Ns/m)	3.115×10^4
e_r	Lateral distance between the symmetrical plane of rail and wheel/rail contact point (m)	0.04
h_r	Vertical distance between the neutral plane of rail and wheel/rail contact point (m)	0.09453
a_r	Vertical distance between the neutral plane of rail and rail base (m)	0.08147
b_r	Half width of rail base (m)	0.075
d_r	The lateral distance between the symmetrical plane of two rails (m)	1.51
f_{11}	Lateral creep coefficient (N)	1.2×10^6
K_n	Linear Hertzian stiffness in the normal direction (N/m)	5.0×10^9

Parameters of 5th American track spectra are $k = 0.25$, $A_v = 0.2095\ \text{cm}^2\text{rad/m}$, $A_a = 0.0762\ \text{cm}^2\text{rad/m}$, $\Omega_c = 0.8245\ \text{rad/m}$, $\Omega_s = 0.8209\ \text{rad/m}$.

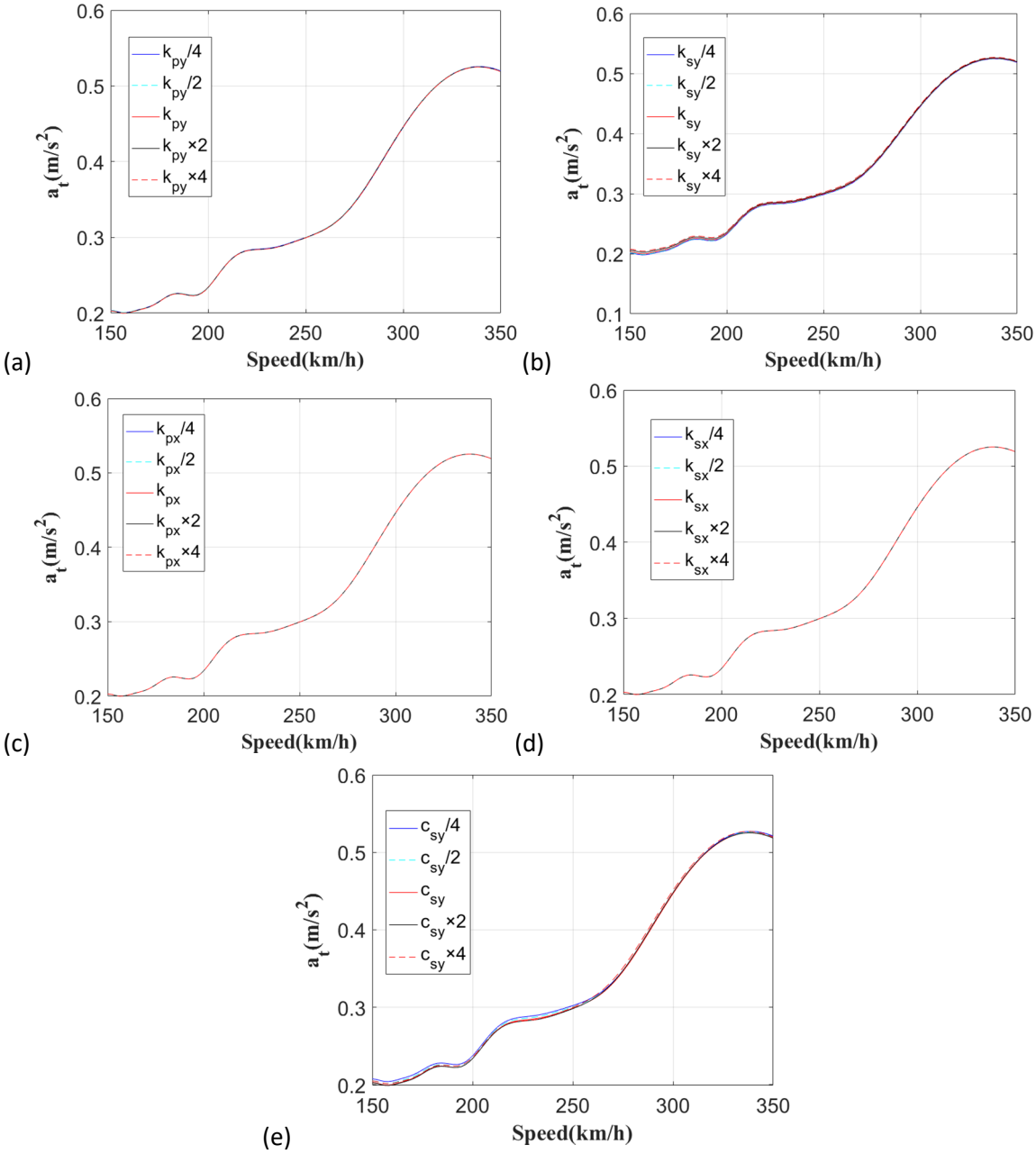

Fig. H-10 The effect of suspension parameters on ride comfort (a) k_{py}, (b) k_{sy}, (c) k_{px}, (d) k_{sx}, (e) c_{sy} at the position of seat 7.

Table H-5 The multiplying factors and weighting functions for different directions and positions

Direction and position	Multiplying factor	Weighting function
Y-axis on the seat-buttock interface	$b_{sy}=1$	W_d
Z-axis on the seat-buttock interface	$b_{sz}=1$	W_k
r_x-axis on the seat-buttock interface	$b_{sr}=0.63$	W_e
Y-axis on the human-backrest interface	$b_{by}=0.5$	W_d
Z-axis on the human-backrest interface	$b_{bz}=0.4$	W_d
Y-axis at the feet	$b_{fy}=0.25$	W_k
Z-axis at the feet	$b_{fz}=0.4$	W_k

Reference

Bendat, J.S. and Piersol, A.G. (2010) *Random data: analysis and measurement procedures*, 4th ed.: John Wiley & Sons.

Bhat, R.B. (1985) Natural Frequencies of Rectangular-Plates Using Characteristic Orthogonal Polynomials in Rayleigh-Ritz Method. *Journal of Sound and Vibration,* 102 (4), 493-499.

Bsi (1987)*: BS 6841:1987 Guide to measurement and evaluation of human exposure to whole-body mechanical vibration and repeated shock*.

Cao, H., Zhang, W. and Miao, B. (2015) Vertical vibration analysis of the flexible carbody of high speed train. *International Journal of Vehicle Structures and Systems,* 7 (2), 55-60.

Carlbom, P. (2000) *Carbody and passengers in rail vehicle dynamics*, Doctoral dissertation, Institutionen för farkostteknik.

Carlbom, P. (2001) Combining MBS with FEM for rail vehicle dynamics analysis. *Multibody system dynamics,* 6 (3), 291-300.

Carlbom, P. and Berg, M. (2002) Passengers, Seats and Carbody in Rail Vehicle Dynamics. *Vehicle System Dynamics,* 37 (sup1), 290-300.

Cheli, F. and Corradi, R. (2011) On rail vehicle vibrations induced by track unevenness: Analysis of the excitation mechanism. *Journal of Sound and Vibration,* 330 (15), 3744-3765.

Cho, Y. and Yoon, Y.S. (2001) Biomechanical model of human on seat with backrest for evaluating ride quality. *International Journal of Industrial Ergonomics,* 27 (5), 331-345.

Corbridge, C., Griffin, M. and Harborough, P. (1989) Seat dynamics and passenger comfort. *Proceedings of the Institution of Mechanical Engineers, Part F: Journal of Rail and Rapid Transit,* 203 (1), 57-64.

Cossalter, V., Doria, A., Garbin, S. and Lot, R. (2006) Frequency-domain method for evaluating the ride comfort of a motorcycle. *Vehicle System Dynamics,* 44 (4), 339-355.

D'errico, J. (2012) *fminsearchbnd, fminsearchcon–File Exchange–MATLAB Central*.

Dempster, W.T. and Gaughran, G.R.L. (2010) Properties of body segments based on size and weight. *Developmental Dynamics,* 120 (1), 33-54.

Desai, R., Guha, A. and Seshu, P. (2018) Multibody Biomechanical Modelling of Human Body Response to Direct and Cross Axis Vibration. *Procedia computer science,* 133, 494-501.

Di Gialleonardo, E., Braghin, F. and Bruni, S. (2012) The influence of track modelling options on the simulation of rail vehicle dynamics. *Journal of Sound and Vibration,* 331 (19), 4246-4258.

Diana, G., Cheli, F., Collina, A., Corradi, R. and Melzi, S. (2002) The Development of a Numerical Model for Railway Vehicles Comfort Assessment Through Comparison With Experimental Measurements. *Vehicle System Dynamics,* 38 (3), 165-183.

Dossing, O. (1984) *Dynamic design verification of a prototype rapid transit train using modal analysis*. Bruel&Kjaer.

Dumitriu, M. (2015) Analysis of the dynamic response in the railway vehicles to the track vertical irregularities. Part II: The numerical analysis. *Journal of Engineering Science and Technology Review,* 8 (4), 32-39.

Ebe, K. (1998) *Predicting overall seat discomfort from static and dynamic characteristics of seats*, PhD thesis, University of Southampton.

Fairley, T.E. (1986) *Predicting the dynamic performance of seats*, PhD thesis, University of Southampton.

Fairley, T.E. (1990) Predicting the transmissibility of a suspension seat. *Ergonomics,* 33 (2), 121-135.

Fairley, T.E. and Griffin, M.J. (1983) Application of mechanical impedance methods to seat transmissibility. Paper presented at Proceedings of International Conference on Noise Control Engineering, Edinburgh, UK.

Fairley, T.E. and Griffin, M.J. (1986) A test method for the prediction of seat transmissibility. Paper presented at SAE International Congress and Exposition.

Fairley, T.E. and Griffin, M.J. (1989) The apparent mass of the seated human body: vertical vibration. *Journal of Biomechanics,* 22 (2), 81-94.

Fairley, T.E. and Griffin, M.J. (1990) The apparent mass of the seated human body in the fore-and-aft and lateral directions. *Journal of Sound and Vibration,* 139 (2), 299–306.

Fard, M. (2011) Structural dynamics characterization of the vehicle seat for NVH performance analysis. Paper presented at SAE 2011 World Congress, Detroit, Michigan, United States, 12-14 April 2011.

Garg, V. and Dukkipati, R. (1984) *Dynamics of Railway Vehicle Systems*. London: Academic press, INC LTD.

Gong, D., Zhou, J.S. and Sun, W.J. (2012) On the resonant vibration of a flexible railway car body and its suppression with a dynamic vibration absorber. *Journal of Vibration and Control,* 19 (5), 649-657.

Gong, W. and Griffin, M.J. (2018) Measuring, evaluating and assessing the transmission of vibration through the seats of railway vehicles. *Proceedings of the Institution of Mechanical Engineers, Part F: Journal of Rail and Rapid Transit,* 232 (2), 384-395.

Griffin, M. (1990) *Handbook of human vibration*. London: Academic press.

Grujicic, M., Pandurangan, B., Arakere, G., Bell, W.C., He, T. and Xie, X. (2009) Seat-cushion and soft-tissue material modeling and a finite element investigation of the seating comfort for passenger-vehicle occupants. *Materials and Design,* 30 (10), 4273-4285.

Hinz, B., Blüthner, R., Menzel, G., Rützel, S., Seidel, H. and Wölfel, H.P. (2006) Apparent mass of seated men—Determination with single- and multi-axis excitations at different magnitudes. *Journal of Sound and Vibration,* 298 (3), 788-809.

Hollander, M., Wolfe, D.A. and Chicken, E. (2013) *Nonparametric statistical methods*, 3rd ed.: John Wiley & Sons.

Huang, Y. and Ferguson, N.S. (2018) Identification of biomechanical nonlinearity in whole-body vibration using a reverse path multi-input-single-output method. *Journal of Sound and Vibration,* 419, 337-351.

Huang, Y. and Griffin, M.J. (2006) Effect of voluntary periodic muscular activity on nonlinearity in the apparent mass of the seated human body during vertical random whole-body vibration. *Journal of Sound and Vibration,* 298 (3), 824-840.

Huang, Y. and Griffin, M.J. (2008) Nonlinear dual-axis biodynamic response of the semi-supine human body during vertical whole-body vibration. *Journal of Sound and Vibration,* 312 (1-2), 296-315.

Ippili, R.K., Davies, P., Bajaj, A.K. and Hagenmeyer, L. (2008) Nonlinear multi-body dynamic modeling of seat–occupant system with polyurethane seat and H-point prediction. *International Journal of Industrial Ergonomics,* 38 (5-6), 368-383.

Iso (1997)*: ISO 2631–1: Mechanical vibration and shock—Evaluation of human exposure to whole-body vibration—Part1: General requirements*. Switzerland: ISO.

Iso (2001)*: ISO 2631-4: Mechanical vibration and shock —Evaluation of human exposure to whole-body vibration —Part 4: Guidelines for the evaluation of the effects of vibration and rotational motion on passenger and crew comfort in fixed-guideway transport systems*. UK: BSI.

Ittianuwat, R., Fard, M. and Kato, K. (2014) The transmission of vibration at various locations on vehicle seat to seated occupant body. Paper presented at INTER-NOISE and NOISE-CON Congress and Conference Proceedings Melbourne, Australia.

Iwnicki, S. (2006) *Handbook of railway vehicle dynamics*. CRC press.

Jalil, N.a.A. and Griffin, M.J. (2007a) Fore-and-aft transmissibility of backrests: Effect of backrest inclination, seat-pan inclination, and measurement location. *Journal of Sound and Vibration,* 299 (1-2), 99-108.

Jalil, N.a.A. and Griffin, M.J. (2007b) Fore-and-aft transmissibility of backrests: Variation with height above the seat surface and non-linearity. *Journal of Sound and Vibration,* 299 (1-2), 109-122.

Kargarnovin, M.H., Younesian, D., Thompson, D. and Jones, C. (2005) Ride comfort of high-speed trains travelling over railway bridges. *Vehicle System Dynamics,* 43 (3), 173-197.

Kim, K.-S., Kim, J. and Kim, K.-J. (2011) Dynamic modeling of seated human body based on measurements of apparent inertia matrix for fore-and-aft/vertical/pitch motion. *Journal of Sound and Vibration,* 330 (23), 5716-5735.

Kim, S.K., White, S.W., Bajaj, A.K. and Davies, P. (2003a) Simplified models of the vibration of mannequins in car seats. *Journal of Sound and Vibration,* 264 (1), 49-90.

Kim, Y.G., Choi, S., Kim, S.W., Kim, Y.M. and Park, T.W. (2009) An Experimental Study on the Ride Comfort of the Korean High-Speed Train. *Experimental Techniques,* 33 (6), 30-37.

Kim, Y.G., Won, H.B.K., Kim, S.W., Park, C.K. and Park, T.W. (2003b) Correlation of evaluation methods of ride comfort for railway vehicles. *Proceedings of the Institution of Mechanical Engineers Part F: Journal of Rail & Rapid Transit,* 217 (2), 73-88.

Kitazaki, S. and Griffin, M.J. (1997) A modal analysis of whole-body vertical vibration, using a finite element model of the human body. *Journal of Sound and Vibration,* 200 (1), 83-103.

Kitazaki, S. and Griffin, M.J. (1998) Resonance behaviour of the seated human body and effects of posture. *Journal of Biomechanics,* 31 (2), 143-149.

Knothe, K.L. and Grassie, S.L. (1993) Modelling of Railway Track and Vehicle/Track Interaction at High Frequencies. *Vehicle System Dynamics,* 22 (3-4), 209-262.

Konowrocki, R. and Bajer, C. (2008) Vibrations due to the passage of a railway vehicle on Straight and Curved Tracks. Paper presented at XXIII Symposium–Vibrations in Physical Systems.

Kumar, V., Rastogi, V. and Pathak, P.M. (2017) Simulation for whole-body vibration to assess ride comfort of a low–medium speed railway vehicle. *Simulation,* 93 (3), 225-236.

Lei, X. (2015) *High speed railway track dynamics—Models, algorithms and applications*. Beijing: Science Press.

Liang, C.C. and Chiang, C.F. (2008) Modeling of a seated human body exposed to vertical vibrations in various automotive postures. *Industrial health,* 46 (2), 125-137.

Ling, L., Xiao, X.B., Xiong, J.Y., Zhou, L., Wen, Z.F. and Jin, X.S. (2014) A 3D model for coupling dynamics analysis of high-speed train/track system. *Journal of Zhejiang University Science A,* 15 (12), 964-983.

Ling, L., Zhang, Q., Xiao, X., Wen, Z. and Jin, X. (2018) Integration of car-body flexibility into train–track coupling system dynamics analysis. *Vehicle System Dynamics,* 56 (4), 485-505.

Liu, C. and Qiu, Y. (2020) Nonlinearity in the localised apparent masses of the seated human body exposed to vertical vibration. *Mechanical Systems and Signal Processing,* 135.

Liu, C., Qiu, Y. and Griffin, M.J. (2015) Finite element modelling of human-seat interactions: vertical in-line and fore-and-aft cross-axis apparent mass when sitting on a rigid seat without backrest and exposed to vertical vibration. *Ergonomics,* 58 (7), 1207-1219.

Lo, L., Fard, M., Subic, A. and Jazar, R. (2013) Structural dynamic characterization of a vehicle seat coupled with human occupant. *Journal of Sound and Vibration,* 332 (4), 1141-1152.

Lu, F., Kennedy, D., Williams, F.W. and Lin, J.H. (2008) Symplectic analysis of vertical random vibration for coupled vehicle–track systems. *Journal of Sound and Vibration,* 317 (1-2), 236-249.

Mandapuram, S., Rakheja, S., Boileau, P.-É., Maeda, S. and Shibata, N. (2010) Apparent mass and seat-to-head transmissibility responses of seated occupants under single and dual axis horizontal vibration. *Industrial health,* 48 (5), 698-714.

Mandapuram, S.C., Rakheja, S., Ma, S., Demont, R.G. and Boileau, P.-É. (2005) Influence of Back Support Conditions on the Apparent Mass of Seated Occupants under Horizontal Vibration. *Industrial Health,* 43 (3), 421-435.

Mansfield, N.J. (2004) *Human response to vibration*. CRC press.

Mansfield, N.J. and Griffin, M.J. (2000) Non-linearities in apparent mass and transmissibility during exposure to whole-body vertical vibration. *Journal of Biomechanics,* 33 (8), 933-941.

Mansfield, N.J. and Lundström, R. (1999) The apparent mass of the human body exposed to non-orthogonal horizontal vibration. *Journal of Biomechanics,* 32 (12), 1269-1278.

Mansfield, N.J. and Maeda, S. (2006) Comparison of the apparent masses and cross-axis apparent masses of seated humans exposed to single- and dual-axis whole-body vibration. *Journal of Sound and Vibration,* 298 (3), 841-853.

Mansfield, N.J. and Maeda, S. (2007) The apparent mass of the seated human exposed to single-axis and multi-axis whole-body vibration. *Journal of Biomechanics,* 40, 2543-2551.

Matsumoto, Y. and Griffin, M.J. (2001) Modelling the dynamic mechanisms associated with the principal resonance of the seated human body. *Clinical Biomechanics,* 16 (Supplement 1), 31-44.

Matsumoto, Y. and Griffin, M.J. (2002a) Effect of Muscle Tension on Non-Linearities in the Apparent Masses of Seated Subjects Exposed to Vertical Whole-Body Vibration. *Journal of Sound and Vibration,* 253 (1), 77-92.

Matsumoto, Y. and Griffin, M.J. (2002b) Non-linear characteristics in the dynamic responses of seated subjects exposed to vertical whole-body vibration. *Transactions-American Society of Mechanical Engineers Journal of Biomechanical Engineering,* 124 (5), 527-532.

Nawayseh, N. and Griffin, M.J. (2003) Non-linear dual-axis biodynamic response to vertical whole-body vibration. *Journal of Sound and Vibration,* 268 (3), 503-523.

Nawayseh, N. and Griffin, M.J. (2004) Tri-axial forces at the seat and backrest during whole-body vertical vibration. *Journal of Sound and Vibration,* 277 (1-2), 309-326.

Nawayseh, N. and Griffin, M.J. (2005a) Non-linear dual-axis biodynamic response to fore-and-aft whole-body vibration. *Journal of Sound and Vibration,* 282 (3-5), 831-862.

Nawayseh, N. and Griffin, M.J. (2005b) Tri-axial forces at the seat and backrest during whole-body fore-and-aft vibration. *Journal of Sound and Vibration,* 281 (3-5), 921-942.

Nawayseh, N. and Griffin, M.J. (2009) A model of the vertical apparent mass and the fore-and-aft cross-axis apparent mass of the human body during vertical whole-body vibration. *Journal of Sound and Vibration,* 319 (1-2), 719-730.

Nguyen, D.-V., Kim, K.-D. and Warnitchai, P. (2009) Simulation procedure for vehicle–substructure dynamic interactions and wheel movements using linearized wheel–rail interfaces. *Finite Elements in Analysis and Design,* 45 (5), 341-356.

Pankoke, S., Buck, B. and Woelfel, H.P. (1998) Dynamic FE model of sitting man adjustable to body height, body mass and posture used for calculating internal forces in the lumbar vertebral disks. *Journal of Sound and Vibration,* 215 (4), 827-839.

Park, S.J., Min, S.N., Lee, H., Subramaniyam, M. and Suh, W.S. (2014) Express Train Seat Discomfort Evaluation using Body Pressure and Anthropometric Data. *Journal of the Ergonomics Society of Korea,* 33 (3), 215-227.

Popp, K., Kruse, H. and Kaiser, I. (1999) Vehicle-Track Dynamics in the Mid-Frequency Range. *Vehicle System Dynamics,* 31 (5-6), 423-464.

Qiu, Y. (2012) A procedure for developing a generic model of a suspension seat with occupant for predicting seat transmissibility. Paper presented at 47th United Kingdom Conference on Human Responses to Vibration, ISVR, University of Southampton, September, 2012.

Qiu, Y. and Griffin, M.J. (2003) Transmission of fore–aft vibration to a car seat using field tests and laboratory simulation. *Journal of Sound and Vibration,* 264 (1), 135-155.

Qiu, Y. and Griffin, M.J. (2004) Transmission of vibration to the backrest of a car seat evaluated with multi-input models. *Journal of Sound and Vibration,* 274 (1-2), 297-321.

Qiu, Y. and Griffin, M.J. (2005) Transmission of roll, pitch and yaw vibration to the backrest of a seat supported on a non-rigid car floor. *Journal of Sound and Vibration,* 288 (4-5), 1197-1222.

Qiu, Y. and Griffin, M.J. (2010) Biodynamic Responses of the Seated Human Body to Single-axis and Dual-axis Vibration. *Industrial Health,* 48 (5), 615-627.

Qiu, Y. and Griffin, M.J. (2011) Modelling the fore-and-aft apparent mass of the human body and the transmissibility of seat backrests. *Vehicle System Dynamics,* 49 (5), 703-722.

Qiu, Y. and Griffin, M.J. (2012) Biodynamic Response of the Seated Human Body to Single-axis and Dual-axis Vibration: Effect of Backrest and Non-linearity. *Industrial Health,* 50 (1), 37-51.

Railways, I.U.O. (1994)*: UIC 513: Guidelines for evaluating passenger comfort in relation to vibration in railway vehicles*. Paris: UIC.

Rawlings, J.O., Pantula, S.G. and Dickey, D.A. (2001) *Applied regression analysis: a research tool*, 2rd ed.: Springer Science & Business Media.

Ren, Z., Sun, S. and Zhai, W. (2005) Study on lateral dynamic characteristics of vehicle/turnout system. *Vehicle System Dynamics,* 43 (4), 285-303.

Shi, H., Luo, R., Wu, P., Zeng, J. and Guo, J. (2014) Application of DVA theory in vibration reduction of carbody with suspended equipment for high-speed EMU. *Science China Technological Sciences,* 57 (7), 1425-1438.

Shi, H. and Wu, P. (2016) Flexible vibration analysis for car body of high-speed EMU. *Journal of Mechanical Science and Technology,* 30 (1), 55-66.

Siefert, A., Pankoke, S. and Wölfel, H.P. (2008) Virtual optimisation of car passenger seats: Simulation of static and dynamic effects on drivers' seating comfort. *International Journal of Industrial Ergonomics,* 38 (5-6), 410-424.

Sivanandam, S.N. and Deepa, S.N. (2007) *Introduction to genetic algorithms*. Springer Science and Business Media.

Stein, G.J., Mucka, P., Chmurny, R., Hinz, B. and Bluthner, R. (2007) Measurement and modelling of x-direction apparent mass of the seated human body-cushioned seat system. *Journal of Biomechanics,* 40 (7), 1493-1503.

Stein, G.J., Múčka, P., Hinz, B. and Blüthner, R. (2009) Measurement and modelling of the y-direction apparent mass of sitting human body–cushioned seat system. *Journal of Sound and Vibration,* 322 (1-2), 454-474.

Sun, W., Zhou, J., Thompson, D. and Gong, D. (2014) Vertical random vibration analysis of vehicle–track coupled system using Green's function method. *Vehicle System Dynamics,* 52 (3), 362-389.

Suzuki, H. (1998) Research trends on riding comfort evaluation in Japan. *Proceedings of the Institution of Mechanical Engineers, Part F: Journal of Rail and Rapid Transit,* 212 (1), 61-72.

Tanifuji, K. (1991) An analysis of the body-bending vibration of a bogie vehicle for an evaluation of the ride quality with deflected airsprings. *Proceedings of the Institution of Mechanical Engineers, Part F: Journal of Rail and Rapid Transit,* 205 (1), 35-42.

Tomioka, T., Suzuki, Y. and Takigami, T. (2003) Three-dimensional flexural vibration of lightweight railway vehicle carbody and a new analytical method for flexural vibration. *Quarterly Report of RTRI,* 44 (1), 15-21.

Tomioka, T. and Takigami, T. (2010) Reduction of bending vibration in railway vehicle carbodies using carbody–bogie dynamic interaction. *Vehicle System Dynamics,* 48 (sup1), 467-486.

Tomioka, T., Takigami, T. and Suzuki, Y. (2006) Numerical analysis of three-dimensional flexural vibration of railway vehicle car body. *Vehicle System Dynamics,* 44 (sup 1), 272-285.

Toward, M.G.R. and Griffin, M.J. (2009) Apparent mass of the human body in the vertical direction: Effect of seat backrest. *Journal of Sound and Vibration,* 327 (3-5), 657-669.

Toward, M.G.R. and Griffin, M.J. (2011) The transmission of vertical vibration through seats: Influence of the characteristics of the human body. *Journal of Sound and Vibration,* 330 (26), 6526-6543.

Tufano, S. and Griffin, M.J. (2013) Nonlinearity in the vertical transmissibility of seating: the role of the human body apparent mass and seat dynamic stiffness. *Vehicle System Dynamics,* 51 (1), 122-138.

Verver, M.M., De Lange, R., Van Hoof, J. and Wismans, J.S. (2005) Aspects of seat modelling for seating comfort analysis. *Applied Ergonomics,* 36 (1), 33-42.

Wang, W., Rakheja, S. and Boileau, P.É. (2004) Effects of sitting postures on biodynamic response of seated occupants under vertical vibration. *International Journal of Industrial Ergonomics,* 34 (4), 289-306.

Wei, L. and Griffin, M.J. (1998a) Mathematical models for the apparent mass of the seated human body exposed to vertical vibration. *Journal of Sound and Vibration,* 212 (5), 855-874.

Wei, L. and Griffin, M.J. (1998b) The prediction of seat transmissibility from measures of seat impedance. *Journal of Sound and Vibration,* 214 (1), 121-137.

Wickens, A.H. (2003) *Fundamentals of Rail Vehicle Dynamics: Guidance and Stability*. Lisse, The Netherlands: Swets & Zeitlinger Publishers.

Wu, X., Rakheja, S. and Boileau, P.E. (1999) Analyses of relationships between biodynamic response functions. *Journal of Sound and Vibration,* 3 (226), 595-606.

Wu, Y.-S. and Yang, Y.-B. (2003) Steady-state response and riding comfort of trains moving over a series of simply supported bridges. *Engineering Structures,* 25 (2), 251-265.

Xu, W.T., Lin, J.H., Zhang, Y.H., Kennedy, D. and Williams, F.W. (2009) Pseudo-excitation-method-based sensitivity analysis and optimization for vehicle ride comfort. *Engineering Optimization,* 41 (7), 699-711.

Yuan, J. (1992) *On the use of artificial springs in the Rayleigh-Ritz method*, PhD thesis, The University of Western Ontario.

Zhai, W., Liu, P., Lin, J. and Wang, K. (2015a) Experimental investigation on vibration behaviour of a CRH train at speed of 350 km/h. *International Journal of Rail Transportation,* 3 (1), 1-16.

Zhai, W., Wang, K. and Cai, C. (2009) Fundamentals of vehicle–track coupled dynamics. *Vehicle System Dynamics,* 47 (11), 1349-1376.

Zhai, W., Wang, S., Zhang, N., Gao, M., Xia, H., Cai, C. and Zhao, C. (2013) High-speed train–track–bridge dynamic interactions – Part II: experimental validation and engineering application. *International Journal of Rail Transportation,* 1 (1-2), 25-41.

Zhai, W., Yang, J., Li, Z. and Han, H. (2015b) Dynamics of high-speed train in crosswinds based on an air-train-track interaction model. *Wind and Structures,* 20 (2), 143-168.

Zhai, W.M., Wang, K.Y. and Lin, J.H. (2004) Modelling and experiment of railway ballast vibrations. *Journal of Sound and Vibration,* 270 (4-5), 673-683.

Zhang, L. and Dupuis, R. (2010) Measurement and identification of dynamic properties of flexible polyurethane foam. *Journal of Vibration and Control,* 17 (4), 517-526.

Zhang, X., Qiu, Y. and Griffin, M.J. (2015a) Developing a simplified finite element model of a car seat with occupant for predicting vibration transmissibility in the vertical direction. *Ergonomics,* 58 (7), 1220-1231.

Zhang, X., Qiu, Y. and Griffin, M.J. (2015b) Transmission of vertical vibration through a seat: Effect of thickness of foam cushions at the seat pan and the backrest. *International Journal of Industrial Ergonomics,* 48, 36-45.

Zhang, X., Qiu, Y. and Griffin, M.J. (2016) Transmission of fore-and-aft vibration to the seat pan, the backrest and the headrest of a car seat. *Proceedings of the Institution of Mechanical Engineers, Part D: Journal of Automobile Engineering,* 230 (6), 736-744.

Zhang, Y.W., Zhao, Y., Zhang, Y.H., Lin, J.H. and He, X.W. (2013) Riding comfort optimization of railway trains based on pseudo-excitation method and symplectic method. *Journal of Sound and Vibration,* 332 (21), 5255-5270.

Zheng, G., Qiu, Y. and Griffin, M.J. (2011) An analytic model of the in-line and cross-axis apparent mass of the seated human body exposed to vertical vibration with and without a backrest. *Journal of Sound and Vibration,* 330 (26), 6509-6525.

Zheng, G., Qiu, Y. and Griffin, M.J. (2012) Vertical and dual-axis vibration of the seated human body: Nonlinearity, cross-axis coupling, and associations between resonances in transmissibility and apparent mass. *Journal of Sound and Vibration,* 331 (26), 5880-5894.

Zheng, G., Qiu, Y. and Griffin, M.J. (2019) Fore-and-aft and dual-axis vibration of the seated human body: Nonlinearity, cross-axis coupling, and associations between resonances in the transmissibility and apparent mass. *International Journal of Industrial Ergonomics,* 69, 58-65.

Zhou, J., Goodall, R., Ren, L. and Zhang, H. (2009) Influences of car body vertical flexibility on ride quality of passenger railway vehicles. *Proceedings of the Institution of Mechanical Engineers, Part F: Journal of Rail and Rapid Transit,* 223 (5), 461-471.